The wild frontier of fusion energy *p. 370*

Invisibility cloaking goes out of sight *pp. 384 & 427*

Were feathers widespread among early dinosaurs? *p. 451*

Science

$10
25 JULY 2014
sciencemag.org

AAAS



SPECIAL ISSUE

Vanishing fauna

Charting and reversing the decline *p. 392*

CONTENTS



384 & 427
Cloaking objects with just the right coating

25 JULY 2014 • VOLUME 345 • ISSUE 6195

NEWS

IN BRIEF

362 Roundup of the week's news

IN DEPTH

364 EBOLA DRUGS STILL STUCK IN LAB
Experts discussed—and rejected—bringing experimental vaccines and therapies to West Africa *By M. Enserink*

365 ROAD HAZARDS THREATEN ROVER
To limit wheel damage from sharp rocks, the Curiosity Mars rover detours into sandy valleys *By E. Hand*

366 NIH INSTITUTE CONSIDERS BROAD SHIFT TO 'PEOPLE' AWARDS
Approach promises freedom from grant writing but could favor established researchers *By J. Kaiser*
▸ PODCAST

367 DENGUE VACCINE TRIAL POSES PUBLIC HEALTH QUANDARY
Experimental vaccine fell short against key strain *By D. Normile*

368 OIL SANDS FIGHT HEATS UP IN U.S.
Environmentalists oppose federal lease in Utah *By D. Malakoff*



FEATURE

370 FUSION'S RESTLESS PIONEERS
Startups with novel technologies are taking on fusion's Goliaths *By D. Clery*



INTRODUCTION

392 Vanishing fauna

NEWS

396 The empty forest
By E. Stokstad

OPINION

400 An animal-rich future
By J. J. Tewksbury and H. S. Rogers

REVIEWS

401 Defaunation in the Anthropocene
R. Dirzo et al.

406 Reversing defaunation: Restoring species in a changing world
P. J. Seddon et al.

ON THE COVER



A male clouded leopard (*Neofelis diardi borneensis*) caught by a camera trap in the lowland rainforest of Borneo. If the cataract in his right eye indicates old age, he has been fortunate. Animals from rare predators to common invertebrates are experiencing a human-caused global decline that often leads to extinction, with consequences for ecosystems and human well-being. See page 392. *Photo: © Sebastian Kennerknecht/Panthera*

SEE ALSO ▸ PERSPECTIVE P. 376 ▸ BOOK REVIEW P. 388 ▸ sciencemag.org/special/vanishing

INSIGHTS

PERSPECTIVES

376 WILDLIFE DECLINE AND SOCIAL CONFLICT
Policies aimed at reducing wildlife-related conflict must address the underlying causes *By J. S. Brashares* et al.
▸ VANISHING FAUNA SECTION P. 392

378 RIBOSOME RESCUE AND NEURODEGENERATION
A mutation in a brain-specific tRNA reveals the link between ribosome maintenance and neuronal cell death *By J. C. Darnell*
▸ REPORT P. 455

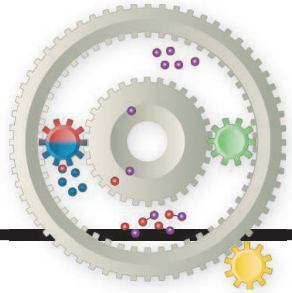
380 ULTRASLOW RELAXATION OF CONFINED DNA
DNA dynamics in tight spaces challenge nature's nanomachines *By Y. R. Chemla and T. Ha*

381 SELF-CONTROL TAMES THE COUPLING OF REACTIVE RADICALS
Iridium complexes use two points of contact to control carbon-carbon bond formation *By G. C. Lloyd-Jones and L. T. Ball*
▸ REPORTS PP. 433 & 437

383 WHY ARE PLANT-POLLINATOR NETWORKS NESTED?
Mutualistic communities maximize their structural stability *By S. Pawar*
▸ RESEARCH ARTICLE P. 416

Published by AAAS

CONTENTS



381, 433, & 437
Intersecting catalytic cycles couple carbons

25 JULY 2014 • VOLUME 345 • ISSUE 6195

384 A CLOAKING COATING FOR MURKY MEDIA
Objects shrouded in fog disappear entirely with simple coating
By D. R. Smith
▸ REPORT P. 427

385 ASTROCYTES EYEBALL AXONAL MITOCHONDRIA
Retinal neurons transfer mitochondria to astrocytes for rapid turnover to meet energy demands *By T. C. Burdett and M. R. Freeman*

BOOKS *ET AL.*

387 THE NSA REPORT
reviewed by K. O'Hara and N. Shadbolt

388 OUR ONCE AND FUTURE PLANET
By P. Woodworth, reviewd by W. E. Stutz
▸ VANISHING FAUNA SECTION P. 392

LETTERS

389 IN DEFENSE OF FENCES
By M. Pfeifer et al.

389 RESPONSE
By R. Woodroffe et al.

390 EARLY AMERICANS: MISSTATED RESULTS
By D. J. Kennett et al.

390 EARLY AMERICANS: RESPECTING ANCESTORS
By D. K. Grayson et al.

390 RESPONSE
By J. C. Chatters

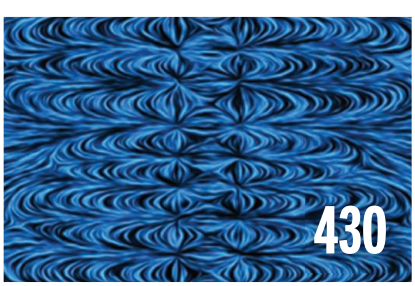


PHOTO: (LEFT) EMILY EDWARDS

RESEARCH

IN BRIEF

413 From *Science* and other journals

RESEARCH ARTICLE

416 ECOLOGICAL NETWORKS
On the structural stability of mutualistic systems *R. P. Rohr* et al.
RESEARCH ARTICLE SUMMARY; FOR FULL TEXT: dx.doi.org/10.1126/science.1253497
▸ PERSPECTIVE P. 383

REPORTS

417 ULTRAFAST OPTICS
Ultrafast optical control by few photons in engineered fiber *R. Nissim* et al.

420 QUANTUM COMPUTING
Defining and detecting quantum speedup *T. F. Rønnow* et al.

424 QUANTUM METROLOGY
Fisher information and entanglement of non-Gaussian spin states *H. Strobel* et al.

427 METAMATERIALS
Invisibility cloaking in a diffusive light scattering medium *R. Schittny* et al.
▸ PERSPECTIVE P. 384

430 QUANTUM SIMULATION
Coherent imaging spectroscopy of a quantum many-body spin system *C. Senko* et al.

DUAL CATALYSIS

433 Single-electron transmetalation in organoboron cross-coupling by photoredox/nickel dual catalysis *J. C. Tellis* et al.

437 Merging photoredox with nickel catalysis: Coupling of α-carboxyl sp^3-carbons with aryl halides *Z. Zuo* et al.
▸ PERSPECTIVE P. 381

440 EXOPLANET DETECTION
Stellar activity masquerading as planets in the habitable zone of the M dwarf Gliese 581 *P. Robertson* et al.

444 PALEOCLIMATE
Synchronization of North Pacific and Greenland climates preceded abrupt deglacial warming *S. K. Praetorius and A. C. Mix*

448 INDUCED EARTHQUAKES
Sharp increase in central Oklahoma seismicity since 2008 induced by massive wastewater injection *K. M. Keranen* et al.

451 DINOSAUR EVOLUTION
A Jurassic ornithischian dinosaur from Siberia with both feathers and scales *P. Godefroit* et al.

455 RNA FUNCTION
Ribosome stalling induced by mutation of a CNS-specific tRNA causes neurodegeneration *R. Ishimura* et al.
▸ PERSPECTIVE P. 378

459 CLATHRIN ADAPTORS
AP2 controls clathrin polymerization with a membrane-activated switch *B. T. Kelly* et al.

463 ACTIN CYTOSKELETON
Mechanism of actin filament pointed-end capping by tropomodulin *J. N. Rao* et al.

DEPARTMENTS

361 EDITORIAL
Ghosts from the past
By David Titley

478 WORKING LIFE
A scientific partnership
By Jim Austin

Science Staff 360
AAAS News & Notes 391
New Products 471
Science Careers 472

SCIENCE (ISSN 0036-8075) is published weekly on Friday, except the last week in December, by the American Association for the Advancement of Science, 1200 New York Avenue, NW, Washington, DC 20005. Periodicals mail postage (publication No. 484460) paid at Washington, DC, and additional mailing offices. Copyright © 2014 by the American Association for the Advancement of Science. The title SCIENCE is a registered trademark of the AAAS. Domestic individual membership and subscription (51 issues): $153 ($74 allocated to subscription). Domestic institutional subscription (51 issues): $1282; Foreign postage extra: Mexico, Caribbean (surface mail) $55; other countries (air assist delivery) $85. First class, airmail, student, and emeritus rates on request. Canadian rates with GST available upon request, GST #1254 88122. Publications Mail Agreement Number 1069624. **Printed in the U.S.A.**
Change of address: Allow 4 weeks, giving old and new addresses and 8-digit account number. **Postmaster:** Send change of address to AAAS, P.O. Box 96178, Washington, DC 20090–6178. **Single-copy sales:** $10.00 current issue, $15.00 back issue prepaid includes surface postage; bulk rates on request. **Authorization to photocopy** material for internal or personal use under circumstances not falling within the fair use provisions of the Copyright Act is granted by AAAS to libraries and other users registered with the Copyright Clearance Center (CCC) Transactional Reporting Service, provided that $30.00 per article is paid directly to CCC, 222 Rosewood Drive, Danvers, MA 01923. The identification code for *Science* is 0036-8075. *Science* is indexed in the *Reader's Guide to Periodical Literature* and in several specialized indexes.

Published by AAAS

Science
AAAS
1200 New York Avenue, NW, Washington, DC 20005
Bateman House, 82-88 Hills Road, Cambridge, UK CB2 1LQ

Editor-in-Chief Marcia McNutt
Executive Editor Monica M. Bradford **News Editor** Tim Appenzeller
Managing Editor, Research Journals Katrina L. Kelner
Deputy Editors Barbara R. Jasny, Andrew M. Sugden(UK), Valda J. Vinson, Jake S. Yeston

Research and Insights

SR. EDITORS Caroline Ash(UK), Gilbert J. Chin, Lisa D. Chong, Maria Cruz(UK), Julia Fahrenkamp-Uppenbrink(UK), Pamela J. Hines, Stella M. Hurtley(UK), Paula A. Kiberstis, Marc S. Lavine(Canada), Kristen L. Mueller, Ian S. Osborne(UK), Beverly A. Purnell, L. Bryan Ray, Guy Riddihough, H. Jesse Smith, Peter Stern(UK), Phillip D. Szuromi, Brad Wible, Nicholas S. Wigginton, Laura M. Zahn **ASSOCIATE EDITORS** Brent Grocholski, Melissa R. McCartney, Margaret M. Moerchen, Jelena Stajic, Sacha Vignieri **BOOK REVIEW EDITOR** Sherman J. Suter **ASSOCIATE LETTERS EDITOR** Jennifer Sills **EDITORIAL MANAGER** Cara Tate **SR. COPY EDITORS** Jeffrey E. Cook, Chris Filiatreau, Cynthia Howe, Harry Jach, Lauren Kmec, Barbara P. Ordway, Trista Wagoner **SR. EDITORIAL COORDINATORS** Carolyn Kyle, Beverly Shields **EDITORIAL COORDINATORS** Ramatoulaye Diop, Joi S. Granger, Lisa Johnson, Anita Wynn **PUBLICATIONS ASSISTANTS** Aneera Dobbins, Jeffrey Hearn, Dona Mathieu, Le-Toya Mayne Flood, Shannon McMahon, Scott Miller, Jerry Richardson, Rachel Roberts(UK), Alice Whaley(UK), Brian White **ADMINISTRATIVE SUPPORT** Janet Clements(UK), Joan Cuthbert(UK), Maryrose Madrid, John Wood(UK)

News

NEWS MANAGING EDITOR John Travis **INTERNATIONAL EDITOR** Richard Stone **DEPUTY NEWS EDITORS** Daniel Clery(UK), Robert Coontz, Elizabeth Culotta, David Grimm, David Malakoff, Leslie Roberts **CONTRIBUING EDITORS** Martin Enserink(Europe), Mara Hvistendahl (Asia) **SR. CORRESPONDENTS** Jeffrey Mervis, Elizabeth Pennisi **NEWS WRITERS** Adrian Cho, Jon Cohen, Jennifer Couzin-Frankel, Carolyn Gramling, Eric Hand, Jocelyn Kaiser, Kelly Servick, Robert F. Service, Erik Stokstad, Emily Underwood **CONTRIBUTING INTERNS** Hassan DuRant, Xochitl Rojas-Rocha, Nadia Whitehead **CORRESPONDENTS** Pallava Bagla(South Asia), Michael Balter(Paris), John Bohannon, Ann Gibbons, Sam Kean, Richard A. Kerr, Eli Kintisch, Kai Kupferschmidt(Berlin), Andrew Lawler, Christina Larson(Beijing), Mitch Leslie, Charles C. Mann, Eliot Marshall, Virginia Morell, Dennis Normile(Tokyo), Heather Pringle, Tania Rabesandratana(Brussels), Gretchen Vogel(Berlin), Lizzie Wade(Mexico City) **CAREERS** Jim Austin(Editor), Donisha Adams **COPY EDITORS** Kara Estelle, Nora Kelly, Jennifer Levin **ADMINISTRATIVE SUPPORT** Scherraine Mack

Executive Publisher Alan I. Leshner
Publisher Beth Rosner **Chief Digital Media Officer** Rob Covey

BUSINESS OPERATIONS AND ADMINISTRATION DIRECTOR Deborah Rivera-Wienhold **BUSINESS SYSTEMS AND FINANCIAL ANALYSIS DIRECTOR** Randy Yi **MANAGER OF FULFILLMENT SYSTEMS** Neal Hawkins **SYSTEMS ANALYST** Nicole Mehmedovich **ASSISTANT DIRECTOR, BUSINESS OPERATIONS** Eric Knott **MANAGER, BUSINESS OPERATIONS** Jessica Tierney **BUSINESS ANALYSTS** Cory Lipman, Cooper Tilton, Celeste Troxler **FINANCIAL ANALYST** Jeremy Clay **RIGHTS AND PERMISSIONS: ASSISTANT DIRECTOR** Emilie David **PERMISSIONS ASSOCIATE** Elizabeth Sandler **RIGHTS, CONTRACTS, AND LICENSING ASSOCIATE** Lili Kiser

MARKETING DIRECTOR Ian King **MARKETING MANAGER** Julianne Wielga **MARKETING ASSOCIATE** Elizabeth Sattler **SR. MARKETING EXECUTIVE** Jennifer Reeves **SR. ART ASSOCIATE, PROJECT MANAGER** Tzeitel Sorrosa **ART ASSOCIATE** Seil Lee **ASSISTANT COMMERCIAL EDITOR** Selby Frame **MARKETING PROJECT MANAGER** Angelissa McArthur **SR. WRITER** Bill Zimmer **PROGRAM DIRECTOR, AAAS MEMBER CENTRAL** Peggy Mihelich **FULFILLMENT SYSTEMS AND OPERATIONS** membership@aaas.org **MANAGER, MEMBER SERVICES** Pat Butler **SPECIALISTS** LaToya Casteel, Javia Flemmings, Latasha Russell **MANAGER, DATA ENTRY** Mickie Napoleoni **DATA ENTRY SPECIALISTS** JJ Regan, Jaimee Wise, Fiona Giblin

DIRECTOR, SITE LICENSING Tom Ryan **DIRECTOR, CORPORATE RELATIONS** Eileen Bernadette Moran **SR. PUBLISHER RELATIONS SPECIALIST** Kiki Forsythe **PUBLISHER RELATIONS MANAGER** Catherine Holland **PUBLISHER RELATIONS, EASTERN REGION** Keith Layson **PUBLISHER RELATIONS, WESTERN REGION** Ryan Rexroth **MANAGER, SITE LICENSE OPERATIONS** Iquo Edim **FULFILLMENT ANALYST** Lana Guz **ASSOCIATE DIRECTOR, MARKETING** Christina Schlecht **MARKETING ASSOCIATES** Thomas Landreth, Minah Kim

DIRECTOR OF WEB TECHNOLOGIES Ahmed Khadr **SR. DEVELOPER** Chris Coleman **DEVELOPER** Dan Berger **SR. PROJECT MANAGER** Trista Smith **SYSTEMS ENGINEER** Luke Johnson **PRODUCT MANAGER** Walter Jones

CREATIVE DIRECTOR, MULTIMEDIA Martyn Green **DIRECTOR OF ANALYTICS** Enrique Gonzales **SR. WEB PRODUCER** Sarah Crespi **WEB PRODUCER** Alison Crawford **VIDEO PRODUCER** Nguyen Nguyen **SOCIAL MEDIA PRODUCER** Meghna Sachdev

DIRECTOR OF OPERATIONS PRINT AND ONLINE Lizabeth Harman **PRINT PRODUCTION DIRECTOR** Wendy K. Shank **PREFLIGHT MANAGER** Marcus Spiegler **ASSISTANT MANAGER ONLINE** Lisa Stanford **ASSISTANT MANAGER PRINT** Rebecca Doshi **SR SPECIALISTS** Steve Forrester, Amy Hardcastle, Jason Hillman, Antoinette Hodal, Tara Kelly, Anthony Rosen **SPECIALISTS** Jacob Hedrick, Nichele Johnston, Yuse Lajiminmuhip, Lori Murphy, Kimberley Oster

DESIGN DIRECTOR Beth Rakouskas **ASSOCIATE ART DIRECTOR** Laura Creveling **SR. ILLUSTRATORS** Chris Bickel, Katharine Sutliff **ILLUSTRATOR** Valerie Altounian **SR. ART ASSOCIATES** Holly Bishop, Preston Huey **ART ASSOCIATES** Kay Engman, Garvin Grullón, Chrystal Smith **SR. PHOTO EDITOR** William Douthitt **PHOTO EDITOR** Leslie Blizard

DIRECTOR, GLOBAL COLLABORATION, CUSTOM PUBLICATIONS, ADVERTISING Bill Moran **EDITOR, CUSTOM PUBLISHING** Sean Sanders: 202-326-6430 **ASSISTANT EDITOR, CUSTOM PUBLISHING** Tianna Hicklin: 202-326-6463 **ADVERTISING MARKETING MANAGER** Justin Sawyers: 202-326-7061 science_advertising@aaas.org **ADVERTISING SUPPORT MANAGER** Karen Foote: 202-326-6740 **ADVERTISING PRODUCTION OPERATIONS MANAGER** Deborah Tompkins **SR. TRAFFIC ASSOCIATE** Christine Hall **SALES COORDINATOR** Shirley Young **ASSOCIATE DIRECTOR, COLLABORATION, CUSTOM PUBLICATIONS/CHINA/TAIWAN/KOREA/SINGAPORE** Ruolei Wu: +86-186 0822 9345, rwu@aaas.org **EAST COAST/E. CANADA** Laurie Faraday: 508-747-9395, FAX 617-507-8189 **WEST COAST/W. CANADA** Lynne Stickrod: 415-931-9782, FAX 415-520-6940 **MIDWEST** Jeffrey Dembksi: 847-498-4520 x3005, Steven Loerch: 847-498-4520 x3006 **UK EUROPE/ASIA** Roger Goncalves: TEL/FAX +41 43 243 1358 **JAPAN** Makiko Hara: +81 (0) 3 6802 4616, FAX +81 (0) 3 6802 4615, ads@sciencemag.jp **CHINA/TAIWAN** Ruolei Wu: +86-186 0822 9345

WORLDWIDE ASSOCIATE DIRECTOR OF SCIENCE CAREERS Tracy Holmes: +44 (0) 1223 326525, FAX +44 (0) 1223 326532 tholmes@science-int.co.uk **CLASSIFIED** advertise@sciencecareers.org **U.S. SALES** Tina Burks: 202-326-6577, Nancy Toema: 202-326-6578 **SALES ADMINISTRATOR** Marci Gallun **EUROPE/ROW SALES** Axel Gesatzki, Sarah Lelarge **SALES ASSISTANT** Kelly Grace **JAPAN** Yuri Kobayashi: +81 (0)90-9110-1719, careerads@sciencemag.jp **CHINA/TAIWAN** Ruolei Wu: +86-186 0822 9345 rwu@aaas.org **MARKETING MANAGER** Allison Pritchard **MARKETING ASSOCIATE** Aimee Aponte

AAAS BOARD OF DIRECTORS RETIRING PRESIDENT, CHAIR Phillip A. Sharp **PRESIDENT** Gerald R. Fink **PRESIDENT-ELECT** Geraldine (Geri) Richmond **TREASURER** David Evans Shaw **CHIEF EXECUTIVE OFFICER** Alan I. Leshner **BOARD** Bonnie L. Bassler, May R. Berenbaum, Carlos J. Bustamante, Claire M. Fraser, Laura H. Greene, Elizabeth Loftus, Raymond Orbach, Inder M. Verma

SUBSCRIPTION SERVICES For change of address, missing issues, new orders and renewals, and payment questions: 866-434-AAAS (2227) or 202-326-6417, FAX 202-842-1065. Mailing addresses: AAAS, P.O. Box 96178, Washington, DC 20090-6178 or AAAS Member Services, 1200 New York Avenue, NW, Washington, DC 20005

INSTITUTIONAL SITE LICENSES 202-326-6755 **REPRINTS:** Author Inquiries 800-635-7181 **COMMERCIAL INQUIRIES** 803-359-4578 **PERMISSIONS** 202-326-6765, permissions@aaas.org **AAAS Member Services** 202-326-6417 or http://membercentral.aaas.org/discounts

Science serves as a forum for discussion of important issues related to the advancement of science by publishing material on which a consensus has been reached as well as including the presentation of minority of conflicting points of view. Accordingly, all articles published in *Science*—including editorials, news and comment, and books reviews—are signed and reflect the individual views of the authors and not official points of view adopted by AAAS or the institutions with which the authors are affiliated.

INFORMATION FOR AUTHORS See pages 680 and 681 of the 7 February 2014 issue or access www.sciencemag.org/about/authors

SENIOR EDITORIAL BOARD
A. Paul Alivisatos, *Lawrence Berkeley Nat'l. Laboratory,* **Ernst Fehr,** *U. of Zürich*
Susan M. Rosenberg, *Baylor College of Medicine,* **Michael S. Turner,** *U. of Chicago*

BOARD OF REVIEWING EDITORS (Statistics board members indicated with **(S)**)

Adriano Aguzzi, *U. Hospital Zürich*
Takuzo Aida, *U. of Tokyo*
Leslie Aiello, *Wenner-Gren Foundation*
Judith Allen, *U. of Edinburgh*
Sonia Altizer, *U. of Georgia*
Virginia Armbrust, *U. of Washington*
Sebastian Amigorena, *Institut Curie*
Kathryn Anderson, *Memorial Sloan-Kettering Cancer Center*
Peter Andolfatto, *Princeton U.*
Meinrat O. Andreae, *Max-Planck Inst. Mainz*
Paola Arlotta, *Harvard U.*
Johan Auwerx, *EPFL*
David Awschalom, *U. of Chicago*
Jordi Bascompte, *Estación Biológica de Doñana CSIC*
Facundo Batista, *London Research Inst.*
Ray H. Baughman, *U. of Texas, Dallas*
David Baum, *U. of Wisconsin*
Mark Bear, *Massachusetts Inst. of Technology*
Kamran Behnia, *ESPCI-ParisTech*
Yasmine Belkaid, *NIAID, NIH*
Philip Benfey, *Duke U.*
Stephen J. Benkovic, *Penn State U.*
Gabriele Bergers, *U. of California, San Francisco*
Christophe Bernard, *Aix-Marseille U.*
Bradley Bernstein, *Massachusettes General Hospital*
Gregory C. Beroza, *Stanford U.*
Peer Bork, *EMBL*
Bernard Bourdon, *Ecole Normale Supérieure de Lyon*
Chris Bowler, *École Normale Supérieure*
Ian Boyd, *U. of St. Andrews*
Emily Brodsky, *U. of California, Santa Cruz*
Ron Brookmeyer, *U. of California Los Angeles* **(S)**
Christian Büchel, *U. Hamburg-Eppendorf*
Joseph A. Burns, *Cornell U.*
William P. Butz, *Population Reference Bureau*
Gyorgy Buzsaki, *New York U. School of Medicine*
Blanche Capel, *Duke U.*
Mats Carlsson, *U. of Oslo*
David Clapham, *Children's Hospital Boston*
David Clary, *U. of Oxford*
Joel Cohen, *Rockefeller U., Columbia U.*
Jonathan D. Cohen, *Princeton U.*
James Collins, *Boston U.*
Robert Cook-Deegan, *Duke U.*
Alan Cowman, *Walter & Eliza Hall Inst.*
Robert H. Crabtree, *Yale U.*
Janet Currie, *Princeton U.*
Jeff L. Dangl, *U. of North Carolina*
Tom Daniel, *U. of Washington*
Frans de Waal, *Emory U.*
Stanislas Dehaene, *Collège de France*
Robert Desimone, *MIT*
Claude Desplan, *New York U.*
Ap Dijksterhuis, *Radboud U. of Nijmegen*
Dennis Discher, *U. of Pennsylvania*
Gerald W. Dorn II, *Washington U. School of Medicine*
Jennifer A. Doudna, *U. of California, Berkeley*
Bruce Dunn, *U. of California, Los Angeles*
Christopher Dye, *WHO*
Todd Ehlers, *U. of Tuebingen*
David Ehrhardt, *Carnegie Inst. of Washington*
Tim Elston, *U. of North Carolina at Chapel Hill*
Gerhard Ertl, *Fritz-Haber-Institut, Berlin*
Barry Everitt, *U. of Cambridge*
Ernst Fehr, *U. of Zurich*
Anne C. Ferguson-Smith, *U. of Cambridge*
Michael Feuer, *The George Washington U.*
Peter Fratzl, *Max-Planck Inst.*
Elaine Fuchs, *Rockefeller U.*
Daniel Geschwind, *UCLA*
Andrew Gewirth, *U. of Illinois*
Karl-Heinz Glassmeier, *TU Braunschweig*
Julia R. Greer, *Caltech*
Elizabeth Grove, *U. of Chicago*
Kip Guy, *St. Jude's Children's Research Hospital*
Taekjip Ha, *U. of Illinois at Urbana-Champaign*
Christian Haass, *Ludwig Maximilians U.*
Steven Hahn, *Fred Hutchinson Cancer Research Center*
Michael Hasselmo, *Boston U.*
Martin Heimann, *Max-Planck Inst. Jena*
Yka Helariutta, *U. of Finland*
James A. Hendler, *Rensselaer Polytechnic Inst.*
Janet G. Hering, *Swiss Fed. Inst. of Aquatic Science & Technology*
Michael E. Himmel, *National Renewable Energy Lab.*
Kai-Uwe Hinrichs, *U. of Bremen*
Kei Hirose, *Tokyo Inst. of Technology*
David Hodell, *U. of Cambridge*
David Holden, *Imperial College*
Lora Hooper, *UT Southwestern Medical Ctr. at Dallas*
Thomas Hudson, *Ontario Inst. for Cancer Research*
Raymond Huey, *U. of Washington*
Steven Jacobsen, *U. of California, Los Angeles*
Kai Johnsson, *EPFL Lausanne*
Peter Jonas, *Inst. of Science & Technology (IST) Austria*
Matt Kaeberlein, *U. of Washington*
William Kaelin Jr., *Dana-Farber Cancer Inst.*
Daniel Kahne, *Harvard U.*
Daniel Kammen, *U. of California, Berkeley*
Masashi Kawasaki, *U. of Tokyo*
Joel Kingsolver, *U. of North Carolina at Chapel Hill*
Robert Kingston, *Harvard Medical School*
Alexander Kolodkin, *Johns Hopkins U.*
Roberto Kolter, *Harvard Medical School*
Alberto R. Kornblihtt, *U. of Buenos Aires*
Leonid Kruglyak, *UCLA*
Thomas Langer, *U. of Cologne*
Mitchell A. Lazar, *U. of Pennsylvania*
David Lazer, *Harvard U.*
Thomas Lecuit, *IBDM*
Virginia Lee, *U. of Pennsylvania*
Stanley Lemon, *U. of North Carolina at Chapel Hill*
Ottoline Leyser, *Cambridge U.*
Marcia C. Linn, *U. of California, Berkeley*
Jianguo Liu, *Michigan State U.*
Luis Liz-Marzan, *CIC biomaGUNE*
Jonathan Losos, *Harvard U.*
Ke Lu, *Chinese Acad. of Sciences*
Christian Lüscher, *U. of Geneva*
Laura Machesky, *CRUK Beatson Inst. for Cancer Research*
Anne Magurran, *U. of St. Andrews*
Oscar Marin, *CSIC & U. Miguel Hernández*
Charles Marshall, *U. of California, Berkeley*
C. Robertson McClung, *Dartmouth College*
Graham Medley, *U. of Warwick*
Yasushi Miyashita, *U. of Tokyo*
Richard Morris, *U. of Edinburgh*
Alison Motsinger-Reif, *NC State U.* **(S)**
Sean Munro, *MRC Lab. of Molecular Biology*
Thomas Murray, *The Hastings Center*
James Nelson, *Stanford U. School of Med.*
Karen Nelson, *J. Craig Venter Institute*
Daniel Neumark, *U. of California, Berkeley*
Timothy W. Nilsen, *Case Western Reserve U.*
Pär Nordlund, *Karolinska Inst.*
Helga Nowotny, *European Research Advisory Board*
Ben Olken, *MIT*
Luke O'Neill, *Trinity College, Dublin*
Joe Orenstein, *U. of California Berkeley & Lawrence Berkeley National Lab*
Harry Orr, *U. of Minnesota*
Andrew Oswald, *U. of Warwick*
Steve Palumbi, *Stanford U.*
Jane Parker, *Max-Planck Inst. of Plant Breeding Research*
Giovanni Parmigiani, *Dana-Farber Cancer Inst.* **(S)**
Donald R. Paul, *U. of Texas, Austin*
John H. J. Petrini, *Memorial Sloan-Kettering Cancer Center*
Joshua Plotkin, *U. of Pennsylvania*
Philippe Poulin, *CNRS*
David Randall, *Colorado State U.*
Colin Renfrew, *U. of Cambridge*
Trevor Robbins, *U. of Cambridge*
Jim Roberts, *Fred Hutchinson Cancer Research Ctr.*
Barbara A. Romanowicz, *U. of California,Berkeley*
Jens Rostrup-Nielsen, *Haldor Topsoe*
Mike Ryan, *U. of Texas, Austin*
Mitinori Saitou, *Kyoto U.*
Shimon Sakaguchi, *Kyoto U.*
Miquel Salmeron, *Lawrence Berkeley National Lab*
Jürgen Sandkühler, *Medical U. of Vienna*
Alexander Schier, *Harvard U.*
Randy Seeley, *U. of Cincinnati*
Vladimir Shalaev, *Purdue U.*
Robert Siliciano, *Johns Hopkins School of Medicine*
Joseph Silk, *Institut d'Astrophysique de Paris*
Denis Simon, *Arizona State U.*
Alison Smith, *John Innes Centre*
Richard Smith, *U. of North Carolina* **(S)**
John Speakman, *U. of Aberdeen*
Allan C. Spradling, *Carnegie Institution of Washington*
Jonathan Sprent, *Garvan Inst. of Medical Research*
Eric Steig, *U. of Washington*
Paula Stephan, *Georgia State U. and National Bureau of Economic Research*
Molly Stevens, *Imperial College London*
V. S. Subrahmanian, *U. of Maryland*
Ira Tabas, *Columbia U.*
Sarah Teichmann, *Cambridge U.*
John Thomas, *North Carolina State U.*
Christopher Tyler-Smith, *The Wellcome Trust Sanger Inst.*
Herbert Virgin, *Washington U.*
Bert Vogelstein, *Johns Hopkins U.*
Cynthia Volkert, *U. of Göttingen*
Douglas Wallace, *Dalhousie U.*
David Wallach, *Weizmann Inst. of Science*
Ian Walmsley, *U. of Oxford*
David A. Wardle, *Swedish U. of Agric. Sciences*
David Waxman, *Fudan U.*
Jonathan Weissman, *U. of California, San Francisco*
Chris Wikle, *U. of Missouri* **(S)**
Ian A. Wilson, *The Scripps Res. Inst.* **(S)**
Timothy D. Wilson, *U. of Virginia*
Rosemary Wyse, *Johns Hopkins U.*
Jan Zaanen, *Leiden U.*
Kenneth Zaret, *U. of Pennsylvania School of Medicine*
Jonathan Zehr, *U. of California, Santa Cruz*
Len Zon, *Children's Hospital Boston*
Maria Zuber, *MIT*

BOOK REVIEW BOARD
David Bloom, *Harvard U.,* **Samuel Bowring,** *MIT,* **Angela Creager,** *Princeton U.,* **Richard Shweder,** *U. of Chicago,* **Ed Wasserman,** *DuPont*

Published by AAAS

EDITORIAL

Ghosts from the past

2014 marks the centennial of the commencement of World War I. One connection between today and that seemingly long-ago war is how we make choices when the future seems obvious only in retrospect, in what former U.S. Secretary of State George P. Shultz refers to as a world "awash in change." Max Hastings, in *Catastrophe 1914: Europe Goes to War*, summarizes his views on how the rulers of Europe allowed World War I to start, then continue with a loss of over 8.6 million soldiers: "It is more appropriate to call them deniers, who preferred to persist with supremely dangerous policies and strategies…."



"...we again face uncertainties and choices of enormous consequence, just as...in 1914."

The parallels between today's political decisions regarding climate change and the decisions that led Europe to World War I are sobering. Those made in 1914 reflected political policies pursued for short-term gains and benefits, institutional hubris, and a failure to imagine and understand the risks. The result was a disaster in many ways, the reverberations from which are still felt a century later.

Once again, nations face a challenge—climate change—which, if left unmanaged, has the potential to bring tremendous pain to hundreds of millions of people and seriously disrupt the existing economic and political orders of the day. Although we do not know exactly how climate change will evolve, we do know that ignoring climate change is tantamount to assuming that there will be no change, an exceedingly unlikely outcome.

So, what to do? Here are three proposals for action to "buy-down" the risk we have accreted: Increase our understanding of the near-term future, and focus on the most dangerous and most probable risks; take the actions needed to maintain society's essential infrastructure: water, food, and a viable coastline; and make the commitments to accelerate our shift to a no-carbon energy future.

We need to have adequate warning of truly extreme environmental conditions or abrupt, unexpected changes. This goal cannot be achieved without substantially improving the ability to monitor Earth's systems. This will lead to a better understanding of when, why, and how the details of climate are changing and improvements of early-warning systems for any sudden changes.

We must devote greater resources to the management and efficient use of fresh water, and its impact on food and energy production. We must address another water challenge—the inexorable rise in sea level, which threatens coastal communities and vital economic and security infrastructure. We must also meet the challenge of ocean acidification, global warming's "silent, evil twin," on ocean ecosystems, the primary source of protein for about 2 billion people.

We must stabilize the climate system by solving the root cause of its changes: unchecked greenhouse gases entering the atmosphere. We must focus the best minds on this challenge, develop the needed technologies, and drive their costs down so that they can be implemented. Ubiquitous, affordable, non–carbon-based power and clean water will change the world for the better.

In 2014, we again face uncertainties and choices of enormous consequence, just as the European powers faced choices in 1914. The data and projections are laid out in front of us, as they were for them. Will we repeat the same mistakes they made a century ago? This is not a political or partisan issue—the atmosphere, water, and ice neither know nor care how anyone votes or thinks. Humanity can perform amazing, nearly miraculous feats. But it requires sustained leadership from all sectors and at all levels. Political leaders must remember those ghosts from history a century ago—and this time avert the crisis.

– David Titley



David Titley is a retired Rear Admiral of the United States Navy and is director of the Center for Solutions to Weather and Climate Risk at The Pennsylvania State University, University Park, PA 16802, USA. E-mail: dwt12@psu.edu

10.1126/science.1258594

IMAGES: (INSET) GETTY IMAGES; (TOP RIGHT) PENNSYLVANIA STATE UNIVERSITY

Downloaded from www.sciencemag.org on July 27, 2014

Published by AAAS

NEWS

19,000,000

Hectares of land needed for new U.S. energy sites by 2040, estimated at the North America Congress for Conservation Biology.

IN BRIEF

AIDS researcher dead in Ukraine crash



Malaysian Airlines flight MH17 was shot down over Ukraine last week.



The 20th International AIDS Conference, held in Melbourne, Australia, this week, was overshadowed by the death of leading researcher Joep Lange and five other delegates who perished when Malaysia Airlines flight MH17 was shot down over Ukraine on 17 July. Colleagues praised Lange (left), who was head of the Amsterdam Institute for Global Health and Development, for his leadership and vision. In a speech at the meeting, David Cooper, head of the Kirby Institute for Infection and Immunity in Society in Sydney, Australia, noted that Lange early on recognized that a single drug against HIV likely would fail. "He single-handedly convinced the pharmaceutical industry that combination chemotherapy was the way to go," Cooper said. Lange then made it his mission to bring the treatment to the world's poor, probably saving "tens of thousands of lives," he said. Also killed in the crash were Lange's partner, Jacqueline van Tongeren, who was communications director at his institute; three others working in the Dutch HIV/AIDS community; and World Health Organization spokesman Glenn Thomas. http://scim.ag/LangeMH17

AROUND THE WORLD

Australia scraps carbon tax

CANBERRA | Bucking global efforts to curtail carbon pollution, the Australian government last week abolished a national carbon tax. The move to "ax the tax" makes Australia the first country in the world to abolish a functioning carbon pricing scheme. Energy researchers condemn the move. The tax repeal is a "dereliction of duty with respect to the rights of young people and future generations," says energy research expert Hugh Outhred of the University of New South Wales in Sydney. The centerpiece of Australia's Clean Energy Act passed in 2012, the carbon tax required 350 of the nation's biggest polluters to purchase carbon credits, valued at AU$23 per ton, if they exceeded their allotted targets. The legislation sparked significant reductions in Australia's carbon dioxide emissions, analysts say. http://scim.ag/Auscarbtax

Lawsuit over golden rice paper

WOBURN, MASSACHUSETTS | Tufts University nutrition scientist Guangwen Tang is suing the American Society for Nutrition (ASN) and Tufts to prevent the retraction of her 2012 nutrition study of golden rice in Chinese children, published in *The American Journal of Clinical Nutrition*. The study aimed to find out how well the body converts golden rice—a



Golden rice may help vitamin A deficiency in children.

PHOTOS: (TOP TO BOTTOM) © MAXIM ZMEYEV/REUTERS; AIGHD/AMC; © ERIK DE CASTRO/REUTERS/CORBIS

Downloaded from www.sciencemag.org on July 27, 2014

Published by AAAS



New Zealand plans to poison stoats and rats to save the brown kiwi and other native birds.

Battle for the birds

New Zealand is beginning its largest pest control effort, aimed at protecting native birds, bats, and snails across more than 708,000 hectares on the south island. The plan is a response to a massive abundance of beech seed, which began in March, due to 2 years of favorable weather. The bumper crop is predicted to cause "a plague of rodents of biblical proportions," said Conservation Minister Nick Smith in a statement. Once the rats and stoats finish the seed, they will likely hunt native species. To knock down the rodent population, workers will set traps and drop poison by helicopter in 29 forests until November. Although the toxic bait, laced with sodium monofluoroacetate, is formulated to minimize deaths to deer and birds, some environmental and farming groups object to its use. The effort will cost between NZ$9 million and NZ$12 million, part of a 5-year, NZ$21 million campaign.

genetically modified crop aimed at fighting vitamin A deficiency—into vitamin A. After a Tufts investigative panel found ethical lapses in the study last year, ASN allegedly asked Tang and her co-authors to withdraw the paper. The scientists declined; Tang, who filed suit 9 July, argued that retraction is tantamount to defamation. One of Tang's supporters says the society has agreed to a 90-day stay before retracting the paper to attempt to settle out of court. http://scim.ag/riceretraction

Remote tribe contracts flu

ACRE, BRAZIL | Members of a long-isolated Amazon tribe have contracted influenza after making voluntary contact with the outside world (*Science*, 11 July, p. 125). Members of the tribe had emerged from the forest along the Upper Envira River late last month, possibly to evade illegal loggers and cocaine traffickers. They spent several weeks with representatives from Brazil's Indian affairs department (FUNAI) and with people from an indigenous village. Late last week, FUNAI announced that the tribespeople had contracted the flu virus, to which they have no immunity—particularly worrying because thousands of such tribespeople live in the Amazon region. A government medical team treated the infected tribespeople and provided them with immunizations, according to FUNAI, but the group then returned to their forest home—a development that alarms many researchers. http://scim.ag/flutribe

Bill would boost NSF funding

WASHINGTON, D.C. | The Senate's Commerce, Science, and Transportation Committee released proposed legislation on 18 July that calls on Congress to increase the National Science Foundation's (NSF's) budget by nearly 40%, to $9.9 billion, by 2019. It also endorses NSF's current policies for reviewing grant proposals and—in sharp contrast to a U.S. House of Representatives bill—emphasizes the importance of the social sciences as part of a balanced research portfolio. The bill, titled the America COMPETES Reauthorization Act of 2014, would replace the 2010 America COMPETES Act, which expired last year. But neither the Senate nor the House is likely to complete action on its reauthorization bill before the November election. http://scim.ag/SenCOMPETES

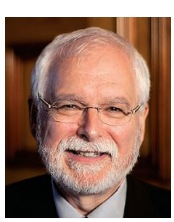
NEWSMAKERS

Three Q's

Neuroscientist **John Donoghue** has spent the past decade working on "BrainGate," brain-machine interfaces that allow paralyzed people to control prosthetic limbs using their minds. This summer, he's leaving Brown University to become director of the new Wyss Center for Bio- and Neuro-Engineering in Geneva, Switzerland.

Q: What's the new Wyss center's mission?
A: The goal is to make neuroprosthetics that will be practical in the real world. A lot of times we do things that look really cool to the media, but are they something that will help people in everyday life?

Q: Does Europe provide a more stable environment for neuroscience research?
A: The U.S. has absolutely extraordinary scientists and neuroscience is amazing here. I am a little disappointed that the U.S. is not investing as heavily as other countries, though. If you look at countries that are investing heavily in industry, education, and science, it's Germany and Switzerland.



Q: Officially you are on a 1-year sabbatical from Brown. Will you go back?
A: I don't know. I love Brown, and I never thought I would even think of going someplace else, but to have the chance to shape something like this—it's hard to turn something that wonderful down.

PHOTOS: (TOP TO BOTTOM) © TRAVEL PICTURES/ALAMY; MIKE COHEA/BROWN UNIVERSITY

Published by AAAS



Health workers carry the body of an Ebola virus victim in Kenema, Sierra Leone, on 25 June 2014.

IN DEPTH

INFECTIOUS DISEASES

Ebola drugs still stuck in lab

Experts discussed—and rejected—bringing experimental vaccines and therapies to West Africa

By **Martin Enserink**

There's little doubt what Erica Ollmann Saphire would do if she had Ebola or knew she had been exposed. The x-ray crystallographer at the Scripps Research Institute in San Diego, California, is leading an international effort to develop a potent mix of monoclonal antibodies against the virus, some of which have already shown promise in animals. Knowing the staggering case fatality rate of this hemorrhagic fever, Ollmann Saphire says she would take the antibodies—never mind that they haven't been tested for safety. "Believe me, I'd run for the freezer and ask for forgiveness instead of permission," she says.

Many Ebola researchers say they, too, would eagerly try the antibodies—or one of the promising candidate drugs, or an experimental Ebola vaccine. And they would love for people in Sierra Leone, Guinea, and Liberia to have access to experimental therapies as well, as the death toll from the largest Ebola outbreak on record climbs past 600. But it's not going to happen.

As the outbreak in West Africa worsened, debates intensified among scientists, government officials, and company executives about bringing some of these unapproved products to Africa on a so-called compassionate use basis—after all, "something is better than nothing," Ollman Saphire says. "I have been on at least half a dozen conference calls about this," says Lisa Hensley, an expert in hemorrhagic fever viruses at the National Institute of Allergy and Infectious Diseases (NIAID) in Frederick, Maryland.

But the organizations fighting Ebola on the ground say they simply can't bring an untested, unlicensed drug to a population that's already distrustful of the teams trying to stamp out the outbreak. "Some people are throwing stones at us," says Armand Sprecher, a public health specialist at the Brussels office of Doctors Without Borders. "There are rumors that we are spreading disease, harvesting organs, and other horrible things. Bringing in unlicensed things to experiment on people could be very counterproductive." A representative for the World Health Organization (WHO) adds that using vaccines now "would not be ethical, feasible, or wise."

Longtime Ebola researchers say they accept that decision, but they're frustrated. "It's very, very disappointing," says Heinz Feldmann of NIAID's Rocky Mountain Laboratories in Hamilton, Montana, who has helped develop a promising vaccine candidate. But Feldmann hopes the tragedy will at least help unclog the product pipeline.

With 1048 reported cases and 632 deaths since March—a 60% fatality rate—the West African outbreak shows no signs of tapering off. People in the affected countries are more mobile than in the central African regions struck by Ebola in the past, Sprecher says, giving the virus more options to spread. What's familiar are the cultural problems in battling Ebola. The measures that will contain the virus—strictly isolating patients, tracing and monitoring their contacts, and burying the dead quickly and safely—are often difficult for the local population to accept.

Despite the media's fascination with Ebola, the disease is exceedingly rare, which has slowed the development of countermeasures. Before the current one, all known outbreaks had caused fewer than 2400 cases, across a dozen African countries over 3 decades. Add the poverty of those countries, and the market for drugs and vaccines looks unpromising. (Complicating matters, Ebola-Zaire, now raging in West Africa, is just the most common of five Ebola species; each needs its own countermeasures.) Most research has been funded by the U.S. government in response to worries about biowarfare and bioterrorism.

But that support hasn't been enough to bring a single product to the market. Feldmann's vaccine, for instance, consists of a livestock pathogen called vesicular stomatitis virus (VSV) in which one gene has been replaced with that for Ebola's surface glycoprotein. It gives rhesus macaques full protection against Ebola-Zaire and saved four out of eight animals when

Too little, too late

A selection of Ebola vaccines and drugs in development. Only TKM-Ebola has entered a phase I trial, which was halted by FDA.

● VACCINES ● DRUGS	DEVELOPERS
● VSV-based vaccines	Profectus BioSciences; Public Health Agency of Canada
● Adenovirus-based vaccines	At least three different labs/companies
● TKM-Ebola (RNAi-based)	Tekmira Pharmaceuticals Corp.
● Nucleoside analog	U.S. Army Medical Research Institute of Infectious Diseases
● Monoclonal antibodies	Many labs/companies
● AVI-7537 (antisense-based)	Sarepta Therapeutics

PHOTO: STRINGER/REUTERS/CORBIS

Downloaded from www.sciencemag.org on July 27, 2014

Published by AAAS

given 30 minutes after an otherwise lethal dose of the virus. But the Public Health Agency of Canada (PHAC) in Winnipeg, Feldmann's previous employer, has yet to take it to phase I safety trials in human volunteers. Profectus BioSciences in Tarrytown, New York, which is developing a similar vaccine, needs some $2 million to produce it under good manufacturing practice standards, a prerequisite for any human study.

A leading drug candidate has more funding and is further advanced, but it also faces obstacles. The compound, identified by U.S. Army researchers and based on RNA interference, is in development at Tekmira Pharmaceuticals Corp., a Burnaby, Canada–based company that has a Pentagon contract worth up to $140 million to produce it. But on 3 July, the company announced that the Food and Drug Administration had put a phase I trial on hold because it wants more data and a change in the protocol to protect participants' safety. Tekmira says it expects to resolve the issue by the end of the year.

Monoclonal antibodies are similarly stymied. In the $28 million NIAID-funded project that Ollmann Saphire is leading, 25 labs from seven countries are pooling their antibodies to see which cocktail best blocks the virus. But again, none of these has entered a phase I trial. The same is true for a powerful nucleoside analog—a small molecule that's cheap to make—developed by the U.S. Army Medical Research Institute of Infectious Diseases. A promising antisense-based compound by Sarepta Therapeutics in Cambridge, Massachusetts, was put on ice after the Pentagon ended its funding in 2012.

Still, an exception was once made for compassionate use of an Ebola therapy. In 2009, when a German researcher pricked her finger with a syringe containing Ebola, the VSV vaccine was rushed from Winnipeg to Hamburg, where she received it 48 hours after the accident and remained healthy. Whether the vaccine helped can't be determined.

But that was a single case in an intensive care unit in a Western hospital where the patient could be monitored closely for side effects and treated if needed, says PHAC virologist Gary Kobinger. Doing the same for hundreds of people in Africa is virtually impossible, he says. Getting informed consent would be a huge challenge. And no drug or vaccine is going to work once patients are very ill, says Ebola researcher Thomas Geisbert of the University of Texas Medical Branch in Galveston; if patients seek care too late, that could create the mistaken impression that the interventions are useless. "If something goes wrong this could be a disaster," Feldmann says. "So we have to work hard and come up with a really good plan for the next outbreak." ■

PHOTO: NASA/JPL-CALTECH/MSSS

PLANETARY SCIENCE

Road hazards threaten rover

To limit wheel damage from sharp rocks, the Curiosity Mars rover detours into sandy valleys

By **Eric Hand**

John Grotzinger, the project scientist for NASA's Curiosity rover, is eager to study the rocks on Mars. But right now he fears them. "Today the rover planners were so tense that they only agreed to drive 10 meters," he says. "It's killing us."

The problem: Daggerlike rocks are tearing into Curiosity's featherweight aluminum wheels. The rover has been returning increasingly alarming pictures of punctures in the metal, which is just 0.75 millimeters thick, and scientists and engineers both on and off the team are concerned. Even Alcoa, one of the world's largest aluminum producers, has offered suggestions for minimizing the damage, says Grotzinger, a planetary scientist at the California Institute of Technology in Pasadena. "I've got a nation of back-seat drivers," he says.



Holes in one of Curiosity's 0.75-mm-thick wheels.

Soon after landing 2 years ago, on 5 August 2012, the rover struck pay dirt, drilling into an ancient lakebed that revealed a formerly habitable environment (*Science*, 24 January, p. 386). And a few months ago, the mission scientists announced that they had found signs of organic molecules called chlorobenzenes, although they don't know whether the compounds derived from meteoritic debris or could be a byproduct of ancient life (*Science*, 28 March, p. 1419). Those findings and others have made them itchy to get to the main event: a mountain, ringed by water-altered sediments, that rises 5.5 kilometers from the middle of Gale crater. For the past year, the rover has been on a fast-track route across swaths of sharp-rocked terrain.

But its latest troubles have forced operators to back off the throttle. By January, mission engineers saw that damage to the wheels was accumulating at an alarming rate. Geologists on the team worked to map the terrain, using instruments on the Mars Reconnaissance Orbiter, and quickly picked out the offending rock formation. It was tightly cemented, retained a history of more craters than surrounding formations, and formed a cap rock, jutting above the landscape. Fractures in the cratered rock have allowed the wind to whittle the rock into sharp pyramidlike pieces.

The mappers charted a new route that took the rover off the cap rock and into narrow, sand-filled valleys. The detour risked trading one hazard for another: ripples of sand piled up 30 to 40 centimeters high in the center of the valleys. Although the miniature sand dunes shouldn't pose much of a problem for the 2-meter-high rover, the team has played it safe by sticking to valley edges, where the ripples taper, says Raymond Arvidson, a planetary scientist at Washington University in St. Louis who has led some of the rerouting efforts. "You don't want to get all six wheels on sand going uphill," he says. The new route paid immediate dividends: Damage rates plummeted, and the odometer ticked along faster. Last month, in one of the valleys, Curiosity drove 143 meters in 1 day—the second longest drive of the entire mission.

Recently the rover climbed back onto cap rock. But engineers at the Jet Propulsion Laboratory (JPL) in Pasadena are working on other ways to ease the wear and tear on the wheels. One is driving backward; Project Manager Jim Erickson likens the benefit to that of dragging a roller bag over a curb rather than pushing it. He says the team is also working on software changes that could cut the torque applied to an individual wheel when it senses a hazardous object.

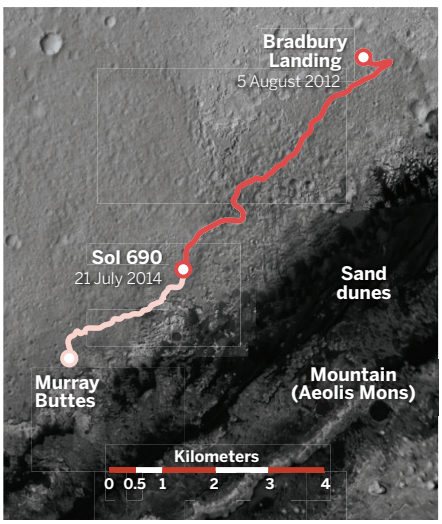
Others are trying to understand how the wheels could ultimately break. In the Mars Yard at JPL, engineers have created a sandy racetrack so that three wheels—half of

Published by AAAS

Corrected 23 July, 2014; see full text.

Rocky road

Two-thirds of the way to its mountain goal, the Curiosity rover has been slowed by damage to its wheels from sharp rocks.



Source: NASA/JPL-Caltech/Univ. of Arizona

Curiosity's chassis, pinned to a pivot—can spin around continuously, accumulating damage. An initial test suggested that the wheels would still work after 25 kilometers of rough terrain, even though some of the zigzagging grousers, or treads, will probably break. With about 8.5 kilometers under the rover's belt, Erickson says he is confident that the mission is more likely to be limited by the radioisotope power generator, which has a decade of power left, than by broken wheels.

Last week, engineers embarked on a new racetrack test, one meant to simulate the effects of continuous cap rock terrain. Under the heat of the midday sun, Michael Newby, a mechanical engineering graduate student from California State University, Northridge, toiled by a rock pile. With a tape measure, he sorted sharp quartzite rocks into two piles of different sizes. They would later be glued to plywood and placed in the racetrack. "We're trying to make it look as natural and random as possible," Newby says.

In any case, the worst of the cap rock terrain may be in the rearview mirror. The rover is nearing the end of a 200-meter stretch of sharp-rock terrain and will soon return to the safety of the sandy valleys. Just one more bad stretch remains in the 3.4 kilometers to Murray Buttes, the gateway to the base of the mountain. And Arvidson points out that there may be a silver lining to the wheel damage: The tears and perforations might actually act as extra cleats during all the sandy travel ahead. "It might actually improve your traction," he says. ■

FUNDING

NIH institute considers broad shift to 'people' awards

Approach promises freedom from grant writing but could favor established researchers

By **Jocelyn Kaiser**

Fund people, not projects. That's long been the philosophy of the largest private, nonprofit U.S. biomedical research funder, the Howard Hughes Medical Institute (HHMI), but the $30 billion U.S. National Institutes of Health (NIH) has remained a bastion of project-based grants. Now, in a major shift, some NIH institutes propose to move large chunks of money away from project grants into this type of no-strings support, which is based not on a specific research plan but on an investigator's promise.



Jon Lorsch is targeting "regular outstanding researchers."

The most far-reaching proposal comes from NIH's basic research institute, the National Institute of General Medical Sciences (NIGMS). It is seeking feedback from the research community on the idea of giving all its roughly 3300 investigators the option of applying to swap their project grants for a single, long-term award based largely on their track record. "This is potentially for the entire constellation of investigators that NIGMS funds," says NIGMS Director Jon Lorsch. But he and others agree that such an approach should be phased in with care to avoid shutting out some scientists.

HHMI adopted the people-not-projects model decades ago, reasoning that long-term support not tied to a specific idea unleashes creativity and frees scientists from writing endless grant proposals. It now supports about 320 investigators at institutions around the country with 5-year awards totaling $1 million a year. Inspired by that example, in 2004 the NIH director's office launched its Pioneer Award, which now funds 70 investigators doing high-risk, high-reward research. The experiment seems to be working: Pioneer Awards produced more innovative and higher impact results, concluded a 2012 study commissioned by NIH that compared the grants with a matched set of NIH's standard R01 project-based grants (see table).

NIH is now encouraging its 27 institutes and centers to launch their own people awards. The objective is to "unbridle scientists a bit," allowing them to "step off the grant treadmill," says Sally Rockey, NIH's deputy director for extramural research.

Furthest along is the National Cancer Institute (NCI), which last month announced a new 7-year award, championed by Director Harold Varmus: a people grant of up

People power

Pioneer Awards beat project grants on five of nine measures (shaded).

	NIH PIONEER AWARDS	MATCHED R01 GRANTS
Number of papers	●	
Papers per grant $	●	●
Citations per awardee	●	●
Citations per grant $	●	●
Citations per paper	●	●
H-index	●	
Journal ranking	●	
Impact	●	
Innovativeness	●	

Source: Institute for Defense Analyses

PHOTO: MIKE CIESIELSKI/NIGMS

Downloaded from www.sciencemag.org on July 27, 2014

Published by AAAS

to $600,000 a year (plus another 50% for overhead costs) that will replace an investigator's project-based grants. (NIH's average R01 covers $282,000 a year in direct costs for 4.3 years.) NCI expects that if it adds 50 of these Outstanding Investigator Awards a year for 7 years, the program will total $317 million a year, or about 16% of the $2 billion that NCI now spends on research grants.

At NIGMS, a people award would replace a standard NIGMS project grant, offering $150,000 to $750,000 a year in direct funding for 5 years. But Lorsch says that unlike NCI and HHMI awards, the so-called Maximizing Investigators' Research Award his institute plans to pilot-test would be intended not just for high-risk research or for "a perceived elite," but also for "regular outstanding researchers."

Several other NIH institutes are also planning people awards, Rockey says. But other funders' experiences could make them cautious. For example, NIH Director Francis Collins noted in a meeting earlier this month that the United Kingdom's Wellcome Trust, which 3 years ago shifted roughly $180 million in annual project grant funding to people awards (*Science*, 13 November 2009, p. 921), is now "rethinking" the program. Collins says Wellcome officials are concerned about the "graying" of its investigators—one risk of basing awards on reputation. Asked for comment, a Wellcome Trust representative pointed to a blog post last week from Director Jeremy Farrar saying that he plans to increase opportunities for early- and mid-career investigators.

Lorsch says NIGMS will give early-stage investigators a boost by judging them through a separate review process that will examine their graduate and postdoctoral records; the institute may also set targets to make sure enough young investigators are funded. But Rockey raises another concern: As an institute funds more long-term awards, the amount of money that turns over each year will go down, which could mean fewer awards overall. Institutes will "need to balance their portfolios," she says.

Howard Garrison, deputy executive director for policy at the Federation of American Societies for Experimental Biology in Bethesda, Maryland, said his group's members are still discussing NIH's plans. "I suspect that views will be mixed," he says, citing "concern about how funding 'people instead of projects' will affect younger scientists." But he adds: "More and more people are frustrated by the continuous struggle for funding, and there is a growing acceptance of the idea that we need to do something different." ■

PHOTO: SANOFI PASTEUR/FLICKR

Corrected 23 July, 2014; see full text.



A pediatric trial of a dengue vaccine produced mixed results.

TROPICAL DISEASES

Dengue vaccine trial poses public health quandary

Experimental vaccine fell short against key strain

By **Dennis Normile**

As scientists and public health officials mull over the puzzling results of the first large efficacy trial of a vaccine for dengue, one thing is clear: "There are complexities we've never seen in any other vaccines," says Annelies Wilder-Smith, a public health specialist at Nanyang Technological University (NTU) in Singapore.

The vaccine, the fruit of decades of public and private sector efforts, reduced the incidence of the mosquito-borne disease overall by 56.5% and, perhaps more significant, cut cases of dengue hemorrhagic fever, a severe form of the disease, by 88.5%. But the vaccine provided only limited protection against dengue 2, one of the four serotypes of the virus, and, mysteriously, it worked best in people who had already recovered from one dengue infection and among older children.

Reported online on 11 July in *The Lancet*, these results will likely leave public health officials in dengue-endemic countries grappling with whether to include the Sanofi Pasteur vaccine in national immunization programs. Its cost, the logistics of delivering three doses over the course of a year, and its limited efficacy in regions where the dengue 2 serotype predominates must all be considered. And because the vaccine works best in preventing second infections, its value in subtropical nations where dengue is not yet firmly entrenched is even more questionable. Joachim Hombach, senior adviser to the World Health Organization (WHO) on immunization and vaccines in Geneva, Switzerland, says the results can "clearly translate" into public health benefits. But each country will have to carefully study the costs, risks, and benefits in light of its own epidemiological situation, he adds.

No one ever thought developing a vaccine for a disease as complicated and poorly understood as dengue would be easy. The four virus serotypes, all spread by the *Aedes aegypti* mosquito, are found throughout the tropics, but one strain or another often predominates in different regions and at different times. A first infection with any of the serotypes typically causes a mild fever, rash, and muscle and joint pain. Patients then have lifelong immunity to that serotype. But infection with a second serotype raises the risk of a little-understood phenomenon called antibody-dependent enhancement, which can cause dengue

Published by AAAS

hemorrhagic fever, with debilitating fatigue, internal bleeding, and occasionally death. WHO puts the annual death toll at 20,000. But the costs of caring for the estimated 500,000 patients with severe dengue yearly "represents an enormous strain to society, to the economy, to the health care system, and may drive households into poverty," Hombach says.

The burden has been steadily growing along with the global move to cities, where flowerpots, discarded tires, and construction site puddles create breeding sites for the opportunistic mosquito. Before 1970, only nine countries had experienced severe dengue epidemics; now the disease is endemic in more than 100 countries, and epidemics have increased in frequency and severity. "Most public health officials in Southeast Asia will tell you that dengue is their biggest concern," says Duane Gubler, a dengue expert at the Duke-NUS Graduate Medical School in Singapore. There are no dengue medications.

Efforts to develop a vaccine stretch back to the 1940s. From the outset, researchers believed that to avoid enhancement a dengue vaccine would have to be tetravalent, providing balanced protection against all four serotypes. This has proved challenging. Among the pioneers was a group at Mahidol University in Bangkok that tried to create a live attenuated vaccine by passaging all four virus serotypes in culture until weakened ones emerged. Sanofi Pasteur partnered with Mahidol to work on the vaccine in the mid-1990s but abandoned the effort in 2004 when it could not properly attenuate one serotype. The company then switched strategies, using a proven yellow fever live attenuated vaccine as a backbone on which to insert the genes for the envelope and membrane proteins from each of the serotypes. The four resulting chimeric vaccines were tested for safety individually and then combined to create the current candidate and tested further. A standard in vitro assay used to predict immunity, called the plaque reduction neutralization test (PRNT), suggested the vaccine would provide roughly equal protection against all four serotypes.

But in September 2012, discouraging news came from a small phase IIb trial in Thailand: In spite of the PRNT results, the tetravalent vaccine provided almost no protection against the dengue 2 virus. By then, Sanofi Pasteur had already launched two large, randomized, double-blind phase III trials: the one just reported, involving more than 10,000 children in five Southeast Asian countries, and another involving more than 20,000 subjects in five countries in Latin America. Results of the second trial will be announced later this year.

In the current trial, efficacies for the four serotypes range from 75% or better against serotypes 3 and 4 down to just 35% for serotype 2. The variation is unsettling news for other groups developing dengue vaccines, most of which have shown some evidence of weakness to one of the serotypes. All are using PRNT to guide their work—a strategy that is now in question. "Positive findings on PRNT are a poor surrogate of immunity," says Eng Eong Ooi, a dengue researcher at Duke-NUS. Researchers are working on more accurate tests, but none is ready for use yet, he says.

Another mystery is why the Sanofi Pasteur vaccine was more effective in people who had already been exposed to dengue. That finding means that "for dengue-naive travelers this vaccine is of little use," says NTU's Wilder-Smith. Gubler thinks it will still be of value in dengue-endemic countries, "because most persons in those countries have already experienced at least one dengue infection" and could be protected from severe disease.

Sanofi Pasteur expects the vaccine to "have a real impact on this disease," says Guillaume Leroy, head of the company's dengue program in Lyon, France, and is aggressively moving forward. The company built a $400 million facility in Neuville-sur-Saône, France, capable of producing 100 million doses of its vaccine per year. But the company is putting off a decision on pricing until after the results of the second efficacy trial are available later this year.

Endemic countries will then be faced with a difficult decision on whether to use a partially effective vaccine or wait for other dengue vaccines in the pipeline. Says Wilder-Smith: "It will be very interesting to see how countries react to this possible vaccine." ■

2.5 billion people
live in dengue-endemic countries (more than **40%** of the world's population)

50–100 million dengue infections
occur worldwide **each year**

500,000 people with severe dengue
require **hospitalization** each year

2.5%
of people with severe dengue **die**

Source: World Health Organization



PHOTO: TAYLOR MCKINNON/GRAND CANYON TRUST/ECOFLIGHT

ENERGY POLICY

Oil sands fight heats up in U.S.

Environmentalists oppose federal lease in Utah

By **David Malakoff**

The battle over oil sands is moving to U.S. soil. Soon, the U.S. Bureau of Land Management (BLM) plans to offer private firms the chance to exploit tar-soaked sandstones beneath 8.5 square kilometers of federal land on Asphalt Ridge, a sagebrush-speckled outcrop near the small town of Vernal, Utah. If successful, the lease sale would open a new frontier in U.S. energy production, easing industry access to land in Utah that could hold up to 19 billion barrels of oil; that's in addition to the nation's roughly 30 billion barrels of conventional oil reserves.

The prospect of developing Utah's vast, untapped deposits alarms environmentalists and conservation scientists, who point to Canada's burgeoning oil sands operations to argue that extraction takes an unacceptable toll on land, water, and global climate. A coalition of environmental groups is vowing to challenge the Asphalt Ridge lease and other similar sales. "Tar sands leasing on federal lands is absolutely the wrong policy if you are serious about preventing the worst effects of climate change," says Taylor McKinnon, director of energy at the Grand Canyon Trust in Flagstaff, Arizona. "The greenhouse emissions and environmental impacts will be enormous."

Downloaded from www.sciencemag.org on July 27, 2014

Published by AAAS



Utah's Asphalt Ridge (*foreground*) is the scene of a sticky fight over oil sands mining.

Asphalt Ridge, its dusty slopes abutted by industrial sites and housing subdivisions, seems an unlikely place to wage an environmental battle. "It's the kind of place where the local high school kids like to go at night to party," McKinnon says. But since the 1800s, petroleum geologists have known that the thick sedimentary formations beneath eastern Utah's Uinta Basin, where Asphalt Ridge is located, are rich in tar sands (also called oil sands)—porous rock laden with bitumen, a heavy viscous oil. The majority of U.S. tar sands are in Utah, mostly under land owned by BLM and other federal agencies. Asphalt Ridge alone could hold a billion barrels.

Oil prices have historically been too low to justify the expense of extracting the oil, which typically requires digging up the rock and heating it or treating it with solvents. And unlike the Canadian tar sands, which sit relatively close to the surface, the Utah deposits can be 300 meters down and require potentially expensive tunneling. Still, in 2005, as energy prices rose, energy firms persuaded Congress to require BLM and other U.S. agencies to establish a plan for developing tar sands on federal lands. Under President George W. Bush, the agencies initially proposed selling tar sands leases on some 174,000 hectares of federal land, but the Obama administration reduced the area to 53,000 hectares in Utah after court challenges by environmental groups.

Critics say that's still too much. It typically takes 2 tons of tar sands to produce a single barrel of oil, they note, meaning mines and waste piles can chew up habitat used by rare or threatened plants and animals. Two or more liters of water are often needed to extract each liter of oil, potentially producing copious amounts of contaminated wastewater. That's a major concern at Asphalt Ridge, researchers say, where water is scarce and contaminated runoff could ultimately flow into streams and rivers holding endangered fish. Extraction can also produce air pollutants. BLM didn't do enough to analyze those issues, the groups argue; nor did it consider how tar sands projects on federal lands would add to the impacts associated with a handful of similar projects under way on Utah's state and private property.

The Obama administration also neglected to tally up the expected greenhouse gas emissions from extraction, environmentalists add, which can be four times greater than conventional oil drilling because of the energy required for processing. "That's a big contradiction," McKinnon says, given the administration's simultaneous vow to curb emissions from other sources, such as coal-fired power plants. The groups want BLM to do a more complete analysis before approving any leases.

BLM officials challenge that critique, saying the agency will closely scrutinize such issues once companies present specific plans for extracting oil. "We won't really know exactly what we are up against until we get a mine plan," says Kent Hoffman, deputy state director of lands and minerals at BLM's Utah office in Salt Lake City. The agency's initial assessment "is not the end of the journey," adds Megan Crandall, the office's chief of external affairs, noting that the Asphalt Ridge leasing process "is being watched very closely" by both environmentalists and industry.

The argument is likely to be settled in court—and the outcome could determine whether the nascent U.S. oil sands industry soon gains easier access to some of the richest deposits on federal lands, or instead gets stuck in a legal and political tar pit. ■

Published by AAAS

FUSION'S RESTLESS PIONEERS

Startups with novel technologies are taking on fusion's Goliaths

By **Daniel Clery**

Something strange is happening in the world of fusion energy research. There's been an outbreak of entrepreneurship, maverick independence, and pioneering spirit. In a field that has come to epitomize the worst of "big science"—slow, overpriced, and heavily engineered—some people are finally saying "enough is enough" and striking out on their own to find another way.

In unassuming industrial units across North America, Europe, and elsewhere, small teams of scientists and engineers supported by either private finance or a mix of government and private funds are working out novel approaches to fusion. They're not just doing research: They're aiming to build financially viable power reactors simpler and cheaper than anything envisaged by publicly funded efforts, and they're hoping to do it a whole lot faster.

So why is this happening? And why now? In the more than 6 decades that researchers have been trying to replicate the sun's source of heat—fusing together atoms to release the energy locked in their nuclei—reactors have grown from tabletop gadgets to multibillion-dollar behemoths. ITER, the multinational facility aiming to show net energy gain for the first time, will weigh in at 23,000 tonnes when complete—three times the weight of the Eiffel Tower—and will cost about $20 billion. The National Ignition Facility (NIF), which uses a different fusion technology, cost $3.5 billion to build.

ITER and NIF are the current torchbearers in the effort to show that a reactor can produce more energy than it consumes. That's a big ask because fusion reactions take a lot of energy to get going: The fuel has to be heated to and held at more than 150 million degrees Celsius. In theory, once the reaction gets started it will heat itself, but no one has come close to achieving that yet. NIF was meant to have produced such an "ignited" fusion burn several years ago, but it is still far from that goal. ITER isn't due to start doing burning experiments until after 2027.

Meanwhile, the huge cost of constructing these facilities has choked off funds for independent fusion programs. Some researchers argue this outcome was inevitable because, in technological terms, ITER and NIF take fusion to extremes. ITER aims to bottle up a tenuous burning plasma in magnetic fields for as long as possible; NIF's strategy is to blast fusion fuel with giant lasers, crushing it to as high a density as possible. Reaching those extremes requires complex technology, high cost, and large size.

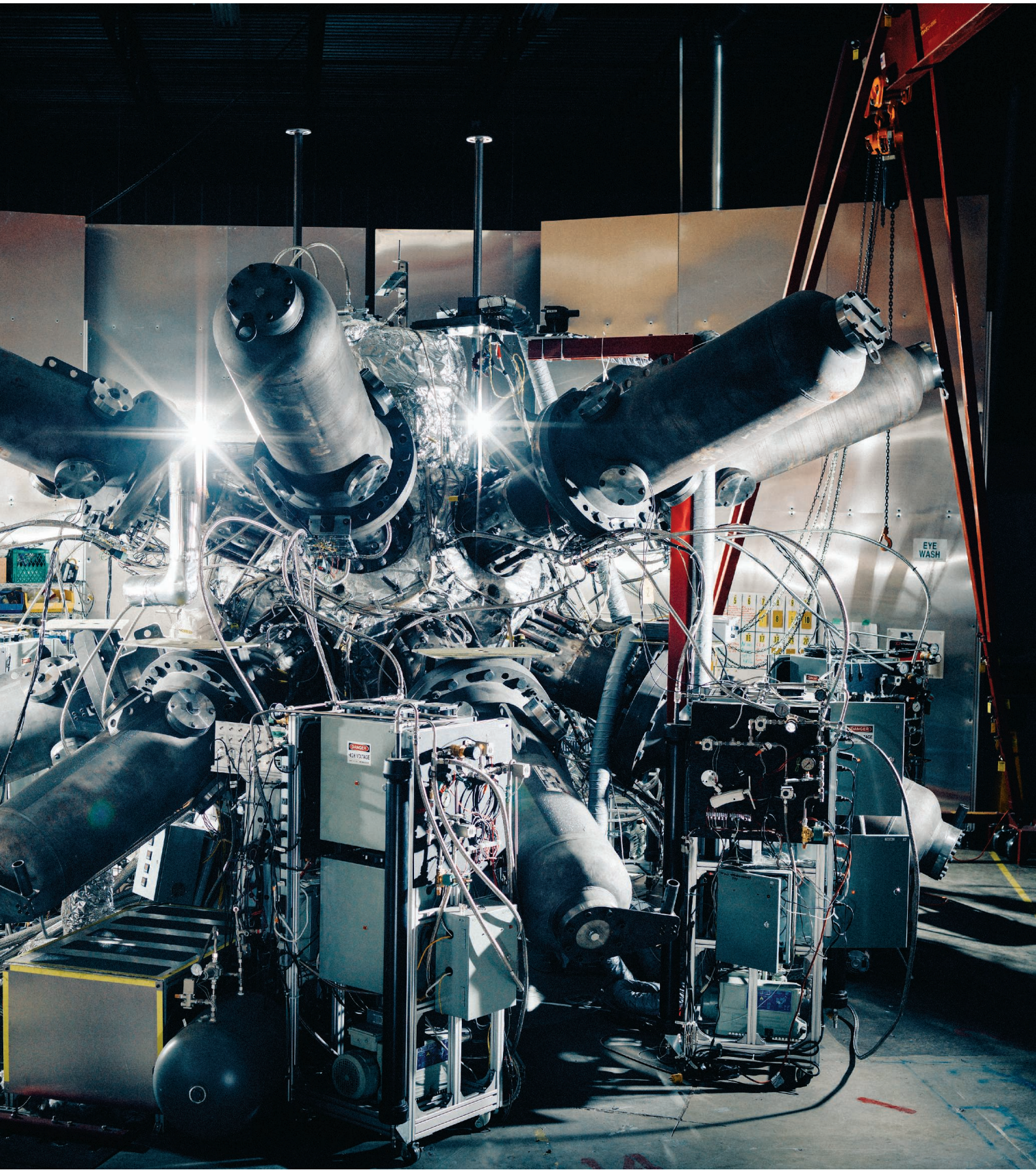


PHOTO: HUBERT KANG PHOTOGRAPHY

General Fusion's machine compresses fuel with giant pistons.

Downloaded from www.sciencemag.org on July 27, 2014

Published by AAAS



Published by AAAS

The dark-horse approaches to fusion, by contrast, steer a middle course between the extremes. Although scientifically plausible, unlike the notorious cold fusion, they have enjoyed relatively little time and funding.

But fusion is a complicated business, involving high-energy particles and colossal temperatures and pressures. To get anywhere, you need sophisticated diagnostics, advanced materials, complex computer simulation—no? Who would be crazy enough to go out and try to build a fusion reactor?

THE STEAMPUNK SOLUTION Michel Laberge was bored. In 2001, he was approaching 40 and for the past 10 years had been designing laser printers for the Canadian company Creo (now part of Eastman Kodak Co.), learning "to make machines fast and cheap." It was time to do something more with his life. He had spent the earlier part of his career studying lasers and their potential for sparking fusion at the University of British Columbia, France's École Polytechnique, and Canada's National Research Council in Ottawa. He knew what a successful fusion reactor could do for the planet. So he cashed in his Creo shares, quit his job, and set out to build one.

Scanning the literature, Laberge came across a 1970s program at the Naval Research Laboratory in Washington, D.C., called LINUS—an early attempt at so-called magnetized target fusion. The LINUS scheme aimed to take fusion fuel, form it into a magnetized ball of plasma, and fire it into a shell of liquid metal, created by putting the metal inside a cylindrical container and spinning it to force the liquid up the walls. Once the shell and plasma were in place, pneumatic pistons would slam into the shell, compressing it and imploding the plasma, boosting its density and temperature. LINUS was closed down in 1980, but Laberge thought it was a great scheme for a power plant. LINUS failed, he says, because 1970s technology wasn't up to the job. "You need to accelerate the pistons, delivering energy very fast, faster than the lifetime of the plasma," he says.

Laberge persuaded a few former colleagues from Creo to invest and, with a small Canadian government grant, built a tabletop device that simulated the effect of pistons with electric pulses. This was enough to produce a few neutrons—Laberge calls them his "marketing neutrons," because neutrons are a sign that fusion reactions are taking place. Then he was off, gathering funds from government and investors and recruiting staff. In 2002, Laberge and his partners formed General Fusion, which now has a staff of more than 60. Since 2009, they have raised CA$62 million, 80% from private sources that include the oil company Cenovus Energy and the investment company of Amazon.com founder Jeff Bezos.

With that money, they built a machine that looks like something straight out of steampunk, a sort of giant robot sea urchin. Around a meter-wide spherical steel reaction chamber are 14 pneumatically driven pistons the size of cannons jutting in all directions. How it works sounds positively apocalyptic. First, the researchers swirl molten lead around the walls of the chamber, creating a vortex with a void in the center; into the void they fire a "compact toroid" of fusion fuel—essentially a smoke ring of plasma. Then the pistons come hammering down at 50 meters per second and slam into plugs in the wall of the chamber, sending a shock wave through the lead. The shock wave crushes the fuel to huge temperature and pressure and—bang!—a small fusion explosion takes place (in theory).

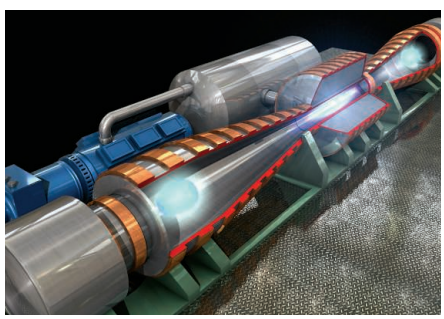
The current setup won't achieve fusion; it's just to validate the compression system. "We're testing seals, pumping, creating shock waves—getting to know the technology," Laberge says. Elsewhere at their headquarters in a light industrial park in Burnaby, Canada, researchers are working on the injector, the plasma gun that will form the balls of fuel and shoot them into the compressor.

As in all such endeavors, they've had their share of problems: Pistons cracked; shock waves caused the liner to spit out droplets of lead; and the plasma cooled too quickly or its density was too low. But the team plans to continue working on the separate elements for another couple of years until they have enough data to predict what it will take to reach breakeven: the point at which the device puts out as much energy as the pistons put in.

At the moment, they expect that will require a monster version of their current setup, with a reaction chamber three times as big, up to 400 pistons hammering its surface, and possibly two opposing plasma injectors firing compact toroids that collide and merge before compression. And that means a whole new level of funding. "We're visiting investors, building relationships, getting ready to raise capital," says Michael Delage, General Fusion's vice president of strategy and corporate development. Convincing people that the technology is viable can take work. "It takes more than one meeting," Delage says.

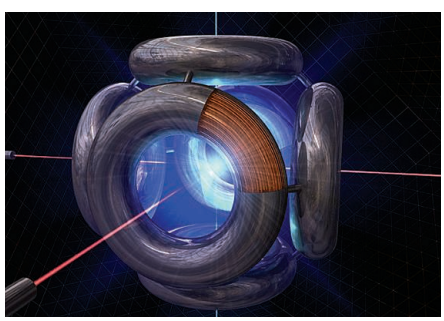
Fusion's middle way

Fusion devices take hot fuel (an ionized gas, or plasma) and squeeze its particles together long enough for nuclei to fuse. Big mainstream projects do that by means of extremely high densities or long confinement times. Smaller private pioneers hope that avoiding such extremes will yield smaller, simpler, cheaper fusion machines. Two promising approaches:



Magnetized target fusion

Magnetized target fusion (MTF) devices first confine the plasma with a magnetic field (as in magnetic fusion) and then crush it (as in inertial fusion). The crushing increases density and temperature and boosts the magnetic field, lengthening confinement time. Most MTF schemes create "compact toroids," or smoke rings of plasma. Electric currents in the plasma create magnetic fields that confine it for a few microseconds while "plasma guns" fire it into a crushing device.



Polywell

A polywell uses electric fields to accelerate fuel nuclei so that they collide and fuse. Typically, six ring-shaped electromagnets arranged in a cube create a magnetic particle trap. Electrons fired into the center stay there and exert a strong electric field that slams fuel nuclei together. The problem is that polywells are leaky: Plasma can escape through gaps in the magnetic field and through the centers of the rings.

PHOTOS: (TOP TO BOTTOM) HELION ENERGY; EMC2 FUSION DEVELOPMENT CORP.

Published by AAAS



Eric Lerner stares into electrodes at the heart of LPP's dense plasma focus device.

PHOTO: LAWRENCEVILLE PLASMA PHYSICS

THE SPACEMAN Eric Lerner is an unlikely fusion scientist. He dropped out of a postgrad physics course and became a successful science writer. In 1991, he published the controversial book *The Big Bang Never Happened*, which depicted an eternal universe dominated not by gravity and quantum mechanics but by plasma physics—a model mainstream cosmologists consider unworkable.

By then, Lerner had already started doing independent research into fusion devices and had latched on to one called a dense plasma focus (DPF), invented in Russia in the 1950s. DPF creates a compact toroid of fusion fuel and then compresses it to tiny size with an electromagnetic effect known as a pinch. After 10 years of research, Lerner won funding from NASA's Jet Propulsion Laboratory to investigate whether DPF could be used for spacecraft propulsion. Seven years later, after spending $300,000, NASA killed the project and Lerner started looking for private sponsors.

After another 7 years, he'd raised $1.2 million, enough to build his own research facility in Middlesex, New Jersey, under the name Lawrenceville Plasma Physics (LPP). This hand-to-mouth existence has continued: Lerner raised another $2 million over the past 5 years from 60 different investors to continue the work. "Compared with other [private fusion] efforts, we're the most technologically advanced but the least well funded," he says.

General Fusion's thumping pneumatic monster makes Lerner's device look like a toy. The heart of the machine is two cylindrical electrodes, one inside the other. The outer electrode—a set of parallel bars arranged in a ring—is just 18 centimeters across, and the entire device is enclosed in a vessel filled with a diffuse gas. A huge electric pulse is discharged from the outer to the inner electrode, creating a doughnut-shaped sheath of plasma that escapes into the vessel. Then the magnetic field caused by the current pinches the doughnut down into a tiny, dense ball of plasma.

The collapsing magnetic field induces an electric field, which drives a beam of electrons through the plasma, heating it to a temperature of billions of degrees. If everything goes according to plan, the ball of plasma—which lasts for only 10 billionths of a second—will get hot and dense enough for fusion to occur.

Lerner says that the device can achieve the necessary temperatures but so far falls short of the needed density of particles. The problem is copper atoms evaporating off the electrodes and polluting the plasma. At the time of writing, LPP had just taken receipt of a new set of tungsten electrodes and completed a crowdfunding campaign to help pay for the $200,000 cost. "I'm pretty convinced that the electrodes will radically reduce impurities and increase density by 100 times," Lerner says.

The LPP team will experiment with the new electrodes until the end of this year and then, if everything looks good, will change over from deuterium fuel to a mixture of hydrogen and boron-11. This fuel is harder to react but does not produce high-energy neutrons, which damage the reactor and make it radioactive. If he can raise another $1 million, Lerner believes he can demonstrate net energy gain by the middle of 2015. "We're very far along compared with the others," Lerner says. "Tri Alpha is three orders of magnitude behind." Tri who?

ENIGMA MACHINE Tri Alpha Energy is the team to beat in privately financed fusion, mainly because it has a huge cash pile: hundreds of millions of dollars. "Tri Alpha is singular in the history of fusion as the only time that amount of money has been invested in a private effort," says Stewart Prager, director of Princeton Plasma Physics Laboratory in New Jersey, America's foremost fusion facility.

The company shrouds itself in mystery. It has no website and makes no public statements. What details are known about its work come from occasional papers in journals or appearances by its staff at conferences. Company managers declined to be interviewed for this article, explaining that they had no need at the moment to publicize their efforts.

Tri Alpha is the brainchild of Norman Rostoker, a Canadian plasma physicist who has worked at Cornell University and the company General Atomics, and is now a professor emeritus at the University of California, Irvine. In 1997, Rostoker, who will turn 89 in August, and two colleagues published a paper in *Science* describing the "Colliding Beam Fusion Reactor" (*Science*, 21 November 1997, p. 1419). They founded Tri Alpha Energy, based in Foothill Ranch, California, the following year.

The company now has more than 150 employees, and investment has come from the likes of Goldman Sachs, Microsoft co-founder Paul Allen, and other venture capitalists. It also has strong connections with Russian researchers, and the prominent Russian politician and businessman Anatoly Chubais is on its board of directors. Much of Tri Alpha's ample funding is rumored to come from Russian oligarchs.

Published by AAAS

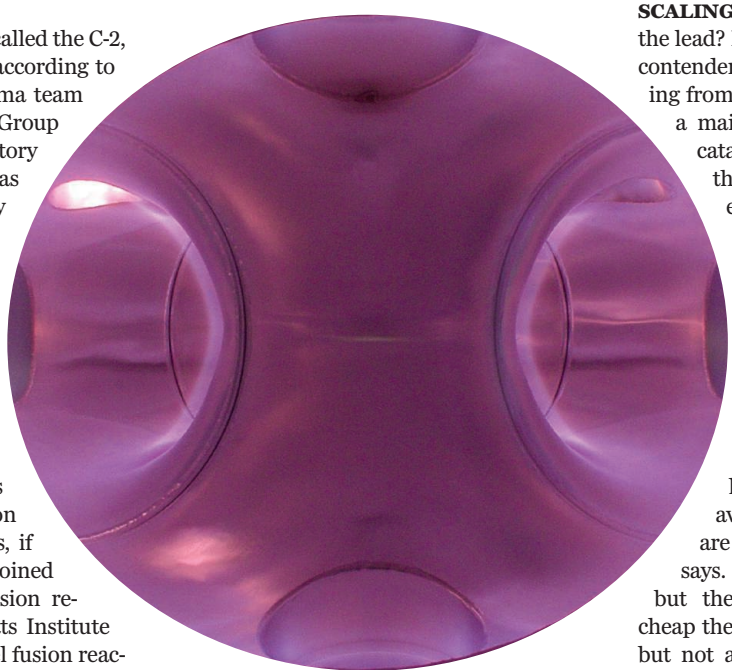
Rostoker's colliding beam reactor works by creating two compact toroids and then accelerating them at the supersonic speed of 250 kilometers per second into a head-on collision. The toroids merge into a toroid known as a field-reversed configuration (FRC), converting their kinetic energy into heat. Extra heating is provided by ion beams. The Tri Alpha team has also developed tricks to lengthen the lifetime of the FRC, reporting lifetimes of up to 4 milliseconds in a 2012 paper in *Physical Review Letters*. Unlike Tri Alpha's rivals, the device does not compress the plasma but instead relies on high temperature and long confinement to spark fusion.

Tri Alpha's current machine, called the C-2, is the length of a tennis court, according to Glen Wurden, magnetized plasma team leader in the Plasma Physics Group at Los Alamos National Laboratory (LANL) in New Mexico, who has visited the facility. "It's a very beautiful machine," he says.

THE VISIONARY Robert Bussard started his career at LANL designing nuclear-powered rocket engines, including the Bussard ramjet, which uses a magnetic field to scoop up interstellar hydrogen to fuel its fusion engine. His ramjet is a common propulsion system in science fiction novels, if not in real spacecraft. Later, he joined forces with Bruno Coppi, a fusion researcher from the Massachusetts Institute of Technology, to develop a novel fusion reactor they called the Riggatron—after the Riggs National Bank, an early backer. Their biggest supporter was Bob Guccione, the flamboyant publisher of magazines including *Penthouse* and *Omni*. But just as they were planning a public flotation, Guccione balked and the project collapsed.

Bussard quickly recovered from that setback and by the mid-1980s had come up with another promising fusion design: the polywell. The polywell is a refinement of another device known as a fusor, perhaps the simplest of fusion reactor designs. A fusor has two usually spherical electrodes made of wire mesh, one inside the other. When the setup is placed in a vacuum chamber filled with fusion fuel and a large voltage is applied across the electrodes, the electric field accelerates ions inward, toward the inner mesh. In theory, the ions fly right through the holes and continue on to the center where they collide with other ions and fuse. The problem is that too many ions hit the inner electrode and are absorbed, cutting the device's efficiency and putting ignition out of reach.

Bussard's idea was to replace the inner electrode with something that was harder to hit: a virtual electrode. The polywell is made up of a number of ring-shaped electromagnets, usually arranged to form a cube. When current is passed through the magnets, they create a field that has a null point in the center of the cube, which traps any charged particles. An electron gun fires electrons through the middle of the rings and they become trapped by the field. Once enough are in place, the electrons act as an electrode, exerting a strong pull on positive ions. Atoms of fuel are puffed in at the corners, become ionized, accelerate into the center, and, with luck, collide with other ions and fuse.



Plasma glows in the core of Tokamak Energy's compact machine.

Bussard set up the Energy/Matter Conversion Corp. (EMC2) in 1985 to research polywells. He won funding from the Department of Defense and later from the U.S. Navy. But Jaeyoung Park, who now leads EMC2, says Bussard was "conceptually very good, but not an experimentalist." In 2005, the Navy cut the company's funding, and Bussard embarked on a publicity campaign, highlighted by a talk at Google headquarters titled "Should Google Go Nuclear?"

In August 2007, the Navy restored its funding with $1.8 million and a new team was assembled at EMC2, including Richard Nebel and Park, both on leave from LANL. Then, in October, Bussard died of multiple myeloma at the age of 79. Nebel and Park were left, so to speak, holding the baby.

The polywell's big problem is confinement: Particles leak out through gaps in the magnetic field. In experiments carried out last October, EMC2 used improved electron guns to build up a high pressure of electrons in the center and showed that confinement was significantly improved. "We've taken a big step forward," Park says. "We were behind Tri Alpha, now we're competing directly."

Despite this success, the Navy told EMC2 that it would be stopping its funding later this year. So Park is back on the money trail, seeking $30 million for a 3-year program to put polywell to the test.

SCALING UP Which of the dark horses is in the lead? It's hard to say. And there are other contenders: companies with projects ranging from a compact version of a tokamak—a mainstream fusion device—to muon-catalyzed fusion, an exotic approach that relies on this heavy cousin of the electron to drag pairs of nuclei close enough together to fuse. Most have produced promising laboratory-scale devices; all have persuaded some venture capital companies and wealthy individuals that their investments could, one day, spawn an immensely lucrative industry.

Mainstream fusion scientists have mixed opinions of the breakaway efforts. "The center line is they are long shots," Princeton's Prager says. "It would be great if they succeed, but they're overstating how quick and cheap their solutions are. There's skepticism but not antagonism." Brian Lloyd, head of the experimental department at the United Kingdom's Culham Centre for Fusion Energy in Abingdon, notes that fusion reactors are complex devices with many interacting subsystems. "Even nations don't go it alone," he says. "It does seem implausible that a private enterprise could undertake that."

The next stage—building a demonstration reactor that can get close to breakeven or even reach ignition—will require a whole new level of funding: not millions of dollars but hundreds of millions. But the startups are undaunted. "There are a lot of potential investors out there, a lot of wealthy individuals prepared to take on a big challenge," says David Kingham, CEO of Tokamak Energy, a British venture working on a compact tokamak. "Private money can sometimes achieve things that public money can't."

Park thinks the chase inspires people. "It's a fascinating subject, it makes people's hearts beat quicker," he says. But will any of these schemes work? "We will never know until someone really cracks it," Park says. But he adds: "I like our chances." ■

PHOTO: TOKAMAK ENERGY LTD.

Published by AAAS

Ribosome stalling and neurodegeneration *p. 378*

Hiding an object's shadow in the fog *p. 384*

PERSPECTIVES

CONSERVATION POLICY

Wildlife decline and social conflict

Policies aimed at reducing wildlife-related conflict must address the underlying causes

By **Justin S. Brashares[1]*, Briana Abrahms[1], Kathryn J. Fiorella[1], Christopher D. Golden[2], Cheryl E. Hojnowski[1], Ryan A. Marsh[1], Douglas J. McCauley[3], Tristan A. Nuñez[1], Katherine Seto[1], Lauren Withey[1]**



Children enslaved for fishing labor in the Brong Ahafo region of Ghana, 2010.

PHOTO: LISA KRISTINE/LISAKRISTINE.COM

U.S. President Obama's recent creation of an interagency task force on wildlife trafficking reflects growing political awareness of linkages between wildlife conservation and national security (*1*). However, this and similar new initiatives in Europe and Asia promote a "war on poachers" that overlooks the ecological, social, and economic complexity of wildlife-related conflict. Input from multiple disciplines is essential to formulate policies that address drivers of wildlife decline and contexts from which associated conflicts ignite.

POLICY

The harvest of wild animals from land and sea provides more than $400 billion annually, supports the livelihoods of 15% of the global population, and is the main source of animal protein for more than a billion of Earth's poorest inhabitants (*2*, *3*). Humans have always depended on wildlife, but the contemporary depletion of wildlife, combined with unprecedented market globalization, has heightened the economic stakes and desperation of consumers. The consequences of wildlife declines are severe and include regional destabilization and the proliferation of terrorism.

Here, we illustrate how wildlife decline may give rise to exploitative labor practices, empower profiteering groups who use violence to control illicit wildlife trades, and promote vigilante resource management. We also describe cases where incorporating interdisciplinary perspectives has improved policy outcomes.

HUMAN TRAFFICKING, ORGANIZED CRIME, AND VIGILANTE GOVERNANCE. Wildlife declines often necessitate increased labor to maintain yields. Harvesters of wildlife resort to acquiring trafficked adults and children to capture ever-scarcer resources while minimizing production costs. A vicious cycle ensues, as resource depletion drives harvesters to increase their use of forced labor to stay competitive.

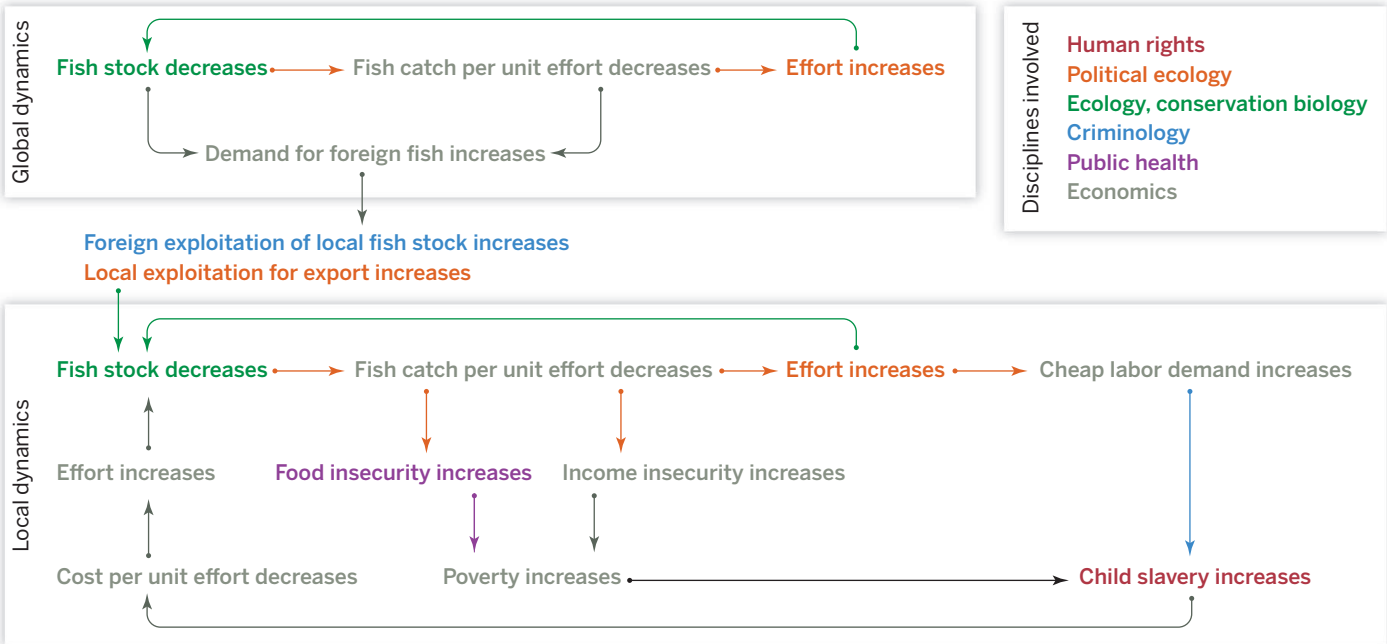
Human trafficking associated with declining fishery harvests is increasing across the globe, exposing connections between fishery decline, poverty, and human exploitation (see the chart and figure) (*4*). Many fishers must travel farther, endure harsher conditions, search deeper, and fish for longer to obtain the types of harvests more readily available a generation ago (*2*). In Thailand, for example, Burmese, Cambodian, and Thai men are increasingly sold to fishing boats, where they may remain at sea for several years without pay, forced to work 18- to 20-hour days (*4*). Starvation, physical abuse, and murder are common on these vessels.

Connections between wildlife depletion and labor injustice are not limited to fisheries. Terrestrial wildlife declines in West Africa have led to exploitative child labor practices (*5*). Communities that for thousands of years met their dietary needs by hunting in neighboring forests must now travel for days to find prey. The region's main source of animal protein, fish, has declined, increasing reliance on terrestrial wildlife (*6*). Cheap child labor enables hunters to extract wildlife from areas that would otherwise be too costly to harvest.

Wildlife-related conflict is not limited to labor injustice. Scarce wildlife species used

Downloaded from www.sciencemag.org on July 27, 2014

Published by AAAS



Global and local drivers. The growth of child slavery in fisheries provides an example of the complex linkages between wildlife decline and social conflict, as well as the multidisciplinary insights necessary to inform policy. In practice, interdisciplinary engagement cannot be easily parsed among simplistic categories, and many perspectives inform each step. Policy action must integrate disciplines to address feedbacks among failing fish stocks, weak governance, uncertain resource tenure, and pressure from international demand.

as luxury goods can draw extraordinary prices. For example, high demand and reduced supply have contributed to record prices in elephant and rhino products, with ivory recently sold for $3000/kg and rhino horn fetching $60,000 to $100,000/kg (*1*, *7*). As in the drug trade, such concentrations of value promote a cascade of social consequences. Huge profits from trafficking luxury wildlife goods have attracted guerilla groups and crime syndicates worldwide. In Africa, the Janjaweed, Lord's Resistance Army, al-Shabab, and Boko Haram poach ivory and rhino horn to fund terrorist attacks (*7*).

Conservationists have lamented the endangerment of species targeted by luxury trades. Yet disciplines beyond conservation biology—such as political science, economics, and international law—must be integrated with ecological perspectives to understand and address feedbacks between wildlife depletion and organized crime (*8*).

Conflict resulting from wildlife scarcity is not always catalyzed by organized crime. When governments lack the political will or capacity to defend access to declining wildlife, local stakeholders may take the job into their own hands, sometimes resorting to violence. These vigilante defense actions often escalate into broader social unrest.

For example, lacking an effective central government since 1991, Somalia's coast guard ceased to defend the country's exclusive economic zone. As foreign fishing vessels proliferated in Somali waters, local fishers seized offending boats and demanded payment. As the number of foreign fishers increased, violence escalated (*9*). Dozens of boats are now ransomed annually by well-armed pirates (many supported by foreign cartels), who long ago traded nets for heavy weaponry. Pirates have justified their actions as necessary to protect their sovereignty over offshore fishing grounds (*9*).

This path from resource defense to violent conflict, facilitated by weak governance, seems to be repeating itself in Benin, Senegal, and Nigeria, which are all witnessing increasing rates of piracy. In the words of a Senegalese fisherman, "in 10 years' time people will go fishing with guns.... We will fight for fish at sea. If we cannot eat, what do you expect us to do?" (*10*).

"wildlife decline may give rise to exploitative labor practices, empower profiteering groups who use violence to control illicit wildlife trades, and promote vigilante resource management."

TOWARD INTEGRATED POLICY. Initiatives like President Obama's wildlife task force, the International Consortium on Combating Wildlife Crime, and the new UN Office on Drug and Crime anti–wildlife trafficking program emphasize enforcement of antipoaching and antitrafficking laws. Such steps are useful but their reach is limited because they target outcomes rather than factors that underlie demand for wildlife. Combating trafficking should only be one part of integrative programs that consider ecological, socioeconomic, and institutional contexts in which wildlife conflict occurs (see the chart).

Several models already exist for such programs. At a global scale, the Intergovernmental Panel on Climate Change has brought together academics, government practitioners, and seasoned policy-makers. The formation of a similarly inclusive and far-reaching problem-based working group is long overdue for addressing the global decline of wildlife.

The Millennium Ecosystem Assessment provides a multidisciplinary platform on which such a working group could be built. The new United for Wildlife collaboration, led by the Duke of Cambridge, offers an organizational framework for integrating law

[1]Department of Environmental Science, Policy, and Management, University of California, Berkeley, CA 94720, USA. [2]Wildlife Health & Health Policy, Health and Ecosystems: Analysis of Linkages (HEAL) Program, Wildlife Conservation Society, Bronx, NY 10460, USA. [3]Department of Ecology, Evolution, and Marine Biology, University of California, Santa Barbara, CA 93106, USA. *Corresponding author. brashares@berkeley.edu

Published by AAAS

enforcement with biodiversity and livelihood conservation. However, such global efforts will only be sustained if the policies they create are enacted with strong funding and unfaltering political engagement.

At local and regional scales, policies that strengthen resource tenure may address both causes and consequences of wildlife conflict. Local governments have headed off social tension created by uncertain resource tenure by giving fishers and hunters exclusive rights to harvest grounds. Fiji's fishery, structured around territorial use rights, offers one example of effective management (*11*). Locally controlled management zones in Namibia have also demonstrated the ability of proactive policies to reduce poaching, stem wildlife decline, and improve local livelihoods (*12*). Government willingness to allow stakeholders to retain the bulk of revenues from harvests has been critical to the persistence of these programs.

Reducing or preventing wildlife conflict by strengthening local resource tenure has broad application but requires strong governance and an international commitment to recognize user rights. Organizations working to stem social conflict must address wildlife decline as a possible driver. Similarly, policies aimed at addressing wildlife decline must consider the social context of wildlife use and the feedbacks between wildlife scarcity and social conflict. Leadership must move beyond superficial reactions to elephant and rhino poaching and consider the complicated fate of the billions of people who rely on our planet's rapidly disappearing wildlife for food and income. ■

REFERENCES AND NOTES

1. Office of the President, *National Strategy for Combating Wildlife Trafficking* (U.S. Office of the President, Washington, DC, 2014).
2. Fisheries and Agriculture Department, *The State of World Fisheries and Aquaculture 2012* (Food and Agriculture Organization of the United Nations, Rome, 2012).
3. J. E. Fa, S. F. Ryan, D. J. Bell, *Biol. Conserv.* **121**, 167 (2005).
4. U.N. Office on Drugs and Crime, *Transnational Organized Crime in the Fishing Industry* (UNDOC, Vienna, 2011).
5. U.S. Department of Labor, Findings on the Worst Forms of Child Labor (2012); www.dol.gov/ilab/reports/child-labor/findings/.
6. J. S. Brashares *et al.*, *Science* **306**, 1180 (2004).
7. L. R. Douglas, K. Alie, *Biol. Conserv.* **171**, 270 (2014).
8. M. L. Gore, *Conserv. Biol.* **25**, 659 (2011).
9. J. Bahadur, *The Pirates of Somalia* (Pantheon Books, New York, 2011).
10. J. Vidal, "Will overfishing by foreigners drive Senegalese fishermen to piracy?" [blog], *The Guardian*, 3 April 2012.
11. R. Weeks, S. D. Jupiter, *Conserv. Biol.* **27**, 1234 (2013).
12. Namibian Association of Community-Based Natural Resource Management Support Organizations, *The State of Community Conservation in Namibia, Annual Report 2012* (NASCO, Windhoek, Namibia, 2013).

ACKNOWLEDGMENTS

This article was greatly improved by suggestions from four anonymous reviewers and supported by a NSF Dynamics of Coupled Natural and Human Systems grant.

10.1126/science.1256734

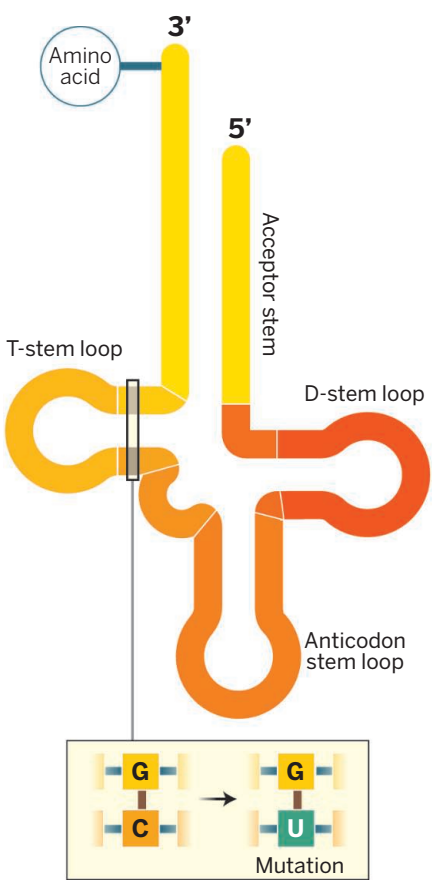
MOLECULAR BIOLOGY

Ribosome rescue and neurodegeneration

A mutation in a brain-specific tRNA reveals the link between ribosome maintenance and neuronal cell death

By **Jennifer C. Darnell**

Many human cognitive and neurodegenerative diseases are caused by alterations in the amounts of specific neuronal proteins, which are maintained at proper levels by regulation of their synthesis and turnover. For example, fragile X syndrome, a neurologic disease characterized by intellectual impairment and many behavioral symptoms including autism (*1*), results from loss of fragile X mental retardation protein (FMRP). FMRP normally reduces the synthesis of synaptic and other proteins (*2*). It achieves this by stalling ribosomes that are translating messenger RNA (mRNA) into protein. Aberrant protein synthesis that arises from the absence of FMRP is linked to neuron dysfunction. On page 455 of this issue, Ishimura *et al.* (*3*) reveal that loss of a protein that functions to release similar stalled ribosomes is linked to neuronal degeneration, but surprisingly, only in the presence of a second mutation in the protein synthesis machinery. This finding informs both critical translation mechanisms in the brain and the impact of modifying genes on disease symptoms. It thereby establishes a paradigm for understanding how a person's genetic makeup affects whether a specific mutation will lead to disease or be tolerated.



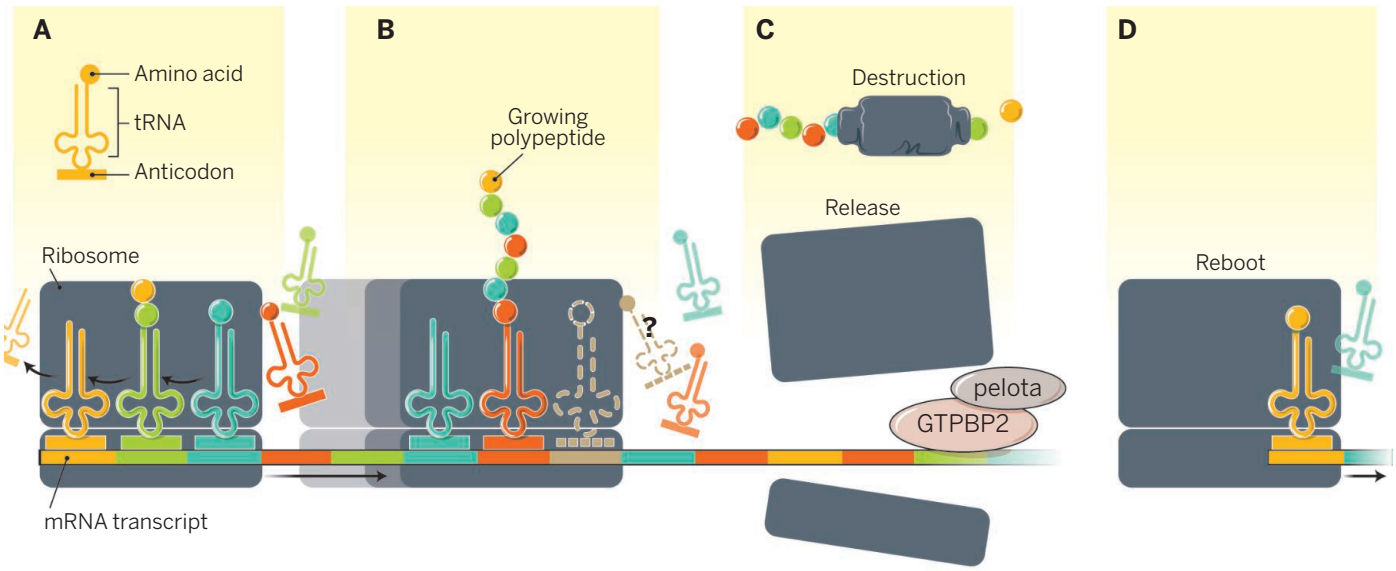
Isodecoder mutation. The predicted secondary structure of a brain-specific tRNA for arginine (in the mouse) is shown (*3*). The box indicates the mutation in the T-stem loop that is linked to neurodegeneration.

Ribosomes move along a strand of mRNA one codon at a time, decoding each group of three nucleotides into an amino acid that is added to a growing polypeptide chain. This decoding involves transfer RNA (tRNA) molecules that recognize a specific mRNA codon by base pairing through their "anticodon" loop. To mediate the translation of mRNA code into a protein, the tRNAs must be "charged" with the appropriate amino acid specified by the anticodon, a reaction catalyzed by very specific enzymes called tRNA synthetases. Neurodegeneration can result from mutation in the domain of a tRNA synthetase responsible for confirming the correct amino acid specified by the anticodon. Such mutations cause the incorporation of the wrong amino acids into neuronal proteins (*4*).

Ishimura *et al.* set out to identify the genomic mutation underlying a form of neurodegeneration. They discovered that neuronal death in mice resulted from a mutation that caused loss of the guanosine triphosphate–binding protein 2 (GTPBP2). GTPBP2 is similar to a class of proteins called ribosome release factors that free ribosomes from mRNA when they have stopped translating protein. Some of these release factors help terminate the newly synthesized protein when the ribosome reaches a codon instructing it to stop. Others rescue stalled ribosomes that have encountered aberrant early stop codons (*5*), have reached the 3′ end of mRNAs lacking a stop codon (*6*), or are stalled at codons

ILLUSTRATION: V. ALTOUNIAN/*SCIENCE*

Published by AAAS



Ribosome release. (**A**) Active translation by a ribosome scans mRNA to synthesize the corresponding protein. (**B**) This process stops if the ribosome cannot find tRNA bearing the appropriate anticodon. (**C**) The ribosome release factor GTPBP2 recruits another factor, pelota, to release the stalled ribosome. The unfinished protein is presumably degraded (perhaps by the proteasome). (**D**) The released ribosomal subunits can begin to synthesize a new protein.

lacking a matching, amino acid–charged tRNA. These latter forms of translational control can result in the degradation of the mRNAs associated with these aberrantly stalled ribosomes (*7*). Ishimura *et al.* show that GTPBP2 functions as a ribosome release factor in this protective pathway (see the second figure).

What Ishimura *et al.* then did is something often missing in similar studies—they tested whether the neurodegenerative effects of the GTPBP2 mutation were the same in the context of several different genetic backgrounds. Surprisingly, they found that loss of GTPBP2 only caused neuronal death in one particular genetic background of mice, the commonly used C57BL/6J strain. This suggested that this mutation was dependent on another gene for its effect. The authors set off on an arduous search for the second gene. They found it in a single nucleotide change in one of the tRNAs that decodes the codon AGA (A, adenine; G, guanine) (see the first figure), causing a marked decrease in its amounts. Remarkably, the authors found that expression of this particular tRNA—one of a set of five that all decode AGA as the amino acid arginine ("isodecoders")—is brain specific. Using elegant ribosome profiling experiments (*8*), Ishimura *et al.* generated a brain-wide map of where ribosomes are stalled, revealing that the mutations may interfere with the brain's ability to make proteins involved in carrying out translation itself, possibly leading to secondary effects on protein synthesis.

The impact of the work by Ishimura *et al.* can be felt on many levels. The authors have discovered a new ribosome release factor and by successfully identifying a modifying gene, have revealed much more about its function. Loss of GTPBP2 is only acutely felt when there is an increased need for it; this need is caused by excessive ribosome stalling that results from limiting amounts of a single tRNA. The further discovery that one tRNA in a set of isodecoders is expressed only in the brain raises the intriguing possibility that additional specific roles remain to be discovered within these gene families.

The strain specificity of the observed neurodegeneration sounds a wake-up call. The C57BL/6J strain is used in many labs, and the work by Ishimura *et al.* uncovers potential defects in brain protein translation in what the field considers to be "wild-type" or normal C57BL/6J mice. If one can extrapolate from the results of additional loss of GTPBP2, which amplifies the effects of limiting amounts of the tRNA, then it is possible that the wild-type mice also have altered synthesis of proteins involved in translation as well as in protein turnover, localization, mRNA processing, synaptic transmission, and regulation of the cytoskeleton.

Ribosome stalling in wild-type C57BL/6J mice may also be exacerbated under conditions where rapid or local synthesis of proteins is required in the brain—for example, when the strength of synapses (points of contact between neurons that facilitate communication) needs to be altered by changing their size, shape, and protein composition during learning. This is especially relevant in cases where this mouse genetic background is used to model human diseases in which a mutation may affect those pathways. The example of fragile X syndrome suggests that caution is warranted in making conclusions about the function of the translational regulatory factor FMRP based on results specific to its loss in only the particular genetic background of C57BL/6J mouse. However, as Ishimura *et al.* demonstrate, such strain specificity can also be a goldmine for discovering informative modifying genes. Both conclusions underscore the need for increased awareness of the effects of genetic background in model studies. ■

Laboratory of Molecular Neuro-Oncology, Rockefeller University, 1230 York Avenue, New York, NY 10065, USA. E-mail: jennifer.darnell@rockefeller.edu

ILLUSTRATION: V. ALTOUNIAN/*SCIENCE*

REFERENCES

1. M. R. Santoro, S. M. Bray, S. T. Warren, *Annu. Rev. Pathol.* **7**, 219 (2012).
2. J.C. Darnell, S.J. Van Driesche, C. Zhang, K.Y. Hung, A. Mele, C.E. Fraser, E.F. Stone, C. Chen, J.J. Fak, S.W. Chi, D.D. Licatalosi, J.D. Richter, R.B. Darnell, *Cell* **146**, 247 (2011).
3. R. Ishimura, G. Nagy, I. Dotu, H. Zhou, X.-L. Yang, P. Schimmel, S. Senju, Y. Nishimura, J.H. Chuang, S.L. Ackerman, *Science* **345**, 455 (2014).
4. J.W. Lee, K. Beebe, L.A. Nangle, J. Jang, C.M. Longo-Guess, S.A. Cook, M.T. Davisson, J.P Sundberg, P. Schimmel, S.L. Ackerman, *Nature* **443**, 50 (2006).
5. S. Kervestin, A. Jacobson, *Nat. Rev. Mol. Cell Biol.* **13**, 700 (2012).
6. T. Tsuboi, K. Kuroha, K. Kudo, S. Makino, E. Inoue, I. Kashima, T. Inada, *Mol. Cell* **46**, 518 (2012).
7. M. K. Doma, R. Parker, *Nature* **440**, 561 (2006).
8. N. T. Ingolia, S. Ghaemmaghami, J. R. Newman, J. S. Weissman, *Science* **324**, 218 (2009).

10.1126/science.1257193

Published by AAAS

BIOPHYSICS

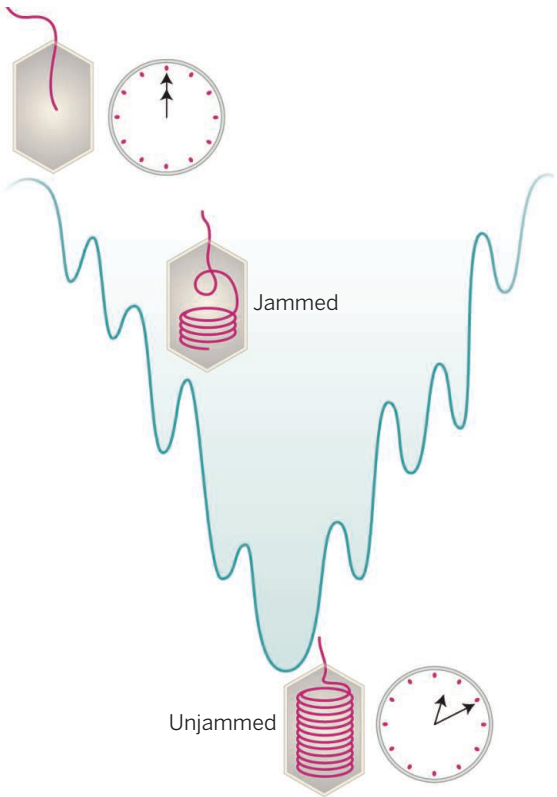
Ultraslow relaxation of confined DNA

DNA dynamics in tight spaces challenge nature's nanomachines

By Yann R. Chemla[1] and Taekjip Ha[1,2]

Polymers are ubiquitous and occur in many diverse forms, including cross-linked synthetic polymers (e.g., rubber and plastic) and biopolymers such as DNA and proteins. DNA has long been used as a model system for polymer science because long, chemically well-defined DNA chains can be prepared using its ability to self-replicate, and because it can be analyzed at the single-molecule level. For instance, the relaxation dynamics of a distorted DNA molecule eventually reverting to its lowest-energy configuration have been investigated extensively (*1*). There has been growing interest in understanding the relaxation of spatially confined polymers. How biopolymers such as DNA and proteins behave under high spatial confinement is important because they often experience such conditions—for example, when DNA passes through a narrow pore during viral packaging or bacterial conjugation. With the advent of nanotechnology (DNA is 2 nm in diameter), it has now become possible to study the relaxation dynamics of DNA confined in one (*2*) and two (*3*) dimensions. Berndsen *et al.* (*4*) have undertaken the first characterization of DNA relaxation under extreme confinement in three dimensions. Remarkably, they find that DNA relaxation under such circumstances is slowed by a factor of more than 60,000, presenting a daunting challenge for the biological machines that need to compact DNA reliably into tight spaces.

Extreme confinement of DNA can be achieved in viruses and bacteriophages (i.e., viruses that infect bacteria). They package their genome to near-crystalline densities in the smallest volume possible—a protein shell called the capsid typically only 50 to 100 nm in its largest dimension. Most double-stranded DNA bacteriophages and many eukaryotic viruses (notably, the herpes virus) use powerful molecular motors to reel in newly replicated viral DNA into empty, preformed capsids. Using the energy of adenosine triphosphate (ATP) hydrolysis, this motor must work against tremendous pressure as high as 2 to 6 megapascals (*5*, *6*). These pressures are believed eventually to drive DNA ejection into new host cells for infection.



A tight fit. During packaging of the viral genome into its capsid, DNA can become kinetically trapped in nonequilibrium conformations, generating high resistances against the packaging motor. Relaxation to the lowest-energy state is extremely slow.

Recent single-molecule measurements (*7*) have provided important new insights into the mechanism of viral DNA packaging. Smith *et al.* (*5*) used optical traps to pull on an individual DNA molecule as it is packaged into a single ϕ29 phage. Their work established that packaging slows down as DNA fills the capsid because of the build-up of internal pressure within the capsid. Berndsen e*t al.* (*4*) used this assay to investigate the dynamics of the confined DNA inside the capsid. During the reaction, they stalled packaging complexes with a non-hydrolyzable ATP analog, then restarted them with ATP after a variable wait ranging from 1 to >10 min. Surprisingly, packaging became faster upon restarting if the ϕ29 capsids were nearly filled to capacity when they were stalled; this finding suggests that densely packed DNA can become kinetically trapped in nonequilibrium conformations that jam the motor. Stalling the motor allows DNA time to relax to its lowest-energy state and to present a lower resistance to packaging, leading to an acceleration of the packaging reaction. The fact that the effect was more pronounced after stalls longer than 10 min indicates that the relaxation time scales must be longer than those of unconfined DNA of the same length by a factor of 60,000 (*1*).

In addition, 1- to 10-s pauses that had been observed during the late stages of packaging became all but eliminated by stalling and restarting of the motor, corroborating an early proposal that these pauses represented the motor's response to local jamming of the DNA (*5*). Late-stage packaging is also marked by increasing variability in speed, suggesting that multiple pathways are used with different resistances. Again, stalling and restarting reduced this variability. These findings suggest that packaged DNA can reorganize over multiple spatial and temporal scales. Several factors may affect DNA mobility under extreme confinement. DNA-DNA interactions play an important role. Spermidine^{3+}, which induces attractive interactions between DNA molecules by neutralizing the negative phosphate charge, increased the pause frequency and duration and the variability in packaging speed. Paradoxically, this DNA condensing agent actually impedes packaging by enhancing DNA-DNA interactions (*8*).

The ultraslow dynamics have a number of implications for the viral packaging mechanism. Because the relaxation time scales in ϕ29 exceed the duration of the entire packaging reaction, the motor must overcome large fluctuations in resistance because of ultraslow DNA dynamics. On the other hand, because cell infection occurs much later in the viral life cycle, presumably allowing more time for the viral DNA to relax to its lowest-energy conformation, the forces

[1]Department of Physics, Center for the Physics of Living Cells, and Center for Biophysics and Computational Biology, Institute for Genomic Biology, University of Illinois at Urbana–Champaign, Urbana, IL 61820, USA. [2]Howard Hughes Medical Institute, University of Illinois at Urbana–Champaign, Urbana, IL 61820, USA. E-mail: ychemla@illinois.edu; tjha@illinois.edu

ILLUSTRATION: P. HUEY/*SCIENCE*

Published by AAAS

that drive DNA ejection into the host are likely to be smaller than those resisting packaging, which may limit the role of pressure in DNA ejection. Berndsen *et al.* propose that relaxation of confined DNA may occur by a reptation-like mechanism, the time scales of which depend on the cube of genome length. If so, relaxation time scales would be even longer for bacteriophages and viruses with genomes longer than that of ϕ29 (e.g., λ, T4, T7, and herpes virus) (*9*). Because the time to complete packaging is expected to be similar for many of these systems (*10*), this potentially presents an even bigger challenge to their packaging motors. Interestingly, under certain conditions, T4 is also known to "unpackage" DNA (*11*), allowing its genome to exit the capsid in a controlled and reversible manner. It is tantalizing to speculate that this mechanism could allow the motor to "unjam" DNA.

A number of issues remain to be addressed. More precise measurements of relaxation times as a function of filling fraction will aid theoretical models of polymers, because such models often lack accurate relaxation time scales. It will also be important to connect the observed slow relaxation to the mechanism of the packaging motor and to the organization of the DNA inside the capsid. Another recent optical trap study (*12*) showed that the motor rotates DNA as it packages it, and that the rotation pitch changes as the capsid becomes filled. This is potentially related to the spool structure proposed for packaged DNA (*13*, *14*). It may be possible to study the prerelaxation conformations of the packaged DNA with the help of recent advances in cryoelectron microscopy. Direct visualization of confined DNA motion by single-molecule imaging may shed additional light on the packaging process. This system illustrates how biological processes exist far from equilibrium and how their study can provide an unexpected testing ground for the underlying physical theories. ■

REFERENCES

1. T. T. Perkins, S. R. Quake, D. E. Smith, S. Chu, *Science* **264**, 822 (1994).
2. W. Reisner *et al.*, *Phys. Rev. Lett.* **94**, 196101 (2005).
3. J. Tang *et al.*, *Macromolecules* **43**, 7368 (2010).
4. Z. T. Berndsen, N. Keller, S. Grimes, P. J. Jardine, D. E. Smith, *Proc. Natl. Acad. Sci. U.S.A.* **111**, 8345 (2014).
5. D. E. Smith *et al.*, *Nature* **413**, 748 (2001).
6. A. Evilevitch, L. Lavelle, C. M. Knobler, E. Raspaud, W. M. Gelbart, *Proc. Natl. Acad. Sci. U.S.A.* **100**, 9292 (2003).
7. Y. R. Chemla, D. E. Smith, *Adv. Exp. Med. Biol.* **726**, 549 (2012).
8. N. Keller *et al.*, *Phys. Rev. Lett.* **112**, 248101 (2014).
9. P. K. Purohit *et al.*, *Biophys. J.* **88**, 851 (2005).
10. V. B. Rao, M. Feiss, *Annu. Rev. Genet.* **42**, 647 (2008).
11. V. I. Kottadiel, V. B. Rao, Y. R. Chemla, *Proc. Natl. Acad. Sci. U.S.A.* **109**, 20000 (2012).
12. S. Liu *et al.*, *Cell* **157**, 702 (2014).
13. M. E. Cerritelli *et al.*, *Cell* **91**, 271 (1997).
14. L. R. Comolli *et al.*, *Virology* **371**, 267 (2008).

10.1126/science.1256359

CATALYSIS

Self-control tames the coupling of reactive radicals

Iridium complexes use two points of contact to control carbon-carbon bond formation

By **Guy C. Lloyd-Jones** *and* **Liam T. Ball**

Highly reactive or unstable chemical reagents are challenging to prepare, store, and safely handle, so chemists frequently generate them in situ from convenient precursors. In an ideal case, the rate of release of the reagent would be matched to the rate of its "capture" in the desired chemical reaction, thereby preventing the reagent from accumulating and minimizing any opportunity for decomposition. However, this synchronization is rarely achieved or even attempted: The rate of release is usually dictated by the conditions of the reaction (*1*), rather than being regulated by capture of the reagent. In this issue, Tellis *et al.* (*2*) on page 433 and Zuo *et al.* (*3*) on page 437 independently report the use of iridium photocatalysis (*4*, *5*) to supply highly reactive radical coupling partners ($R^{\cdot}$) to a nickel-catalyzed carbon-carbon bond-forming process (see the figure). Intriguingly, the two points of contact between the iridium and nickel cycles enforce autoregulated release of the radical, ensuring its efficient capture by nickel rather than its decomposition via other pathways.

Transition metal catalysts for the carbon-to-carbon coupling of complementary pairs of appropriately functionalized molecular building blocks are now a mainstay in modern organic synthesis, at least for unsaturated carbon sites (ones with double or triple bonds). Efficient coupling at saturated sites ("C_{sp3}" where the carbon has four single bonds) remains troublesome. An important difference between these processes is that C_{sp3} coupling generates three-dimensional molecular architectures that are of key importance to the pharmaceutical, agrochemical, and materials industries (*6*).

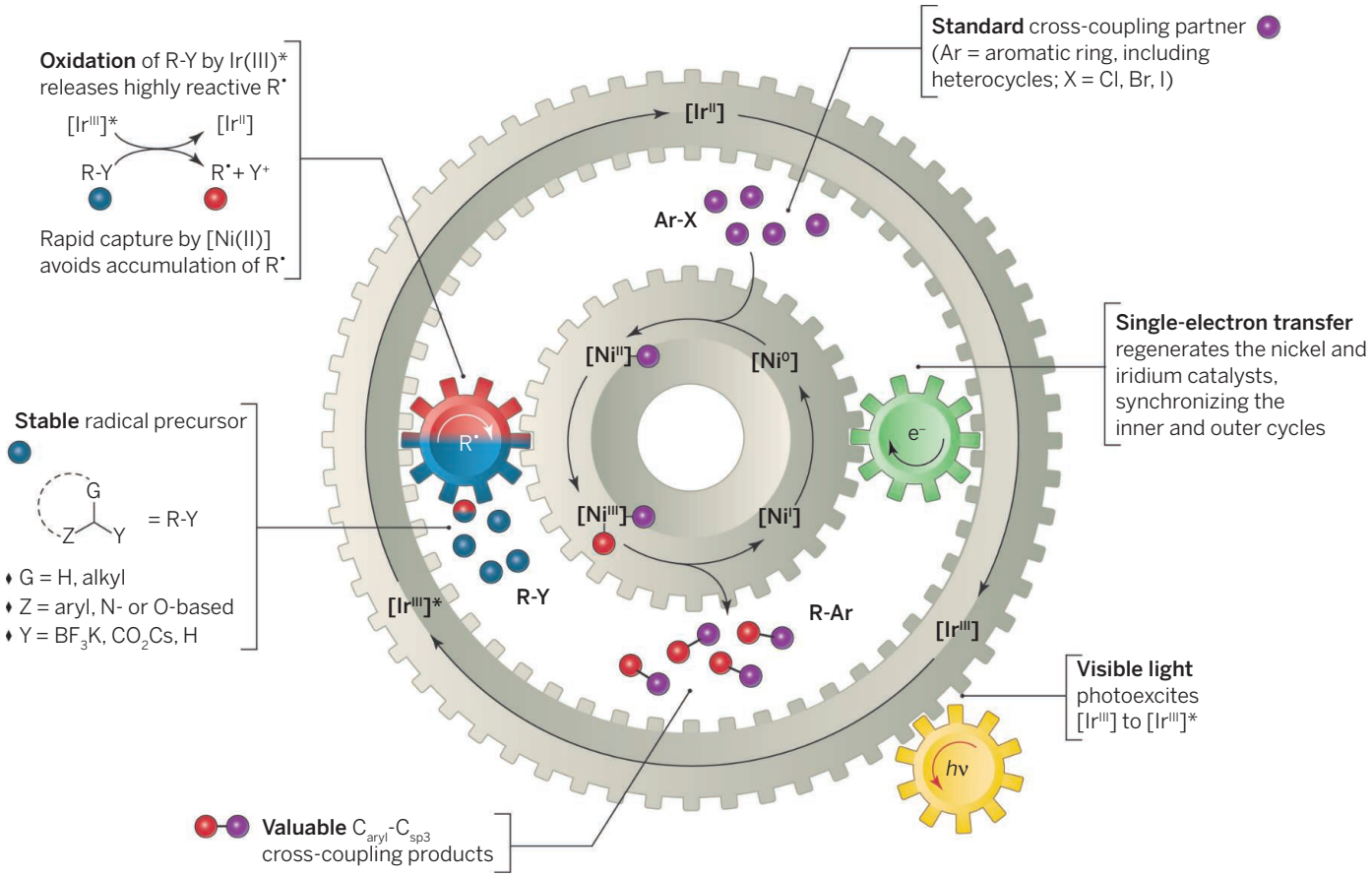
There are three primary reasons that C_{sp3} reaction centers are ill-suited to cross-coupling. The first is that the organic component transfers sluggishly to the metal catalyst. This problem precedes two more—the resulting organometallic species are frequently unstable, and also only slowly undergo the desired C-C bond formation ("reductive elimination"), exacerbating the instability problem (*7*). Cases of successful C_{sp3} couplings typically must address all three issues. The slow transfer is tackled by use of highly reactive C_{sp3} nucleophiles (the electron-rich component), which are inherently hard to control. The other two issues are suppressing side reactions at the metal center and accelerating the reductive elimination, which can be addressed through careful tuning of the metal catalyst (for example, altering its ligand sphere).

'The system is an example of an underexploited approach in synthesis: "autoregulated release" of reactive intermediates by synchronization of multiple catalytic cycles, a phenomenon that is ubiquitous in biochemistry.'

The reports of Tellis *et al.* and Zuo *et al.* offer an alternative and innovative solution to all three issues. The authors report high-yielding and selective formation of a new bond between an aromatic (benzene-like) ring and a C_{sp3} moiety ("R") with an aromatic halide ("Ar-X") coupling partner, and convenient precursor sources of the C_{sp3} component, in reactions that are simple to conduct and of substantial scope. At the heart of the new process is a photoexcited iridium complex ([Ir(III)]*) that oxidizes stable C_{sp3} precursors (R-Y, where Y is BF_3K, CO_2Cs, or H) to their corresponding organoradicals ($R^{\cdot}$), highly reactive species in which the sp^3 carbon now bears an unpaired electron. The radical does not accumulate, but instead is captured by an aryl-nickel(II) complex that "awaits" its arrival. Not only does the use of an organoradical overcome the usual reluctance for formation of the

School of Chemistry, University of Edinburgh, Edinburgh EH9 3JJ, UK. E-mail: guy.lloyd-jones@ed.ac.uk; liam.ball@ed.ac.uk

Published by AAAS



Driving chemistry with epicyclic gears. A schematic representation of cooperative iridium (outer) and nickel (inner) catalytic cycles for the cross-coupling of a stable radical precursor (blue spheres, R-Y) with an aryl halide (purple spheres, Ar-X), driven by an external source of visible light ($h\nu$). Two points of contact (smaller cogs on the left and right sides) synchronize the inner and outer cycles, ensuring autoregulated release of a highly reactive radical (red spheres, R•) to the awaiting nickel(II)-aryl intermediate.

C_{sp3} organometallic cross-coupling intermediate, it also generates a nickel(III) species that more readily undergoes reductive elimination, avoiding competing decomposition. A single electron transfer then reoxidizes the spent iridium photocatalyst and provides a nickel(0) species for addition to the Ar-X, thereby closing and synchronizing the two cycles.

The whole process proceeds under remarkably mild reaction conditions: The iridium photocatalysis is driven by visible light (simply using a household light bulb), avoiding ultraviolet photodegradation of the organic coupling partners. The organoradicals smoothly add to the nickel catalyst at ambient temperature, and unlike most couplings, there is no requirement for a strong exogenous base. Overall, these mild conditions suggest that the process can be extended to a wider range of coupling partners, including other unsaturated or saturated halides, or their more environmentally friendly equivalents (e.g., phenol derivatives), as well as radical precursors that do not benefit from a stabilizing group (Z in the figure). An important target for future development will be gaining access to single-enantiomer products, via full stereoconvergence of racemic radical precursors (R-Y) (*8*), the feasibility of which Tellis *et al.* preliminarily explored.

Consideration of the overarching mechanisms proposed for the couplings reveals that this first example of the successful confluence of iridium and nickel catalytic cycles relies on more than just the relay of an organoradical from one cycle to the other. The single-electron transfer provides a second point of contact between the two cycles, as illustrated by the gear systems in the figure. Neither cycle can operate independently of the other; the turnover of one cycle both determines and is controlled by the other. It is this "self-control" in the liberation of highly unstable radical reagents from the C_{sp3} component that facilitates their productive coupling, instead of their decomposition, as would occur if they were released en masse.

The system is an example of an underexploited approach in synthesis: "autoregulated release" of reactive intermediates by synchronization of multiple catalytic cycles, a phenomenon that is ubiquitous in biochemistry. This analysis also shows that, by modulating the relative concentrations of the two catalysts and by judicious choice of their initial point of entry into the system, the distribution of catalytic intermediates can be constrained to be predominantly in one or the other hemisphere of a cycle. This manipulation of the location of the so-called "catalyst resting state" provides wide-ranging opportunities for the development of novel catalyst systems for synthesis and for the installation of new modes of selectivity into ones already known (*9*). ■

REFERENCES

1. A. J. J. Lennox, G. C. Lloyd-Jones, *J. Am. Chem. Soc.* **134**, 7431 (2012).
2. J. C. Tellis, D. N. Primer, G. A. Molander, *Science* **345**, 433 (2014).
3. Z. Zuo *et al.*, *Science* **345**, 437 (2014).
4. D. M. Schultz, T. P. Yoon, *Science* **343**, 1239176 (2014).
5. C. K. Prier, D. A. Rankic, D. W. C. MacMillan, *Chem. Rev.* **113**, 5322 (2013).
6. F. Lovering, J. Bikker, C. Humblet, *J. Med. Chem.* **52**, 6752 (2009).
7. R. Jana, T. P. Pathak, M. S. Sigman, *Chem. Rev.* **111**, 1417 (2011).
8. C. J. Cordier, R. J. Lundgren, G. C. Fu, *J. Am. Chem. Soc.* **135**, 10946 (2013).
9. L. A. Evans, N. S. Hodnett, G. C. Lloyd-Jones, *Angew. Chem. Int. Ed.* **51**, 1526 (2012).

10.1126/science.1256755

ILLUSTRATION: GUY C. LLOYD-JONES AND LIAM T. BALL; ADAPTED BY P. HUEY/*SCIENCE*

Published by AAAS

ECOLOGY

Why are plant-pollinator networks nested?

Mutualistic communities maximize their structural stability

By **Samraat Pawar**

Interactions between species in a community may be mutually beneficial, competitive, or exploitative. The resulting ecological networks strongly influence the population dynamics of species (*1*). Nonrandom features of such networks may reflect organizing processes. For example, mutualistic networks such as plant-pollinator communities are "nested." Specialist pollinator species visit plant species that are subsets of those visited by more generalist pollinators (see the figure). But what drives the emergence of nestedness? On page 416 of this issue, Rohr *et al.* (*2*) provide theoretical and empirical evidence for the decade-old idea that nestedness prevails because it stabilizes mutualistic networks.

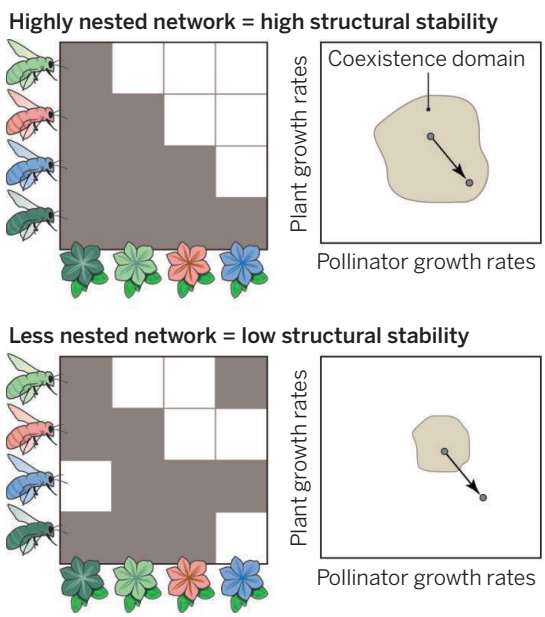
Different studies have produced conflicting results about the consequences of nestedness at the community level (*3*–*5*). Rohr *et al.* argue that these conflicts arise because most studies have focused on how nestedness affects Lyapunov stability. This type of stability analysis is concerned with whether, for a given community, population trajectories will return to an equilibrium point after they are perturbed from it (say, due to sudden reduction in the population densities of one or more species). Instead, Rohr *et al.* study whether nestedness improves structural stability. In ecological communities, structural stability analyses aim to determine whether a network feature (such as nestedness) widens or constricts the feasible region for multispecies coexistence when biological parameters are varied (*1*) (see the figure).

This shift from Lyapunov stability to structural stability, originally suggested in 1974 (*1*), has profound implications. Any equilibrium of a community cannot be permanent because real communities are not static: Individual species may undergo changes, e.g., in their growth rate, and the species composition of the community may change, e.g., when phenotypically different individuals immigrate or emigrate. Such changes are even more likely when individuals respond to changes in environmental conditions such as temperature (*6*). This is why it is necessary to ask whether a system will be structurally stable to changes in biological parameters.

Rohr *et al.* investigate how structurally stable mutualistic networks are to changes in the intrinsic growth rates of species. Intrinsic growth rate is a fundamental biological parameter that determines the absolute fitness of species' populations and varies with the metabolic rate (rate of energy use) of individuals. The intrinsic growth rate has typically been treated as a fixed parameter across all species in a community (*4*, *5*, *7*). Combining theory and data on the network structure of 23 communities, Rohr *et al.* show that more nested mutualistic networks permit multispecies coexistence for a wider range of species growth rates: They are more structurally stable (see the figure).

Rohr *et al.*'s results imply that if a community can explore a full range of species growth rates during assembly, nestedness is the configuration most likely to be observed because of the structural stability that it imparts. This is an important step toward reconciling previous results based on Lyapunov stability. However, it remains to be shown how maximization of structural stability affects Lyapunov stability. Insights may come from studies that allow ecological networks to assemble through a stochastic exploration of species growth rate combinations (*8*–*10*). These studies have found that as communities assemble, they become more resistant to invasions by new species, likely because they have come close to the center of the coexistence domain of growth rates (see the figure). At the same time, these communities tend to be less resilient (that is, they return more slowly to equilibrium after perturbations). This fragility may explain previous results showing that nestedness undermines resilience to perturbations (*4*, *11*).

Future work must take two critical factors into account. First, Rohr *et al.* study variations in growth rates independently of interspecific and intraspecific interaction parameters. Yet, these three sets of parameters are not independent and will covary, because they all depend on the metabolic rates of individuals. For example, both interaction and growth rates scale with body size (*12*, *13*). Second, the methods and the results of Rohr *et al.* cannot directly be applied to consumer-resource systems and only to certain classes of competitive systems. This is a crucial limitation that future work must strive to overcome, because mutualistic systems are typically embedded in a larger, more complex network of interactions that also include competitive and consumer-resource interactions. ■



Nestedness and structural stability. According to Rohr *et al.* (*1*), a highly nested network (top, fully nested in this case) has a high structural stability. This means that species can coexist over larger ranges of species' growth rates (gray shaded coexistence domain). A less nested network (bottom) will have lower structural stability (a smaller coexistence domain). Thus, perturbations to plant or pollinator growth rates can more easily displace an equilibrium point of the community out of the coexistence domain, resulting in one or more populations going extinct.

Department of Life Sciences, Imperial College London, Silwood Park, Ascot, Berkshire SL5 7PY, U K. E-mail: s.pawar@imperial.ac.uk

ILLUSTRATION: P. HUEY/*SCIENCE*

REFERENCES

1. R. M. May, *Stability and Complexity in Model Ecosystems* (Princeton Univ. Press, Princeton, NJ, 1974).
2. R. P. Rohr, S. Saavedra, J. Bascompte, *Science* **345**, 1253497 (2014).
3. S. Allesina, S. Tang, *Nature* **483**, 205 (2012).
4. U. Bastolla *et al.*, *Nature* **458**, 1018 (2009).
5. S. Suweis *et al.*, *Nature* **500**, 449 (2013).
6. A. I. Dell *et al.*, *Proc. Natl. Acad. Sci. U.S.A.* **108**, 10591 (2011).
7. A. James *et al.*, *Nature* **487**, 227 (2012).
8. S. Pawar, *J. Theor. Biol.* **259**, 601 (2009).
9. T. Fukami, *Popul. Ecol.* **46**, 137 (2004).
10. R. Law, R. D. Morton, *Ecology* **77**, 762 (1996).
11. P. P. A. Staniczenko, J. C. Kopp, S. Allesina, *Nat. Commun.* **4**, 1391 (2013).
12. S. Pawar *et al.*, *Nature* **486**, 485 (2012).
13. S. Tang, S. Pawar, S. Allesina, *Ecol. Lett.* 10.1111/ele.12312 (2014).

10.1126/science.1256466

Published by AAAS

METAMATERIALS

A cloaking coating for murky media

Objects shrouded in fog disappear entirely with simple coating

By **David R. Smith**

For centuries, magicians have created the illusion of invisibility with the assistance of smoke and mirrors: Mirrors redirect light and fool our eyes; smoke conceals the trickery. The concept of redirecting light has become routine in the ongoing development of "invisibility cloaks"—constructs of specially designed materials that can route light around an object, making it appear as if both the object and cloak are empty space. On page 427 of this issue, Schittny *et al.* (*1*) show how to use the other half of the magicians' tool kit, showing that objects in a smoky or "diffusive" environment can be perfectly hidden from sight.

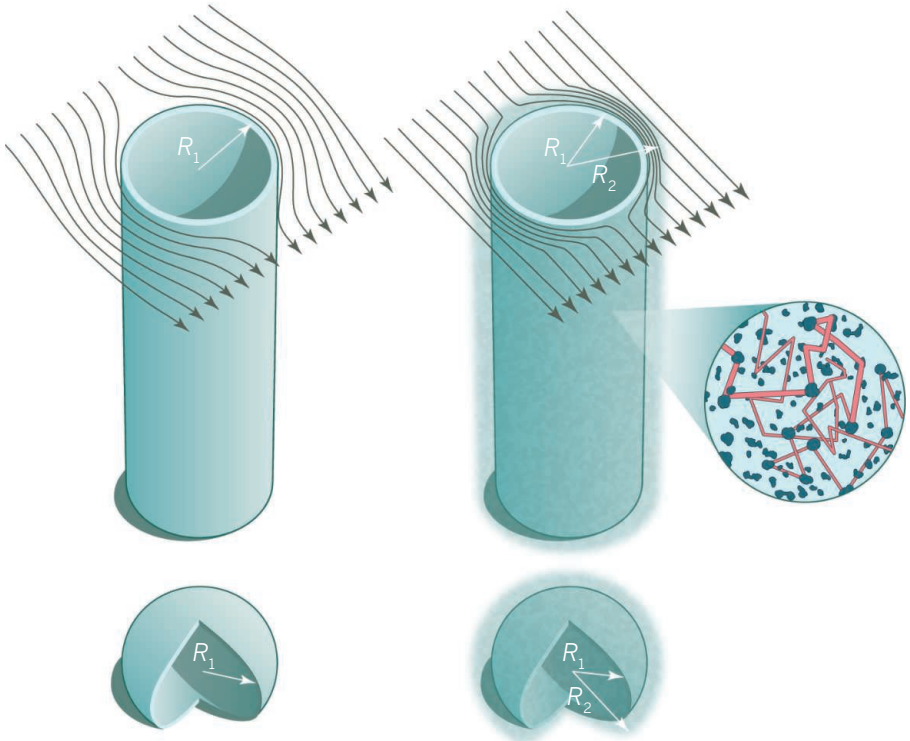
Although the challenges in creating an invisibility cloak are substantial, key advances in artificial materials—or metamaterials—during the past decade kept alive the dream of true invisibility. The requirements for an optical cloak are indeed stringent. A ray of light entering a cloak must not be reflected and must emerge from the cloak as if having passed through an equivalent region of empty space. A handful of theorems require that such a cloak must consist of a material with both electric and magnetic response, be anisotropic, and have properties that vary continuously throughout the cloak volume. Naturally occurring materials do not have enough flexibility to meet these requirements.

Motivated by the increasingly complex materials that were becoming achievable using metamaterials, Pendry *et al.* (*2*) suggested a new design tool, transformation optics, for cloaking. The propagation of light and other electromagnetic waves through a medium is described by Maxwell's equations; the material enters solely through two parameters: the electric permittivity, ε, and the magnetic permeability, μ. A conceptually simple coordinate transformation to Maxwell's equations produces an exact specification for a cloak, which can be represented as values of ε and μ that vary throughout the cloak structure. Schurig *et al.* (*3*) used this approach to demonstrate a metamaterial invisibility cloak at microwave frequencies.

While transformation optics allows for a perfect optical cloak, this cloak is ultimately limited by fundamental physics. Cloaking requires that a light ray traveling through the cloak arrive at the observer at the same time as a ray that would have passed through empty space. The diverted ray takes a longer path and would need to travel faster than the speed of light in vacuum, which Einstein's theory of special relativity rules out. A slight loophole in this limitation allows the ideal cloak to work over a very small bandwidth. Other types of wave phenomena do not possess the inviolable speed-of-light limitation. Transformation optical cloaks for sound waves, for example, can be much more easily realized, as recently demonstrated by Zigoneanu *et al.* (*4*).

If the object to be cloaked is much smaller than the wavelength of light, then the light need not be diverted to such an extent, and one might imagine cloaking would be considerably easier. Indeed, Alù and Engheta (*5*) suggested that a simple material coating could be applied to small objects in such a way that the composite would not scatter light. This approach of a material coating is obviously limited because subwavelength objects are effectively beyond the diffraction limit and not visually detectable anyway. However, the coating idea works for other physical phenomena that are not waves and do not have a wavelength as a parameter. To manage heat flow, for example, Xu *et al.* recently showed that a material with an appropriately chosen thermal conductivity could be fashioned into an extremely thin coating to achieve cloaking-like behavior—in this instance, keeping a desired area of a heated plate cool (*6*).

The idea that a simple coating could work as a cloak for heat flow and other physical phenomena prompted Schittny *et al.* to take another look at optical cloaking. Although light traveling in empty space is governed by the wave equation, light traveling through a fog or similarly dense, murky medium no longer travels in a straight



Cloaking in diffusive media. In a smoky or other strongly scattering medium, light propagates by bouncing randomly from one particulate to the next. As a result, light transport is better described by the mechanism of diffusion as opposed to wave mechanics (as shown on the right). In this diffusive regime, an invisibility cloak can be created by simply wrapping the object (with radius R_1) to be hidden with a thin shell of homogeneous composite material (which increases the radius to R_2). The trick developed by Schittny *et al.* is to select the diffusion constant of the cloak material in such a way that it perfectly cancels any scattering from the underlying object.

ILLUSTRATION: P. HUEY/*SCIENCE*

Center for Metamaterials and Integrated Plasmonics and Department of Electrical and Computer Engineering, Duke University, Durham, NC 27708, USA.
E-mail: drsmith@ee.duke.edu

Published by AAAS

line. Instead, the light bounces around—or diffuses—among the particulates in the medium, effectively traveling at a much lower speed than in vacuum. In this diffusive regime, Maxwell's equations no longer govern light transport; instead, the much simpler diffusion equation, known as Fick's law, takes precedence, with the diffusivity D being the sole material parameter that needs to be controlled, rather than the ε and μ of Maxwell's equations.

To investigate the cloaking of light in the diffusive regime, Schittny *et al.* immerse either a metal cylinder or sphere into a tank of water mixed with paint. The paint flakes in water form a suspension that, for light, produces a strongly scattering, diffusive medium—analogous to the smoke that a magician might use to obscure the audience's view. Patterns of light projected from a computer monitor are used to illuminate the cylinder, which blocks the light and forms a shadow easily viewed by the observer. Around the roughly 3-cm diameter of the cylinder, a material coating only 3 mm thick is applied, with a diffusivity designed to perfectly offset the scattering from the metal object. As a result, the entire object is rendered invisible relative to the medium—that is, the shadow is removed, and the light pattern from the monitor restored (see the figure).

So, while cloaking an object in empty space for light waves remains an unrealized goal, Schittny *et al.* have shown that if we alter the environment, slowing the light down and perhaps confusing it a bit, we can actually render objects completely invisible. It is a remarkable result in terms of its simplicity and yet completeness. Schittny *et al.* have cleverly changed the properties of the environment to achieve optical cloaking, rather than trying to create the challenging and inherently limited cloak for free space. Because the goal of invisibility is often to provide camouflage—where an object might go unnoticed relative to its environment, like a gecko changing its color to match the background scenery—the diffusive cloak is an intriguing concept and one that represents a convincing step forward for invisibility research. ■

REFERENCES

1. R. Schittny, M. Kadic, T. Bückmann, M. Wegener, *Science* **345**, 427 (2014).
2. J. B. Pendry, D. Schurig, D. R. Smith, *Science* **312**, 1780 (2006).
3. D. Schurig *et al.*, *Science* **314**, 977 (2006).
4. L. Zigoneanu, B.-I. Popa, S. A. Cummer, *Nat. Mater.* **13**, 352 (2014).
5. A. Alù, N. Engheta, *Phys. Rev. E Stat. Nonlin. Soft Matter Phys.* **72**, 016623 (2005).
6. H. Xu, X. Shi, F. Gao, H. Sun, B. Zhang, *Phys. Rev. Lett.* **112**, 054301 (2014).

10.1126/science.1256753

ILLUSTRATION: V. ALTOUNIAN/*SCIENCE*

NEUROSCIENCE

Astrocytes eyeball axonal mitochondria

Retinal neurons transfer mitochondria to astrocytes for rapid turnover to meet energy demands

By **Thomas C. Burdett** *and* **Marc R. Freeman**

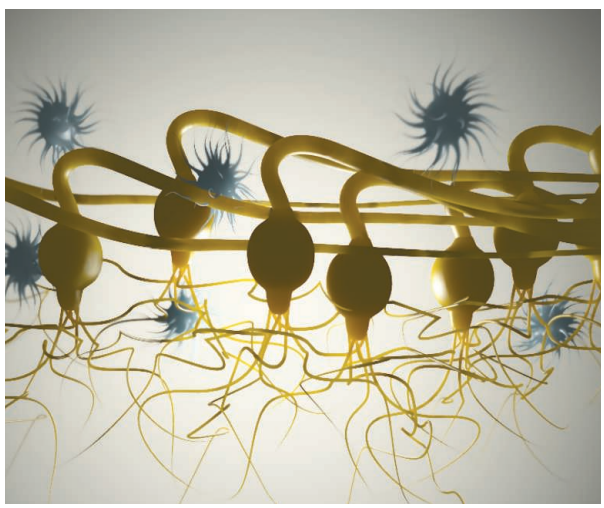
Sustaining a healthy population of mitochondria in a neuron requires a balance of de novo biogenesis of new mitochondria or mitochondrial components and removal of damaged mitochondrial membrane, proteins, and DNA (*1*, *2*). Recent evidence suggests that mitochondria must be actively transported between the cell body and axon (*2*). A new study by Davis *et al.* (*3*) offers a surprising alternative: Axons expel mitochondria to neighboring astrocytes for degradation. This unexpected finding might reshape how we think of mitochondrial disposal in the nervous system.

Axons enable long-distance communication in the nervous system by propagating signals to distant synapses at extraordinary lengths from the neuronal cell body. Axons within the spinal tract of the blue whale (perhaps the longest in nature) are estimated to exceed 30 m in length, and the longest human axons extend an average of 1 m from the base of the spine to the toes. By comparison, a neuronal cell body is less than 100 μm in diameter (*4*). Thus, long axons can represent the majority of a neuron's volume and pose a major logistical challenge to ship nutrients, organelles, and other biomaterials essential for maintaining axon integrity, synaptic connectivity, and neuronal function (*2*, *4*).

The active transport of organelles and vesicles, as well as the maintenance of membrane potential along the length of the axon, are energetically demanding tasks that require a constant supply of adenosine triphosphate from axonal mitochondria (*5*). As such, mitochondria must be both properly distributed and functioning efficiently to maintain neuronal energy homeostasis and neural activity (*2*, *6*).

Most newly formed mitochondria are transported from the cell body down the length of the axon and often fuse with resident mitochondria along the way (*2*). Mitochondrial fusion and fission together constitute an important quality-control mechanism that is believed to help adjust mitochondrial length and vitality, replenish supplies of biomolecules, and dilute out defective mitochondrial components (*1*). Such maintenance is essential not only for proper bioenergetic function, but also to prevent the release of reactive oxygen species or molecules that trigger programmed cell death (apoptosis) from partially depolarized mitochondria (*7*, *8*).

Ultimately, aged mitochondria are believed to become damaged irreparably, at which point cells discard them or fission off sections to be degraded through an autophagy-based process (mitophagy). Autophagosomes form around mitochondria, which then fuse with lysosomes, delivering digestive enzymes and accomplishing their degradation (*1*, *9*). Neuronal autophagosomes likely mature by fusing with endosomes and lysosomes during retrograde transport



Eye on mitochondria. Retinal ganglion cells in the optic nerve head of the mouse are enwrapped by astrocytes and rapidly turn over mitochondria to meet high metabolic demands.

Published by AAAS

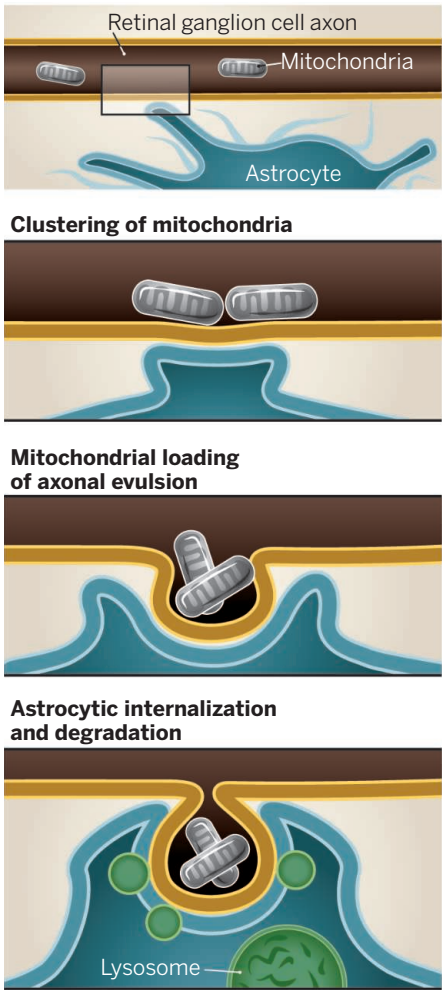
from the axon to the cell body (*10*). How or where mitophagy is induced in the axon, or precisely how many mitochondria are eliminated by autophagy versus alternate mechanisms (axonal or otherwise), is not clear (*11*).

A study of retinal ganglion cells at the optic nerve head in a mouse revealed that membrane-bound vesicles that were shed from their axons were internalized by surrounding astrocytes (*12*). Davis *et al.* further analyzed this shedding event. Using scanning electron microscopy and cell-specific labeling, they identified mitochondria as one of the major constituents of the shed axonal evulsions. A clear continuum of events was observed whereby mitochondria clustered in axons near sites of astrocyte membranes, evulsions from axons were filled with mitochondria, and shed evulsions were internalized by astrocytes. The authors further determined that the mitochondria-rich evulsions were degraded in astrocytes, as the organelles colocalized with lysosomal markers and were surrounded by astrocyte membranes.

To trace the fate of these mitochondria-rich evulsions in astrocytes, Davis *et al.* targeted a red/green, acid-resistant/acid-sensitive fluorescent protein to neuronal mitochondria. In healthy mitochondria, red and green signals colocalize, whereas the green fluorescence is eliminated in an acidic lysosomal environment. The authors confirmed that mitochondria undergoing lysosomal degradation were not in axons but in surrounding glia (astrocytes). They also detected degraded neuronal mitochondrial DNA in astrocytes. The study provides compelling evidence that retinal ganglion cells can transfer mitochondria to astrocytes for destruction rather than sending the organelles down the axon to the cell body for recycling. In addition, Davis *et al.* show that a majority of axonal mitochondria in the optic nerve head undergo degradation in surrounding astrocytes. This process therefore represents a major route for mitochondrial disposal from these neurons.

Retinal ganglion cells are particularly energy-hungry cells and may demand a level of mitochondrial turnover that exceeds axonal transport capacity. Their axons project through a variety of target regions in the brain, are unmyelinated in the retina but myelinated for the remainder of their length, and experience stressors such as light, varying intraocular pressure, and poor oxygen supply (*13*). Such an environment could stand in contrast to the more protected regions of the brain and nerve tracts, and so this may be a specialization of these neurons.

Department of Neurobiology, Howard Hughes Medical Institute, University of Massachusetts Medical School, Worcester, MA 01605, USA. E-mail: marc.freeman@umassmed.edu



Transmitophagy. Mitochondria cluster in the axon of a retinal ganglion cell in the optic nerve head. This forms an evulsion that is internalized by a nearby astrocyte. Mitochondria are then degraded in lysosomes.

However, one could also imagine low levels of transcellular mitochondrial degradation being dismissed as artifactual in these tissues or going wholly unnoticed because they are only readily identified by electron microscopy or with a fluorescent marker. Indeed, this phenomenon appears to be more widely used in the nervous system, as Davis *et al.* report the identification of similar mitochondria-rich protrusions in the superficial layers of the cerebral cortex of young mice.

Davis *et al.* have named this process of transcellular degradation of mitochondria "transmitophagy." But although cell-autonomous mitophagy is an autophagic event, it remains to be determined whether axonal mitochondria transferred to astrocytes are degraded by an autophagic process or a phagocytic event; both would result in the association of transferred material with lysosomal compartments. Key next steps include determining whether these particles are enclosed in a double membrane-bound vesicle, implying autophagy, or a single membrane-bound phagosome-like vesicle. Equally important is exploring whether this process is regulated by autophagic, phagocytic, or other signaling pathways.

The process of transmitophagy not only goes against dogma—cells don't necessarily autonomously destroy all of their own mitochondria—but it raises many intriguing questions about the biology of mitochondria, axons, and astrocytes. For instance, how do mitochondria tag themselves for disposal, cluster at the appropriate axonal site, and load themselves into these evulsions? It is also not clear whether this transcellular degradation process is specific for mitochondria, or is used to dispose of other axonal organelles. How astrocytes discriminate between axonal evulsions and healthy axonal material, and ultimately drive uptake and disposal of the correct target is also a curiosity. What drives the formation of evulsions, loading, and pinching off is also an open question. The finding also raises the question of whether signals are sent from the axon to the astrocyte to ensure uptake.

Even if transmitophagy is rare in healthy neuronal populations, it will be necessary to determine whether each neuron has the intrinsic capability to use this mechanism to dispose of unwanted mitochondria, if we wish to understand neuronal physiology, and whether it is up-regulated in response to stress or disease. Interestingly, Davis *et al.* noted an increase of transmitophagy in retinal ganglion cells after exposure to rotenone, an inhibitor of mitochondrial respiratory chain complex I. Autophagosomes containing mitochondria reportedly accumulate in neurodegenerative disease models (*9*, *14*). In these situations, transmitophagy may compensate for interruptions in axonal transport by intracellular aggregates or disruption of microtubule networks. Going forward, it will be exciting to explore a possible increase of transmitophagy as a neuroprotective target. ■

REFERENCES

1. R. J. Youle, A. M. van der Bliek, *Science* **337**, 1062 (2012).
2. Z. H. Sheng, *J. Cell Biol.* **204**, 1087 (2014).
3. C. H. Davis *et al.*, *Proc. Natl. Acad. Sci. U.S.A.* **111**, 9633 (2014).
4. D. H. Smith, *Prog. Neurobiol.* **89**, 231 (2009).
5. B. M. Morrison, Y. Lee, J. D. Rothstein, *Trends Cell Biol.* **23**, 644 (2013).
6. M. Sajic *et al.*, *PLOS Biol.* **11**, e1001754 (2013).
7. F. A. Court, M. P. Coleman, *Trends Neurosci.* **35**, 364 (2012).
8. D. Weaver *et al.*, *Mol. Cell* **54**, 870 (2014).
9. S. Maday, E. L. F. Holzbaur, *Autophagy* **8**, 858 (2012).
10. S. Maday *et al.*, *J. Cell Biol.* **196**, 407 (2012).
11. G. Ashrafi, T. L. Schwarz, *Cell Death Differ.* **20**, 31 (2013).
12. J. V. Nguyen *et al*, *Proc. Natl. Acad. Sci. U.S.A.* **108**, 1176 (2011).
13. D. Y. Yu *et al.*, *Prog. Retin. Eye Res.* **36**, 217 (2013).
14. Q. J. Wang *et al.*, *J. Neurosci.* **26**, 8057 (2006).

10.1126/science.1258295

ILLUSTRATION: V. ALTOUNIAN/*SCIENCE*

Published by AAAS

SURVEILLANCE OVERSIGHT

Who guards the guardians?

By **Kieron O'Hara** *and* **Nigel Shadbolt**



The NSA Report
Liberty and Security in a Changing World
The President's Review Group on Intelligence and Communications Technologies. Richard A. Clarke, Michael J. Morell, Geoffrey R. Stone, Cass R. Sunstein, and Peter Swire
Princeton University Press, 2014. 283 pp.

In an impressive display of tact, the word "Snowden" does not appear in the report of the U.S. President's Review Group on Intelligence and Communications Technologies. Nevertheless, the former system administrator's revelations demanded a serious response. *The NSA Report* certainly provides that, with 46 far-reaching recommendations.

The report signals the need for correction. Following 9/11, the USA PATRIOT Act (2001) was rushed into law, an early fusillade in the war on terror. Combined with the amended (2008) Foreign Intelligence Surveillance Act—"scrutinized" by the Foreign Intelligence Surveillance Court, whose procedures appear unbalanced and unchallenged—we have seen the emergence of new behaviors, such as "collect everything, minimize later." There is now no need to show probable cause, and retroactive immunity is provided for companies that provide the bulk data. To many, these developments appear to undermine the American way of life while claiming to defend it.



The report is a brilliantly readable guide to the world Snowden revealed; its clarity of analysis, proceeding from fundamental principles, impeccable. Its starting point is the U.S. Constitution, which seeks to "provide for the common defense … and secure the Blessings of Liberty to ourselves and our Posterity." The authors firmly reject the view that these positions conflict, arguing that "privacy is a central aspect of liberty, and it must be safeguarded."

We need to adapt surveillance practice to a multipolar world. The report argues that national security has to be balanced not only against privacy but also against other functions of government. The United States has to promote relations with its allies and to ensure that American firms are not unnecessarily disadvantaged abroad. Vital especially from the point of view of science and engineering is the need to maintain the integrity of the Internet and the Web. These global sociotechnical systems cannot function without trust in their integrity. When social networks have been appropriated by Russian oligarchs and artificially created by the United States to sow dissent in Cuba, it is obvious that rich information can be used against us or a whole nation. In this context, the recommendation to minimize the use government can make of legally acquired information is welcome. Rumors swirl about backdoors inserted into security technology at the behest of the U.S. (and Chinese) intelligence communities. The group's report is deadpan on this, writing in generalities. It is worth pointing out that the practice, if indeed prevalent, is borderline insane for all parties—a form of mutually assured destruction that may ultimately have to be limited by treaties akin to those restricting other technologies.

Foreign states have been outraged (however hypocritically) by spying on their leaders and commercial companies; one suspects little of that was terrorism-related. In response, Brazil was within an ace of insisting that data about Brazilians should be held on servers in Brazil, and even so its Marco Civil da Internet (2014) extends Brazilian law to cover any online service used by Brazilians. The European Union might react strongly, too, while Vladimir Putin has argued that the Internet is a CIA project. The balkanization of the Internet has never felt closer.

Against this background, the report's discussion of the treatment of non-U.S. persons is important, arguing that on the Internet the national-international distinction has virtually collapsed. The recommendation that disseminating information about non-U.S. persons only be done to protect U.S. national security is powerful and welcome. Would any president outlaw diplomatic or commercial spying? Probably not, but the review group makes a strong case. The application of the Privacy Act of 1974 to non-U.S. persons in the absence of specific suspicions is appropriate in the age of the cloud and consistent with the current policy of the Department of Homeland Security. It would help dispel the corrosive distrust, which is so damaging to the Internet.

The report is very sound on the invasive nature of metadata and the uselessness of much of this intelligence. The controversial recommendation to consider a civilian National Security Agency director follows from the nonobvious observation that recent intelligence-gathering has been driven by combat in Iraq and Afghanistan. But counterterrorism is not always a military matter, and so the recommendation logically reasserts the primacy of nonmilitary considerations.

The report is necessarily handicapped by the impossibility of predicting the future balance of power among president, Congress, media, and the so-called intelligence-industrial complex, and so it is hard to say that the recommended institutions will succeed where the current ones have failed. Recommendations for transparency are weakened by acceptance of the imperative to protect the integrity of intelligence programs. Doesn't this just beg the question? Government is many actors, not one, and we shouldn't underestimate their tendency to fight against one another in pursuit of individual targets. But overall separation and limitation of powers was at the heart of the U.S. Constitution. The vigilance that "is required in every age to maintain liberty" has to be applied not only to our enemies but also to those who would protect us. Governments around the world would do well to reflect on the principles that underpin *The NSA Report* and relate them to their own intelligence-gathering activities.

10.1126/science.1256398

The reviewers are at the Web and Internet Science Group, Electronics and Computer Science, University of Southampton, Highfield, Southampton SO17 1BJ, UK. E-mail: kmo@ecs.soton.ac.uk

PHOTO: MIGUEL JUAREZ LUGO/ZUMA PRESS/CORBIS

Downloaded from www.sciencemag.org on July 27, 2014

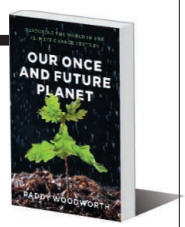
Published by AAAS

ENVIRONMENT

Repairing ecosystems

By **William E. Stutz**

Our Once and Future Planet
Restoring the World in the Climate Change Century
Paddy Woodworth
University of Chicago Press, 2013. 529 pp.



A few years ago, in an effort to become more aware of the ecological problems facing humanity, I started a personal list of threatened and degraded ecosystems around the world. The list produced more despair than enlightenment, and I gave it up. Paddy Woodworth's *Our Once and Future Planet* offers a belated but welcome counterweight to my abandoned list. He focuses on the relatively young field of restoration ecology, whose practitioners include scientists, philosophers, engineers, civil servants, and citizen volunteers undertaking nothing less than the regeneration and restoration of those same degraded ecosystems across the globe.

Woodworth, an Irish journalist whose two previous books focused on Spanish political struggles and Basque culture, has produced a hybrid volume. He intersperses a clear and thoughtful description of the historical and theoretical underpinnings of restoration ecology with detailed accounts of projects from around the world. Highlights include country-wide efforts to remove invasive trees in South Africa after the end of apartheid, the transformation of ill-fated farmland to native bush habitat in Western Australia, and the conservation and restoration of quickly disappearing bog lands in Ireland. These case studies are well chosen to illustrate the variety of challenges and approaches facing restorationists in their efforts to combat the loss of important and diverse ecosystems.

With such a young field, it is not surprising to find numerous tensions among practitioners. Through reflections on the primary literature and his interviews of many of the major players, Woodworth skillfully dissects the arguments surrounding the purpose and direction of ecological restoration. Most prominent is the debate over whether we should attempt to recreate or model restored ecosystems after "historical references"—natural assemblages of plants and animals that existed at some point in the past. This approach has dominated the field since its inception but has been repeatedly challenged by ecologists such as Roy Hobbs and even seen as "hopelessly nostalgic." By their reckoning, climate change will doom attempts to recreate historical ecosystems to failure. Instead, restoration ecologists need to embrace "novel ecosystems," assemblages of flora and fauna with no historical analogues. Whether such novel ecosystems will satisfy many of the goals of restoration ecology remains an open question.

The debate around just what those goals should be is almost as contentious as debates over novel ecosystems. Should restoration take into account "ecosystem services" such as food production, water retention, and soil formation? Or should the focus be on the restoration of nature for its own sake, with, as philosopher Bill Jordan puts it, "a studied disregard of human interests"? From this debate stem corollary discussions about the necessity of removing beneficial nonnative species and whether local communities and governments are motivated more by aesthetic or economic interests when deciding to spend money on restoration.

Because the book encompasses his own journey into the field, both literally and figuratively, Woodworth makes brief but effective use of narrative techniques to enhance his presentation. His descriptions of the people he meets are often charming and revealing. Ecologist Dan Janzen memorably "sits at his computer, totally focused, lean and muscular body stripped to the waist, long silver hair flowing like an Old Testament prophet's," while his partner in restoration Winnie Hallwachs's "Quakerish dress and diffident manner mask a powerful personality—a very useful gambit … for blending smoothly into the gender-conservative Costa Rican establishment." Woodworth also extensively quotes the scientists, project managers, and citizens he interviewed, allowing their conflicting views on restoration tactics or theory to push the narrative along.

Despite Woodworth's ambitious international itinerary, there is a conspicuous absence of restoration examples from some fast-growing and conflict-ridden regions such as South and East Asia and tropical Africa. One wonders whether hard-fought restorations in places like Costa Rica or New Zealand are truly representative of global efforts or simply islands of ecological progress on a planet of deteriorating landscapes.

In addition, Woodworth's account makes it difficult not to see the success of large-scale restoration projects as inextricably linked to the tireless efforts and political skills of their founders. As leaders such as Janzen, Guy Preston, and Keith Bradby relinquish their roles atop the organizations they have long embodied, what will become of the restorations they initiated? More broadly, what are the consequences of depending so heavily on extraordinary individuals to get projects off the ground?

Despite these concerns, I commend Woodworth for immersing himself in the field of restoration ecology so completely over the eight-year period spent writing the book. While not completely reversing my initial pessimism about Earth's ecological fate, *Our Once and Future Planet* makes a convincing case that we have, however hesitantly, begun a journey toward "'restoring the future.'"

10.1126/science.1256060



Easy to misread. The seemingly ancient oak woodlands around the medieval monastic churches of Glendalough, Ireland, cover slopes that were bare in the 19th century.

PHOTO: PADDY WOODWORTH/COURTESY UNIVERSITY OF CHICAGO PRESS

The reviewer is at the Department of Ecology and Evolutionary Biology, University of Colorado, Boulder, CO 80309–0334, USA. E-mail: william.stutz@colorado.edu

Downloaded from www.sciencemag.org on July 27, 2014

Published by AAAS





PHOTOS: (DOGS) ROGER DE LA HARPE/WWW.AFRICAIMAGERY.COM; (ELEPHANTS) LAUREN EVANS/WWW.GEOG.CAM.AC.UK/PEOPLE/L.EVANS AND WWW.SPACEFORGIANTS.ORG

Downloaded from www.sciencemag.org on July 27, 2014

LETTERS

Edited by **Jennifer Sills**

In defense of fences

HUMAN-DRIVEN HABITAT fragmentation reduces global biodiversity and ecosystem functioning (*1*). R. Woodroffe *et al.* ("To fence or not to fence," Perspective, 4 April, p. 46) claim that fencing, despite some positive outcomes (*2*, *3*), overwhelmingly exacerbates fragmentation and negatively affects wildlife conservation. They suggest that fencing should only be considered as a last resort and that fence removal is important for climate change preparedness.

Woodroffe *et al.* underplay the critical role fences play in habitat conservation and protection of livelihoods in tropical Africa, where scattered islands of natural habitat persist amidst a sea of agricultural encroachment, spared often through physical demarcation of protected area boundaries (*4*). In Africa, biomass extraction and subsistence/smallholder agriculture remain the dominant drivers of degradation (*5*). Although fencing can be problematic, especially for gene-flow [but see (*6*)] and large-scale mammal migration, it successfully arrests the gradual erosion of habitats, combats poaching, and can facilitate wildlife tolerance among communities (*7*).

Woodroffe *et al.* cite growing populations of unfenced carnivores/megaherbivores in North America as a model for other regions. Yet in Africa, the notion of rural communities enthusiastically sharing dwindling environmental space with wildlife is an ideal for which both wildlife and the rural poor suffer considerable costs (*8*). While it may be tempting to generalize across biogeographic realms, the billion-strong African population is expected to quadruple this century (*9*), with rising demands for land and increased potential for human-wildlife conflict. There is little evidence that large, sometimes dangerous, animals can successfully move through agricultural landscapes in the absence of fences, and it would be unwise to assume that islands of irreplaceable biodiversity would remain intact should fencing be removed.

Fences should be recognized as a fundamental conservation tool that may often be the best option for a specific set of circumstances. Decisions on fencing must be based on context-dependent evaluation of all alternatives, rather than dismissed as a last resort.

M. Pfeifer,[1,2]* C. Packer,[3] A. C. Burton,[4,5] S. T. Garnett,[6] A. J. Loveridge,[7] D. MacNulty,[8] P. J. Platts[2]

[1]Forest Ecology and Conservation Lab, Department of Life Sciences, Imperial College London, Ascot, SL5 7PY, UK. [2]York Institute for Tropical Ecosystems, Environment Department, University of York, York, YO10 5DD, UK. [3]Department of Ecology, Evolution and Behavior, University of Minnesota, St. Paul, MN 55108, USA. [4]Alberta Innovates Technology Futures, Victoria, BC V8Z 7X8, Canada. [5]Department of Biology, University of Victoria, Victoria, BC V8W 2Y2, Canada. [6]Research Institute for the Environment and Livelihoods, Charles Darwin University, Darwin, NT 0909, Australia. [7]Wildlife Conservation Research Unit, Department of Zoology, Oxford University, Oxford, OX13 5QL, UK. [8]Department of Wildland Resources, Utah State University, Logan, UT 84322, USA.

*Corresponding author.
E-mail: m.pfeifer@imperial.ac.uk

REFERENCES

1. S. H. M. Butchart *et al.*, *Science* **328**, 1164 (2010).
2. C. Packer *et al.*, *Ecol. Lett.* **16**, 635 (2013).
3. C. Packer *et al.*, *Ecol. Lett.* **16**, 1414-e4 (2013).
4. A. G. Bruner, R. E. Gullison, R. E. Rice, G. A. B. da Fonseca, *Science* **291**, 125 (2001).
5. B. Fisher, *Nat. Geosci.* **3**, 375 (2010).
6. M. Trinkel *et al.*, *Anim. Conserv.* **11**, 138 (2008).
7. M. J. Somers, M. Hayward, *Fencing for Conservation* (Springer, New York, 2012).
8. A. Balmford, T. Whitten, *Oryx* **37**, 238 (2003).
9. United Nations, ESA/P/WP.227 (2013); http://esa.un.org/.

Response

THE CONCLUSION OF PFEIFER *et al.*—that wildlife fencing should be context-dependent—echoes our own call for fencing decisions to be based on realistic assessments of the costs and benefits. We did not, as Pfeifer *et al.* suggest, state that fencing impacts were invariably negative, nor did we express a view that fence removal was imperative.

Pfeifer *et al.* emphasize circumstances in which fences encircle isolated wildlife areas embedded in a matrix of human activity. However, as stated in our Perspective, many fences are constructed within contiguous wildlife habitat. Some of these fences are constructed for conservation purposes (e.g., to contain rhinos within a well-guarded area) and some serve other purposes (e.g., to delineate private property). Whatever their purpose, the resulting barriers to wildlife movement will have environmental impacts that should be considered when deciding whether to construct or remove fences.

We agree with Pfeifer *et al.* that appropriately designed and well-maintained fences may contribute to wildlife conservation in small areas that are irretrievably isolated by human development. However, even in these circumstances, the likely benefits and costs need to be assessed carefully. As

Published by AAAS

detailed in our Perspective, the anticipated benefits of fencing are often not realized, and so the prospects of success need to be realistically evaluated. Moreover, it is important to bear in mind that patches of wildlife habitat may be less isolated than they appear. In contrast with Pfeifer *et al.*'s statement, there is growing evidence of dispersal between apparently isolated wildlife areas, for example by tigers (*1*), wolves (*2*), and elephants (*3*). Such movements across the human-dominated matrix may improve the viability of relatively isolated populations, and the consequences of breaking such connectivity through fencing need to be carefully considered.

We cited the paucity of fencing around reserves in North America as an illustration of alternatives rather than a model for other regions. Tolerance of wildlife movement in and out of many North American national parks may be related to sustainable use (including recreational hunting) on adjoining lands. This approach may or may not be appropriate elsewhere, but its success indicates that fencing is not the only way for societies to conserve large mammals while also pursuing economic development.

Fencing interventions are often less straightforward than they seem, and may have lasting and irreversible impacts. Conservationists need to pay attention to both positive and negative impacts, and consider a range of interventions, not just fencing, to design long-term solutions to wildlife conservation.

Rosie Woodroffe,[1]* Simon Hedges,[2] Sarah Durant[1,2]

[1]Institute of Zoology, Zoological Society of London, London, NW1 4RY, UK. [2]Wildlife Conservation Society, Bronx, NY 10460, USA.

*Corresponding author. E-mail: rosie.woodroffe@ioz.ac.uk

REFERENCES

1. P. A. Reddy *et al.*, *PLOS ONE* **7**, 9 (2012).
2. P. Ciucci, W. Reggioni, L. Maiorano, L. Boitani, *J. Wildlife Manage.* **73**, 1300 (2009).
3. N. Pinter-Wollman, L. A. Isbell, L. A. Hart, *Biol. Conserv.* **142**, 1116 (2009).

Early Americans: Misstated results

IN THE 16 MAY ISSUE of *Science*, we were part of a research team that reported the analysis of a late Pleistocene–age human skeleton found below sea level within a cave on Mexico's Yucatan Peninsula (*1*). Mitochondrial DNA extracted from this individual's tooth identified a subhaplogroup that is found today only among Native Americans. Based on our findings, we hypothesized that the morphological differences between these early people and modern Native Americans resulted from in situ evolution rather than separate ancestry. In the accompanying News & Analysis story "Bones from a watery 'black hole' confirm first American origins" (16 May, p. 680), M. Balter quoted J. C. Chatters discussing ideas that are his alone. Chatters is quoted as characterizing early Native Americans "with their large skulls and more forward-projecting faces" as a "human 'wild type'" distinct from modern Native Americans "with rounder and flatter faces" that "reflect a more 'domestic' form." The quoted comments do not reflect the research results and interpretations reported in our paper, and we do not endorse the ideas presented in this section of the News article. Our study has no bearing on the sociobehavioral life of ancestral Americans or other human populations. We joined the Hoyo Negro project because of our interest in understanding the physical, cultural, and genetic diversity of human beings through time and across space.

Douglas J. Kennett,[1]* Yemane Asmerom,[2] Brian M. Kemp,[3] Victor Polyak,[2] Deborah A. Bolnick,[4] Ripan S. Malhi,[5] Brendan J. Culleton[1]

[1]Department of Anthropology and Institutes of Energy and the Environment, Pennsylvania State University, University Park, PA 16802, USA. [2]Department of Earth and Planetary Sciences, University of New Mexico, Albuquerque, NM 87131–0001, USA. [3]Department of Anthropology and School of Biological Sciences, Washington State University, Pullman, WA 99164, USA. [4]Department of Anthropology and Population Research Center, University of Texas at Austin, Austin, TX 78712, USA. [5]Institute of Genomic Biology, University of Illinois, Urbana-Champaign, IL 61801, USA.

*Corresponding author. E-mail: djk23@psu.edu

REFERENCE

1. J. C. Chatters *et al.*, *Science* **344**, 750 (2014).

Early Americans: Respecting ancestors

AS ANTHROPOLOGISTS, archaeologists, and biologists, and as members of the National Academy of Sciences, we were startled to read J. C. Chatters' statement that the cranial morphology of early Native Americans "represented a human 'wild type,'" whereas more recent Native American cranial morphology reflected a "domesticated" form ("Bones from a watery 'black hole' confirm first American origins," M. Balter, News & Analysis, 16 May, p. 680). We are deeply offended by Chatters' implicit comparison of early Americans to the wild ancestors of today's domesticated animals.

We are disheartened to learn that there are those who continue to believe that cranial morphology carries implications of a presumed "wild" state. By so doing, they demean the very people they attempt to understand.

D. K. Grayson,[1]* D. J. Meltzer,[2] J. E. Buikstra,[3] K. V. Flannery,[4] C. S. Fowler,[5] J. Marcus,[4] J. F. O'Connell,[6] D. R. Piperno,[7] J. A. Sabloff,[8] B. D. Smith,[9] D. H. Thomas,[10] E. Willerslev,[11] M. A. Zeder[9]

[1]Department of Anthropology and Quaternary Research Center, University of Washington, Seattle, WA 98185, USA. [2]Department of Anthropology, Southern Methodist University, Dallas, TX 75275, USA. [3]School of Human Evolution and Social Change, Arizona State University, Tempe, AZ 85287, USA. [4]Museum of Anthropological Archaeology, University of Michigan, Ann Arbor, MI 48109, USA. [5]Department of Anthropology, University of Nevada, Reno, NV 89557, USA. [6]Department of Anthropology, University of Utah, Salt Lake City, UT 84112, USA. [7]Program in Human Ecology and Archaeobiology and Smithsonian Tropical Research Institute (Panama), National Museum of Natural History, Smithsonian Institution, Washington, DC 20560, USA. [8]Santa Fe Institute, Santa Fe, NM 87501, USA. [9]Program in Human Ecology and Archaeobiology, National Museum of Natural History, Smithsonian Institution, Washington, DC 20560, USA. [10]Division of Anthropology, American Museum of Natural History, New York, NY 10024, USA. [11]Centre for GeoGenetics, Natural History Museum of Denmark, University of Copenhagen, DK-1350 Copenhagen K, Denmark.

*Corresponding author. E-mail: grayson@uw.edu

Response

THE IDEAS I DISCUSSED with Balter, which were abbreviated in the story, are excerpted from a peer-reviewed article by me titled "Wild-type colonizers and high frequencies of violence among the Paleoamericans" (*1*). Domestication is not a foreign concept in discussions of human evolution. Literature on human self-domestication includes, among others, contributions by Leach (*2*) and Taylor (*3*). It is important to remember that, as Darwin effectively demonstrated more than 140 years ago in his *Descent of Man* (*4*), humans are subject to the same evolutionary processes as other species.

James C. Chatters

Applied Paleoscience, Bothell, WA 98011, USA. E-mail: paleosci@gmail.com

REFERENCES

1. J. C. Chatters, in *Violence and Warfare Among Prehistoric Hunter-Gatherers: Re-examining a Pacified Past*, M. Allen, T. Jones, Eds. (Left Coast Press, Walnut Creek, CA, 2014), pp. 70–96.
2. H. M. Leach, *Curr. Anthropol.* **44**, 349 (2003).
3. J. Taylor, *Not a Chimp: The Hunt to Find the Genes that Make Us Human* (Oxford Univ. Press, Oxford, 2009).
4. C. Darwin, *The Descent of Man and Selection in Relation to Sex* (John Murray, London, 1871).

Published by AAAS

At FDA, speedier approval could add uncertainty over risks

By **Kathy Wren**



In 1988, days after AIDS activists protested at the FDA for greater access to experimental drugs, the agency announced new regulations to speed up approval for certain medical products.

Officials at the Food and Drug Administration (FDA) must wrestle with a difficult paradox. Since the early 1960s, after the thalidomide tragedy, the agency has been charged with protecting the public from unsafe and ineffective medical products. At the same time, across society, the demand for faster access to new therapies has risen. As patients exhaust treatment options for serious or life-threatening conditions, their tolerance for risk may grow.

In an effort to balance prudence and innovation, the FDA has implemented a variety of new regulatory pathways to expedite the approval of new drugs and medical devices that meet certain conditions. But the benefits of these accelerated approaches must be weighed against their drawbacks, speakers cautioned at a 13 June event at AAAS headquarters in Washington, DC. The meeting was cosponsored by AAAS; the Program on Regulation, Therapeutics, and Law within the Division of Pharmacoepidemiology and Pharmacoeconomics of Brigham and Women's Hospital/Harvard Medical School; and the National Center for Health Research.

Scientific evidence is paramount to balancing the multiple demands on the Obama Administration, according to FDA Commissioner Margaret Hamburg. "At the end of the day, we have to be guided by science in everything we do. It has to be our compass," she said in a keynote address.

Several of these speedier approval pathways are specifically designed to allow FDA validation based on studies measuring "surrogate end points." Certain cholesterol levels, for example, have been proven to adequately reflect a patient's risk of having a heart attack, so a drug that reduces those levels may be presumed to lower cardiovascular mortality.

Forty-nine percent of the drug approvals by the FDA from 2005 to 2012 were based on surrogate end points, according to a study by Joseph Ross, an assistant professor of medicine and of public health at the Yale University School of Medicine. The numbers varied by medical specialty, with a full 80% of cancer drug approvals relying on these measurements.

As speedier approval pathways allow the use of surrogate measures in a wider variety of conditions, fewer of these measures are subject to the rigorous validation required of earlier FDA-authorized surrogates such as cholesterol levels or systolic blood pressure.

"We need to do better studies to validate whether these surrogates are as good as we think, and not just assume things about them," said Jerry Avorn, a professor of medicine at Harvard Medical School and chief of the Division of Pharmacoepidemiology and Pharmacoeconomics at Brigham and Women's Hospital.

Speakers at the meeting cited study design as another area of concern. While randomized, controlled clinical trials are the gold standard in medical research, this type of study is not always used when testing new medical products for FDA approval. And it is particularly rare for new devices, which are subject to different regulatory procedures from prescription drugs.

More than 90% of all new medical devices are not tested in clinical trials at all, according to Diana Zuckerman, president of the National Center for Health Research. And, when Rita Redberg, a cardiologist at the University of California, San Francisco, School of Medicine, investigated the approval of cardiovascular devices in the highest-risk category over an 8-year period, she found that only one-third were approved on the basis of a randomized clinical trial.

In some cases, bypassing a controlled trial may cost lives. An intracranial stent called the Wingspan Stent System was approved for use in stroke prevention on the basis of a 45-person study, according to Redberg. Instead of using a randomized control group, the researchers compared the patients' outcomes to those in a previous study. The FDA approved the Wingspan stent via the "humanitarian device exemption," which is intended to encourage the development of devices for treating rare diseases.

Later, a larger, randomized, controlled trial known as the SAMPRISS trial determined that 1 out of every 11 patients who received the Wingspan stent experienced a stroke or died. An FDA committee agreed that these data did not support the stent's use for stroke, and the agency recommended narrowing the official list of ways that the device should be used.

The SAMPRISS trial was able to gather data effectively because it required anyone using the device to be enrolled in the trial, and it may thus be a good model for future postmarket studies, Redberg suggested.

View the 2013 AAAS Annual Report
www.aaas.org/annual-report

CREDIT: FLICKR/FDAPHOTOS

Downloaded from www.sciencemag.org on July 27, 2014

Published by AAAS



Animals are rapidly disappearing from forests in Borneo and across the world.

PHOTO: CHRISTIAN ZIEGLER

Downloaded from www.sciencemag.org on July 27, 2017

Vanishing fauna

By **Sacha Vignieri**

During the Pleistocene epoch, only tens of thousands of years ago, our planet supported large, spectacular animals. Mammoths, terror birds, giant tortoises, and saber-toothed cats, as well as many less familiar species such as giant ground sloths (some of which reached 7 meters in height) and glyptodonts (which resembled car-sized armadillos), roamed freely. Since then, however, the number and diversity of animal species on Earth have consistently and steadily declined. Today we are left with a relatively depauperate fauna, and we continue to lose animal species to extinction rapidly. Although some debate persists, most of the evidence suggests that humans were responsible for extinction of this Pleistocene fauna, and we continue to drive animal extinctions today

INSIDE

NEWS
The empty forest *p. 396*

OPINION
An animal-rich future *p. 400*

REVIEWS
Defaunation in the Anthropocene *p. 401*

Reversing defaunation: Restoring species in a changing world *p. 406*

SEE ALSO
▸ PERSPECTIVE p. 376
▸ BOOK REVIEW p. 388

Published by AAAS

through the destruction of wild lands, consumption of animals as a resource or a luxury, and persecution of species we see as threats or competitors.

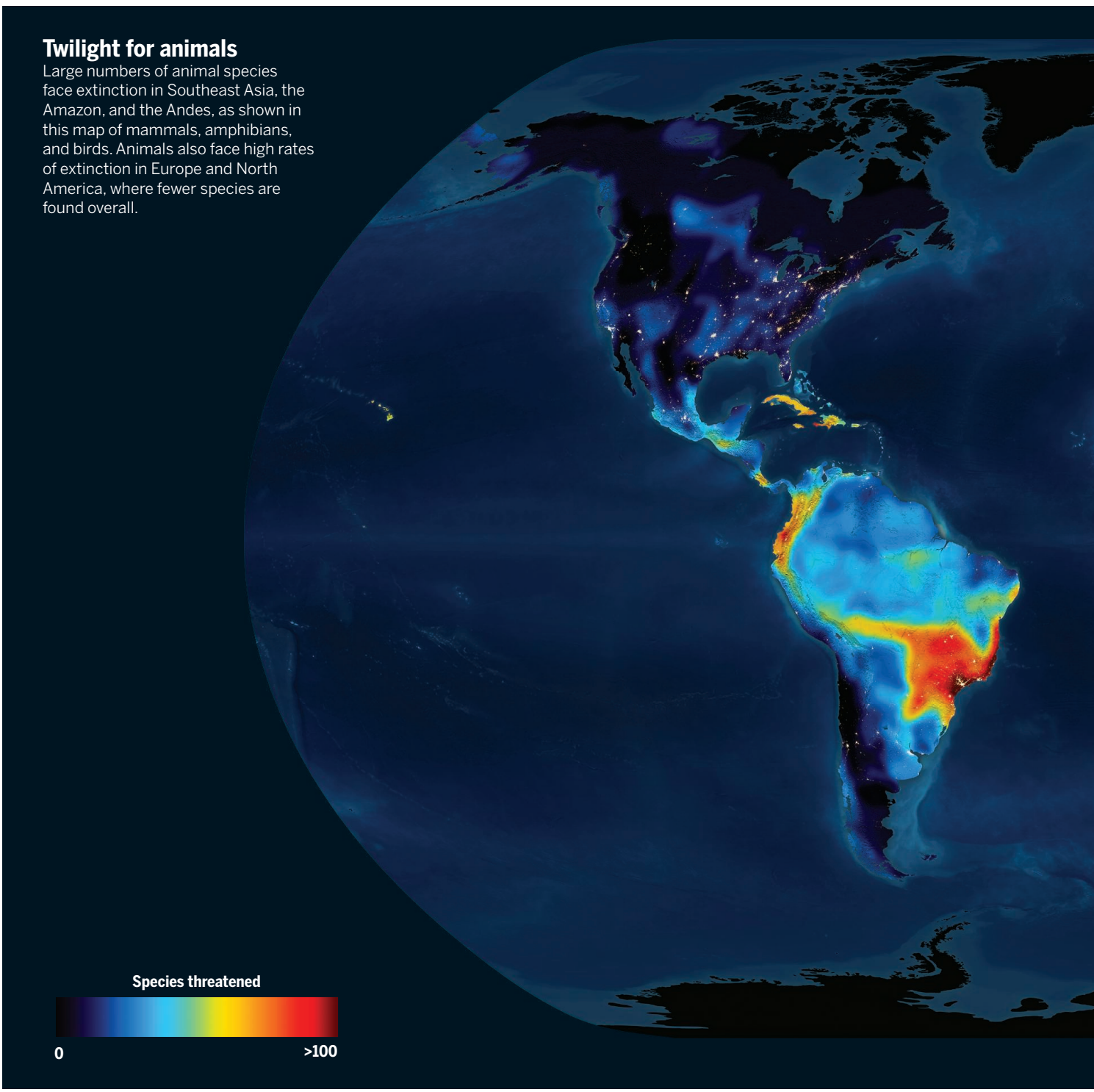
Such global loss of animal species, or defaunation, is increasingly recognized as a problem akin to deforestation in terms of scale and impact. Though for emotional or aesthetic reasons we may lament the loss of large charismatic species, such as tigers, rhinos, and pandas, we now know that loss of animals, from the largest elephant to the smallest beetle, will also fundamentally alter the form and function of the ecosystems upon which we all depend (see Dirzo *et al.*, p. 401).

Identifying the drivers of these extinctions is straightforward, but stemming the loss is a daunting challenge. Animal species continue to decline in, and disappear from, even large, long-protected reserves, due both to direct impacts, such as poaching, and indirect ecological feedbacks, such as habitat fragmentation. Though hunting and poaching might seem obvious candidates for targeted policy and management interventions, there are complex social issues underlying these activities that will require coordinated and cooperative actions by nations (see Brashares *et al.*, p. 376).

While stemming this loss remains a chal-

Twilight for animals

Large numbers of animal species face extinction in Southeast Asia, the Amazon, and the Andes, as shown in this map of mammals, amphibians, and birds. Animals also face high rates of extinction in Europe and North America, where fewer species are found overall.



MAP: FÉLIX PHARAND-DESCHÊNES (VISUALIZATION), CLINTON JENKINS (DATA PROCESSING), IUCN/BIRDLIFE INTERNATIONAL (DATA)

Published by AAAS

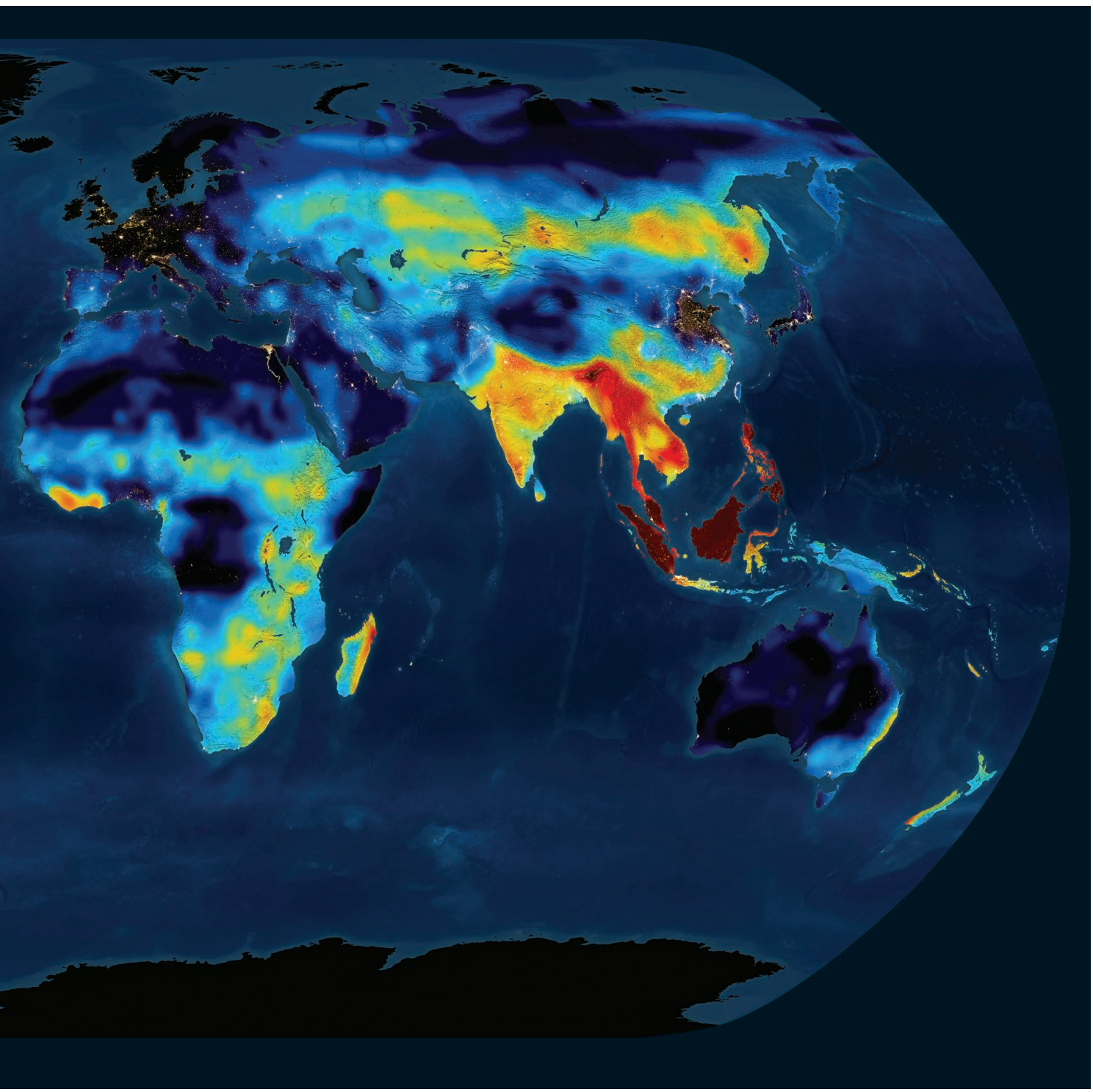
lenging goal, attempts to reverse the extinction trend are increasing. Such "refaunation" efforts involve a variety of approaches, including breeding animals in captivity, with the hope of reintroducing them to the wild, and assisting recolonization of areas where species have become locally extinct (see Seddon *et al.*, p. 406). Active reversal of animal extinctions is proving just as challenging as preventing extinctions in the first place, but a few success stories provide some hope.

ONLINE

View slideshow at sciencemag.org/special/vanishing

Many note and mourn the loss of animals but have not recognized that the impacts of this loss go beyond an aesthetic and emotional need to maintain animals as a part of nature. Current research reveals startling rates of animal declines and extinctions and confirms the importance of these species to ecosystems (see Stokstad, p. 396). Further, and more broadly, it suggests that if we are unable to end or reverse the rate of their loss, it will mean more for our own future than a broken heart or an empty forest. ■

This special issue has been edited by Sacha Vignieri, Andrew M. Sugden, and Elizabeth Pennisi.



Published by AAAS



A suspension bridge helps researchers study changes to the forest in Lambir Hills National Park.

PHOTO: CHRISTIAN ZIEGLER

Downloaded from www.sciencemag.org on July 27, 2014

Published by AAAS

The empty forest

A beleaguered national park in Borneo hints at what can happen when animals disappear

By **Erik Stokstad**

Darkness comes quickly at Lambir Hills National Park in western Borneo. The cicadas fall silent, and tree frogs start to chirp softly. Tourists and day hikers have left the ancient forest, so it is a good time to look for the slow loris, a shy arboreal primate. But one night, while ecologist Rhett Harrison was searching for wildlife, a man stepped out of the shadows. The hunter scowled; he knew he wasn't allowed to shoot the animals in the park. No one spoke. The man raised his bakakuk, a homemade shotgun. Unarmed and helpless, Harrison slowly backed away.

The encounter was a rare, heart-stopping event in several years of research at the park in the mid-1990s. Usually, Harrison only heard distant gunshots echoing through the forest or came across snares. But the cost of the hunting became clear with time. In Lambir—one of the most diverse forests in the world—the richness of animals has declined precipitously over the last 3 decades, work by Harrison and others has shown. Flying foxes, sun bears, gibbons, rhinoceros hornbills. All gone. "It's empty of large wildlife," says Richard Corlett of the Xishuangbanna Tropical Botanical Garden in Menglun, China. "There's been dramatic and rapid change."



PHOTO: KAREN KASMAUSKI

Deer and pigs are primary targets of hunters looking for meat to sell or eat.

Lambir is not alone in its defaunation, a process in which an ecosystem loses animals. Much of Asia, Africa, and Latin America also suffers from poaching and overhunting. In some places, the quarry are elephants, tigers, or other high-value species for the international black market. Elsewhere, hunters are just trying to put meat on the dinner table. "It's an epidemic that's going through tropical forest reserves," says Harrison, who works for the World Agroforestry Centre in Kunming, China.

In 1992, Kent Redford, then of the University of Florida, brought widespread attention to the potential fallout from this epidemic, arguing that the forest itself could not survive without the animals that help plants reproduce. "We must not let a forest full of trees fool us into believing that all is well," he wrote in *BioScience*. "An empty forest is a doomed forest."

Since then, researchers have been documenting animal losses and their consequences for a wide range of species and ecosystems including pollinators in farm fields and sharks on coral reefs. Lambir is a key case study. Long-term research on its vegetation is revealing how a forest changes when it loses the herbivores that once thinned saplings and the fruit eaters that dispersed seeds. Borneo is also the scene of more hopeful developments, as researchers and nongovernmental organizations seek ways to stem the damage. "Overhunting is bad for both people and wildlife," says Jedediah Brodie of the University of British Columbia, Vancouver, in Canada. "If we can make hunting sustainable, then it's a win-win."

What is not sustainable is the millions of metric tons of meat harvested in central Africa and the Amazon each year, or the impact of China's burgeoning demand for bear gallbladders and other animal parts used in traditional medicine. In the forests of Laos and Vietnam, few animals heavier than 80 grams can now be found. "There is deafening silence," says Carlos Peres of the University of East Anglia in Norwich, U.K.

Researchers exploring the impacts of defaunation consistently find that it favors plants with wind-dispersed seeds over those that rely on animals to disperse their seeds. In Panama, S. Joseph Wright of the Smithsonian Tropical Research Institute and colleagues have linked hunting to an increase

Published by AAAS





While some researchers study insects in the park, others have probed the fate of plants based on their fruit or seed.

in woody vines called lianas, which cast their seeds into the wind. Other studies in Peru, Thailand, and Nigeria have also shown changing patterns of plant distributions. But long-term studies in Lambir offered researchers a closer look at what happens to a forest as ever more animals disappear.

BORNEO'S INDIGENOUS NOMADS, the Penan, long made a living by hunting, but their impact was minimal. They would move their forest camps when the sago palm became scarce and game, as they put it, turned shy. In addition, their communities were small relative to the forest.

Life for the Penan and other peoples began to change rapidly in the 1970s. Loggers carved roads into previously isolated areas, making it easier for outsiders and migrants to hunt deep in the forest. They would take game back to village markets or sell it to the work camps. Although the Indonesian government had long since banned guns, dangerous homemade shotguns proliferated. Even more devastating has been the use of snares, which indiscriminately kill animals.

Yet well into the 1980s, Lambir (established in 1975) was reachable only by a dirt logging road. It would wash out in the rainy season, giving the park some protection. Helmeted hornbills filled the sky with the whoosh of their wings. Hunters covet these magnificent birds, because artisans carve the casque, a large, ivorylike protrusion on its upper beak. "It was as near to an undisturbed forest you could have had at that time," Harrison says.

Now, after decades of logging, the park is a lonely island in a sea of oil palm plantations. The road to the park was paved in 1987, easing access by tourists and nearby residents of Miri, the center of Borneo's petroleum industry. Its 6952 hectares contain waterfalls and sparkling pools. The trees growing on the clay soil are gargantuan, dwarfing those of the Amazon. "It's like being in a gothic cathedral," says Peter Ashton, a retired botanist who set up research plots there in 1964. The warm, moist air, smelling a bit like cigars, buzzes with insects. To many, especially newcomers, the park looks pristine.



But the forest is not what it was. The helmeted hornbill was long gone by the time Harrison arrived in 1994 to start his doctoral research on fig trees. And other species, such as the swan-sized rhinoceros hornbill and the gibbon, seemed rarer than they should have been. "I felt there was something wrong," Harrison recalls. It wasn't a big leap to suspect hunting. In addition to hearing the blasts of shotguns, he came across snares and evidence of hunters' camps.

In the evening, when Harrison and his colleagues drove to Miri, they would sometimes see sport hunters parked in large four-wheel-drive vehicles, shining spotlights into the forest to catch reflections of wild eyes. In the city, curio shops sold earrings made from hornbill casques. Vendors in the open-air market hawked small mammals in cages, ready to be cooked or taken home as pets.

Years later, Harrison decided to pull together the data about the decline in animal species. He went through previous records, interviewed older researchers, and walked his own surveys. The situation appeared grim: A camera-trap survey in 2004 detected only one bearded pig in 8 months. And when Harrison spent 6 months in the park in 2007, he couldn't find a single animal that weighed more than a kilogram. Not all animals are gone; small birds, rodents, and geckos persist, for example.

Harrison decided to explore the consequences of these losses, taking advantage of the data that the Smithsonian has collected at Lambir since 1991. Every 5 years, researchers and staff members spend about 9 months measuring each and every one of the 370,000 trees and saplings in a

PHOTOS: CHRISTIAN ZIEGLER (3)

Published by AAAS





Orangutans and rhinoceros hornbills are gone from Lambir, leaving only small creatures such as geckos (*lower left*).

52-hectare plot. Harrison and colleagues pored over books and museum records to figure out how these trees disperse their seeds. Then they analyzed how common each species was across the plant surveys.

The changes were dramatic. For all species, they found that the density of the saplings had increased by 25%, likely from the paucity of deer and other herbivores that thin new growth. The higher density of saplings could be a problem, as overcrowding can promote the spread of plant diseases. Even though there were more saplings, their diversity has fallen by 1.9% since 1992, they reported online in March 2013 in *Ecology Letters*.

This is large and rapid change for a rainforest, Harrison says, and it's due to the loss of seed dispersal by animals. Another impact: Compared with wind-dispersed species, saplings of fruit trees became more clustered around the adults, especially tightly so for species with large fruit. Eventually, the distribution of adult trees may shift, and some species could disappear.

A FIRM CONCLUSION ABOUT THE FATE of the forest is still elusive, as much is unknown about the demography of trees. "It can be overwhelming to go into a rainforest and try to understand anything," Brodie says. "There's just so much going on." Even Redford, who in 2011 established Archipelago Consulting in Portland, Maine, doesn't want to oversell the risk. "It's my suspicion that there is a lot more hype than data about



how everything goes to hell once the big animals are gone," he says. It could be that small, reclusive animals will take over the role of dispersing seeds, for example.

Lisa Curran of Stanford University, an anthropologist who studies land use change and biodiversity in Borneo, even questions how big a role hunting has played in Lambir's loss of fauna. The park may be simply too small to support many large animals, she says. And because it's surrounded by plantations, animals emigrating from other areas can't easily replenish the population.

Some officials and activists in various parts of Borneo are nevertheless taking action against overhunting and illegal trade, with mixed success. Enforcing hunting bans can be a challenge. This past December, wildlife rangers raided an open-air market in the state of Sabah. They confiscated 160 kilograms of unlicensed meat from sambar and barking deer. Angry villagers then hurled stones and machetes, damaging vehicles and injuring an officer. Many conservation groups shy away from confronting overhunting, because they don't want to be seen as hurting local livelihoods.

But some groups are helping head off poaching and illegal logging. For example, staff with the HUTAN-Kinabatangan Orang-utan Conservation Project patrol part of a 26,000-hectare wildlife sanctuary in northeast Borneo. And some local communities have stepped up as well. Sungai Wain Protection Forest, an upland reserve on the east side of Borneo, was protected after the nearby city of Balikpapan realized its importance for providing water for the local petroleum refinery. It retains abundant wildlife, including many rare birds and mammals. "You don't need a really great forest," Harrison says. "What you need is protection from hunting."

As for Lambir, many think the outlook is gloomy, at least in the short term. But not long ago, rhinoceros hornbills—the state emblem of Sarawak—were spotted in a nearby park. "I think the significance is huge," Harrison says. "It suggests that if hunting is controlled, at least some species like the hornbills that can fly substantial distances could reestablish." The hornbills might become an emblem of hope, a testament to the capacity of nature to heal. ■

PHOTOS: (LEFT TO RIGHT) CHRISTIAN ZIEGLER; © THOMAS MARENT/MINDEN PICTURES/CORBIS

Published by AAAS

OPINION

An animal-rich future

The rate at which animals are vanishing from this planet is one of the signatures of this age, as sure a sign of human dominance as our impact on Earth's nitrogen, phosphorus, and carbon cycles. This disappearance of animals from the world's ecosystems is generally a by-product of human activity, not an intentional act. Animals do matter to people, but on balance, they matter less than food, jobs, energy, money, and development. As long as we continue to view animals in ecosystems as irrelevant to these basic demands, animals will lose.

If we accept that humans now shape the future of this planet, the future for existing and extirpated fauna will depend on vision as much as on science. What type of world do we want to pass on, and what role do animals have in that world?

A responsible vision must include the dominating influence of people on the planet. The near future is likely to include 8 to 9 billion people, 3 billion more people in the middle class, a doubling of the terrestrial footprint of cities, and a transformation of global food and energy systems. A vision that includes a vital future for animals requires thinking beyond "restoration" and even beyond "rewilding." To maintain the animal diversity of the present and restore the animal abundance of the past, we must place animals squarely in a world where human systems are integrated with functioning natural systems. We cannot focus on recreating the ecosystems of the past—our impacts are making this untenable in most places—but we must not give up on nature or wildness, either.



"A vision that includes a vital future for animals requires thinking beyond 'restoration' and even beyond 'rewilding.'"

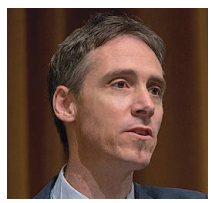
To begin, we need to recognize the importance of animals in all socioecological systems, pristine and human-dominated, terrestrial and marine. When we consider the benefits of a world rich with animals, we should shift some of our focus to systems where many people depend on animals. As an example, 2.6 billion people depend on ocean animals for protein.

In addition, we will have to grapple with tricky issues, such as those associated with the management of novel ecosystems and species substitution. There is also the potential application of synthetic biology, but the positive and negative impacts must be fully explored. How do we reduce the risks of ecosystem-level experimentation? When considering whether to introduce a new species into a system to replace the loss of another, for example, we must weigh the consequences of no intervention against the consequences of actions taken to recover ecological function. This is not a trivial exercise, as the ecological, economic, and cultural impact of an animal within an ecosystem is dynamic, and often obscured by complex ecological dynamics, shifting baselines (what a natural system "should" be like), and changing cultural norms. A full understanding of the relevant natural history, as well as the values of the people with a stake in the outcome, will be essential to any path forward. This is not entirely new territory, as our successes and failures in biological control can serve as a guide.

We cannot give up on the difficult species—the species that do not coexist well with people and require large areas for their survival. Conservation of these animals will hinge on recognition of their full value—ecological, economic, and cultural—by those with the power to protect them. A country with many large animals has as much right to development as a country without, and thus the global community must find pathways that would allow communities sharing their land with these animals to benefit from their presence.

Defaunation is a global issue. A world without animals represents a loss to humanity as much as a loss to ecology.

– Joshua J. Tewksbury and Haldre S. Rogers



Joshua J. Tewksbury is director of the Luc Hoffmann Institute at the World Wide Fund for Nature, Gland, Switzerland. E-mail: jewksbury@wwfint.org



Haldre S. Rogers is a faculty fellow in the Department of BioSciences, Rice University, Houston, TX, USA.

10.1126/science.1258601

PHOTOS: (LEFT) PAUL ROLLISON/FLICKR; (TOP RIGHT) NEXUS 2014/WATER FOOD CLIMATE AND ENERGY CONFERENCE; (BOTTOM RIGHT) SUSANNAH BARR

Downloaded from www.sciencemag.org on July 27, 2014

Published by AAAS

REVIEW

Defaunation in the Anthropocene

Rodolfo Dirzo,[1]* Hillary S. Young,[2] Mauro Galetti,[3] Gerardo Ceballos,[4] Nick J. B. Isaac,[5] Ben Collen[6]

We live amid a global wave of anthropogenically driven biodiversity loss: species and population extirpations and, critically, declines in local species abundance. Particularly, human impacts on animal biodiversity are an under-recognized form of global environmental change. Among terrestrial vertebrates, 322 species have become extinct since 1500, and populations of the remaining species show 25% average decline in abundance. Invertebrate patterns are equally dire: 67% of monitored populations show 45% mean abundance decline. Such animal declines will cascade onto ecosystem functioning and human well-being. Much remains unknown about this "Anthropocene defaunation"; these knowledge gaps hinder our capacity to predict and limit defaunation impacts. Clearly, however, defaunation is both a pervasive component of the planet's sixth mass extinction and also a major driver of global ecological change.

In the past 500 years, humans have triggered a wave of extinction, threat, and local population declines that may be comparable in both rate and magnitude with the five previous mass extinctions of Earth's history (*1*). Similar to other mass extinction events, the effects of this "sixth extinction wave" extend across taxonomic groups, but they are also selective, with some taxonomic groups and regions being particularly affected (*2*). Here, we review the patterns and consequences of contemporary anthropogenic impact on terrestrial animals. We aim to portray the scope and nature of declines of both species and abundance of individuals and examine the consequences of these declines. So profound is this problem that we have applied the term "defaunation" to describe it. This recent pulse of animal loss, hereafter referred to as the Anthropocene defaunation, is not only a conspicuous consequence of human impacts on the planet but also a primary driver of global environmental change in its own right. In comparison, we highlight the profound ecological impacts of the much more limited extinctions, predominantly of larger vertebrates, that occurred during the end of the last Ice Age. These extinctions altered ecosystem processes and disturbance regimes at continental scales, triggering cascades of extinction thought to still reverberate today (*3*, *4*).

The term defaunation, used to denote the loss of both species and populations of wildlife (*5*), as well as local declines in abundance of individuals, needs to be considered in the same sense as deforestation, a term that is now readily recognized and influential in focusing scientific and general public attention on biodiversity issues (*5*). However, although remote sensing technology provides rigorous quantitative information and compelling images of the magnitude, rapidity, and extent of patterns of deforestation, defaunation remains a largely cryptic phenomenon. It can occur even in large protected habitats (*6*), and yet, some animal species are able to persist in highly modified habitats, making it difficult to quantify without intensive surveys.

Analyses of the impacts of global biodiversity loss typically base their conclusions on data derived from species extinctions (*1*, *7*, *8*), and typically, evaluations of the effects of biodiversity loss draw heavily from small-scale manipulations of plants and small sedentary consumers (*9*). Both of these approaches likely underestimate the full impacts of biodiversity loss. Although species extinctions are of great evolutionary importance, declines in the number of individuals in local populations and changes in the composition of species in a community will generally cause greater immediate impacts on ecosystem function (*8*, *10*). Moreover, whereas the extinction of a species often proceeds slowly (*11*), abundance declines within populations to functionally extinct levels can occur rapidly (*2*, *12*). Actual extinction events are also hard to discern, and International Union for Conservation of Nature (IUCN) threat categories amalgamate symptoms of high risk, conflating declining population and small populations so that counts of threatened species do not necessarily translate into extinction risk, much less ecological impact (*13*). Although the magnitude and frequency of extinction events remain a potent way of communicating conservation issues, they are only a small part of the actual loss of biodiversity (*14*).

The Anthropocene defaunation process

Defaunation: A pervasive phenomenon

Of a conservatively estimated 5 million to 9 million animal species on the planet, we are likely losing ~11,000 to 58,000 species annually (*15*, *16*). However, this does not consider population extirpations and declines in animal abundance within populations.

Across vertebrates, 16 to 33% of all species are estimated to be globally threatened or endangered (*17*, *18*), and at least 322 vertebrate species have become extinct since 1500 (a date representative of onset of the recent wave of extinction; formal definition of the start of the Anthropocene is still being debated) (table S1) (*17*, *19*, *20*). From an abundance perspective, vertebrate data indicate a mean decline of 28% in number of individuals across species in the past four decades (fig. S1, A and B) (*14*, *21*, *22*), with populations of many iconic species such as elephant rapidly declining toward extinction (*19*).

Loss of invertebrate biodiversity has received much less attention, and data are extremely limited. However, data suggest that the rates of decline in numbers, species extinction, and range contraction among terrestrial invertebrates are at least as severe as among vertebrates (*23*, *24*). Although less than 1% of the 1.4 million described invertebrate species have been assessed for threat by the IUCN, of those assessed, ~40% are considered threatened (*17*, *23*, *24*). Similarly, IUCN data on the status of 203 insect species in five orders reveal vastly more species in decline than increasing (Fig. 1A). Likewise, for the invertebrates for which trends have been evaluated in Europe, there is a much higher proportion of species with numbers decreasing rather than increasing (*23*). Long-term distribution data on moths and four other insect orders in the UK show that a substantial proportion of species have experienced severe range declines in the past several decades (Fig. 1B) (*19*, *25*). Globally, long-term monitoring data on a sample of 452 invertebrate species indicate that there has been an overall decline in abundance of individuals since 1970 (Fig. 1C) (*19*). Focusing on just the Lepidoptera (butterflies and moths), for which the best data are available, there is strong evidence of declines in abundance globally (35% over 40 years) (Fig. 1C). Non-Lepidopteran invertebrates declined considerably more, indicating that estimates of decline of invertebrates based on Lepidoptera data alone are conservative (Fig. 1C) (*19*). Likewise, among pairs of disturbed and undisturbed sites globally, Lepidopteran species richness is on average 7.6 times higher in undisturbed than disturbed sites, and total abundance is 1.6 times greater (Fig. 1D) (*19*).

Patterns of defaunation

Although we are beginning to understand the patterns of species loss, we still have a limited understanding of how compositional changes in communities after defaunation and associated disturbance will affect phylogenetic community structure and phylogenetic diversity (*26*). Certain lineages appear to be particularly susceptible to human impact. For instance, among vertebrates, more amphibians (41%) are currently considered

[1]Department of Biology, Stanford University, Stanford, CA 94305, USA. [2]Department of Ecology, Evolution, and Marine Biology, University of California Santa Barbara, Santa Barbara, CA 93106, USA. [3]Departamento de Ecologia, Universidade Estadual Paulista, Rio Claro, SP, 13506-900, Brazil. [4]Instituto de Ecología, Universidad Nacional Autónoma de México, AP 70-275, México D.F. 04510, Mexico. [5]Natural Environment Research Council (NERC) Centre for Ecology and Hydrology, Benson Lane, Crowmarsh Gifford, Oxfordshire, OX10 8BB, UK. [6]Centre for Biodiversity and Environment Research, Department of Genetics, Evolution and Environment, University College London, Gower Street, London WC1E 6BT, UK.
*Corresponding author. E-mail: rdirzo@stanford.edu

threatened than birds (17%), with mammals and reptiles experiencing intermediate threat levels (*27*).

Although defaunation is a global pattern, geographic distribution patterns are also decidedly nonrandom (*28*). In our evaluation of mammals (1437 species) and birds (4263 species), the number of species per 10,000 km^2 in decline (IUCN population status "decreasing") varied across regions from a few to 75 in mammals and 125 in birds (Fig. 2), with highest numbers in tropical regions. These trends persist even after factoring in the greater species diversity of the tropics (*29*, *30*). Similarly, most of 177 mammal species have lost more than 50% of their range (*9*).

The use of statistical models based on life history characteristics (traits) has gained traction as a way to understand patterns of biodiversity loss (*31*). For many vertebrates, and a few invertebrates, there has been excellent research examining the extent to which such characteristics correlate with threat status and extinction risk (*32*–*34*). For example, small geographic range size, low reproductive rates, large home range size, and large body size recur across many studies and diverse taxa as key predictors of extinction risk, at least among vertebrates. However, these "extinction models" have made little impact on conservation management, in part because trait correlations are often idiosyncratic and context-dependent (*31*).

We are increasingly aware that trait correlations are generally weaker at the population level than at the global scale (*31*, *35*). Similarly, we now recognize that extinction risk is often a synergistic function of both intrinsic species traits and the nature of threat (*32*, *34*–*37*). For example, large body size is more important for predicting risk in island birds than mainland birds (*34*) and for

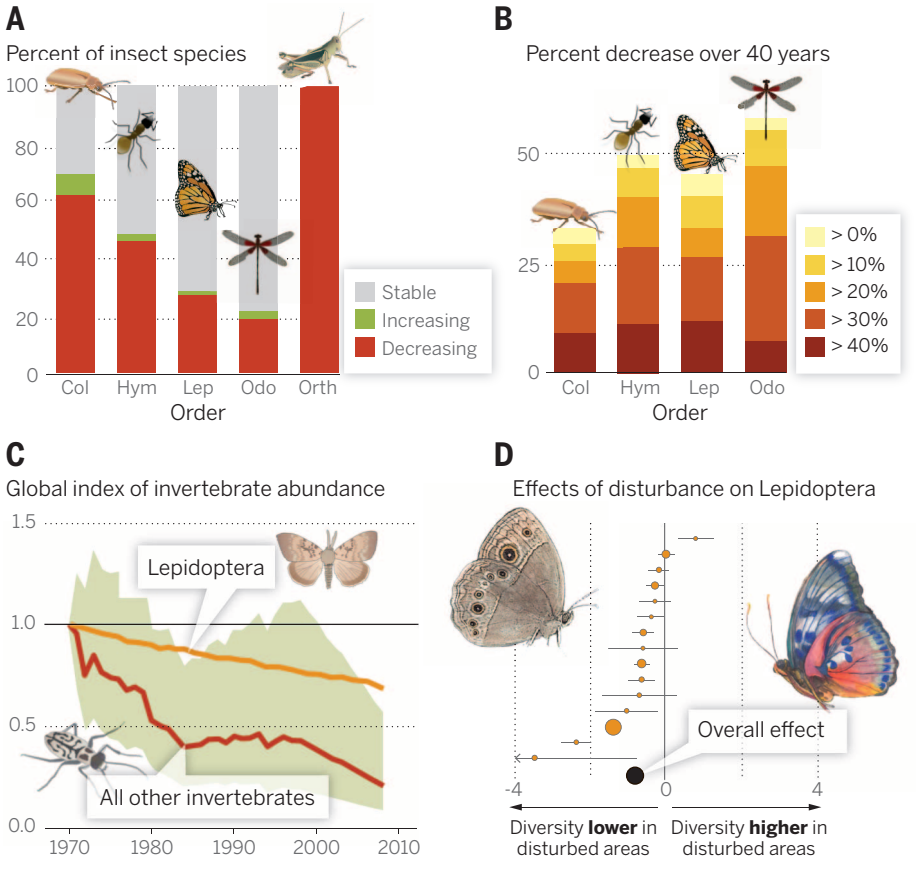


Fig. 1. Evidence of declines in invertebrate abundance. (**A**) Of all insects with IUCN-documented population trends, 33% are declining, with strong variation among orders (*19*). (**B**) Trends among UK insects (with colors indicating percent decrease over 40 years) show 30 to 60% of species per order have declining ranges (*19*). (**C**) Globally, a compiled index of all invertebrate population declines over the past 40 years shows an overall 45% decline, although decline for Lepidoptera is less severe than for other taxa (*19*). (**D**) A meta-analysis of effects of anthropogenic disturbance on Lepidoptera, the best-studied invertebrate taxon, shows considerable overall declines in diversity (*19*).

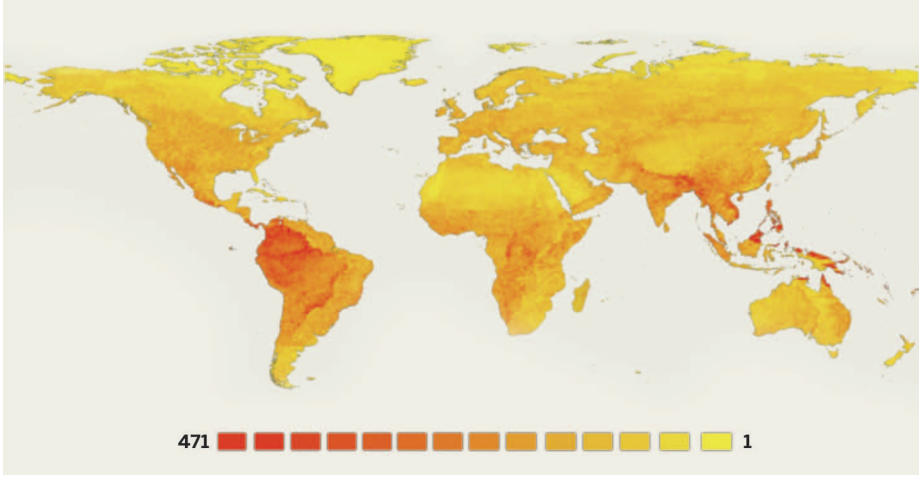


Fig. 2. Global population declines in mammals and birds. The number of species defined by IUCN as currently experiencing decline, represented in numbers of individuals per 10,000 km^2 for mammals and birds, shows profound impacts of defaunation across the globe.

tropical mammals than for temperate ones (*36*). However, increasingly sophisticated approaches help to predict which species are likely to be at risk and to map latent extinction risk (*38*), holding great promise both for managing defaunation and identifying likely patterns of ecological impact (*39*). For instance, large-bodied animals with large home ranges often play specific roles in connecting ecosystems and transferring energy between them (*40*). Similarly, species with life history characteristics that make them robust to disturbance may be particularly competent at carrying zoonotic disease and therefore especially important at driving disease emergence (*41*, *42*).

The relatively well-established pattern of correlation between body size and risk in mammals creates a predictable size-selective defaunation gradient (Fig. 3) (*19*, *36*, *43*). For instance, there are strong differences in body mass distributions among mammals that (i) became extinct in the Pleistocene [<50,000 years before the present (B.P.)], (ii) went recently extinct (<5000 years B.P., Late Holocene and Anthropocene), (iii) are currently threatened with extinction (IUCN category "threatened" and above), and (iv) extant species not currently threatened (Fig. 3), all showing greater vulnerability of larger-bodied species. The myriad consequences of such differential defaunation have been quantified via the experimental manipulation of the large wildlife in an African savanna (Fig. 4 and table S3), revealing substantial effects on biodiversity, ecological processes, and ecosystem functioning.

Multiple unaddressed drivers of defaunation

The long-established major proximate drivers of wildlife population decline and extinction in terrestrial ecosystems—namely, overexploitation, habitat destruction, and impacts from invasive species—remain pervasive (*18*). None of these major drivers have been effectively mitigated at the global scale (*14*, *18*). Rather, all show increasing trajectories in recent decades (*14*). Moreover, several newer threats have recently emerged, most notably anthropogenic climate disruption, which will likely soon compete with habitat loss as the most important driver of defaunation (*44*). For example, ~20% of the landbirds in the western hemisphere are predicted to go extinct because of climate change by 2100 (*45*). Disease, primarily involving human introduced pathogens, is also a major and growing threat (*46*).

Although most declining species are affected by multiple stressors, we still have a poor understanding of the complex ways in which these drivers interact and of feedback loops that may exist (*7*, *11*). Several examples of interactions are already well documented. For example, fragmentation increases accessibility to humans, compounding threats of reduced habitat and exploitation (*47*). Similarly, land-use change is making it difficult for animals to expand their distributions into areas made suitable by climate change (*25*, *48*). Feedbacks among these and other drivers seem more likely to amplify the effects of defaunation than to dampen them (*11*).

Consequences of defaunation

Because animal loss represents a major change in biodiversity, it is likely to have important effects on ecosystem functioning. A recent meta-analyses of biodiversity-ecosystem function studies suggests that the impact of biodiversity losses on ecosystem functions is comparable in scale with that of other global changes (such as pollution and nutrient deposition) (*9*). However, most efforts to quantify this relationship have focused largely on effects of reduced producer diversity, which may typically have much lower functional impacts than does consumer loss (*49*, *50*). Efforts to quantify effects of changes in animal diversity on ecosystem function, particularly terrestrial vertebrate diversity, remain more limited (*19*, *51*).

Impacts on ecosystem functions and services

We examined several ecosystem functions and services for which the impacts of defaunation have been documented that are either a direct result of anthropogenic extirpation of service-providing animals or occur indirectly through cascading effects (Fig. 5).

Pollination

Insect pollination, needed for 75% of all the world's food crops, is estimated to be worth ~10% of the economic value of the world's entire food supply (*52*). Pollinators appear to be strongly declining globally in both abundance and diversity (*53*). Declines in insect pollinator diversity in Northern Europe in the past 30 years have, for example, been linked to strong declines in relative abundance of plant species reliant on those pollinators (*54*). Similarly, declines in bird pollinators in New Zealand led to strong pollen limitation, ultimately reducing seed production and population regeneration (Fig. 5H) (*55*).

Pest control

Observational and experimental studies show that declines in small vertebrates frequently lead to multitrophic cascades, affecting herbivore abundance, plant damage, and plant biomass (*56*).

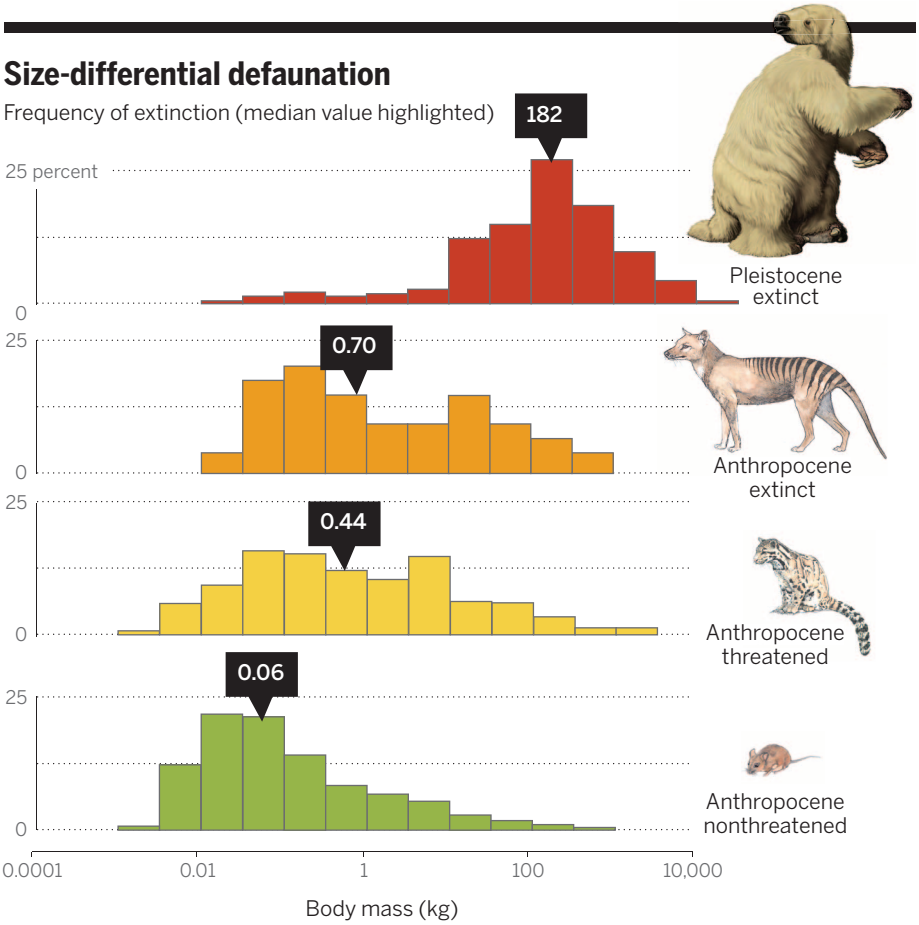


Fig. 3. Extinction and endangerment vary with body size. Comparing data on body size of all animals that are known to have gone extinct in Pleistocene or are recently extinct (<5000 years B.P.) shows selective impact on animals with larger body sizes (median values denoted with black arrow). Differences in body masses between distributions of currently threatened and nonthreatened species suggest ongoing patterns of size-differential defaunation (Kolmogorv-Smirnov test, $K = 1.3$, $P < 0.0001$) (*19*). [Animal image credits: giant sloth, C. Buell; others, D. Orr]

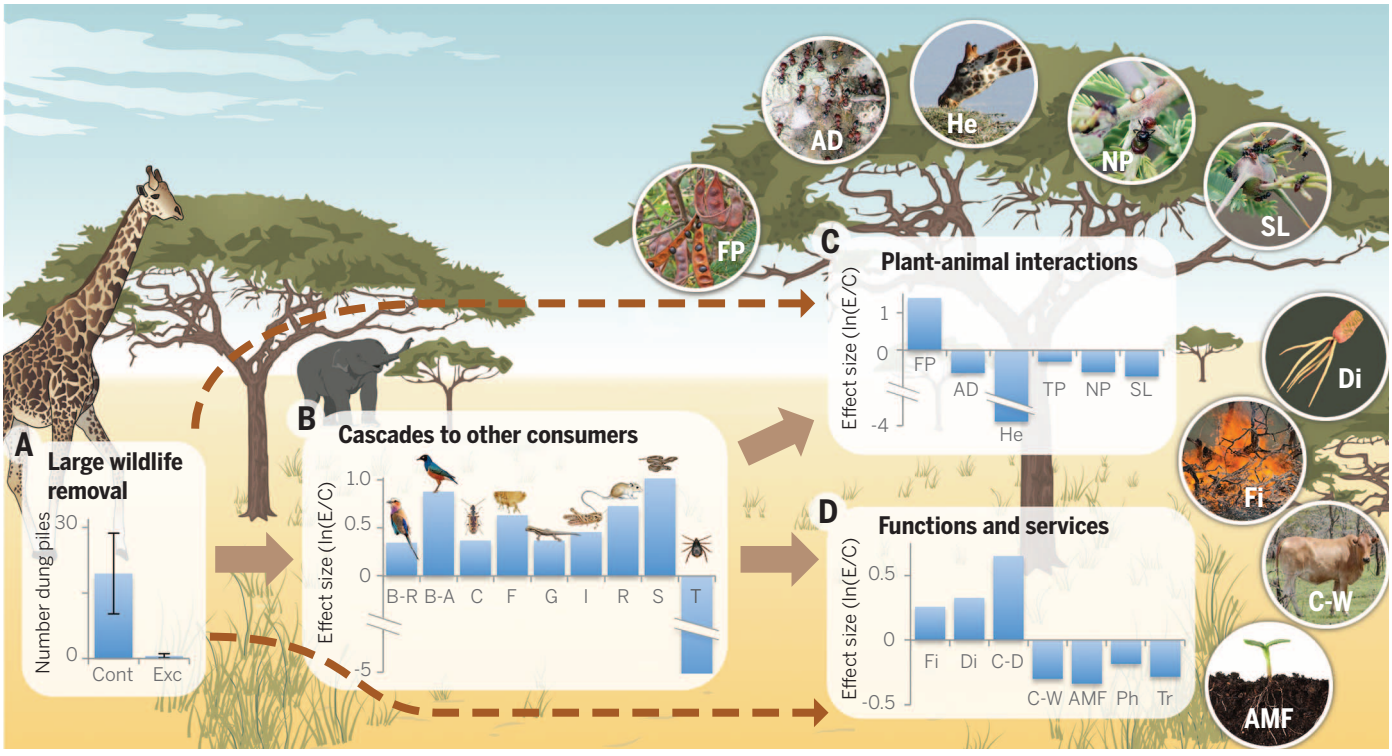


Fig. 4. Results of experimental manipulation simulating differential defaunation. As a model of the pervasive ecosystem effects of defaunation, in just one site (the Kenya Long Term Exclosure Experiment), the effects of selective large-wildlife (species >15 kg) removal drive strong cascading consequences on other taxa, on interactions, and on ecosystem services (*81*). (**A**) In this experiment, large wildlife are effectively removed by fences, as evidenced by mean difference in dung abundance (±1 SE) between control and exclosure plots. (**B**) This removal leads to changes in the abundance or diversity of other consumer groups. Effects were positive for most of these small-bodied consumers—including birds (B-R, bird species richness; B-A, granivorous bird abundance), Coleoptera (C), fleas (F), geckos (G), insect biomass (I), rodents (R), and snakes (S)—but negative for ticks (T). (**C**) Experimental defaunation also affects plant-animal interactions, notably altering the mutualism between ants and the dominant tree, *Acacia drepanolobium* and driving changes in fruit production (FP), ant defense by some species (AD), herbivory of shoots (He), thorn production (TP), nectary production (NP), and spine length (SL). (**D**) Large-wildlife removal also causes major effects on ecosystem functions and services, including changes to fire intensity (Fi), cattle production in both dry (C-D) and wet (C-W) seasons, disease prevalence (D), infectivity of arbuscular mycorrhizae fungi (AMF), photosynthetic rates (Ph), and transpiration rates (TR). Data in (B) to (D) are effect size [ln(exclosure metric/control metric)] after large-wildlife removal. Although this experiment includes multiple treatments, these results represent effects of full exclosure treatments; details on treatments and metrics are provided in table S3. [Photo credits: T. Palmer, H. Young, R. Sensenig, and L. Basson]

Cumulatively, these ubiquitous small-predator trophic cascades can have enormous impacts on a wide variety of ecological functions, including food production. For example, arthropod pests are responsible for 8 to 15% of the losses in most major food crops. Without natural biological control, this value could increase up to 37% (*57*). In the United States alone, the value of pest control by native predators is estimated at $4.5 billion annually (*58*).

Nutrient cycling and decomposition

The diversity of invertebrate communities, particularly their functional diversity, can have dramatic impacts on decomposition rates and nutrient cycling (*59*–*61*). Declines in mobile species that move nutrients long distances have been shown to greatly affect patterns of nutrient distribution and cycling (*62*). Among large animals, Pleistocene extinctions are thought to have changed influx of the major limiting nutrient, phosphorus, in the Amazon by ~98%, with implications persisting today (*3*).

Water quality

Defaunation can also affect water quality and dynamics of freshwater systems. For instance, global declines in amphibian populations increase algae and fine detritus biomass, reduce nitrogen uptake, and greatly reduce whole-stream respiration (Fig. 5E) (*63*). Large animals, including ungulates, hippos, and crocodiles, prevent formation of anoxic zones through agitation and affect water movement through trampling (*64*).

Human health

Defaunation will affect human health in many other ways via reductions in ecosystem goods and services (*65*), including pharmaceutical compounds, livestock species, biocontrol agents, food resources, and disease regulation. Between 23 and 36% of all birds, mammals, and amphibians used for food or medicine are now threatened with extinction (*14*). In many parts of the world, wild-animal food sources are a critical part of the diet, particularly for the poor. One recent study in Madagascar suggested that loss of wildlife as a food source will increase anemia by 30%, leading to increased mortality, morbidity, and learning difficulties (*66*). However, although some level of bushmeat extraction may be a sustainable service, current levels are clearly untenable (*67*); vertebrate populations used for food are estimated to have declined by at least 15% since 1970 (*14*). As previously detailed, food production may decline because of reduced pollination, seed dispersal, and insect predation. For example, loss of pest control from ongoing bat declines in North America are predicted to cause more than $22 billion in lost agricultural productivity (*68*). Defaunation can also affect disease transmission in myriad ways, including by changing the abundance, behavior, and competence of hosts (*69*). Several studies demonstrate increases in disease prevalence after defaunation (*41*, *42*, *70*). However, the impacts of defaunation on disease are far from straightforward (*71*), and few major human pathogens seem to fit the criteria that would make such a relationship pervasive (*71*). More work is

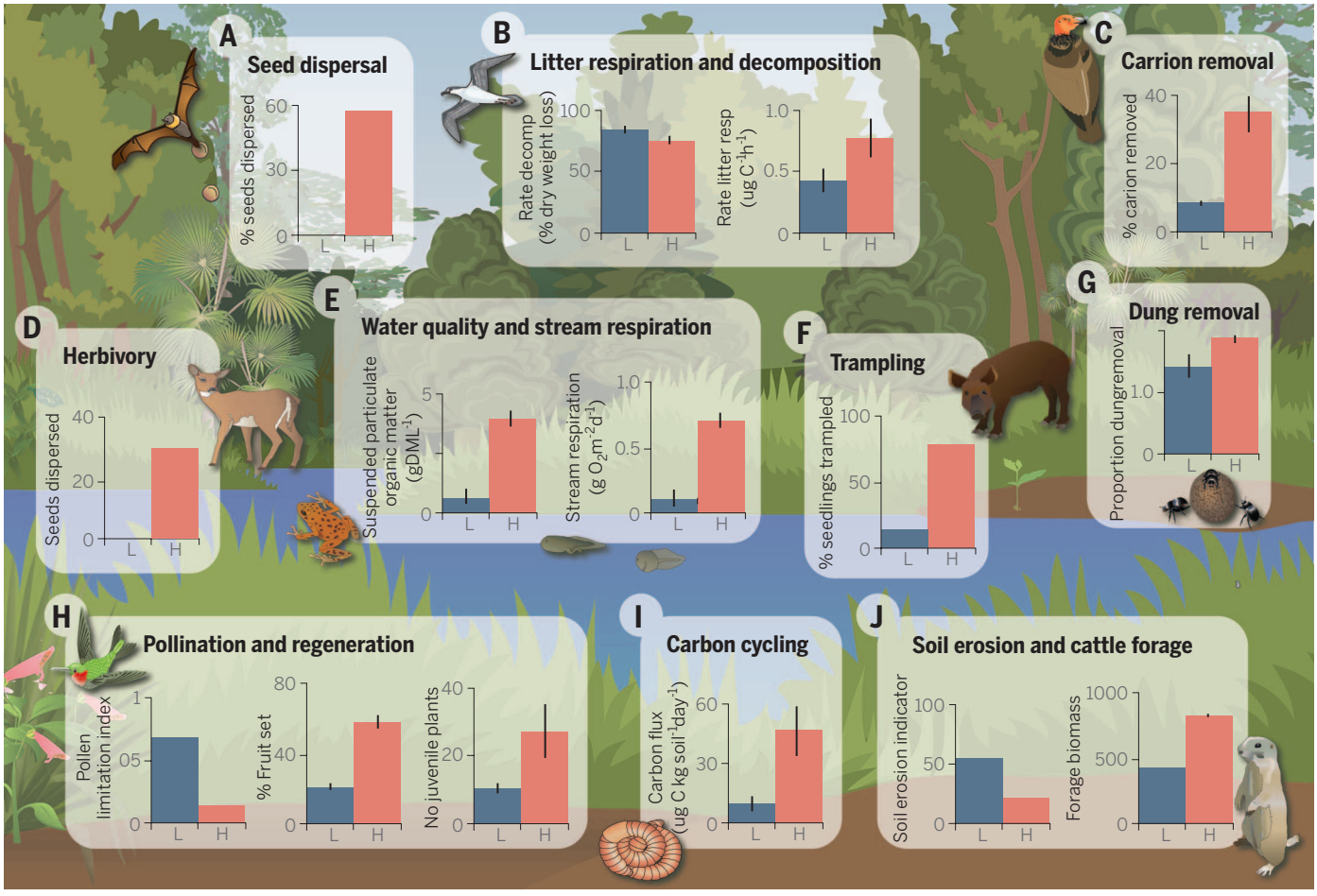


Fig. 5. Consequences of defaunation on ecosystem functioning and services. Changes in animal abundance from low (blue, L) to high (red, H) within a region have been shown to affect a wide range of ecological processes and services (*19*), including (**A**) seed dispersal (flying foxes), (**B**) litter respiration and decomposition (seabirds), (**C**) carrion removal (vultures), (**D**) herbivory (large mammals), (**E**) water quality and stream restoration (amphibians), (**F**) trampling of seedlings (mammals), (**G**) dung removal (dung beetles), (**H**) pollination and plant recruitment (birds), (**I**) carbon cycling (nematodes), and (**J**) soil erosion and cattle fodder (prairie dogs).

urgently needed to understand the mechanisms and context-dependence of defaunation-disease relationships in order to identify how defaunation will affect human disease.

Impacts on evolutionary patterns

The effects of defaunation appear not to be merely proximally important to the ecology of affected species and systems but also to have evolutionary consequences. Several studies have detected rapid evolutionary changes in morphology or life history of short-lived organisms (*72*) or human-exploited species (*73*). Because defaunation of vertebrates often selects on body size, and smaller individuals are often unable to replace fully the ecological services their larger counterparts provide, there is strong potential for cascading effects that result from changing body-size distributions (*74*). Still poorly studied are the indirect evolutionary effects of defaunation on other species, not directly affected by human defaunation. For example, changes in abundance or composition of pollinators or seed dispersers can cause rapid evolution in plant mating systems and seed morphology (*75*, *76*). There is a pressing need to understand the ubiquity and importance of such "evolutionary cascades" (*77*).

Synthesis and ways forward

This Review indicates that a widespread and pervasive defaunation crisis, with far-reaching consequences, is upon us. These consequences have been better recognized in the case of large mammals (*78*, *79*). Yet, defaunation is affecting smaller and less charismatic fauna in similar ways. Ongoing declines in populations of animals such as nematodes, beetles, or bats are considerably less evident to humans yet arguably are more functionally important. Improved monitoring and study of such taxa, particularly invertebrates, will be critical to advance our understanding of defaunation. Ironically, the cryptic nature of defaunation has strong potential to soon become very noncryptic, rivaling the impact of many other forms of global change in terms of loss of ecosystem services essential for human well-being.

Although extinction remains an important evolutionary impact on our planet and is a powerful social conservation motivator, we emphasize that defaunation is about much more than species loss. Indeed, the effects of defaunation will be much less about the loss of absolute diversity than about local shifts in species compositions and functional groups within a community (*80*). Focusing on changes in diversity metrics is thus unlikely to be effective for maintaining adequate ecological function, and we need to focus on predicting the systematic patterns of winners and losers in the Anthropocene and identify the traits that characterize them because this will provide information on the patterns and the links to function that we can then act on.

Cumulatively, systematic defaunation clearly threatens to fundamentally alter basic ecological functions and is contributing to push us toward global-scale "tipping points" from which we may not be able to return (*7*). Yet despite the dramatic rates of defaunation currently being observed, there is still much opportunity for action. We must more meaningfully address immediate drivers of defaunation: Mitigation of animal overexploitation and land-use change are two feasible, immediate actions that can be taken (*44*). These actions can also buy necessary time to address the other critical driver, anthropogenic climate disruption.

However, we must also address the often nonlinear impacts of continued human population growth and increasingly uneven per capita consumption, which ultimately drive all these threats (while still fostering poverty alleviation efforts). Ultimately, both reduced and more evenly distributed global resource consumption will be necessary to sustainably change ongoing trends in defaunation and, hopefully, eventually open the door to refaunation. If unchecked, Anthropocene defaunation will become not only a characteristic of the planet's sixth mass extinction, but also a driver of fundamental global transformations in ecosystem functioning.

REFERENCES AND NOTES

1. A. D. Barnosky *et al.*, *Nature* **471**, 51–57 (2011).
2. M. Cardillo *et al.*, *Philos. R. Soc. London B. Biol.* **275**, 1441–1448 (2008).
3. C. E. Doughty, A. Wolf, Y. Malhi, *Nat. Geosci.* **6**, 761–764 (2013).
4. J. L. Gill, J. W. Williams, S. T. Jackson, K. B. Lininger, G. S. Robinson, *Science* **326**, 1100–1103 (2009).
5. R. Dirzo, in *Global Biodiversity in a Changing Environment: Scenarios for the 21st Century*, F. S. Chapin, O. E. Sala, E. Huber-Sannwald, Ed. (Springer, New York, 2001), pp. 251–276.
6. C. A. Peres, E. Palacios, *Biotropica* **39**, 304–315 (2007).
7. A. D. Barnosky *et al.*, *Nature* **486**, 52–58 (2012).
8. G. Ceballos, P. R. Ehrlich, *Science* **296**, 904–907 (2002).
9. D. U. Hooper *et al.*, *Nature* **486**, 105–108 (2012).
10. K. J. Gaston, R. A. Fuller, *Trends Ecol. Evol.* **23**, 14–19 (2008).
11. B. W. Brook, N. S. Sodhi, C. J. Bradshaw, *Trends Ecol. Evol.* **23**, 453–460 (2008).
12. T. Säterberg, S. Sellman, B. Ebenman, *Nature* **499**, 468–470 (2013).
13. A. Ø. Mooers, D. P. Faith, W. P. Maddison, *PLOS One* **3**, e3700 (2008).
14. S. H. M. Butchart *et al.*, *Science* **328**, 1164–1168 (2010).
15. C. Mora, A. Rollo, D. P. Tittensor, *Science* **443**, 295 (2013).
16. B. R. Scheffers, L. N. Joppa, S. L. Pimm, W. F. Laurance, *Trends Ecol. Evol.* **27**, 501–510 (2012).
17. IUCN, The IUCN Red List of Threatened Species (2013); available at www.iucnredlist.org.
18. M. Hoffmann *et al.*, *Science* **330**, 1503–1509 (2010).
19. Materials and methods are available as supplementary materials on *Science* Online.
20. G. Ceballos, A. García, P. R. Ehrlich, *J. Cosmol.* **8**, 1821 (2010).
21. B. Collen *et al.*, *Conserv. Biol.* **23**, 317–327 (2009).
22. Living Planet Rport, "Living Planet Report 2012: Biodiversity, biocapacity and better choices" (WWF, Zoological Society of London, Global Footprint Network, European Space Agency, London, 2012).
23. B. Collen, M. Böhm, R. Kemp, J. Baillie, *Spineless: Status and Trends of the World's Invertebrates* (Zoological Society of London, London, 2012).
24. B. Collen, J. E. M. Baillie, *Science* **329**, 140 (2010).
25. R. Fox *et al.*, *J. Appl. Ecol.* 10.1111/1365-2664.12256 (2014).
26. J. Cavender-Bares, K. H. Kozak, P. V. Fine, S. W. Kembel, *Ecol. Lett.* **12**, 693–715 (2009).
27. J. Schipper *et al.*, *Science* **322**, 225–230 (2008).
28. S. L. Pimm *et al.*, *Science* **344**, 1246752 (2014).
29. R. Dirzo, P. H. Raven, *Annu. Rev. Environ. Resour.* **28**, 137–167 (2003).
30. C. N. Jenkins, S. L. Pimm, L. N. Joppa, *Proc. Natl. Acad. Sci. U.S.A.* **110**, E2602–E2610 (2013).
31. M. Cardillo, E. Meijaard, *Trends Ecol. Evol.* **27**, 167–171 (2012).
32. A. D. Davidson, M. J. Hamilton, A. G. Boyer, J. H. Brown, G. Ceballos, *Proc. Natl. Acad. Sci. U.S.A.* **106**, 10702–10705 (2009).
33. E. Öckinger *et al.*, *Ecol. Lett.* **13**, 969–979 (2010).
34. T. M. Lee, W. Jetz, *Philos. R. Soc. London B. Biol.* **278**, 1329–1338 (2011).
35. M. J. Pocock, P. Roy, *Philos. R. Soc. London B. Biol.* **278**, 1532–1538 (2011).
36. S. A. Fritz, O. R. P. Bininda-Emonds, A. Purvis, *Ecol. Lett.* **12**, 538–549 (2009).
37. G. Cowlishaw, R. A. Pettifor, N. J. Isaac, *Philos. R. Soc. London B. Biol.* **276**, 63–69 (2009).
38. M. Cardillo, G. M. Mace, J. L. Gittleman, A. Purvis, *Proc. Natl. Acad. Sci. U.S.A.* **103**, 4157–4161 (2006).
39. H. Hillebrand, B. Matthiessen, *Ecol. Lett.* **12**, 1405–1419 (2009).
40. D. J. McCauley *et al.*, *Ecol. Appl.* **22**, 1711–1717 (2012).
41. F. Keesing *et al.*, *Nature* **468**, 647–652 (2010).
42. P. T. Johnson, D. L. Preston, J. T. Hoverman, K. L. Richgels, *Nature* **494**, 230–233 (2013).
43. M. Di Marco *et al.*, *Conserv. Biol.* 10.1111/cobi.12249 (2014).
44. O. E. Sala *et al.*, *Science* **287**, 1770–1774 (2000).
45. C. H. Sekercioglu, S. H. Schneider, J. P. Fay, S. R. Loarie, *Conserv. Biol.* **22**, 140–150 (2008).
46. K. F. Smith, D. F. Sax, K. D. Lafferty, *Conserv. Biol.* **20**, 1349–1357 (2006).
47. C. A. Peres, *Conserv. Biol.* **14**, 240–253 (2000).
48. S. T. Jackson, D. F. Sax, *Trends Ecol. Evol.* **25**, 153–160 (2010).
49. J. Reiss, J. R. Bridle, J. M. Montoya, G. Woodward, *Trends Ecol. Evol.* **24**, 505–514 (2009).
50. B. J. Cardinale *et al.*, *Nature* **486**, 59–67 (2012).
51. B. J. Cardinale *et al.*, *Nature* **443**, 989–992 (2006).
52. N. Gallai, J.-M. Salles, J. Settele, B. E. Vaissière, *Ecol. Econ.* **68**, 810–821 (2009).
53. S. G. Potts *et al.*, *Trends Ecol. Evol.* **25**, 345–353 (2010).
54. J. C. Biesmeijer *et al.*, *Science* **313**, 351–354 (2006).
55. S. H. Anderson, D. Kelly, J. J. Ladley, S. Molloy, J. Terry, *Science* **331**, 1068–1071 (2011).
56. D. S. Karp *et al.*, *Ecol. Lett.* **16**, 1339–1347 (2013).
57. E.-C. Oerke, *J. Agric. Sci.* **144**, 31–43 (2006).
58. J. E. Losey, M. Vaughan, *Bioscience* **56**, 311–323 (2006).
59. M. O. Gessner *et al.*, *Trends Ecol. Evol.* **25**, 372–380 (2010).
60. T. B. Atwood *et al.*, *Nat. Geosci.* **6**, 191–194 (2013).
61. D. Hawlena, M. S. Strickland, M. A. Bradford, O. J. Schmitz, *Science* **336**, 1434–1438 (2012).
62. H. S. Young, D. J. McCauley, R. B. Dunbar, R. Dirzo, *Proc. Natl. Acad. Sci. U.S.A.* **107**, 2072–2077 (2010).
63. M. Whiles *et al.*, *Ecosystems (N.Y.)* **16**, 146–157 (2013).
64. J. P. Wright, C. G. Jones, A. S. Flecker, *Oecologia* **132**, 96–101 (2002).
65. S. S. Myers *et al.*, *Proc. Natl. Acad. Sci. U.S.A.* **110**, 18753–18760 (2013).
66. C. D. Golden, L. C. Fernald, J. S. Brashares, B. J. Rasolofoniaina, C. Kremen, *Proc. Natl. Acad. Sci. U.S.A.* **108**, 19653–19656 (2011).
67. J. E. Fa, C. A. Peres, J. Meeuwig, *Conserv. Biol.* **16**, 232–237 (2002).
68. J. G. Boyles, P. M. Cryan, G. F. McCracken, T. H. Kunz, *Science* **332**, 41–42 (2011).
69. R. S. Ostfeld, F. Keesing, *Annu. Rev. Ecol. Evol. Syst.* **43**, 157–182 (2012).
70. H. S. Young *et al.*, *Proc. Natl. Acad. Sci. U.S.A.* 10.1073/pnas.1404958111 (2014).
71. C. L. Wood *et al.*, *Ecology* **95**, 817–832 (2014).
72. S. R. Palumbi, *Science* **293**, 1786–1790 (2001).
73. C. T. Darimont *et al.*, *Proc. Natl. Acad. Sci. U.S.A.* **106**, 952–954 (2009).
74. M. Galetti, C. I. Donatti, M. A. Pizo, H. C. Giacomini, *Biotropica* **40**, 386–389 (2008).
75. S. A. Bodbyl Roels, J. K. Kelly, *Evolution* **65**, 2541–2552 (2011).
76. M. Galetti *et al.*, *Science* **340**, 1086–1090 (2013).
77. J. A. Estes, J. S. Brashares, M. E. Power, *Am. Nat.* **181** (suppl. 1), S76–S99 (2013).
78. J. A. Estes *et al.*, *Science* **333**, 301–306 (2011).
79. W. J. Ripple *et al.*, *Science* **343**, 1241484 (2014).

ACKNOWLEDGMENTS

D. Orr, L. Gillespie, B. Rossman, R. Pringle, C. Bello, T. August, G. Powney, F. Pedrosa, and M. Pires helped in providing or analyzing data and producing figures. P. Ehrlich, T. Young, S. Vignieri, and two anonymous reviewers read a previous draft and offered constructive comments. Butterfly Conservation, the British Dragonfly Society, Bees Wasps and Ants Recording Society, the Ground Beetle Recording Scheme, and Bird Life International provided access to unpublished data. We thank Conselho Nacional de Desenvolvimento Científico e Tecnológico, Fundação para o Desenvolvimento do Unesp, Fundação de Amparo à Pesquisa do Estado de São Paulo, NERC, Joint Nature Conservation Committee, NSF, and Universidad Nacional Autonoma de Mexico for financial support. Vector images are courtesy of University of Maryland Center for Environmental Science.

SUPPLEMENTARY MATERIALS

www.sciencemag.org/content/345/6195/401/suppl/DC1
Materials and Methods
Figs. S1 to S6
Tables S1 to S3
References (*80*–*167*)

10.1126/science.1251817

REVIEW

Reversing defaunation: Restoring species in a changing world

Philip J. Seddon,[1]* Christine J. Griffiths,[2] Pritpal S. Soorae,[3] Doug P. Armstrong[4]

The rate of biodiversity loss is not slowing despite global commitments, and the depletion of animal species can reduce the stability of ecological communities. Despite this continued loss, some substantial progress in reversing defaunation is being achieved through the intentional movement of animals to restore populations. We review the full spectrum of conservation translocations, from reinforcement and reintroduction to controversial conservation introductions that seek to restore populations outside their indigenous range or to introduce ecological replacements for extinct forms. We place the popular, but misunderstood, concept of rewilding within this framework and consider the future role of new technical developments such as de-extinction.

Recent analyses have shown that the rate of biodiversity loss has not slowed despite global commitments made through the 2002 Convention on Biological Diversity (*1*). Projected future extinction rates for terrestrial species might exceed current rates of extinction (*2*). A key component of biodiversity loss is defaunation, the loss or depletion of animal species from ecological communities (*3*, *4*). Such losses can reduce the stability of

ecological communities (*5*), with cascading effects (*3*).

In situ conservation measures—including the creation and management of protected areas, increasing connectivity between wildlife populations, and reduction of the impacts of predation and hunting—can achieve some success where the amount of habitat remaining is sufficient for viable populations (*6*). Increasingly, however, more intensive forms of threatened species management are required to address local extinctions and impending threats to critical areas of habitat. Progress in reversing defaunation is emerging from conservation translocations—the intentional movement of animals to restore populations (*7*) (Fig. 1).

Population restoration: Reintroduction and reinforcement

The intentional movement and release of animals has occurred for millennia, but the use of translocations to address conservation objectives is barely 100 years old (*8*). In recent decades, there has been an increase in the number of species that are the focus of conservation translocations to restore and enhance populations; for vertebrates alone, at least 124 species were translocated during 1900–1992, and this had risen to 199 species by 1998 and to 424 species by 2005 (*9*). Two types of translocation for population restoration are recognized: (i) reinforcements, involving the release of an organism into an existing population of conspecifics to enhance population viability, and (ii) reintroductions, where the intent is to reestablish a population in an area after local extinction (*7*) (Fig. 1). The critical feature of these translocations is the release of animals into their indigenous range, the known or inferred distribution derived from historical records or other evidence (*7*).

Previous work has shown that conservation translocation projects, as with other types of conservation management, show a marked taxonomic bias toward birds (33% of projects, whereas birds make up 18% of species represented in nature) and mammals (41% of projects versus 8% of species), particularly the larger, more charismatic species, almost irrespective of the degree of threat or vulnerability (*10*). Recent data on reinforcements show that this bias toward birds and mammals is continuing (*11*). For conservation translocations in general, relatively few invertebrate, reptile, amphibian, or fish species are represented relative to their prevalence in nature (Fig. 2). The global distribution of species' translocations suggests a geographic bias also, with most activity in developed regions (Fig. 2).

The ultimate objective of any reintroduction is the establishment of a self-sustaining population and, using this definition, reviews of reintroduction outcomes have indicated generally low success rates (*12*), as low as 23% (*13*). Concern over high failure rates prompted analyses of the factors associated with translocation success. In 1989, the first comprehensive review looked at the reintroduction and reinforcement of 93 species of native birds and mammals (*12*). This data set was updated, and 181 mammal and bird programs were reanalyzed in 1998 (*14*). Both studies identified habitat quality at the release site, release into the core of a species range, and total numbers released as determinants of success (*12*, *14*). An independent analysis of a broader taxonomic range of animal translocations over 20 years highlighted the greater likelihood of success associated with the release of wild versus captive animals and confirmed the importance of larger founder group sizes (*13*).

Reintroduced populations go through a period of relatively small population size where the risks of inbreeding and loss of genetic variation is high; the challenge, therefore, is to minimize loss of genetic variation by creating large effective population sizes (*15*). The key determinants of the genetic diversity retained in a reintroduction will be the total number of founders and the proportion contributing genetically to the next generations (*16*). Thus, even when a large population results, there might be considerable loss of genetic diversity during the early stages of population establishment (*17*), and the number of founders necessary for preservation of genetic diversity might be substantially greater than that required for population establishment and growth (*18*). Low initial population sizes might also make reintroduced populations vulnerable to Allee effects, which might have contributed to past reintroduction failures, although this link has not been shown (*19*). Reinforcement of existing populations can increase population size, prevent Allee effects, and increase genetic diversity, but also carries a risk of loss of local adaptation and the introduction of pathogens, particularly from captive breeding programs (*11*).

Simple classification of any reintroduction as success or failure to result in a self-sustaining population is of limited use because the time scale for success evaluation is important, and there are examples of successful projects failing at a later stage (*13*). The International Union for Conservation of Nature (IUCN) guidelines advocate that projects make clear definitions of success in relation to three phases of any reintroduction: establishment, growth, and regulation, with future population persistence assessed through population viability analysis (*7*). Assessment of success or of the causes of failure can be made only through adequate postrelease monitoring (*20*). Monitoring is needed also to facilitate meta-analyses (*13*), to track genetic diversity (*16*), and to evaluate the performance of reintroduced populations and the possible impacts on recipient ecosystems (*21*).

Conservation introductions

Perhaps the greatest challenge facing practitioners of species or ecosystem restoration is the definition of a target state (*22*). Attempts to return a system to some historical condition make somewhat arbitrary decisions about how far back in time to go. Historical restoration reference states vary according to the history of human occupation, with pre-European settlement conditions often held up as the baseline (*23*). However, a desire to return to some past state makes some assumptions, including the implication that near-pristine conditions existed in pre-European times and that historical restoration targets will be sustainable with changing climate (*22*). It is now recognized that past species distributions do not indicate current suitability and that current species' distribution does not guarantee future suitability (*24*). Climate change, in tandem with human-facilitated species invasions and land transformation, contribute to the creation of novel ecosystems: systems that differ in composition and function from past systems (*25*).

If we acknowledge that restoration and maintenance of species within their indigenous ranges will remain a foundation of conservation efforts, the realization that a return to a completely natural world is not achievable frees us to think about more radical types of conservation translocation. Conservation introductions involve the movement and release of an organism outside its indigenous range (*7*). Two types of conservation introduction are recognized by the IUCN: assisted colonization and ecological replacement (Fig. 1).

Assisted colonization

In 1985, Peters and Darling (*26*) suggested that climate change might alter habitat suitability for species confined within protected areas, effectively stranding them in increasingly unsuitable sites. They proposed the translocation of individuals into new reserves encompassing habitat that was or would become appropriate. Possibly because of the low profile of global climate change, the unreliability of early predictive models of climate, and the radical nature of the proposal, the idea of proactive translocation initially gained little traction (*27*). However, there is growing acknowledgment that conservation managers could take action to address climate-induced changes in species' habitats where individuals of affected species are unable to naturally colonize new areas as habitat suitability shifts (*28*–*30*). Understandably, given the devastating ecological impact wrought by invasive species, assisted colonization has been greeted with extreme skepticism, which has promoted a vigorous debate in the literature (*31*, *32*). The 2013 IUCN guidelines define assisted colonization in broad terms as the intentional movement of an organism outside its indigenous range to avoid extinction of populations due to current or future threats (*7*). Under this definition, far from being a radical new translocation approach, assisted colonization is already being applied as a conservation tool in Australasia to protect, on predator-free islands, populations of species, such as the kakapo

[1]Department of Zoology, University of Otago, Post Office Box 56, Dunedin, New Zealand. [2]School of Biological Sciences, University of Bristol, Woodland Road, Bristol BS8 1UG, UK. [3]Environment Agency, Abu Dhabi, United Arab Emirates. [4]Institute of Natural Resources, Massey University, Private Bag 11222, Palmerston North, New Zealand.
***Corresponding author. E-mail: philip.seddon@otago.ac.nz**

(*Strigops habroptilus*), threatened by predation from exotic mammalian predators in mainland habitat (*24*). The creation of a disease-free population of Tasmanian devils (*Sarcophilus harrisii*) outside the species' indigenous range in Tasmania (*33*) also fits this definition.

The 2013 IUCN guidelines place great emphasis on feasibility and risk analysis as essential components of any conservation translocation. Given the uncertainties involved in moving species outside their range, assisted colonization is inherently more risky than "traditional" translocations such as reintroductions. New approaches for understanding and managing risk under uncertainty are being applied to conservation introduction planning, including quantitative risk analysis (*34*), active adaptive management (*35*), and structured decision-making (*36*). Where protection from threats in the indigenous range is unfeasible and where appropriate habitat can be identified elsewhere, application of carefully planned assisted colonizations might become more acceptable (*37*).

A critical aspect in planning for assisted colonization is selection of suitable release sites that match the biotic and abiotic needs of the focal species (*7*) under future climate scenarios. Climate-envelope models have been used to determine species' future habitat suitability to guide some of the first experimental assisted colonizations of two butterfly species to sites ~35 and ~65 km beyond their indigenous range in northern England (*38*). But static bioclimatic envelope models might not adequately account for species' ability to disperse or for changing demographic processes as habitat quality shifts. More complex integrative climate suitability models will be required (*39*), although these too can never be perfect predictors of complex environments. Improved approaches to predict future habitat suitability explicitly integrate species distribution data with population dynamics or physiology. For example, stochastic population modeling combined with habitat suitability models predict how the vital rates of hihi (*Notiomystis cincta*), a New Zealand endemic passerine, could be influenced by climate change, with at least two populations potentially at risk of extinction (*40*). Ecoenergetic and hydrological models were integrated to evaluate the long-term suitability of habitat for the Western swamp tortoise (*Psuedemydura umbrina*) and extended to identify new regions that would meet the tortoise's thermodynamic requirements under a range of warmer and drier climates predicted by 2030 (*41*). Future developments around assisted colonization planning will include the

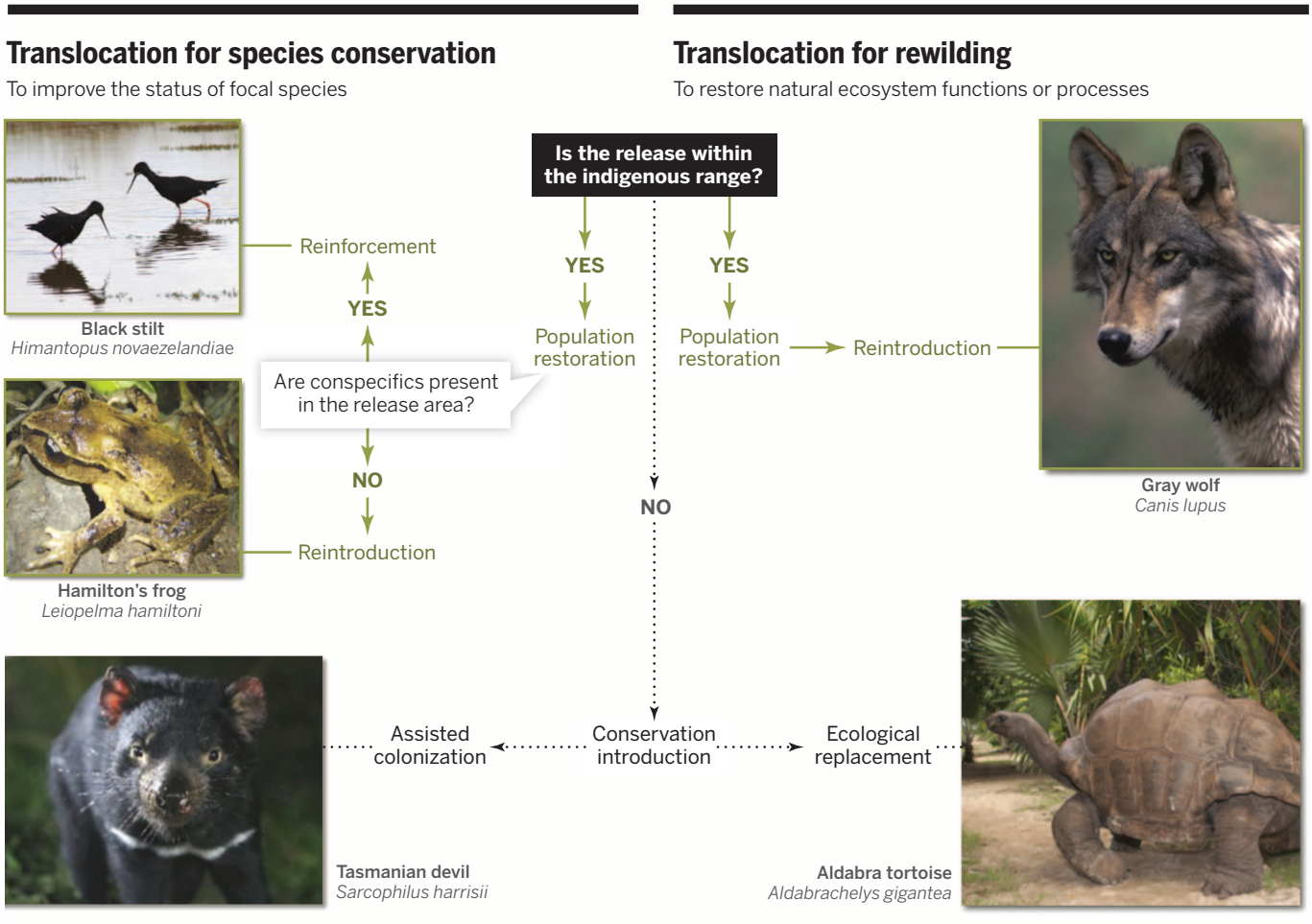


Fig. 1. The conservation translocation spectrum [based on (*7*)]. Translocations with the primary objective of improving the status of the focal species are a species conservation tool, and releases can take place inside or outside the indigenous range. Releases inside the indigenous range may be for reinforcements, as illustrated by the black stilt (*68*), or reintroductions, for example, of amphibians, such as Hamilton's frog (*69*). Releases outside the indigenous range for species conservation are assisted colonizations, e.g., Tasmanian devil (*33*). Translocations with the primary objective of restoring ecosystem functions are a component of rewilding and may include reintroductions, e.g., gray wolf (*46*). Rewilding releases outside the indigenous range might be justified if an ecological function has been lost due to extinction, e.g., dispersal of large-seeded plants by giant tortoises (*70*). Releases may have both objectives, but these should be explicitly stated as each will require specific targets and outcome monitoring. [Photo credits: black stilt (P. Guilford), Hamilton's frog (P. Bishop), Tasmanian devil (G. King), gray wolf (B. Quayle), Aldabra giant tortoise (M. Whittaker)]

application of fully integrated models that combine climatic suitability, habitat availability, population dynamics, and mechanistic movement models of dispersal (*39*, *42*). These may involve a single species or two or more interacting species.

Ecological replacements

Biodiversity can increase ecosystem stability by buffering the effects of environmental change, resisting species invasions, and preventing secondary extinctions after species losses (*43*). Species extinctions reduce interaction network diversity (*44*) and can lead to cascading effects, including the loss of other species and their biotic interactions (*45*). Where only local extinction occurs, critical ecosystem functions might be reinstated through reintroductions; for example, the reintroduction of wolves into Yellowstone National Park in 1995–1996 restored direct effects on their prey and a range of indirect effects (*46*). The global extinction of a species, however, means that restoration of functions might be achieved only through introduction of functionally similar exotic species.

The 2013 IUCN guidelines define ecological replacement as a form of conservation introduction involving the release of an appropriate substitute species to reestablish an ecological function lost through extinction. Although the rationale for ecological replacement is different from that of assisted colonization, the two terms have often been used interchangeably in the literature [e.g., (*47*)]. Although, in some situations, an assisted colonization to prevent extinction of the focal species could serve in parallel to restore an ecosystem function outside the indigenous range (*47*), in many cases, the most appropriate ecological replacements might not be endangered species. Recognition of ecological replacement as a valid conservation tool represents a departure from the single-species focus that once characterized conservation translocations and conforms more closely to the current global conservation emphasis on restoring natural processes rather than addressing only extinction risk (*48*).

There has been interest in the replacement of ecological functions once performed by extinct

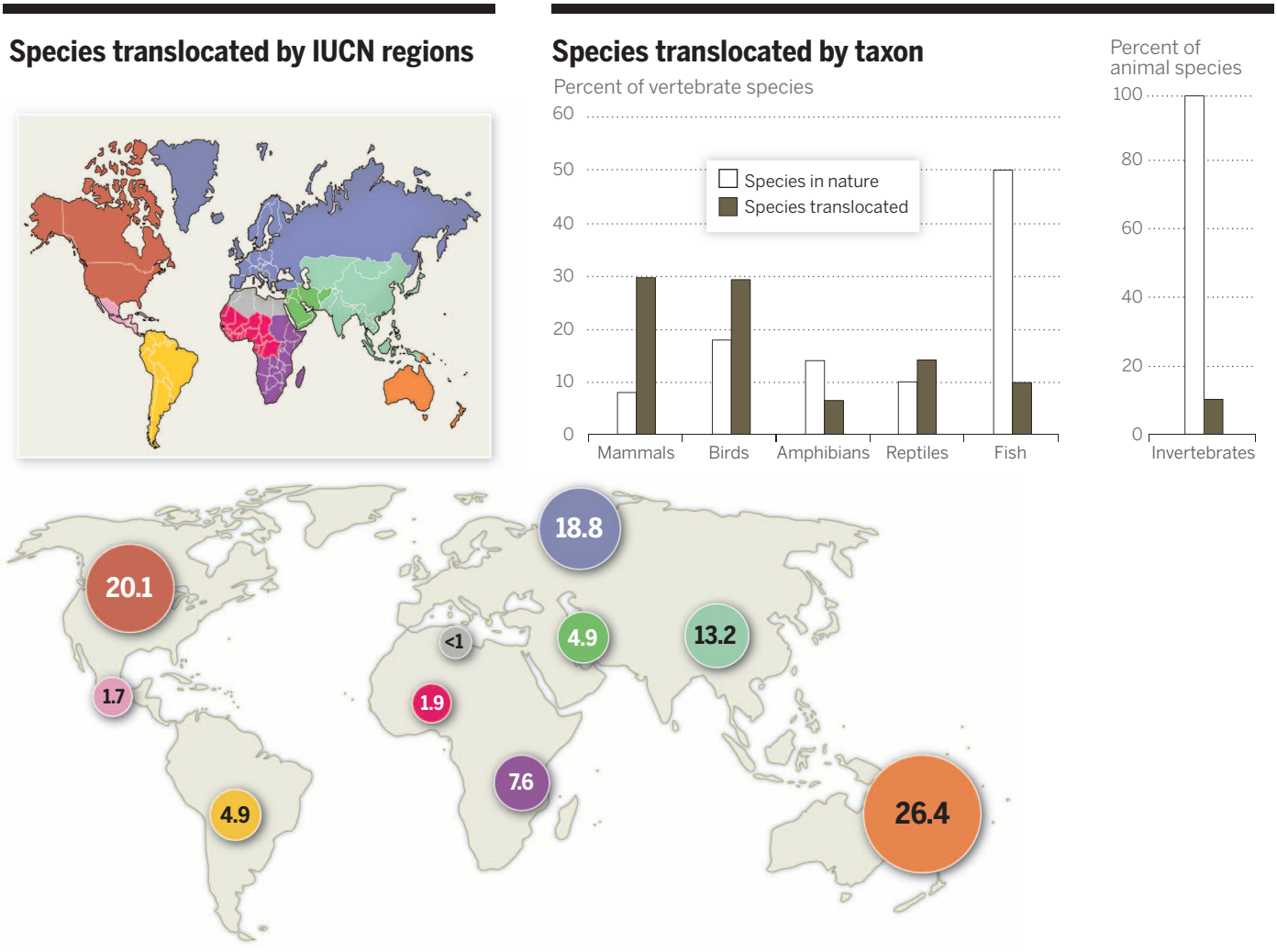


Fig. 2. Global and taxonomic range of conservation translocations. The proportions of 303 species that have been translocated for conservation purposes, by IUCN region (main map—the larger the circle the greater the proportion of species), and by taxon (inset bar chart: shaded bars are proportions of species translocated out of the total of 303; unshaded bars are proportions of species in nature. Because invertebrate species are estimated to be >99% of all animal species in nature, for clarity, the relative proportion of invertebrates in nature and the proportion of invertebrate species that have been translocated out of the total of 303 animal species are presented on the right; the proportions relative to vertebrate species only are on the left. [Data from (*10*).] The color inset map shows the 10 IUCN regions; west to east, these are North America and Caribbean, Meso-America, South America, North Africa, Central and West Africa, East and Southern Africa, West Asia and the Middle East, Europe and the Mediterranean, Asia, and Oceania (source iucn.org). Data on the 303 species was derived from downloadable project summaries available at iucnsscrsg.org. Base map source: commons.wikimedia.org

megafauna, because they would have had large ecosystem impacts in relation to their abundance (*49*, *50*). The megafaunal concept must, however, be viewed as context-dependent, because in island ecosystems, the largest native frugivore may be an order of magnitude lighter than those in continental systems, yet loss of large island frugivores can result in more sizable cascading effects owing to the lower functional redundancy on islands (*51*). The most important application of ecological replacements to date has been in the restoration of herbivory and seed dispersal functions in island ecosystems. Extinction of large frugivores can disrupt seed dispersal, interrupt recruitment, and reduce genetic variation of large-seeded fleshy-fruited plants (*52*); it can also drive rapid evolutionary reduction in seed size, affecting seed survival (*45*). There is evidence of the ecosystem-engineering role of giant tortoises, as tortoises are important dispersers of large-seeded plants, and their grazing and trampling is critical for creating and maintaining some vegetation communities (*53*). To restore grazing functions and the seed dispersal of native large-seeded plants, exotic Aldabra giant tortoises (*Aldabrachelys gigantea*) have been introduced to Mauritian offshore islands to replace the extinct Mauritian *Cylindraspis* species (*54*, *55*) (Fig. 3). Not only has seed dispersal resumed, but passage through the tortoise gut also improves seed germination success (*55*). Further projects are planned or under way to use ecologically similar species of giant tortoise to reinstate processes lost with the extinction of endemic giant tortoises in the islands of Madagascar, the Galapagos, the Mascarenes, the Seychelles, and the Caribbean (*56*).

The future challenge is the identification of suitable replacements to perform the desired ecosystem functions within a given system. The longer the time since the extinction of the original form, the greater the uncertainty about the best substitute. The best replacements might not be closely related taxa. If and when risk and uncertainty are adequately evaluated, radical substitutions could be considered, such as the use of tortoises as replacements for moa-nalo, a group of extinct gooselike ducks, in Hawaii (*57*). The focus must be more on reinstatement of functions and processes to restore degraded ecosystems (*58*) and to enhance ecosystem resilience, rather than on restoration to some arbitrary historical state. For any conservation introduction, the risk of unintended effects must be evaluated and weighed against the expected benefits (*7*). The greatest progress will come from carefully designed experimental substitutions using species that can be readily monitored and managed (*58*) and easily removed should the manifestation of unwanted effects reach some predetermined threshold.

Rewilding

In 1998, the concept of "rewilding" was proposed as a "fourth current in the modern conservation movement" that would complement the protection of representative biotic elements (*59*). The original concept of rewilding was built around the keystone role played by wide-ranging, large animals—particularly carnivores—able to maintain ecosystem structure, resilience, and diversity through top-down trophic interactions (*46*, *59*). Rewilding would entail restoration of "big wilderness" through the creation and management of large, strict, core protected areas, enhanced connectivity between core reserves, and critically, the restoration of keystone species (*59*). The term rewilding is going through a surge in popularity in the media, but its original meaning is often misinterpreted or lost. Rewilding has been widely and variously misused to mean: (i) the reintroduction of any recently extirpated species; (ii) the rehabilitation of ecosystems through reintroductions; (iii) the return of an ecosystem to a prehuman state; or (iv) the release of nonnative, rather than native, species. The increased

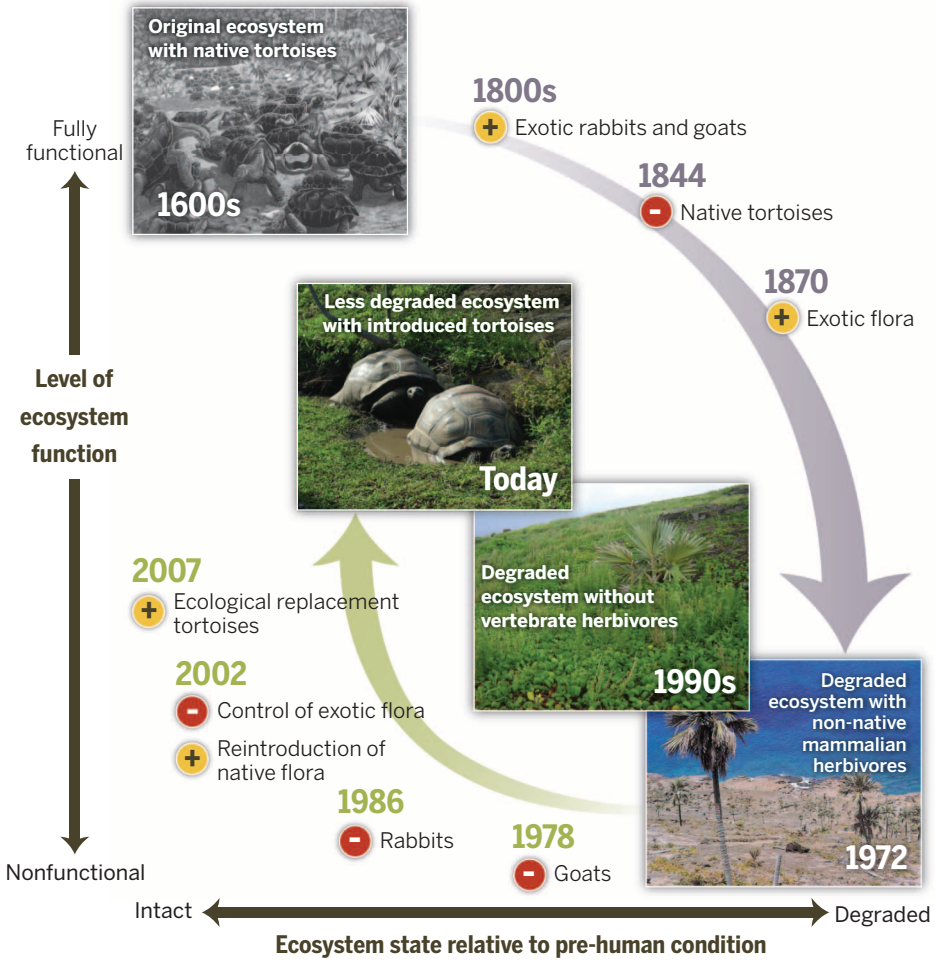


Fig. 3. Rebuilding ecosystems by removing invasive species and introducing ecological replacements. The extinction (−) of keystone ecosystem engineers, such as the Mauritian giant tortoises (*Cylindraspis* species), and the addition (+) of non-native mammalian herbivores and invasive plants degraded (gray arrow) Round Island's ecosystem. The restoration phase (green arrow) first entailed the eradication of goats and rabbits. Without vertebrate herbivory, exotic vegetation flourished, suppressing native plants adapted to tortoises' grazing pressure. Restoration efforts then focused on weeding invasive flora and rebuilding the native plant community, although weeding was costly and limited in spatial area. A long-term, more cost-effective solution sought to restore the grazing and seed dispersal functions once performed by the giant tortoises. In 2007, a small population of Aldabra giant tortoises was introduced as part of a reversible experiment to restore and increase ecosystem resilience (*68*). Tortoises are preferentially grazing the fast-growing exotic plants and avoiding much of the native vegetation believed to have evolved to withstand the high density of Mauritian giant tortoises. [Image credits: Giant tortoise 1600s (J. P. Hulme), giant tortoises today (Z. Ahamud), 1990s (C. Griffiths), 1972 (C. Jouanin)]

use and misuse of the term rewilding has been perhaps due to controversy around the proposed introduction of megafauna to North America to replace species lost 13,000 years ago (*60*). Pleistocene rewilding is at its core true to the original concept of rewilding, as it recognizes the important ecosystem-shaping role of large vertebrates, but made a major departure by arguing for the ecological replacement of long-extinct species. The radical nature of the Pleistocene rewilding concept spawned other, similarly controversial suggestions—such as the introduction of elephants to Australia to control invasive plants (*61*)—but also usefully reenergized the debate on ecological replacements as a valid conservation tool.

Where does this leave rewilding as a concept? The most valuable redefinition of rewilding replaces the "keystone species restoration" component with "species reintroduction to restore ecosystem functioning" (*50*). More broadly though, the restoration of ecosystem function could also involve the introduction of ecological replacements (*50*). This harmonizes rewilding with the current conservation translocation framework (Fig. 1). There is a distinction between translocation for species conservation—where the primary objective is to improve the status of the focal species through reinforcement, reintroduction, or assisted colonization—and translocation for rewilding—where the objective is to restore natural ecosystem functions or processes. Translocation for rewilding could entail population restoration through reintroduction, where releases occur in the indigenous range with the primary aim of restoring some ecological function. A rewilding translocation could also take the form of a conservation introduction through ecological replacement using suitable substitute species.

In its original form, rewilding was seen as a way to restore wilderness, the implication being that there would be large areas of land where human influence was minimal and ongoing management interventions unnecessary. The restoration of keystone species would facilitate the recovery of other "habitat-creating" species and the recovery of natural disturbance regimes (*59*). Oostvaardersplassen (OVP) is a 6000-ha state-owned polder 40 km north of Amsterdam, Netherlands. In the 1980s, the ecologist Frans Vera began to recreate an ecosystem shaped by grazing of large ungulates (*62*), unregulated by large predators. Red deer (*Cervus elaphus*) were released, along with back-bred Konik horses (*Equus ferus caballus*), and the domestic descendants of the Auroch, Heck cattle, as replacements for extinct Auroch (*Bos primigenius*) and Tarpan (*Equs przewalski gmelini*). Rather than seeking the preservation or restoration of indigenous biodiversity, OVP is one manifestation of a European vision of rewilding, as the restoration of ecological processes to create untamed landscapes reminiscent of ecological conditions at the end of the Pleistocene (*63*). The challenge is uncertainty over the emergent properties and climax equilibrium vegetation of the area, but the emphasis is on minimizing human interventions.

However, restoration that aspires to exclude human influence and activity has been challenged as being unobtainable or unsustainable. The positive average annual population growth rates for the larger carnivores, the golden jackal (*Canis aureus*), gray wolf (*Canis lupus*), Eurasian lynx (*Lynx lynx*), Iberian lynx (*Lynx pardinus*), and wolverine (*Gulo gulo*), in Europe between 1961 and 2005 (*64*), for example, has shifted emphasis away from preventing extinctions and prompted thinking toward future planning under a new model of coexistence between predators and humans over large spatial scales (*65*). This reshaping of rewilding acknowledges that humans are an integral part of, not apart from, nature and recasts the retrospective goals of restoring "wilderness" as future-oriented visions of creating "wildness" in which ecological processes, such as predator-prey interactions, are managed within landscapes shared by humans and wildlife (*65*).

Future prospects and implications

With official IUCN recognition of a spectrum of conservation translocation tools, the emphasis has now shifted to how best to apply these approaches to maximize conservation benefit while minimizing the risk of unintended consequences. Particularly for the inherently more uncertain conservation introductions, the focus needs to be on development and application of rigorous methods to match species to habitats while evaluating risk. The IUCN guidelines (*7*) provide a framework for dealing with the complexities of conservation translocations and are sufficiently comprehensive to be able to accommodate new developments. The prospect of species de-extinction, the resurrection of extinct species using selective breeding or the clonal technologies of synthetic biology potentially broadens the range of species and associated processes we might seek to restore. De-extinction of multiple species will occur at some future time, but one question that must be addressed is which species? Because the goals of de-extinction relate to ecological enrichment, selection of de-extinction candidates should be guided by the feasibility and risks of their release into suitable habitat (*66*).

Daniel Pauly (*67*) called attention to "shifting baselines" in fisheries—a concept extended to encompass the gradual attrition in people's expectations of what the natural world around them should look like, whereby each generation grows up within a slightly more impoverished natural biodiversity. Defaunation is a major contributing factor to this extinction of experience. Translocations for the restoration of populations of threatened species, for reestablishment of ecological functions and processes, and for the re-creation of wildness provide a foundation for resetting public aspirations for biodiversity. Conservation translocation projects provide a powerful means to reconnect people with their natural heritage, to engage them as conservation partners, and to make them stewards of the wild animals and habitats around them.

Part of this reconnection with nature will entail a new appreciation of the concept of wild, moving away from increasingly unobtainable concepts of self-sustaining wildlife populations within pristine landscapes untouched by human influence. We are moving instead toward understanding the value of restoring and sustaining species and their habitats, possibly in novel configurations, with ongoing management, and with the needs of humans both acknowledged and integrated.

REFERENCES AND NOTES

1. S. H. M. Butchart *et al.*, *Science* **328**, 1164–1168 (2010).
2. H. M. Pereira *et al.*, *Science* **330**, 1496–1501 (2010).
3. R. Dirzo *et al.*, *Science* **345**, 401–406 (2014).
4. H. C. Giacomini, M. Galetti, *Biol. Conserv.* **163**, 33–41 (2013).
5. B. J. Cardinale *et al.*, *Nature* **486**, 59–67 (2012).
6. M. E. Soulé, G. H. Orians, Eds., *Conservation Biology: Research Priorities for the Next Decade* (Society for Conservation Biology, Island Press, Washington, DC, 2001).
7. IUCN, *Guidelines for Reintroductions and Other Conservation Translocations* (IUCN SSC, Gland, Switzerland, ed. 1.0, 2013).
8. J. G. Ewen, D. P. Armstrong, K. A. P. Parker, P. J. Seddon, Eds, *Reintroduction Biology: Integrating Science and Management* (Wiley-Blackwell, West Sussex, UK, 2012).
9. P. J. Seddon, D. P. Armstrong, R. F. Maloney, *Conserv. Biol.* **21**, 303–312 (2007).
10. P. J. Seddon, P. S. Soorae, F. Launay, *Anim. Conserv.* **8**, 51–58 (2005).
11. J. Champagnon, J. Elmberg, M. Guillemain, M. Gauthier-Clerc, J.-D. Lebreton, *J. Nat. Conserv.* **20**, 231–241 (2012).
12. B. Griffith, J. M. Scott, J. W. Carpenter, C. Reed, *Science* **245**, 477–480 (1989).
13. J. Fischer, D. B. Lindenmayer, *Biol. Conserv.* **96**, 1–11 (2000).
14. C. M. Wolf, T. Garland Jr., B. Griffith, *Biol. Conserv.* **86**, 243–255 (1998).
15. L. F. Keller *et al.*, in *Reintroduction Biology: Integrating Science and Management*, J. G. Ewen, D. P. Armstrong, K. A. P. Parker, P. J. Seddon, Eds. (Wiley-Blackwell, West Sussex, UK, 2012), pp. 360–394.
16. J. J. Groombridge *et al.*, in *Reintroduction Biology: Integrating Science and Management*, J. G. Ewen, D. P. Armstrong, K. A. P. Parker, P. J. Seddon, Eds. (Wiley-Blackwell, West Sussex, UK, 2012), pp. 395–440.
17. I. G. Jamieson, R. C. Lacy, in *Reintroduction Biology: Integrating Science and Management*, J. G. Ewen, D. P. Armstrong, K. A. P. Parker, P. J. Seddon, Eds. (Wiley-Blackwell, West Sussex, UK, 2012), pp. 441–475.
18. L. N. Tracy, G. P. Wallis, M. G. Efford, I. G. Jamieson, *Anim. Conserv.* **14**, 439–446 (2011).
19. A. Deredec, F. Courchamp, *Ecoscience* **14**, 440–451 (2007).
20. W. J. Sutherland *et al.*, *Conserv. Lett.* **3**, 229–235 (2010).
21. D. P. Armstrong, P. J. Seddon, *Trends Ecol. Evol.* **23**, 20–25 (2008).
22. S. T. Jackson, R. J. Hobbs, *Science* **325**, 567–569 (2009).
23. A. S. Thorpe, A. G. Stanley, *J. Appl. Ecol.* **48**, 275–279 (2011).
24. C. D. Thomas, *Trends Ecol. Evol.* **26**, 216–221 (2011).
25. R. J. Hobbs, E. S. Higgs, C. Hall, Eds., *Novel Ecosystems: Intervening in the New Ecological World Order* (Wiley-Blackwell, West Sussex, UK, 2013).
26. R. L. Peters, J. D. S. Darling, *Bioscience* **35**, 707–717 (1985).
27. N. E. Heller, E. S. Zavaleta, *Biol. Conserv.* **142**, 14–32 (2009).
28. J. S. McLachlan, J. J. Hellmann, M. W. Schwartz, *Conserv. Biol.* **21**, 297–302 (2007).
29. M. L. Hunter Jr., *Conserv. Biol.* **21**, 1356–1358 (2007).
30. O. Hoegh-Guldberg *et al.*, *Science* **321**, 345–346 (2008).

31. S. R. Loss, L. A. Terwilliger, A. C. Peterson, *Biol. Conserv.* **144**, 92–100 (2010).
32. N. Hewitt *et al*., *Biol. Conserv.* **144**, 2560–2572 (2011).
33. B. Nogardy, *Ecos* **25**, 13036 www.ecosmagazine.com/?paper=EC13036 (2013).
34. T. M. Lee, W. Jetz, *Proc. Biol. Sci.* **278**, 1329–1338 (2011).
35. E. McDonald-Madden, M. C. Runge, H. P. Possingham, T. G. Martin, *Nat. Climate Change* **1**, 261–265 (2011).
36. M. W. Schwartz, T. G. Martin, *Ann. N. Y. Acad. Sci.* **1286**, 15–28 (2013).
37. B. M. H. Larson, C. Palmer, *Ethics. Policy Environ.* **16**, 16–18 (2013).
38. S. G. Willis *et al*., *Conserv. Lett.* **2**, 46–51 (2009).
39. B. Huntley *et al*., *Ecography* **33**, 621–626 (2010).
40. A. L. M. Chauvenet, J. G. Ewen, D. Armstrong, N. Pettorelli, *J. Appl. Ecol.* **50**, 1330–1340 (2013).
41. N. Mitchell *et al*., *Biology* **2**, 1–25 (2012).
42. L. M. J. Travis *et al*., *Oikos* **122**, 1532–1540 (2013).
43. A. S. MacDougall, K. S. McCann, G. Gellner, R. Turkington, *Nature* **494**, 86–89 (2013).
44. J. M. Tylianakis, E. Laliberté, A. Nielsen, J. Bascompte, *Biol. Conserv.* **143**, 2270–2279 (2010).
45. M. Galetti *et al*., *Science* **340**, 1086–1090 (2013).
46. W. J. Ripple *et al*., *Science* **343**, 1241484 (2014).
47. I. D. Lunt *et al*., *Biol. Conserv.* **157**, 172–177 (2013).
48. M. W. Cadotte, K. Carscadden, N. Mirotchnick, *J. Appl. Ecol.* **48**, 1079–1087 (2011).
49. M. Pedrono *et al*., *Biol. Conserv.* **159**, 501–506 (2013).
50. C. Sandom *et al*., in *Key Topics in Conservation Biology 2*, D. W. MacDonald, K. J. Willis, Eds. (Wiley-Blackwell, West Sussex, UK, 2013), pp. 430–451.
51. D. M. Hansen, M. Galetti, *Science* **324**, 42–43 (2009).
52. P. R. Guimarães, M. Galetti, P. Jordano, *PLOS ONE* **3**, e1745 (2008).
53. J. P. Gibbs, C. Marquez, E. J. Sterling, *Restor. Ecol.* **16**, 88093 (2008).
54. C. J. Griffiths *et al*., *Restor. Ecol.* **18**, 1–7 (2010).
55. C. J. Griffiths, D. M. Hansen, C. G. Jones, N. Zuël, S. Harris, *Curr. Biol.* **21**, 762–765 (2011).
56. D. M. Hansen, C. J. Donlan, C. J. Griffiths, K. J. Campbell, *Ecography* **33**, 272–284 (2010).
57. S. Reardon, *New Sci.* **221**, 40–43 (2014).
58. R. T. Corlett, *Biol. Conserv.* **163**, 13–21 (2013).
59. M. Soulé, R. Noss, *Wild Earth* **1998** (Fall), 1-11 (1998).
60. J. Donlan, *Nature* **436**, 913–914 (2005).
61. D. Bowman, *Nature* **482**, 30 (2012).
62. F. W. M. Vera, *Br. Wildlife* **20** (suppl.), 28–36 (2009).
63. J. Lorimer, C. Driessen, *Trans. Inst. Br. Geogr.* **3**, 169–181 (2013).
64. S. Deinet *et al*., 2013. *Wildlife Comeback in Europe: The Recovery of Selected Mammal and Bird Species* (Final report to Rewilding Europe by ZSL, Birdlife International, and the European Bird Census Council, London, UK; Zoological Society of London, London, 2013).
65. L. Boitani, L. D. C. Linnell, in *Rewilding European Landscapes*, H. Periera, L. Navarro, Eds. (Springer Science, Dordrecht, 2014).
66. P. J. Seddon, A. Moehrenschlager, J. Ewen, *Trends Ecol. Evol.* **29**, 140–147 (2014).
67. D. Pauly, *Trends Ecol. Evol.* **10**, 430 (1995).
68. R. J. Keedwell, R. F. Maloney, D. P. Murray, *Biol. Conserv.* **105**, 369–374 (2002).
69. J. M. Germano, P. J. Bishop, *Conserv. Biol.* **23**, 7–15 (2009).
70. C. J. Griffiths, N. Zuël, C. G. Jones, Z. Ahamud, S. Harris, *Conserv. Biol.* **27**, 690–700 (2013).

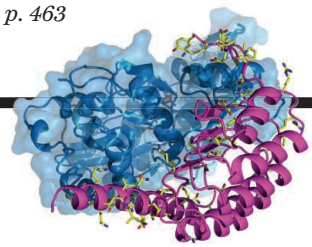
ACKNOWLEDGMENTS

We are grateful to P. Bishop, L. Boitani, S. Clelland, P. Guilford, Y. van Heezik, M. Knight, D. Mallon, R. Maloney, A. Moehrenschlagar, N. Mooney, J. Olden, M. Stanley Price, and two anonymous referees, who variously shared their insights, facilitated access to literature or images, or gave valuable feedback on early versions of the manuscript. K. Miller assisted with formatting the figures.

10.1126/science.1251818

RESEARCH

How tropomodulin binds and caps the pointed end of actin
Rao et al. *p. 463*



IN *SCIENCE* JOURNALS

Edited by **Stella Hurtley**



Artist's view of the new species

DINOSAUR EVOLUTION

Feathers, not just for the birds?

Theropod dinosaurs, thought to be the direct ancestors of birds, sported birdlike feathers. But were they the only feathery dino group? Godefroit *et al.* describe an early neornithischian dinosaur with both early feathers and scales. This seemingly feathery nontheropod dinosaur shows that feathers were not unique to the ancestors of birds and may even have been quite widespread. — SNV

Science, this issue p. 451

RNA FUNCTION

Problems making proteins kills nerve cells

Neurodegeneration is associated with a variety of different diseases, but its cellular roots are often obscure. Ishimura *et al.* find that mutant mice whose brain cells start to die rapidly soon after birth have lost the function of two vital cellular components (see the Perspective by Darnell). The first is a protein that releases stalled ribosomes stuck on messenger RNA (mRNA); the second is a transfer RNA (tRNA), which reads the code for arginine in the mRNA. This tRNA is expressed predominantly in the central nervous system. The lack of the tRNA leads to increased ribosomal stalling at arginine codons, which, when left uncorrected, blocks protein synthesis and proves fatal. — GR

Science, this issue p. 455; see also p. 378

CYSTIC FIBROSIS

In CF, two drugs are no better than one

Cystic fibrosis (CF), a disabling lung disease, is caused by mutations in a protein called CFTR, which acts as a channel to move chloride ions into and out of cells. Ivacaftor, the only targeted drug available, does not work well for the severest, most common form of disease. Cholon *et al.* and Veit *et al.* now explain why efforts to improve CF treatment by combining ivacaftor with new drugs have failed. Ivacaftor increases mutant CFTR's activity, but it only works when CFTR is on the cell surface. The new drugs under development bring mutant CFTR to the surface, but combining the two types of drugs has not been effective because ivacaftor also makes CFTR less stable, so cells remove it quickly from their membranes. — YN

Sci. Transl. Med. **6**, 246ra96, 246ra97 (2014).

METAMATERIALS

To cast no shadow in a murky medium

Cloaks can hide objects from view, but what about their shadows? Schittny *et al.* devised a cloak to remove even the shadow of an object embedded in a murky medium in front of a computer screen (see the Perspective by Smith). They engineered a core-shell structure within which an object could be hidden and tailored the optical properties of the cloak to match that of the medium. Light was routed around the cloak, leaving no trace of the hidden object. — ISO

Science, this issue p. 427; see also p. 384

CELL BIOLOGY

Changing skin cells in development with TGF-β

Transforming growth factor–β (TGF-β) makes some cells stop dividing, separate from one another, and start migrating. This process, called the epithelial-to-mesenchymal transition, occurs during normal development and can help cancers progress. D'Souza *et al.* cultured skin cells and measured changes in their proteins as they underwent this process. TGF-β caused thousands of protein changes that varied depending on how long

PHOTOS: (TOP TO BOTTOM) RAO *ET AL.*; ANDREY ATUCHIN

Downloaded from www.sciencemag.org on July 27, 2014

Published by AAAS

cells were exposed to TGF-β. The protein changes correlated with changes in cell behavior. The authors modeled the network of interacting proteins affected by TGF-β, creating a road map that can explain how TGF-β influences cell behavior. — JDB

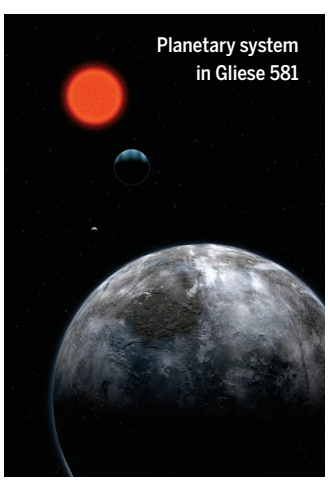
Sci. Signal. **7**, rs5 (2014).

QUANTUM METROLOGY

Subtle entanglement in an atomic cloud

In the quantum world, atoms can be correlated with each other—"entangled"—which reduces the uncertainty in the knowledge of some of their properties. Physicists then use this reduced uncertainty to perform precision measurements. Strobel *et al.* made an unusual type of entangled state consisting of hundreds of ultracold Rb atoms. These methods may in the future be able to generate states that will be more useful in precision measurement. — JS

Science, this issue p. 424



Planetary system in Gliese 581

EXOPLANET DETECTION

Tricky star plays sleight-of-light

Two signatures in starlight thought to be written by extrasolar planets may turn out to be forgeries. Astronomers often attribute periodic shifts in a star's apparent motion toward and away from us to the tug of orbiting planets. Robertson *et al.* studied archival spectra of the star Gliese 581 to assess another potential cause: magnetic activity on the star's surface. The signals once attributed to two planet candidates instead resulted from the combined effect of starspots and stellar rotation. Planet hunters be warned—correct for stellar activity in your data analyses. — MMM

Science, this issue p. 440

INDUCED EARTHQUAKES

Wastewater disposal linked to earthquakes

The number of earthquakes is increasing in regions with active unconventional oil and gas wells, where water pumped at high pressure breaks open rock containing natural gas, leaving behind wastewater in need of disposing. Keranen *et al.* show that the steep rise in earthquakes in Oklahoma, USA, is likely caused by fluid migration from wastewater disposal wells. Twenty percent of the earthquakes in the central United States could be attributed to just four of the wells. Injected fluids in high-volume wells triggered earthquakes over 30 km away. — NW

Science, this issue p. 448

CLATHRIN ADAPTORS

A membrane-activated switch to bind clathrin

Clathrin-mediated endocytosis—the process by which cells take up nutrients and signals within clathrin-coated vesicles—is very well understood. Kelly *et al.* reveal an unanticipated layer of regulation in this process. The proteins AP2 and clathrin are the major constituents of endocytic clathrin-coated vesicles. AP2 and clathrin stick together through a clathrin-binding motif in AP2. The authors now show that AP2's clathrin-binding motif is normally buried within the core of the AP2 protein. AP2 only ejects its clathrin-binding motif and recruits clathrin if it is associated with the correct cell membrane and an endocytic cargo. — SMH

Science, this issue p. 459

IN OTHER JOURNALS

Edited by **Kristen Mueller** *and* **Jesse Smith**



The common marmoset has a sequenced genome

GENOMICS

Marmoset DNA shows why it's small

A New World monkey joins a growing list of primate species with sequenced genomes, improving genomicists' ability to tell what genes make primates—and humans—unique. Brazil's common marmoset is unusual among primates: It is tiny—the size of a guinea pig—and always produces twins. During development, the twins share placental blood supply; after birth, each carries stem cells from the other that produce foreign blood cells with no ill effect. The Marmoset Genome Sequencing and Analysis Consortium fouwnd five genes likely involved in making the monkey small and eight genes that may help it adjust its metabolism and temperature control to deal with being tiny. — EP

Nat. Genet. 10.1038/ng.3042 (2014).

OPTICAL IMAGING

Stealthy spying on a moving target

Ghost imaging can create an image of a moving target without the target ever knowing that it is being watched. The traditional way to observe an object, either stationary or in motion, is to illuminate it and use the light that it reflects or scatters to create an image on a detector such as a camera. However, the observation of the object can itself be detected, which compromises the stealth of the process. Ghost imaging, a technique that forms an image with photons that have never even come into contact with the object, has been used to detect objects at rest, and now Li *et al.* show that it also can be used to reconstruct the image of moving targets, such as the small wafer that they use in their demonstration. — ISO

Appl. Phys. Lett. **104**, 251120 (2014).

TRANSCRIPTION

TRF2 gets transcription started, too

Transcribing DNA into RNA involves an intricate dance of proteins and nucleic acids. Transcription starts at specific promoter sequences near genes, including one called the TATA box. For most genes, a protein called TBP binds to the

PHOTOS: (LEFT TO RIGHT) ESO; © PETE OXFORD/MINDEN PICTURES/CORBIS

Published by AAAS

ALSO IN *SCIENCE* JOURNALS

Edited by **Stella Hurtley**

ECOLOGICAL NETWORKS

A structural approach to species interactions

What determines the stability of ecological networks? Rohr *et al.* devised a conceptual approach to study interactions between species that emphasizes the role of network structure (see the Perspective by Pawar). Using the example of mutualistic networks of communities of plants and their pollinator species, they show how the structure of networks can determine the persistence of the interactions. Network structures and architectures observed in nature intrinsically match the most stable solution. This approach has promise for application to questions of ecological community stability under global change. — AMS

Science, this issue p. 416; see also p. 383

DUAL CATALYSIS

A bright outlook for carbon coupling

In contemporary organic chemistry, it is straightforward to forge bonds between unsaturated carbons (i.e., carbons already engaged in double bonds) using cross-coupling catalysis. The protocol runs into some trouble, however, if one or both starting carbon centers are saturated (purely single-bonded). Tellis *et al.* and Zuo *et al.* independently found that combining a second, light-activated catalyst with a nickel cross-coupling catalyst could achieve selective coupling of saturated and unsaturated reagents (see the Perspective by Lloyd-Jones and Ball). Their methods rely on single-electron transfer from the light-activated catalyst to the saturated carbon, thereby enhancing its reactivity more effectively than the two-electron mechanisms prevailing in traditional protocols. — JSY

Science, this issue p. 433, p. 437; see also p. 381

QUANTUM COMPUTING

How to benchmark a quantum computer

Quantum machines offer the possibility of performing certain computations much faster than their classical counterparts. However, how to define and measure quantum speedup is a topic of debate. Rønnow *et al.* describe methods for fairly evaluating the difference in computational power between classical and quantum processors. They define various types of quantum speedup and consider quantum processors that are designed to solve a specific class of problems. — ISO

Science, this issue p. 420

ULTRAFAST OPTICS

Toward the control of light with light

Optic fibers form the backbone of the communications sector and carry huge amounts of data around the globe. Nissim *et al.* show that small perturbations within the core of a fiber give rise to interactions between photons. The strength of the interaction could be controlled by carefully characterizing and splicing together different lengths of fiber. The interactions between the photons were enhanced so that a strong signal beam could be switched off with just a few photons. — ISO

Science, this issue p. 417

QUANTUM SIMULATION

Characterization of a quantum simulator

Ultracold gases can be used to simulate the behavior of more complicated systems, such as solid materials. Senko *et al.* developed a method similar to nuclear magnetic resonance that can be used to validate the properties of such simulators. They demonstrated the method on an array of interacting trapped ions that simulate magnetism. A modulated magnetic field resonantly enhanced the transfer of the population between the different configurations of the system. The authors varied the modulation frequency to measure the energy of each configuration and mapped the effective interactions. — JS

Science, this issue p. 430

PALEOCLIMATE

Climates conspire together to make big changes

The regional climates of the North Pacific and North Atlantic fluttered between synchrony and asynchrony during the last deglaciation, with correspondingly more and less intense effects on the rest of the world, researchers have found. The climate system can be highly nonlinear, meaning that small changes in one part can lead to much larger changes elsewhere. This type of behavior is especially evident during transitions from glacial to interglacial conditions, when climate is affected by a wide variety of time-varying influences and is relatively unstable. Praetorius and Mix present a record of North Pacific climate over the past 18,000 years. When the climates of the more local high-latitude Pacific and Atlantic sectors varied in parallel, large, abrupt climate fluctuations occurred on a more global scale. — HJS

Science, this issue p. 444

ACTIN CYTOSKELETON

Making tropomodulin find the right point

Actin filaments are a key component of the cell's cytoskeleton. Actin filaments have a characteristic polarized architecture with a so-called barbed end and a pointed end—so described because of how the filaments look under the electron microscope when they are coated with tropomyosin. Rao *et al.* describe crystal structures of a protein that uniquely binds and caps the pointed end of actin filaments. This protein, tropomodulin, binds to several actin subunits and to a couple of tropomyosin molecules, which generates a high-affinity specific cap to the filaments by combining low-affinity interactions. — SMH

Science, this issue p. 463

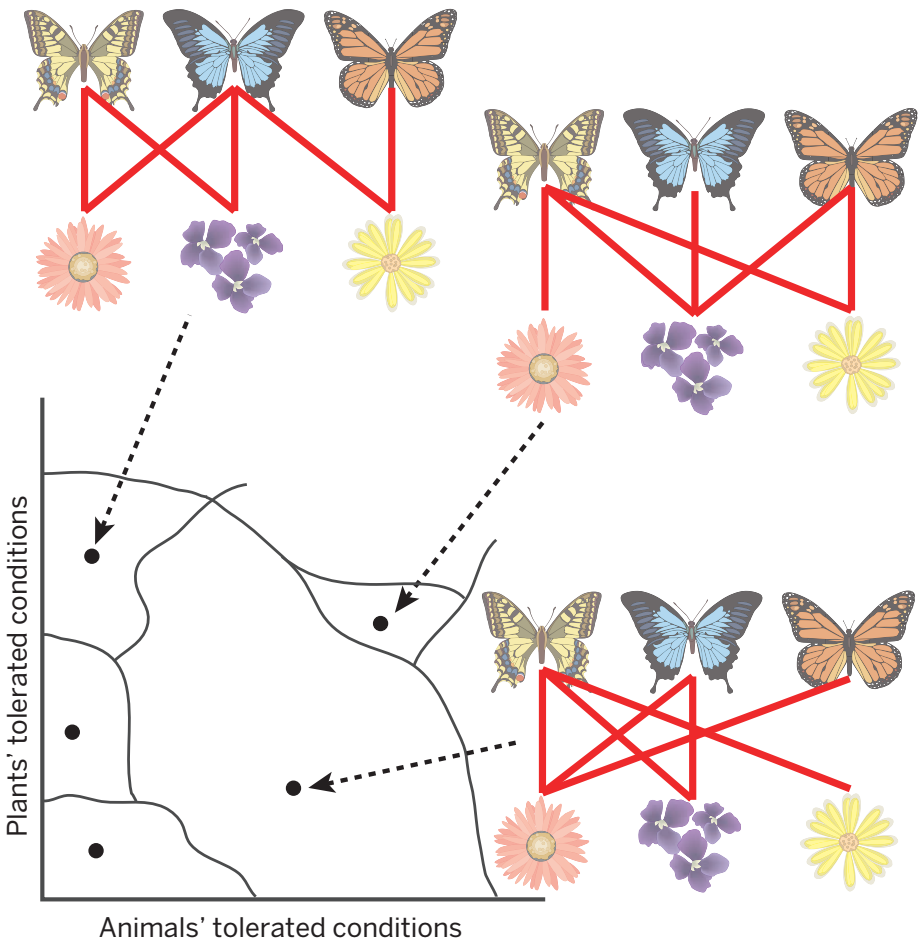
Published by AAAS

RESEARCH ARTICLE SUMMARY

ECOLOGICAL NETWORKS

On the structural stability of mutualistic systems

Rudolf P. Rohr,[1,2] Serguei Saavedra,[1] Jordi Bascompte[1]*



The architecture of plant-animal mutualistic networks modulates the range of conditions leading to the stable coexistence of all species. The area of the different domains represents the structural stability of a model of mutualistic communities with a given network architecture. The nested networks observed in nature—illustrated here by the network at the bottom—lead to a maximum structural stability.

INTRODUCTION: Several major developments in theoretical ecology have relied on either dynamical stability or numerical simulations, but oftentimes, they have found contradictory results. This is partly a result of not rigorously checking either the assumption that a steady state is feasible—meaning, all species have constant and positive abundances—or the dependence of results to model parameterization. Here, we extend the concept of structural stability to community ecology in order to account for these two problems. Specifically, we studied the set of conditions leading to the stable coexistence of all species within a community. This shifts the question from asking whether we can find a feasible equilibrium point for a fixed set of parameter values, to asking how large is the range of parameter values that are compatible with the stable coexistence of all species.

ON OUR WEBSITE

Read the full article at http://dx.doi.org/10.1126/science.1253497

RATIONALE: We begin by disentangling the conditions of global stability from the conditions of feasibility of a steady state in ecological systems. To quantify the domain of stable coexistence, we first find its center (the structural vector of intrinsic growth rates). Next, we determine the boundaries of such a domain by quantifying the amount of variation from the structural vector tolerated before one species goes extinct. Through this two-step approach, we disentangle the effects of the size of the feasibility domain from how close a solution is to its boundary, which is at the heart of previous contradictory results. We illustrate our method by exploring how the observed architecture of mutualistic networks between plants and their pollinators or seed dispersers affects their domain of stable coexistence.

RESULTS: First, we determined the network architecture that maximizes the structural stability of mutualistic systems. This corresponds to networks with a maximal level of nestedness, a small trade-off between the number and intensity of interactions a species has, and a high level of mutualistic strength within the constraints of global stability. Second, we found that the large majority of observed mutualistic networks are close to this optimum network architecture, maximizing the range of parameters that are compatible with species coexistence.

CONCLUSION: Structural stability has played a major role in several fields such as evolutionary developmental biology, in which it has brought the view that some morphological structures are more common than others because they are compatible with a wider range of developmental conditions. In community ecology, structural stability is the sort of framework needed to study the consequences of global environmental change—by definition, large and directional—on species coexistence. Structural stability will serve to assess both the range of variability a given community can withstand and why some community patterns are more widespread than others. ■

[1]Integrative Ecology Group, Estación Biológica de Doñana–Consejo Superior de Investigaciones Científicas (EBD-CSIC), Calle Américo Vespucio s/n, E-41092 Sevilla, Spain. [2]Unit of Ecology and Evolution, Department of Biology, University of Fribourg, Chemin du Musée 10, CH-1700 Fribourg, Switzerland.

*Corresponding author. E-mail: bascompte@ebd.csic.es

Cite this article as: R. Rohr *et al.*, *Science* **345**, 1253497 (2014). DOI: 10.1126/science.1253497

Published by AAAS

RESEARCH ARTICLE

ECOLOGICAL NETWORKS

On the structural stability of mutualistic systems

Rudolf P. Rohr,[1,2]* Serguei Saavedra,[1]* Jordi Bascompte[1]†

In theoretical ecology, traditional studies based on dynamical stability and numerical simulations have not found a unified answer to the effect of network architecture on community persistence. Here, we introduce a mathematical framework based on the concept of structural stability to explain such a disparity of results. We investigated the range of conditions necessary for the stable coexistence of all species in mutualistic systems. We show that the apparently contradictory conclusions reached by previous studies arise as a consequence of overseeing either the necessary conditions for persistence or its dependence on model parameterization. We show that observed network architectures maximize the range of conditions for species coexistence. We discuss the applicability of structural stability to study other types of interspecific interactions.

A prevailing question in ecology [particularly since May's seminal work in the early 1970s (*1*)] is whether, given an observed number of species and their interactions, there are ways to organize those interactions that lead to more persistent communities. Conventionally, studies addressing this question have either looked into local stability or used numerical simulations (*2*–*4*). However, these studies have not yet found a unified answer (*1*, *5*–*12*). Therefore, the current challenge is to develop a general framework in order to provide a unified assessment of the implications of the architectural patterns of the networks we observe in nature.

Main approaches in theoretical ecology

Dynamical stability and feasibility

Studies based on the mathematical notions of local stability, *D*-stability, and global stability have advanced our knowledge on what makes ecological communities stable. In particular, these studies explore how interaction strengths need to be distributed across species so that an assumed feasible equilibrium point can be stable (*1*–*4*, *13*–*17*). By definition, a feasible equilibrium point is that in which all species have a constant positive abundance across time. A negative abundance makes no sense biologically, and an abundance of zero would correspond to an extinct species.

The dynamical stability of a feasible equilibrium point corresponds to the conditions under which the system returns to the equilibrium point after a perturbation in species abundance. Local stability, for instance, looks at whether a system will return to an assumed feasible equilibrium after an infinitesimally small perturbation (*1*–*3*, *13*). *D*-stability, in turn, looks at the local stability of any potential feasible equilibrium that the system may have (*15*–*17*). More generally, global stability looks at the stability of any potential feasible equilibrium point after a perturbation of any given amplitude (*14*–*17*). A technical definition of these different types of dynamical stability and their relationship is provided in (*18*).

In most of these stability studies, however, a feasible equilibrium point is always assumed without rigorously studying the set of conditions allowing its existence (*5*, *14*, *15*, *19*). Yet in any given system, we can find examples in which we satisfy only one, both, or none of the feasibility and stability conditions (*3*, *16*, *17*, *19*). This means that without a proper consideration of the feasibility conditions, any conclusion for studying the stable coexistence of species is based on a system that may or may not exist (*3*, *5*, *19*).

To illustrate this point, consider the following textbook example of a two-species competition system

$$\begin{cases} \frac{dN_1}{dt} = N_1(\alpha_1 - \beta_{11}N_1 - \beta_{12}N_2) \\ \frac{dN_2}{dt} = N_2(\alpha_2 - \beta_{21}N_1 - \beta_{22}N_2) \end{cases} \quad (1)$$

where N_1 and N_2 are the abundances of species 1 and 2; β_{11} and β_{22} are their intraspecific competition strengths; β_{12} and β_{21} are their interspecific competition strengths; and α_1 and α_2 are their intrinsic growth rates. An equilibrium point of the system is a pair of abundances N_1^* and N_2^* that makes the right side of the ordinary differential equation system equal to zero.

Although the only condition necessary to guarantee the global stability of any feasible equilibrium point in this system is that the interspecific competition strengths are lower than the intraspecific ones ($\beta_{12}\beta_{21} < \beta_{11}\beta_{22}$), the feasibility conditions are given by $N_1^* = \frac{\beta_{22}\alpha_1 - \beta_{12}\alpha_2}{\beta_{11}\beta_{22} - \beta_{12}\beta_{21}} > 0$ and $N_2^* = \frac{\beta_{11}\alpha_2 - \beta_{21}\alpha_1}{\beta_{11}\beta_{22} - \beta_{12}\beta_{21}} > 0$ (*3*, *4*, *19*). This implies that if we set, for example, $\beta_{11} = \beta_{22} = 1$, $\beta_{12} = \beta_{21} = 0.5$, $\alpha_1 = 1$, and $\alpha_2 = 2$, we fulfill the stability condition but not the feasibility condition, whereas if we set $\beta_{11} = \beta_{22} = 0.5$, $\beta_{12} = \beta_{21} = 1$, and $\alpha_1 = \alpha_2 = 1$, we can satisfy the feasibility condition but not the stability one. To have a stable and feasible equilibrium point, we need to set, for instance, $\beta_{11} = \beta_{22} = 1$, $\beta_{12} = \beta_{21} = 0.5$, and $\alpha_1 = \alpha_2 = 1$ (a graphical illustration is provided in Fig. 1).

The example above confirms the importance of verifying both the stability and the feasibility conditions of the equilibrium point when analyzing the stable coexistence of species (*3*–*5*, *19*). Of course, we can always fine-tune the parameter values of intrinsic growth rates so that the system is feasible (*16*, *17*). This strategy, for example, has been used when studying the success probability of an invasive species (*20*). However, when fixing the parameter values of intrinsic growth rates, we are not anymore studying the overall effect of interspecific interactions on the stable coexistence of species. Rather, we are answering the question of how interspecific interactions increase the persistence of species for a given parameterization of intrinsic growth rates. As we will show below, this is also the core of the problem in studies that are based on arbitrary numerical simulations.

Numerical simulations

Numerical simulations have provided an alternative and useful tool with which to explore species coexistence in large ecological systems in which analytical solutions are precluded (*3*). With this approach, one has as a prerequisite to parameterize the dynamical model, or a least to have a good estimate of the statistical distribution from which these parameters should be sampled. However, if one chooses an arbitrary parameterization without an empirical justification, any study has a high chance of being inconclusive for real ecosystems because species persistence is strongly dependent on the chosen parameterization.

To illustrate this point, we simulated the dynamics of an ecological model (*6*) with three different parameterizations of intrinsic growth rates (*21*). Additionally, these simulations were performed over an observed mutualistic network of interactions between flowering plants and their pollinators located in Hickling Norfolk, UK (table S1), a randomized version of this observed network, and the observed network without mutualistic interactions (we assume that there is only competition among plants and among animals). As shown in Fig. 2, it is possible to find a set of intrinsic growth rates so that any network that we analyze is completely persistent and, at the same time, the alternative networks are less persistent.

This observation has two important implications. First, this means that by using different parameterizations for the same dynamical model

[1]Integrative Ecology Group, Estación Biológica de Doñana–Consejo Superior de Investigaciones Científicas (EBD-CSIC), Calle Américo Vespucio s/n, E-41092 Sevilla, Spain. [2]Unit of Ecology and Evolution, Department of Biology, University of Fribourg, Chemin du Musée 10, CH-1700 Fribourg, Switzerland.
*These authors contributed equally to this work. †Corresponding author. E-mail: bascompte@ebd.csic.es

and network of interactions, one can observe from all to a few of the species surviving. Second, this means that each network has a limited range of parameter values under which all species coexist. Thus, by studying a specific parameterization, for instance, one could wrongly conclude that a random network has a greater effect on community persistence than that of an observed network, or vice versa (*10*–*12*). This sensitivity to parameter values clearly illustrates that the conclusions that arise from studies that use arbitrary values in intrinsic growth rates are not about the effects of network architecture on species coexistence, but about which network architecture maximizes species persistence for that specific parameterization.

Traditional studies focusing on either local stability or numerical simulations can lead to apparently contradictory results. Therefore, we need a different conceptual framework to unify results and seek for appropriate generalizations.

Structural stability

Structural stability has been a general mathematical approach with which to study the behavior of dynamical systems. A system is considered to be structurally stable if any smooth change in the model itself or in the value of its parameters does not change its dynamical behavior (such as the existence of equilibrium points, limit cycles, or deterministic chaos) (*22*–*25*). In the context of ecology, an interesting behavior is the stable coexistence of species—the existence of an equilibrium point that is feasible and dynamically stable. For instance, in our previous two-species competition system there is a restricted area in the parameter space of intrinsic growth rates that leads to a globally stable and feasible solution as long as $\rho < 1$ (Fig. 3, white area). The higher the competition strength ρ, the larger the size of this restricted area (Fig. 3) (*19*, *26*). Therefore, a relevant question here is not only whether or not the system is structurally stable, but how large is the domain in the parameter space leading to the stable coexistence of species.

To address the above question, we recast the mathematical definition of structural stability to that in which a system is more structurally stable, the greater the area of parameter values leading to both a dynamically stable and feasible equilibrium (*27*–*29*). This means that a highly structurally stable ecological system is more likely to be stable and feasible by handling a wider range of conditions before the first species becomes extinct. Previous studies have used this approach in low-dimensional ecological systems (*3*, *19*). Yet because of its complexity, almost no study has fully developed this rigorous analysis for a system with an arbitrary number of species. An exception has been the use of structural stability to calculate an upper bound to the number of species that can coexist in a given community (*6*, *30*).

Here, we introduce this extended concept of structural stability into community ecology in order to study the extent to which network architecture—strength and organization of interspecific interactions—modulates the range of conditions compatible with the stable coexistence of species. As an empirical application of our framework, we studied the structural stability of mutualistic systems and applied it on a data set of 23 quantitative mutualistic networks (table S1). We surmise that observed network architectures increase the structural stability and in turn the likelihood of species coexistence as a function of the possible set of conditions in an ecological system. We discuss the applicability of our framework to other types of interspecific interactions in complex ecological systems.

Structural stability of mutualistic systems

Mutualistic networks are formed by the mutually beneficial interactions between flowering plants and their pollinators or seed dispersers (*31*). These mutualistic networks have been shown to share a nested architectural pattern (*32*). This nested architecture means that typically, the mutualistic interactions of specialist species are proper subsets of the interactions of more generalist species (*32*). Although it has been repeatedly shown that this nested architecture may arise from a combination of life history and complementarity constraints among species (*32*–*35*), the effect of this nested architecture on community persistence continues to be a matter of strong debate. On the one hand, it has been shown that a nested architecture can facilitate the maintenance of species coexistence (*6*), exhibit a flexible response to environmental disturbances (*7*, *8*, *36*), and maximize total abundance (*12*). On the other hand, it has also been suggested that this nested

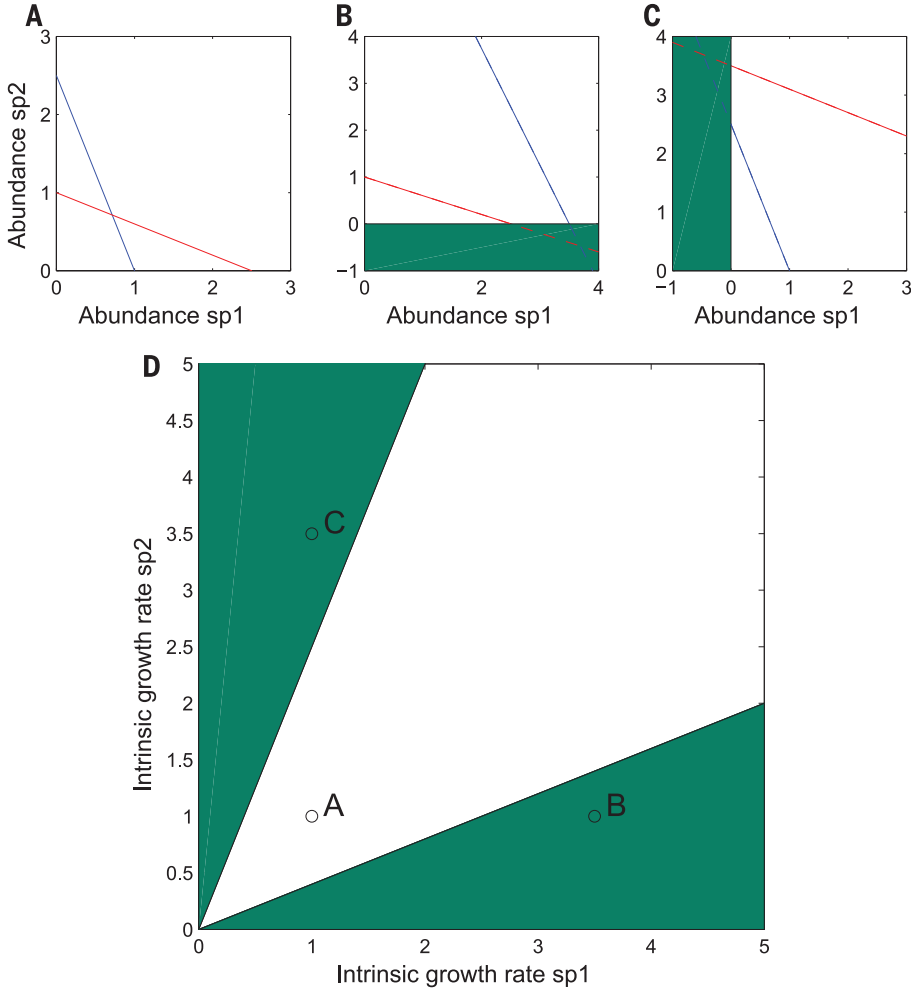


Fig. 1. Stability and feasibility of a two-species competition system. For the same parameters of competition strength (which grant the global stability of any feasible equilibrium), (**A** to **C**) represent the two isoclines of the system. Their intersection gives the equilibrium point of the system (*3*, *19*). Scenario (A) leads to a feasible equilibrium (both species have positive abundances at equilibrium), whereas in scenarios (B) and (C), the equilibrium is not feasible (one species has a negative abundance at equilibrium). (**D**) represents the area of feasibility in the parameter space of intrinsic growth rates, under the condition of global stability. This means that when the intrinsic growth rates of species are chosen within the white area, the equilibrium point is globally stable and feasible. In contrast, when the intrinsic growth rates of species are chosen within the green area, the equilibrium point is not feasible. Points "A," "B," and "C" indicate the parameter values corresponding to (A) to (C), respectively.

architecture can minimize local stability (*9*), have a negative effect on community persistence (*10*), and have a low resilience to perturbations (*12*). Not surprisingly, the majority of these studies have been based on either local stability or numerical simulations with arbitrary parameterizations [but, see (*6*)].

Model of mutualism

To study the structural stability and explain the apparently contradictory results found in studies of mutualistic networks, we first need to introduce an appropriate model describing the dynamics between and within plants and animals. We use the same set of differential equations as in (*6*). We chose these dynamics because they are simple enough to provide analytical insights and yet complex enough to incorporate key elements—such as saturating, functional responses (*37*, *38*) and interspecific competition within a guild (*6*)—recently adduced as necessary ingredients for a reasonable theoretical exploration of mutualistic interactions. Specifically, the dynamical model has the following form

$$\begin{cases} \dfrac{dP_i}{dt} = P_i\left(\alpha_i^{(P)} - \sum_j \beta_{ij}^{(P)} P_j + \dfrac{\sum_j \gamma_{ij}^{(P)} A_j}{1 + h\sum_j \gamma_{ij}^{(P)} A_j}\right) \\ \dfrac{dA_i}{dt} = A_i\left(\alpha_i^{(A)} - \sum_j \beta_{ij}^{(A)} A_j + \dfrac{\sum_j \gamma_{ij}^{(A)} P_j}{1 + h\sum_j \gamma_{ij}^{(A)} P_j}\right) \end{cases} \quad (2)$$

where the variables P_i and A_i denote the abundance of plant and animal species i, respectively.

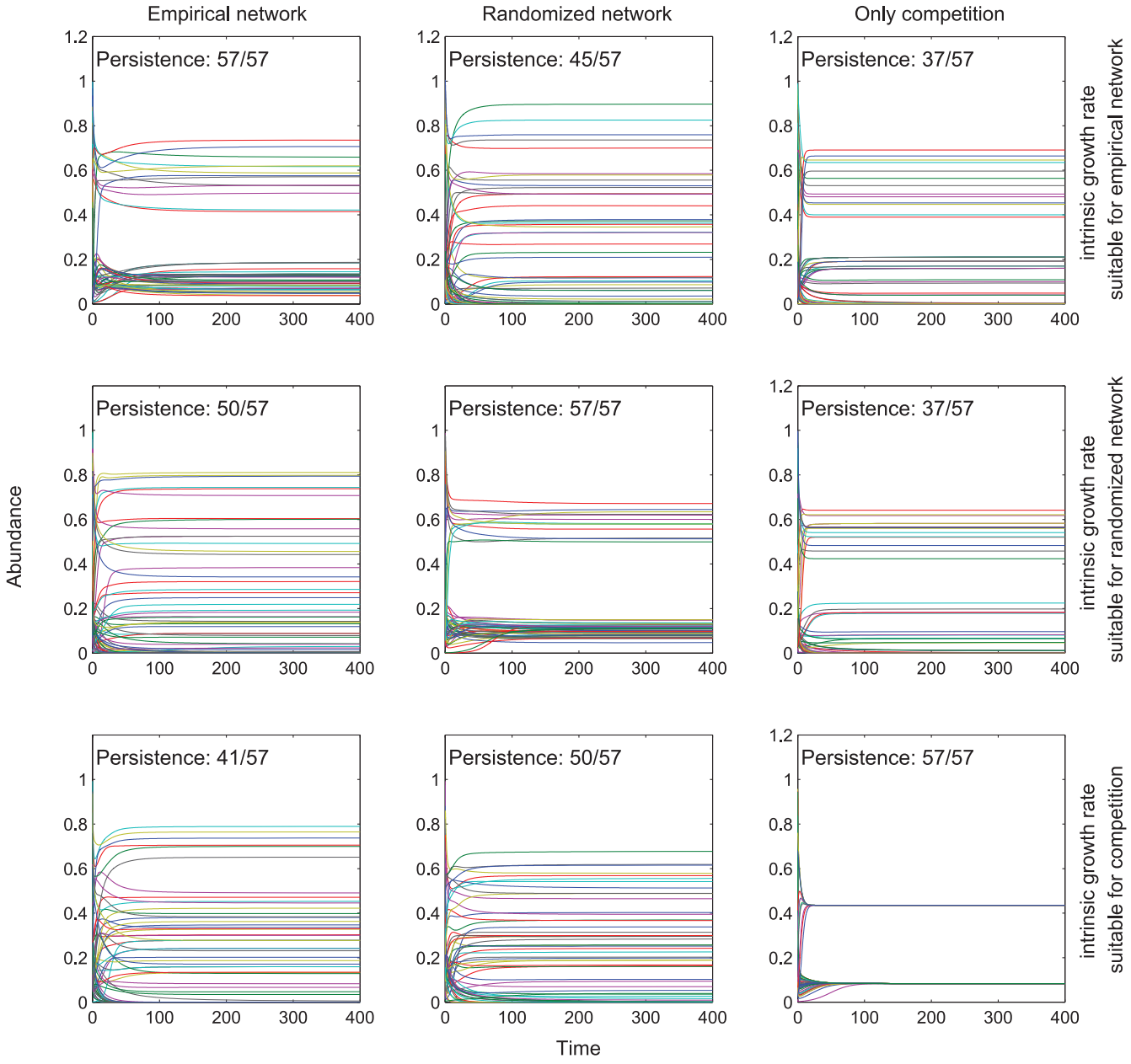


Fig. 2. Numerical analysis of species persistence as a function of model parameterization. This figure shows the simulated dynamics of species abundance and the fraction of surviving species (positive abundance at the end of the simulation) using the mutualistic model of (*6*). Simulations are performed by using an empirical network located in Hickling, Norfolk, UK (table S1), a randomized version of this network using the probabilistic model of (*32*), and the network without mutualism (only competition). Each row corresponds to a different set of growth rate values. It is always possible to choose the intrinsic growth rates so that all species are persistent in each of the three scenarios, and at the same time, the community persistence defined as the fraction of surviving species is lower in the alternative scenarios.

The parameters of this mutualistic system correspond to the values describing intrinsic growth rates (α_i), intra-guild competition (β_{ij}), the benefit received via mutualistic interactions (γ_{ij}), and the saturating constant of the beneficial effect of mutualism (h), commonly known as the handling time. Because our main focus is on mutualistic interactions, we keep as simple as possible the competitive interactions for the sake of analytical tractability. In the absence of empirical information about interspecific competition, we use a mean field approximation for the competition parameters (*6*), where we set $\beta_{ii}^{(P)} = \beta_{ii}^{(A)} = 1$ and $\beta_{ij}^{(P)} = \beta_{ij}^{(A)} = \rho < 1$ ($i \neq j$).

Following (*39*), the mutualistic benefit can be further disentangled by $\gamma_{ij} = (\gamma_0 y_{ij})/(k_i^{\delta})$, where $y_{ij} = 1$ if species i and j interact and zero otherwise, k_i is the number of interactions of species i, γ_0 represents the level of mutualistic strength, and δ corresponds to the mutualistic trade-off. The mutualistic strength is the per capita effect of a certain species on the per capita growth rate of their mutualistic partners. The mutualistic trade-off modulates the extent to which a species that interacts with few other species does it strongly, whereas a species that interacts with many partners does it weakly. This trade-off has been justified on empirical grounds (*40*, *41*). The degree to which interspecific interactions y_{ij} are organized into a nested way can be quantified by the value of nestedness N introduced in (*42*).

We are interested in quantifying the extent to which network architecture (the combination of mutualistic strength, mutualistic trade-off, and nestedness) modulates the set of conditions compatible with the stable coexistence of all species—the structural stability. In the next sections, we explain how this problem can be split into two parts. First, we explain how the stability conditions can be disentangled from the feasibility conditions as it has already been shown for the two-species competition system. Specifically, we show that below a critical level of mutualistic strength ($\gamma_0 < \gamma_0^r$), any feasible equilibrium point is granted to be globally stable. Second, we explain how network architecture modulates the domain in the parameter space of intrinsic growth rates, leading to a feasible equilibrium under the constraints of being globally stable (given by the level of mutualistic strength).

Stability condition

We investigated the conditions in our dynamical system that any feasible equilibrium point needs to satisfy to be globally stable. To derive these conditions, we started by studying the linear Lotka-Volterra approximation ($h = 0$) of the dynamical model (Eq. 2). In this linear approximation, the model reads

$$\begin{bmatrix} \frac{dP}{dt} \\ \frac{dA}{dt} \end{bmatrix} = \mathrm{diag}\left(\begin{bmatrix} P \\ A \end{bmatrix}\right) \times \left(\begin{bmatrix} \alpha^{(P)} \\ \alpha^{(A)} \end{bmatrix} - \underbrace{\begin{bmatrix} \beta^{(P)} & -\gamma^{(P)} \\ -\gamma^{(A)} & \beta^{(A)} \end{bmatrix}}_{:=B} \begin{bmatrix} P \\ A \end{bmatrix} \right) \quad (3)$$

where the matrix B is a two-by-two block matrix embedding all the interaction strengths.

Conveniently, the global stability of a feasible equilibrium point in this linear Lotka-Volterra model has already been studied (*14*–*17*, *43*). Particularly relevant to this work is that an interaction matrix that is Lyapunov–diagonally stable grants the global stability of any potential feasible equilibrium (*14*–*18*).

Although it is mathematically difficult to verify the condition for Lyapunov diagonal stability, it is known that for some classes of matrices, Lyapunov stability and Lyapunov diagonal stability are equivalent conditions (*44*). Symmetric matrices and Z-matrices (matrices whose off-diagonal elements are nonpositive) belong to those classes of equivalent matrices. Our interaction strength matrix B is either symmetric when the mutualistic trade-off is zero ($\delta = 0$) or is a Z-matrix when the interspecific competition is zero ($\rho = 0$). This means that as long as the real parts of all eigenvalues of B are positive (*18*), any feasible equilibrium point is globally stable. For instance, in the case of $\rho < 1$ and $\gamma_0 = 0$, the interaction matrix B is symmetric and Lyapunov–diagonally stable because its eigenvalues are $1 - \rho$, $(S_A - 1)\rho + 1$, and $(S_P - 1)\rho + 1$.

For $\rho > 0$ and $\delta > 0$, there are no analytical results yet demonstrating that Lyapunov diagonal stability is equivalent to Lyapunov stability. However, after intensive numerical simulations we conjecture that the two main consequences of Lyapunov diagonal stability hold (*45*). Specifically, we state the following conjectures: Conjecture 1: If B is Lyapunov-stable, then B is D-stable. Conjecture 2: If B is Lyapunov-stable, then any feasible equilibrium is globally stable.

We found that for any given mutualistic trade-off and interspecific competition, the higher the level of mutualistic strength, the smaller the maximum real part of the eigenvalues of B (*45*). This means that there is a critical value of mutualistic strength (γ_0^r) so that above this level, the matrix B is not any more Lyapunov-stable. To compute γ_0^r, we need only to find the critical value of γ_0 at which the real part of one of the eigenvalues of the interaction-strength matrix reaches zero (*45*). This implies that at least below this critical value

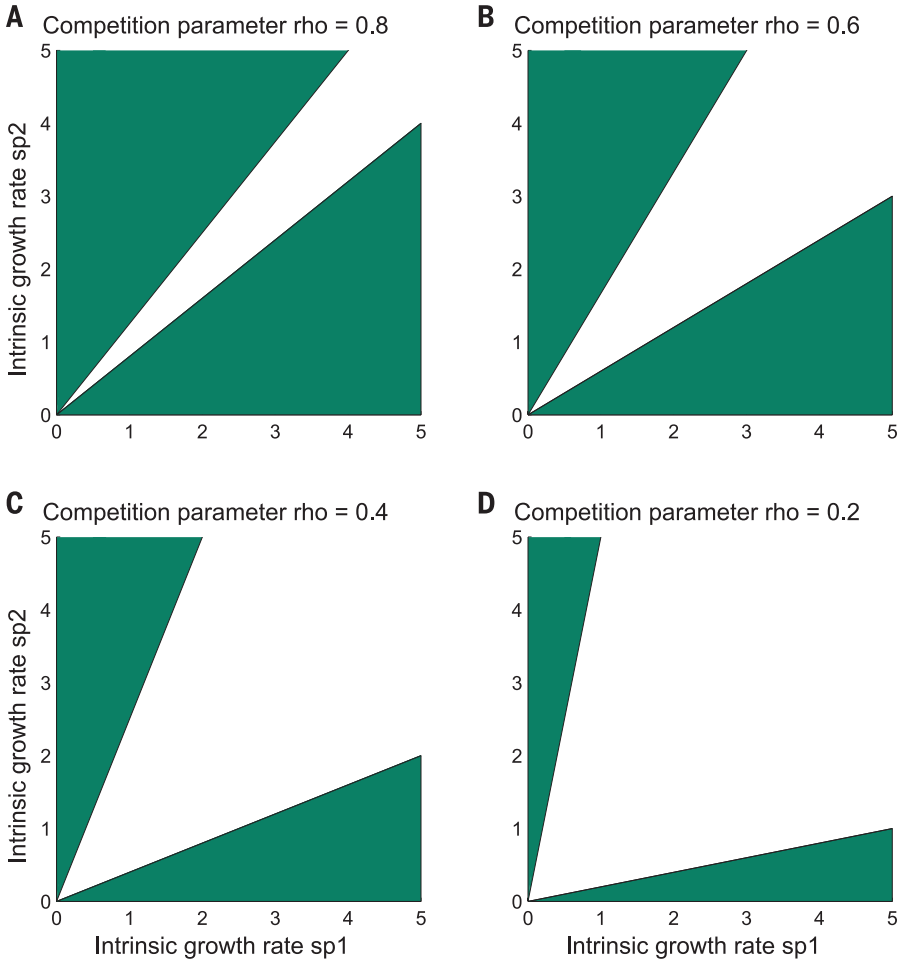


Fig. 3. Structural stability in a two-species competition system. The figure shows how the range of intrinsic growth rates leading to the stable coexistence of the two species (white region) changes as a function of the competition strength. (**A** to **D**) Decreasing interspecific competition increases the area of feasibility, and in turn, the structural stability of the system. Here, $\beta_{11} = \beta_{22} = 1$, and $\beta_{12} = \beta_{21} = \rho$. Our goal is extending this analysis to realistic networks of species interactions.

$\gamma_0 < \gamma_0^r$, any feasible equilibrium is granted to be locally and globally stable according to conjectures 1 and 2, respectively. We can also grant the global stability of matrix B by the condition of being positive definite, which is even stronger than Lyapunov diagonal stability (*14*). However, this condition imposes stronger constraints on the critical value of mutualistic strength than does Lyapunov stability (*39*).

Last, we studied the stability conditions for the nonlinear Lotka-Volterra system (Eq. 2). Although the theory has been developed for the linear Lotka-Volterra system, it can be extended to the nonlinear dynamical system. To grant the stability of any feasible equilibrium ($P_i > 0$ and $A_i > 0$ for all i) in the nonlinear system, we need to show that the above stability conditions hold on the following two-by-two block matrix (*14*, *43*)

$$B_{nl} := \begin{bmatrix} \beta_{ij}^{(P)} & -\dfrac{\gamma_{ij}^{(P)}}{1+h\sum_k \gamma_{ik}^{(P)} A_k} \\ -\dfrac{\gamma_{ij}^{(A)}}{1+h\sum_k \gamma_{ik}^{(A)} P_k} & \beta_{ij}^{(A)} \end{bmatrix} \quad (4)$$

B_{nl} differs from B only in the off-diagonal block with a decreased mutualistic strength. This implies that the critical value of mutualistic strength for the nonlinear Lotka-Volterra system is larger than or equal to the critical value for the linear system (*45*). Therefore, the critical value γ_0^r derived from the linear Lotka-Volterra system (from the matrix B) is already a sufficient condition to grant the global stability of any feasible equilibrium in the nonlinear case. However, this does not imply that above this critical value of mutualistic strength, a feasible equilibrium is unstable. In fact, when the mutualistic-interaction terms are saturated ($h > 0$), it is possible to have feasible and locally stable equilibria for any level of mutualistic strength (*39*, *45*).

Feasibility condition

We highlight that for any interaction strength matrix B, whether it is stable or not, it is always possible to find a set of intrinsic growth rates so that the system is feasible (Fig. 2). To find this set of values, we need only to choose a feasible equilibrium point so that the abundance of all species is greater than zero ($A_i^* > 0$ and $P_j^* > 0$) and find the vector of intrinsic growth rates so that the right side of Eq. 2 is equal to zero: $\alpha_i^{(P)} = \sum_j \beta_{ij}^{(P)} P_j^* - \dfrac{\sum_j \gamma_{ij}^{(P)} A_j^*}{1+h\sum_j \gamma_{ij}^{(P)} A_j^*}$ and $\alpha_i^{(A)} = \sum_j \beta_{ij}^{(A)} A_j^* - \dfrac{\sum_j \gamma_{ij}^{(A)} P_j^*}{1+h\sum_j \gamma_{ij}^{(A)} P_j^*}$. This reconfirms that the stability and feasibility conditions are different and that they need to be rigorously verified when studying the stable coexistence of species (*3*, *16*, *17*, *19*). This also highlights that the relevant question is not whether we can find a feasible equilibrium point, but how large is the domain of intrinsic growth rates leading to a feasible and stable equilibrium point. We call this domain the feasibility domain.

Because the parameter space of intrinsic growth rates is substantially large ($\mathbf{R}^S$, where S is the total number of species), an exhaustive numerical search of the feasibility domain is impossible. However, we can analytically estimate the center of this domain with what we call the structural vector of intrinsic growth rates. For example, in the two-species competition system of Fig. 4A the structural vector is the vector (in red), which is in the center of the domain leading to feasibility of the equilibrium point (white region). Any vector of intrinsic growth rates collinear to the structural vector guarantees the feasibility of the equilibrium point—that is, guarantees species coexistence. Because the structural vector is the center of the feasibility domain, then it is also the vector that can tolerate the strongest deviation before leaving the feasibility domain—that is, before having at least one species going extinct.

In mutualistic systems, we need to find one structural vector for animals and another for plants. These structural vectors are the set of intrinsic growth rates that allow the strongest perturbations before leaving the feasibility domain. To find these structural vectors, we had to transform the interaction-strength matrix B to an effective competition framework (*45*). This results in an effective competition matrix for plants and a different one for animals (*6*), in which these matrices represent respectively the apparent competition among plants and among animals, once taking into account the indirect effect via their mutualistic partners. With a nonzero mutualistic trade-off ($\delta > 0$), the effective competition matrices are nonsymmetric, and in order to find the structural vectors, we have to use the singular decomposition approach—a generalization of the eigenvalue decomposition. This results in a left and a right structural vector for plants and for animals in the effective competition framework. Last, we need to move back from the effective competition framework in order to obtain a left and right vector for plants ($\alpha_L^{(P)}$ and $\alpha_R^{(P)}$) and animals ($\alpha_L^{(A)}$ and $\alpha_R^{(A)}$) in the observed mutualistic framework. The full derivation is provided in the supplementary materials (*45*).

Once we locate the center of the feasibility domain with the structural vectors, we can approximate the boundaries of this domain by quantifying the amount of variation from the structural vectors allowed by the system before having any of the species going extinct—that is, before losing the feasibility of the system. To quantify this amount, we introduced proportional random perturbations to the structural vectors, numerically generated the new equilibrium points (*21*), and measured the angle or the deviation between the structural vectors and the perturbed vectors (a graphical example is provided in Fig. 4A). The deviation from the structural vectors is quantified, for the plants, by $\eta_P(\alpha^{(P)}) = [1 - \cos(\theta_L^{(P)})\cos(\theta_R^{(P)})]/[\cos(\theta_L^{(P)})\cos(\theta_R^{(P)})]$, where $\theta_L^{(P)}$ and $\theta_R^{(P)}$ are, respectively, the angles between $\alpha^{(P)}$ and $\alpha_L^{(P)}$ and between $\alpha^{(P)}$ and $\alpha_R^{(P)}$. The parameter $\alpha^{(P)}$ is any perturbed vector of intrinsic growth rates of plants. The deviation from the structural vector of animals is computed similarly.

As shown in Fig. 4B, the greater the deviation of the perturbed intrinsic growth rates from the structural vectors, the lower is the fraction of surviving species. This confirms that there is a restricted domain of intrinsic growth rates centered on the structural vectors compatible with the stable coexistence of species. The greater the tolerated deviation from the structural vectors

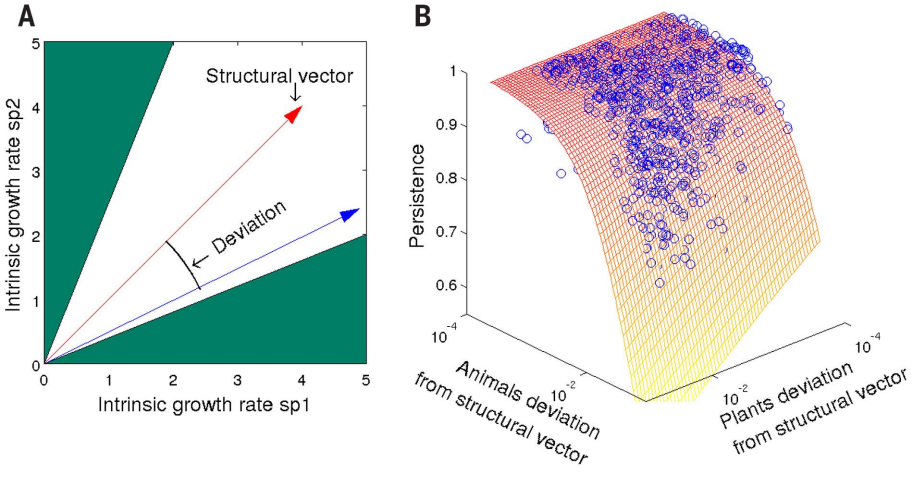


Fig. 4. Deviation from the structural vector and community persistence. (**A**) The structural vector of intrinsic growth rates (in red) for the two-species competition system of Fig. 1. The structural vector is the vector in the center of the domain leading to the feasibility of the equilibrium point (white region) and thus can tolerate the largest deviation before any of the species go extinct. The deviation between the structural vector and any other vector (blue) is quantified by the angle between them. (**B**) The effect of the deviation from the structural vector on intrinsic growth rates on community persistence defined as the fraction of model-generated surviving species. The example corresponds to an observed network located in North Carolina, USA (table S1), with a mutualistic trade-off $\delta = 0.5$ and a maximum level of mutualistic strength $\gamma_0 = 0.2402$. Blue symbols represent the community persistence, and the surface represents the fit of a logistic regression ($R^2 = 0.88$).

within which all species coexist, the greater the feasibility domain, and in turn the greater the structural stability of the system.

Network architecture and structural stability

To investigate the extent to which network architecture modulates the structural stability of mutualistic systems, we explored the combination of alternative network architectures (combinations of nestedness, mutualistic strength, and mutualistic trade-off) and their corresponding feasibility domains.

To explore these combinations, for each observed mutualistic network (table S1) we obtained 250 different model-generated nested architectures by using an exhaustive resampling model (*46*) that preserves the number of species and the expected number of interactions (*45*). Theoretically, nestedness ranges from 0 to 1 (*42*). However, if one imposes architectural constraints such as preserving the number of species and interactions, the effective range of nestedness that the network can exhibit may be smaller (*45*). Additionally, each individual model-generated nested architecture is combined with different levels of mutualistic trade-off δ and mutualistic strength γ_0. For the mutualistic trade-off, we explored values $\delta \in [0, ..., 1.5]$ with steps of 0.05 that allow us to explore sublinear, linear, and superlinear trade-offs. The case $\delta = 0$ is equivalent to the soft mean field approximation studied in (*6*). For each combination of network of interactions and mutualistic trade-off, there is a specific critical value γ_0^r in the level of mutualism strength γ_0 up to which any feasible equilibrium is globally stable. This critical value γ_0^r is dependent on the mutualistic trade-off and nestedness. However, the mean mutualistic strength $\overline{\gamma} = \langle \gamma_{ij} \rangle$ shows no pattern as a function of mutualistic trade-off and nestedness (*45*). Therefore, we explored values of $\gamma_0 \in [0, ..., \gamma_0^r]$ with steps of 0.05 and calculated the new generated mean mutualistic strengths. This produced a total of 250 × 589 different network architectures (nestedness, mutualistic trade-off, and mean mutualistic strength) for each observed mutualistic network.

We quantified how the structural stability (feasibility domain) is modulated by these alternative network architectures in the following way. First, we computed the structural vectors of intrinsic growth rates that grant the existence of a feasible equilibrium of each alternative network architecture. Second, we introduced proportional random perturbations to the structural vectors of intrinsic growth rates and measured the angle or deviation ($\eta_{(A)}$, $\eta_{(P)}$) between the structural vectors and the perturbed vectors. Third, we simulated species abundance using the mutualistic model of (*6*) and the perturbed growth rates as intrinsic growth rate parameter values (*21*). These deviations lead to parameter domains from all to a few species surviving (Fig. 4).

Last, we quantified the extent to which network architecture modulates structural stability by looking at the association of community persistence with network architecture parameters, once taking into account the effect of intrinsic growth rates. Specifically, we studied this association using the partial fitted values from a binomial regression (*47*) of the fraction of surviving species on nestedness (N), mean mutualistic strength ($\overline{\gamma}$), and mutualistic trade-off (δ), while controlling for the deviations from the structural vectors of intrinsic growth rates ($\eta_{(A)}$, $\eta_{(P)}$). The full description of this binomial regression and the calculation of partial fitted values are provided in (*48*). These partial fitted values are the contribution of network architecture to the logit of the probability of species persistence, and in turn, these values are positively proportional to the size of the feasibility domain.

Results

We analyzed each observed mutualistic network independently because network architecture is constrained to the properties of each mutualistic system (*11*). For a given pollination system located in the KwaZulu-Natal region of South Africa, the extent to which its network architecture modulates structural stability is shown in Fig. 5. Specifically, the partial fitted values are plotted as a function of network architecture. As shown in Fig. 5A, not all architectural combinations have the same structural stability. In particular, the architectures that maximize structural stability (reddish/darker regions) correspond to the following properties: (i) a maximal level of nestedness, (ii) a small (sublinear) mutualistic trade-off, and (iii) a high level of mutualistic strength within the constraint of any feasible solution being globally stable (*49*).

A similar pattern is present in all 23 observed mutualistic networks (*45*). For instance, using three different levels of interspecific competition

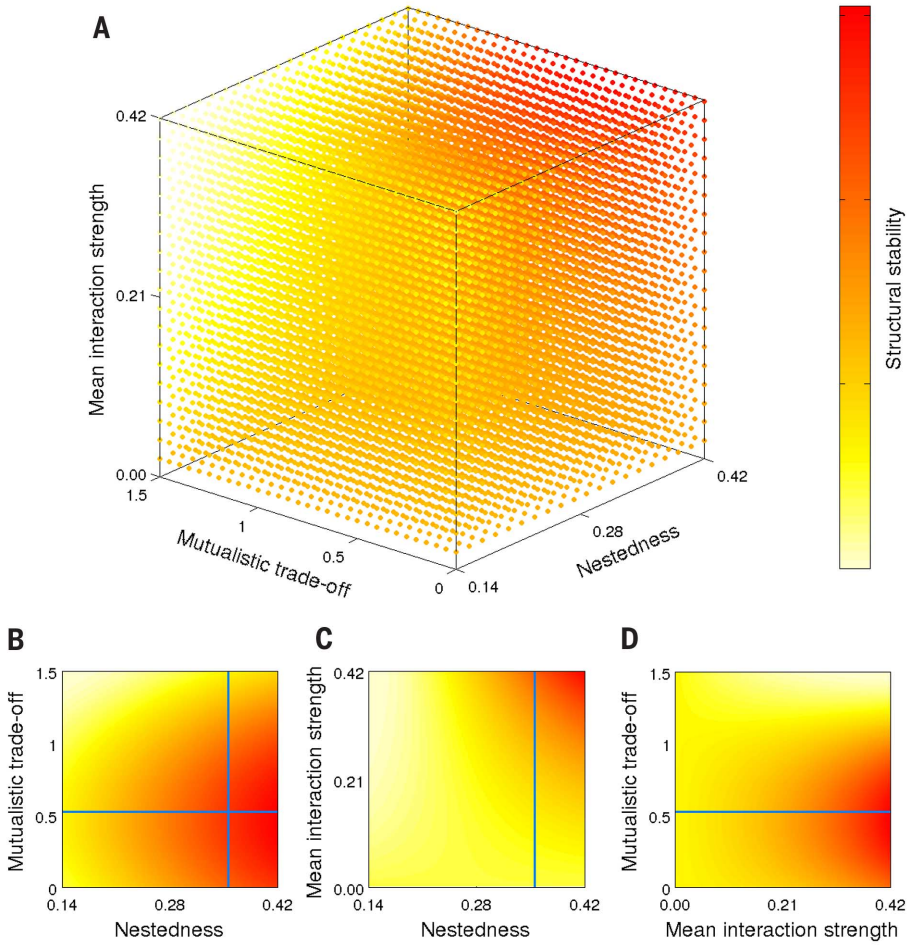


Fig. 5. Structural stability in complex mutualistic systems. For an observed mutualistic system with 9 plants, 56 animals, and 103 mutualistic interactions located in the grassland asclepiads in South Africa (table S1) (*58*), (**A**) corresponds to the effect—colored by partial fitted residuals—of the combination of different architectural values (nestedness, mean mutualistic strength, and mutualistic trade-off) on the domain of structural stability. The reddish/darker the color, the larger the parameter space that is compatible with the stable coexistence of all species, and in turn the larger the domain of structural stability. (**B**), (**C**), and (**D**) correspond to different slices of (A). Slice (B) corresponds to a mean mutualistic strength of 0.21, slice (C) corresponds to the observed mutualistic trade-off, and slice (D) corresponds to the observed nestedness. Solid lines correspond to the observed values of nestedness and mutualistic trade-offs.

(ρ = 0.2, 0.4, 0.6), we always find that structural stability is positively associated with nestedness and mutualistic strength (*45*). Similarly, structural stability is always associated with the mutualistic trade-off by a quadratic function, leading quite often to an optimal value for maximizing structural stability (*45*). These findings reveal that under the given characterization of interspecific competition, there is a general pattern of network architecture that increases the structural stability of mutualistic systems.

Yet, one question remains to be answered: Is the network architecture that we observe in nature close to the maximum feasibility domain of parameter space under which species coexist? To answer this question, we compared the observed network architecture with theoretical predictions. To extract the observed network architecture, we computed the observed nestedness from the observed binary interaction matrices (table S1) following (*42*). The observed mutualistic trade-off δ is estimated from the observed number of visits of pollinators or fruits consumed by seed-dispersers to flowering plants (*41*, *50*, *51*). The full details on how to compute the observed trade-off is provided in (*52*). Because there is no empirical data on the relationship between competition and mutualistic strength that could allow us to extract the observed mutualistic strength γ_0, our results on nestedness and mutualistic trade-off are calculated across different levels of mean mutualistic strength.

As shown in Fig. 5, B to D, the observed network (blue solid lines) of the mutualistic system located in the grassland asclepiads of South Africa actually appears to have an architecture close to the one that maximizes the feasibility domain under which species coexist (reddish/darker region). To formally quantify the degree to which each observed network architecture is maximizing the set of conditions under which species coexist, we compared the net effect of the observed network architecture on structural stability against the maximum possible net effect. The maximum net effect is calculated in three steps.

First, as outlined in the previous section, we computed the partial fitted values of the effect of alternative network architectures on species persistence (*48*). Second, we extracted the range of nestedness allowed by the network given the number of species and interactions in the system (*45*). Third, we computed the maximum net effect of network architecture on structural stability by finding the difference between the maximum and minimum partial fitted values within the allowed range of nestedness and mutualistic trade-off between $\delta \in [0, ..., 1.5]$. All the observed mutualistic trade-offs have values between $\delta \in [0, ..., 1.5]$. Last, the net effect of the observed network architecture on structural stability corresponds to the difference between the partial fitted values for the observed architecture and the minimum partial fitted values extracted in the third step described above.

Looking across different levels of mean mutualistic strength, in the majority of cases (18 out of 23, $P = 0.004$, binomial test) the observed network architectures induce more than half the value of the maximum net effect on structural stability (Fig. 6, red solid line). These findings reveal that observed network architectures tend to maximize the range of parameter space—structural stability—for species coexistence.

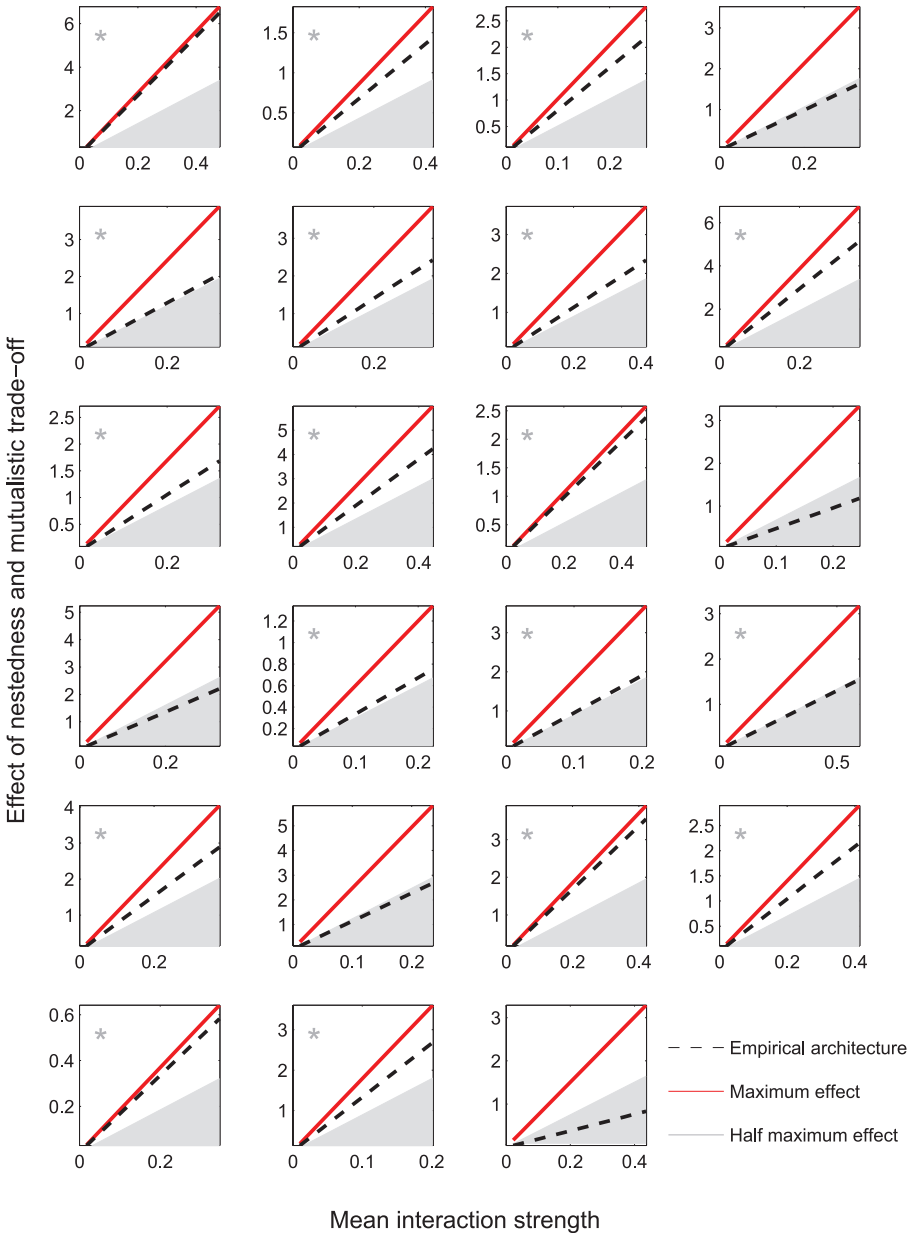


Fig. 6. Net effect of network architecture on structural stability. For each of the 23 observed networks (table S1), we show how close the observed feasibility domain (partial fitted residuals) is as a function of the network architecture to the theoretical maximal feasibility domain. The network architecture is given by the combination of nestedness and mutualistic trade-off (*x* axis) across different values of mean mutualistic strength (*y* axis). The solid red and dashed black lines correspond to the maximum net effect and observed net effect, respectively. In 18 out of 23 networks (indicated by asterisks), the observed architecture exhibits more than half the value of the maximum net effect (gray regions). The net effect of each network architecture is system-dependent and cannot be used to compare across networks.

Structural stability of systems with other interaction types

In this section, we explain how our structural stability framework can be applied to other types of interspecific interactions in complex ecological systems. We first explain how structural stability can be applied to competitive interactions. We proceed by discussing how this competitive approach can be used to study trophic interactions in food webs.

For a competition system with an arbitrary number of species, we can assume a standard set of dynamical equations given by $\frac{dN_i}{dt} = N_i(\alpha_i - \sum_j \beta_{ij} N_j)$, where $\alpha_i > 0$ is the intrinsic growth rate, $\beta_{ij} > 0$ is the competition interaction strength, and N_i is the abundance of species i. Recall that the Lyapunov diagonal stability of the interaction matrix β would imply the global stability of any feasible equilibrium point. However, in nonsymmetric competition matrices Lyapunov stability does not always imply Lyapunov diagonal stability (*53*). This establishes that we should work with a restricted class of competition matrices such as the ones derived from the niche space of (*54*). Indeed, it has been demonstrated that this class of competition matrices are Lyapunov diagonally stable and that this stability is independent of the number of species (*55*). For a competition system with a symmetric interaction-strength matrix, the structural vector is equal to its leading eigenvector. For other appropriate classes of matrices, we can compute the structural vectors in the same way as we did with the effective competition matrices of our mutualistic model and numerically simulate the feasibility domain of the competition system. In general, following this approach we can verify that the lower the average interspecific competition, the higher is the feasibility domain, and in turn, the higher is the structural stability of the competition system.

In the case of predator-prey interactions in food webs, so far there is no analytical work demonstrating the conditions for a Lyapunov–diagonally stable system and how this is linked to its Lyapunov stability. Moreover, the computation of the structural vector of an antagonistic system is not a straightforward task. However, we may have a first insight about how the network architecture of antagonistic systems modulates their structural stability by transforming a two-trophic–level food web into a competition system among predators. Using this transformation, we are able to verify that the higher the compartmentalization of a food web, then the higher is its structural stability. There is no universal rule to study the structural stability of complex ecological systems. Each type of interaction poses their own challenges as a function of their specific population dynamics.

Discussion

We have investigated the extent to which different network architectures of mutualistic systems can provide a wider range of conditions under which species coexist. This research question is completely different from the question of which network architectures are aligned to a fixed set of conditions. Previous numerical analyses based on arbitrary parameterizations were indirectly asking the latter, and previous studies based on local stability were not rigorously verifying the actual coexistence of species. Of course, if there is a good empirical or scientific reason to use a specific parameterization, then we should take advantage of this. However, because the set of conditions present in a community can be constantly changing because of stochasticity, adaptive mechanisms, or global environmental change, we believe that understanding which network architectures can increase the structural stability of a community becomes a relevant question. Indeed, this is a question much more aligned with the challenge of assessing the consequences of global environmental change—by definition, directional and large—than with the alternative framework of linear stability, which focuses on the responses of a steady state to infinitesimally small perturbations.

We advocate structural stability as an integrative approach to provide a general assessment of the implications of network architecture across ecological systems. Our findings show that many of the observed mutualistic network architectures tend to maximize the domain of parameter space under which species coexist. This means that in mutualistic systems, having both a nested network architecture and a small mutualistic trade-off is one of the most favorable structures for community persistence. Our predictions could be tested experimentally by exploring whether communities with an observed network architecture that maximizes structural stability stand higher values of perturbation. Similarly, our results open up new questions, such as what the reported associations between network architecture and structural stability tell us about the evolutionary processes and pressures occurring in ecological systems.

Although the framework of structural stability has not been as dominant in theoretical ecology as has the concept of local stability, it has a long tradition in other fields of research (*29*). For example, structural stability has been key in evolutionary developmental biology to articulate the view of evolution as the modification of a conserved developmental program (*27*, *28*). Thus, some morphological structures are much more common than others because they are compatible with a wider range of developmental conditions. This provided a more mechanistic understanding of the generation of form and shape through evolution (*56*) than that provided by a historical, functionalist view. We believe ecology can also benefit from this structuralist view. The analogous question here would assess whether the invariance of network architecture across diverse environmental and biotic conditions is due to the fact that such a network structure is the one increasing the likelihood of species coexistence in an ever-changing world.

REFERENCES AND NOTES

1. R. M. May, Will a large complex system be stable? *Nature* **238**, 413–414 (1972). doi: 10.1038/238413a0; pmid: 4559589
2. A. R. Ives, S. R. Carpenter, Stability and diversity of ecosystems. *Science* **317**, 58–62 (2007). doi: 10.1126/science.1133258; pmid: 17615333
3. T. J. Case, *An Illustrated Guide to Theoretical Ecology* (Oxford Univ. Press, Oxford, UK, 2000).
4. S. L. Pimm, *Food Webs* (Univ. Chicago Press, Chicago, 2002).
5. A. Roberts, The stability of a feasible random ecosystem. *Nature* **251**, 607–608 (1974). doi: 10.1038/251607a0
6. U. Bastolla *et al.*, The architecture of mutualistic networks minimizes competition and increases biodiversity. *Nature* **458**, 1018–1020 (2009). doi: 10.1038/nature07950; pmid: 19396144
7. T. Okuyama, J. N. Holland, Network structural properties mediate the stability of mutualistic communities. *Ecol. Lett.* **11**, 208–216 (2008). doi: 10.1111/j.1461-0248.2007.01137.x; pmid: 18070101
8. E. Thébault, C. Fontaine, Stability of ecological communities and the architecture of mutualistic and trophic networks. *Science* **329**, 853–856 (2010). doi: 10.1126/science.1188321; pmid: 20705861
9. S. Allesina, S. Tang, Stability criteria for complex ecosystems. *Nature* **483**, 205–208 (2012). doi: 10.1038/nature10832; pmid: 22343894
10. A. James, J. W. Pitchford, M. J. Plank, Disentangling nestedness from models of ecological complexity. *Nature* **487**, 227–230 (2012). doi: 10.1038/nature11214; pmid: 22722863
11. S. Saavedra, D. B. Stouffer, "Disentangling nestedness" disentangled. *Nature* **500**, E1–E2 (2013). doi: 10.1038/nature12380; pmid: 23969464
12. S. Suweis, F. Simini, J. R. Banavar, A. Maritan, Emergence of structural and dynamical properties of ecological mutualistic networks. *Nature* **500**, 449–452 (2013). doi: 10.1038/nature12438; pmid: 23969462
13. A. M. Neutel, J. A. Heesterbeek, P. C. De Ruiter, Stability in real food webs: Weak links in long loops. *Science* **296**, 1120–1123 (2002). doi: 10.1126/science.1068326; pmid: 12004131
14. B. S. Goh, Global stability in many-species systems. *Am. Nat.* **111**, 135–143 (1977). doi: 10.1086/283144
15. D. O. Logofet, Stronger-than-lyapunov notions of matrix stability, or how flowers help solve problems in mathematical ecology. *Linear Algebra Appl.* **398**, 75–100 (2005). doi: 10.1016/j.laa.2003.04.001
16. D. O. Logofet, *Matrices and Graphs: Stability Problems in Mathematical Ecology* (CRC Press, Boca Raton, FL, 1992).
17. Y. M. Svirezhev, D. O. Logofet, *Stability of Biological Communities* (Mir Publishers, Moscow, Russia, 1982).
18. Any matrix B is called Lyapunov-stable if the real parts of all its eigenvalues are positive, meaning that a feasible equilibrium at which all species have the same abundance is at least locally stable. A matrix B is called D-stable if DB is a Lyapunov-stable matrix for any strictly positive diagonal matrix D. D-stability is a stronger condition than Lyapunov stability in the sense that it grants the local stability of any feasible equilibrium (*15*). In addition, a matrix B is called Lyapunov diagonally stable if there exists a strictly positive diagonal matrix D so that $DB + B^tD$ is a Lyapunov-stable matrix. This notion of stability is even stronger than D-stability in the sense that it grants not only the local stability of any feasible equilibrium point, but also its global stability (*14*). A Lyapunov–diagonally stable matrix has all of its principal minors positive. Also, its stable equilibrium (which may be only partially feasible; some species may have an abundance of zero) is specific (*57*). This means that there is no alternative stable state for a given parameterization of intrinsic growth rates (*55*). We have chosen the convention of having a minus sign in front of the interaction-strength matrix B. This implies that B has to be positive Lyapunov-stable (the real parts of all eigenvalues have to be strictly positive) so that the equilibrium point of species abundance is locally stable. This same convention applies for D-stability and Lyapunov–diagonal stability.
19. J. H. Vandermeer, Interspecific competition: A new approach to the classical theory. *Science* **188**, 253–255 (1975). doi: 10.1126/science.1118725; pmid: 1118725
20. T. J. Case, Invasion resistance arises in strongly interacting species-rich model competition communities. *Proc. Natl. Acad. Sci. U.S.A.* **87**, 9610–9614 (1990). doi: 10.1073/pnas.87.24.9610; pmid: 11607132
21. All simulations were performed by integrating the system of ordinary differential equations by using the function ode45 of Matlab. Species are considered to have gone extinct when their abundance is lower than 100 times the machine precision. Although we present the results of our simulations with a fixed value of $\rho = 0.2$ and $h = 0.1$, our results are robust to this choice as long as $\rho < 1$ (*45*). In our dynamical system, the units of the parameters are abundance for N, 1/time for α and h, and 1/(time · biomass) for β and γ. Abundance and time can be any unit (such as biomass and years), as long as they are constant for all species.
22. V. I. Arnold, *Geometrical Methods in the Theory of Ordinary Differential Equations* (Springer, New York, ed. 2, 1988).
23. R. V. Solé, J. Valls, On structural stability and chaos in biological systems. *J. Theor. Biol.* **155**, 87–102 (1992). doi: 10.1016/S0022-5193(05)80550-8
24. A. N. Kolmogorov, Sulla teoria di volterra della lotta per l'esistenza. *Giornale Istituto Ital. Attuari* **7**, 74–80 (1936).

25. Y. A. Kuznetsov, *Elements of Applied Bifurcation Theory* (Springer, New York, ed. 3, 2004).
26. J. H. Vandermeer, The community matrix and the number of species in a community. *Am. Nat.* **104**, 73–83 (1970). doi: 10.1086/282641
27. P. Alberch, E. A. Gale, A developmental analysis of an evolutionary trend: Digital reduction in amphibians. *Evolution* **39**, 8–23 (1985). doi: 10.2307/2408513
28. P. Alberch, The logic of monsters: Evidence for internal constraints in development and evolution. *Geobios* **22**, 21–57 (1989). doi: 10.1016/S0016-6995(89)80006-3
29. R. Thom, *Structural Stability and Morphogenesis* (Addison-Wesley, Boston, 1994).
30. U. Bastolla, M. Lässig, S. C. Manrubia, A. Valleriani, Biodiversity in model ecosystems, I: Coexistence conditions for competing species. *J. Theor. Biol.* **235**, 521–530 (2005). doi: 10.1016/j.jtbi.2005.02.005; pmid: 15935170
31. J. Bascompte, Disentangling the web of life. *Science* **325**, 416–419 (2009). doi: 10.1126/science.1170749; pmid: 19628856
32. J. Bascompte, P. Jordano, C. J. Melián, J. M. Olesen, The nested assembly of plant-animal mutualistic networks. *Proc. Natl. Acad. Sci. U.S.A.* **100**, 9383–9387 (2003). doi: 10.1073/pnas.1633576100; pmid: 12881488
33. J. N. Thompson, *The Geographic Mosaic of Coevolution* (Univ. Chicago Press, Chicago, 2005).
34. E. L. Rezende, J. E. Lavabre, P. R. Guimarães, P. Jordano, J. Bascompte, Non-random coextinctions in phylogenetically structured mutualistic networks. *Nature* **448**, 925–928 (2007). doi: 10.1038/nature05956; pmid: 17713534
35. S. Saavedra, F. Reed-Tsochas, B. Uzzi, A simple model of bipartite cooperation for ecological and organizational networks. *Nature* **457**, 463–466 (2009). doi: 10.1038/nature07532; pmid: 19052545
36. L. A. Burkle, J. C. Marlin, T. M. Knight, Plant-pollinator interactions over 120 years: Loss of species, co-occurrence, and function. *Science* **339**, 1611–1615 (2013). doi: 10.1126/science.1232728; pmid: 23449999
37. D. H. Wright, A simple, stable model of mutualism incorporating handling time. *Am. Nat.* **134**, 664–667 (1989). doi: 10.1086/285003
38. J. N. Holland, T. Okuyama, D. L. DeAngelis, Comment on "Asymmetric coevolutionary networks facilitate biodiversity maintenance." *Science* **313**, 1887b (2006). doi: 10.1126/science.1129547; pmid: 17008511
39. S. Saavedra, R. P. Rohr, V. Dakos, J. Bascompte, Estimating the tolerance of species to the effects of global environmental change. *Nat. Commun.* **4**, 2350 (2013). doi: 10.1038/ncomms3350; pmid: 23945469
40. R. Margalef, *Perspectives in Ecological Theory* (Univ. Chicago Press, Chicago, 1968).
41. D. P. Vázquez *et al*., Species abundance and asymmetric interaction strength in ecological networks. *Oikos* **116**, 1120–1127 (2007). doi: 10.1111/j.0030-1299.2007.15828.x
42. M. Almeida-Neto, P. Guimarães, P. R. Guimarães Jr., R. D. Loyola, W. Urlich, A consistent metric for nestedness analysis in ecological systems: Reconciling concept and measurement. *Oikos* **117**, 1227–1239 (2008). doi: 10.1111/j.0030-1299.2008.16644.x
43. B. S. Goh, Stability in models of mutualism. *Am. Nat.* **113**, 261–275 (1979). doi: 10.1086/283384
44. Y. Takeuchi, N. Adachi, H. Tokumaru, Global stability of ecosystems of the generalized volterra type. *Math. Biosci.* **42**, 119–136 (1978). doi: 10.1016/0025-5564(78)90010-X
45. Materials and methods are available as supplementary materials on *Science* Online.
46. R. P. Rohr, R. E. Naisbit, C. Mazza, L.-F. Bersier, Matching-centrality decomposition and the forecasting of new links in networks. arXiv:1310.4633 (2013).
47. P. McCullagh, J. A. Nelder, *Generalized Linear Models* (Chapman and Hall, London, ed. 2, 1989), chap. 4.
48. For a given network, we look at the association of the fraction of surviving species with the deviation from the structural vector of plants $\eta_{(P)}$ and animals $\eta_{(A)}$, nestedness N, mutualistic trade-off δ, and mean level of mutualistic strength $\overline{\gamma} = \langle \gamma_{ij} \rangle$ using the following binomial generalized linear model (*47*): logit(probability of surviving) $\sim \log(\eta_A) + \log(\eta_P) + \overline{\gamma} + \overline{\gamma}^2 + \overline{\gamma} \cdot N + \overline{\gamma} \cdot N^2 + \overline{\gamma} \cdot \delta + \overline{\gamma}\delta^2$. Obviously, at a level of mutualism of zero (γ = 0), nestedness and mutualistic trade-off cannot influence the probability of a species to survive. We have to include an interaction between the mean level of mutualism and the nestedness and mututalistic trade-off. We have also included a quadratic term in order to take into account potential nonlinear effects of nestedness, mutualistic trade-off, and mean level of mutualistic strength. The effect of network architecture is confirmed by the significant likelihood ratio between the full model and a null model without such a network effect ($P < 0.001$) for all the observed empirical networks. The effect of network architecture on structural stability can be quantified by the partial fitted values defined as follows: partial fitted values $= \hat{\beta}_1\overline{\gamma} + \hat{\beta}_2\overline{\gamma}^2 + \hat{\beta}_3\ \overline{\gamma} \cdot N + \hat{\beta}_4\overline{\gamma} \cdot N^2 + \hat{\beta}_5\overline{\gamma} \cdot \delta + \hat{\beta}_6\overline{\gamma} \cdot \delta^2$, where $\hat{\beta}_1 \cdots \hat{\beta}_6$ are the fitted parameters corresponding to the terms $\overline{\gamma}$ to $\overline{\gamma} \cdot \delta^2$, respectively.
49. J. Bascompte, P. Jordano, J. M. Olesen, Asymmetric coevolutionary networks facilitate biodiversity maintenance. *Science* **312**, 431–433 (2006). doi: 10.1126/science.1123412; pmid: 16627742
50. P. Turchin, I. Hanski, An empirically based model for latitudinal gradient in vole population dynamics. *Am. Nat.* **149**, 842–874 (1997). doi: 10.1086/286027; pmid: 18811252
51. P. Jordano, J. Bascompte, J. M. Olesen, Invariant properties in coevolutionary networks of plant-animal interactions. *Ecol. Lett.* **6**, 69–81 (2003). doi: 10.1046/j.1461-0248.2003.00403.x
52. To estimate the mutualistic trade-off, δ, from an empirical point of view, we proceed as follows. First, there is available data on the frequency of interactions. Thus, q_{ij} is the observed number of visits of animal species j on plant species i. This quantity has been proven to be the best surrogate of per capita effects of one species on another (γ_{ij}^P and γ_{ij}^A) (*41*). Second, the networks provide information on the number of species one species interacts with (its degree or generalization level; k_i^A and k_i^P). Following (*41*, *50*, *51*), the generalization level of a species has been found to be proportional to its abundance at equilibrium. Thus, the division of the total number of visits by the product of the degree of plants and animals can be assumed to be proportional to the interaction strengths. Mathematically, we obtain two equations, one for the effect of the animals on the plants and vice versa: $(q_{ij})/(k_i^P k_j^A) \propto \gamma_{ij}^P$ and $(q_{ij})/(k_i^A k_j^P) \propto \gamma_{ij}^A$. Introducing the explicit dependence between interaction strength and trade-of—for example, $\gamma_{ij}^P = \gamma_0/(k_i^P)^\delta$ and $(q_{ij})/(k_i^P k_j^A) \propto (\gamma_0)/[(k_i^P)^\delta]$—we obtain $(q_{ij})/(k_i^P k_j^A) \propto (\gamma_0)/[(k_i^P)^\delta]$ and $(q_{ij})/(k_i^A k_j^P) \propto (\gamma_0)/[(k_i^A)^\delta]$. In order to estimate the value of δ, we can just take the logarithm on both sides of the previous equations for the data excluding the zeroes. Then, δ is simply given by the slope of the following linear regressions:

$$\log\left(\frac{q_{ij}}{k_i^P k_j^A}\right) = a^P - \delta\log\left(k_i^P\right) \text{ and } \log\left(\frac{q_{ij}}{k_i^A k_j^P}\right) = a^A - \delta\log\left(k_i^A\right),$$

where a^P and a^A are the intercepts for plants and animals, respectively. These two regressions are performed simultaneously by lumping together the data set. The intercept for the effect of animals on plants (a^P) may not be the same as the intercept for the effect of the plants on the animals (a^A).
53. The competition matrix given by $\beta = \begin{bmatrix} 3 & 3.1 & 1 \\ 5 & 5 & 6 \\ 4 & 1 & 3 \end{bmatrix}$ is Lyapunov-stable but not *D*-stable. Because Lyapunov diagonal stability implies *D*-stability, this matrix is also not Lyapunov–diagonally stable.
54. R. MacArthur, Species packing and competitive equilibria for many species. *Theor. Pop. Biol.* **1**, 1–11 (1970).
55. T. J. Case, R. Casten, Global stability and multiple domains of attraction in ecological systems. *Am. Nat.* **113**, 705–714 (1979). doi: 10.1086/283427
56. D. W. Thompson, *On Growth and Form* (Cambridge Univ. Press, Cambridge, UK, 1992).
57. Y. Takeuchi, N. Adachi, The existence of globally stable equilibria of ecosystem of the generalised Volterra type. *J. Math. Biol.* **10**, 401–415 (1980). doi: 10.1007/BF00276098
58. J. Ollerton, S. D. Johnson, L. Cranmer, S. Kellie, The pollination ecology of an assemblage of grassland asclepiads in South Africa. *Ann. Bot. (Lond.)* **92**, 807–834 (2003). doi: 10.1093/aob/mcg206; pmid: 14612378

ACKNOWLEDGMENTS

We thank U. Bastolla, L.-F. Bersier, V. Dakos, A. Ferrera, M. A. Fortuna, L. J. Gilarranz, S. Kéfi, J. Lever, B. Luque, A. M. Neutel, A. Pascual-García, D. B. Stouffer, and J. Tylianakis for insightful discussions. We thank S. Baigent for pointing out the counter-example in (*53*). Funding was provided by the European Research Council through an Advanced Grant (J.B.) and FP7-REGPOT-2010-1 program under project 264125 EcoGenes (R.P.R.). The data are publicly available at www.web-of-life.es.

SUPPLEMENTARY MATERIALS

www.sciencemag.org/content/345/6195/1253497/suppl/DC1
Materials and Methods
Figs. S1 to S14
Table S1
References (*59*–*61*)
17 March 2014; accepted 3 June 2014
10.1126/science.1253497

REPORTS

ULTRAFAST OPTICS

Ultrafast optical control by few photons in engineered fiber

R. Nissim,* A. Pejkic,* E. Myslivets, B. P. Kuo, N. Alic, S. Radic†

Fast control of a strong optical beam by a few photons is an outstanding challenge that limits the performance of quantum sensors and optical processing devices. We report that a fast and efficient optical gate can be realized in an optical fiber that has been engineered with molecular-scale accuracy. Highly efficient, distributed phase-matched photon-photon interaction was achieved in the fiber with locally controlled, nanometer-scale core variations. A three-photon input was used to manipulate a Watt-scale beam at a speed exceeding 500 gigahertz. In addition to very fast beam control, the results provide a path to developing a new class of sensitive receivers capable of operating at very high rates.

The prospect of light-wave digital processors has motivated a decades-long pursuit of the optical transistor (*1*–*4*). The optical gate should control an intense beam with only a few photons (*3*) and be fast. Intuitively, by replacing electron carriers with massless photons, faster switching can be expected (*3*). Although desirable, the original transistor analogy also faces fundamental differences between light-wave and electronic carriers. Where electrons are easily manipulated in submicrometer structures (*5*), the interaction between photons is extremely weak (*6*). This weakness is countered by strong-field (*7*) or highly nonlinear material (*8*) serving as a photon-photon mediator. In practice, spatial (*7*) or spectral (*2*, *4*, *8*) resonances are necessary to efficiently manipulate photons. Recent experiments (*1*, *2*, *4*, *7*, *8*) have shown that direct, few-photon control is viable and can lead to transistor-like behavior. Unfortunately, the operating frequencies remain orders of magnitude below the terahertz rate relevant to light-wave communication. Resonant engineering, used to increase interaction efficiency, also induces spectral inhibition: Although very efficient, resonant devices are inherently slow (*3*).

However, an efficient optical gate can, at least in principle, also be fast if the nonlinear mechanism mediating photon-photon interaction remains spectrally uninhibited. Four-photon mixing (FPM) in a Kerr material (*9*, *10*) is an example of such interaction: It is both fast (*11*) and efficient in waveguides with a large product of nonlinearity γ and length L (*11*). In this regard, silica fiber represents a nearly ideal physical platform: With optical loss α below 0.0003 dB/m, its exceptional transparency (*12*) means that kilometer-scale interaction lengths can be used to offset the weak glass nonlinearity (*12*, *13*) and guarantee a γL product in excess of 100 W^{-1}. This advantage (*14*) can be fully realized only if phase matching is controlled by local dispersion (*15*). Unfortunately, local fiber dispersion, defined by its transverse geometry, varies a lot with small core fluctuations (*16*) (Fig. 1). Until recently, control of such small variations was not considered feasible (*15*), particularly over long scales.

We show that silica fiber core can be controlled with subnanometer precision and be used for fast, few-photon control. We find that the strongest interaction between few- and many-photon beams does not occur in ideal, constant core fibers. Instead, the optimal photon control requires a small but finite and specific core variation comparable to the size of a silicon-oxygen molecular ring (*16*). To demonstrate the feasibility of such distributed, microscopically controlled photon-photon interaction, we switched a 1.49-W beam by using a classically attenuated, 520-GHz bandwidth pulse containing an average of three photons. These measurements reveal that FPM in a fiber with a unique core profile is a nonreciprocal process, contrary to the well-established notion of directional invariance in passive waveguides (*17*).

In the simplified notion of few-photon control of a strong beam (Fig. 2A), weak input signal induces depletion of the many-photon pump via phase-matched FPM. Parametric mixing annihilates pump photons and recreates them at new (signal/idler) frequencies. In ideal fiber with constant core radius r, the instantaneous pump power $P(z)$ defines the local gain peak as separation between the pump (ω_P) and signal (ω_s) frequencies $\Omega = \omega_S - \omega_P \sim \sqrt{P(z)/r}$ (*12*). With signal amplification, the pump is depleted and the maximum-gain frequency Ω is shifted away from the signal. In contrast, when phase matching is controlled locally, the maximum-gain frequency Ω can be maintained even when the pump is depleted (Fig. 2B). To adjust the phase matching, the fiber core can be adjusted to

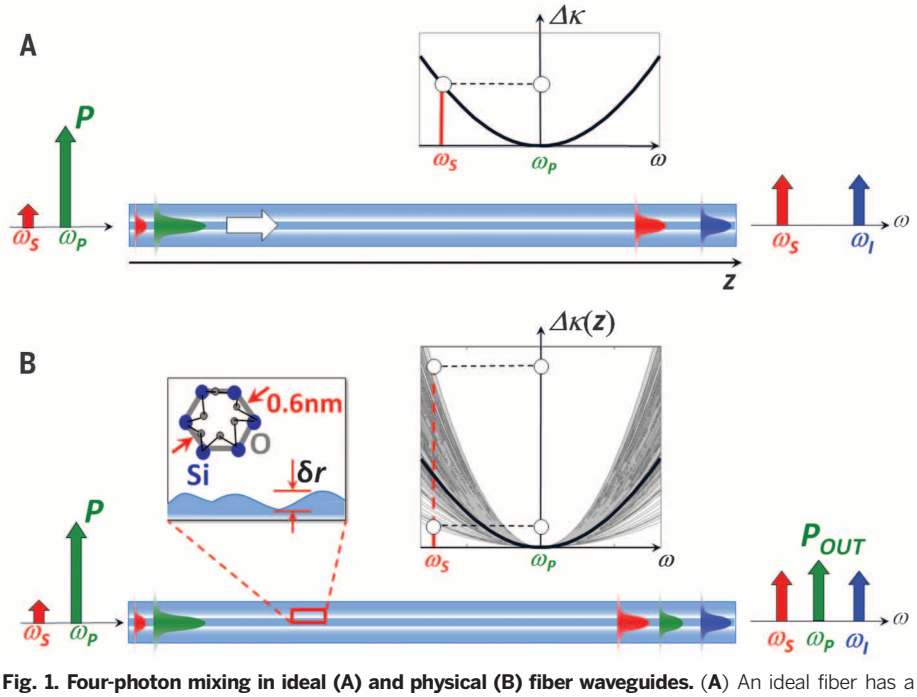


Fig. 1. Four-photon mixing in ideal (A) and physical (B) fiber waveguides. (**A**) An ideal fiber has a constant transverse geometry, and the phase matching imposed on pump k_P signal k_I, and idler k_S wave vectors $2k_P - k_S - k_I = \Delta\kappa$ results in spatially invariant dispersion $\Delta\kappa(\omega)$ (inset). With weak signal and strong pump inputs, sufficiently long phase-matched nonlinear fiber leads to complete pump depletion $P_{OUT} \sim 0$. (**B**) In a physical fiber, the core size fluctuates, with the fundamental limit set by the diameter of the Si-O molecular ring. This variation leads to a $\Delta\kappa(\omega, z)$ that randomly fluctuates along the fiber (inset). Stochastic phase matching results in random, suboptimal pump depletion.

Department of Electrical and Computer Engineering, University of California, San Diego, La Jolla, CA 92093, USA.
*These authors contributed equally to this work. †Corresponding author. E-mail: sradic@ucsd.edu

adapt to the depleted pump power and maintain the optimal pump-signal frequency separation: $\Omega \sim \sqrt{P(z)/r(z)} = \text{constant}$, where $r(z)$ represents a unique core variation function. This simple model, while establishing the need for local core control, is also inaccurate because it does not account for the higher-order mixing products generated in efficient FPM interaction (*13*). To describe such a many-beam photon exchange in a spatially varying nonlinear waveguide, it is necessary to use the nonlinear Schrodinger (NLS) model (*13*).

The NLS model indeed predicts the existence of an optimum core fluctuation (Fig. 2C). The extinction ratio (*ER*), defined as the ratio of the output pump power in the absence of the input signal to the output pump power in the presence of the input signal, was calculated for a fiber ensemble with randomly generated core variations. Similar to physical fibers (*12*), ensemble members differed at the nanometer scale: Each had unique local dispersion defined by random core variations and limited by standard deviation σ below 5 nm. To illustrate this important notion, consider two fibers that are identical in terms of global parameters but also possess the same standard core variation σ = 2.2 nm (Fig. 2C, inset). Although macroscopically indistinguishable, the two samples possess drastically different switching performance. In the first sample, a 300-nW signal depletes a 4.5×10^6 times stronger (1.39 W) beam efficiently (*ER* = 12.3 dB), with no effect in the second sample (*ER* = 0.3 dB). This extreme sensitivity to core fluctuations is even more remarkable when viewed in the context of glass structure: Its basic building block, the Si-O molecular ring, has a 0.6-nm diameter (*16*) and defines the ultimate precision with which physical fiber core can be realized. Unfortunately, Fig. 2C implies that even if one succeeds in fabricating fiber with molecular-scale transverse precision (~1 nm), this would still not guarantee the ability to build a few-photon switch. Facing this fundamental limit, it would appear that few-photon control in silica fiber is not feasible, even in principle. However, recent progress made in fiber measurement now allows both core selection (*18*) and synthesis (*19*) with subnanometer precision.

Although the localized stress technique can generate an arbitrary core variation profile (*19*), it can also perturb the native birefringence of the fiber. We therefore avoided this path in order to decouple the stochastic dispersion from any induced polarization effects. The fabrication-imposed limit was instead circumvented by selecting specific fiber segments with the desired core variation. Following this idea, it is necessary to first measure, with subnanometer precision, a fiber that is much longer than the switching device length. The ability to perform such a measurement in a nondestructive manner and over a long scale was established by a countercolliding Brillouin scanning technique (*18*). First, kilometers of fiber samples were measured and core variations were recorded to generate a nanoscale signature library. Although a necessary step, this alone was not sufficient to engineer an optimum few-photon FPM interaction. A specific core fluctuation profile corresponding to the maximum pump depletion also had to be identified. This was guided by a coupled-mode calculation (*13*) predicting that a strong (1.5 W) pump can be depleted by a 100-nW signal if the γPL-product exceeds 10. The search for the optimum core variation was constrained by the requirement that the FPM occurs in a fiber shorter than $L \sim 10/15\ \text{W}^{-1}\,\text{km}^{-1}/1\ \text{W} \sim 600$ m, with the assumption of standard confinement ($\gamma \sim 15\ \text{W}^{-1}\,\text{km}^{-1}$). The calculation resulted in a unique core variation profile that indeed could be closely approximated by combining two distinct fiber sections from the core fluctuation library (Fig. 3).

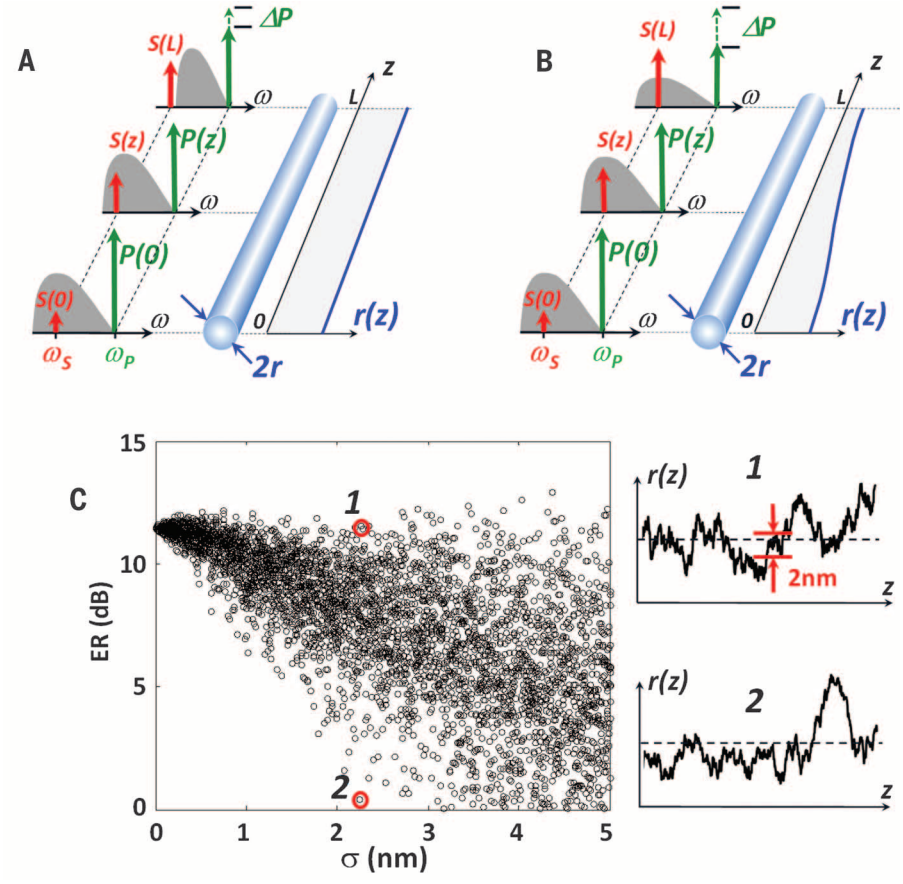


Fig. 2. Four-photon mixing in fibers with nanometer-scale core variations. (**A**) Maximum parametric gain in a homogeneous fiber is defined by the instantaneous pump power *P*. With pump depletion, the gain peak shifts away from the signal *S* at frequency ω_S, preventing further pump-signal photon transfer. The shaded area represents the magnitude of parametric gain. (**B**) By varying the core size, local phase matching can be controlled to maintain the gain peak position even when the pump is depleted. (**C**) *ER* calculated by the nonlinear Schrodinger model. Each point represents a unique core variation function.

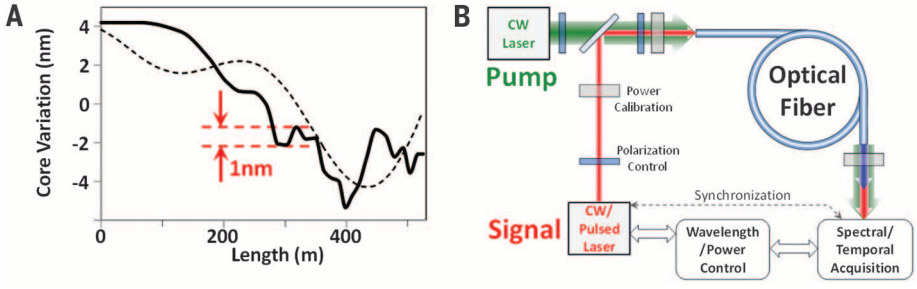


Fig. 3. Photon switching in fiber with optimal core. (**A**) Calculated (dotted) and measured (solid) core variation functions selected for few-photon switching experiments. Core variation is plotted as a deviation from the mean core size. The unique core variation was created by combining two distinct fiber sections identified from the measurement library; the splice was applied at z = 245.2 m. (**B**) Experimental schematics for static and fast switching characterization. A CW laser (pump) was combined with classically attenuated weak CW or pulsed signal and launched into the nonlinear fiber.

Subsequently, we investigated the efficiency and speed of few-photon control. In the first set of measurements, the depletion of a high-power pump seeded by a small continuous wave (CW) signal was characterized. To eliminate any effect of Brillouin scattering, the high-power CW pump was converted into quasi-CW, 1-ns pulse with 1.59-W peak power. The pump depletion map (Fig. 4A) illustrates the static transfer characteristics of the photon gate when the pump was centered at 1554 nm. The static measurement accuracy (±0.065 dB) imposed the minimum observable depletion level, limiting the smallest input signal power to 30 nW during the measurement. To estimate the maximum bandwidth of the control signal pulse, we consider a 1-dB pump depletion level that is ~10 times above the measurement accuracy. For an input control power of 178 nW, the signal can be tuned over 520 GHz (line N1 in Fig. 4A) while maintaining the minimum 1-dB pump depletion level. This underestimates the true pump depletion level: The 178-nW signal positioned in the middle of this frequency range (point P in Fig. 4A) will lead to higher (~2 dB) pump depletion. However, even with this constraint, it is possible to estimate the minimum photon number in the control pulse allowed by this fiber: A 2.5-ps-long pulse with peak power of 178 nW contains less than three photons, indicating the feasibility of few-photon switching at a 500-GHz rate.

The same experimental architecture was used to test the nonreciprocity hypothesis of this work by inverting the physical direction of the FPM interaction. Indeed, if a unique core variation function leads to optimum photon switching, then a directionally inverted process would be suboptimal. Consequently, the input and output ports of the fiber were swapped, and the CW depletion map was measured again (Fig. 4B). We note the striking differences between the responses shown in Fig. 4, A and B, with respect to both the maximum pump depletion and the depletion-bandwidth product.

Although useful in estimating the performance of few-photon control, these static depletion measurements alone cannot accurately quantify the ultrafast switching response because wide signal bandwidth precludes the assumption of monochromatic phase matching. Consequently, in the second set of measurements, we investigated the pump depletion induced by an ultrafast signal. To approach the maximum bandwidth predicted by the 1-dB static depletion measurement, a 2.45-ps pulse was generated using a continuously tunable, cavity-less source (see the supplementary materials), attenuated, and used to deplete a 1.45-W pump centered at 1554 nm. Instantaneous pump depletion was acquired by a high-sensitivity parametric sampling gate (see the supplementary materials). The sampling gate bandwidth was larger than a terahertz, thus guaranteeing undistorted pump depletion capture. Figure 4C shows pump depletion traces corresponding to input signal pulses with an average of 3, 5, 7, and 15 photons, respectively.

These results prove the basic importance of nanometer-scale fiber core control in distributed FPM interactions. Although this report addresses the feasibility of few-photon switching in locally controlled fiber, it is not difficult to predict the broader implications of this approach, specifically with respect to photon sensors operating in previously forbidden regimes. The most interesting of these rests on the notion that long-scale, locally controlled FPM triggers a multifrequency photon avalanche, inducing massive pump photon annihilation by a few-photon signal stimulus. However, it is also clear that much work remains before its ultimate limit is reached. To accomplish that, a new class of fibers that minimize stochastic dispersion fluctuations (*20*, *21*) while inhibiting parasitic and noise mechanisms must be created.

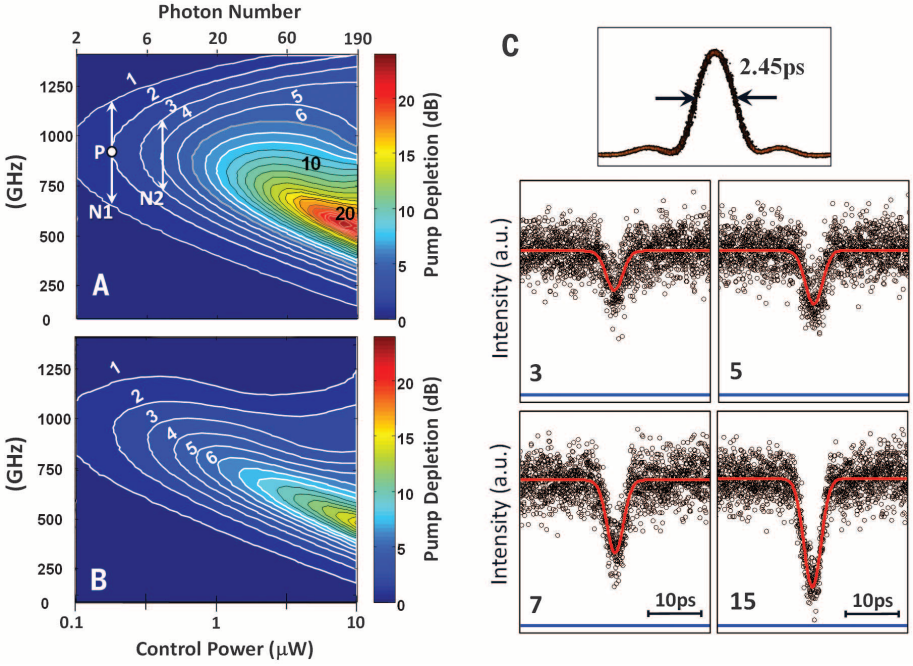


Fig. 4. Static and ultrafast photon control response. (**A**) Measured bandwidth-depletion map for fiber shown in Fig. 3; 1-dB pump depletion corresponds to a 3-photon pulse (N1), and 3-dB pump depletion corresponds to an 8-photon pulse (N2). Pump-signal spectral separation was measured with 12-GHz resolution. Control power was varied with 1-dB step. (**B**) FPM nonreciprocity. Bandwidth-depletion map obtained by reversing the direction of pump and signal propagation. Horizontal axis indicates power in the input (control) pulse (bottom) and the corresponding average photon count (top). (**C**) Pump depletion induced by a 2.45-ps control pulse (top) in the case when it contains an average of 3, 5, 7, and 15 photons. Red curves indicate the average sampling value; blue line indicates the zero-intensity level.

REFERENCES AND NOTES

1. J. Hwang *et al.*, *Nature* **460**, 76–80 (2009).
2. M. Bajcsy *et al.*, *Phys. Rev. Lett.* **102**, 203902 (2009).
3. B. Dayan, Y. Silberberg, *Nat. Photonics* **3**, 429–430 (2009).
4. A. M. C. Dawes, L. Illing, S. M. Clark, D. J. Gauthier, *Science* **308**, 672–674 (2005).
5. I. Ferrain, C. A. Colinge, J.-P. Colinge, *Nature* **479**, 310–316 (2011).
6. G. Raybon *et al.*, *Proc. Opt. Fiber Commun. Conf.*, paper FD10-1, 17–22 March, Anaheim, CA (2002).
7. K. M. Birnbaum *et al.*, *Nature* **436**, 87–90 (2005).
8. D. A. Braje, V. Balic, G. Y. Yin, S. E. Harris, *Phys. Rev. A* **68**, 041801 (2003).
9. R. H. Stolen, A. Ashkin, *Appl. Phys. Lett.* **22**, 294–296 (1973).
10. N. Matsuda, R. Shimizu, M. Mitsumori, H. Kosaka, K. Edamatsu, *Nat. Photonics* **3**, 95–98 (2009).
11. G. I. Stegeman, R. H. Stolen, *J. Opt. Soc. Am. B* **6**, 652–662 (1989).
12. M. Hirano, T. Nakanishi, T. Okuno, M. Onishi, *IEEE J. Sel. Top. Quantum Electron.* **15**, 103–113 (2009).
13. M. E. Marhic, *FOPAs, Oscillators and Related Devices* (Cambridge Univ. Press, Cambridge, 2008).
14. P. A. Andrekson, H. Sunnerud, S. Oda, T. Nishitani, J. Yang, *Opt. Express* **16**, 10956–10961 (2008).
15. S. Radic, *IEEE J. Sel. Top. Quantum Electron.* **18**, 670–680 (2012).
16. R. L. Mozzi, B. E. Warren, *J. Appl. Cryst.* **2**, 164–172 (1969).
17. M. E. Marhic, G. Kalogerakis, L. G. Kazovsky, *Electron. Lett.* **42**, 519–520 (2006).
18. E. Myslivets, N. Alic, S. Radic, *J. Lightwave Technol.* **28**, 3478–3487 (2010); www.opticsinfobase.org/jlt/abstract.cfm?URI=jlt-28-23-3478.
19. E. Myslivets *et al.*, *IEEE Photon. Technol. Lett.* **21**, 1807–1809 (2009).
20. B. P.-P. Kuo, J. M. Fini, L. Grüner-Nielsen, S. Radic, *Opt. Express* **20**, 18611–18619 (2012).
21. B. P.-P. Kuo, M. Hirano, S. Radic, *Opt. Express* **20**, 18422–18431 (2012).

ACKNOWLEDGMENTS

This research is based on work supported by the Office of the Director of National Intelligence (ODNI), Intelligence Advanced Research Projects Activity (IARPA).

SUPPLEMENTARY MATERIALS

www.sciencemag.org/content/345/6195/417/suppl/DC1
Materials and Methods
Supplementary Text
Figs. S1 to S3
References (*22*–*26*)

10 March 2014; accepted 4 June 2014
Published online 19 June 2014;
10.1126/science.1253125

QUANTUM COMPUTING

Defining and detecting quantum speedup

Troels F. Rønnow,[1] Zhihui Wang,[2,3] Joshua Job,[3,4] Sergio Boixo,[5,6] Sergei V. Isakov,[7] David Wecker,[8] John M. Martinis,[9] Daniel A. Lidar,[2,3,4,6,10] Matthias Troyer[1]*

The development of small-scale quantum devices raises the question of how to fairly assess and detect quantum speedup. Here, we show how to define and measure quantum speedup and how to avoid pitfalls that might mask or fake such a speedup. We illustrate our discussion with data from tests run on a D-Wave Two device with up to 503 qubits. By using random spin glass instances as a benchmark, we found no evidence of quantum speedup when the entire data set is considered and obtained inconclusive results when comparing subsets of instances on an instance-by-instance basis. Our results do not rule out the possibility of speedup for other classes of problems and illustrate the subtle nature of the quantum speedup question.

The interest in quantum computing originates in the potential of a quantum computer to solve certain computational problems much faster than is possible classically. Examples are the factoring of integers (*1*) and the simulation of quantum systems (*2*, *3*). In these examples, a quantum algorithm is exponentially faster than the best known classical algorithm. According to the extended Church-Turing thesis, all classical computers are equivalent up to polynomial factors (*4*). Similarly, all proposed models of quantum computation are polynomially equivalent, so that a finding of exponential quantum speedup will be model-independent. In other cases, in particular on small devices or when the quantum speedup is polynomial, defining and detecting quantum speedup becomes more subtle.

Denoting the time used by a specific classical device or algorithm to solve a problem of size N by $C(N)$ and the time used on the quantum device by $Q(N)$, we define quantum speedup as the asymptotic behavior of the ratio

$$S(N) = \frac{C(N)}{Q(N)} \qquad (1)$$

for $N \to \infty$. Subtleties appear in the choice of classical algorithms and in defining $C(N)$ and $Q(N)$ if the runtime depends not just on the size N of a problem but also on the specific problem instance and in extrapolating to the asymptotic limit.

Depending on our knowledge of classical algorithms for a given problem, we may consider four different types of quantum speedup. The optimal scenario is one of a provable quantum speedup, where there exists a proof that no classical algorithm can outperform a given quantum algorithm. The best known example is Grover's search algorithm (*5*), which, in the query complexity setting, exhibits a provable quadratic speedup over the best possible classical algorithm (*6*). A strong quantum speedup was defined in (*7*) by using the performance of the best classical algorithm for $C(N)$, whether such an algorithm is known or not. Unfortunately, the performance of the best classical algorithm is unknown for many interesting problems. In the case of factoring, for example, a proof of a classical super-polynomial lower bound is not known. A less ambitious goal is therefore desirable, and thus one usually defines quantum speedup (without additional adjectives) by comparing it with the best available classical algorithm instead of the best possible classical algorithm.

A weaker scenario is one where a quantum algorithm is designed to make use of quantum effects, but it is not known whether these quantum effects provide an advantage over classical algorithms or where a device is a putative or candidate quantum information processor. To capture this scenario, which is of central interest

[1]Theoretische Physik, ETH (Eidgenössische Technische Hochschule) Zurich, 8093 Zurich, Switzerland. [2]Department of Chemistry, University of Southern California, Los Angeles, CA 90089, USA. [3]Center for Quantum Information Science and Technology, University of Southern California, Los Angeles, CA 90089, USA. [4]Department of Physics, University of Southern California, Los Angeles, CA 90089, USA. [5]Google, 150 Main Street, Venice Beach, CA 90291, USA. [6]Information Sciences Institute, University of Southern California, Los Angeles, CA 90089, USA. [7]Google, Brandschenkestrasse 110, 8002 Zurich, Switzerland. [8]Quantum Architectures and Computation Group, Microsoft Research, Redmond, WA 98052, USA. [9]Department of Physics, University of California Santa Barbara, CA 93106–9530, USA. [10]Department of Electrical Engineering, University of Southern California, Los Angeles, CA 90089, USA.
*Corresponding author. E-mail: troyer@phys.ethz.ch

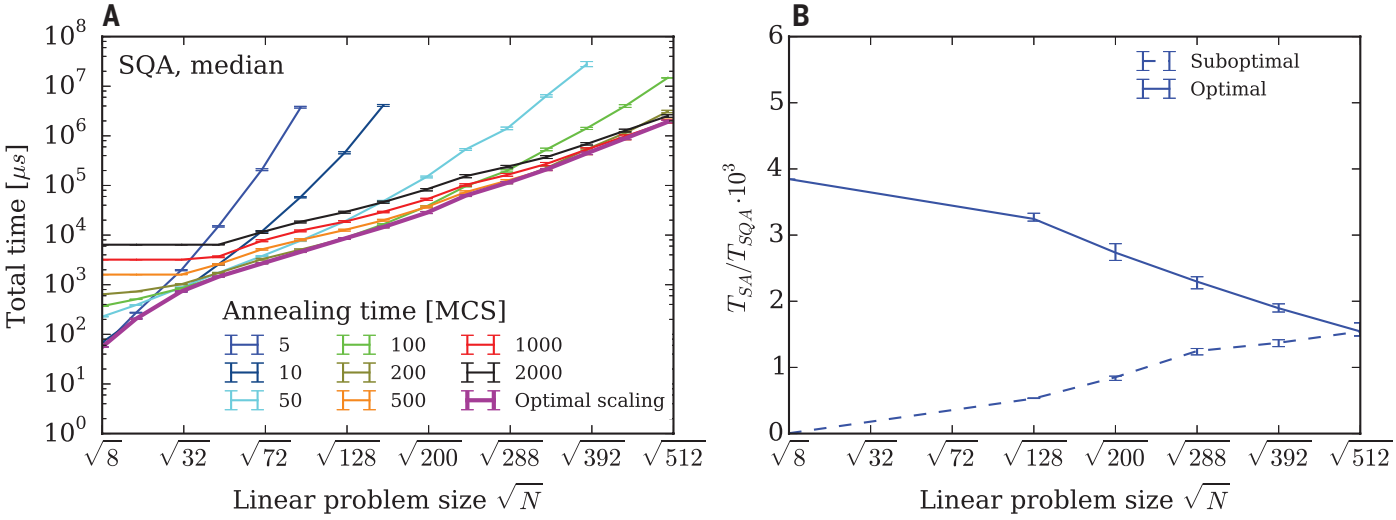


Fig. 1. Pitfalls when detecting speedup. (**A**) The typical (median) time to find a ground state at least once with 99% probability for spin glasses with ±1 couplings using SQA at constant t_a. The lower envelope of the curves at constant t_a corresponds to the total effort at $t_a^{opt}(N)$ and can be used to infer the asymptotic scaling. The initial, relatively flat slope at fixed N is due to suboptimal performance at small N values and should therefore not be interpreted as speedup. Annealing times are given in units of Monte Carlo steps (MCS), corresponding to one update per spin. (**B**) The speedup of SQA over SA for two cases. If SQA is run suboptimally at small sizes by choosing a fixed large t_a = 10,000 MCS (dashed line), a speedup is feigned. This is due to suboptimal performance on small sizes and not indicative of the real asymptotic behavior when both codes are run optimally (solid line). Error bars indicate statistical errors.

to us in this work, we define limited quantum speedup as a speedup obtained when compared specifically with classical algorithms that "correspond" to the quantum algorithm in the sense that they implement the same algorithmic approach, but on classical hardware. A natural example is quantum annealing (*8*, *9*) or adiabatic quantum optimization (*10*) implemented on a candidate physical quantum information processor versus corresponding classical algorithms such as simulated annealing (SA) (*11*) (which performs annealing on a classical Monte Carlo simulation of the Ising spin glass and makes no use of quantum effects) or simulated quantum annealing (SQA) (*12*, *13*) (a classical algorithm mimicking quantum annealing in a path-integral quantum Monte Carlo simulation). In this comparison, a limited quantum speedup would be a demonstration that quantum effects improve the annealing algorithm.

To illustrate the subtleties in detecting quantum speedup, even after a classical reference algorithm is chosen, we compared the performance of an experimental 503-qubit D-Wave Two (DW2, D-Wave Systems, Incorporated, Burnaby, Canada) device to classical algorithms and analyzed the evidence for quantum speedup on the benchmark problem of random spin glass instances. Specifically, we considered the problem of finding the ground state of an Ising spin glass model described by a "problem Hamiltonian"

$$H_{\mathrm{Ising}} = -\sum_{i\in\mathcal{V}} h_i\sigma_i^z - \sum_{(i,j)\in\mathcal{E}} J_{ij}\sigma_i^z\sigma_j^z \qquad (2)$$

with N binary variables $\sigma_i^z = \pm 1$. The local fields $\{h_i\}$ and couplings $\{J_{ij}\}$ are fixed and define a problem instance of the Ising model. The spins occupy the vertices $\mathcal{V}$ of a graph $G = \{\mathcal{V}, \mathcal{E}\}$ with edge set $\mathcal{E}$. We will consider the distributions of the time to solution over many random spin glass problems instances with zero local fields on the Chimera graph realized by the DW2 device [see supplementary materials (*14*) for a definition of that graph and why we choose $h_i = 0$]. This problem is NP-hard (*15*), and all known classical algorithms scale super-polynomially not only for the hardest but also for typical instances. Although quantum mechanics is not expected to reduce the super-polynomial scaling to polynomial, a quantum algorithm might still scale better with problem size N than any classical algorithm.

The D-Wave devices (*16*–*19*) are designed to be physical realizations of quantum annealing using superconducting flux qubits and programmable fields $\{h_i\}$ and couplings $\{J_{ij}\}$. Quantum annealing is implemented by initializing the system in the ground state of a transverse magnetic field $H_X = -\sum_{i\in\mathcal{V}}\sigma_i^x$, where the σ's denote the Pauli matrices; H_X is turned off adiabatically, while H_{Ising} is turned on simultaneously. A measurement of each qubit in the computational basis then determines the ground state of H_{Ising} with a probability affected by many factors, including thermal excitations and implementation errors (*20*). Tests on D-Wave One (DW1) (*21*) and DW2 devices (*22*) have shown that for small problem sizes the device correlates well with the predictions of a quantum master equation. For larger problem sizes, a 108-qubit DW1 device correlated well with SQA (*20*), which indicates that, despite decoherence and coupling to a thermal bath, the behavior of the device is consistent with it actually performing quantum annealing (*23*, *24*). However, for these benchmarks both SQA and the DW1 device are also well described by a semi-classical mean-field version of SQA (*25*), which raises the question of whether quantum effects play an important role. The approach adopted here, of seeking evidence of a (limited) quantum speedup, directly addresses the crucial question of whether large-scale quantum effects create a potential for the devices to outperform classical algorithms. To test this possibility, we compared the performance of a DW2 device to two "corresponding" classical algorithms: SA and SQA.

Because quantum speedup concerns the asymptotic scaling of $S(N)$, we considered the subtleties of estimating it from small N and inefficiencies at small N that can fake or mask a speedup. In the context of annealing, the optimal choice of the annealing time t_a turns out to be crucial for estimating asymptotic scaling. To illustrate this, we first considered the time to solution using SA and SQA run at different fixed t_a values, independent of N. Figure 1A shows the scaling of the median total annealing time [over 1000 different random instances on the D-Wave Chimera graph; see supplementary materials (*14*)] for SQA to find a solution at least once with probability $P = 0.99$. Corresponding times for SA are shown in fig. S10. We observed that at constant t_a, as long as t_a is long enough to find the ground state almost every time, the scaling of the total effort is at first relatively flat. The total effort then rose more rapidly, once one reached N values for which the chosen t_a is too short, and the success probabilities were thus low, requiring many repetitions. Extrapolations to $N \to \infty$ need to consider the lower envelope of all curves, which corresponds to choosing an optimal annealing time $t_a^{\mathrm{opt}}(N)$ for each N.

Figure 1B demonstrates that, when using fixed t_a values, no conclusion can be drawn from annealing (simulated or in a device) about the asymptotic scaling. The initial slow increase at constant t_a is misleading, and instead the optimal annealing time t_a^{opt} needs to be used for each N. To illustrate this, we show (Fig. 1B) the real "speedup" ratio of the scaling of SA and SQA (actually a slowdown) and a fake speedup resulting from a constant and excessively long t_a for SQA. Because SA outperforms SQA on our benchmark set, it is our algorithm of choice in the comparisons with the DW2 reported below.

A related issue is the scaling of hardware resources (computational gates and memory) with problem size, which must be identical for the devices we compare. A device whose hardware resources scale as N can achieve an intrinsic parallel speedup compared with a fixed

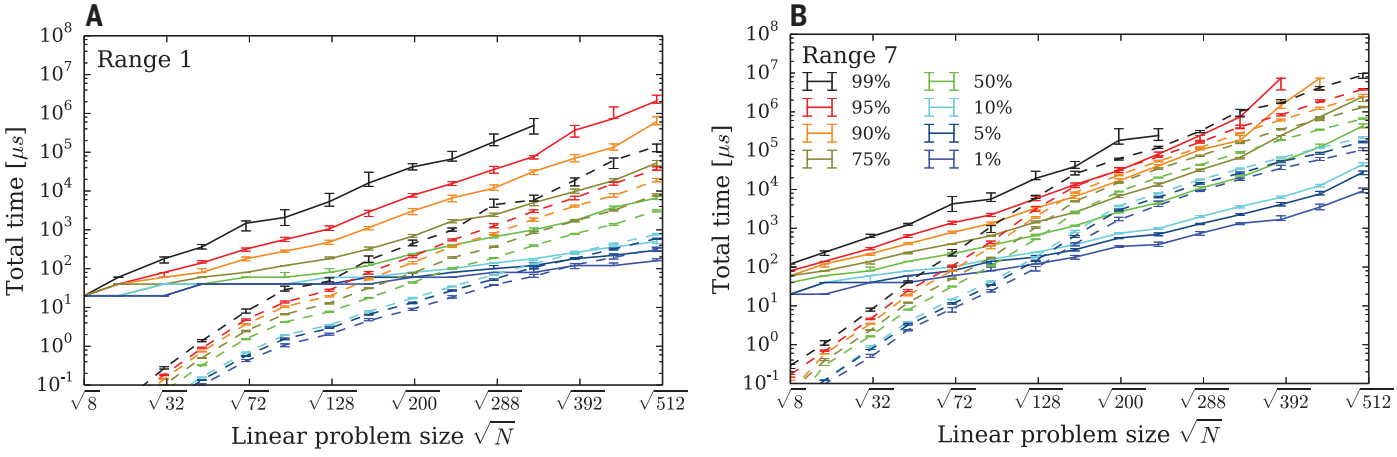


Fig. 2. Scaling of time to solution for $r = 1$ (A) and $r = 7$ (B). Shown is the scaling of the pure annealing time to find the ground state at least once with a probability $P = 0.99$ for various quantiles of hardness for simulated annealing (SA, dashed) and the DW2 (solid). The solid lines terminate for the highest quantiles because the DW2 did not solve the hardest instances for large problem sizes within the maximum number of repetitions (at least 32,000) of the annealing we performed.

size device. Such is the case for the DW2, which uses N (out of 512) qubits, $\mathcal{O}(N)$ couplers, and $\mathcal{O}(N)$ classical logical control gates to solve a spin glass instance with N spin variables in time $T_{\mathrm{DW}}(N)$. Considering quantum speedup for $N \to \infty$, we need to compare a (hypothetical) larger DW2 device with the number of qubits and couplers growing as $\mathcal{O}(N)$ to a (hypothetical) classical device with $\mathcal{O}(N)$ gates or processing units. Because SA (and SQA) are perfectly parallelizable for the bipartite Chimera graphs realized by the DW2, we can relate the scaling of the time $T_{\mathrm{C}}(N)$ on such a device to the time $T_{\mathrm{SA}}(N)$ for SA on a fixed-size classical central processing unit (CPU) by $T_{\mathrm{C}}(N) \sim T_{\mathrm{SA}}/N$ and obtain

$$S(N) = \frac{T_{\mathrm{C}}(N)}{T_{\mathrm{DW}}(N)} \sim \frac{T_{\mathrm{SA}}(N)}{T_{\mathrm{DW}}(N)} \frac{1}{N} \qquad (3)$$

We lastly addressed the question of how to measure time when the time to solution depends on the specific problem instance. When a device is used as a tool for solving computational problems, the question of interest is to determine which device is better for almost all possible problem instances. If instead the focus is on the underlying physics of a device, then it might suffice to find a subclass of instances where a speedup is exhibited. These two questions lead to different quantities of interest.

To illustrate the considerations, we now turn to our results. Figure 2 shows the scaling of the time to find the ground state for various quantiles, from the easiest instances (1%) to the hardest (99%), comparing the DW2 and SA. We chose the values of the couplings J_{ij} from $2r$ discrete values $\{n/r\}$, with $n \in \pm\{1, \ldots, r-1, r\}$, and call r the range. Because we do not a priori know the hardness of a given problem instance, we have to assume the worst case and perform a sufficient number of repetitions R to be able to solve even the hardest problem instances. Hence, the scaling for the highest quantiles is the most informative. Here, we considered only the pure annealing times, ignoring setup and readout times that scale subdominantly [see (*14*) for wall-clock results].

We observed for both the DW2 and the SA, for sufficiently large N, that the total time to solution for each quantile q scaled as $\exp(c_q\sqrt{N})$ (with $c_q > 0$ a constant) as reported previously for SA and SQA (*20*). The origin of the $\sqrt{N}$ exponent is well understood for exact solvers as reflecting the treewidth of the Chimera graph (*14*, *26*). Whereas the SA code was run at a $t_{\mathrm{a}}^{\mathrm{opt}}$ for each N, the DW2 has a minimal $t_{\mathrm{a}} = 20\ \mu\mathrm{s}$, which is longer than the optimal time for all problem sizes (*14*). Therefore, the observed slope of the DW2 data can only be taken as a lower bound for the asymptotic scaling. With this in mind, we observed similar scaling for SA and the DW2 for $N \gtrsim 200$.

How can we probe for a speedup in light of this similar scaling? With algorithms such as SA or quantum annealing, where the time to solution depends on the problem instance, it is impractical to experimentally find the hardest problem instance. If instead we target a fraction

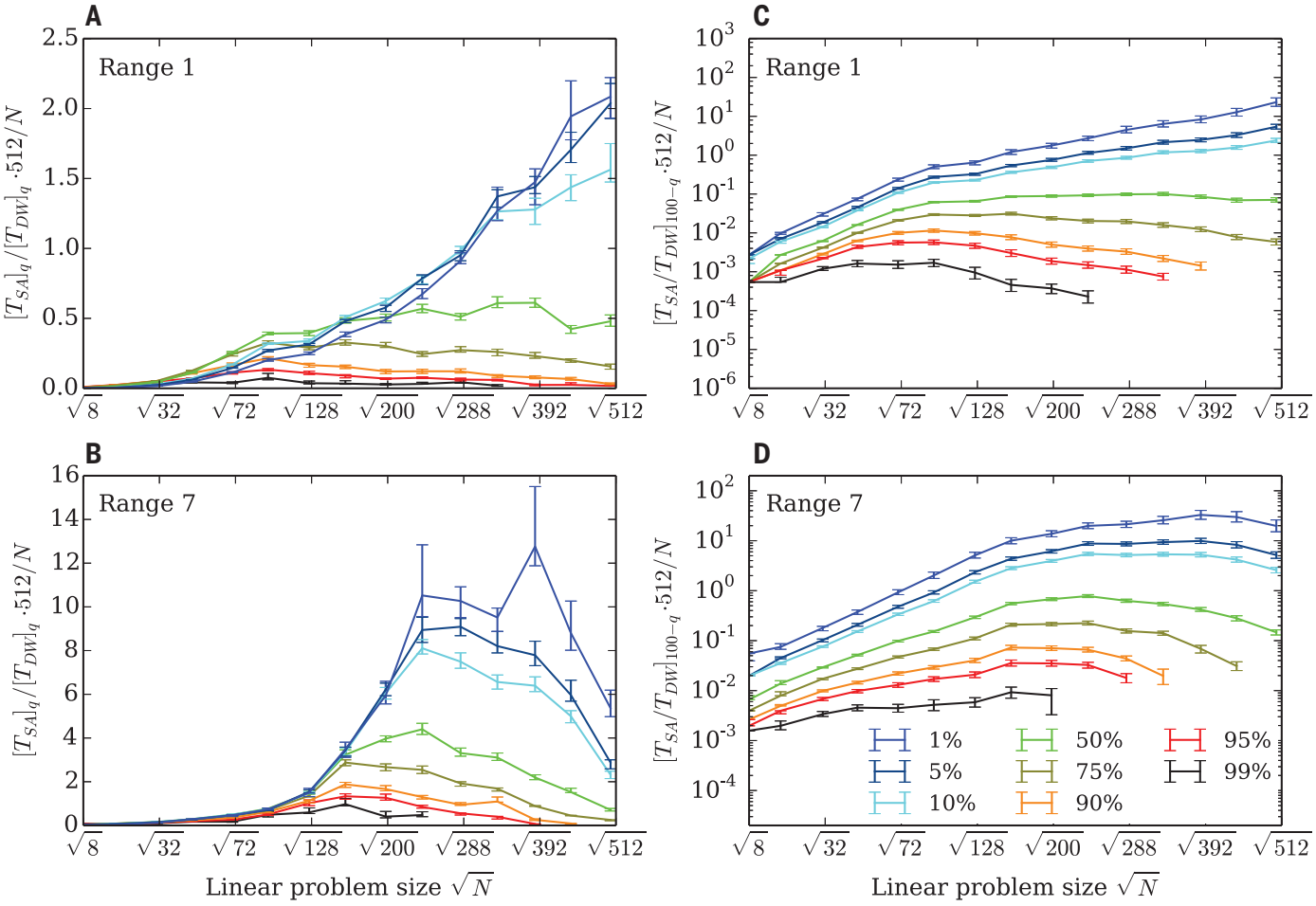


Fig. 3. Speedup of the DW2 compared to SA. (**A** and **B**) For the RofQs, and (**C** and **D**) for the QofRs. For a random variable X with distribution $p(x)$ and values in $x \in [0, \infty)$, we defined, as usual, the qth quantile as $\int_0^{x_q} p(x)dx = q/100$, which we solved for x_q and plotted as a function of $\sqrt{N}$. In the QofR case, we used x_{100-q} so that high quantiles still corresponded to instances that are hard for the DW2. We terminated the curves when the DW2 does not find the ground state for large N at high percentiles. In these plots, we multiplied Eqs. 4 and 5 by 512 so that the speedup value at $N = 512$ directly compares one DW2 processor against one classical CPU. An overall positive slope suggests a possible limited quantum speedup, subject to the caveats discussed in the text. A negative slope indicates that SA outperforms the DW2.

of q% of the instances, then we should consider the qth quantile in the scaling plots shown in Fig. 2. The appropriate speedup quantity is then the ratio of these quantiles (RofQ). Denoting a quantile q of a random variable X by $[X]_q$, we define this as

$$S_q^{\mathrm{RofQ}}(N) = \frac{[T_{\mathrm{SA}}(N)]_q}{[T_{\mathrm{DW}}(N)]_q}\frac{1}{N} \quad (4)$$

Plotting this quantity for the DW2 versus SA in Fig. 3, A and B, we found no evidence for a limited quantum speedup in the interesting regime of large N and large q (almost all instances). That is, although for all quantiles and for both ranges the initial slope was positive, when N and q became large enough we observed a turnaround and eventually a negative slope. Although we observed a positive slope for quantiles smaller than the median, this is of limited interest because we have not been able to identify a priori which instances will be easy. Taking into account that because of the fixed suboptimal annealing times the speedup defined in Eq. 4 is an upper bound, we conclude that there is no evidence of a speedup over SA for this particular benchmark.

$S_q^{RofQ}(N)$ measures the speedup while comparing different sets of instances for DW and SA, each determined by the respective quantile. Now we consider instead whether there is a speedup for a (potentially small) subset of the same problem instances. To this end, we study the scaling of the ratios of the time to solution for individual instances and display in Fig. 3, C and D, the scaling of various quantiles of the ratio (QofR)

$$S_q^{\mathrm{QofR}}(N) = \left[\frac{T_{\mathrm{SA}}(N)}{T_{\mathrm{DW}}(N)}\right]_q \frac{1}{N} \quad (5)$$

For r = 7, all the quantiles bend down for sufficiently large N, so that there is no evidence of a limited quantum speedup. There does seem to be an indication of such a speedup compared to SA in the low quantiles for r = 1, that is, for those instances whose speedup ratio was high. However, the instances contributing here are not run at t_a^{opt}, and more work is needed to establish that the potential r = 1 speedup result persists for those instances for which one can be sure that t_a is optimal.

Next we consider the distribution of solution times at a fixed problem size. This does not address the speedup question, because no scaling can be extracted, but illuminates instead the question of correlation between the performance of the DW2 and SA. To this end, we performed individual comparisons for each instance and show in Fig. 4, A and B, the time to solution for the same instances for the DW2 and SA. We observed a wide scatter [in agreement with the DW1 results of (*20*)] and found that, although the DW2 is sometimes up to 10 times faster in pure annealing time, there are many cases where it is ≥100 times slower.

It is not yet known whether a quantum annealer or even a perfectly coherent adiabatic quantum optimizer can exhibit (limited) quantum speedup at all, although there are promising indications from theory (*27*), simulation (*13*), and experiments on spin glass materials (*9*). Experimental tests are thus important. There are several candidate explanations for the absence of a clear quantum speedup in our tests. Perhaps quantum annealing simply does not provide any advantages over simulated (quantum) annealing or other classical algorithms for the problem class we have studied (*28*), or perhaps the noisy implementation in the DW2 cannot realize quantum speedup and is thus not better than classical devices. Alternatively, a speedup might be masked by calibration errors, improvements might arise from error correction (*29*), or other problem classes might exhibit a speedup. Future studies will probe these alternatives and aim to determine whether one can find a class of problem instances for which an unambiguous speedup over classical hardware can be observed.

Although we used specific processors and algorithms for illustration, the considerations about a reliable determination of quantum speedup presented here are general. For any speedup analysis, use of the same scaling of hardware resources for both quantum and classical devices is required to disentangle parallel and quantum speedup. And, for any quantum algorithm where the runtime must be determined experimentally, a careful extrapolation to large problem sizes is important to avoid mistaking inefficiencies at small problem sizes for signs of quantum speedup.

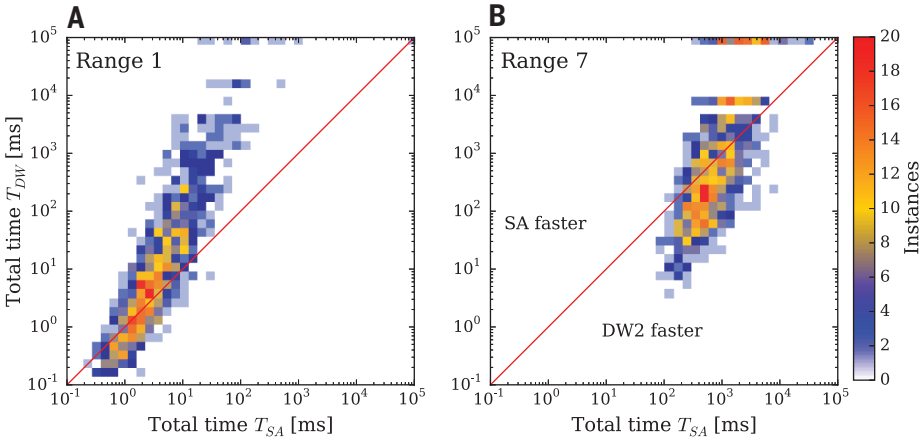


Fig. 4. Instance-by-instance comparison of annealing times. Shown are scatter plots of the pure annealing time for the DW2 compared with SA using an average over 16 gauges [see (*14*)] on the DW2 for (**A**) r = 1 and (**B**) r = 7. The color scale indicates the number of instances in each square. Instances below the diagonal red line are faster on the DW2; those above are faster using SA. Instances for which the DW2 did not find the solution with 10,000 repetitions per gauge are shown at the top of the frame (no such instances were found for SA).

REFERENCES AND NOTES

1. P. W. Shor, in *Proceedings 35th Annual Symposium on Foundations of Computer Science* (IEEE, New York, 1994), pp. 124–134.
2. R. Feynman, *Int. J. Theor. Phys.* **21**, 467–488 (1982).
3. S. Lloyd, *Science* **273**, 1073–1078 (1996).
4. I. Parberry, *SIGACT News* **18**, 54–67 (1986).
5. L. K. Grover, *Phys. Rev. Lett.* **79**, 325–328 (1997).
6. C. Bennett, E. Bernstein, G. Brassard, U. Vazirani, *SIAM J. Comput.* **26**, 1510–1523 (1997).
7. A. Papageorgiou, J. F. Traub, *Phys. Rev. A* **88**, 022316 (2013).
8. T. Kadowaki, H. Nishimori, *Phys. Rev. E* **58**, 5355–5363 (1998).
9. J. Brooke, D. Bitko, T. F. Rosenbaum, G. Aeppli, *Science* **284**, 779–781 (1999).
10. E. Farhi *et al.*, *Science* **292**, 472–475 (2001).
11. S. Kirkpatrick, C. D. Gelatt Jr., M. P. Vecchi, *Science* **220**, 671–680 (1983).
12. R. Martoňák, G. E. Santoro, E. Tosatti, *Phys. Rev. B* **66**, 094203 (2002).
13. G. E. Santoro, R. Martonák, E. Tosatti, R. Car, *Science* **295**, 2427–2430 (2002).
14. See supplementary materials on *Science* Online. The supplementary materials provide details about the classical simulation algorithms, the DW2 device, the procedure used to determine annealing times, and additional data on scaling with problem size.
15. F. Barahona, *J. Phys. Math. Gen.* **15**, 3241–3253 (1982).
16. R. Harris *et al.*, *Phys. Rev. B* **82**, 024511 (2010).
17. M. W. Johnson *et al.*, *Supercond. Sci. Technol.* **23**, 065004 (2010).
18. A. J. Berkley *et al.*, *Supercond. Sci. Technol.* **23**, 105014 (2010).
19. M. W. Johnson *et al.*, *Nature* **473**, 194–198 (2011).
20. S. Boixo *et al.*, *Nat. Phys.* **10**, 218–224 (2014).
21. S. Boixo, T. Albash, F. M. Spedalieri, N. Chancellor, D. A. Lidar, http://arxiv.org/abs/1212.1739 (2012).
22. W. Vinci, T. Albash, A. Mishra, P. A. Warburton, D. A. Lidar, http://arxiv.org/abs/1403.4228 (2014).
23. J. A. Smolin, G. Smith, http://arxiv.org/abs/1305.4904 (2013).
24. L. Wang *et al.*, http://arxiv.org/abs/1305.5837 (2013).
25. S. W. Shin, G. Smith, J. A. Smolin, U. Vazirani, http://arxiv.org/abs/1401.7087 (2014).
26. V. Choi, *Quantum Inf. Process.* **10**, 343–353 (2011).
27. R. D. Somma, D. Nagaj, M. Kieferová, *Phys. Rev. Lett.* **109**, 050501 (2012).
28. H. G. Katzgraber, F. Hamze, R. S. Andrist, *Phys. Rev. X* **4**, 021008 (2014).
29. K. L. Pudenz, T. Albash, D. A. Lidar, *Nat. Commun.* **5**, 3243 (2014).
30. S. Isakov, I. Zintchenko, T. Rønnow, M. Troyer, http://arxiv.org/abs/1401.1084 (2014).

ACKNOWLEDGMENTS

We thank N. Allen, M. Amin, E. Farhi, M. Mohseni, H. Neven, and C. McGeoch for useful discussions and comments and I. Zintchenko for providing the an_ss_ge_nf_bp simulated annealing code before publication of the code with (*30*). This project was supported by the Swiss National Science Foundation through the

National Center of Competence in Research Quantum Science and Technology, the Army Research Office (ARO) Multidisciplinary University Research Initiative (MURI) grant no. W911NF11-1-0268, ARO grant no. W911NF-12-1-0523, the Lockheed Martin Corporation, and Microsoft Research. Simulations were performed on clusters at Microsoft Research and ETH Zurich an on supercomputers of the Swiss Center for Scientific Computing.

We acknowledge hospitality of the Aspen Center for Physics, supported by NSF grant PHY-1066293.

SUPPLEMENTARY MATERIALS
www.sciencemag.org/content/345/6195/420/DC1
Supplementary Text
Figs. S1 to S10
Tables S1 and S2
References (*31*–*37*)

17 February 2014; accepted 10 June 2014
Published online 19 June 2014;
10.1126/science.1252319

QUANTUM METROLOGY

Fisher information and entanglement of non-Gaussian spin states

Helmut Strobel,[1]* Wolfgang Muessel,[1] Daniel Linnemann,[1] Tilman Zibold,[1] David B. Hume,[1] Luca Pezzè,[2] Augusto Smerzi,[2] Markus K. Oberthaler[1]

Entanglement is the key quantum resource for improving measurement sensitivity beyond classical limits. However, the production of entanglement in mesoscopic atomic systems has been limited to squeezed states, described by Gaussian statistics. Here, we report on the creation and characterization of non-Gaussian many-body entangled states. We develop a general method to extract the Fisher information, which reveals that the quantum dynamics of a classically unstable system creates quantum states that are not spin squeezed but nevertheless entangled. The extracted Fisher information quantifies metrologically useful entanglement, which we confirm by Bayesian phase estimation with sub–shot-noise sensitivity. These methods are scalable to large particle numbers and applicable directly to other quantum systems.

Multiparticle entangled states are the key ingredients for advanced quantum technologies (*1*). Various types have been achieved in experimental settings ranging from ion traps (*2*), photonic systems (*3*), and solid state circuits (*4*) to Bose-Einstein condensates. For the latter, squeezed states (*5*, *6*) have been generated (*7*–*12*), and a rich class of entangled non-Gaussian states is predicted to be obtainable (*13*), including maximally entangled Schrödinger cat states (*14*, *15*). The production of these fragile states in large systems remains a challenge, and efficient methods for characterization are necessary because full state reconstruction becomes intractable. Here, we generate a class of non-Gaussian many-particle entangled states and reveal their quantum properties by studying the distinguishability of experimental probability distributions.

A measure of the distinguishability with respect to small phase changes of the state is provided by the Fisher information F (*16*). It is related to the highest attainable interferometric phase sensitivity by the Cramer-Rao bound $\Delta\theta_{CR} = 1/\sqrt{F}$ (*17*). This limit follows from general statistical arguments for a measurement device with fluctuating output (*18*). The Fisher information is limited by quantum fluctuations of the input state as well as the performance of the device. Even in the absence of technical noise, the Fisher information of a classical input state is $F \leq N$ because of the intrinsic granularity of N independent particles, which translates into the shot-noise limit $\Delta\theta \geq 1/\sqrt{N}$ for phase estimation. This classical bound can be surpassed with a reduction of the input fluctuations by introducing entanglement between the N particles (*5*). These states, known as squeezed states, are fully characterized by mean and variance of the observable and already used in precision measurements (*19*–*21*). In contrast, non-Gaussian quantum states can have increased fluctuations of the observable but nevertheless allow surpassing shot-noise limited performance. A textbook example is the Schrödinger cat state characterized by macroscopic fluctuations but achieving the best interferometric performance allowed by quantum mechanics, that is, at the fundamental Heisenberg limit $F = N^2$ (*22*). In general, the class of states that are entangled and useful for sub–shot-noise phase estimation is identified by the Fisher information criterion $F > N$ (*13*). Exploiting these resources requires probabilistic methods for phase estimation, such as maximum likelihood or Bayesian analysis (*23*), which go beyond standard evaluation of averages.

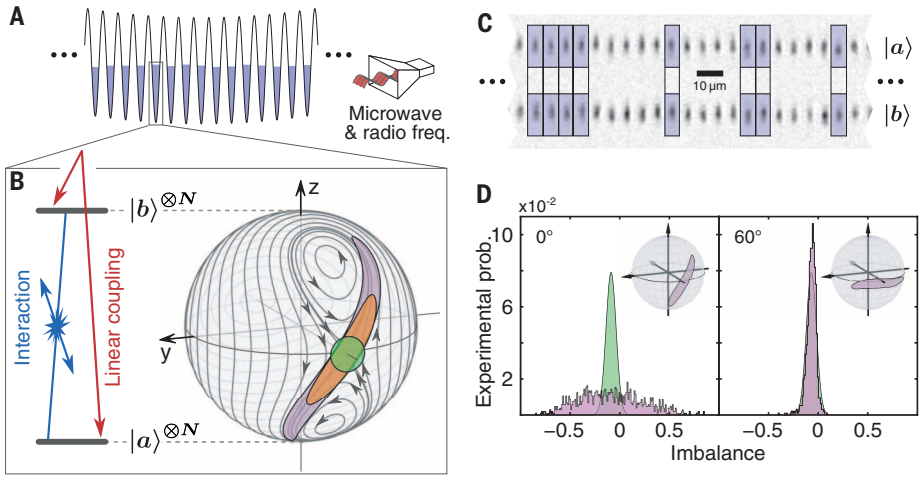


Fig. 1. Preparation and detection of non-Gaussian entangled states. (**A**) Array of Bose-Einstein condensates in an optical lattice potential addressed by microwave and radio frequency fields. (**B**) The interplay of nonlinear interaction (blue) and weak Rabi coupling (red) between the internal states $|a\rangle$ and $|b\rangle$ results in an unstable fixed point in the classical phase space. The state of the system is visualized on a generalized Bloch sphere with radius $J = N/2$. Gray lines indicate trajectories of the mean-field equations of motion (*18*). The initial coherent spin state (green) ideally evolves into a squeezed state (orange) followed by non-Gaussian states at later evolution times (violet). Edges of shaded areas are contours of the Husimi distribution for $N = 380$ at $1/e^2$ of its maximum. (**C**) Experimental absorption picture showing the site- and state-resolved optical lattice after a Stern-Gerlach separation. Shaded boxes indicate the sites with a total atom number in the range of 380 ± 15, which are selected for further analysis. (**D**) Example histograms of the imbalance $z = 2J_z/N$ after nonlinear evolution of 25 ms and final rotation (angles indicated in the graphs) compared with the ideal coherent spin state of identical N (green Gaussian).

[1]Kirchhoff-Institut für Physik, Universität Heidelberg, Im Neuenheimer Feld 227, 69120 Heidelberg, Germany. [2]QSTAR (Quantum Science and Technology in Arcetri), INO-CNR (Istituto Nazionale di Ottica–Consiglio Nazionale delle Ricerche), and LENS (European Laboratory for Nonlinear Spectroscopy), Largo Enrico Fermi 2, 50125 Firenze, Italy.
*Corresponding author. E-mail: fisherinformation@matterwave.de

A paradigm physical process that exhibits the transition from Gaussian to non-Gaussian states is the time evolution of a quantum state initially prepared at an unstable classical fixed point. Our experimental system is an array of interacting binary Bose-Einstein condensates of ^{87}Rb with additional linear coupling of the two internal states (Fig. 1, A and B), which allows for the controlled realization of such unstable fixed point dynamics (*24*). The linear coupling, realized with microwave and radio frequency magnetic fields, also permits precise rotations for initial state preparation and final state manipulation before readout (Fig. 1, B and D). For a coherent state initially centered on the unstable fixed point, the quantum dynamics leads to spin squeezed states for short evolution times; subsequently, the squeezed states transform into non-Gaussian states on an experimentally feasible time scale (*14*) (Fig. 1B).

For the characterization of non-Gaussian states, higher moments, or even the full probability distributions, have to be accessed experimentally. For this, the setup (*8*) has been extended to realize up to 35 individual condensates in a single experiment, which permits the acquisition of sufficient statistics in a narrow window of ±15 for the final atom number. The populations of the atomic states $|a\rangle = |F = 1, m_F = 1\rangle$ and $|b\rangle = |F = 2, m_F = -1\rangle$ are destructively detected for each individual condensate by state-selective absorption imaging with high spatial resolution (Fig. 1C) (*25*). By repeating the experiment (typically many thousands of times), we measure the experimental probability distributions of the population imbalance $z = (N_b - N_a)/N$ along defined directions by applying the corresponding spin rotation before detection. The analysis window for $N = N_b + N_a$ is adjusted according to the independently determined time scale of atom loss (*18*) to follow the time evolution starting with $\langle N \rangle = 470$. Figure 1D shows examples of observed distributions for two different orientations and an evolution time of 25 ms; the distributions are consistent with the theoretically expected structure of the state (Fig. 1B).

Detailed insight can be gained by repeating this measurement for various angles (here in steps of 10°) allowing for the maximum-likelihood reconstruction of the density matrix in the symmetric subspace (*18*). The tomography results obtained from 32,500 experimental realizations (Fig. 2A) confirm qualitatively the expected behavior; at short evolution times, the state has a squeezed shape, whereas at later times the characteristic bending dynamics appears as expected from the presence of the two stable fixed points above and below the equator.

Analyzing the variance of z for the same data as a function of the tomography angle (Fig. 2B) shows that the time evolution leads to suppressed fluctuations at 15 ms. Extracting the spin squeezing parameter ξ^2 (*18*), we find that the minimum is $\xi^2_{\mathrm{min}} = -4.5 \pm 0.2$ dB below the standard quantum limit, which demonstrates entanglement (*5*). For all results reported here, the photon shot noise of the absorption imaging of ±4 atoms is not subtracted. For longer time evolution, the bending dynamics leads to increased fluctuations in all directions, that is, tomography angles. After 25 ms, spin squeezing is lost, and we find that $\xi^2_{\mathrm{min}} = -0.2 \pm 0.3$ dB. However, experimental extraction of the Fisher information (detailed below, Fig. 2C) reveals that useful entanglement is still present although spin squeezing is vanishing, that is, $F/N \geq 1/\xi^2$ (*13*). At 26 ms, spin squeezing is completely lost, whereas the Fisher information still indicates the presence of quantum resources ($F/N > 1$). In the Gaussian regime up to 23 ms, we observe that Fisher information and the inverse spin squeezing agree as expected, $F/N \approx 1/\xi^2$, because these states are fully characterized by their variance.

Our method for extraction of the Fisher information circumvents the experimentally intractable full reconstruction of the density matrix and has its basis in a specific set of experimental probability distributions $P_z(\theta)$ after small rotations θ of the quantum state. In Fig. 3A, we show distributions for the state created at 26 ms and the optimal tomography angle of 58° (Fig. 2C) after small rotations about the y axis (Fig. 3C, inset). The distributions feature a pronounced peak and long tails characteristic for the bent state. The main effect of the small rotation is a continuous shift of the distribution toward increasing imbalance for larger angles θ.

The analysis for extraction of the Fisher information builds on the statistical distance (*26*, *27*) of these distribution functions. We use a Euclidean distance in the space of probability amplitudes $\sqrt{P_z}$ known as Hellinger distance (*18*), defined as $d^2_{\mathrm{H}}(\theta) = \frac{1}{2}\sum_z [\sqrt{P_z(\theta)} - \sqrt{P_z(0)}]^2$, where $P_z(\theta)$ is the experimental probability distribution at angle θ. Figure 3C shows $d^2_{\mathrm{H}}(\theta)$ as a function of θ for three different evolution times and the respective optimal tomography angles. A resampling method (*18*) is used to extract error bars and reduce the statistical bias. The observed quadratic behavior is expected from the Taylor expansion $d^2_{\mathrm{H}}(\theta) = (F/8)\theta^2 + \mathcal{O}(\theta^3)$ (eq. S11), which reveals the close connection between Hellinger distance and Fisher information; this relationship is used to extract F from the curvature of $d^2_{\mathrm{H}}(\theta)$. The gray shaded area in Fig. 3C indicates the region that is not accessible to separable states; for them, the Fisher information is limited to $F/N \leq 1$, resulting in a d^2_{H} curvature smaller than $N/8$. For the initially prepared state, we found a Fisher information of

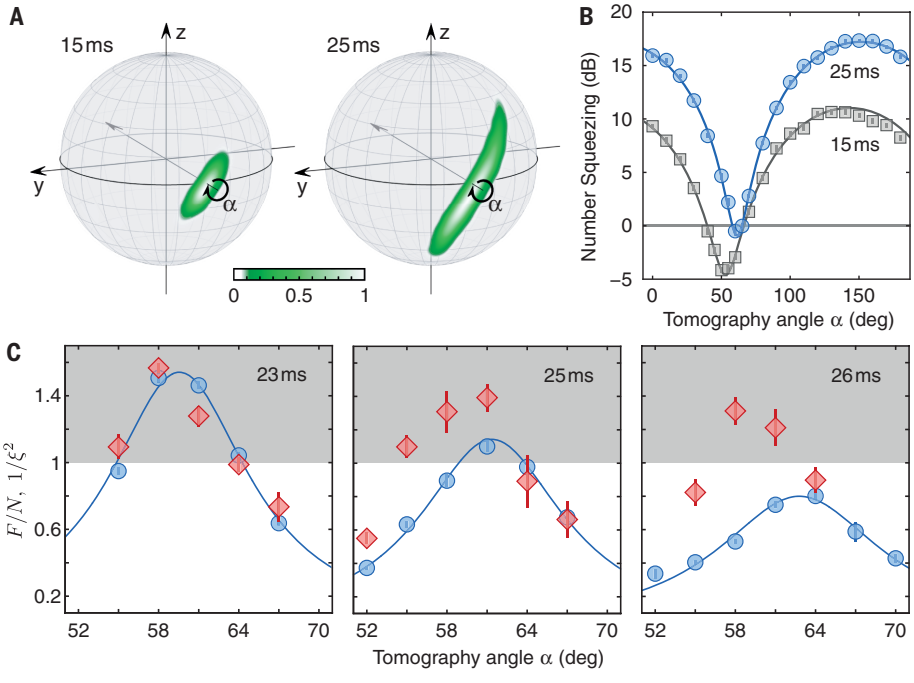


Fig. 2. Entangled state characterization. (**A**) Tomographic reconstruction of the experimental state after evolution times of 15 and 25 ms. The Husimi projections [scaled amplitude is brightness-coded (*18*)] confirm the creation of an elongated state and the subsequent distortion of the Gaussian shape. (**B**) A variance analysis of the particle number difference reveals maximum spin squeezing of −4.5 ± 0.2 dB for 15 ms and −0.2 ± 0.3 dB for 25 ms. (**C**) Comparison of the normalized Fisher information F/N (red diamonds) for $N = 380 \pm 15$ atoms and the inverted spin squeezing factor $1/\xi^2$ (blue circles). The gray shaded areas are only accessible for nonseparable (entangled) states. For 26 ms, spin squeezing cannot identify the entanglement that is detected by the Fisher information. Lines are sinusoidal fits; error bars of the Fisher information represent the 68% confidence interval of the Hellinger distance method.

$F/N = 0.91 \pm 0.04 < 1$, which is expected for a separable state. All given error margins are ±1 SE. For a subsequent evolution of 26 ms, the measured Hellinger distances lie in the regime of nonseparability. This reveals entanglement in a regime where no spin squeezing is present. For the intermediate evolution time of 15 ms, we extract a Fisher information $F/N = 2.2 \pm 0.2$, which confirms entanglement in the Gaussian spin squeezed state. For obtaining the experimental points in Fig. 2C, this procedure is performed at a given evolution time for different tomography angles. The reported values for the Fisher information are limited by experimental imperfections, detection noise, and atom loss, which especially affect the fragile non-Gaussian states. For the ideal time evolution, monotonically increasing Fisher information is expected, whereas the available spin squeezing is limited to $1/\xi^2 \approx 18$ (–12.6 dB). The ideal theoretical model prediction is $F/N \approx 90$ (–19.5 dB) for the evolution time when spin squeezing vanishes (*18*).

There is a direct connection between Fisher information and sensitivity in parameter estimation. In an interferometric context, high sensitivity, indicated by a large value of F, means fast change of the output distribution with the phase θ, that is, high statistical speed $\partial d_H/\partial\theta = \sqrt{F/8}$ with respect to the parameter change. For the quantum state at 25 ms, the enhanced Fisher information reveals quantum resources beyond the standard quantum limit in a range of tomography angles. In Fig. 4A, we show explicitly through an analysis of mean and variance that averaging of the observable z does not surpass shot-noise limited performance for rotations about the y axis [corresponding, for example, to a phase shift inside a Ramsey interferometer (*18*)].

However, the resource can be harnessed with model-independent Bayesian estimation by using the experimental probability distributions $P_z(\theta)$. For this, we use an independent data set taken with the setting ($\alpha = 58°, \theta = \theta_0 = 0°$) and 25 ms of evolution time, which we divide into sequences $\{z_1, ..., z_m\}$ each containing m realizations. To obtain realistic measurement conditions, we discard the previous knowledge on the true value of the phase θ_0 [Bayesian estimation with flat prior (*18*)]. For each distribution $P_z(\theta_i)$, we calculate the likelihood $\mathcal{L}(\theta_i) = \prod_{j=1}^{m} P_{z_j}(\theta_i)$, which corresponds to the conditional probability to obtain the sequence $\{z_1, ..., z_m\}$ if the phase setting had been θ_i. For sufficiently large m, we expect a Gaussian distribution $\mathcal{L}(\theta) \propto \exp[-(\theta-\theta_c)^2/2\sigma^2]$ centered at θ_c with the Bayesian phase uncertainty σ (*18*). Thus, σ can be extracted from a quadratic fit to $\log\mathcal{L}(\theta)$ (Fig. 4B, inset). We find a fast convergence of σ^2 to the expected value $1/mF$ (Cramer-Rao bound for m measurements) already for $m \gtrsim 2$ (Fig. 4B). This explicitly shows phase uncertainty below the standard quantum limit in agreement with the Fisher information obtained from the Hellinger distance method described above.

Fisher information serves to verify entanglement in the absence of spin squeezing and quantifies

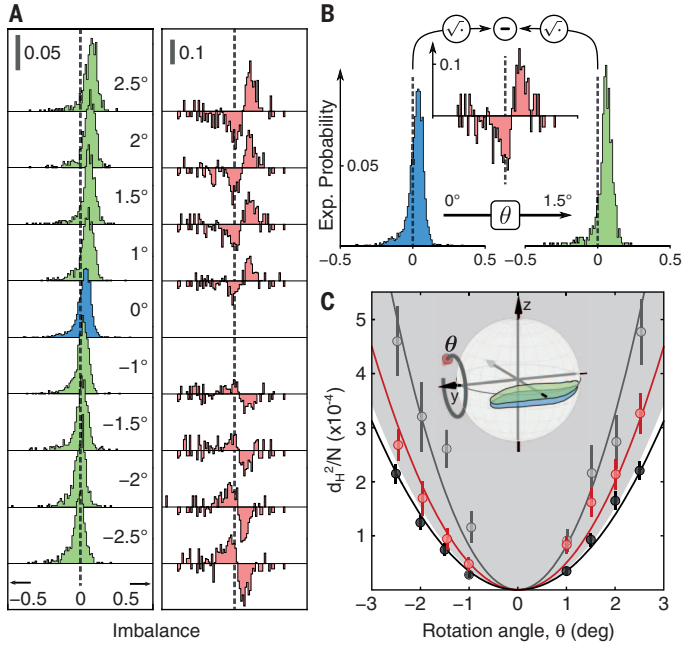


Fig. 3. Experimental extraction of the Fisher information. (**A**) Examples of experimental histograms of z (left) after 26 ms of evolution time obtained for the tomography angle $\alpha = 58°$ and additional small rotation angles θ about the y axis [see inset of (C)]. The blue histogram is used as a reference for the following analysis. The right column shows the square-root differences between the respective histogram and the reference [see (B)]. Gray bars indicate the vertical scales [see axes in (B)]. (**B**) Extraction of the squared Hellinger distance (example of $\theta = 1.5°$). Probability amplitudes $\sqrt{P_z}$ for $\theta = 1.5°$ (green) and $\theta = 0°$ (blue) are subtracted for each bin (red), and these differences are squared and summed to obtain the squared Hellinger distance. (**C**) Squared Hellinger distance for three evolution times. A reference measurement (black) with the initial coherent spin state (0 ms evolution) lies slightly outside the nonclassical region (gray shaded area). The spin squeezed state (gray, 15-ms evolution) surpasses the classical limit. After 26 ms [red points, histograms shown in (A)], the state has a non-Gaussian shape, is not spin squeezed, but still performs beyond the standard quantum limit. Error bars indicate the statistical 68% confidence interval obtained by a resampling procedure (*18*). The curvature of the quadratic fit is proportional to F/N.

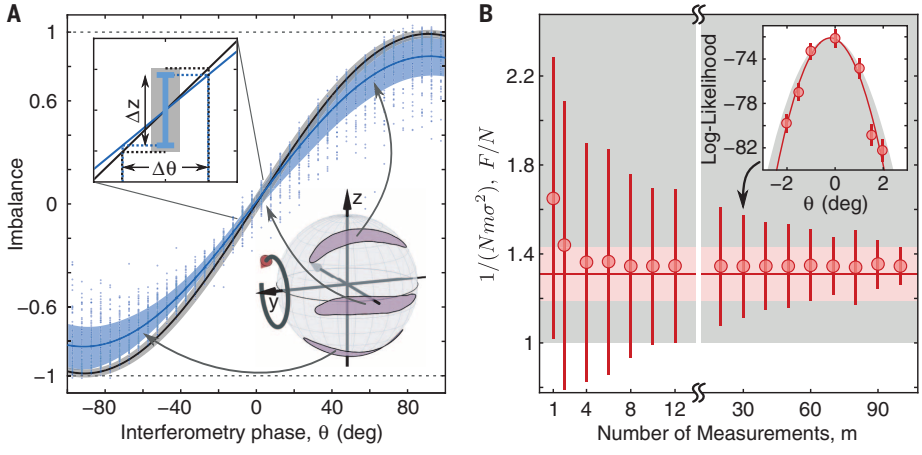


Fig. 4. Quantum enhanced phase sensitivity in the absence of spin squeezing. (**A**) A rotation on the Bloch sphere by the angle θ (right inset) is formally equivalent to the action of a Ramsey interferometer with relative phase shift θ (fig. S5). Interference fringe of z (blue line with 68% confidence interval) with the state after 25-ms evolution and subsequent tomography rotation of 61°; reference measurement with a coherent spin state (black line with gray confidence region). The phase sensitivity Δθ deduced from standard error propagation via the slope of the interferometer fringe (left inset) does not surpass the standard quantum limit. (**B**) Bayesian analysis with the tomography angle for maximal Fisher information (58°). For each sequence of length m, a quadratic fit to log $\mathcal{L}$ is used to extract the Gaussian variance σ^2 of $\mathcal{L}$ (inset), which corresponds to the phase sensitivity. The value of $1/(Nm\sigma^2)$ as a function of m shows fast convergence to the extracted F/N obtained with the Hellinger distance method (red line with 68% confidence region). The error bars indicate the standard deviation of a single sequence. Gray shaded regions are only accessible with entanglement in the system.

the quantum resource for improved phase estimation. The presented method does not depend on the special shape of the probability distributions and is not limited to small particle numbers. It is therefore broadly applicable to the efficient characterization of highly entangled states, relevant for further improvement of atom interferometers (*8*, *11*, *12*, *19*, *20*, *28*–*30*) toward the ultimate Heisenberg limit (*22*). More generally, it can be applied to any phenomenon characterizable by the distinguishability of quantum states, as in quantum phase transitions (*31*), quantum Zeno dynamics (*32*), and quantum information protocols (*1*).

REFERENCES AND NOTES

1. M. A. Nielsen, I. L. Chuang, *Quantum Computation and Quantum Information* (Cambridge Univ. Press, Cambridge, 2000).
2. R. Blatt, D. Wineland, *Nature* **453**, 1008–1015 (2008).
3. J.-W. Pan *et al.*, *Rev. Mod. Phys.* **84**, 777–838 (2012).
4. B. Vlastakis *et al.*, *Science* **342**, 607–610 (2013).
5. A. Sørensen, L.-M. Duan, J. I. Cirac, P. Zoller, *Nature* **409**, 63–66 (2001).
6. D. J. Wineland, J. J. Bollinger, W. M. Itano, D. J. Heinzen, *Phys. Rev. A* **50**, 67–88 (1994).
7. J. Estève, C. Gross, A. Weller, S. Giovanazzi, M. K. Oberthaler, *Nature* **455**, 1216–1219 (2008).
8. C. Gross, T. Zibold, E. Nicklas, J. Estève, M. K. Oberthaler, *Nature* **464**, 1165–1169 (2010).
9. M. F. Riedel *et al.*, *Nature* **464**, 1170–1173 (2010).
10. C. D. Hamley, C. S. Gerving, T. M. Hoang, E. M. Bookjans, M. S. Chapman, *Nat. Phys.* **8**, 305–308 (2012).
11. T. Berrada *et al.*, *Nat. Commun.* **4**, 2077 (2013).
12. B. Lücke *et al.*, *Science* **334**, 773–776 (2011).
13. L. Pezzé, A. Smerzi, *Phys. Rev. Lett.* **102**, 100401 (2009).
14. A. Micheli, D. Jaksch, J. I. Cirac, P. Zoller, *Phys. Rev. A* **67**, 013607 (2003).
15. J. I. Cirac, M. Lewenstein, K. Mølmer, P. Zoller, *Phys. Rev. A* **57**, 1208–1218 (1998).
16. R. A. Fisher, *Proc. Camb. Philos. Soc.* **22**, 700–725 (1925).
17. C. W. Helstrom, *Quantum Detection and Estimation Theory* (Academic Press, New York, 1976).
18. Materials and methods are available as supplementary materials on *Science* Online.
19. R. J. Sewell *et al.*, *Phys. Rev. Lett.* **109**, 253605 (2012).
20. C. F. Ockeloen, R. Schmied, M. F. Riedel, P. Treutlein, *Phys. Rev. Lett.* **111**, 143001 (2013).
21. R. Schnabel, N. Mavalvala, D. E. McClelland, P. K. Lam, *Nat. Commun.* **1**, 121 (2010).
22. V. Giovannetti, S. Lloyd, L. Maccone, *Phys. Rev. Lett.* **96**, 010401 (2006).
23. R. Krischek *et al.*, *Phys. Rev. Lett.* **107**, 080504 (2011).
24. T. Zibold, E. Nicklas, C. Gross, M. K. Oberthaler, *Phys. Rev. Lett.* **105**, 204101 (2010).
25. W. Muessel *et al.*, *Appl. Phys. B* **113**, 69–73 (2013).
26. W. K. Wootters, *Phys. Rev. D* **23**, 357–362 (1981).
27. S. L. Braunstein, C. M. Caves, *Phys. Rev. Lett.* **72**, 3439–3443 (1994).
28. J. Appel *et al.*, *Proc. Natl. Acad. Sci. U.S.A.* **106**, 10960–10965 (2009).
29. I. D. Leroux, M. H. Schleier-Smith, V. Vuletić, *Phys. Rev. Lett.* **104**, 250801 (2010).
30. Z. Chen, J. G. Bohnet, S. R. Sankar, J. Dai, J. K. Thompson, *Phys. Rev. Lett.* **106**, 133601 (2011).
31. P. Zanardi, M. G. A. Paris, L. Campos Venuti, *Phys. Rev. A* **78**, 042105 (2008).
32. A. Smerzi, *Phys. Rev. Lett.* **109**, 150410 (2012).

ACKNOWLEDGMENTS

We thank J. Tomkovič, E. Nicklas, and I. Stroescu for technical help and discussions. This work was supported by the Forschergruppe FOR760, the Deutsche Forschungsgemeinschaft, the Heidelberg Center for Quantum Dynamics, and the European Commission small or medium-scale focused research project QIBEC (Quantum Interferometry with Bose-Einstein condensates, contract no. 284584). W.M. acknowledges support by the Studienstiftung des deutschen Volkes. D.B.H. acknowledges support from the Alexander von Humboldt Foundation. L.P. acknowledges financial support by Ministero dell'Istruzione, dell'Università e della Ricerca through Fondo per gli Investimenti della Ricerca di Base project no. RBFR08H058. QSTAR is the Max Planck Institute of Quantum Optics, LENS, Istituto Italiano di Tecnologia, Università degli Studi di Firenze Joint Center for Quantum Science and Technology in Arcetri.

SUPPLEMENTARY MATERIALS

www.sciencemag.org/content/345/6195/424/suppl/DC1
Materials and Methods
Figs. S1 to S5
References (*33*–*38*)

24 December 2013; accepted 3 June 2014
10.1126/science.1250147

METAMATERIALS

Invisibility cloaking in a diffusive light scattering medium

Robert Schittny,[1,2] Muamer Kadic,[1,3] Tiemo Bückmann,[1,2] Martin Wegener[1,2,3]*

In vacuum, air, and other surroundings that support ballistic light propagation according to Maxwell's equations, invisibility cloaks that are macroscopic, three-dimensional, broadband, passive, and that work for all directions and polarizations of light are not consistent with the laws of physics. We show that the situation is different for surroundings leading to multiple light scattering, according to Fick's diffusion equation. We have fabricated cylindrical and spherical invisibility cloaks made of thin shells of polydimethylsiloxane doped with melamine-resin microparticles. The shells surround a diffusively reflecting hollow core, in which arbitrary objects can be hidden. We find good cloaking performance in a water-based diffusive surrounding throughout the entire visible spectrum and for all illumination conditions and incident polarizations of light.

With an invisibility cloak (*1*–*5*), light is guided in a detour around an object to be hidden so that it emerges behind as though no object was there. Ideally, this concerns the direction, amplitude, and timing of light. In vacuum (or air) and for macroscopic objects much larger than the wavelength of light, this geometrical detour means that the local velocity of light must exceed the vacuum speed of light somewhere. For broadband operation—in the absence of wavelength dependence—the phase velocity of light equals its energy velocity. Furthermore, according to the theory of relativity, energy and mass are equivalent, and transport of mass faster than the vacuum speed of light is not possible. Thus, ideal passive broadband invisibility cloaking of macroscopic objects in vacuum (or air) is not consistent (*4*, *5*) with relativity and Maxwell's equations of electromagnetism.

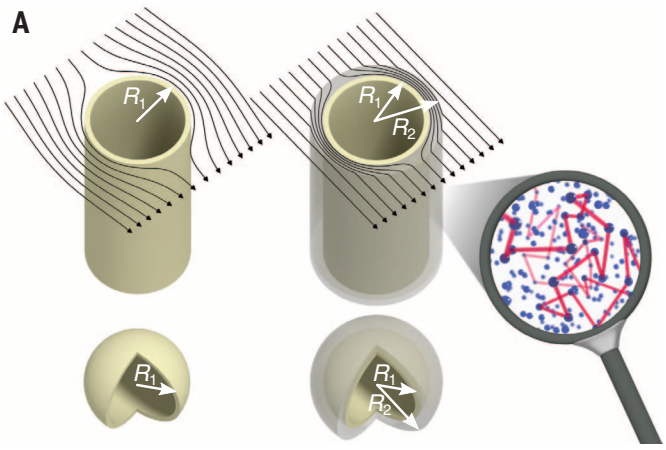
Nevertheless, inspired by transformation optics (*1*–*3*) based on Maxwell's equations, many interesting cloaking experiments have been performed (*6*–*12*). All of these cloaks, however, are either narrow in bandwidth or not macroscopic, do not properly recover the time-of-flight (or phase), work only for restricted polarizations or directions of light, or exhibit combinations of these limitations.

In many practical instances, light does not propagate ballistically—it cannot be described adequately by the macroscopic Maxwell equations for continua. For example, in clouds, fog, milk, frosted glass, or in other systems containing many randomly distributed scattering centers, every photon of visible light performs a random walk. Effectively, this random walk slows down light propagation with respect to vacuum and scrambles any incident polarization. Multiple light scattering can also lead to coherent speckles (*13*) and to Anderson localization (*14*, *15*). For a broad range of settings, however, multiple light scattering is well described by the diffusion of photons (*14*).

We demonstrate that passive broadband invisibility cloaking of macroscopic objects for all incident directions and polarizations of light is possible in the regime of light diffusion.

In 1855, Fick postulated his diffusion equation (*16*), which was then followed by a microscopic derivation on the basis of statistical mechanics (*17*). Our diffusion experiments have been inspired (*18*, *19*) by recent work on thermal cloaking: Whereas early cloaking structures designed with coordinate transformations contained many alternating layers of effectively low and high heat conductivity (*20*), more recent thermal cloaks (*21*, *22*) work for just one pair of layers with low and high heat conductivity. Such core-shell structures have also successfully been used for static magnetic cloaking (*23*). Intuitively, the combination of core and shell can be thought of as a single period of a highly anisotropic laminate metamaterial (*24*). It is known theoretically (*24*, *25*) that core-shell geometries can be perfectly undetectable in the stationary case, assuming a spatially constant gradient of the temperature (or magnetic field or photon density, for example) across the cloak. Recently, it has become clear that these cloaks also work for nonconstant gradients (*21*, *22*). Core-shell geometries allow for cloaks that are thin as compared with the size of the object they hide (*21*–*23*).

[1]Institute of Applied Physics, Karlsruhe Institute of Technology (KIT), D-76128 Karlsruhe, Germany. [2]Deutsche Forschungsgemeinschaft (DFG)–Center for Functional Nanostructures (CFN), KIT, D-76128 Karlsruhe, Germany. [3]Institute of Nanotechnology, KIT, D-76021 Karlsruhe, Germany.
***Corresponding author. E-mail: martin.wegener@kit.edu**



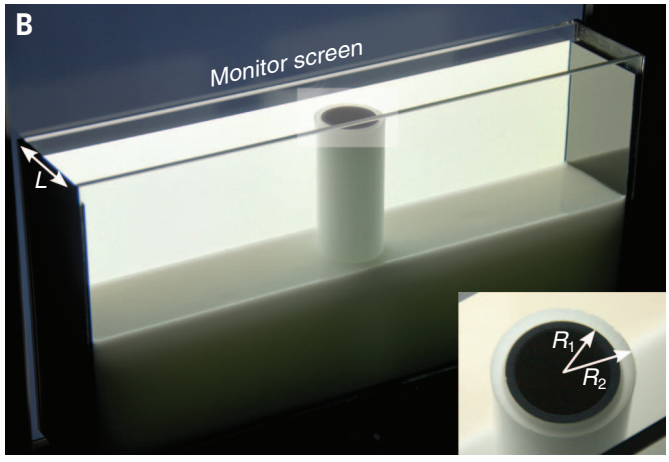


Fig. 1. Cloaking principle and experimental setup. (**A**) Illustration of the cylindrical and spherical core-shell invisibility cloaks for diffusive light. The outer radii for core R_1 and shell R_2 are indicated. The corresponding light diffusivities are D_1 and D_2, and that of the surrounding is D_0. The streamlines visualize the photon-current-density vector field $\vec{j}$ (the analog of the Poynting vector for ballistic light transport) as calculated from Fick's diffusion equation for homogeneous illumination for obstacle (left) and cloak (right). Parameters are $R_2/R_1 = 1.24$, $D_1 = 0$, and $D_2/D_0 = 4.72$. The magnifying glass exhibits an artistic microscopic view of light transport in diffusive media containing many randomly distributed scatterers. (**B**) Photograph of the experimental setup. The diameters of the cylinders used in Fig. 2 (spheres in Fig. 3) are $2R_1 = 32.1$ mm and $2R_2 = 39.8$ mm ($2R_1 = 33.2$ mm and $2R_2 = 39.9$ mm), and the tank thickness is $L = 60$ mm.

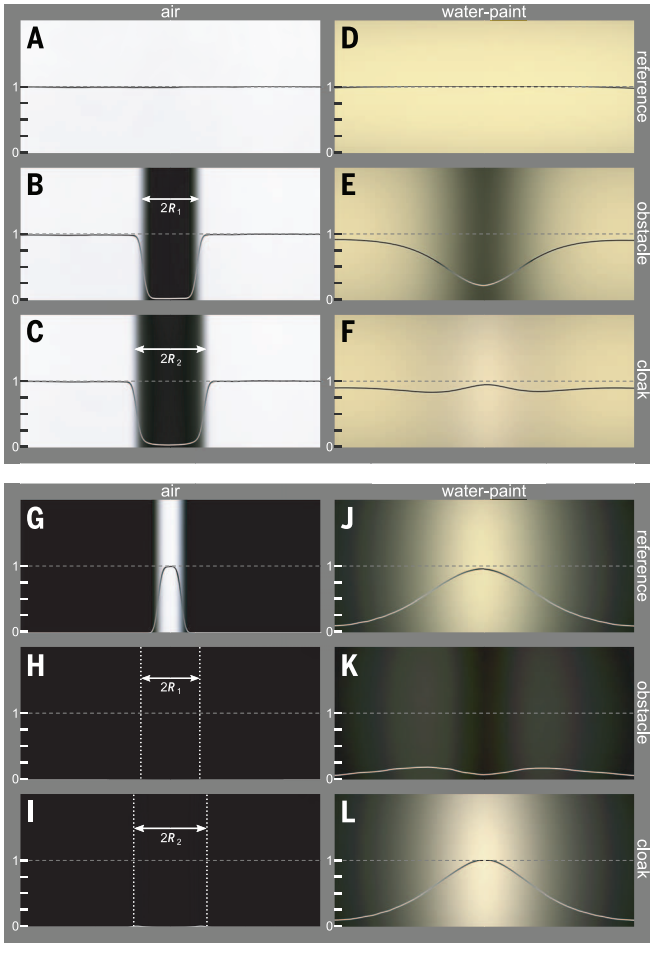


Fig. 2. Measurement results for cylindrical geometry. (**A** to **F**) True-color photographs of light emerging from the setup (Fig. 1B) for homogeneous illumination with white light. The first row is the plain surrounding ("reference"); in the second row, the cylindrical core ("obstacle") is added; and in the third row, the cylindrical core-shell structure ("cloak") is added. In (A) to (C), the surrounding is the empty tank ("air"). In (D) to (F), the tank is filled with de-ionized water and 0.35% white paint ("water-paint"). Obstacle and cloak are centered in the tank, with their cylinder axes oriented along the vertical direction. The curves superimposed onto the photographs are horizontal cuts of the normalized intensity along the gray dashed line. All images and cuts within one column are shown on the identical intensity scale. Obstacle and cloak cast a pronounced shadow in air. In the water-paint surrounding, the obstacle still casts a pronounced diffusive shadow (center is four times darker), whereas the intensity variation around a mean is less than ±10% for the cloak. (**G** to **L**) As (A) to (F), but for line-like illumination (G).

The blueprint for our light-diffusion invisibility cloaks (Fig. 1A) contains either a cylindrical or a spherical core with zero light diffusivity $D_1 = 0$ and radius R_1, which effectively suppresses the flow of photons within. Thus, we can carve out the core's interior, opening up a space for objects to be hidden within. When illuminated from one side, the bare zero-diffusivity core reduces the photon current on the downstream side; this obstacle casts a diffusive shadow. To compensate for this reduced photon current, the core is surrounded by a layer with diffusivity D_2 and radius $R_2 > R_1$. Given the photon diffusivity of the homogeneous surrounding D_0, a mathematical connection of D_2 and R_2 and the other parameters can be obtained (*24*, *26*). For example, for the cylindrical geometry in our experiments with $R_2/R_1 = 1.24$, we calculate a moderate, hence feasible, diffusivity contrast of $D_2/D_0 = 4.72$—and for the spherical geometry in our experiments with $R_2/R_1 = 1.20$, we calculate a similar diffusivity contrast of $D_2/D_0 = 3.06$—for negligible losses (*26*). This core-shell structure is the cloak. The cloak also restores the photon flux in the backward and sideward directions (Fig. 1A).

In the experimental setup (Fig. 1B), the three light diffusivities are realized in rather different ways. For the core, we used a hollow stainless-steel cylinder (or sphere) that is coated with a thin layer of acrylic white paint (*26*), which serves as a diffusive reflector. The metal guarantees that no light can enter the inside of the cloak. The shell is composed of polydimethylsiloxane (PDMS), doped with dielectric 10-μm-diameter melamine-resin particles at a concentration of 1 mg/ml (*26*). For the surrounding diffusive medium within which the cloak is placed, we used a cuboid tank with an inner volume 35.5 by 16 by 6 cm filled with de-ionized water to which white wall dispersion paint (*26*) is added (in Fig. 1B, the tank is only partially filled for illustration). This allows for the

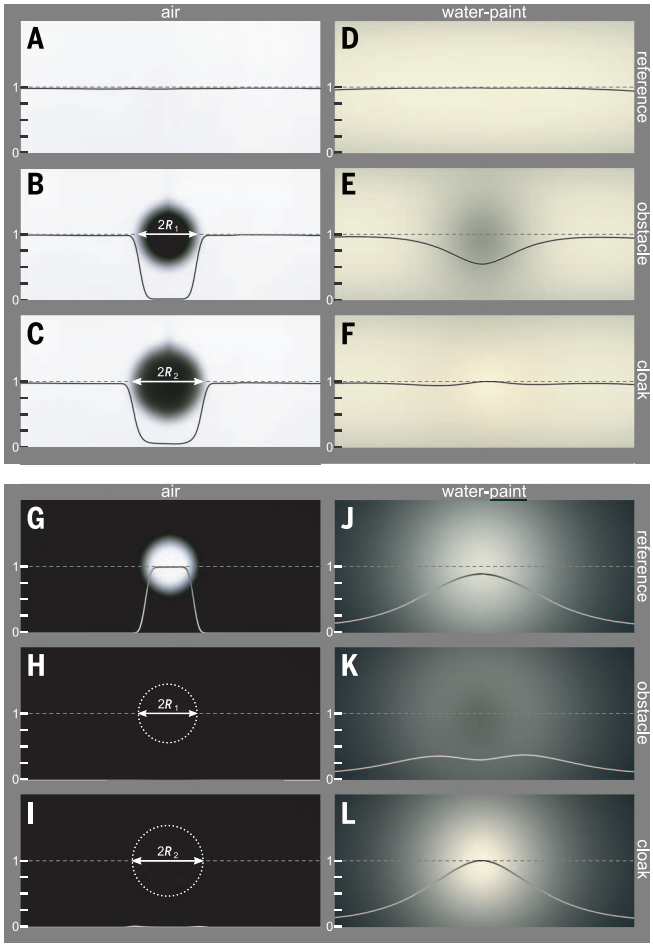


Fig. 3. Measurement results for spherical geometry. (**A** to **L**) Results are as Fig. 2, A to L, respectively, but for a spherical rather than a cylindrical cloak. Obstacle and cloak are again centered in the tank. Here, the concentration of white paint in de-ionized water is 0.175%.

experimental conditions in our model experiments to be varied readily. We adjusted the paint concentration and thus the diffusivity empirically so as to obtain good cloaking behavior. We chose this approach because a reliable quantitative a priori calculation of the effective photon diffusivities would be demanding. This approach also automatically compensates for the effect of losses (*26*). One side of the tank is illuminated by a liquid-crystal display (LCD) flat screen computer monitor, which is in direct contact with one of the Plexiglas walls. The monitor allows us to conveniently vary the spatial pattern of illumination. We took optical images of the other side of the tank using a digital camera located at a distance of ~0.5 m, with its optical axis normal to the LCD screen.

For all cases, we show results for white-light illumination using either air or the water-paint mixture, respectively, as surroundings in the tank (Fig. 2). Homogeneous illumination of the empty tank, the reference, is shown in Fig. 2A; a shadow for the obstacle is shown in Fig. 2B; and an even more pronounced shadow for the cloak is shown in Fig. 2C. The cloak has not been designed for air as its surroundings. Both obstacle and cloak are centered with respect to the tank. The same sequence is shown in Fig. 2, D to F, but for the water-paint surrounding. Light emerging from the reference (Fig. 2D) has been subject to diffusive light scattering. As to be expected, we again found a nearly homogeneous light distribution. The yellowish color indicates that blue light is partially absorbed in the water-paint mixture (*26*). For the obstacle (Fig. 2E), a pronounced diffusive shadow was observed. For the cloak (Fig. 2F), this shadow disappears, leaving behind only a small relative modulation of the light intensity within the image. These small imperfections [(*23*) for comparison] can be traced back to residual absorption losses (*26*). The absence of major color distortions beyond the overall yellowish appearance (which occurs for the reference already) indicates that cloaking works well for the red, green, and blue components of visible light.

An invisibility cloak should also work for any other possible illumination condition. An extreme example is a pointlike or a line-like illumination (Fig. 2G). Diffusive-light invisibility cloaking remains very good even under these extremely nonhomogeneous illumination conditions (Fig. 2, J to L).

Figure 3 exhibits the same as Fig. 2, but for a spherical instead of a cylindrical geometry. By symmetry of this cloak, it is clear that the cloak is omnidirectional. It is $2R_2/\lambda \approx$ five orders of magnitude larger than the operation wavelength λ and works throughout the entire visible spectrum, qualifying as a broadband cloak. This is the evidence for our above claim of having achieved an omnidirectional passive broadband macroscopic invisibility cloak in the diffusive regime—attributes that are fundamentally impossible in the ballistic regime.

All experimental results (Figs. 2 and 3) agree well with calculations (*26*) based on diffusion theory (figs. S3 and S4). On this basis, we estimate (*26*) that the used stationary limit of Fick's diffusion equation remains applicable down to time scales of 100 ns, which is equivalent to 10^7 image frames per second.

Last, as an application of diffusive-light invisibility cloaking, we suggest that one could insert metal bars, which are almost as thick as the glass, into a bathroom frosted-glass window to prevent burglary. Usually, these bars would immediately be visible via the diffusive shadow they cast. By adding thin diffusive cloaking shells around the metal bars, the window would again appear as a homogeneously bright milky glass.

REFERENCES AND NOTES

1. J. B. Pendry, D. Schurig, D. R. Smith, *Science* **312**, 1780–1782 (2006).
2. U. Leonhardt, *Science* **312**, 1777–1780 (2006).
3. V. M. Shalaev, *Science* **322**, 384–386 (2008).
4. D. A. B. Miller, *Opt. Express* **14**, 12457–12466 (2006).
5. H. Hashemi, B. Zhang, J. D. Joannopoulos, S. G. Johnson, *Phys. Rev. Lett.* **104**, 253903 (2010).
6. D. Schurig *et al*., *Science* **314**, 977–980 (2006).
7. R. Liu *et al*., *Science* **323**, 366–369 (2009).
8. J. Valentine, J. Li, T. Zentgraf, G. Bartal, X. Zhang, *Nat. Mater.* **8**, 568–571 (2009).
9. L. H. Gabrielli, J. Cardenas, C. B. Poitras, M. Lipson, *Nat. Photonics* **3**, 461–463 (2009).
10. T. Ergin, N. Stenger, P. Brenner, J. B. Pendry, M. Wegener, *Science* **328**, 337–339 (2010).
11. T. Ergin, J. Fischer, M. Wegener, *Phys. Rev. Lett.* **107**, 173901 (2011).
12. X. Chen *et al*., *Nat. Commun.* **2**, 176 (2011).
13. J. W. Goodman, *Speckle Phenomena in Optics* (Ben Roberts & Company, Greenwood Village, CO 2007).
14. C. M. Soukoulis, Ed., *Photonic Crystals and Light Localization in the 21st Century* (Springer, New York, 2001).
15. T. Schwartz, G. Bartal, S. Fishman, M. Segev, *Nature* **446**, 52–55 (2007).
16. A. Fick, *Ann. Phys.* **170**, 59–86 (1855).
17. A. Einstein, *Ann. Phys.* **322**, 549–560 (1905).
18. S. Guenneau, T. M. Puvirajesinghe, *J. R. Soc. Interface* **10**, 20130106 (2013).
19. M. Wegener, *Science* **342**, 939–940 (2013).
20. R. Schittny, M. Kadic, S. Guenneau, M. Wegener, *Phys. Rev. Lett.* **110**, 195901 (2013).
21. H. Xu, X. Shi, F. Gao, H. Sun, B. Zhang, *Phys. Rev. Lett.* **112**, 054301 (2014).
22. T. Han *et al*., *Phys. Rev. Lett.* **112**, 054302 (2014).
23. F. Gömöry *et al*., *Science* **335**, 1466–1468 (2012).
24. G. W. Milton, *The Theory of Composites* (Cambridge Univ. Press, Cambridge, UK, 2002).
25. A. Alù, N. Engheta, *Phys. Rev. E Stat. Nonlin. Soft Matter Phys.* **72**, 016623 (2005).
26. Materials and methods are available as supplementary materials on *Science* Online.

ACKNOWLEDGMENTS

We thank A. Naber (KIT) and X. He (visitor at KIT) for discussions and J. Westhauser (KIT) for technical assistance. We acknowledge support by the DFG-CFN through subproject A1.5 and by the Karlsruhe School of Optics & Photonics (KSOP). We also thank the Hector Fellow Academy for support.

SUPPLEMENTARY MATERIALS

www.sciencemag.org/content/345/6195/427/suppl/DC1
Materials and Methods
Supplementary Text
Figs. S1 to S4
Table S1

8 April 2014; accepted 27 May 2014
Published online 5 June 2014;
10.1126/science.1254524

QUANTUM SIMULATION

Coherent imaging spectroscopy of a quantum many-body spin system

C. Senko,[1]* J. Smith,[1] P. Richerme,[1] A. Lee,[1] W. C. Campbell,[2] C. Monroe[1]

Quantum simulators, in which well-controlled quantum systems are used to reproduce the dynamics of less understood ones, have the potential to explore physics inaccessible to modeling with classical computers. However, checking the results of such simulations also becomes classically intractable as system sizes increase. Here, we introduce and implement a coherent imaging spectroscopic technique, akin to magnetic resonance imaging, to validate a quantum simulation. We use this method to determine the energy levels and interaction strengths of a fully connected quantum many-body system. Additionally, we directly measure the critical energy gap near a quantum phase transition. We expect this general technique to become a verification tool for quantum simulators once experiments advance beyond proof-of-principle demonstrations and exceed the resources of conventional computers.

Certain classes of quantum many-body systems, including high-temperature superconductors and spin liquids, are believed to be fundamentally inaccessible to classical modeling (*1*). For example, interacting spin systems described by the Ising model can be mapped to NP-complete computational problems (*2*) and have been applied to understanding neural networks (*3*) and social behavior (*4*), yet quickly become theoretically intractable because of the exponential number of possible spin configurations (*5*).

Quantum simulations (*6*–*8*), in which well-controlled quantum objects like photons (*9*) or ultracold atoms (*10*, *11*) are induced to emulate other quantum systems, are a promising alternative for accessing such problems. However, as these systems approach theoretically intractable physics, validating quantum simulation results will become a major challenge (*1*, *12*). Here, we introduce a technique for performing coherent imaging spectroscopy on the Hamiltonian of an interacting many-body spin system. We use spectroscopic imaging to infer spin-spin interaction strengths and directly measure the critical energy gap near a quantum phase transition.

Ultracold atomic systems are particularly well suited for simulating interacting spin systems, with the ability to prepare known input states, engineer tunable interaction patterns, and measure individual particles (*10*, *11*). Our experiment uses trapped ions to simulate chains of spin-1/2 particles subject to effective magnetic fields and long-range, inhomogenous Ising couplings generated by optical dipole forces (*13*–*19*). This results in an effective N-spin Hamiltonian (with the Planck constant $\hbar = 1$)

$$H_{\text{eff}} = \sum_{i<j} J_{i,j}\sigma_i^x\sigma_j^x + B(t)\sum_i \sigma_i^y, \qquad (1)$$

where σ_i^γ ($\gamma = x, y, z$) is the Pauli matrix for spin i along direction γ; $J_{i,j} \sim J_0|i-j|^{-\alpha}$ is a long-range coupling strength between spins i and j with $J_0 > 0$ and α tunable between 0 and 3 (*13*); and $B(t)$ is the energy associated with a time-dependent transverse magnetic field (*20*).

The ability to generate antiferromagnetic $J_{i,j}$ couplings of varying interaction range (*13*, *17*, *18*) has recently attracted much interest in contexts such as studying the spread of correlations after a quench (*21*, *22*), observing prethermalization of a quantum system (*23*, *24*), and directly measuring response functions (*25*). Developing a general protocol to measure the spin-spin couplings will be an important validation goal. Previous experiments have fully characterized the interactions in small systems using techniques that may be difficult to scale up, such as Fourier decomposition of multispin dynamics (*14*) or manipulating each of the $\sim N^2/2$ pairs of spins separately using electromagnetic field gradients for frequency (*26*) or spatial addressing (*27*). By contrast, the protocol we introduce below allows the couplings

[1]Joint Quantum Institute, University of Maryland, Department of Physics, and National Institute of Standards and Technology, College Park, MD 20742, USA. [2]Department of Physics and Astronomy, University of California, Los Angeles, CA 90095, USA.
*Corresponding author. E-mail: csenko@umd.edu

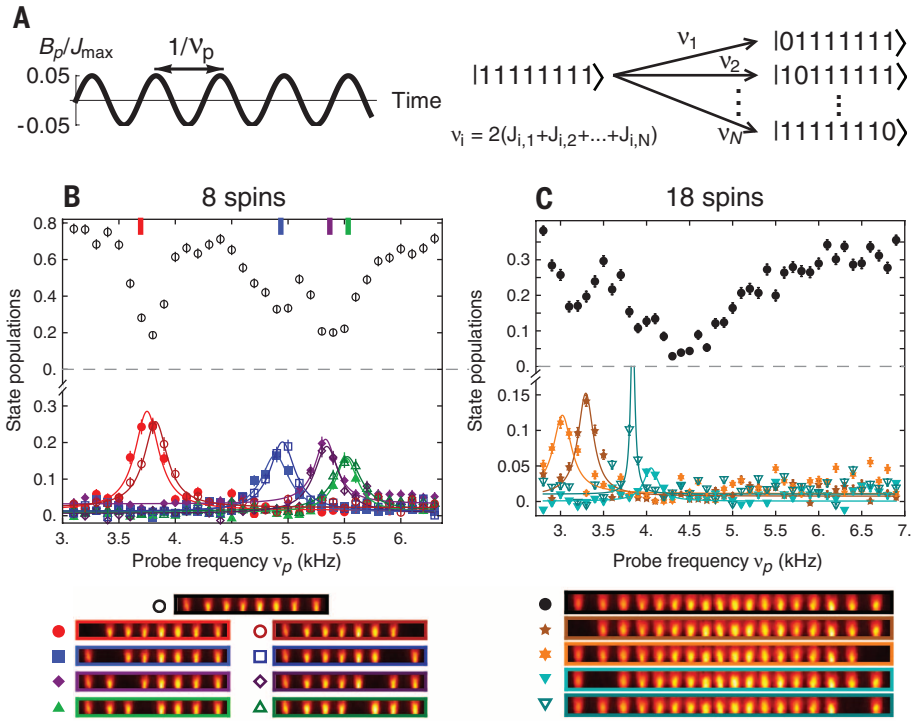


Fig. 1. Principle of coherent imaging spectroscopy. (**A**) The transverse field term B_p drives transitions between states when its modulation frequency matches an allowed energy splitting (such as between the state with all spins up along x and any single-defect state with a single spin down). (**B**) Measured populations in specific spin states (see legend, bottom, where a fluorescing (dark) ion represents $|1\rangle$ [$|0\rangle$)] versus the frequency of the probe field for a system of eight spins initialized in $|11111111\rangle$ before probing. Solid curves are Lorentzians fit to the data sets; the energy splittings predicted from Eq. 1 are indicated with colored bars at the top of the frame. Error bars represent statistical error from performing 1000 repetitions of each experiment. (**C**) Measured populations versus the frequency of the probe field for a system of 18 spins. The left-right asymmetry is attributed to slight misalignment of the laser beams. Despite the low fidelity of the initial state (35% in the $|1111111111111111\rangle$ state), these energy splittings are still clearly visible.

to be measured by taking ~N frequency spectra and requires only global interactions and site-resolved measurements.

The spin-1/2 particles are represented by a string of $^{171}Yb^{+}$ ions confined in a linear Paul trap. The spin states $|\downarrow\rangle_z$ and $|\uparrow\rangle_z$ are encoded in the magnetic-field-insensitive ($m_F = 0$) hyperfine states of the ground electronic manifold (*28*). The spin-spin couplings and effective magnetic fields derive from lasers that globally illuminate the ion chain, driving stimulated Raman transitions between the spin states (*14*, *20*). State initialization comprises optical pumping into the $|\downarrow\downarrow\downarrow\cdots\rangle_z$ state followed by a coherent rotation to polarize all spins along the desired axis. After applying the spin-spin couplings and the probe field(s) described above, the individual spin states are read out along any axis by performing a coherent rotation from that axis to the measurement basis $|\downarrow\rangle_z$ and $|\uparrow\rangle_z$, then collecting state-dependent fluorescence onto a charge-coupled device imager with site-resolving optics (*20*).

We measure the energy splittings in our spin system using a weakly modulated transverse field as a probe.

$$B(t) = B_0 + B_p \sin(2\pi\nu_p t) \qquad (2)$$

When the probe frequency ν_p is matched to the energy difference $|E_a - E_b|$ between two eigenstates $|a\rangle$ and $|b\rangle$, the field will drive transitions between the two states if there is a nonzero matrix element $\langle b|B(t)\sum_i \sigma_i^y|a\rangle \neq 0$. For example, in the weak-field regime $B(t) << J_0$, the Hamiltonian eigenstates are symmetric combinations of the σ^x eigenstates, and the matrix element $\langle b|B(t)\sum_i \sigma_i^y|a\rangle$ is nonzero only when $|a\rangle$ and $|b\rangle$ differ by the orientation of exactly one spin.

In the weak-field regime, a transition at a single frequency can easily be monitored, and its stability can provide a good proxy for the entire Hamiltonian. Each splitting depends on multiple spin-spin couplings—for example, a transition from $|1111\cdots\rangle$ to $|0111\cdots\rangle$, where $|1\rangle$ ($|0\rangle$) denotes the σ^x eigenstate $|\uparrow\rangle_x$ ($|\downarrow\rangle_x$), requires energy

$$\Delta E = 2(J_{1,2} + J_{1,3} + \cdots + J_{1,N}) \qquad (3)$$

These splittings are therefore sensitive to changes in the motional mode structure or the laser intensities at each of the ions.

We demonstrate the mapping of individual energy splittings in the weak-field regime $B(t)/J_0 << 1$ in Fig. 1. The spins are prepared along the x direction in $|111\cdots\rangle$, and a probe field corresponding to $B(t) = (100\ \text{Hz})\sin(2\pi\nu_p t)$ is applied for 3 ms, which is sufficient to transfer more than 50% of the population between states, before measuring along x. These parameters allow resolution of the energy differences in an eight-spin system while still accommodating the few ms decoherence time scale in our system (*18*).

Population transfer is clearly seen when ν_p is resonant with an energy splitting (e.g., Fig. 1, B and C). We quantify the energy of a particular state relative to the initial state by fitting Lorentzians to the spectra (*20*). The spectral positions are insensitive to state preparation and measurement error, which affects only the contrast of these resonances, as seen in Fig. 1C with $N = 18$ spins.

A sequence of multiple probe frequencies (shown in fig. S1) can be used to populate any desired spin configuration with a global beam in no more than $\lfloor N/2 \rfloor$ pulses. We can transfer population into any of the 32 eigenstates of a five-spin system by starting in either the $|11111\rangle$ or $|00000\rangle$ and applying at most two pulses of the transverse field. This system is small enough to also measure the entire relative energy spectrum, which scales exponentially with system size. Starting from the states $|11111\rangle$, $|00000\rangle$, $|10101\rangle$, and $|01010\rangle$ [the last two of which are prepared using an adiabatic ramp of a transverse field (*18*)], we use single and multiple frequency drives to measure all possible energy splittings.

Figure 2 shows the measured spectrum of this five-spin system, obtained by direct addition of the measured energy splittings, compared to that given by the interactions estimated from the same data (as detailed below). An examination of the full spectrum of a many-body quantum system is generally difficult to achieve and shows the versatility of this form of many-body spectroscopy.

We can also use modulated transverse fields to prepare arbitrary coherent quantum states, which can be used to probe many-body quantum dynamics (*24*). An example protocol for preparing a specific spin configuration is shown in fig. S1.

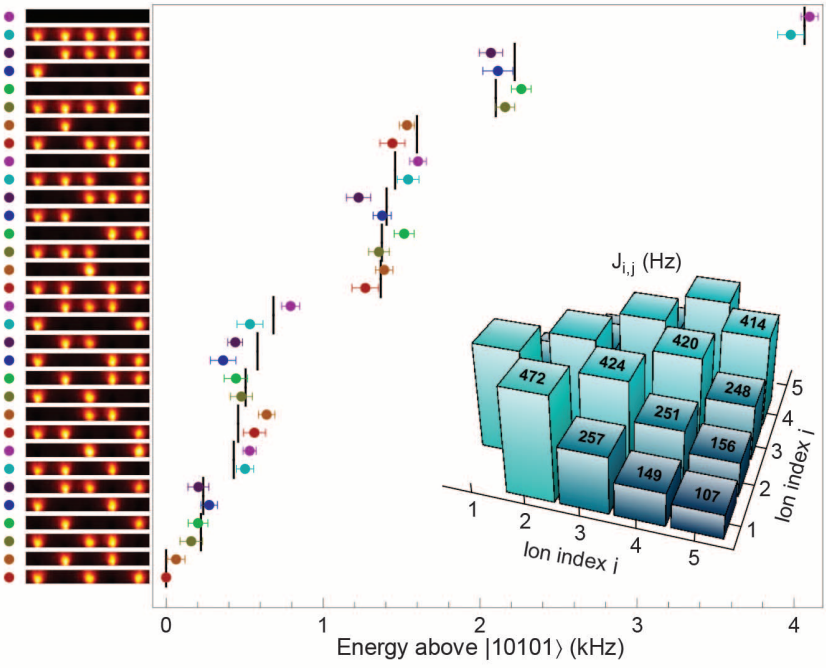


Fig. 2. Reconstructed energy spectrum. In a system of five spins, the energy of each spin configuration above the $|10101\rangle$ ground state (colored points) is compared to the calculated energies (black lines). Calculations are based on the spin-spin couplings estimated from the same energy measurements (inset). Error bars include statistical errors and an estimate of systematic error due to experimental drifts.

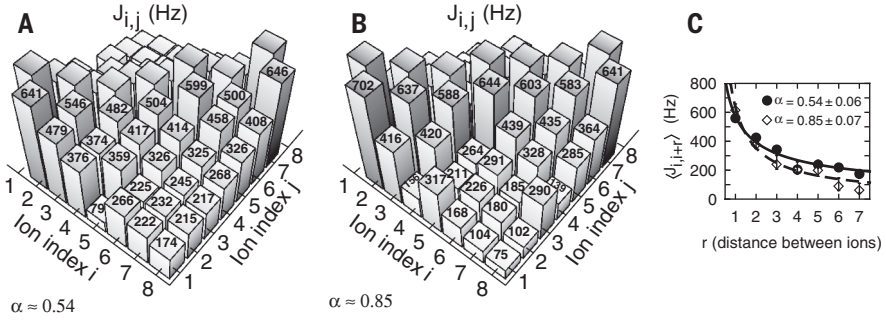


Fig. 3. Experimentally determined spin-spin coupling profiles. The couplings were measured in a system of eight spins for two sets of trap parameters, corresponding to a more long-range or more short-range interaction profile. (**A**) and (**B**) depict the individual elements of the measured coupling matrix. (**C**) plots measured average interactions against ion separation and shows fits to a power law J_0/r^{α}. The error in α is an estimate of the standard error in the fit parameter; this takes into account the errors in the $J_{i,j}$ estimates based on fit error and statistical error in population measurements (*20*).

In general, subjecting a left-right symmetric state to a global resonant probe field prepares symmetric superpositions of states that exhibit a degree of entanglement, although this is difficult to detect without individual rotations for readout.

We generate entanglement by subjecting an initial state $|111\cdots11\rangle$ to multiple frequencies simultaneously, such that all of the possible transitions are driven equally. After an appropriate time, the system will ideally be driven into a W-type state of the form

$$|\Psi_W\rangle = \frac{1}{\sqrt{N}}\left(e^{i\phi_0}|011\cdots11\rangle + e^{i\phi_1}|101\cdots11\rangle + \cdots + e^{i\phi_1}|111\cdots01\rangle + e^{i\phi_0}|111\cdots10\rangle\right) \quad (4)$$

where the phases ϕ_i depend on the relative phase of the applied modulation frequencies. Entanglement can then be detected using global measurements of the magnetization along various directions of the Bloch sphere (*29*). In particular, we use a witness operator

$$W_{ss} = (N-1)(< J_x^2 > - < J_x >^2) + \frac{N}{2} - < J_y^2 > - < J_z^2 > \quad (5)$$

where $J_\gamma \equiv \frac{1}{2}\sum_{i=1}^{N}\sigma_i^\gamma$ (with appropriate phases) and angle brackets denote ensemble averages. This spin-squeezing observable will always be positive for separable states, so measurement of a negative value certifies that at least two particles are entangled. We prepare an entangled state of four spins by applying two simultaneous frequencies of the modulated transverse field to the state $|1111\rangle$ with an appropriate relative phase for 1.8 ms and measure the resulting state along the Bloch sphere directions x, y, and z to obtain the witness shown above. This certifies that the full state is entangled. Moreover, individual spin-state imaging allows us to trace over any given spin or pair of spins and apply the witness to this reduced density matrix. Table S1 displays these data, which is consistent with entanglement in every possible reduced state.

Many-body spectroscopy using a transverse probe field further enables determination of each individual spin-spin coupling J_{ij}. Using only $N+1$ scans of the probe frequency, we can measure $\binom{N}{2} = N(N-1)/2$ energy splittings and thus determine the entire interaction matrix of $\binom{N}{2}$ couplings (e.g., Eq. 3). For example, one scan probes the state $|1111\cdots\rangle$ and yields the N energy splittings to the single-defect states. Then, as in fig. S1, N additional scans starting from each single-defect state determine $N-1$ further energy splittings. In total, these $N+1$ scans yield N^2 measurements [N from the first probe scan and $N(N-1)$ from the rest]. Because of the parallel processing enabled by imaging individual spin states, the number of measurements to evaluate all spin-spin couplings scales only linearly with the system size (*20*). We perform this verification protocol on a system of eight spins with two different interaction ranges. We can measure the full interaction matrix with five frequency scans; because of the left-right symmetry, single-defect states are populated in pairs and only four scans are necessary to probe all eight of the defect states. In contrast, mapping all 2^N energies (as done above with five spins) would already require ~100 scans for an eight-spin system. The obtained matrix agrees well with theory; roughly 70% of measured interactions match the prediction within 1σ standard error. We observe a distinction in the coupling matrices for differently chosen ranges of spin-spin interactions (Fig. 3).

Finally, we probe energy levels at nonzero transverse field B_0, including near the critical region $B_0 \approx < J >$. Determining the critical energy gap Δ, at which the energy difference between the ground and lowest coupled excited states is minimized, is useful because this parameter determines the ability to perform an adiabatic sweep of the transverse field (*19*, *30*). However, measuring the critical gap is difficult in general because of the inability to measure or even know the instantaneous eigenbasis.

The protocol described in Fig. 1 is effective even when there is a small dc field B_0 (Fig. 4, A and B) but breaks down near the critical region. However, for a finite-size ferromagnetic system, measurements along a different axis of the Bloch sphere (here, $\hat{x}+\hat{y}$) allow us to still observe transitions from the ground to the first coupled excited state near the critical gap (Fig. 4, C and D). As shown in Fig. 4E, these experiments allow us to map the lowest coupled excited state from $B_0 = 0$ beyond the critical energy gap Δ. The downward drift in energies near $B_0 = 0$ can be attributed to drifts in laser and trap parameters as the experiments progressed from higher to lower fields. An alternative protocol, which follows the time evolution after a quench, has recently been proposed for measuring the critical gap and may scale better for larger systems (*31*).

Our technique will no doubt benefit from further refinements borrowing from the extensive literature of spectroscopic methods developed in other fields, such as nuclear magnetic

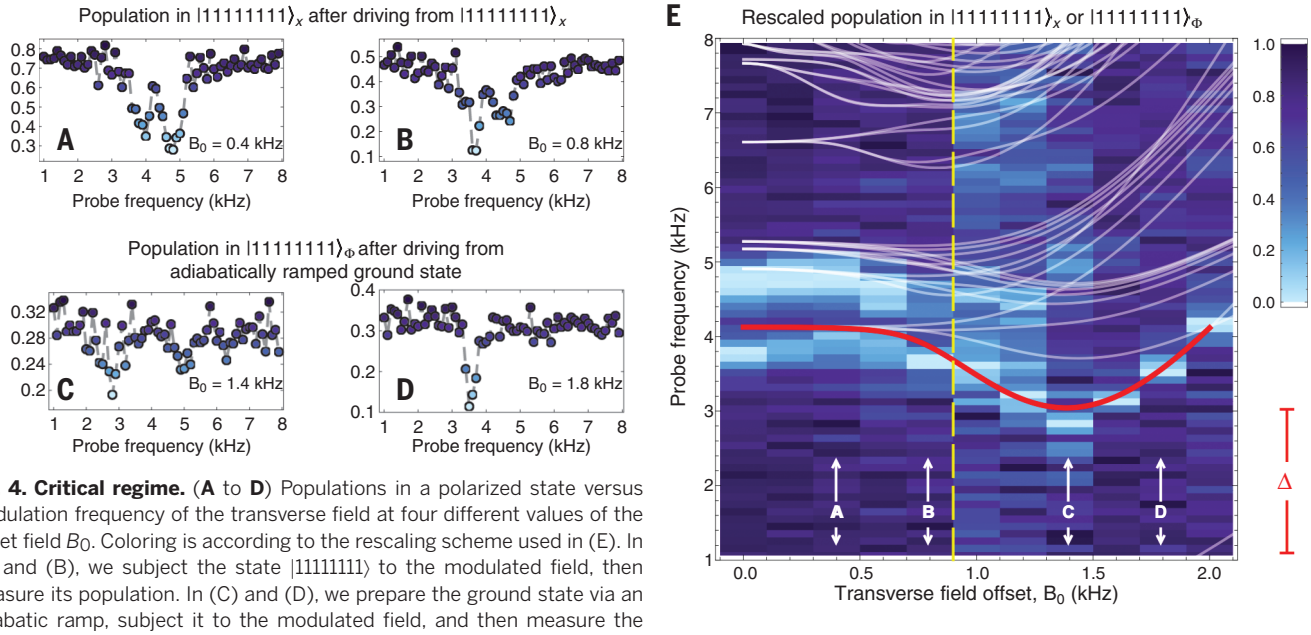


Fig. 4. Critical regime. (**A** to **D**) Populations in a polarized state versus modulation frequency of the transverse field at four different values of the offset field B_0. Coloring is according to the rescaling scheme used in (E). In (A) and (B), we subject the state $|11111111\rangle$ to the modulated field, then measure its population. In (C) and (D), we prepare the ground state via an adiabatic ramp, subject it to the modulated field, and then measure the population in $|\uparrow\uparrow\uparrow\uparrow\uparrow\uparrow\uparrow\uparrow\rangle_\phi$. (**E**) Rescaled populations in $|11111111\rangle$ (left of the dashed line) or $|\uparrow\uparrow\uparrow\uparrow\uparrow\uparrow\uparrow\uparrow\rangle_\phi$ (right of the dashed line) versus static field offset B_0 and modulation frequency. Calculated energy levels, based on measurements of trap and laser parameters, are overlaid as thin white lines, and the lowest coupled excited state as a thick red line, showing the critical gap Δ at position C. The energy of the ground state is always taken to be zero.

resonance (*32*). In addition, the protocol developed here is general and will affect experiments with ion traps and other platforms as system sizes increase, both in full calibrations of the coupling matrix and in the ability to observe a single quantity that serves as a proxy for the entire Hamiltonian.

REFERENCES AND NOTES

1. J. I. Cirac, P. Zoller, *Nat. Phys.* **8**, 264–266 (2012).
2. B. A. Cipra, *SIAM News* **33** (6), 654 (2000); www.siam.org/pdf/news/654.pdf.
3. E. Schneidman, M. J. Berry 2nd, R. Segev, W. Bialek, *Nature* **440**, 1007–1012 (2006).
4. S. Liu, L. Ying, S. Shakkottai, in *48th Annual Allerton Conference on Communication, Control, and Computing* (IEEE, New York, 2010), pp. 570–576.
5. H. T. Diep, Ed., *Frustrated Spin Systems* (World Scientific, Singapore, 2005).
6. R. Feynman, *Int. J. Theor. Phys.* **21**, 467–488 (1982).
7. S. Lloyd, *Science* **273**, 1073–1078 (1996).
8. *Nature Physics*, Insight Issue: "Quantum Simulation" **8**, 264 (2012).
9. A. Aspuru-Guzik, P. Walther, *Nat. Phys.* **8**, 285–291 (2012).
10. R. Blatt, C. F. Roos, *Nat. Phys.* **8**, 277–284 (2012).
11. I. Bloch, J. Dalibard, S. Nascimbene, *Nat. Phys.* **8**, 267–276 (2012).
12. P. Hauke, F. M. Cucchietti, L. Tagliacozzo, I. Deutsch, M. Lewenstein, *Rep. Prog. Phys.* **75**, 082401 (2012).
13. D. Porras, J. I. Cirac, *Phys. Rev. Lett.* **92**, 207901 (2004).
14. K. Kim *et al.*, *Phys. Rev. Lett.* **103**, 120502 (2009).
15. K. Kim *et al.*, *Nature* **465**, 590–593 (2010).
16. R. Islam *et al.*, *Nat. Commun.* **2**, 377 (2011).
17. J. W. Britton *et al.*, *Nature* **484**, 489–492 (2012).
18. R. Islam *et al.*, *Science* **340**, 583–587 (2013).
19. P. Richerme *et al.*, *Phys. Rev. A* **88**, 012334 (2013).
20. Materials and methods are available as supplementary material on *Science* Online.
21. J. Schachenmayer, B. P. Lanyon, C. F. Roos, A. J. Daley, *Phys. Rev. X* **3**, 031015 (2013).
22. P. Hauke, L. Tagliacozzo, *Phys. Rev. Lett.* **111**, 207202 (2013).
23. M. van den Worm, B. C. Sawyer, J. J. Bollinger, M. Kastner, *New J. Phys.* **15**, 083007 (2013).
24. Z.-X. Gong, L.-M. Duan, *New J. Phys.* **15**, 113051 (2013).
25. M. Knap *et al.*, *Phys. Rev. Lett.* **111**, 147205 (2013).
26. A. Khromova *et al.*, *Phys. Rev. Lett.* **108**, 220502 (2012).
27. P. Jurcevic *et al.*, *Nature* **511**, 202–205 (2014).
28. S. Olmschenk *et al.*, *Phys. Rev. A* **76**, 052314 (2007).
29. G. Tóth, C. Knapp, O. Gühne, H. J. Briegel, *Phys. Rev. Lett.* **99**, 250405 (2007).
30. E. E. Edwards *et al.*, *Phys. Rev. B* **82**, 060412 (2010).
31. B. Yoshimura, W. C. Campbell, J. K. Freericks, http://arxiv.org/abs/1402.7357 (2014).
32. R. R. Ernst, G. Bodehausen, A. Wokaun, *Principles of Nuclear Magnetic Resonance in One and Two Dimensions* (Clarendon Press, Oxford, 1987).

ACKNOWLEDGMENTS

We thank J. Freericks, B. Yoshimura, E. Edwards, S. Will, Z.-X. Gong, M. Foss-Feig, and A. Gorshkov for helpful discussions. This work is supported by the U.S. Army Research Office (ARO) award no. W911NF0710576 with funds from the *Defense Advanced Research Projects Agency* Optical Lattice Emulator Program, ARO award no. W911NF0410234 with funds from the Intelligence Advanced Research Projects Activity *Multi-Qubit Coherent Operations* Program, and the NSF Physics Frontier Center at the Joint Quantum Institute.

SUPPLEMENTARY MATERIALS

www.sciencemag.org/content/345/6195/430/suppl/DC1
Materials and Methods
Fig. S1
Table S1
References (*33*–*35*)

28 January 2014; accepted 3 June 2014
10.1126/science.1251422

DUAL CATALYSIS

Single-electron transmetalation in organoboron cross-coupling by photoredox/nickel dual catalysis

John C. Tellis,* David N. Primer,* Gary A. Molander†

The routine application of C_{sp3}-hybridized nucleophiles in cross-coupling reactions remains an unsolved challenge in organic chemistry. The sluggish transmetalation rates observed for the preferred organoboron reagents in such transformations are a consequence of the two-electron mechanism underlying the standard catalytic approach. We describe a mechanistically distinct single-electron transfer-based strategy for the activation of organoboron reagents toward transmetalation that exhibits complementary reactivity patterns. Application of an iridium photoredox catalyst in tandem with a nickel catalyst effects the cross-coupling of potassium alkoxyalkyl- and benzyltrifluoroborates with an array of aryl bromides under exceptionally mild conditions (visible light, ambient temperature, no strong base). The transformation has been extended to the asymmetric and stereoconvergent cross-coupling of a secondary benzyltrifluoroborate.

The immense impact of transition metal–catalyzed cross-coupling has been well recognized, with the Suzuki-Miyaura reaction in particular emerging as a preferred method for the construction of C-C bonds in both industrial and academic settings (*1*). Traditionally, cross-coupling reactions employ a three-step catalytic cycle (Fig. 1): (i) oxidative addition of an organic halide at Pd^0, (ii) transmetalation of an organometallic nucleophile to an organopalladium(II) electrophile, and (iii) reductive elimination from a diorganopalladium(II) species, releasing the coupled product and regenerating the Pd^0 catalyst (*1*, *2*). Although these methods are highly effective for C_{sp2}-C_{sp2} coupling, extension to C_{sp3} centers has proven challenging because of lower rates of oxidative addition and transmetalation, as well as the propensity of the alkylmetallic intermediates to undergo facile β-hydride elimination (*2*). Recent advances in ligand technology and the use of alternative metals, such as nickel, have greatly expanded the scope of the electrophilic component, extending even to sterically hindered and unactivated alkyl substrates, and have largely succeeded in retarding problematic β-hydride elimination (*3*). Despite the progress achieved in advancement of the other fundamental steps, transmetalation has remained largely unchanged since the inception of cross-coupling chemistry. As such, cross-couplings conducted under the traditional mechanistic manifold typically result in transmetalations that are rate-limiting (*4*).

To date, strategies aimed at accelerating the rate of transmetalation of C_{sp3}-hybridized boronic acid reagents have been largely rudimentary. In most cases, excess base and high temperature are used, thereby limiting functional group tolerance and augmenting deleterious side reactions (*5*). Stoichiometric Ag and Cu salts have been shown to improve transmetalation efficiency in some systems (*6*–*8*), although the mechanism by which the acceleration is achieved is unclear (*9*), thus limiting their widespread application. Often, the only viable alternative to overcome a slow transmetalation is to abandon the readily available boronic acids and make use of more reactive organometallic reagents. Thus, alkylboranes, alkylzincs, or the corresponding Grignard reagents—all of which lack functional group tolerance and are unstable to air—are often used for alkyl cross-coupling (*1*).

The challenge of alkylboron transmetalation was recognized to arise directly from mechanistic limitations inherent in the two-electron nature of the conventional process, wherein reactivity is inversely proportional to heterolytic C-B bond strength, thus predisposing C_{sp3} nucleophiles for failure in cross-coupling reactions (*10*, *11*). Rather than attempting to override the inherent biases of the conventional transmetalation pathway, we anticipated that development of an activation mode based on single-electron transfer (SET) chemistry would constitute a more efficient strategy for engaging this class of reagents (Fig. 1). Trends in homolytic C-B bond strength (*12*) dictate that such a reaction manifold would exhibit reactivity trends complementary to that of a traditional cross-coupling, with C_{sp3}-hybridized nucleophiles now ideally primed for successful implementation.

The first challenge associated with the realization of this ideal is the oxidative profile of radical capture at a transition metal center ($R\bullet + M^n \rightarrow R\text{-}M^{n+1}$), which necessitates a subsequent reduction to maintain the redox neutrality of a traditional transmetalation. Here, application of visible-light photoredox catalysis (*13*, *14*), was envisioned to satisfy the requirements of this unique series of SETs. Encouragement in this

Roy and Diana Vagelos Laboratories, Department of Chemistry, University of Pennsylvania, Philadelphia, PA 19104, USA.
*These authors contributed equally to this work. **†Corresponding author. E-mail: gmolandr@sas.upenn.edu**

regard was found in the work of Sanford and Glorius, who had demonstrated that cooperative catalysis between transition metals and photoredox catalysts is indeed possible (*15*–*17*). Potassium organotrifluoroborates were identified as promising partners in this new class of cross-couplings, as previous reports have documented their ability to function as carbon radical sources upon single-electron oxidation (*18*, *19*). Furthermore, Akita and co-workers have used $Ir[dFCF_3ppy]_2(bpy)PF_6$ ($dFCF_3ppy$ = 2-(2,4-difluorophenyl)-5-(trifluoromethyl)pyridine; bpy = bipyridine) as a catalyst for the oxidation of activated potassium organotrifluoroborates, demonstrating the feasibility of their implementation in the proposed single-electron transmetalation manifold (*20*, *21*).

Studies were initiated with nickel as a result of its high reactivity toward organic halides and its favorable single-electron redox potentials. We anticipated that the combination of a monomeric Ni(0) catalyst **1** and an aryl halide **2** would result in rapid oxidative addition, generating Ni(II) species **3**. Concomitantly, visible-light irradiation of $Ir[dFCF_3ppy]_2(bpy)PF_6$ **4** would generate the excited-state complex **5**, the reduction potential of which is sufficiently high [electrochemical potential of reduction E_{red} = +1.21 V (*22*, *23*)] to induce single-electron oxidation of an activated alkyltrifluoroborate **6** [electrochemical potential of oxidation E_{ox} = –1.10 V (*20*)], affording the desired alkyl radical **7** upon fragmentation. Subsequent capture of the alkyl radical at Ni(II) would then yield high-valent Ni(III) intermediate **9**, which was expected to undergo reductive elimination to generate the desired cross-coupled product **10** and Ni(I) complex **11**. From here, reduction of **11** [E_{red} > –1.10 V (*24*, *25*)] by the reduced form of the photocatalyst **8** [E_{ox} = +1.37 V (*21*)] would regenerate both the Ni(0) catalyst **1** and the Ir catalyst **4**, closing the dual catalytic cycle.

As a proof of concept, this dual catalytic single-electron transmetalation approach was applied to the cross-coupling of benzylic trifluoroborates and aryl bromides (Fig. 2). Our efforts were quickly rewarded, as a catalytic system consisting of photocatalyst **4**, $Ni(COD)_2$ (COD = 1,5-cyclooctadiene), 4,4-di-*tert*-butyl-2,2′-bipyridine (dtbbpy) as ligand, and 2,6-lutidine as an additive effected the cross-coupling of potassium benzyltrifluoroborate and bromobenzonitrile in 89% yield upon exposure to visible light from a 26-W compact fluorescent light bulb at room temperature for 24 hours. Control reactions performed in the absence of photocatalyst, Ni catalyst, or light resulted in no detectable product formation, confirming the essential role of each of these components in the dual catalytic process (*26*).

We next analyzed the scope of the reaction with regard to both the benzylic trifluoroborate and aryl halide. As expected, electronic modification of the trifluoroborate component had a moderate effect on reaction yield, with more electron-rich, and thus more highly stabilized, radical precursors (**16** and **18**) performing better than those substituted with electron-withdrawing groups (**15** and **17**). Substrates possessing an ortho substituent were well tolerated, as evidenced by isolation of product **13** in 82% yield. The reaction also exhibited increased efficiency on a larger scale, as diarylmethane **12** was isolated in 97% yield on a 5.5-mmol scale with reduced catalyst loading [1 mol % **4** and 1.5 mol % of Ni $(COD)_2$ and ligand].

High levels of versatility and functional group tolerance were observed with regard to the aryl halide partner. Substrates bearing electrophilic functional groups that would be incompatible with more highly reactive organometallic nucleophiles were well tolerated. Protic functional groups, including amide **27**, sulfonamide **39**, phenol **26**, pyrazole **32**, and -NHBoc **28**, could also be used. Substrates possessing substituents ortho to the halide (**25**, **37**) were tolerated, albeit in diminished yield. The absence of a strong base permitted the coupling of amino acid derivative **28** with no observable epimerization, demonstrating the potential utility of this method for late-stage functionalization of peptides or for use with molecules containing other base-sensitive functional groups.

A variety of nitrogen-containing heteroaryl bromides—classically challenging yet highly valued substrates because of their prevalence in biologically active compounds (*27*)—performed well under the optimized reaction conditions. Pyridine substrates were coupled in all possible regioisomeric configurations (**29**, **30**, **31**, **33**). Other important *N*-heterocycles, including pyrimidine **34**, indole **35**, and quinoline **37**, proved to be competent partners. Although five-membered heterocyclic bromides generally exhibited poor reactivity, electron-deficient thienyl bromides were coupled in moderate yields, leading to **38** and **39**.

Several practical and more sustainable features derive from this approach to cross-coupling. Previous approaches to the cross-coupling of benzylboron compounds with aryl halides have required excess (3 equiv) aqueous base and temperatures no lower than 60°C (*28*–*30*). Furthermore, the present reaction makes use of air-stable and inexpensive bipyridine ligands with low loading of the Ni catalyst. A derivative of photocatalyst **4** has recently been made commercially available and is similarly effective in promoting the desired reactivity.

The reported cross-coupling reactions generally exhibited levels of efficiency and functional group tolerance equal to or surpassing those of traditional cross-coupling reactions on similar substrates. Most reactions cleanly afforded the desired product, with the remaining mass balance consisting of only unreacted aryl halide. Competing homocoupling of the trifluoroborate to afford bibenzyl derivatives was undetectable by crude high-performance liquid chromatography analysis, allowing use of only a slight excess (1.2 equiv) of this reaction partner, which is typical in traditional Suzuki-Miyaura cross-couplings. Also of note is the compatibility of this reaction manifold with functional groups susceptible to

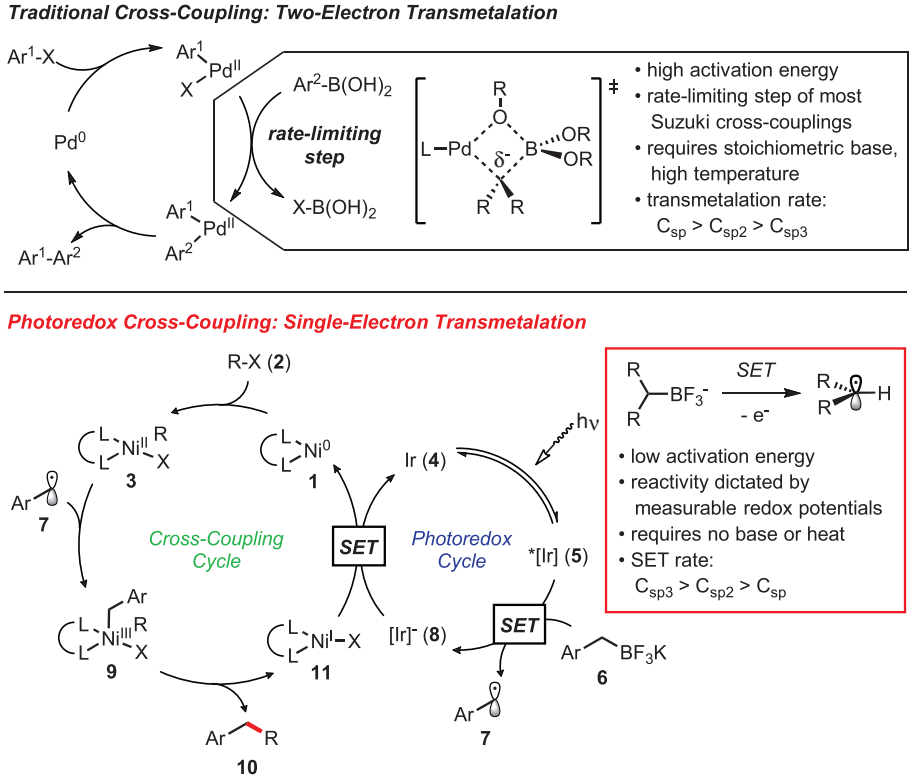


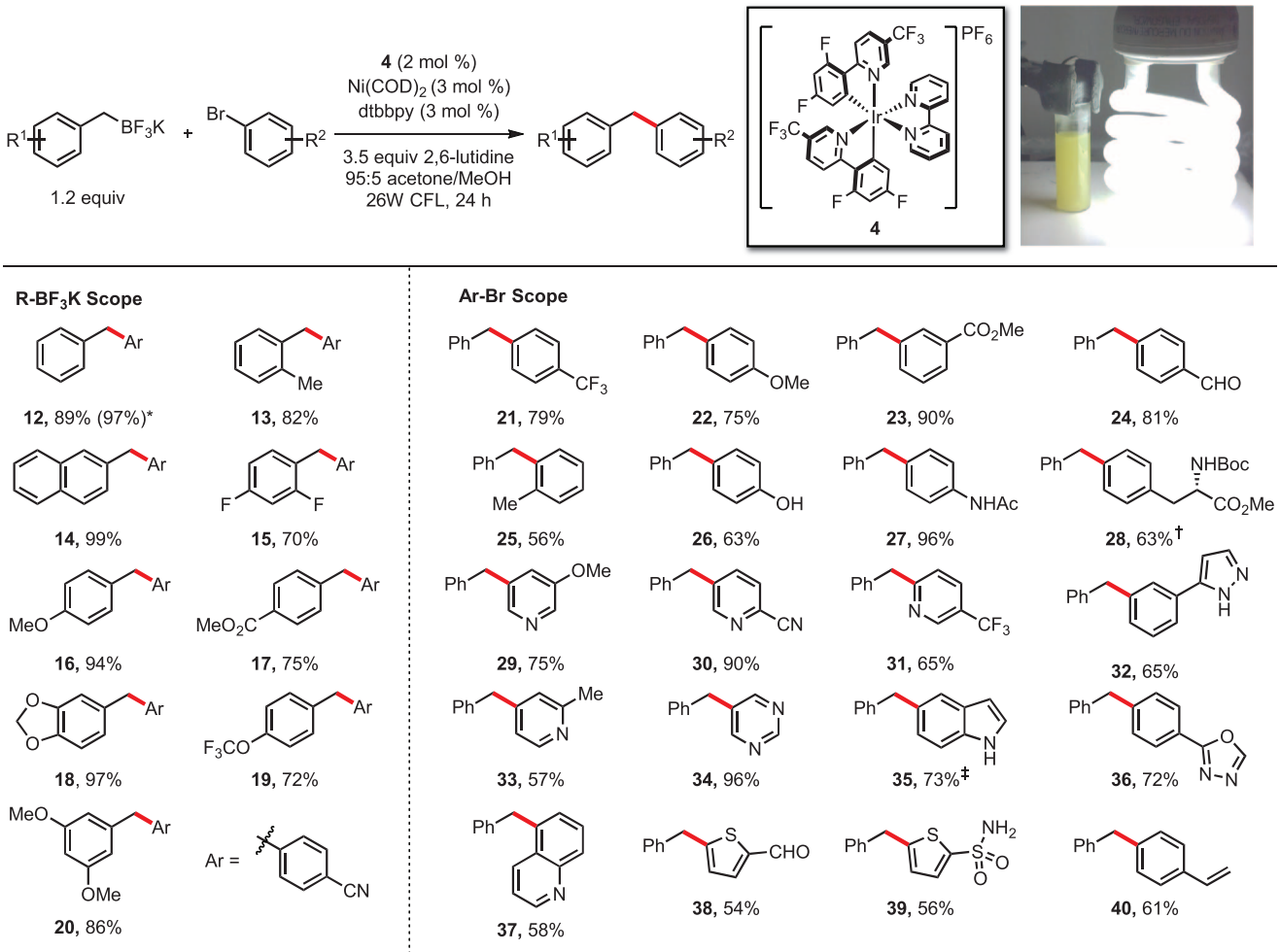
Fig. 1. Comparison of transmetalation in the palladium-catalyzed Suzuki-Miyaura cross-coupling and the proposed single-electron transmetalation in photoredox/nickel cross-coupling. Ir = $Ir[dFCF_3ppy]_2(bpy)PF_6$, R = generic organic subunit, Ar = aryl group.

single-electron oxidation or potentially reactive toward the radical intermediates, including phenol, anilide, and thienyl substructures, as well as five-membered nitrogen heterocycles. Remarkably, even 4-bromostyrene could be used as an electrophile without competitive radical capture or polymerization, affording diarylmethane **40** in 61% yield. The surprising compatibility of the reaction manifold with this substrate may suggest a mechanistic scenario more complex than that proposed in Fig. 1. However, the radical nature of the activation mode is strongly supported by the previous studies of Akita (*20*, *21*) and our own experiments using chiral ligand scaffolds and racemic secondary alkyl nucleophiles (see below).

As a demonstration of the broader potential of the application of single-electron transmetalation in this dual catalytic cross-coupling, the conditions optimized for use with primary benzylic trifluoroborates were directly applied to the cross-coupling of a secondary (α-alkoxy)alkyltrifluoroborate (Fig. 3). Comparable single-electron oxidation potentials (*20*, *21*) serve as the singular commonality between these structurally dissimilar reagents. Thus, C-C bond formation via single-electron transmetalation proceeded smoothly under these extremely mild and unoptimized conditions. The differential reactivity between the two-electron and single-electron transmetalation processes is underscored by the stark differences in conditions previously reported for (α-alkoxy)alkyltrifluoroborate cross-coupling (5 equiv CsOH, 105°C, 24 hours) versus those described herein (*31*). The observed reactivity also serves to demonstrate tolerance of substrates possessing β-hydrogens—a characteristic that is requisite for any general method for the cross-coupling of alkyl substructures.

To highlight further the differences between the activation mode reported here and that of traditional cross-coupling, we performed a competition experiment between potassium benzyltrifluoroborate and potassium phenyltrifluoroborate. Exposure of these two nucleophiles to the photoredox cross-coupling conditions resulted in isolation of diarylmethane product **12** in 91% isolated yield, with no observable biaryl formation (Fig. 4). The ability to engage a C_{sp3}-hybridized organometallic reagent selectively in a transition metal–catalyzed C-C bond-forming reaction in the presence of an equivalent C_{sp2}-hybridized organometallic represents a striking reversal of the reactivity hierarchy of previously reported cross-coupling reactions. This effectively demonstrates the complementary reactivity patterns observed between the single-electron and two-electron transmetalation modes.

Another important implication of the single-electron transmetalation manifold is related to the stereochemical outcome of the alkyl transfer. Nearly all cross-coupling reactions of stereodefined nucleophiles reported heretofore have demonstrated the transmetalation event to be stereospecific (*32*). Thus, enantioenriched products may only be accessed from nonracemic and configurationally stable organometallic reagents, which are often difficult to access. Isolated examples of stereoconvergence in transmetalation



* Reaction performed on 1.0 g (5.5 mmol) ArBr with 1 mol % **4**, 1.5 mol % $Ni(COD)_2$, and 1.5 mol % dtbbpy. † Reaction performed with 3 mol % **4**, 5 mol % $Ni(COD)_2$, and 5 mol % dtbbpy. ‡ 55% isolated pure, 18% isolated as mixture with bromide starting material

Fig. 2. Photoredox cross-coupling of benzylic trifluoroborates and aryl bromides. All yields are percent isolated yield of pure material after chromatography. Reactions were performed on aryl halide (0.5 mmol). Boc = *tert*-butoxycarbonyl, Me = methyl, Ph = phenyl, Ac = acetyl.

exist, specifically in the context of secondary benzylmagnesium reagents, a pyrrolidine-based organozinc, and a diastereoconvergent cross-coupling of substituted cyclohexylzinc reagents (*33*–*36*). Stereoconvergence in the former is thought to be enabled by dynamic kinetic resolution of the configurationally unstable Grignard reagent; the origin of selectivity in the latter is not fully understood. None of these approaches constitute a general strategy for stereoconvergent transmetalation beyond the scope of the directly explored reagents.

In contrast, the stereochemical outcome of the single-electron transmetalation is dictated by facial selectivity of the addition of a prochiral alkyl radical to a ligated Ni center. Thus, application of a chiral ligand framework renders this process asymmetric and provides a general reaction manifold in which stereoconvergent transmetalation can be achieved. Well-known stereoconvergent cross-couplings of alkyl halides, which putatively undergo a similar mechanistic step, provide guidance for selection of appropriate ligand scaffolds to maximize the stereoselectivity of the radical capture (*37*). Indeed, when we used commercially available ligand **L1** under slightly modified conditions, racemic trifluoroborate **44** was engaged in stereoconvergent cross-coupling with methyl 3-bromobenzoate, affording 1,1-diarylethane product **45** in 52% yield and a promising enantiomeric ratio of 75:25 (Fig. 4). The observed stereoconvergence serves as an effective mechanistic probe that supports the role of the organotrifluoroborate as a carbon radical precursor, provides evidence that the radical is intercepted by the ligated Ni complex, and suggests that C-C bond formation occurs via reductive elimination from Ni.

This preliminary result strongly implies that high levels of stereoselectivity are possible in the photoredox cross-coupling of secondary alkyl nucleophiles with appropriate modification of reaction conditions and ligand structure. Refinement of this approach to asymmetric cross-coupling will provide a powerful advancement to the field by alleviating the need for synthesis of enantioenriched organometallic reagents. Taken together, our findings effectively validate the single-electron transmetalation manifold and dual photoredox/cross-coupling cycle as a viable alternative to conventional cross-coupling of C_{sp3}-hybridized nucleophiles.

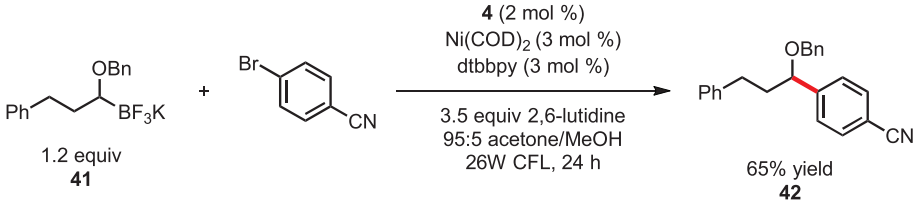


Fig. 3. Photoredox cross-coupling of a secondary (α-alkoxy)alkyltrifluoroborate with 4-bromobenzonitrile.

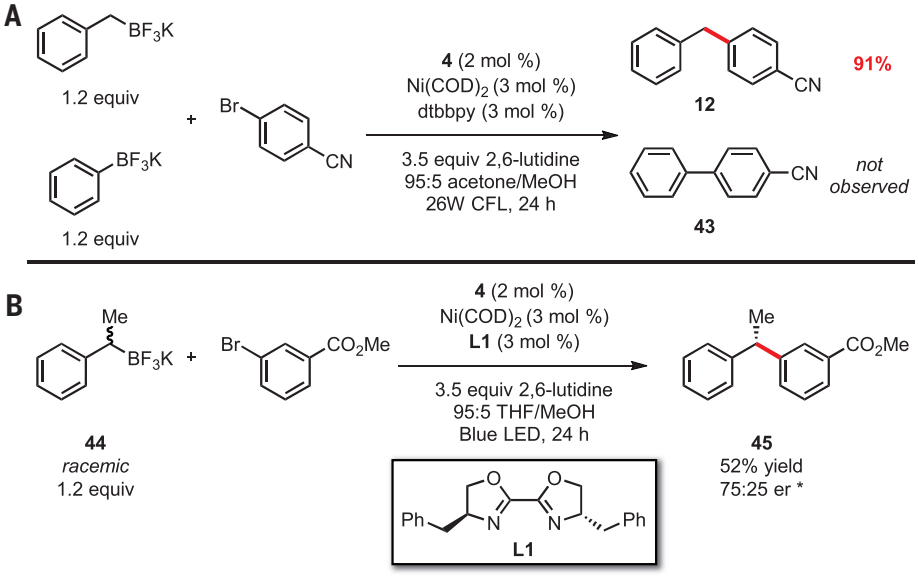


Fig. 4. Probing chemo- and stereoselectivity. (**A**) Competition experiment between potassium benzyltrifluoroborate and potassium phenyltrifluoroborate under photoredox cross-coupling conditions. (**B**) Stereoconvergent cross-coupling of a racemic trifluoroborate **44** and aryl bromide to afford an enantioenriched product. Reactions were performed on aryl bromide (0.5 mmol). *Determined by chiral supercritical fluid chromatography (SFC). †Absolute configuration was assigned as (*S*) on the basis of data reported in the literature. er = enantiomeric ratio.

REFERENCES AND NOTES

1. A. de Meijere, F. Diederich, Eds., *Metal-Catalyzed Cross-Coupling Reactions* (Wiley-VCH, Weinheim, Germany, ed. 2, 2004).
2. J. F. Hartwig, *Organotransition Metal Chemistry: From Bonding to Catalysis* (University Science, Sausalito, CA, 2010).
3. A. Rudolph, M. Lautens, *Angew. Chem. Int. Ed.* **48**, 2656–2670 (2009).
4. L. S. Hegedus, B. C. G. Soderberg, *Transition Metals in the Synthesis of Complex Organic Molecules* (University Science, Sausalito, CA, ed. 3, 2010).
5. H. Doucet, *Eur. J. Org. Chem.* **2008**, 2013–2030 (2008).
6. D. Imao, B. W. Glasspoole, V. S. Laberge, C. M. Crudden, *J. Am. Chem. Soc.* **131**, 5024–5025 (2009).
7. G. Zou, Y. K. Reddy, J. R. Falck, *Tetrahedron Lett.* **42**, 7213–7215 (2001).
8. J. Z. Deng *et al.*, *Org. Lett.* **11**, 345–347 (2009).
9. M. Aufiero, F. Proutiere, F. Schoenebeck, *Angew. Chem. Int. Ed.* **51**, 7226–7230 (2012).
10. Transmetalation rates of organoboron compounds adhere to trends established for the corresponding organostannanes.
11. J. W. Labadie, J. K. Stille, *J. Am. Chem. Soc.* **105**, 6129–6137 (1983).
12. A. Finch, P. J. Gardner, E. J. Pearn, G. B. Watts, *Trans. Faraday Soc.* **63**, 1880–1888 (1967).
13. C. K. Prier, D. A. Rankic, D. W. C. MacMillan, *Chem. Rev.* **113**, 5322–5363 (2013).
14. D. M. Schultz, T. P. Yoon, *Science* **343**, 1239176 (2014).
15. D. Kalyani, K. B. McMurtrey, S. R. Neufeldt, M. S. Sanford, *J. Am. Chem. Soc.* **133**, 18566–18569 (2011).
16. Y. Ye, M. S. Sanford, *J. Am. Chem. Soc.* **134**, 9034–9037 (2012).
17. B. Sahoo, M. N. Hopkinson, F. Glorius, *J. Am. Chem. Soc.* **135**, 5505–5508 (2013).
18. J. W. Lockner, D. D. Dixon, R. Risgaard, P. S. Baran, *Org. Lett.* **13**, 5628–5631 (2011).
19. G. A. Molander, V. Colombel, V. A. Braz, *Org. Lett.* **13**, 1852–1855 (2011).
20. Y. Yasu, T. Koike, M. Akita, *Adv. Synth. Catal.* **354**, 3414–3420 (2012).
21. K. Miyazawa, Y. Yasu, T. Koike, M. Akita, *Chem. Commun.* **49**, 7249–7251 (2013).
22. All electrochemical potentials are calculated versus the saturated calomel electrode (SCE).
23. M. Lowry *et al.*, *Chem. Mater.* **17**, 5712–5719 (2005).
24. C. Cannes, E. Labbé, M. Durandetti, M. Devaud, J. Y. Nédélec, *J. Electroanal. Chem.* **412**, 85–93 (1996).
25. The reduction of (bpy)$NiBr_2$ is observed as a two-electron wave at −1.1 V, implying that reduction of (bpy)NiBr to (bpy)Ni^0 occurs at a more positive potential.
26. See supplementary materials on *Science* Online.
27. M. E. Welsch, S. A. Snyder, B. R. Stockwell, *Curr. Opin. Chem. Biol.* **14**, 347–361 (2010).
28. P. Jain, S. Yi, P. T. Flaherty, *J. Heterocycl. Chem.* **50**, (S1), E166–E173 (2013).
29. A. Flaherty, A. Trunkfield, W. Barton, *Org. Lett.* **7**, 4975–4978 (2005).
30. G. A. Molander, T. Ito, *Org. Lett.* **3**, 393–396 (2001).
31. G. A. Molander, S. R. Wisniewski, *J. Am. Chem. Soc.* **134**, 16856–16868 (2012).
32. L. Li, C.-Y. Wang, R. Huang, M. R. Biscoe, *Nat. Chem.* **5**, 607–612 (2013).
33. T. Hayashi, M. Tajika, K. Tamao, M. Kumada, *J. Am. Chem. Soc.* **98**, 3718–3719 (1976).
34. T. Hayashi *et al.*, *J. Am. Chem. Soc.* **104**, 180–186 (1982).
35. C. J. Cordier, R. J. Lundgren, G. C. Fu, *J. Am. Chem. Soc.* **135**, 10946–10949 (2013).
36. K. Moriya, P. Knochel, *Org. Lett.* **16**, 924–927 (2014).
37. H. Q. Do, E. R. R. Chandrashekar, G. C. Fu, *J. Am. Chem. Soc.* **135**, 16288–16291 (2013).

ACKNOWLEDGMENTS

Supported by NIH (grant R01 GM-081376) and Pfizer. We thank Frontier Scientific for providing all of the organoboron precursors used in our work.

SUPPLEMENTARY MATERIALS

www.sciencemag.org/content/345/6195/433/suppl/DC1
Materials and Methods
Supplementary Text
Figs. S1 to S9
NMR spectra
References (*38*–*54*)

19 March 2014; accepted 27 May 2014
Published online 5 June 2014;
10.1126/science.1253647

DUAL CATALYSIS

Merging photoredox with nickel catalysis: Coupling of α-carboxyl sp^3-carbons with aryl halides

Zhiwei Zuo, Derek T. Ahneman, Lingling Chu, Jack A. Terrett, Abigail G. Doyle,* David W. C. MacMillan*

Over the past 40 years, transition metal catalysis has enabled bond formation between aryl and olefinic (sp^2) carbons in a selective and predictable manner with high functional group tolerance. Couplings involving alkyl (sp^3) carbons have proven more challenging. Here, we demonstrate that the synergistic combination of photoredox catalysis and nickel catalysis provides an alternative cross-coupling paradigm, in which simple and readily available organic molecules can be systematically used as coupling partners. By using this photoredox-metal catalysis approach, we have achieved a direct decarboxylative sp^3–sp^2 cross-coupling of amino acids, as well as α-O– or phenyl-substituted carboxylic acids, with aryl halides. Moreover, this mode of catalysis can be applied to direct cross-coupling of C_{sp^3}–H in dimethylaniline with aryl halides via C–H functionalization.

Visible light photoredox catalysis has emerged in recent years as a powerful technique in organic synthesis. This class of catalysis makes use of transition metal polypyridyl complexes that, upon excitation by visible light, engage in single-electron transfer (SET) with common functional groups, activating organic molecules toward a diverse array of valuable transformations (*1*–*5*). Much of the utility of photoredox catalysis hinges on its capacity to generate nontraditional sites of reactivity on common substrates via low-barrier, open-shell processes, thereby fostering the use of abundant and inexpensive starting materials.

Over the past century, transition metal-catalyzed cross-coupling reactions have evolved to be among the most used C–C and C–heteroatom bond-forming reactions in chemical synthesis. In particular, nickel catalysis has provided numerous avenues to forge carbon–carbon bonds via a variety of well-known coupling protocols (Negishi, Suzuki-Miyaura, Stille, Kumada, and Hiyama couplings, among others) (*6*, *7*). The broad functional group tolerance of these reactions enables a highly modular building block approach to molecule construction. Organometallic cross-coupling methods are traditionally predicated on the use of aryl or vinyl boronic acids, zinc halides, stannanes, or Grignard fragments that undergo addition to a corresponding aryl or vinyl halide partner.

We recently questioned whether visible-light photoredox and nickel transition metal catalysis might be successfully combined to create a dual catalysis platform for modular C–C bond formation (Fig. 1) (*8*–*14*). Through a synergistic merger of these two activation modes, we hoped to deliver a mechanism by which feedstock chemicals that contain common yet nontraditional leaving groups (C_{sp^3}–CO_2H or C_{sp^3}–H bonds) could serve as useful coupling partners. Among many advantages, this multicatalysis strategy would enable a modular approach to sp^3–sp^2 or sp^3–sp^3 bond formations that is not currently possible by using either photoredox or transition metal catalysis alone. We sought to develop a general method that would exploit naturally abundant, inexpensive, and orthogonal functional handles (e.g., C–CO_2H, C–H with C–Br, or C–I).

We proposed that two interwoven catalytic cycles might be engineered to simultaneously generate (i) an organometallic nickel(II) species via the oxidative addition of a Ni(0) catalyst to an aryl (Ar), alkenyl, or alkyl halide coupling partner and (ii) a carbon-centered radical generated through a photomediated oxidation event (Fig. 2). Given that organic radicals are known to rapidly combine with Ni(II) complexes (*15*, *16*), we hoped that this dual catalysis mechanism would successfully converge in the form of Ni(III)(Ar)(alkyl) that, upon reductive elimination, would deliver our desired C–C fragment coupling product. One of our laboratories has demonstrated that photoredox catalysis affords access to α-amino radicals by two distinct methods: via decarboxylation of a carboxylic acid or by an oxidation, deprotonation sequence with *N*-aryl or trialkyl amines (*17*, *18*). The other laboratory has explored Ni-catalyzed cross-coupling reactions with iminium ions that proceed via a putative α-aminonickel intermediate (*19*–*21*). Given our respective research areas, we sought to jointly explore the capacity of a nickel (II) aryl species to intercept a photoredox-generated α-amino radical, thereby setting the stage for the fragment coupling. We recognized that the sum of these two catalytic processes could potentially overcome a series of limitations that exist for each of these catalysis methods in their own right.

A detailed description of our proposed mechanistic cycle for the decarboxylative coupling is outlined in Fig. 2. We presumed that initial irradiation of heteroleptic iridium(III) photocatalyst $Ir[dF(CF_3)ppy]_2(dtbbpy)PF_6$ [$dF(CF_3)ppy$ = 2-(2,4-difluorophenyl)-5-(trifluoromethyl)pyridine, dtbbpy = 4,4′-di-*tert*-butyl-2,2′-bipyridine] (**1**) would produce the long-lived photoexcited $*Ir^{III}$ state **2** (exposure time τ = 2.3 μs) (*22*). Deprotonation of the α-amino acid substrate **3** with base and oxidation by the excited-state $*Ir^{III}$ complex {$E_{1/2}^{red}$ [$*Ir^{III}/Ir^{II}$] = +1.21 V versus saturated calomel electrode (SCE) in CH_3CN} (*22*) via a SET event would then generate a carboxyl radical, which upon rapid loss of CO_2 would deliver

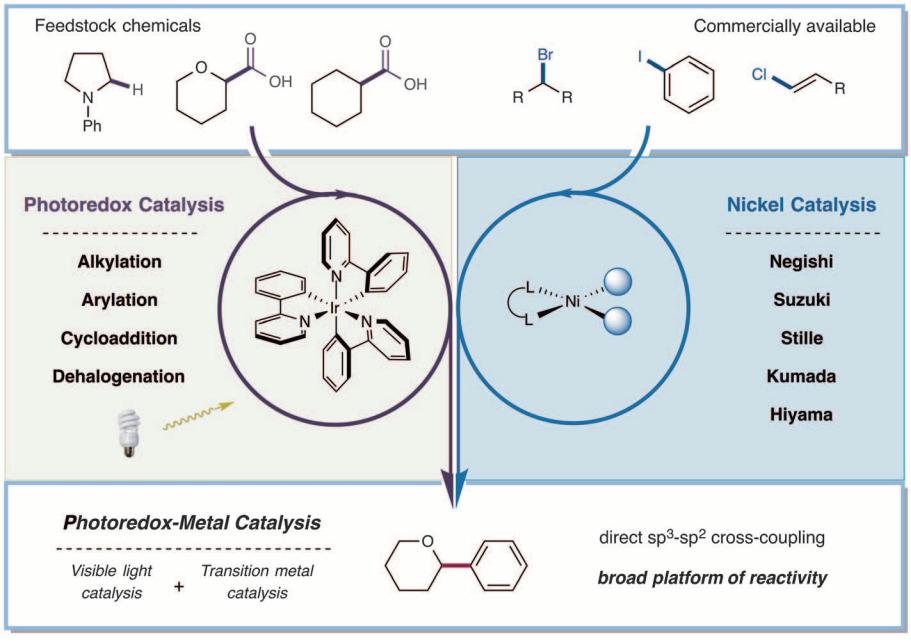
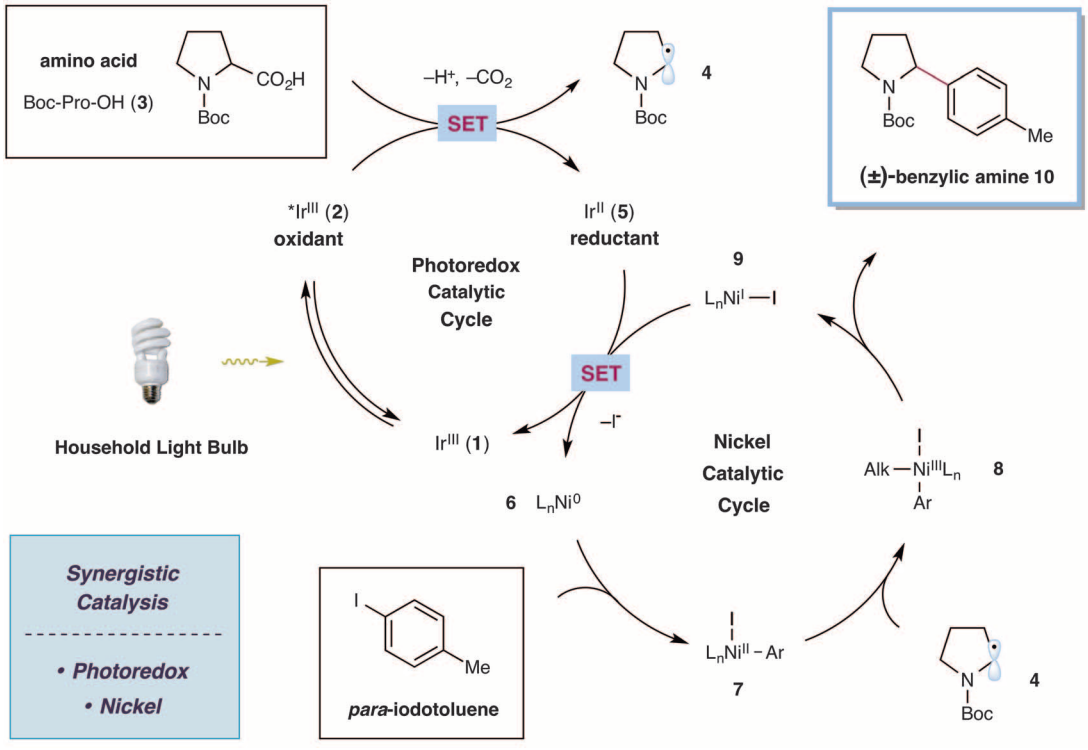
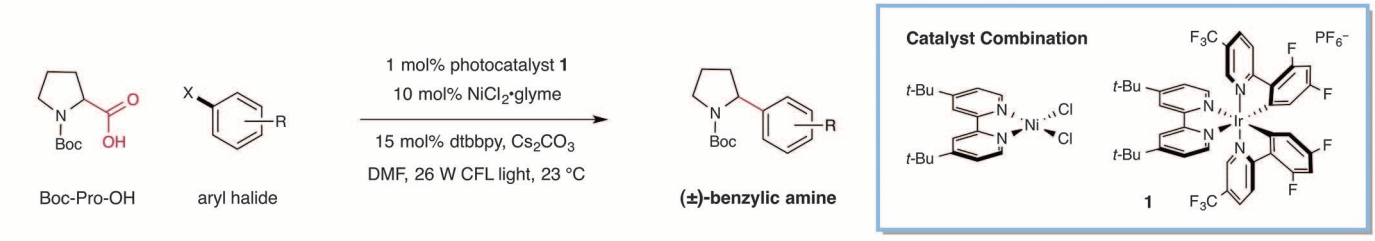


Fig. 1. The merger of photoredox and nickel catalysis yields access to direct sp^3-sp^2 cross-coupling. R, alkyl group.

Merck Center for Catalysis at Princeton University, Princeton, NJ 08544, USA.
*Corresponding author. E-mail: agdoyle@princeton.edu (A.G.D.); dmacmill@princeton.edu (D.W.C.M.)





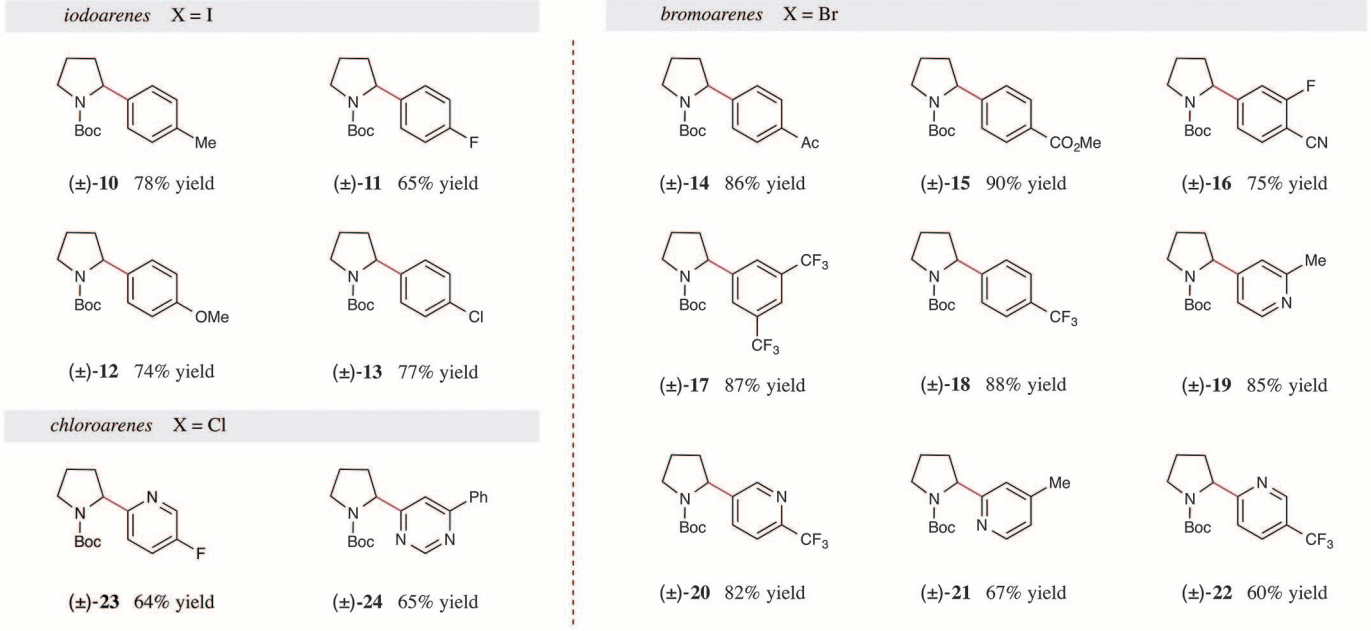


Fig. 2. Proposed mechanistic pathway of photoredox-nickel-catalyzed decarboxylative arylation. Me, methyl group; L, ligand; Alk, alkyl group.

Fig. 3. Photoredox-nickel catalyzed decarboxylative cross-coupling: aryl halide scope. CFL, compact fluorescent light; Bu, butyl group; Ac, acetyl group.

the α-amino radical **4** and the corresponding Ir^{II} species **5**. Given the established oxidation potential of prototypical amino acid carboxylate salts, we expected this process to be thermodynamically favorable [*tert*-butyl carbamoyl (Boc)–Pro-OCs, $E_{1/2}^{red}$ = +0.95 V versus SCE in CH_3CN) (*17*). Concurrently with this photoredox cycle, we hoped that oxidative addition of the Ni(0) species **6** into an aryl halide would produce the Ni(II) intermediate **7**. We anticipated that this Ni(II)-aryl species would rapidly intercept the α-amino radical **4**, forming the organometallic Ni(III) adduct **8**. Subsequent reductive elimination would forge the requisite C–C bond while delivering the desired α-amino arylation product **10** and expelling the Ni(I) intermediate **9**. Last, SET between the Ir^{II} species **5** and the Ni complex **9** would accomplish the exergonic reduction of Ni(I) to Ni(0) {on the basis of the established two-electron reduction potential of Ni(II) to Ni(0), we presume that reduction of Ni(I) to Ni(0) should be thermodynamically favorable, $E_{1/2}^{red}$ [Ni^{II}/Ni^{0}] = –1.2 V versus SCE in *N*,*N*´-dimethylformamide (DMF)} by the Ir^{II} species **5** {$E_{1/2}^{red}$ [Ir^{III}/Ir^{II}] = –1.37 V versus SCE in CH_3CN} (*22*, *23*), thereby completing both the photoredox and the nickel catalytic cycles simultaneously.

With this mechanistic hypothesis in hand, we first examined the proposed coupling by using *N*-Boc proline, *para*-iodotoluene, and a wide range of photoredox and ligated nickel catalysts. To our delight, we found that the combination of Ir[dF(CF_3)ppy]$_2$(dtbbpy)PF_6 and $NiCl_2$•glyme (glycol ether), dtbbpy, in the presence of 1.5 equivalents of Cs_2CO_3 base and white light from a 26-W compact fluorescent bulb, achieved the desired fragment coupling in 78% yield. During our optimization studies, we found that use of a bench-stable Ni(II) source, such as $NiCl_2$•glyme, was sufficient to generate the arylation product with comparable efficiency to a Ni(0) source. We attribute this result to in situ photocatalytic reduction of Ni(II) to Ni(0) via two discrete SET events, with excess amino acid likely serving as the sacrificial reductant to access the active Ni catalyst {$E_{1/2}^{red}$ [Ni^{II}/Ni^{0}] = –1.2 V versus SCE in DMF} (*23*). We believe that it is unlikely that the Ni(II)(Ar)X intermediate **7** undergoes a SET event to form Ni(I)Ar, given the poorly matched reduction potentials of the species involved {compare with $E_{1/2}^{red}$ [Ni^{II}ArX/Ni^{I}Ar] = –1.7 V versus SCE in CH_3CN and $E_{1/2}^{red}$ [Ir^{III}/Ir^{II}] = –1.37 V versus SCE in CH_3CN} (*22*, *24*). However, we recognize that an alternative pathway could be operable wherein the oxidative addition step occurs from the Ni(I) complex to form a Ni(III) aryl halide adduct. In this pathway, photocatalyst-mediated reduction of the aryl-Ni(III) salt to the corresponding Ni(II) species followed by the α-amino radical addition step would then form the same productive Ni(III) adduct **8**, as shown in Fig. 2. Given that (i) Ni(0) complexes undergo oxidative addition more readily than Ni(I) complexes with aryl halides (*25*) and (ii) Ni(II) complexes are believed to rapidly engage with sp^3 carbon-centered radicals to form Ni(III) species (enabling sp^3–sp^2 and sp^3–sp^3 C–C bond formations) (*15*, *16*), we favor the dual-catalysis mechanism outlined in Fig. 2.

Having established the optimal conditions for this photoredox-nickel decarboxylative arylation, we focused our attention on the scope of the aryl halide fragment. As shown in Fig. 3, a wide range of aryl iodides are amenable to this dual-catalysis strategy, including both electron-rich and electron-deficient arenes (**10** to **13**, *65*

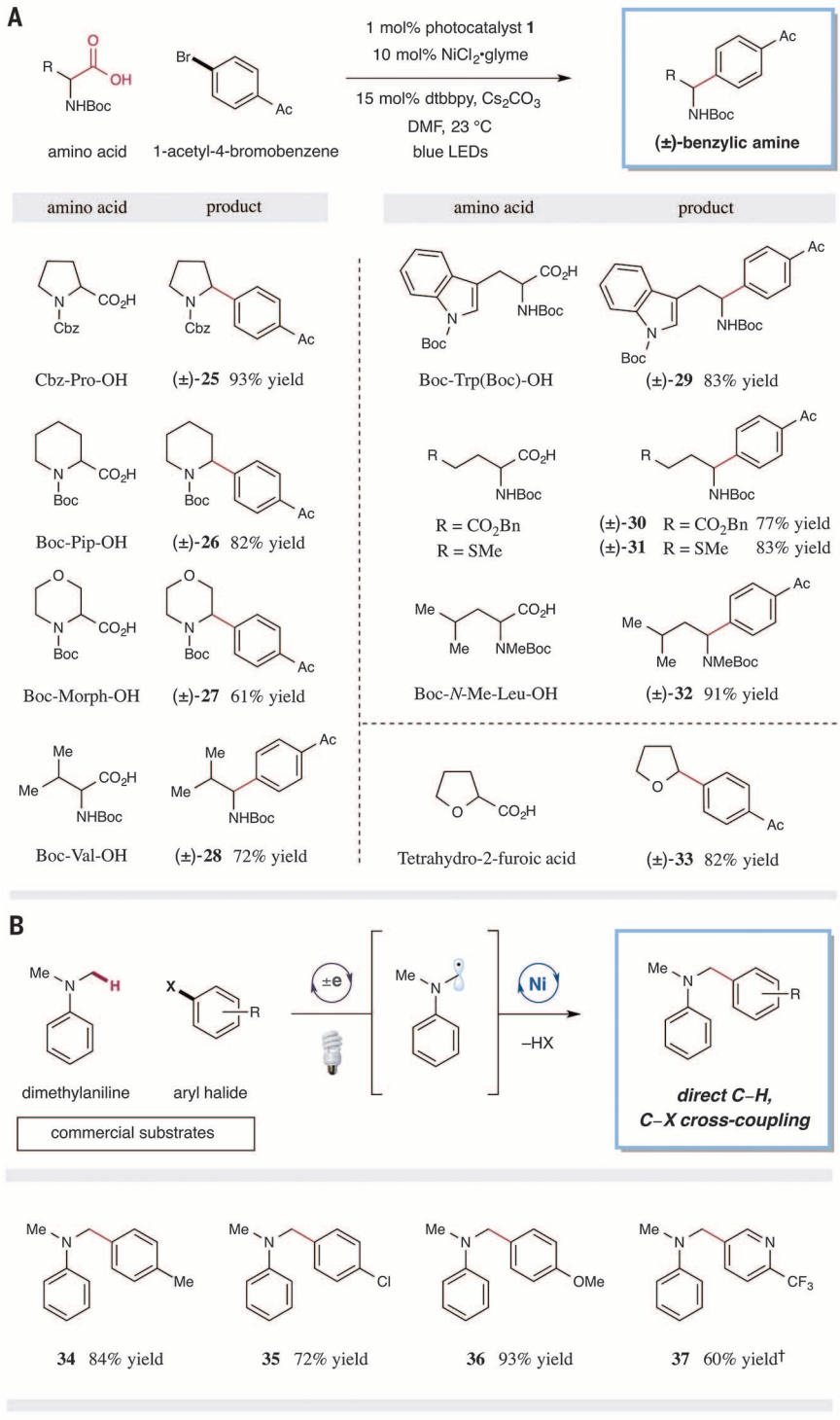


Fig. 4. Amino acid coupling partners and C_{sp^3}–H, C–X cross-coupling. (**A**) Evaluation of the amino acid coupling partner in the decarboxylative-arylation protocol. Ac, acetyl group; LED, light-emitting diode. (**B**) The direct C_{sp^3}–H, C–X cross-coupling via photoredox-nickel catalysis. All yields listed in Figs. 3 and 4 are isolated yields. Reaction conditions for (A) are the same as in Fig. 3. Reaction conditions for (B) are as follows: photocatalyst **1** [1 mole % (mol %)]; $NiCl_2$·glyme (10 mol %), dtbbpy (15 mol %), KOH (3 equiv.), DMF, 23°C, 26-W light. *Iodoarenes used as aryl halide, X = I. †Bromoarene used, X = Br.

to 78% yield). Many aryl bromides function effectively as well, including those that contain functional groups as diverse as ketones, esters, nitriles, trifluoromethyl groups, and fluorides (**14** to **18**, 75 to 90% yield). Heteroaromatics, in the form of differentially substituted bromopyridines, are also efficient coupling partners (**19** to **22**, 60 to 85% yield). Moreover, aryl chlorides are competent substrates if the arenes, such as pyridines and pyrimidines, are electron-deficient (**23** and **24**, 64 and 65% yield). Only products **15** and **19** in Fig. 3 would be accessible by using our previously reported photoredox arylation strategy. Moreover, we are unaware of the general use of C_{sp^3}-bearing carboxylic acids as reaction substrates in transition metal catalysis, an illustration of the tremendous scope expansion that is attainable by using this dual catalysis technology. These reactions are typically complete in 72 hours at larger scale and 48 hours on smaller scale (see supplementary text).

Next, we investigated the nature of the carboxylic acid coupling partner, as highlighted in Fig. 4A. A wide variety of α-amino acids function effectively in this protocol, including various *N*-Boc and *N*-benzyl carbamoyl (*N*-Cbz) protected heterocycles (**25** to **27**, 61 to 93% yield). Acyclic α-amino acids, containing indole, ester, and thioether functionalities, are also readily tolerated (**28** to **32**, 72 to 91% yield). α-oxycarboxylic acids can function as proficient coupling partners, producing α-arylated ethers in high yield over a single step (**33**, 82% yield). Moreover, we have also found that various phenyl acetic acid substrates function in this coupling protocol with high efficiency (>78% yield, see supplementary text).

To further demonstrate the utility of this dual-catalysis strategy, we sought to demonstrate the direct functionalization of C_{sp^3}–H bonds with coupling partners derived from aryl or alkyl halides. Given that our decarboxylation-arylation mechanism involves the rapid addition of an α-amino radical to a Ni(II) salt, we sought to generate an analogous α-nitrogen carbon–centered radical via a photoredox-driven *N*-phenyl (*N*-Ph) oxidation, α-C–H deprotonation sequence using aniline-based substrates (*18*). We presumed that this photomediated *N*-Ph oxidation mechanism would provide an alternative pathway to the open-shell carbon intermediate (corresponding to **4**, Fig. 2) and should similarly intercept the putative Ni(II) intermediate **8**. Assuming that the remaining dual-catalysis mechanism would be analogous to that shown in Fig. 2, we expected that a range of direct C_{sp^3}–H functionalization protocols should be possible. Indeed, we were able to demonstrate that dimethylaniline undergoes α-amine coupling with a variety of aryl halides in the presence of $Ir[dF(CF_3)ppy]_2(dtbbpy)PF_6$ and $NiCl_2$•glyme (Fig. 4B). Electron-deficient and electron-rich iodoarenes give moderate to high yields (**34** to **36**, 72 to 93% yield). Moreover, aryl bromides are competent coupling partners, enabling the installation of medicinally important heterocyclic motifs (**37**, 60% yield). Last, control experiments have revealed that the combination of light, photoredox catalyst **1**, and the $NiCl_2$•dtbbpy complex is essential for product formation in all examples listed in Figs. 3 and 4. This reaction represents a powerful foray into direct C–H activation using orthogonal cross-coupling reactivity.

REFERENCES AND NOTES

1. D. A. Nicewicz, D. W. C. MacMillan, *Science* **322**, 77–80 (2008).
2. M. A. Ischay, M. E. Anzovino, J. Du, T. P. Yoon, *J. Am. Chem. Soc.* **130**, 12886–12887 (2008).
3. J. M. R. Narayanam, J. W. Tucker, C. R. J. Stephenson, *J. Am. Chem. Soc.* **131**, 8756–8757 (2009).
4. D. S. Hamilton, D. A. Nicewicz, *J. Am. Chem. Soc.* **134**, 18577–18580 (2012).
5. M. T. Pirnot, D. A. Rankic, D. B. C. Martin, D. W. C. MacMillan, *Science* **339**, 1593–1596 (2013).
6. M. R. Netherton, G. C. Fu, *Adv. Synth. Catal.* **346**, 1525–1532 (2004).
7. A. Rudolph, M. Lautens, *Angew. Chem. Int. Ed.* **48**, 2656–2670 (2009).
8. The successful merger of photoredox and transition metal catalysis has been demonstrated for the specific installation of unique functionality (e.g., CF_3) (*9*–*14*).
9. M. Osawa, H. Nagai, M. Akita, *Dalton Trans.* **2007**, 827–829 (2007).
10. D. Kalyani, K. B. McMurtrey, S. R. Neufeldt, M. S. Sanford, *J. Am. Chem. Soc.* **133**, 18566–18569 (2011).
11. Y. Ye, M. S. Sanford, *J. Am. Chem. Soc.* **134**, 9034–9037 (2012).
12. M. Rueping *et al.*, *Chemistry* **18**, 5170–5174 (2012).
13. B. Sahoo, M. N. Hopkinson, F. Glorius, *J. Am. Chem. Soc.* **135**, 5505–5508 (2013).
14. X. Z. Shu, M. Zhang, Y. He, H. Frei, F. D. Toste, *J. Am. Chem. Soc.* **136**, 5844–5847 (2014).
15. S. Biswas, D. J. Weix, *J. Am. Chem. Soc.* **135**, 16192–16197 (2013).
16. S. L. Zultanski, G. C. Fu, *J. Am. Chem. Soc.* **135**, 624–627 (2013).
17. Z. Zuo, D. W. C. MacMillan, *J. Am. Chem. Soc.* **136**, 5257–5260 (2014).
18. A. McNally, C. K. Prier, D. W. C. MacMillan, *Science* **334**, 1114–1117 (2011).
19. T. J. A. Graham, J. D. Shields, A. G. Doyle, *Chem. Sci.* **2**, 980 (2011).
20. K. T. Sylvester, K. Wu, A. G. Doyle, *J. Am. Chem. Soc.* **134**, 16967–16970 (2012).
21. J. D. Shields, D. T. Ahneman, T. J. A. Graham, A. G. Doyle, *Org. Lett.* **16**, 142–145 (2014).
22. M. S. Lowry *et al.*, *Chem. Mater.* **17**, 5712–5719 (2005).
23. M. Durandetti, M. Devaud, J. Perichon, *New J. Chem.* **20**, 659 (1996).
24. Y. H. Budnikova, J. Perichon, D. G. Yakhvarov, Y. M. Kargin, O. G. Sinyashin, *J. Organomet. Chem.* **630**, 185–192 (2001).
25. C. Amatore, A. Jutand, *Organometallics* **7**, 2203–2214 (1988).

ACKNOWLEDGMENTS

The authors are grateful for financial support provided by the NIH General Medical Sciences (grants NIHGMS R01 GM103558-01 and R01 GM100985-01) and gifts from Merck, Amgen, Eli Lilly, and Roche. Z.Z. and L.C. are grateful for postdoctoral fellowships from the Shanghai Institute of Organic Chemistry. The authors thank G. Molander and co-workers for graciously offering to concurrently publish a related study that was submitted slightly ahead of our own.

SUPPLEMENTARY MATERIALS

www.sciencemag.org/content/345/6195/437/suppl/DC1
Material and Methods
Supplementary Text
Tables S1 and S2
Data
References (*26*–*34*)

1 May 2014; accepted 27 May 2014
Published online 5 June 2014;
10.1126/science.1255525

EXOPLANET DETECTION

Stellar activity masquerading as planets in the habitable zone of the M dwarf Gliese 581

Paul Robertson,[1,2]* Suvrath Mahadevan,[1,2,3] Michael Endl,[4] Arpita Roy[1,2,3]

The M dwarf star Gliese 581 is believed to host four planets, including one (GJ 581d) near the habitable zone that could possibly support liquid water on its surface if it is a rocky planet. The detection of another habitable-zone planet—GJ 581g—is disputed, as its significance depends on the eccentricity assumed for d. Analyzing stellar activity using the Hα line, we measure a stellar rotation period of 130 ± 2 days and a correlation for Hα modulation with radial velocity. Correcting for activity greatly diminishes the signal of GJ 581d (to 1.5 standard deviations) while significantly boosting the signals of the other known super-Earth planets. GJ 581d does not exist, but is an artifact of stellar activity which, when incompletely corrected, causes the false detection of planet g.

At a distance of 6.3 parsecs, the M dwarf star Gliese 581 (GJ 581) is believed to host a system of planets discovered using the Doppler radial velocity (RV) technique (*1*–*3*) and a debris disk (*4*). It is considered a local analog to compact M dwarf planetary systems found by the Kepler spacecraft (*5*, *6*).

Although the periods and orbital parameters of the inner planets b (P = 5.36 days) and c (P = 12.91 days) are unchanged since their initial discovery (*1*, *2*), the period of planet d was revised from 82 to 66 days (*2*, *3*) upon the discovery of a fourth planet e (P = 3.15 days). Using a combination of data from the High Accuracy Radial Velocity Planet Searcher (HARPS) spectrograph and the High Resolution Echelle Spectrometer (HIRES), planets f (P = 433 days) and g (P = 36.5 days) were reported (*7*), and their existence promptly questioned (*8*) using additional data from HARPS. Although the reported

planet f is now believed not to exist, the existence of planet g is still claimed by some groups. Vogt *et al.* (*9*) argue for a five-planet circular model (including g) based on dynamical stability, whereas studies based on Bayesian statistics (*10*) and correlated noise (*11*, *12*) find no evidence for the existence of g. At close to half the period of d, its RV signal strongly depends on the eccentricity assumed for the fit to planet d (*9*, *13*). The existence of planet d itself has been questioned; an analysis using a correlated noise model (*11*) reduced its significance to 2 SD, although d is still widely believed to exist by the astronomy community. The Gliese 581 system is also of great interest because three of the planets (c, d, and g) have all been considered at one time to be among the first exoplanets likely to host habitable environments if they were rocky (*2*, *7*, *14*, *15*), with d still being considered an excellent candidate. This system continues to be studied intensively [e.g., (*16*)]. Because stellar activity is an important source of noise at the RV amplitudes of the GJ 581 planets, we seek herein to investigate the effects of stellar activity on the RVs of GJ 581 in more detail.

Our analysis of correlation between the RVs and stellar activity indicators focuses on the publicly available spectra from the HARPS spectrograph (based on data obtained from the European Southern Observatory Science Archive Facility under request no. 58160). We adopted the newest published HARPS RVs (*8*) and measured activity indicators for the Hα ($I_{H\alpha}$) (*17*) and Na I D (I_D) (*18*) lines using the spectra. Using the cross-correlation functions (CCFs) included with the HARPS spectra, we have calculated the bisector inverse slopes (BIS) as well. We have excluded one spectrum from our analysis, because it is likely a flare event. Visual inspection of the spectra reveals that I_D is contaminated by strong night sky sodium emission lines, which are difficult to correct without sky fibers. We therefore constrained our RV analysis to Hα to minimize error.

The RVs of GJ 581 are dominated by the signal of planet b. Upon removing this dominant signal, we detect significant anticorrelation in the RV residuals with $I_{H\alpha}$. For the entire data set (239 spectra), the Pearson correlation coefficient is $r = -0.31$ [probability of no correlation, $P(r) = 5 \times 10^{-7}$]. Examining the BIS for the HARPS data, we also see evidence for a correlation ($r = 0.44$ over the most active period) between BIS and $I_{H\alpha}$, as might be expected if stellar activity is the cause of some RV shifts for GJ 581 (fig. S10).

Frequency analysis of the activity indices indicates that their variability—and thus the induced RV signal—is associated with stellar rotation (fig. S1). The periodogram of $I_{H\alpha}$ shows a strong peak at 125 days, with an additional peak at 138 days caused by phase changes in the rotation signal. The best fit to the time-series $I_{H\alpha}$ data is obtained when we model individual sinusoids to the periods from December 2005 to September 2007 and January 2010 to July 2011, when the $I_{H\alpha}$ root mean square (RMS) is twice

[1]Department of Astronomy and Astrophysics, The Pennsylvania State University, University Park, PA 16802, USA. [2]Center for Exoplanets and Habitable Worlds, The Pennsylvania State University, University Park, PA 16802, USA. [3]The Penn State Astrobiology Research Center, The Pennsylvania State University, University Park, PA 16802, USA. [4]McDonald Observatory, The University of Texas at Austin, Austin, TX 78712–1206, USA.
*Corresponding author. E-mail: pmr19@psu.edu

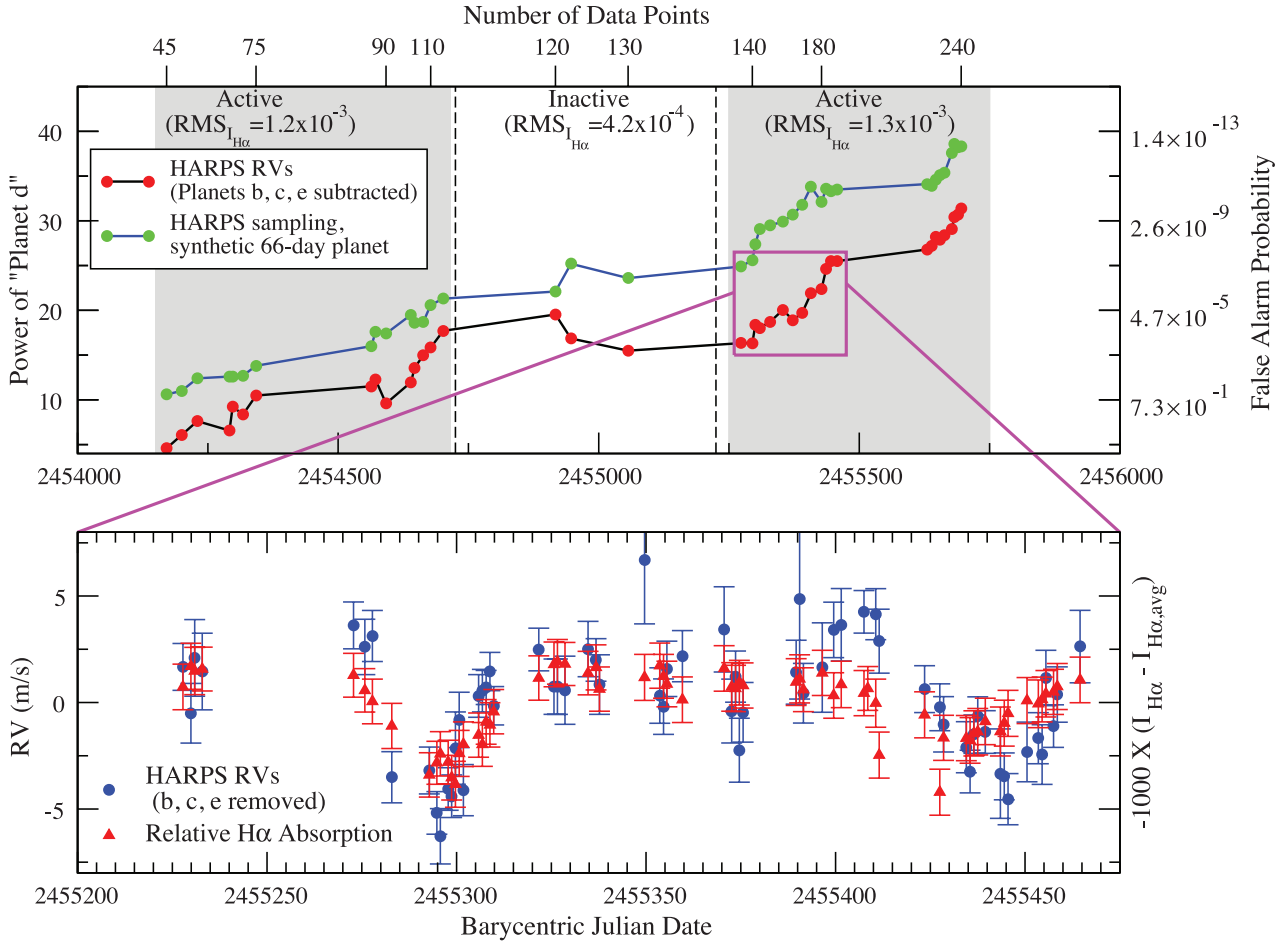


Fig. 1. (**Top**) Periodogram power of d as a function of time and number of HARPS RVs. The power is reported at every five observations. We show the actual RVs after removing planets b, c, and e (black/red), along with the Keplerian signal of an eccentric 66-day planet sampled with the time stamps and uncertainties of the HARPS sampling (blue/green). Qualitative levels of stellar activity, based on the $I_{H\alpha}$ index, are shown for different time periods. (**Bottom**) HARPS RVs (blue) for the region outlined in pink. Planets b, c, and e have been modeled and removed from the RVs. We overlay our Hα index (red), scaled to facilitate visual comparison. RV and Hα are strongly correlated, indicating that the remaining Doppler signal is caused by stellar activity.

as high as during the "quiescent" periods in 2005 and 2009. The sinusoidal models yield an average rotation period of 130 ± 2 days, whereas the phase and (to a lesser extent) amplitude vary.

The changing phase and amplitude of the activity-induced stellar rotation signal induce a variable effect on the RVs, implying that the slope of the RV-activity correlation is not strictly constant. Instead of evaluating the RV-activity correlation as one fit over the entire data set, we have examined RV as a function of $I_{H\alpha}$ over each observing season in the HARPS archive. For the December 2005 to September 2007 and January 2010 to July 2011 time frames, we have combined two seasons, because $I_{H\alpha}$ shows a coherent rotation signal across the seasons, suggesting that the activity behavior remains approximately constant over these times.

We find significant RV-$I_{H\alpha}$ anticorrelations (r = −0.45, −0.55, and −0.48) for three of the five epochs. These three epochs have RMS values of 1.22×10^{-3}, 1.10×10^{-3}, and 1.31×10^{-3} in $I_{H\alpha}$, as opposed to $RMS_{IH\alpha} = 4.81 \times 10^{-4}$ and 4.19×10^{-4} in the other seasons, suggesting that the star is approximately twice as active during these times. Although we have removed planets b, c, and e from the RVs, we find that once planet b has been removed, the correlation coefficients do not change significantly before and after removing c and e. The anticorrelation is particularly striking for the 2010 season, shown in Fig. 1.

We correct the HARPS RVs by subtracting the best-fit RV-$I_{H\alpha}$ relation from each of the three epochs for which we observed a significant anticorrelation, leaving the other epochs unchanged. A new RV model then can be used to evaluate the effect of the activity correction on the known exoplanets and to determine whether any additional signals exist. We detect the known planets b, c, and e using the generalized Lomb-Scargle periodogram (*19*) (Fig. 2). For planets c and e, we observe significant increases in signal power upon correcting for activity. The power of planet c increases from 53.5 to 57.6, while the power of e increases from 23.5 to 30.3. Formally, false-alarm probability (FAP) [from (*11*)] scales approximately as $e^{-P}\sqrt{P}$ for a Lomb-Scargle periodogram with power P; thus, the power increase translates to a decrease in FAP by a factor of 60 for planet c and 800 for planet e.

In contrast, the power of planet d drops from 31.4 to 11.6 after we apply our activity correction. As shown in Fig. 1, the periodogram power increases as a planet would during periods of high activity but decreases over the epoch with lowest $RMS_{IH\alpha}$. Planet d has a reported period of 66 days, which is roughly equal to half the stellar rotation period, suggesting that it is a harmonic that loses significance when the rotation signal is removed via decorrelating with $I_{H\alpha}$.

In Table 1, we list the parameters of our three-planet model to the activity-corrected HARPS RVs. We fit the RVs using the GaussFit (*20*) and Systemic (*21*) software packages, finding good agreement between the two. Our model does not differ much from previous fits to planets b, c, and e (*3*, *8*, *9*), except that planet e no longer shows any eccentricity after the activity correction. In the corrected RVs, the 66-day signal appears only at the 1.5-SD significance level in the residual periodogram, and the 33- or 36-day signal does not appear at all. We conclude that the three-planet solution with activity-induced variability fully explains the observations.

We assert that the periodic RV signal at 66 days is an artifact induced by the stellar rotation rather than an exoplanet. Previous studies (*3*, *7*) discounted starspot-induced rotational modulation as the origin of RV signals corresponding to planets d and g because the low photometric variability of the star suggests that any spots present should be too small to create the observed signals. However, spatially localized magnetic

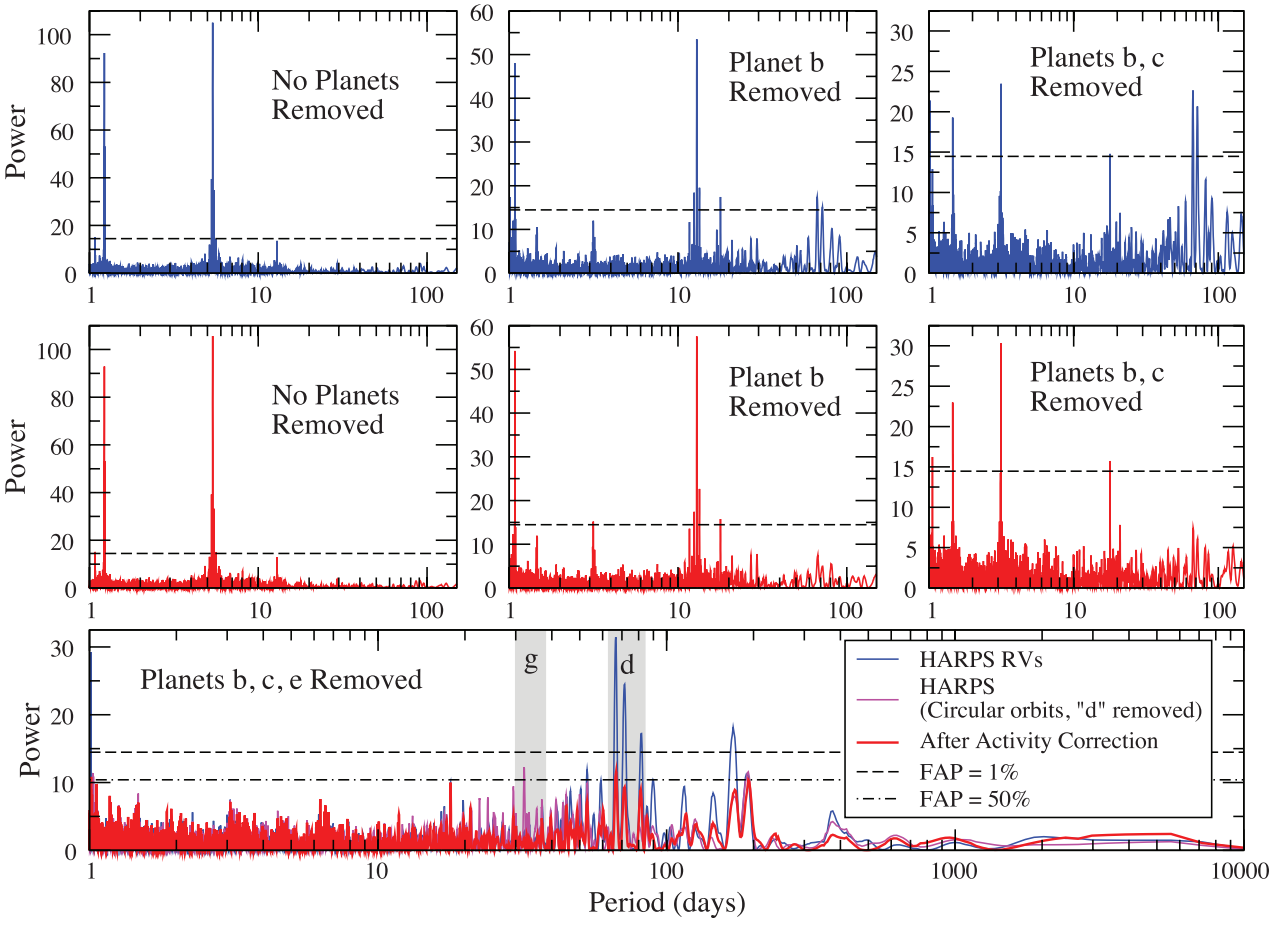


Fig. 2. Periodograms for the HARPS RVs before (blue) and after (red) correcting for stellar activity, with the planets successively subtracted. In the bottom panel, we also show (pink) the periodogram after subtracting four circular Keplerian signals, illustrating that the signal interpreted as 581 g (*7*, *9*) was caused by fitting a sinusoidal signal to the 581d signal and performing, in essence, an incomplete correction for stellar activity.

activity has been observed to influence RV in M stars without producing spots with high optical contrast. Striking similarities exist with our observed activity-RV correlation results for GJ 581 and those reported for Barnard's star, a slow-rotating, photometrically quiet M dwarf of similar spectral type. Observations with the Ultraviolet and Visual Echelle Spectrograph (UVES) found an RV-$I_{H\alpha}$ anticorrelation value of $r = -0.498$, almost identical to that observed herein (*22*). Kürster *et al.* attribute this phenomenon to magnetically active regions that stimulate Hα emission but do not produce spots of high contrast. These regions impede local convection, leading to an RV shift. Evidence for a relation between chromospheric activity, Hα emission, and convective suppression has also been observed in the form of a temperature/radius dependence on Hα activity for low-mass stars (*23*). The anticorrelation (i.e., the negative slope) for RV versus $I_{H\alpha}$ suggests that the stellar lines used for RV determination are emitted from a region of convective overshoot.

Although the activity-induced RV we observe may not be due to "typical" dark starspots, localized, rotating regions that magnetically alter the convective velocity field would create RV signatures equivalent to spots. In the absence of simultaneous high-precision photometric monitoring, it is difficult to deduce the relative contributions of these different mechanisms. We therefore refer to these as active regions (ARs) hereafter. A single rotating starspot creates an RV signal at the rotation period and injects power at a number of its harmonics, primarily $P_{rot}/2$, $P_{rot}/3$, and $P_{rot}/4$ (*24*). For the purposes of exploring the qualitative impact of such ARs on RV, a starspot model should suffice. For a rotation period of 130 days, the activity-induced RV signal always includes significant power near the period of planet d. We present two hypotheses for the lack of an observed signal at the periodogram around 130 days. One explanation lies in the geometry of the star and its ARs. The shape of an activity-induced RV signal changes as a function of the stellar inclination and the latitudes of the ARs, sometimes transferring RV power out of the rotation period into its harmonics. As an illustration, in an analysis using the SOAP (Spot Oscillation and Planet) code (*24*) (fig. S7), for an inclination of 50° for the star [consistent with that of its debris disk (*4*)] and spots near the stellar equator, the spot-induced RVs are dominated by the 66-day signal. A more important factor, though, is that for the 2010 to 2011 observing epoch, the Hα activity contains two signals of roughly equal power at 128 and 69 days, indicating the presence of two ARs instead of one. In this epoch, we find (fig. S4) that the activity-RV correlation is driven by the 69-day signal rather than the rotation period, indicating that activity is injecting RV power at half the rotation period while two ARs are present. The addition of power at half the rotation period for 109 of 240 observations explains the dominance of the $P_{rot}/2$ signal.

Our activity analysis also helps explain why the signal ascribed to planet d is not observed in the Keck/HIRES RVs alone (*11*). We have computed $I_{H\alpha}$ for the HIRES spectra, which we show alongside the HARPS measurements in Fig. 3. The HIRES data only cover the last portion of the active phase from December 2005 to September 2007 and have very little coverage in 2010 to 2011, where two ARs drive the 66-day period. Coupled with the higher reported error bars of HIRES compared with HARPS, this yields a non-detection of the 66-day signal.

The signal of the 33- or 36-day "planet g," the existence of which has already been called into question, is also an artifact of stellar rotation because no hint of it remains after the activity correction. Close to $P = P_{rot}/4$, it is another harmonic of the rotation period. Furthermore, the signal is only observed when fitting a circular orbit to "planet d," as shown in the bottom panel of Fig. 2 (*7*–*9*). By fitting a circular Keplerian model to the 66-day signal, Vogt *et al.* (*7*) essentially performed an incomplete stellar activity correction, and the signal of "planet g" was simply leftover noise created by stellar activity.

The impact of stellar activity on the GJ 581 system demonstrates the crucial importance of understanding and treating the presence of activity signals in the quest for low-mass planets. Our activity correction clearly distinguishes between planetary and stellar signals and reduces the astrophysical noise in the data sufficiently that the signals of very low-mass planets are recovered at much higher significance. This analysis also naturally explains the correlated (red) noise seen in analysis of the HARPS and HIRES data (*11*).

Given the advantages of RV surveys of slow-rotating low-mass M dwarfs for RV searches, the physical mechanism that inhibits the convective motion in the stellar atmosphere should be the

Table 1. Orbital solution for GJ 581 planets after correcting for stellar activity. AU, astronomical units; BJD, barycentric Julian date.

Orbital parameter	Planet b	Planet c	Planet e
Period P (days)	5.3686 ± 0.0001	12.914 ± 0.002	3.1490 ± 0.0002
Periastron passage T_0 (BJD −2,450,000)	4751.76 ± 0.01	4759.2 ± 0.1	4752.33 ± 0.05
RV amplitude K (m/s)	12.6 ± 0.2	3.3 ± 0.2	1.7 ± 0.2
Eccentricity e	0.00 ± 0.03	0.00 ± 0.06	0.00 ± 0.06
Semimajor axis a (AU)	0.04061 ± 0.00003	0.0721 ± 0.0003	0.02815 ± 0.00006
Minimum mass $M \sin i$ ($M_\oplus$)	15.8 ± 0.3	5.5 ± 0.3	1.7 ± 0.2
Zero-point RV offset (m/s)	−0.52 ± 0.1		
RMS (m/s)	2.12		

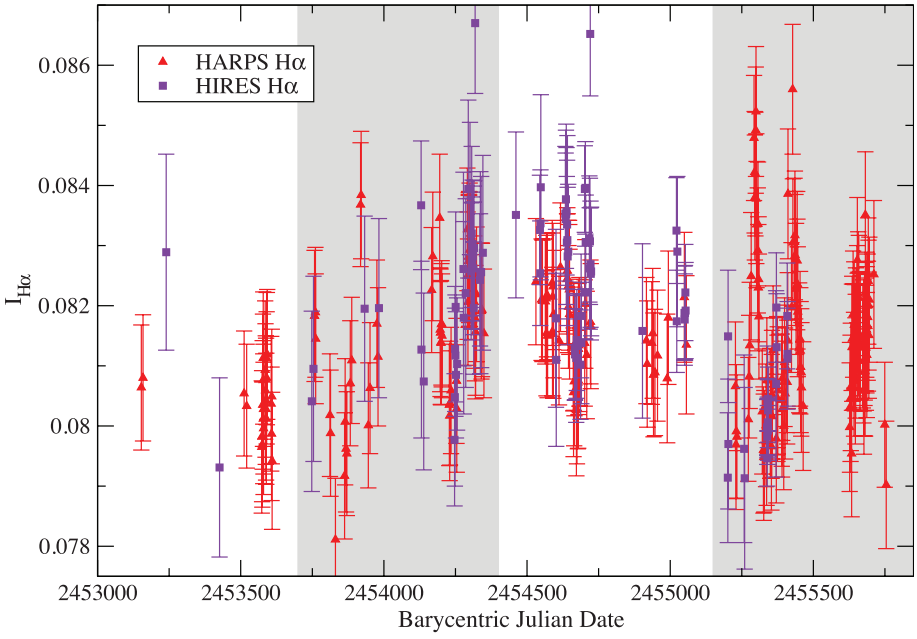


Fig. 3. Hα indices from HARPS (red) and HIRES (purple). The periods of greatest rotational modulation are shaded. Note the sparse HIRES coverage in the last shaded region, where the signal of the 66-day signal is strongest in both RV and $I_{H\alpha}$.

focus of additional scrutiny. Magnetic activity that impedes the local convective velocity in solar-type stars is invariably accompanied by a dark starspot, so the low contrast of spots in the ARs of Barnard's star and GJ 581 may be a feature unique to low-mass stars. More robust theoretical modeling of magnetohydrodynamics in the atmospheres of old, low-mass stars is required to fully understand this phenomenon.

GJ 581d and (the now less widely believed to exist) GJ 581 g were considered to be among the first exoplanets likely to host habitable environments if they were rocky (*7*, *15*). Given the small number of habitable-zone (HZ) (*25*) planets discovered by Doppler surveys around M dwarfs, the removal of GJ 581d affects the RV-based estimate of $\eta_\oplus$ (the fraction of stars hosting low-mass planets in their HZs) around M stars. This has been estimated as $\eta_\oplus = 0.41^{+0.54}_{-0.13}$ by the HARPS M dwarf survey (*26*). The exclusion of GJ 581d reduces the rate to 33%, still within the stated error limits. More precise estimates of $\eta_\oplus$ for M stars from Kepler exist [e.g., (*5*)], but the various HZ limits used by these estimates prevent direct comparison. Although GJ 581 may still be dynamically capable of accommodating terrestrial-mass planets in its HZ, we see no evidence at this time for additional planets in the activity-corrected residuals around our three-planet model.

REFERENCES AND NOTES

1. X. Bonfils *et al*., *Astron. Astrophys.* **443**, L15–L18 (2005).
2. S. Udry *et al*., *Astron. Astrophys.* **469**, L43–L47 (2007).
3. M. Mayor *et al*., *Astron. Astrophys.* **507**, 487–494 (2009).
4. J.-F. Lestrade *et al*., *Astron. Astrophys.* **548**, A86 (2012).
5. C. D. Dressing, D. Charbonneau, *Astrophys. J.* **767**, 95 (2013).
6. R. K. Kopparapu, *Astrophys. J. Lett.* **767**, L8 (2013).
7. S. S. Vogt *et al*., *Astrophys. J.* **723**, 954–965 (2010).
8. T. Forveille *et al*., ArXiv 1109.2505 (2011); http://arxiv.org/abs/1109.2505.
9. S. S. Vogt, R. P. Butler, N. Haghighipour, *Astron. Nachr.* **333**, 561–575 (2012).
10. P. C. Gregory, *Mon. Not. R. Astron. Soc.* **415**, 2523–2545 (2011).
11. R. V. Baluev, *Mon. Not. R. Astron. Soc.* **429**, 2052–2068 (2013).
12. A. P. Hatzes, *Astron. Nachr.* **334**, 616–624 (2013).
13. M. Tadeu dos Santos, G. G. Silva, S. Ferraz-Mello, T. A. Michtchenko, *Celestial Mech. Dyn. Astron.* **113**, 49–62 (2012).
14. F. Selsis *et al*., *Astron. Astrophys.* **476**, 1373–1387 (2007).
15. R. D. Wordsworth *et al*., *Astrophys. J. Lett.* **733**, L48 (2011).
16. D. A. Joiner, C. Sul, D. Dragomir, S. R. Kane, M. E. Kress, *Astrophys. J.*, ArXiv 1404.4381 (2014).
17. P. Robertson, M. Endl, W. D. Cochran, S. E. Dodson-Robinson, *Astrophys. J.* **764**, 3 (2013).
18. R. F. Díaz, C. Cincunegui, P. J. D. Mauas, *Mon. Not. R. Astron. Soc.* **378**, 1007–1018 (2007).
19. M. Zechmeister, M. Kürster, *Astron. Astrophys.* **496**, 577–584 (2009).
20. W. H. Jefferys, M. J. Fitzpatrick, B. E. McArthur, *Celestial Mech.* **41**, 39–49 (1988).
21. S. Meschiari *et al*., *Publ. Astron. Soc. Pac.* **121**, 1016–1027 (2009).
22. M. Kürster *et al*., *Astron. Astrophys.* **403**, 1077–1087 (2003).
23. K. G. Stassun, K. M. Kratter, A. Scholz, T. J. Dupuy, *Astrophys. J.* **756**, 47 (2012).
24. I. Boisse, X. Bonfils, N. C. Santos, *Astron. Astrophys.* **545**, A109 (2012).
25. R. K. Kopparapu *et al*., *Astrophys. J.* **765**, 131 (2013).
26. X. Bonfils *et al*., *Astron. Astrophys.* **549**, A109 (2013).

ACKNOWLEDGMENTS

We acknowledge support from NSF grants AST-1006676, AST-1126413, AST-1310885, The Penn State Astrobiology Research Center, and the NASA Astrobiology Institute (NNA09DA76A) in our pursuit of precise RVs in the near infrared. This work was supported by funding from the Center for Exoplanets and Habitable Worlds. The Center for Exoplanets and Habitable Worlds is supported by the Pennsylvania State University, the Eberly College of Science, and the Pennsylvania Space Grant Consortium. M.E. is supported by NASA through the Origins of Solar Systems Program grant NNX09AB30G and grant AST-1313075 from the NSF. This research has made use of the Keck Observatory Archive (KOA), which is operated by the W. M. Keck Observatory and the NASA Exoplanet Science Institute (NExScI), under contract with the National Aeronautics and Space Administration. We thank C. Bender for assistance in studying telluric absorption in the vicinity of Hα. The data produced for this study are included in table S3 of the supplementary materials.

SUPPLEMENTARY MATERIALS

www.sciencemag.org/content/345/6195/440/suppl/DC1
Materials and Methods
Figs. S1 to S10
Tables S1 to S3
References (*27*–*32*)

12 March 2014; accepted 17 June 2014
Published online 3 July 2014;
10.1126/science.1253253

PALEOCLIMATE

Synchronization of North Pacific and Greenland climates preceded abrupt deglacial warming

Summer K. Praetorius* and Alan C. Mix

Some proposed mechanisms for transmission of major climate change events between the North Pacific and North Atlantic predict opposing patterns of variations; others suggest synchronization. Resolving this conflict has implications for regulation of poleward heat transport and global climate change. New multidecadal-resolution foraminiferal oxygen isotope records from the Gulf of Alaska (GOA) reveal sudden shifts between intervals of synchroneity and asynchroneity with the North Greenland Ice Core Project (NGRIP) $\delta^{18}O$ record over the past 18,000 years. Synchronization of these regions occurred 15,500 to 11,000 years ago, just prior to and throughout the most abrupt climate transitions of the last 20,000 years, suggesting that dynamic coupling of North Pacific and North Atlantic climates may lead to critical transitions in Earth's climate system.

Abrupt climate transitions observed during the last deglaciation (*1*, *2*) and within the last glacial interval (*3*) demonstrate that internal climate feedbacks can amplify the effects of relatively weak external climate forcing. Understanding the mechanisms involved in generating past abrupt transitions, which have led to regional warming events of ~10°C within 3 to 60 years (*2*), will help to assess the dynamic nature of climate tipping points.

Fluctuations in the Atlantic Meridional Overturning Circulation (AMOC) are often invoked to explain millennial-scale climate changes in the North Atlantic region (*4*–*6*), as well as the so-called bipolar seesaw, which reflects changes in net oceanic heat transport between the southern and northern hemispheres (*7*, *8*). An interocean seesaw also has been proposed to operate between the North Atlantic and North Pacific, such that poleward heat transport and/or deep-water formation increases in the North Pacific during times of weakened AMOC strength (*9*–*11*). This remains uncertain, however, because models show conflicting responses for the North Pacific (*10*–*13*). Paleoclimate reconstructions are similarly in conflict; some support an interocean seesaw (*9*, *11*, *14*), whereas others suggest in-phase behavior between the North Atlantic and North Pacific (*15*, *16*), and still other studies suggest a blend of northern (atmospheric) and southern (oceanic) influences (*17*, *18*). If an Atlantic-Pacific seesaw exists, low northward heat transport in one ocean might be partly compensated by high northward heat transport in the other. Conversely, synchronous variations in the two oceans would tend to amplify climate changes in the high northern latitudes by either enhancing or diminishing meridional heat transport.

Changes in the AMOC and Arctic sea ice have been identified as "tipping elements" in the climate system (*19*); both are influenced by poleward heat transport and have the potential for rapid transitions (10 to 100 years) to a new climate state, accompanied by climate and ecosystem effects that are to some degree irreversible (*19*). Several diagnostic signs of approach to a tipping point have been proposed, including enhanced spatial correlation (i.e., interconnection or dynamic coupling), increase in short-term variability (i.e., flickering), and critical slowing down (i.e., increased autocorrelation) (*20*–*22*). Some paleoclimate records document flickering and enhanced variance preceding the abrupt onset of Holocene and Bølling warmth (*23*, *24*), but evidence for increased autocorrelation before these transitions has been mixed (*20*, *24*, *25*), leading to debate as to whether these transitions are true climate bifurcations (*24*). No paleoclimate records have yet shown symptoms of dynamic coupling (see supplementary materials for illustrative model). Here, we document the onset of enhanced correlation between North Pacific and North Atlantic climate variability that shortly precedes the most abrupt warming events of the last deglaciation.

College of Earth, Ocean, and Atmospheric Sciences, Oregon State University, Corvallis, OR 97331, USA.
***Corresponding author: E-mail: spraetor@coas.oregonstate.edu**

This new finding supports the idea that these abrupt transitions were unstable tipping points and points to a possible mechanism that could have pushed the system toward a climatic bifurcation.

We developed a high-resolution planktonic foraminiferal $\delta^{18}O$ record as a composite from three sediment cores in the Gulf of Alaska (GOA) spanning the last 18,000 years (Fig. 1 and fig. S4). Exceptionally high sedimentation rates provide sample resolutions similar to that of polar ice cores; average sample spacing is ~80 years in the Holocene [0 to 11 thousand years ago (ka)], ~10 years in the deglacial interval (11 to 14.6 ka), and ~35 years during late glacial time (14.7 to 18 ka). Age controls include 39 planktonic foraminiferal radiocarbon dates, and a marine reservoir age constrained by a tephra deposit dated on land (see supplementary materials).

The GOA $\delta^{18}O$ record integrates local temperature, salinity, and global ice volume signals, whereas the North Greenland Ice Core Project (NGRIP) $\delta^{18}O$ record (*26*) reflects local temperature, moisture transport, and global ice volume. The temperature component of these $\delta^{18}O$ records is inversely related (in marine carbonates higher $\delta^{18}O$ is colder, whereas in ice cores lower $\delta^{18}O$ is colder); therefore, a high negative correlation implies synchronization. The cross correlation was evaluated in moving time windows for the raw records, as well as for ice-volume–corrected, and low-pass– and

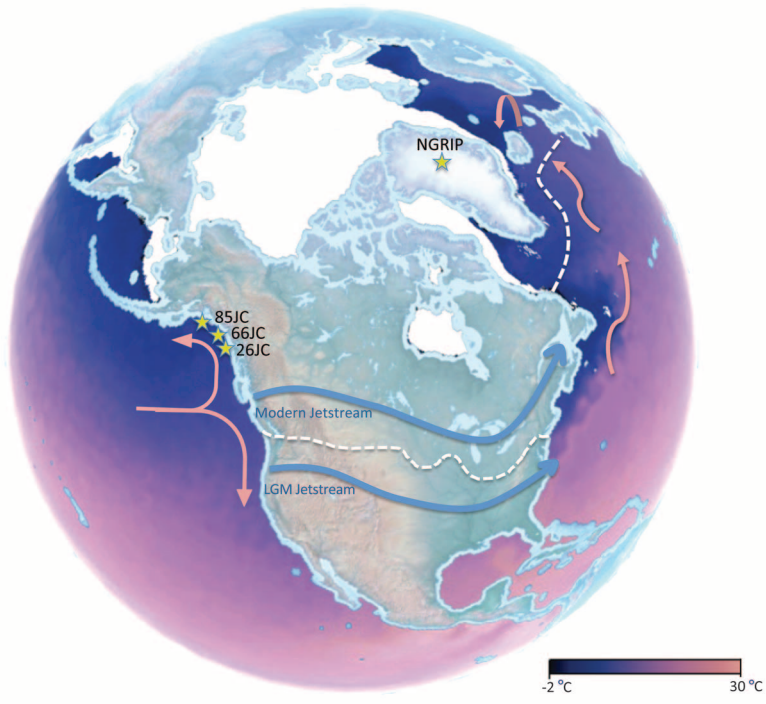


Fig. 1. Map of Gulf of Alaska and NGRIP core locations. Base map shows average sea surface temperature and sea-ice extent for December, 1985 to 2005 (neo.sci.gsfc.nasa.gov). Pink arrows depict surface currents, with overturning indicated in the Norwegian seas. Dashed white line across North America depicts the approximate extent of the Laurentide ice sheet (LIS) during the Last Glacial Maximum (LGM) (*45*). Dashed white line across the North Atlantic depicts the extension of winter sea ice during the LGM (*46*). Changes in the height and extent of the LIS and sea-ice margins could have affected the atmospheric pathways connecting the GOA and Greenland. Blue arrows across North America represent the schematic differences in the position of the jetstream between the modern and LGM climate states.

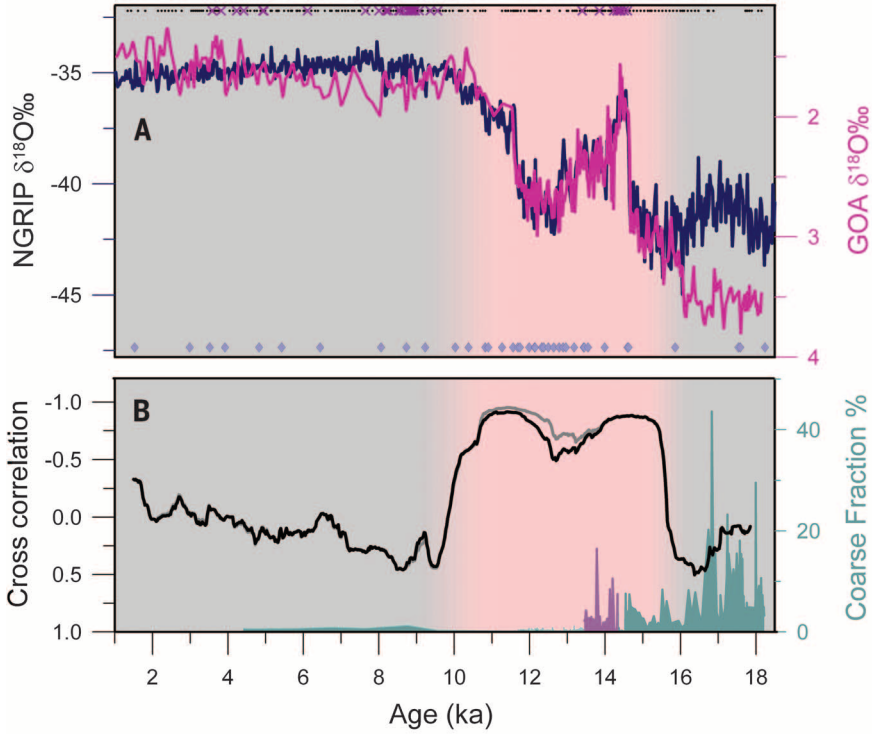


Fig. 2. Comparison of GOA and NGRIP climate variability. (**A**) The 25-year linearly interpolated GOA $\delta^{18}O$ record (rose line, inverted axis) is plotted with the NGRIP $\delta^{18}O$ record (dark blue) (*26*). Radiocarbon age controls plotted as blue diamonds. The purple Xs near the top of the plot indicate times when the subtropical planktonic species *O. universa* was present in the faunal assemblages, whereas the black dots indicate samples in which they were not present. (**B**) A 2000-year moving windowed cross correlation between the records is shown for the original GOA age model (black line, inverted axis) and for an alternative age model that is tuned to Greenland (gray line). The pink shading represents the time period of synchronization between records (see Fig. 3 for expanded view), whereas the gray shading reflects times with either no significant correlation or a seesaw-like mode between records. The coarse fraction percent [green shading in (B)] is dominated by IRD from 18.5 to 14.7 ka and virtually disappears near the onset of the Bølling. The peaks in coarse fraction from 14.5 to 13.5 ka are all dominated by volcanic ash in the sediments (purple shading).

high-pass–filtered deconvolutions of the data. Although we cannot exclude local salinity effects in the GOA record, alkenone paleotemperature reconstructions from the North Pacific and Bering Sea track planktonic foraminiferal $\delta^{18}O$, indicating that a large component of the North Pacific $\delta^{18}O$ changes reflect upper-ocean temperature (*16*, *27*, *28*) (fig. S7). Similarly, NGRIP $\delta^{18}O$ covaries with marine paleotemperature records from the subpolar North Atlantic (*29*) (fig. S7).

The GOA $\delta^{18}O$ and NGRIP $\delta^{18}O$ are positively correlated (temperatures inversely related) from 17.5 to 15.5 ka (equivalent in time to Atlantic Heinrich Stadial 1, HS1) (Fig. 2). The NGRIP $\delta^{18}O$ record documents a warming trend from 18 to 16 ka, followed by a cooling from 16 to 15 ka. The GOA record shows high $\delta^{18}O$ values (colder and/or saltier) from 18 to 16 ka, and the onset of warming and/or freshening starting around 16 ka. Abundant ice-rafted debris (IRD) in the GOA sediments during this interval documents a sustained input of icebergs, which would tend to decrease the local surface salinity and $\delta^{18}O$ through the addition of meltwater. Therefore, the relatively high $\delta^{18}O$ during an interval of enhanced IRD delivery indicates that North Pacific temperatures remained cold until 16 ka. IRD deposition peaked in the GOA from 17.5 to 16.5 ka, consistent with other observations in the North Pacific (*14*, *18*) and coincident with the timing of Heinrich Event 1 (H1) in the North Atlantic (*30*).

Initial GOA warming at 16 ka coincides with the shift from the "Big Dry" to "Big Wet" events in western North America (*31*), supporting a role for enhanced North Pacific heat and moisture transport to the Great Basin Lakes. This GOA warming also coincides with a pause of Antarctic warming from 16 to 15.5 ka (*8*) and a slowing of atmospheric CO_2 rise from 16 to 14.5 ka (*32*, *33*). North Pacific diatom species in the Bering Sea imply sea-ice retreat at ~16 ka (*27*), coincident with a pullback of Arctic sea ice (*34*).

Starting at ~15.5 ka, several hundred years before abrupt warming into the Bølling Interstade at 14.6 ka, NGRIP and GOA $\delta^{18}O$ become synchronized (highly negatively correlated; Fig. 2). The negative correlation persists until ~11 ka, with a near one-to-one correlation for the intervals that encompass the abrupt warming transitions into the Bølling and Holocene interstadials. Disappearance of IRD at the onset of the Bølling Interstade in the GOA records indicates rapid retreat of Cordilleran outlet glaciers onto land at 14.8 ka (*18*). The presence of the subtropical planktonic foraminiferal species *Orbulina universa* in the faunal assemblages of the GOA record during the Bølling and early Holocene suggests that these intervals were warmer than today and involved the incursion of water masses from the south (*35*). Such warm events in the GOA coincide with intervals of high meridional overturning in the North Atlantic (*6*), implying that poleward heat transport increased in both oceans during these times.

After the abrupt warming into the Bølling Interstade (14.7 to 14.1 ka), the GOA and NGRIP $\delta^{18}O$ records remain synchronized but with a weaker negative correlation (from –0.5 to –0.8) during stepwise cooling events within the Allerød (14.1 to 12.9 ka) and Younger Dryas (YD; 12.9 to 11.7 ka) intervals, reflecting slight offsets in the timing of these events between records (see supplementary materials). An alternative age model based on tuning the GOA record to the NGRIP record (without violating the ash date) results in only minor changes to the original age model (Fig. 3) and improves the cross correlation between the GOA and NGRIP records throughout this interval (from –0.65 to –0.90; Fig. 2). Variations in marine reservoir of up to 200 years are plausible and within the range of modern spatial variability, but the combination of the ash date on land and the close correlation between GOA and Greenland preclude larger surface-ocean reservoir ages in this interval (Fig. 3).

GOA and NGRIP again become highly synchronized (r = –0.90) just before abrupt warming into the Holocene. After this warming, the windowed

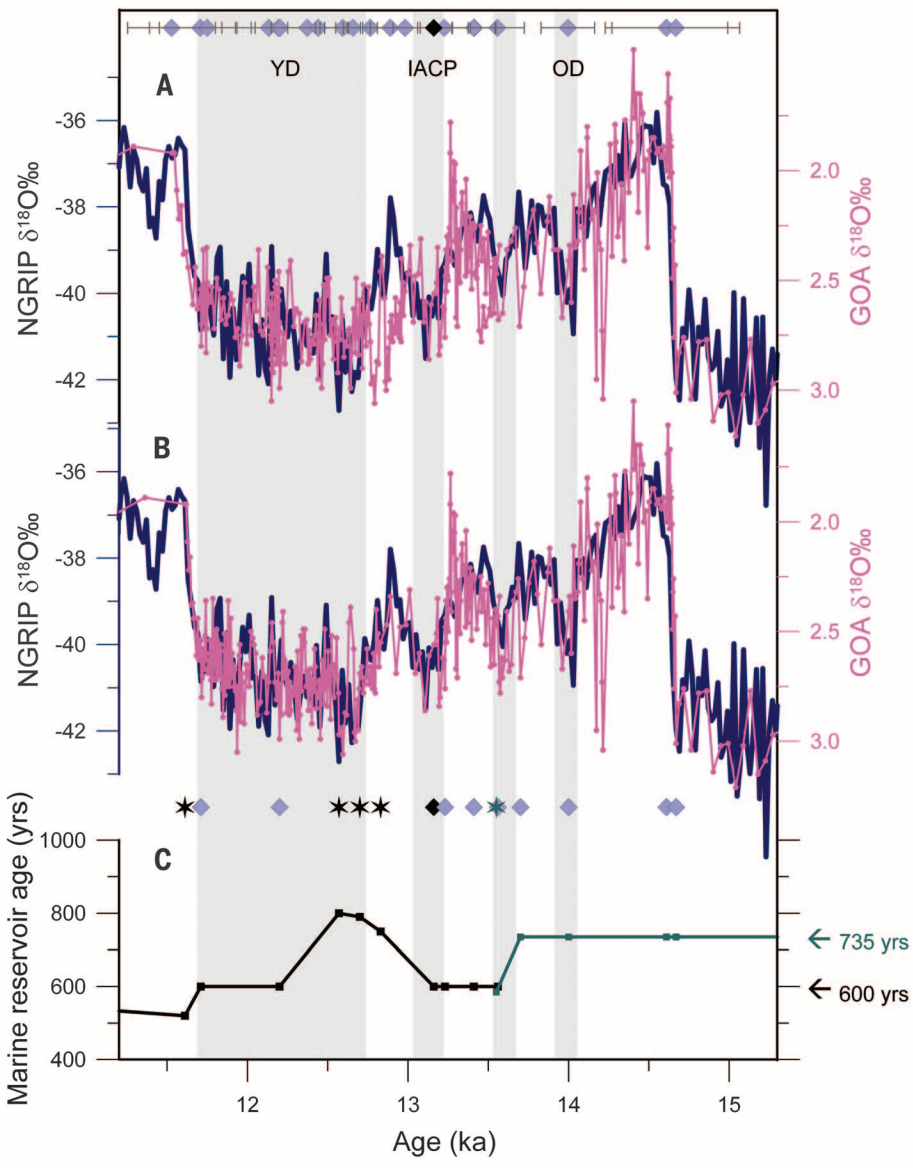


Fig. 3. Age model tuning. (**A** and **B**) Comparison of the raw GOA data (pink, inverted axis) with the 20-year NGRIP record (dark blue) (*26*) on the original age model (A) and on an age model that is tuned to the NGRIP record (B). The blue diamonds in (A) represent radiocarbon age controls with ±2σ uncertainty, and the black diamond indicates the MEd tephra layer (see supplementary materials). The age controls for the tuned record are shown in (B), with the tie points to the NGRIP record shown as black stars for core EW0408-66JC and a green star for core EW0408-26JC. The blue diamonds are the retained radiocarbon age controls from the original age model, and the black diamond is the MEd tephra layer. (**C**) Changes in marine reservoir age that result from the difference in the original and tuned age models for core EW0408-66JC (black) and EW0408-26JC (green). These differences are within the combined uncertainty of the two age models. The gray bars encompass the major climate reversals in the NGRIP record: YD: Younger Dryas, IACP: Inter-Allerød Cold Period, OD: Older Dryas.

correlation between GOA and NGRIP changes sign at ~10 ka, suggesting a return to Pacific-Atlantic seesaw or decoupled behavior in an interglacial state similar to that of late-glacial time. Within the Holocene, asynchronous behavior includes cooling of GOA from 10 to 8 ka, followed by gradual warming; in opposition to this pattern, cooling in NGRIP is initiated after 8 ka and persists throughout the Holocene. Ice-volume–corrected, low-pass–filtered $\delta^{18}O$ records show a more pronounced seesaw pattern (high positive correlation) in the Holocene and HS1 than the raw or high-pass records (Fig. 4). This suggests that the long-term (>2000 years) trends are inversely related during these times, but the short-term variability is either not sufficiently resolved or decoupled between basins during the Holocene and HS1.

Variance increases within the GOA and NGRIP records before the abrupt warming transitions into the Bølling and Holocene (Fig. 4). High-frequency variance in the GOA peaks from 15 to 11.5 ka, coincident with the interval of synchronization, whereas in NGRIP high-frequency variance peaks slightly earlier. Both records show greater short-term variance during abrupt warming into the Bølling relative to the later warming into the Holocene, suggesting that earlier warming, beginning from relatively extreme glacial conditions, was the more abrupt climatic event in these two locations.

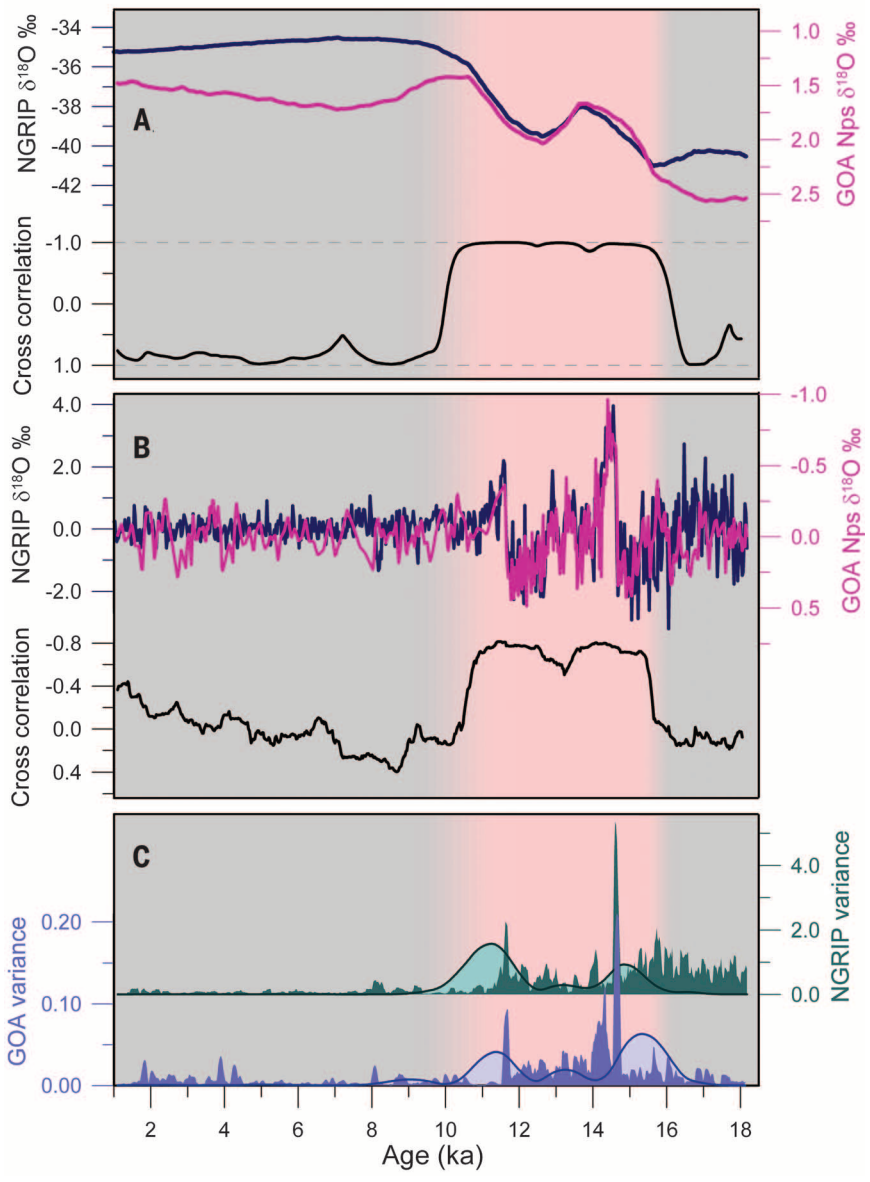


Fig. 4. Low-pass– and high-pass–filtered data. (**A** and **B**) Evaluation of the cross correlation between the ice-volume–corrected, low-pass–filtered [2000-year moving average (A)] and high-pass–filtered records [residuals from 2000-year moving average (B)] of NGRIP (dark blue) (*26*) and GOA on the tuned age model (rose, inverted axis). The 2000-year moving window cross correlation between the GOA and NGRIP records are shown in black for the low-pass– (A) and high-pass–filtered (B) records. Dashed gray lines in (A) reflect one-to-one positive and negative correlations. (**C**) Panel shows the variance for the high-pass and low-pass records. A 200-year windowed variance is shown for NGRIP (dark green) and GOA (dark blue) for the high-pass records, and a 2000-year windowed variance is shown for NGRIP (light green) and GOA (light blue). The transitions into the Bølling and Holocene are clearly identifiable in the peaks in the high-pass variance and the abrupt shifts in the $\delta^{18}O$ records at 14.7 and 11.7 ka.

Thus, we find evidence for intervals of both synchronous and asynchronous climate variability between the GOA and NGRIP regions. Synchronization and an increase in variance preceded and extended through abrupt warming events, consistent with theory that highly connected systems are more susceptible to unstable tipping points (*21*) (see supplementary materials). Possible mechanisms to regulate the modes of connectivity between regions could be related to (i) ice elevation in North America, (ii) the opening of Bering Strait, or (iii) routing of fresh water in the North Atlantic or Southern Ocean. During the Last Glacial Maximum (LGM), topographic steering of the jetstream around an expanded North American ice sheet and sea-ice margin would have reduced the direct atmospheric connection between the GOA and Greenland (*36*, *37*). A gradual fall in ice height following H1 could have caused an abrupt reorganization of atmospheric circulation that set up a stronger meridional flow in the North Atlantic (*38*), thereby strengthening the interocean atmospheric coupling (Fig. 1). Linkages between the North Pacific and North Atlantic may also depend on whether the Bering Strait is open or closed (*10*, *13*, *39*), which could signal a role for the incursion of low-salinity waters from the Arctic in the reversion to interocean seesaw during the early Holocene (*40*). Alternatively, models suggest that freshwater forcing near West Antarctica triggers synchronous warming in the North Pacific and North Atlantic (*41*), whereas meltwater inputs near Greenland create antiphased responses in the North Atlantic and North Pacific (*10*, *11*).

The last glacial termination demonstrates several symptoms of threshold behavior, including greater spatial organization through synchronization of the North Pacific and Greenland/North Atlantic variability (this study), elevated variance [this study and (*23*, *24*)], and enhanced autocorrelation of some climatic indicators just before the abrupt Bølling and Holocene transitions (*20*, *25*). The new highly resolved evidence we present here for interocean dynamic coupling between the NGRIP record in the Atlantic sector and GOA records in the Pacific Sector suggests that synchronization of poleward heat transport in both oceans is an important catalyst for abrupt warming transitions within the Northern Hemisphere. Although a tipping point may be crossed in an instant, large-scale climate systems that include ice sheets or deep ocean circulation may have substantial inertia, such that the full response may play out dynamically over an extended period of time, constituting a "tipping interval."

In the modern climate system, models suggest a tight coupling of short-term (<200 years) ocean-atmosphere interactions between the North Pacific

and North Atlantic and indicate the potential for amplification of decadal-scale variability through interbasin resonance (*42*, *43*). Before the 1970s, variability in poleward heat fluxes and storm tracks in the North Pacific and North Atlantic regions were uncorrelated; more recently, highly correlated behavior has emerged (*44*). Our study documents that the development of such teleconnected variability between these regions is a fundamentally important phenomenon associated with rapid warming, suggesting that such properties may be high-priority targets for detailed monitoring in the future.

REFERENCES AND NOTES

1. R. B. Alley *et al.*, *Nature* **362**, 527–529 (1993).
2. J. P. Steffensen *et al.*, *Science* **321**, 680–684 (2008).
3. W. Dansgaard *et al.*, *Nature* **364**, 218–220 (1993).
4. W. S. Broecker, D. M. Peteet, D. Rind, *Nature* **315**, 21–26 (1985).
5. P. U. Clark *et al.*, *Science* **293**, 283–287 (2001).
6. J. F. McManus, R. Francois, J.-M. Gherardi, L. D. Keigwin, S. Brown-Leger, *Nature* **428**, 834–837 (2004).
7. W. S. Broecker, *Paleoceanography* **13**, 119–121 (1998).
8. J. B. Pedro *et al.*, *Clim. Past* **7**, 671–683 (2011).
9. D. C. Lund, A. C. Mix, *Paleoceanography* **13**, 10–19 (1998).
10. O. A. Saenko, A. Schmittner, A. J. Weaver, *J. Clim.* **17**, 2033–2038 (2004).
11. Y. Okazaki *et al.*, *Science* **329**, 200–204 (2010).
12. A. Timmermann, F. Justino, F.-F. Jin, U. Krebs, H. Goosse, *Clim. Dyn.* **23**, 353–370 (2004).
13. Y. M. Okumura, C. Deser, A. Hu, A. Timmermann, S. P. Xie, *J. Clim.* **22**, 1424–1445 (2009).
14. H. Gebhardt *et al.*, *Paleoceanography* **23**, PA4212 (2008).
15. J. P. Kennett, L. B. Ingram, *Nature* **377**, 510–514 (1995).
16. L. Max *et al.*, *Paleoceanography* **27**, PA3213 (2012).
17. A. C. Mix *et al.*, *Geophys. Monogr.* **112**, 127–148 (1999).
18. M. H. Davies *et al.*, *Paleoceanography* **26**, PA2223 (2011).
19. T. M. Lenton *et al.*, *Proc. Natl. Acad. Sci. U.S.A.* **105**, 1786–1793 (2008).
20. V. Dakos *et al.*, *Proc. Natl. Acad. Sci. U.S.A.* **105**, 14308–14312 (2008).
21. V. Dakos, E. H. van Nes, R. Donangelo, H. Fort, M. Scheffer, *Theor. Ecol.* **3**, 163–174 (2010).
22. M. Scheffer *et al.*, *Science* **338**, 344–348 (2012).
23. J. Bakke *et al.*, *Nat. Geosci.* **2**, 202–205 (2009).
24. T. M. Lenton, V. N. Livina, V. Dakos, M. Scheffer, *Clim. Past.* **8**, 1127–1139 (2012).
25. V. N. Livina, T. M. Lenton, *Geophys. Res. Lett.* **34**, L03712 (2007).
26. S. O. Rasmussen *et al.*, *J. Geophys. Res.* **111**, D06102 (2006).
27. B. E. Caissie, J. Brigham-Grette, K. T. Lawrence, T. D. Herbert, M. S. Cook, *Paleoceanography* **25**, PA1206 (2010).
28. J. A. Barron, L. Heusser, T. Herbert, M. Lyle, *Paleoceanography* **18**, PA1020 (2003).
29. C. Waelbroeck *et al.*, *Nature* **412**, 724–727 (2001).
30. E. Bard, F. Rostek, J. L. Turon, S. Gendreau, *Science* **289**, 1321–1324 (2000).
31. W. Broecker, A. E. Putnam, *Quat. Sci. Rev.* **57**, 17–25 (2012).
32. E. Monnin *et al.*, *Earth Planet. Sci. Lett.* **224**, 45–54 (2004).
33. B. Lemieux-Dudon *et al.*, *Quat. Sci. Rev.* **29**, 8–20 (2010).
34. T. M. Cronin *et al.*, *Quat. Sci. Rev.* **29**, 3415–3429 (2010).
35. H. Asahi, K. Takahashi, *Prog. Oceanogr.* **72**, 343–363 (2007).
36. F. Justino, A. Timmermann, U. Merkel, E. P. Souza, *J. Clim.* **18**, 2826–2846 (2005).
37. F. S. R. Pausata, C. Li, J. J. Wettstein, M. Kageyama, K. H. Nisancioglu, *Clim. Past* **7**, 1089–1101 (2011).
38. D. J. Ullman, A. N. LeGrande, A. E. Carlson, F. S. Anslow, J. M. Licciardi, *Clim. Past* **10**, 487–507 (2014).
39. G. Shaffer, J. Bendtsen, *Nature* **367**, 354–357 (1994).
40. M. H. Davies *et al.*, *Earth Planet. Sci. Lett.* **397**, 57–66 (2014).
41. A. J. Weaver, O. A. Saenko, P. U. Clark, J. X. Mitrovica, *Science* **299**, 1709–1713 (2003).
42. L. Wu, Z. Liu, *J. Clim.* **18**, 331–349 (2005).
43. C. Li, L. Wu, Q. Wang, L. Qu, L. Zhang, *Clim. Dyn.* **32**, 753–765 (2009).
44. E. K. M. Chang, *J. Clim.* **17**, 4230–4244 (2004).
45. A. S. Dyke, in *Quaternary Glaciations: Extent and Chronology*, J. Ehlers, P. L. Gibbard, Eds. (Elsevier, Amsterdam, 2004), pp. 373–424.
46. M. Sarnthein, U. Plaufmann, M. Weinelt, *Paleoceanography* **18**, 1047 (2003).

ACKNOWLEDGMENTS

We thank B. Jensen and D. Froese for the tephra analyses; J. Southon for assistance with radiocarbon samples; A. Ross, J. Padman, and J. McKay of the College of Earth, Ocean and Atmospheric Sciences Stable Isotope Lab; and five anonymous reviewers. This work was supported by NSF grants AGS-0602395 (Project PALEOVAR) and OCE-1204204 to A.C.M., and an NSF graduate research fellowship to S.K.P. The data can be found in the supplementary online materials and at the National Oceanic and Atmospheric Administration Paleoclimate Database.

SUPPLEMENTARY MATERIALS

www.sciencemag.org/content/345/6195/444/suppl/DC1
Materials and Methods
Supplementary Text
Figs. S1 to S11
Tables S1 and S2
References (*47*–*66*)

10 February 2014; accepted 24 June 2014
10.1126/science.1252000

INDUCED EARTHQUAKES

Sharp increase in central Oklahoma seismicity since 2008 induced by massive wastewater injection

K. M. Keranen,[1]* M. Weingarten,[2] G. A. Abers,[3]† B. A. Bekins,[4] S. Ge[2]

Unconventional oil and gas production provides a rapidly growing energy source; however, high-production states in the United States, such as Oklahoma, face sharply rising numbers of earthquakes. Subsurface pressure data required to unequivocally link earthquakes to wastewater injection are rarely accessible. Here we use seismicity and hydrogeological models to show that fluid migration from high-rate disposal wells in Oklahoma is potentially responsible for the largest swarm. Earthquake hypocenters occur within disposal formations and upper basement, between 2- and 5-kilometer depth. The modeled fluid pressure perturbation propagates throughout the same depth range and tracks earthquakes to distances of 35 kilometers, with a triggering threshold of ~0.07 megapascals. Although thousands of disposal wells operate aseismically, four of the highest-rate wells are capable of inducing 20% of 2008 to 2013 central U.S. seismicity.

Seismicity in the United States midcontinent surged beginning in 2008 (*1*), predominantly within regions of active unconventional hydrocarbon production (*2*–*6*). In Arkansas, Texas, Ohio, and near Prague, Oklahoma, recent earthquakes have been linked to wastewater injection (*2*–*7*), although alternative interpretations have been proposed (*1*, *8*). Conclusively distinguishing human-induced earthquakes solely on the basis of seismological data remains challenging.

Seismic swarms within Oklahoma dominate the recent seismicity in the central and eastern United States (*9*), contributing 45% of magnitude (M) 3 and larger earthquakes between 2008 and 2013 (*10*). No other state contributed more than 11%. A single swarm, beginning in 2008 near Jones, Oklahoma, accounts for 20% of seismicity in this region (*10*). East of Jones, the damaging 2011 moment magnitude (M_w) 5.7 earthquake near Prague, Oklahoma, was likely induced by wastewater injection (*2*, *8*, *11*, *12*), the highest magnitude to date. These earthquakes are part of a 40-fold increase in seismicity within Oklahoma during 2008 to 2013 as compared to 1976 to 2007 (Fig. 1, inset A) (*10*). Wastewater disposal volumes have also increased rapidly, nearly doubling in central Oklahoma between 2004 and 2008. Many studies of seismicity near disposal wells rely upon statistical relationships between the relative timing of seismicity, disposal well location, and injected water volume to evaluate a possible causal relationship (*3*–*7*, *13*).

Here we focused on the Jones swarm and compared modeled pore pressure from hydrogeological models to the best-constrained earthquake hypocenters (*14*). Using data from local U.S. Geological Survey NetQuake accelerometers, the Earthscope Transportable Array, and a small local seismic network (fig. S1), we generated a catalog of well-located earthquakes between 2010 and 2013. Event-station distances were predominantly less than 10 km (fig. S2D), and all earthquakes were recorded on at least one seismometer within 20 km of the initial hypocenter. To study pore pressure changes at earthquake hypocenters and the apparent migration in seismicity, we developed a three-dimensional hydrogeological model of pore pressure diffusion from injection wells.

The Jones swarm began within 20 km of high-rate wastewater disposal wells, among the highest rate in Oklahoma, between two regions of fluid injection (Fig. 2). The four high-rate wells are southwest of Jones in southeast Oklahoma City (SE OKC) and dispose of ~4 million barrels per month (*15*) (Fig. 3). The target injection depth is 2.2 to 3.5 km into the Cambrian-Ordovician

[1]Department of Earth and Atmospheric Sciences, Cornell University, Ithaca, NY, USA. [2]Department of Geological Sciences, University of Colorado, Boulder, CO, USA. [3]Lamont-Doherty Earth Observatory of Columbia University, Palisades, NY, USA. [4]U.S. Geological Survey, Menlo Park, CA, USA.
***Corresponding author. E-mail: keranen@cornell.edu** †Present address: Department of Earth and Atmospheric Sciences, Cornell University, Ithaca, NY, USA.

Arbuckle Group (fig. S3), a dolomitized carbonate; one disposal well ends near Precambrian basement. The large disposal wells are within dewatering plays (fig. S4). Dewatering production wells produce substantial wastewater volumes with initially up to 200 times as much water per barrel of oil as conventional production wells (*16*, *17*). The rate of wastewater disposal in central Oklahoma has gradually increased since the mid-1990s (fig. S5), but disposal rates jumped after 2004 as high-rate injection wells began operating, including the first of the SE OKC wells in 2005 (Fig. 3) (*15*). Seismic moment release escalated in the Jones swarm in 2009, concurrent with the initial reported application

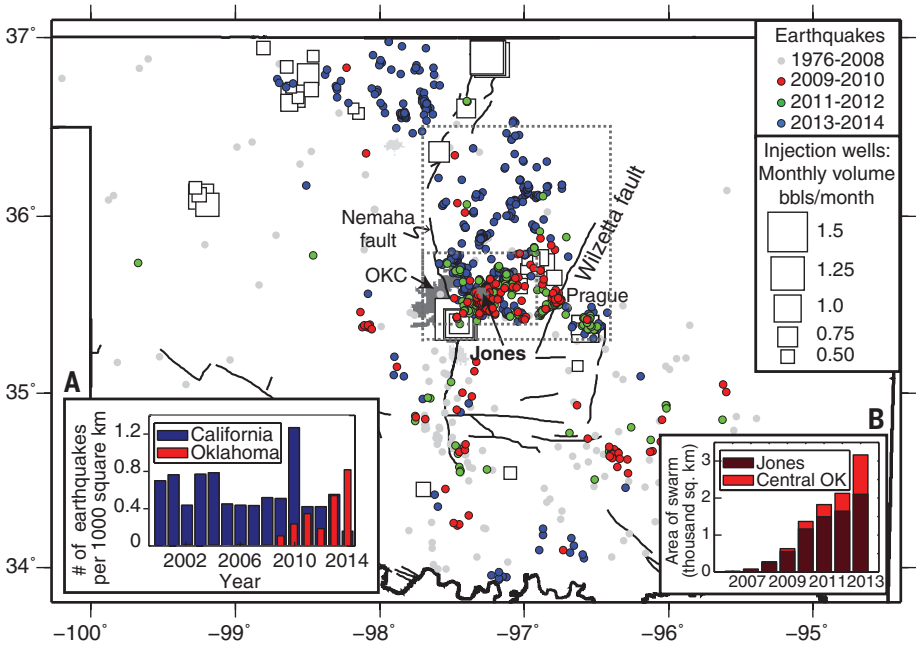


Fig. 1. Earthquakes in Oklahoma between 1976 and 2014. Earthquakes are $M > 1$ from the NEIC catalog (*10*). Black lines are faults (*26*–*28*). Small and large dashed gray boxes outline the areas used for analysis of the Jones swarm and of central Oklahoma, respectively, in inset B. OKC: Oklahoma City. **Inset A:** Comparison of *M*3+ earthquake rate in Oklahoma and California, normalized by area. California is ~2.3 times larger than Oklahoma. 2014 earthquakes are through the first 4 months. **Inset B:** Expanding area of the Jones and the broader central Oklahoma swarms. Regions were divided into 5 km by 5 km grid cells, and any cell with an earthquake was considered part of the swarm. Swarm area per year is inclusive of all prior years.

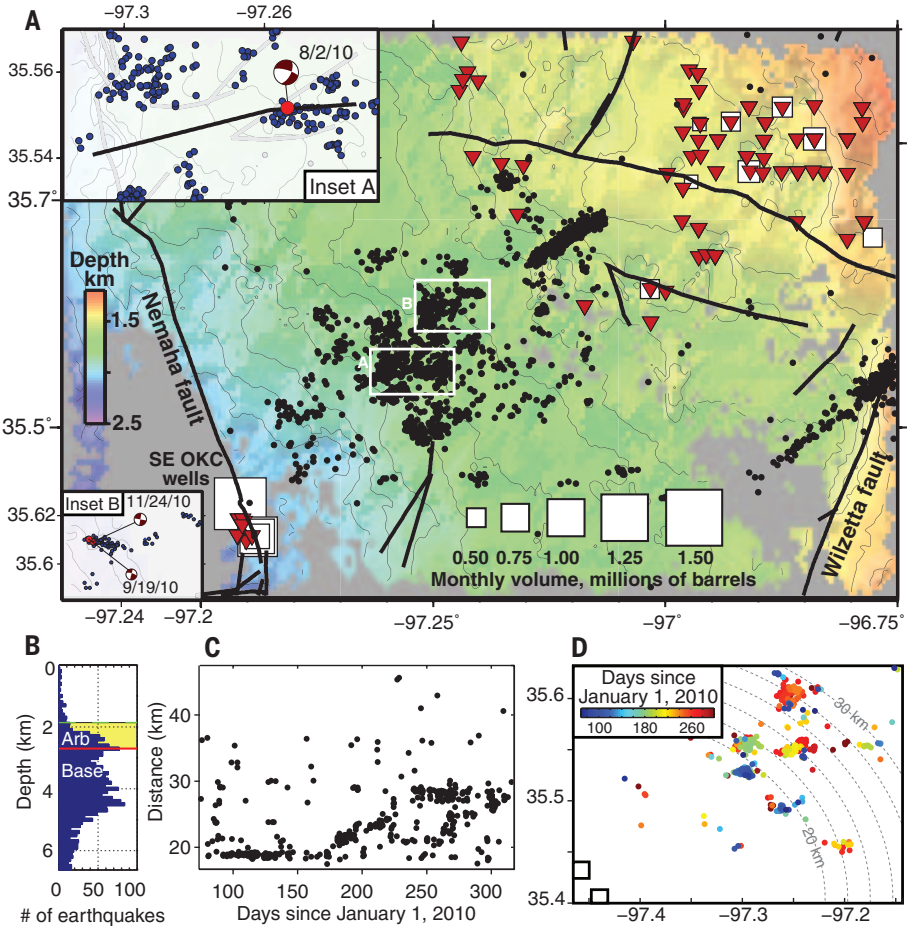


Fig. 2. Earthquake catalog and swarm migration. (**A**) Jones earthquake catalog March 2010 to March 2013 using local stations. Squares are injection wells operating at an average rate ≥ 400,000 barrels per month (*15*, *29*); triangles are high–water production wells. Background color and contours represent depth to the top of the Hunton Group (*15*). The Hunton Group is higher in section than the Arbuckle Group but has more data on formation depth. (**B**) Earthquake depth histogram; earthquakes are dominantly in sediment and upper basement. (**C**) Distance of each March to October 2010 Jones earthquake to the SE OKC disposal wells. The dense region of the swarm increases in distance between days 150 and 250 in 2010. (**D**) Map view of Jones earthquakes during March to October 2010, colored by time. Semicircles are equidistant lines from SE OKC disposal wells. Faults at greater distance from the wells become active at later times. Details of two of these fault planes are shown in insets of Fig. 2A and are discussed in the text.

of positive wellhead pressure at the SE OKC wells (Fig. 3B).

Earthquakes in our catalog primarily nucleated either within the Arbuckle Group or within the upper 2 km of basement, with 22 to 33% above basement (Fig. 2B and fig. S6). Well-constrained earthquake hypocenters from March to October 2010 migrated northeast from the initial swarm centroid near Jones at 0.1 to 0.15 km/day (Fig. 2, C and D), followed by a broad spread in seismicity. Earthquake hypocenters are not diffusely distributed; instead, relocated aftershock sequences of individual earthquakes (*18*) illuminate narrow faults parallel to one plane of calculated focal mechanisms (*19*) (Fig. 2A, insets). An earthquake on 2 August 2010 ruptured a portion of a 7-km-long mapped fault; if the entire fault had ruptured, earthquake scaling laws suggest a maximum magnitude of ~*M*6.0 (*20*). Earthquakes later in 2010 ruptured an unmapped east-southeast– to west-northwest–trending fault, at an oblique angle to the overall northeast-southwest migration direction of the swarm. Although the swarm of seismicity migrates to the northeast parallel to structural dip, the individual faults, as evidenced by earthquake lineations, are not preferentially oriented in this direction.

Our hydrogeological model simulated injection into the Arbuckle Group using reported injection rates at 89 wells within 50 km of the Jones swarm between 1995 and 2012 (*14*). The wells include the four high-rate wells in SE OKC and 85 wells to the northeast of Jones. The model predicts a region of high fluid pressure perturbation spreading radially eastward from the SE OKC wells and a lesser perturbation around the lower-rate wells to the northeast (Fig. 4). The high pore pressure increase occurs within the Arbuckle Group and in the upper 1 to 2 km of the basement in our model; nearly all earthquakes occur within this same depth range (Fig. 2B). The migrating front of the Jones earthquake swarm corresponds closely to the expanding modeled pressure perturbation away from the SE OKC wells, which reaches 25 km from the wells by December 2009 and ~35 km by December 2012. The pore pressure change modeled at each hypocenter indicates a critical threshold of ~0.07 MPa, above which earthquakes are triggered. This threshold is compatible with prior observations that static stress changes of as little as ~0.01 to 0.1 MPa are sufficient to trigger earthquakes when faults are near failure in the ambient stress field (*21*–*23*).

Our results indicate that for modeled diffusivities, ~85% of the pore pressure perturbation is contributed by the four high-rate SE OKC wells. The 85 wells to the northeast contribute ~15% additional pore pressure change at the center of the Jones swarm by the end of 2012 and may contribute to the triggering of earthquakes particularly outside the region affected by the SE OKC wells (fig. S7). The modeled dominance of the SE OKC wells is attributable to their high rate; these wells include one of the largest wells in the state and three closely spaced wells 3.5 km away with a combined monthly volume of ~3 million barrels per month. The only other Oklahoma wells of similar size, in northern Oklahoma (fig. S8), are on the boundary of a second rapidly growing seismic swarm (Fig. 1). The summed rate of this well cluster near SE OKC is higher than previous cases of reported induced seismicity (Fig. 3A), including several times higher than the high-rate disposal wells linked to earthquakes near Dallas–Fort Worth, Texas, and Cleburne, Texas (*5*–*7*). Comprehensive compilations of injection well rates for other high-injection states, including Texas and California, are not yet accessible.

We view the expanding Jones earthquake swarm as a response to regionally increased pore pressure from fluids primarily injected at the SE OKC wells. As the pressure perturbation expanded and encountered faults at various orientations, critically stressed, optimally oriented faults are expected to rupture first (*24*). Additional faults at near-optimal orientations may rupture after further pressure increase (Fig. 4). As fluid pressure continues to

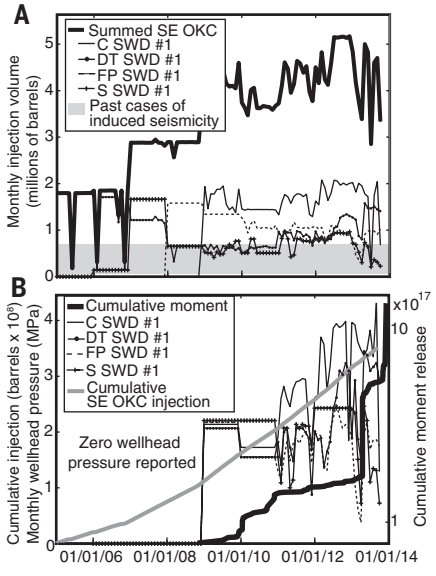


Fig. 3. Fluid injection reported in the four high-rate SE OKC wells. (**A**) Sum and individual monthly injection volumes and (**B**) wellhead pressure and cumulative, summed injected volume (*15*). The DT SWD #1, FP SWD #1, and S SWD #1 wells are in close proximity; the C SWD #1 well is ~3.5 km away. Gray shading denotes injection rates for notable past cases of induced seismicity for reference (table S1). Cumulative seismic moment in (B) is calculated from *M*3+ earthquakes from 2005 to January 2014 (*10*) for earthquakes within the box outlining the Jones swarm in Fig. 1.

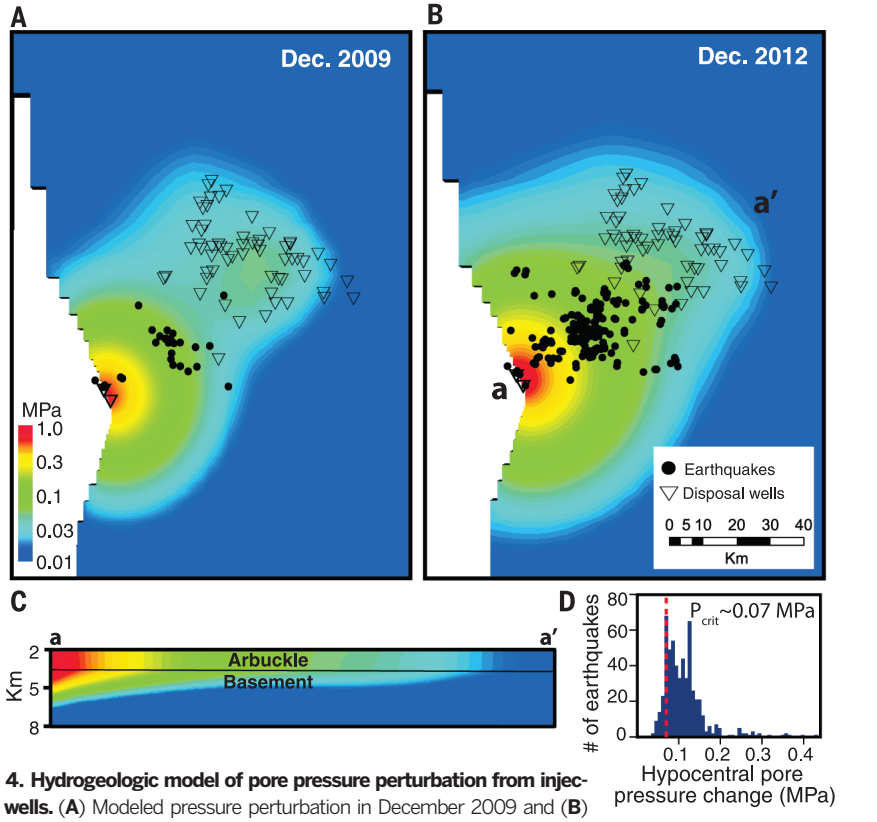


Fig. 4. Hydrogeologic model of pore pressure perturbation from injection wells. (**A**) Modeled pressure perturbation in December 2009 and (**B**) in December 2012 with a hydraulic diffusivity of 2 m^2/s (*14*). The model includes the four high-rate SE OKC wells and 85 wells northeast of the Jones swarm near the West Carney field. The modeled pressure perturbation is dominated by fluid injected at the high-rate SE OKC wells. Earthquakes are plotted from 2008 to 2009 (A) and 2008 to 2012 (B) (*10*). (**C**) Vertical cross section through model results. Pore pressure rises in the Arbuckle Group and uppermost basement. (**D**) Pore pressure increase at the hypocenter of each earthquake in our local catalog. A pore pressure increase of ~0.07 MPa is the modeled triggering threshold. Modeled pore pressure rises throughout much of the swarm area for hydraulic diffusivity between 1 and 4 m^2/s (fig. S7).

propagate away from the wells and disturbs a larger and larger volume, the probability increases that fluid pressure will encounter a larger fault and induce a larger-magnitude earthquake. The absence of earthquakes in regions above the critical pressure threshold may result from either a lack of faults or lack of well-oriented, critically stressed faults. Alternatively, fluid flow may preferentially migrate along bedding structure (Fig. 2A).

Though seven earthquakes were recorded in 2006 to 2009 near the base of the SE OKC wellbores (*10*), the main swarm began ~15 km to the northeast (fig. S9), despite the high modeled pressure perturbation near the wells. Earthquakes in 2009 primarily occurred, within location uncertainty, near injection wells or on the nearest known faults to the northeast of the wells (fig. S9). Focal mechanisms near the swarm onset indicate fault planes at orientations favorable to failure (*19*) (Fig. 2, inset B). Faults subparallel to the north-northwest–south-southeast–trending Nemaha fault would not be well oriented for failure in the regional ~N70E stress regime (*25*) and would require substantially larger pressure increase to fail. Recent earthquakes near the fault may be evidence for continued pressure increase. This 50-km-long segment of the Nemaha fault is capable of hosting a *M*7 earthquake based on earthquake scaling laws (*20*), and the fault zone continues for hundreds of kilometers. The increasing proximity of the earthquake swarm to the Nemaha fault presents a potential hazard for the Oklahoma City metropolitan area.

Our earthquake relocations and pore pressure models indicate that four high-rate disposal wells are capable of increasing pore pressure above the reported triggering threshold (*21*–*23*) throughout the Jones swarm and thus are capable of triggering ~20% of 2008 to 2013 central and eastern U.S. seismicity. Nearly 45% of this region's seismicity, and currently nearly 15 $M > 3$ earthquakes per week, may be linked to disposal of fluids generated during Oklahoma dewatering and after hydraulic fracturing, as recent Oklahoma seismicity dominantly occurs within seismic swarms in the Arbuckle Group, Hunton Group, and Mississippi Lime dewatering plays. The injection-linked seismicity near Jones occurs up to 35 km away from the disposal wells, much further than previously considered in existing criteria for induced seismicity (*13*). Modern, very high-rate injection wells can therefore affect regional seismicity and increase seismic hazard. Regular measurements of reservoir pressure at a range of distances and azimuths from high-rate disposal wells could verify our model and potentially provide early indication of seismic vulnerability.

REFERENCES AND NOTES

1. W. L. Ellsworth, *Science* **341**, 1225942 (2013).
2. K. Keranen, H. Savage, G. Abers, E. Cochran, *Geology* **41**, 699–702 (2013).
3. W.-Y., *J. Geophys. Res.* **118**, 3506–3518 (2013).
4. S. Horton, *Seismol. Res. Lett.* **83**, 250–260 (2012).
5. C. Frohlich, C. Hayward, B. Stump, E. Potter, *Bull. Seismol. Soc. Am.* **101**, 327–340 (2011).
6. A. H. Justinic, B. Stump, C. Hayward, C. Frohlich, *Bull. Seismol. Soc. Am.* **103**, 3083–3093 (2013).
7. C. Frohlich, *Proc. Natl. Acad. Sci. U.S.A.* **109**, 13934–13938 (2012).
8. A. McGarr, *J. Geophys. Res.* **119**, 1008–1019 (2014).
9. The Central and Eastern United States is considered the portion of the contiguous United States east of 109°W.
10. ANSS catalog, United States Geological Survey, http://earthquake.usgs.gov/earthquakes/search/, accessed 4/1/2014.
11. N. J. van der Elst, H. M. Savage, K. M. Keranen, G. A. Abers, *Science* **341**, 164–167 (2013).
12. D. F. Sumy, E. S. Cochran, K. M. Keranen, M. Wei, G. A. Abers, *J. Geophys. Res.* **119**, 1904–1923 (2014).
13. S. D. Davis, C. Frohlich, *Seismol. Res. Lett.* **64**, 207–224 (1993).
14. Information on materials and methods is available on *Science* Online.
15. Oklahoma Corporation Commission Imaging Web Application, http://imaging.occeweb.com/
16. D. Chernicky, *World Oil* (2000); www.worldoil.com/September-2000-Major-reserve-increase-obtained-by-dewatering-high-water-saturation-reservoirs.html.
17. K. E. Murray, *Environ. Sci. Technol.* **47**, 4918–4925 (2013).
18. F. Waldhauser, W. L. Ellsworth, *Bull. Seismol. Soc. Am.* **90**, 1353–1368 (2000).
19. A. A. Holland, *Seismol. Res. Lett.* **84**, 876–890 (2013).
20. D. L. Wells, K. J. Coppersmith, *Bull. Seismol. Soc. Am.* **84**, 974–1002 (1994).
21. P. A. Reasenberg, R. W. Simpson, *Science* **255**, 1687–1690 (1992).
22. L. Seeber, J. G. Armbruster, *Nature* **407**, 69–72 (2000).
23. R. Stein, *Nature* **402**, 605–609 (1999).
24. M. D. Zoback, J. Townend, B. Grollimund, *Int. Geol. Rev.* **44**, 383–401 (2002).
25. M. L. Zoback, *J. Geophys. Res.* **97**, 11703–11728 (1992).
26. K. V. Luza, J. E. Lawson, *Oklahoma Geological Survey Spec. Pub.* **81-3**, 1–67 (1981).
27. S. P. Gay, *Shale Shaker* **54**, 39–49 (2003).
28. L. E. Gatewood, in *Geology of Giant Petroleum Fields*, AAPG Memoir **14**, M. T. Halbouty, Ed. (American Association of Petroleum Geologists Tulsa, OK, 1970).
29. Monthly average volume was calculated by using reported volumes for any month with nonzero volume in data available from 1995 through 2012 (*15*). Injection rates over 90% larger than the median monthly value in a given year for each well were removed from calculations to remove data entry errors.

ACKNOWLEDGMENTS

This research benefited from discussion with E. Cochran, W. Ellsworth, and participants in a U.S. Geological Survey (USGS) Powell Center Working Group on Understanding Fluid Injection Induced Seismicity (M.W., B.A.B., and S.G. are part of this group). C. Hogan identified many *P* and *S* phases. K.M.K was partially supported by USGS National Earthquake Hazards Reduction Program (NEHRP) grant G13AP00025, M.W. was partially supported by the USGS Powell Center grant G13AC00023, and G.A.A. was partially supported by NEHRP grant G13AP00024. This project used seismic data from EarthScope's Transportable Array, a facility funded by the National Science Foundation. Seismic waveforms are from the Incorporated Research Institutions for Seismology Data Management Center and the USGS CWB Query. Well data are from the Oklahoma Corporation Commission and the Oklahoma Geological Survey. Lists of wells and the local earthquake catalog are available as supplementary materials on *Science* Online.

SUPPLEMENTARY MATERIALS

www.sciencemag.org/content/345/6195/448/suppl/DC1
Materials and Methods
Figs. S1 to S10
Tables S1 to S9
References (*30*–*41*)

8 May 2014; accepted 24 June 2014
Published online 3 July 2014;
10.1126/science.1255802

DINOSAUR EVOLUTION

A Jurassic ornithischian dinosaur from Siberia with both feathers and scales

Pascal Godefroit,[1]* Sofia M. Sinitsa,[2] Danielle Dhouailly,[3] Yuri L. Bolotsky,[4] Alexander V. Sizov,[5] Maria E. McNamara,[6,7] Michael J. Benton,[7] Paul Spagna[1]

Middle Jurassic to Early Cretaceous deposits from northeastern China have yielded varied theropod dinosaurs bearing feathers. Filamentous integumentary structures have also been described in ornithischian dinosaurs, but whether these filaments can be regarded as part of the evolutionary lineage toward feathers remains controversial. Here we describe a new basal neornithischian dinosaur from the Jurassic of Siberia with small scales around the distal hindlimb, larger imbricated scales around the tail, monofilaments around the head and the thorax, and more complex featherlike structures around the humerus, the femur, and the tibia. The discovery of these branched integumentary structures outside theropods suggests that featherlike structures coexisted with scales and were potentially widespread among the entire dinosaur clade; feathers may thus have been present in the earliest dinosaurs.

The origin of birds is one of the most-studied diversification events in the history of life. Principal debates relate to the origin of key avian features such as wings, feathers, and flight (*1*–*9*). Numerous finds from China have revealed that diverse theropods possessed feathers and various degrees of flight capability (*4*–*9*). The identification of melanosomes in non-avian theropods (*10*, *11*) confirms that fully birdlike feathers originated within Theropoda at least 50 million years before *Archaeopteryx*.

But were feathers more widespread among dinosaurs? Quill-like structures have been reported in the ornithischians *Psittacosaurus* (*12*) and *Tianyulong* (*13*), but whether these were true feathers, or some other epidermal appendage, is unclear. Bristlelike epidermal appendages occur in pterosaurs, some early theropods (*14*), and extant mammals ("hairs"), and so the *Psittacosaurus*

[1]Directorate 'Earth and History of Life,' Royal Belgian Institute of Natural Sciences, Rue Vautier 29, B-1000 Brussels, Belgium. [2]Institute of Natural Resources, Ecology and Cryology, 26 Butin Street, 672 014 Chita, Russia. [3]UJF-CNRS FRE 3405, AGIM, Université Joseph Fourier, Site Santé, 38 706 La Tronche, France. [4]Institute of Geology and Nature Management, FEB RAS, 1 Relochny Street 675 000, Blagoveschensk, Russia. [5]Institute of the Earth Crust, SB RAS, 128 Lermontov Street, Irkutsk, 664 033 Irkutsk, Russia. [6]School of Biological, Earth and Environmental Science, University College Cork, Cork, Ireland. [7]School of Earth Sciences, University of Bristol, Bristol BS8 1RJ, UK.
*Corresponding author. E-mail: pascal.godefroit@naturalsciences.be

and *Tianyulong* filaments might have evolved independently of the feathers of theropods.

Here we report a new ornithischian dinosaur, *Kulindadromeus zabaikalicus*, with diverse epidermal appendages, including grouped filaments that we interpret as avianlike feathers. This suggests that all Dinosauria could have had feathers and that feathers arose for purposes of insulation and signaling and were only later co-opted for flight (*10*, *11*).

The new dinosaur comes from the Kulinda locality (Cherynyshevsky District of Chita Region, southeastern Siberia, Russia; fig. S1), from the base of the Ukureyskaya Formation, dated as Middle to Late Jurassic (*15*). The dinosaur bones are associated with abundant, well-preserved fossils of plants, insect larvae, and freshwater crustaceans that suggest deposition in a low-energy, probably lacustrine, freshwater environment. The sequence includes tuff deposits and ignimbrites that indicate local volcanic activity (*15*).

The description of *Kulindadromeus zabaikalicus* (*15*) is based on six partial skulls and several hundred disarticulated skeletons unearthed from two neighboring monospecific bone beds. Each individual skeletal element is represented by a single morphotype, and all of the observed morphological differences can easily be explained by ontogenetic and intraspecific variation, as confirmed by the detailed study of the partial skeletons (*15*). Therefore, there is no indication that more than one basal ornithischian is present. Many of the bones are strongly iron-stained, suggesting partial replacement during diagenesis.

Kulindadromeus zabaikalicus is differentiated from all other dinosaurs by the following

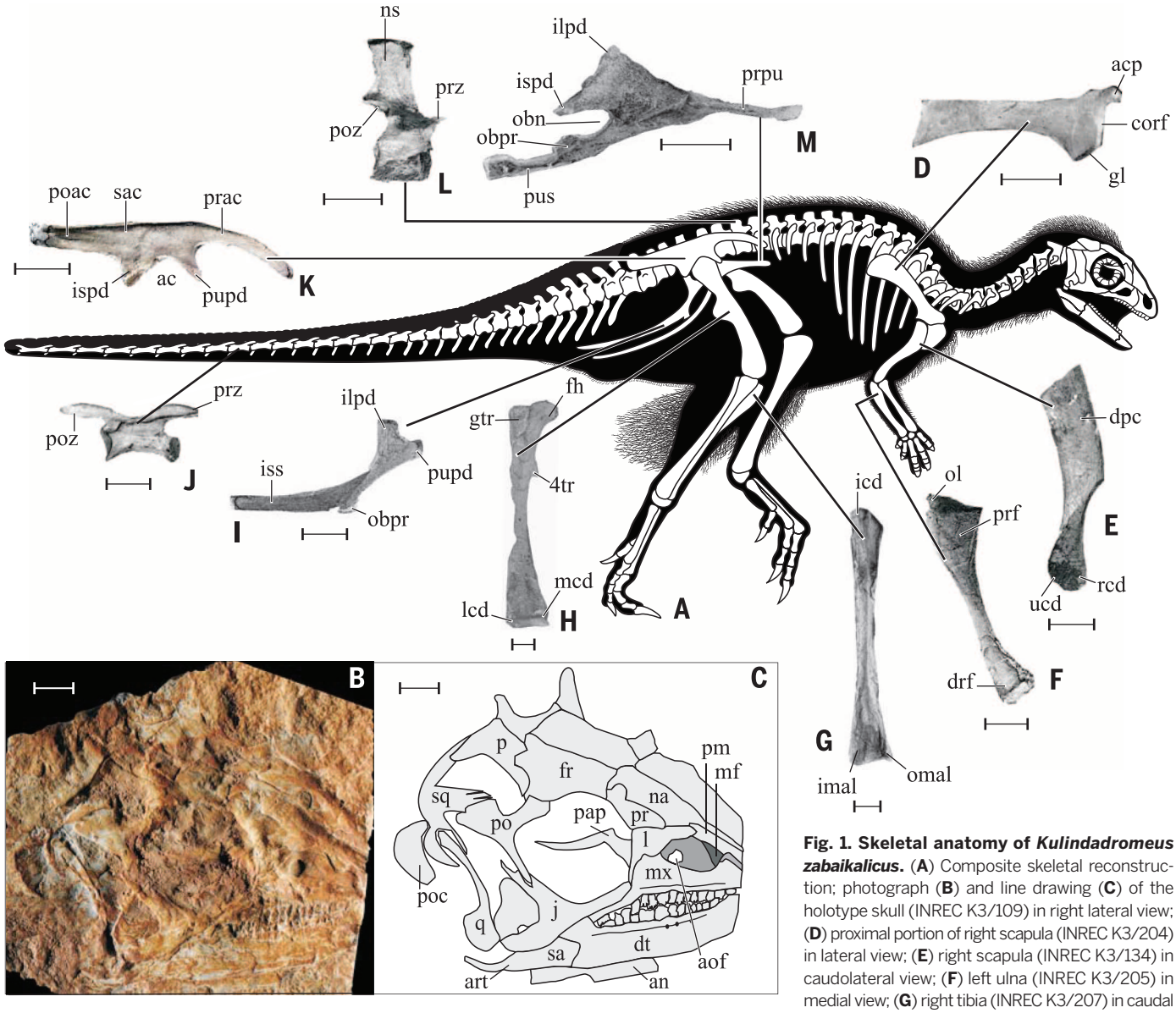


Fig. 1. Skeletal anatomy of *Kulindadromeus zabaikalicus*. (**A**) Composite skeletal reconstruction; photograph (**B**) and line drawing (**C**) of the holotype skull (INREC K3/109) in right lateral view; (**D**) proximal portion of right scapula (INREC K3/204) in lateral view; (**E**) right scapula (INREC K3/134) in caudolateral view; (**F**) left ulna (INREC K3/205) in medial view; (**G**) right tibia (INREC K3/207) in caudal view; (**H**) right femur (INREC K3/206) in cranial view; (**I**) right ischium (INREC K3/124) in lateral view; (**J**) distal caudal vertebra (INREC K3/202) in right lateral view; (**K**) mirror image of left ilium (INREC K3/113) in lateral view; (**L**) dorsal vertebra (INREC 3/112) in right lateral view; (**M**) mirror image of left pubis (INREC K3/114) in lateral view. Scale bars, 10 mm. Abbreviations: ac, acetabulum; acp, acromial process; an, angular; aof, antorbital fossa; art, articular; cor, coracoid facet; dpc, deltopectoral crest; drf, distal radial facet; dt, dentary; fh, femoral head; fr, frontal; gl, glenoid; ilpd, iliac peduncle; imal, inner malleolus; ispd, ischial peduncle; iss, ischial shaft; j, jugal; l, lacrimal; lcd, lateral condyle; mcd, medial condyle; mf, maxillary fenestra; mx, maxilla; na, nasal; obn, obturator notch; obpr, obturator process; ns, neural spine; ol, olecranon process; omal, outer malleolus; p, parietal; pap, palpebral; pm, premaxilla; po, postorbital; poac, postacetabular process; poc, paroccipital process; poz, postzygapophysis; pr, prefrontal; prac, preacetabular process; prf, proximal radial facet; prpu, prepubic process; prz, prezygapophysis; pupd, pubic peduncle; pus, pubic shaft; q, quadrate; qj, quadratojugal; rap, rostral ascending process; rcd, radial condyle; sa, surangular; sac, supraacetabular crest; sq, squamosal; ucd, ulnar condyle; 4tr, fourth trochanter.

characters (Fig. 1, and figs. S4 to S7): maxilla with rostral ascending process much lower than caudal ascending process and maxillary fenestra larger than antorbital fenestra; jugal with notched postorbital ramus; postorbital with dorsoventrally expanded caudal ramus; dorsoventrally slender postacetabular process on ilium; and deep extensor fossae on metatarsals II to IV (*15*).

It was a small, 1.5-m-long bipedal herbivore, with a short skull, plant-eating teeth, elongate hindlimbs, short forelimbs, and an elongate tail (Fig. 1). Phylogenetic analysis (figs. S10 and S11) (*15*) recovers *Kulindadromeus* as a basal member of Neornithischia [all genasaurians more closely related to *Parasaurolophus walkeri* than to *Ankylosaurus magniventris* or *Stegosaurus stenops* (*16*)] and the sister taxon for Cerapoda [*Parasaurolophus walkeri*, *Triceratops horridus*, their most recent common ancestor, and all descendants (*16*)].

The key features of *Kulindadromeus* relate to its integument. Numerous, varied, exceptionally preserved integumentary features are associated, often in direct connection, with the bones and vary in morphology among different body regions. They comprise three types of scales and three types of featherlike structures. Small (<3.5 mm long) imbricated and hexagonal scales, resembling the scutella in modern birds (*17*), are associated with the distal parts of the tibiae in *Kulindadromeus* (Fig. 2A and fig. S8E). Smaller (<1 mm) rounded and nonoverlapping scales occur around the manus, tarsus (Fig. 2A and fig. S8E), metatarsus, and pes (fig. S8F), resembling the reticula along the plantar face of the pes in modern birds (*17*). The tail of *Kulindadromeus* is covered by at least five longitudinal rows of slightly arched scales (Fig. 2, B and C, and fig. S8, A to D). The largest scales (~20 mm long and 10 mm wide) occur along the proximal part of the tail. The caudal scales of *Kulindadromeus* are thin (<100 μm), unornamented, and slightly imbricated, each scale covering part of the adjacent distal one (Fig. 2C and fig. S8, B to D). They are clearly different from the thicker, sculptured, and nonoverlapping osteoderms in thyreophoran ornithischians (*18*) and from the proportionally thicker and smaller scales in iguanodontian ornithopods (*19*), more closely resembling epidermal scales. The preservation of the scales as carbonaceous remains suggests that they are unlikely to be osteoderms, because the bones (which also comprise calcium phosphate in vivo) display a quite different preservational pathway. Each scale forms a triangular anterior spur that covers the preceding one, so that adjacent elements are interconnected by a clip-like system. Proximally, at the level of the base of the tail (Fig. 2C), the scales become progressively smaller and more rounded and do not overlap.

Monofilaments are widely distributed around the thorax (Fig. 2, G to I), on the back, and around the head (Fig. 2, D to F). Those above the head are thin (~0.15 mm in diameter), short (10 to 15 mm long), and curved, with no preferred orientation. The thoracic and abdominal filaments are wider (0.2 to 0.3 mm) and longer (20 to 30 mm). These monofilaments are shorter and thinner than the long bristlelike structures on the proximal part of the tail in *Psittacosaurus* (*12*) and the filamentous structures in *Tianyulong* (*13*). They more closely resemble the monofilaments in the basal coelurosaur *Sinosauropteryx* (*20*) and are similar to morphotype 1 in a recent evolutionary model of feathers (*21*).

Kulindadromeus also shows compound, nonshafted integumentary structures along the humerus and femur (Fig. 3, A to F, and fig. S9).

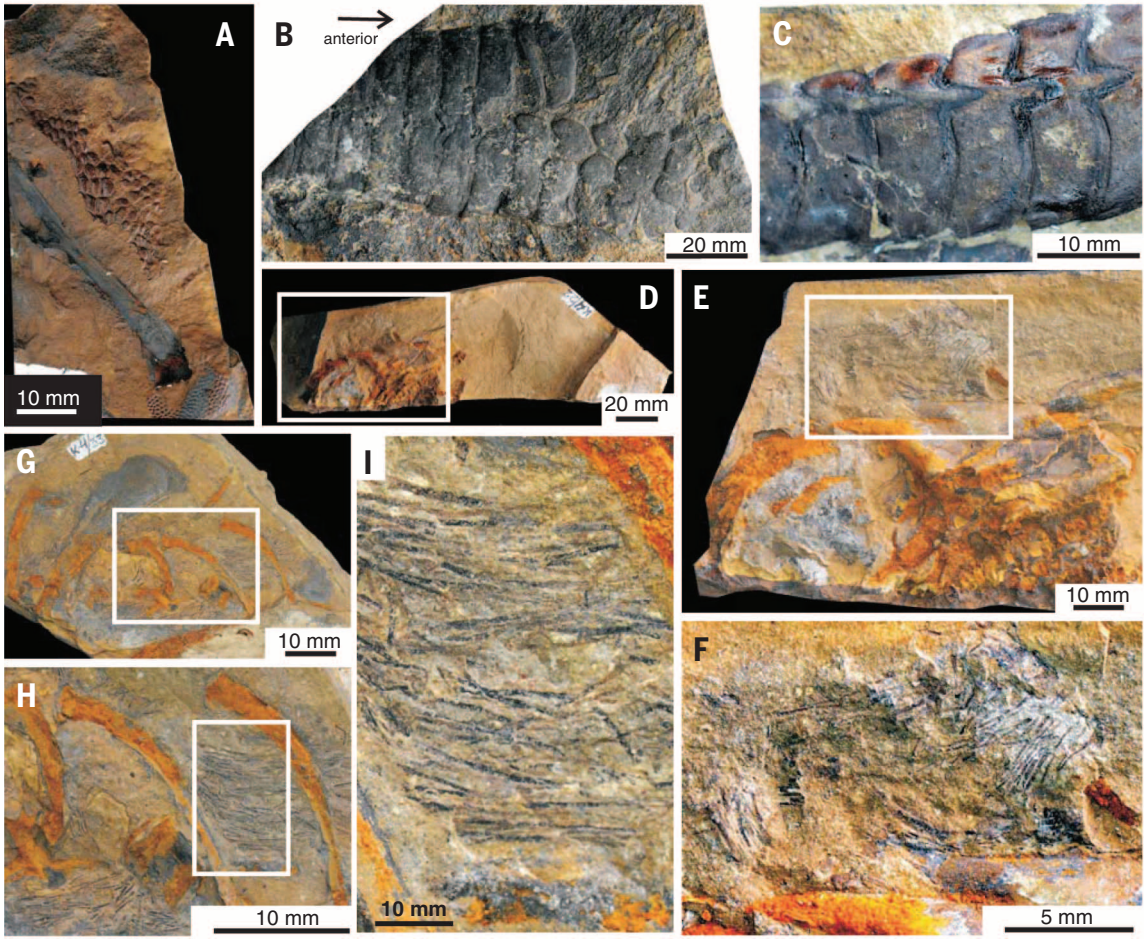


Fig. 2. Epidermal scales and featherlike structures of *Kulindadromeus zabaikalicus*. (**A**) Scales around the distal tibia and the tarsus (INREC K4/57); (**B**) double row of scales above the proximal part of the tail (INREC K4/94) in dorsal view; (**C**) close-up of the left row of caudal scales (INREC K4/117) in dorsal view; (**D**) partial skull (INREC K4/22) in right lateral view, with (**E** and **F**) detail of areas indicated in (D) and (E) showing filamentous structures; (**G**) left part of ribcage (INREC K4/33), with (**H** and **I**) detail of areas indicated in (G) and (H) showing filamentous structures.

These occur as groups of six or seven filaments that converge proximally and arise from the central regions of a basal plate. Individual filaments are 10 to 15 mm long. Those on the humerus are wider (0.2 to 0.4 mm) and straighter than those on the femur (0.1 to 0.2 mm). These groups of filaments are similar to feather morphotype 3 (*21*, *22*) and resemble the down feathers of some modern chicken breeds, such as the Silkie, which are devoid of barbules (*17*). The basal plates are also larger on the humerus (3 to 4 mm wide) than on the femur (2 to 3 mm); they are arranged in a hexagonal pattern, but they remain distinctly separated from each other, contrasting with the contiguous distribution of the scales on the distal forelimb, hindlimb, and tail in *Kulindadromeus* and also with the feathered scales that cover the tarsometatarsus of some living birds (*17*). Whether the basal plates represent modified scales or calamus-like structures remains unclear and requires further investigation.

An additional integumentary morphotype occurs along the proximal part of the tibia in *Kulindadromeus* (Fig. 3, G to J): Clusters of six or seven ribbon-shaped elements appear more or less bundled together proximally, close to the bone surface. Each individual element is 15 to 20 mm long and 1.5 to 3 mm wide, with a dark median axis along its length (Fig. 3, H to J). Careful removal of a thin superficial carbonaceous sheet reveals the presence of ~10 thin (50 to 100 μm) internal parallel filaments within each ribbon-shaped element (Fig. 3J). This is an arrangement that has never previously been reported and that could represent a third feather-like morphotype in *Kulindadromeus*.

The presence of both simple and compound filamentous structures in *Kulindadromeus*

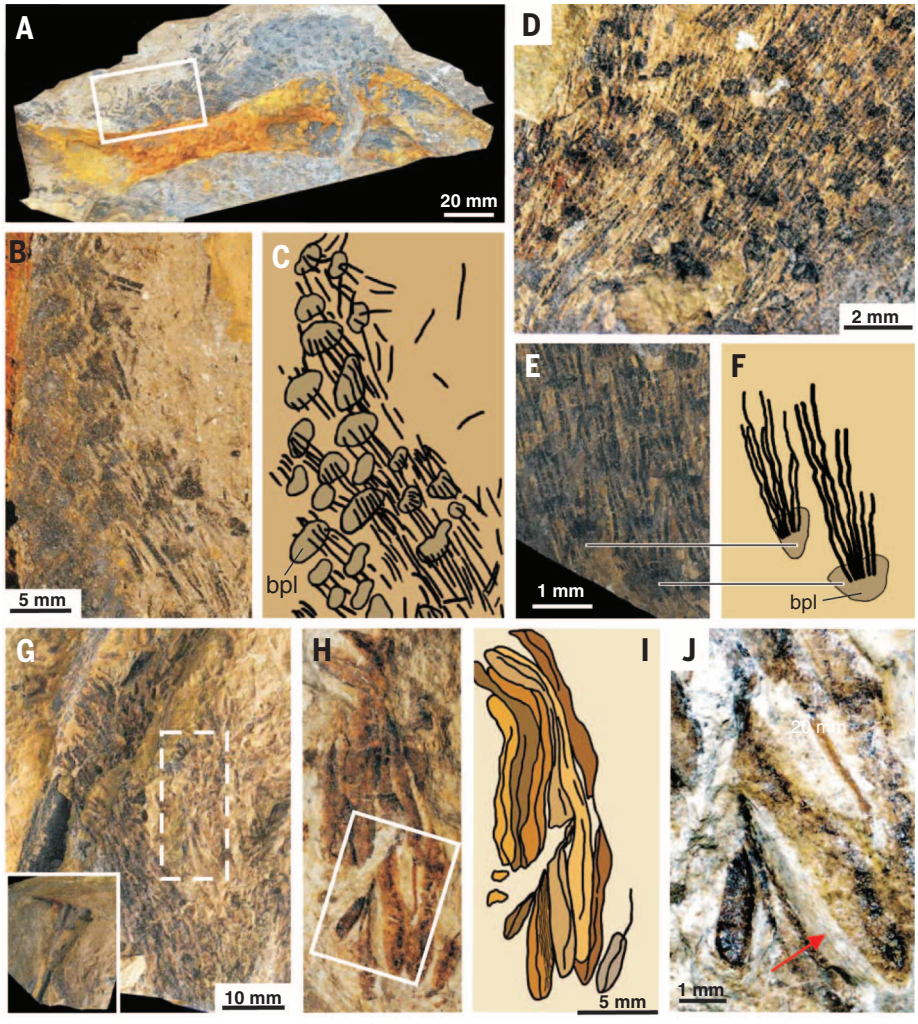


Fig. 3. Featherlike structures in *Kulindadromeus zabaikalicus*. (**A**) Right humerus and proximal part of right radius and ulna (INREC K4/115), with detail (**B**) and interpretative drawing (**C**) of compound structures around the right humerus; (**D** and **E**) compound structures around femur (counterpart of INREC K4/116) with (**F**) interpretative drawing of (E); (**G**) ribbonlike structures around proximal part of tibia (INREC K4/44); the inset shows the slab at lower magnification. (**H**) Detail of area indicated in (G) with interpretive drawing (**I**) and further details of ribbonlike structures (**J**); the superficial carbonaceous sheet has been removed during preparation, revealing an internal structure of thin parallel filaments (red arrow). Abbreviation: bpl, basal plate.

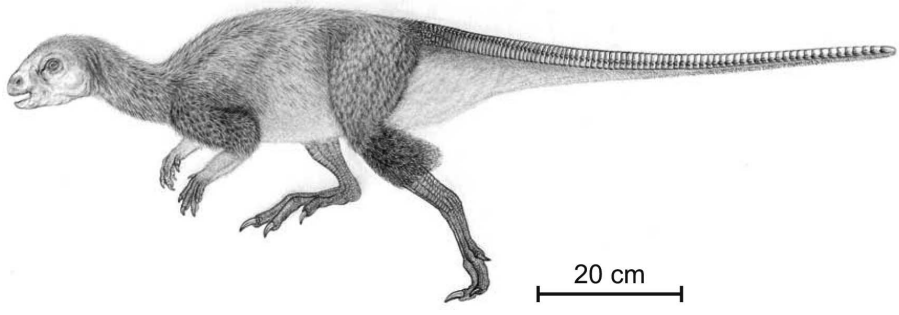


Fig. 4. Reconstruction of *Kulindadromeus zabaikalicus*. A basal ornithopod dinosaur, with feathers and scales, from the Middle to Late Jurassic of southeastern Siberia. [Drawing by Pascale Golinvaux (Royal Belgian Institute of Natural Sciences)]

(Fig. 4) supports the hypothesis that the integumentary structures in Ornithischia, already described in *Psittacosaurus* (*12*) and *Tianyulong* (*13*), could be homologous to the "protofeathers" in non-avian theropods. In any case, it indicates that those protofeather-like structures were probably widespread in Dinosauria, possibly even in the earliest members of the clade. Further, the ability to form simple monofilaments and more complex compound structures is potentially nested within the archosauromorph clade, as exemplified by *Longisquama* (*23*), pterosaurs (*24*), ornithischians, and theropods (including birds).

In *Kulindadromeus* and most ornithuromorph birds (*17*, *25*), the distal hindlimb is extensively covered by scales and devoid of featherlike structures. This condition might thus be primitive in dinosaurs. Both paleontological and genetic evidence, however, suggests that the pedal scales of ornithuromorph birds are secondarily derived from feathers. In avialan evolution, leg feathers were reduced gradually in a distal-to-proximal direction, with eventual loss of the distal feathers and appearance of pedal scales in ornithuromorphs (*25*). Further, evo-devo experiments (*26*, *27*) show that feathers in extant birds are the default fate of the avian epidermis, and that the formation of avian scales requires the inhibition of feather development. The local formation of scales requires the inhibition of epidermal outgrowth, regulated by the *sonic hedgehog* pathway; this inhibition is partially lost in the case of breeds with feathered feet (*27*). Therefore, it is possible that the extensively scaled distal hindlimbs in *Kulindadromeus* might be explained by similar local and partial inhibition in the development of featherlike structures. The preservation of featherlike structures and scales in the basal neornithischian *Kulindadromeus*, and their similarity to structures that are present in diverse theropods and ornithuromorph birds, thus strongly suggest that deep homology mechanisms (*28*) explain the complex distribution of skin appendages within dinosaurs (*23*).

REFERENCES AND NOTES

1. M. A. Norell, X. Xu, *Annu. Rev. Earth Planet. Sci.* **33**, 277–299 (2005).
2. T. Lingham-Soliar, A. Feduccia, X. Wang, *Proc. Biol. Sci.* **274**, 2823 (2007).
3. F. Zhang, Z. Zhou, G. Dyke, *Geol. J.* **41**, 395 (2006).
4. T. Lingham-Soliar, *Proc. Biol. Sci.* **275**, 775–780 (2008).
5. D. Hu, L. Hou, L. Zhang, X. Xu, *Nature* **461**, 640–643 (2009).
6. S. L. Brusatte *et al.*, *Earth Sci. Rev.* **101**, 68–100 (2010).
7. X. Xu, H. You, K. Du, F. Han, *Nature* **475**, 465–470 (2011).
8. P. Godefroit *et al.*, *Nat. Commun.* **4**, 1394 (2013).
9. P. Godefroit *et al.*, *Nature* **498**, 359–362 (2013).
10. F. Zhang *et al.*, *Nature* **463**, 1075–1078 (2010).
11. Q. Li *et al.*, *Science* **327**, 1369–1372 (2010).
12. G. Mayr, D. S. Peters, G. Plodowski, O. Vogel, *Naturwissenschaften* **89**, 361–365 (2002).
13. X.-T. Zheng, H.-L. You, X. Xu, Z.-M. Dong, *Nature* **458**, 333–336 (2009).
14. O. W. M. Rauhut, C. Foth, H. Tischlinger, M. A. Norell, *Proc. Natl. Acad. Sci. U.S.A.* **109**, 11746–11751 (2012).
15. See the supplementary materials on *Science* Online.
16. R. J. Butler, P. Upchurch, D. B. Norman, *J. Syst. Palaeontology* **6**, 1–40 (2008).
17. A. M. Lucas, P. R. Stettenheim, *Avian Anatomy, Integument* (U.S. Department of Agriculture, Washington, DC, 1972).
18. M. K. Vickarious, T. Maryanska, D. B. Weishampel, in *The Dinosauria 2nd edn*, D. B. Weishampel, P. Dodson, H. Osmolska, Eds. (Univ. of California Press, Berkeley, CA, 2004), pp. 363–392.
19. P. R. Bell, *PLOS ONE* **7**, e31295 (2012).
20. P. J. Currie, P. J. Chen, *Can. J. Earth Sci.* **38**, 1705–1727 (2001).
21. X. Xu, X. Zheng, H. You, *Nature* **464**, 1338–1341 (2010).
22. F. Zhang, Z. Zhou, X. Xu, X. Wang, C. Sullivan, *Nature* **455**, 1105–1108 (2008).
23. M. Buchwitz, S.Voigt, *Paläontol. Z.* **86**, 313 (2012).
24. X. Wang, Z. Zhou, F. Zhang, X. Xu, *Chin. Sci. Bull.* **47**, 226 (2002).
25. X. Zheng *et al.*, *Science* **339**, 1309–1312 (2013).
26. D. Dhouailly, *J. Anat.* **214**, 587–606 (2009).
27. F. Prin, D. Dhouailly, *Int. J. Dev. Biol.* **48**, 137–148 (2004).
28. N. Shubin, C. Tabin, S. Carroll, *Nature* **388**, 639–648 (1997).

ACKNOWLEDGMENTS

We thank A. B. Ptitsyn for making fossils available for study; Ph. Claeys, J.-M. Baele, and I. Y. Bolosky for help and comments on the manuscript; and P. Golinvaux, J. Dos Remedios Esteves, C. Desmedt, and A. Vandersypen for the drawings and reconstructions. This study was supported by Belgian Science Policy grant BL/36/62 to P.G. and by Natural Environment Research Council Standard Grant NE/I027630/1 awarded to M.J.B.

SUPPLEMENTARY MATERIALS

www.sciencemag.org/content/345/6195/451/suppl/DC1
Materials and Methods
Supplementary Text
Figs. S1 to S11
References (*29*–*55*)

13 March 2014; accepted 23 June 2014
10.1126/science.1253351

RNA FUNCTION

Ribosome stalling induced by mutation of a CNS-specific tRNA causes neurodegeneration

Ryuta Ishimura,[1]* Gabor Nagy,[1]* Ivan Dotu,[2] Huihao Zhou,[3] Xiang-Lei Yang,[3] Paul Schimmel,[3] Satoru Senju,[4] Yasuharu Nishimura,[4] Jeffrey H. Chuang,[2] Susan L. Ackerman[1]†

In higher eukaryotes, transfer RNAs (tRNAs) with the same anticodon are encoded by multiple nuclear genes, and little is known about how mutations in these genes affect translation and cellular homeostasis. Similarly, the surveillance systems that respond to such defects in higher eukaryotes are not clear. Here, we discover that loss of GTPBP2, a novel binding partner of the ribosome recycling protein Pelota, in mice with a mutation in a tRNA gene that is specifically expressed in the central nervous system causes ribosome stalling and widespread neurodegeneration. Our results not only define GTPBP2 as a ribosome rescue factor but also unmask the disease potential of mutations in nuclear-encoded tRNA genes.

In higher eukaryotes, the nuclear genome typically contains several hundred transfer RNA (tRNA) genes, which fall into isoacceptor groups, each representing an anticodon (*1*). Relative to the total number of tRNA genes, the number of isodecoders—i.e., tRNA molecules with the same anticodon but differences in the tRNA body—increases dramatically with organismal complexity, which leads to speculation that isodecoders might not be fully redundant with one another (*2*). Overexpression of reporter constructs with rare codons that are decoded by correspondingly low-abundance tRNAs in bacteria and yeast, or mutations in single-copy mitochondrial tRNA genes, may result in stalled elongation complexes (*3*–*5*). However, the consequences of mutations in multicopy, nuclear-encoded tRNA isodecoder genes or in the surveillance systems that eliminate the effect of such tRNA mutations are not known in higher eukaryotes.

The *nmf205* mutation was identified in an *N*-ethyl-*N*-nitorosurea mutagenesis screen of C57BL/6J (B6J) mice for neurological phenotypes (*6*). B6J-*nmf205*$^{-/-}$ mice were indistinguishable from wild-type mice at 3 weeks of age but showed clear truncal ataxia at 6 weeks (movie S1). Mice died at 8 to 9 weeks with severe locomotor deficits. Progressive apoptosis of neurons in the inner granule layer (IGL) in the mutant cerebellum was initially observed between 3 and 4 weeks of age (Fig. 1, A to H). Apoptosis of mutant granule cells in the dentate gyrus, CA2 pyramidal neurons, and layer IV cortical neurons occurred between 5 and 8 weeks of age (Fig. 1, I and J, and fig. S1, A to H). Further, many neurons in the retina—including photoreceptors and amacrine, horizontal, and ganglion cells—degenerated during this time (Fig. 1, K and L, and fig. S1, I to T).

[1]Howard Hughes Medical Institute and The Jackson Laboratory, 600 Main Street, Bar Harbor, ME 04609, USA. [2]The Jackson Laboratory for Genomic Medicine, 263 Farmington Avenue, Farmington, CT 06030, USA. [3]The Skaggs Institute for Chemical Biology, The Scripps Research Institute, 10550 North Torrey Pines Road, La Jolla, CA 92037, USA. [4]Department of Immunogenetics, Graduate School of Medical Sciences, Kumamoto University, Honjo 1-1-1, Chuo-ku, Kumamoto 860-8556, Japan.
*These authors contributed equally to this work. **†Corresponding author. E-mail: susan.ackerman@jax.org**

Histological analysis of other organs did not reveal obvious pathology nor was neurodegeneration observed in mice heterozygous for this mutation.

We identified the *nmf205* mutation as a point mutation in the consensus splice donor site of intron 6 of *Gtpbp2* that results in misspliced mRNAs with premature stop codons (fig. S2). Accordingly, Western blot analysis of mutant cerebellar extracts failed to detect GTPBP2 (Fig. 2A). Complementation tests using *nmf205* mice and mice with a targeted deletion of *Gtpbp2* confirmed that loss of *Gtpbp2* results in neurodegeneration (fig. S3).

GTPBP2 shares domain homology with a translational guanosine triphosphatase family that is characterized by the no-go and nonstop decay pathways ribosome-recycling protein Hbs1 and the eukaryotic release factor eRF3, which bind Dom34 and eRF1, respectively (fig. S4A) (*7*–*9*). Although no interaction was observed between GTPBP2 and eRF1 in coimmunoprecipitation assays, Pelota (the mammalian Dom34 homolog) was immunoprecipitated by GTPBP2 (Fig. 2B). The glutathione *S*-transferase–GTPBP2 fusion protein (GST-GTPBP2) also pulled down Pelota from brain extracts, which demonstrated that GTPBP2 can interact with endogenous Pelota (Fig. 2C). Affinity capture of bacterially expressed GTPBP2 by Pelota demonstrated that these proteins directly interact (Fig. 2D).

Analysis of mice from our mapping cross and B6J.BALB^{Chr1} congenic mice revealed that homo- or heterozygosity for a BALB/cJ-derived locus (*Mod205*) on distal chromosome 1 suppressed neurodegeneration in *nmf205*$^{-/-}$ and *Gtpbp2*$^{-/-}$ mice (fig. S5). Mutant mice carrying this BALB locus routinely survived to 18 months or longer. Further analysis of multiple other inbred strains including C57BL/6NJ (B6N) suggested that neurodegeneration in B6J-*nmf205*$^{-/-}$ mice is likely due to an epistatic mutation in the B6J strain (table S1).

One single-nucleotide polymorphism (SNP) in the *Mod205* region, *rs46447118*, was determined to be a T in the B6J genome but a C in all other tested strains (fig. S6A). This SNP resides at nucleotide 50 in the stem of the T loop of *n-Tr20*, one of five isodecoders of the nuclear-encoded tRNA$^{Arg}_{UCU}$ family (fig. S6, B and C). Orthologs of *n-Tr20* are widely found in both vertebrates and invertebrates (fig. S6D). We assayed *n-Tr20* aminoacylation and found that the majority of this tRNA was charged in the B6N brain, but very low levels were observed in B6J (Fig. 3A). Mutations in the T stem of tRNAs have been shown to affect pre-tRNA processing and function (*10*, *11*). In agreement, a 105-nucleotide (nt) band was detected in the B6J brain, which was confirmed to be the pre-tRNA retaining the leader and trailer sequences (Fig. 3B and fig. S7A). In wild-type brains, the pre-tRNA is 115 nt, which suggests the C-to-T mutation changes the length of the primary transcript. Examination of *n-Tr20* processing in reciprocal congenic strains confirmed that this mutation underlies the observed maturation defect (fig. S7B).

To confirm that loss of mature *n-Tr20* underlies neurodegeneration in B6J-*nmf205*$^{-/-}$ mice (which are mutant for both *Gtpbp2* and *n-Tr20*), B6J mice transgenically expressing wild-type *n-Tr20* and harboring the *nmf205* mutation (Tg; *nmf205*$^{-/-}$) were examined (fig. S8, A and B). At 6 months of age, neuron death was greatly attenuated in the brain and retina (Fig. 3C).

Although *Gtpbp2* is widely expressed (fig. S4B) (*12*, *13*), pathology in mice lacking this gene is restricted to the CNS. In contrast to other members of the tRNA$^{Arg}_{UCU}$ family, expression of *n-Tr20* and its human ortholog were surprisingly confined to the CNS (Fig. 3D and fig. S8, C and D). In addition, overall expression of the tRNA$^{Arg}_{UCU}$ isodecoder family was higher in the CNS than in other tissues (Fig. 3D). Compared with levels of processed *n-Tr20* in age-matched B6N brains, which show steady postnatal expression, levels in the B6J brain fell from 50% of B6N levels at postnatal day 0 (P0) to 19% by P30 (Fig. 3E), and a concomitant increase in immature *n-Tr20* was also observed. Although B6J brains have a slight increase in expression of the other members of the tRNA$^{Arg}_{UCU}$ family, a dramatic reduction in the B6J total tRNA$^{Arg}_{UCU}$ pool was observed, which demonstrated that *n-Tr20* normally makes up ~60% of the expression of this isodecoder family (Fig. 3F and fig. S9). Spatial differences in processing of mutant *n-Tr20* were also observed within the B6J brain with significantly lower levels of processed and higher levels of unprocessed *n-Tr20* in the cerebellum compared with the cortex and hippocampus (Fig. 3G). Together, these data define a CNS-specific tRNA in which levels of mature transcript correlate with the onset and severity of cell death in *Gtpbp2*-deficient mice.

We hypothesized that the *n-Tr20* mutation causes ribosome stalling at AGA codons that is exacerbated in the absence of *Gtpbp2*. To test this, we generated ribosome-profiling libraries

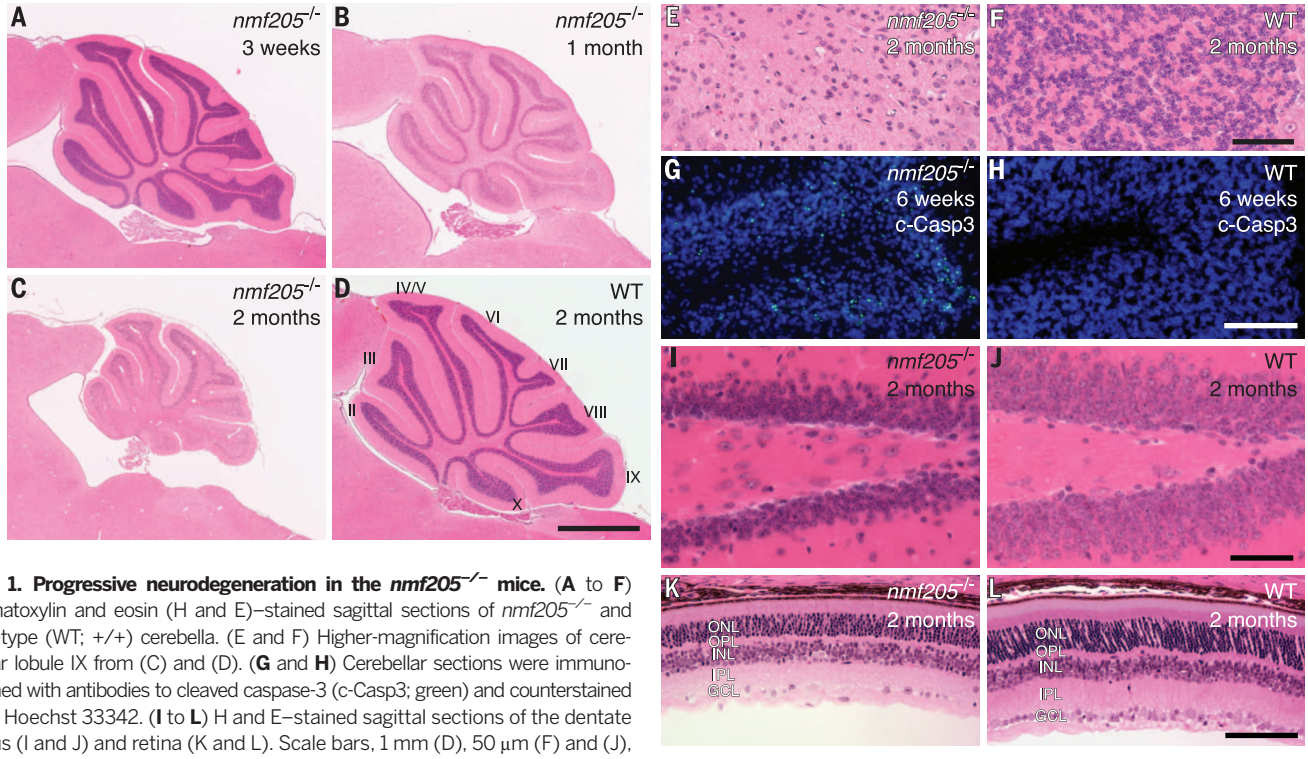
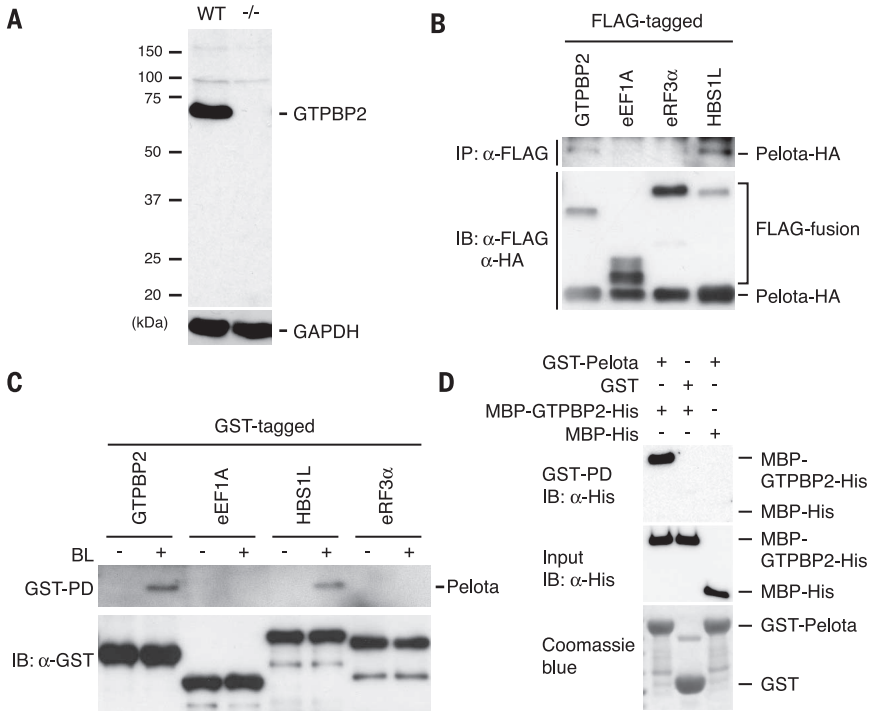


Fig. 1. Progressive neurodegeneration in the *nmf205*$^{-/-}$ mice. (**A** to **F**) Hematoxylin and eosin (H and E)–stained sagittal sections of *nmf205*$^{-/-}$ and wild-type (WT; +/+) cerebella. (E and F) Higher-magnification images of cerebellar lobule IX from (C) and (D). (**G** and **H**) Cerebellar sections were immunostained with antibodies to cleaved caspase-3 (c-Casp3; green) and counterstained with Hoechst 33342. (**I** to **L**) H and E–stained sagittal sections of the dentate gyrus (I and J) and retina (K and L). Scale bars, 1 mm (D), 50 μm (F) and (J), and 100 μm (H) and (L). ONL, outer nuclear layer; OPL, outer plexiform layer; INL, inner nuclear layer; IPL, inner plexiform layer; GCL, ganglion cell layer.

from cerebella of 3-week-old B6J (*n-Tr20* mutant), B6J.B6N^{n-Tr20} (*n-Tr20* wild-type), B6J-*nmf205*$^{-/-}$ (*Gtpbp2*$^{-/-}$; *n-Tr20* mutant), and B6J.B6N^{n-Tr20}; *nmf205*$^{-/-}$ (*Gtpbp2*$^{-/-}$; *n-Tr20* wild-type) mice (*14*–*16*). We calculated the pause strength for each codon in the ribosome A site for every gene (figs. S10 to S14). Consistent with prior studies, we observed thousands of strong pauses (P of ≥10 standard deviations above background), including a



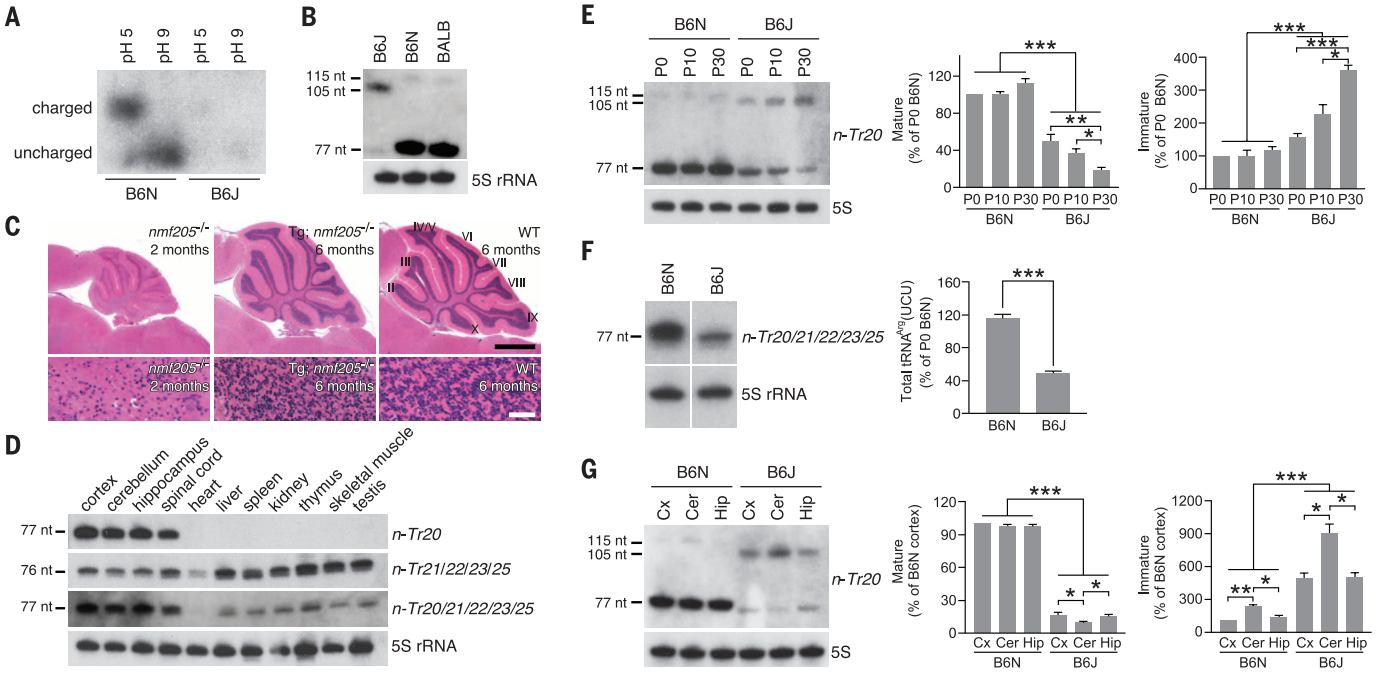


Fig. 2. The *nmf205* mutation disrupts the Pelota-interacting protein, GTPBP2. (**A**) Western blot analysis of GTPBP2 in wild-type (WT, +/+) and *nmf205*$^{-/-}$ (−/−) cerebellar extracts using antibodies to the N-terminal of GTPBP2. Glyceraldehyde-3-phosphate dehydrogenase (GAPDH) was used as a loading control. (**B**) Coimmunoprecipitation (IP) from human embryonic kidney–293T cells cotransfected with FLAG-fusion proteins as indicated, and Pelota fused to hemagglutinin (Pelota-HA). Input levels were determined by immunoblotting (IB). (**C**) GST pull-down (PD) assay of brain lysate (BL). The pull-down eluate and GST-fused baits were immunoblotted as indicated. (**D**) Bacterially expressed myelin basic protein (MBP) fused with GTPBP2 and labeled with histidine (MGP-GTPBP2-His) or MBP-His were purified and were incubated with GST or GST-Pelota. GST pull-down products (top) and input (middle and bottom) were immunoblotted with anti-His antibody (two and middle) or visualized by Coomassie blue (bottom).

Fig. 3. Mutation of the CNS-specific tRNA^{Arg} gene *n-Tr20* underlies *nmf205*-mediated neurodegeneration. (**A**) Acylated (pH 5) and deacylated (pH 9) *n-Tr20* detected by Northern blot analysis of acid gels from polyacrylamide gel electrophoresis. (**B**) Northern blot analysis of *n-Tr20* in brain RNA from P30 mice. (**C**) H and E–stained sagittal sections of cerebella from 2-month-old B6J-*nmf205*$^{-/-}$ (*nmf205*$^{-/-}$), 6-month-old Tg(n-Tr20^{B6N}) 609; B6J-*nmf205*$^{-/-}$, and 6-month-old wild-type (WT; B6J) mice. Higher magnification images of lobule IX from top panels are shown at the bottom . Scale bars in (C): 1 mm (top) and 50 μm (bottom). (**D**) Northern blot analysis of *n-Tr20*, its isodecoders, and all tRNA$^{Arg}_{UCU}$ genes. Ribosomal RNA (5*S* rRNA) was used as loading control. (**E**) Northern blot analysis of *n-Tr20* in P0, P10, and P30 B6N and B6J brain RNA. Mature and immature *n-Tr20* transcripts were quantified relative to the P0 B6N brain. (**F**) Northern blot analysis of *n-Tr20* in the P30 B6N and B6J cortex (Cx), cerebellum (Cer), and hippocampus (Hip). Mature and immature *n-Tr20* was quantified relative to the B6N cortex. (**G**) Northern blot analysis of B6N and B6J P30 brain RNA using pooled probes to *n-Tr20/21/22/23/25* tRNAs. Bands were quantified relative to the P0 B6N brain. Error bars indicate SEMs. All data are representative of independent experiments with three or more mice. *P < 0.05, **P < 0.005 and ***P < 0.0005 (two-tailed Student's t test).

well-studied pause in *Xbp1*, in each genotype (Fig. 4, A and B; fig. S15A; tables S2, A to H; and table S3) (*16*, *17*). However, no significant differences in pause number occurred between genotypes.

We then determined the number of pauses at AGA codons (Fig. 4C and fig. S15B). In the B6J.B6N^{n-Tr20} and B6J.B6N^{n-Tr20}; *nmf205*$^{-/-}$ cerebellum, few strong AGA pauses were observed (Fig. 4D and tables S2, I to P). Demonstrating the effect of impaired *n-Tr20* processing, a threefold increase in strong AGA pauses was observed in the B6J cerebellum. However, the number of AGA pauses increased dramatically in the B6J-*nmf205*$^{-/-}$ cerebellum (Fig. 4, D and E, and fig. S16). Although only a limited number of AGA codons exhibited strong pausing (P ≥ 10), strong pause sites and scores overall showed significant concordance in biological replicates (*18*) (fig. S14 and table S4). Gene ontology analysis of transcripts with strong pauses in the B6J-*nmf205*$^{-/-}$ cerebellum showed enrichment for translation-related genes, among others (table S2Q).

Reads at AGA codons in B6J and B6J-*nmf205*$^{-/-}$ cerebella were 1.6 and 2.8 times background expectations, respectively, whereas unusual AGA pausing was not observed in cerebellar libraries from B6J.B6N^{n-Tr20} and B6J.B6N^{n-Tr20}; *nmf205*$^{-/-}$ mice (Fig. 4F). To determine whether the increase in ribosome pausing in the B6J and B6J-*nmf205*$^{-/-}$ mice is specific to AGA codons, we compared codon frequency at (P ≥ 10) pause sites to the overall codon usage in transcripts. Although minor deviations were observed for several other codons,

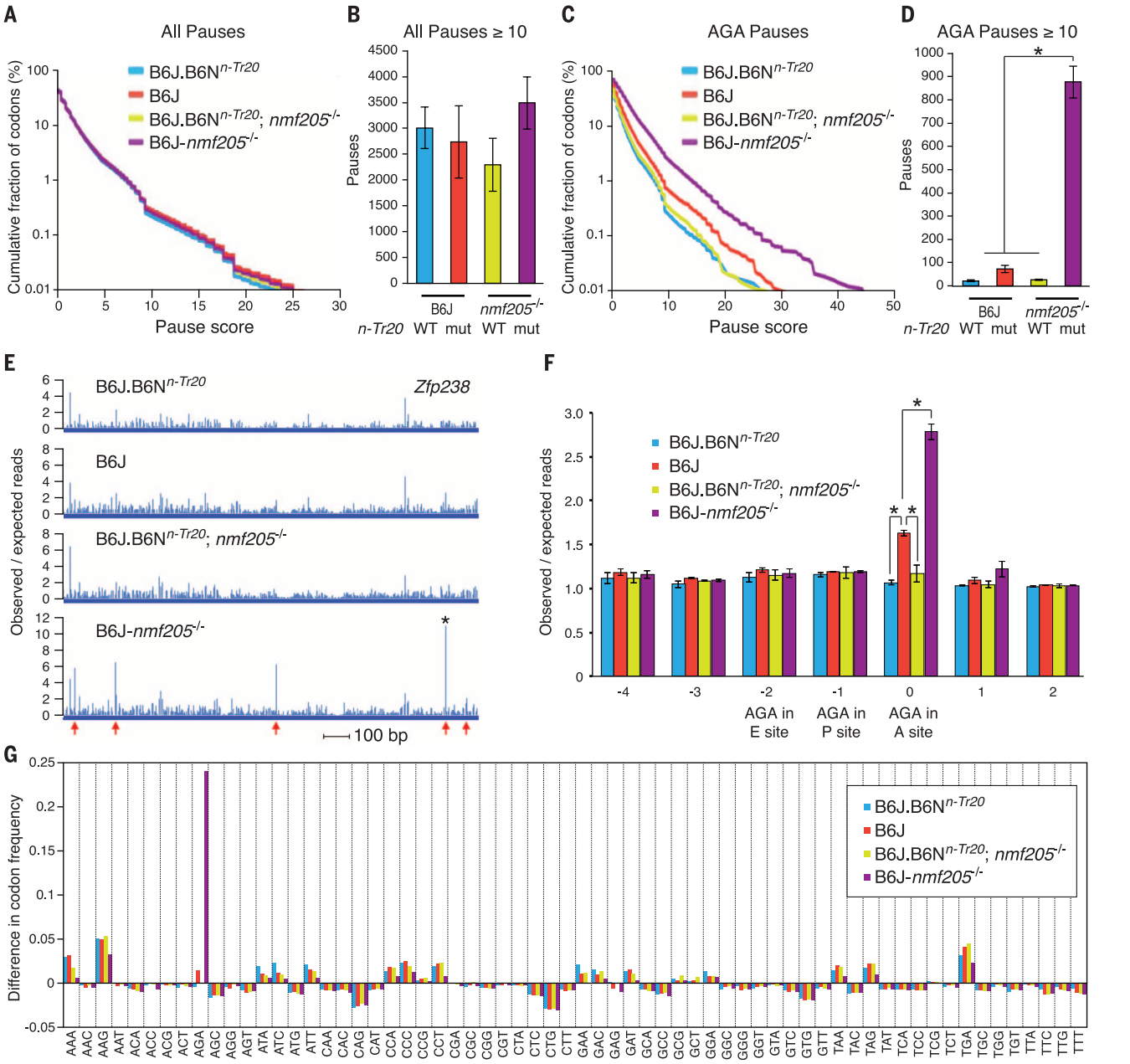


Fig. 4. The *n-Tr20* mutation induces ribosome stalling, which is resolved by GTPBP2. (**A**) Cumulative distribution of pauses at all codons averaged between replicates. (**B**) The mean number of pauses ≥10 standard deviations above the background translation levels of their genes (P ≥ 10). (**C**) Cumulative distribution of pause scores at AGA codons averaged between replicates. (**D**) The mean number of pauses (P ≥ 10) at AGA codons. (**E**) Read profile for *Zfp238* coding sequence. Asterisk (*) indicates an AGA pause with P = 45. (See fig. S16.) Arrows indicate AGA codons. (**F**) Average pausing magnitude at AGA codons, calculated by dividing genome-wide observed reads at AGA codons by expected reads. Expectations are based on read densities in genes containing an AGA. Error bars indicate standard deviations across biological replicates. *$P < 0.05$ (two-tailed Student's t test). (**G**) Difference in the codon frequency observed in the A site at pauses (P ≥ 10) versus the genome-wide codon frequency.

the strain-specific AGA effect was much larger than any other effect, which demonstrated that the increase in ribosome pausing during translation in the B6J and B6J-*nmf205*$^{-/-}$ cerebellum occurs specifically at AGA codons (Fig. 4G).

Our data demonstrate that loss of function of a nuclear encoded tRNA induces ribosome stalling that is normally resolved by GTPBP2 (fig. S17). Note that Hbs1l, another ubiquitously expressed Pelota-binding partner, does not rescue neurodegeneration in the absence of GTPBP2, which is consistent with nonoverlapping functions of these proteins (fig. S4B) (*19*). In addition, the tissue-specific expression of *n-Tr20* suggests that the regulation of individual isodecoder tRNAs may enable translational regulation in mammals. Further, our finding of a pathogenic mutation in one isodecoder of a five-member gene family underlines the possible deleterious consequences of epistatic mutations in individual members of cytoplasmic tRNA genes that could affect the readout of other mutations, including synonymous SNPs. Finally, these data also emphasize the potential for regulation and disease of mutations in individual members of multicopy gene families.

REFERENCES AND NOTES

1. Genomic tRNA database; http://gtrnadb.ucsc.edu.
2. J. M. Goodenbour, T. Pan, *Nucleic Acids Res.* **34**, 6137–6146 (2006).
3. J. R. Buchan, I. Stansfield, *Biol. Cell* **99**, 475–487 (2007).
4. S. D. Moore, R. T. Sauer, *Mol. Microbiol.* **58**, 456–466 (2005).
5. K. Rooijers, F. Loayza-Puch, L. G. Nijtmans, R. Agami, *Nat. Commun.* **4**, 2886 (2013).
6. D. Goldowitz *et al.*, *Brain Res. Mol. Brain Res.* **132**, 105–115 (2004).
7. T. E. Dever, R. Green, *Cold Spring Harb. Perspect. Biol.* **4**, a013706 (2012).
8. V. P. Pisareva, M. A. Skabkin, C. U. Hellen, T. V. Pestova, A. V. Pisarev, *EMBO J.* **30**, 1804–1817 (2011).
9. C. J. Shoemaker, D. E. Eyler, R. Green, *Science* **330**, 369–372 (2010).
10. L. Levinger, D. Serjanov, *RNA Biol.* **9**, 283–291 (2012).
11. L. Levinger *et al.*, *J. Biol. Chem.* **270**, 18903–18909 (1995).
12. H. Kudo, S. Senju, H. Mitsuya, Y. Nishimura, *Biochem. Biophys. Res. Commun.* **272**, 456–465 (2000).
13. M. Watanabe *et al.*, *Gene* **256**, 51–58 (2000).
14. N. T. Ingolia, G. A. Brar, S. Rouskin, A. M. McGeachy, J. S. Weissman, *Nat. Protoc.* **7**, 1534–1550 (2012).
15. N. T. Ingolia, S. Ghaemmaghami, J. R. Newman, J. S. Weissman, *Science* **324**, 218–223 (2009).
16. N. T. Ingolia, L. F. Lareau, J. S. Weissman, *Cell* **147**, 789–802 (2011).
17. K. Yanagitani, Y. Kimata, H. Kadokura, K. Kohno, *Science* **331**, 586–589 (2011).
18. Materials and methods are available as supplementary material on *Science* Online.
19. N. R. Guydosh, R. Green, *Cell* **156**, 950–962 (2014).

ACKNOWLEDGMENTS

Data were deposited in GenBank (GSE56127). We thank The Jackson Laboratory sequencing, histology, microinjection, and multimedia services for their assistance. We also thank K. Brown for mouse husbandry assistance and W. Frankel for comments on the manuscript. This work was supported in part by an institutional CORE grant CA34196 (JAX) and a National Science Foundation Award 0850155 to J.H.C. as part of the American Recovery and Reinvestment Act. S.L.A. is an investigator of the Howard Hughes Medical Institute.

SUPPLEMENTARY MATERIALS

www.sciencemag.org/content/345/6195/455/suppl/DC1
Materials and Methods
Figs. S1 to S17
Tables S1 to S4
References (*20*–*24*)
Movie S1

16 December 2013; accepted 5 June 2014
10.1126/science.1249749

CLATHRIN ADAPTORS

AP2 controls clathrin polymerization with a membrane-activated switch

Bernard T. Kelly,[1]* Stephen C. Graham,[2] Nicole Liska,[1] Philip N. Dannhauser,[3] Stefan Höning,[4] Ernst J. Ungewickell,[3] David J. Owen[1]*

Clathrin-mediated endocytosis (CME) is vital for the internalization of most cell-surface proteins. In CME, plasma membrane–binding clathrin adaptors recruit and polymerize clathrin to form clathrin-coated pits into which cargo is sorted. Assembly polypeptide 2 (AP2) is the most abundant adaptor and is pivotal to CME. Here, we determined a structure of AP2 that includes the clathrin-binding β2 hinge and developed an AP2-dependent budding assay. Our findings suggest that an autoinhibitory mechanism prevents clathrin recruitment by cytosolic AP2. A large-scale conformational change driven by the plasma membrane phosphoinositide phosphatidylinositol 4,5-bisphosphate and cargo relieves this autoinhibition, triggering clathrin recruitment and hence clathrin-coated bud formation. This molecular switching mechanism can couple AP2's membrane recruitment to its key functions of cargo and clathrin binding.

Clathrin adaptors provide an essential physical bridge connecting clathrin, which itself lacks membrane binding activity (*1*), to the membrane and to embedded transmembrane protein cargo. A central player in clathrin-mediated endocytosis (CME) is the AP2 (assembly polypeptide 2) complex (Fig. 1A and fig. S1), which both coordinates clathrin-coated pit (CCP) formation and binds the many cargo proteins that contain acidic dileucine and Yxxϕ endocytic motifs (Y denotes Tyr; x, any amino acid; and ϕ, a bulky hydrophobic residue) through its membrane-proximal core (*2*, *3*). Cargo binding is activated by a large-scale conformational change from the "locked" or inactive cytosolic form to an "open" or active form driven by localization to membranes containing the plasma membrane phosphoinositide phosphatidylinositol 4,5-bisphosphate [PtdIns(4,5)P_2] (*4*, *5*). The C-terminal "appendages" of the α and β2 subunits bind other clathrin adaptors as well as CCV (clathrin-coated vesicle) assembly and disassembly accessory factors (*3*, *6*–*8*). The flexible hinge separating the β2 appendage from the β2 trunk binds the N-terminal β-propeller of the clathrin heavy chain by using a canonical clathrin box motif [LLNLD; L, Leu; N, Asn; D, Asp (Fig. 1, A and B) (*9*)]. The β2 appendage domain also binds clathrin, albeit weakly, but both interactions are necessary for robust clathrin binding (*10*).

A version of AP2 comprising full-length β2, μ2, and σ2 subunits and the α trunk domain (FLβ.AP2) (Fig. 1B) (*11*) was expressed in *Escherichia coli*, avoiding contamination with other CCV components inherent to purification from brain tissue (*12*, *13*). Despite most FLβ.AP2 possessing an intact β2 subunit (Fig. 1, C to E), it bound clathrin very poorly in pulldowns when immobilized either on glutathione sepharose beads (Fig. 1C) or via its N-terminal His_6 tag [similarly positioned to the β2 PtdIns(4,5)P_2 binding site (Fig. 1B) (*4*, *5*)] to liposomes containing the nickel-attached nitrilotriacetic acid–dioleoylglycerosuccinyl (NiNTA-DGS) (Fig. 1E): In both cases, the FLβ.AP2 will be in its locked cytosolic conformation (*4*). FLβ.AP2 also failed to stimulate clathrin cage assembly efficiently at physiological pH (Fig. 1D). In contrast, the isolated β2 hinge-appendage [glutathione *S*-transferase (GST)-β2-h+app (fig. S1)] bound clathrin efficiently (Fig. 1C) and stimulated cage assembly (Fig. 1D). We next compared clathrin recruitment to synthetic liposomes composed of dioleoylphosphatidylcholine and dioleoylphosphatidylethanolamine supplemented either with NiNTA-DGS or with a mixture of PtdIns(4,5)P_2 and a lipid-linked YxxΦ endocytic motif (*5*, *11*, *14*). β2-h+app fused to His_6-tagged epsin N-terminal homology (ENTH) domain (His_6-ENTH-β2-h+app), which can bind NiNTA-DGS or PtdIns(4,5)P_2, recruited clathrin efficiently to both types of liposomes. In contrast, FLβ.AP2 recruited clathrin only when bound to PtdIns(4,5)P_2- and YxxΦ-containing liposomes (Fig. 1E). Thus, no additional proteins are required to prevent clathrin binding to AP2 in solution, consistent with immunoprecipitation data (*15*). We conclude that the clathrin-binding activity of AP2 is autoinhibited in the cytosol to restrict inappropriate clathrin recruitment and that only upon encountering its physiological membrane ligands [PtdIns(4,5)P_2 and cargo] can AP2 recruit clathrin efficiently. Previous reports that AP2 purified from brain could bind and polymerize clathrin (*12*) were likely due to other contaminating clathrin adaptors, such as AP180 (*13*).

We were unable to crystallize FLβ.AP2, so we determined the structure of a form of AP2 (βhingeHis_6.AP2) whose β2 (residues 1 to 650) includes the clathrin box–containing hinge but not the β2 appendage. The structure closely

[1]Cambridge Institute for Medical Research (CIMR), Department of Clinical Biochemistry, University of Cambridge, Hills Road, Cambridge CB2 0XY, UK. [2]Department of Pathology, University of Cambridge, Tennis Court Road, Cambridge CB2 1QP, UK. [3]Department of Cell Biology, Center of Anatomy, Hannover Medical School, Carl-Neuberg Strasse 1, D-30625 Hannover, Germany. [4]Institute of Biochemistry I and Center for Molecular Medicine Cologne, University of Cologne, Joseph-Stelzmann-Strasse 52, 50931 Cologne, Germany.
***Corresponding author. E-mail: btk1000@cam.ac.uk (B.T.K.); djo30@cam.ac.uk (D.J.O.)**

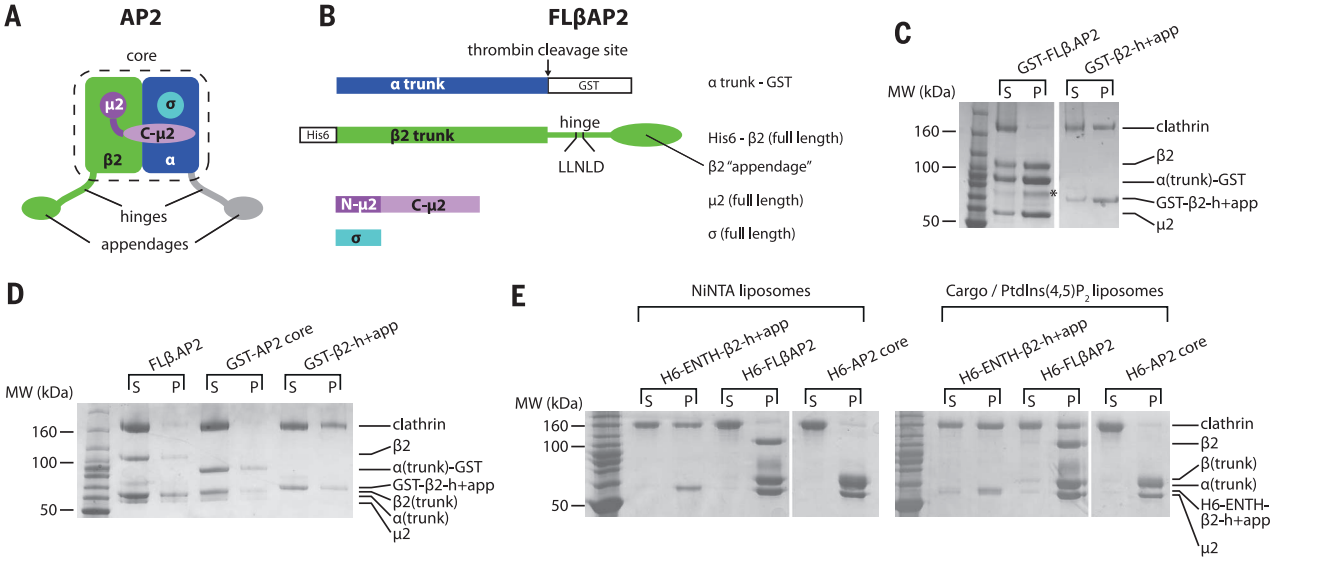


Fig. 1. AP2 can bind clathrin only when it is attached to a PtdIns(4,5)P_2-and cargo-containing membrane. (**A**) AP2 schematic, color-coded by subunit: α, blue; β2, green; N-μ2, dark magenta; C-μ2, pale magenta; σ, cyan. The unstructured α and β2 hinge and appendage subdomains, together with the core of the complex, are indicated. Parts shown in gray are not present in FLβ.AP2. Schematics of constructs are shown in fig. S1. (**B**) FLβ.AP2 showing the positions of the clathrin box and purification tags. (**C**) Coomassie-stained SDS–polyacrylamide gel electrophoresis (SDS-PAGE) of glutathione-sepharose pull-downs using GST-FLβ.AP2 or GST-β2-h+app. Supernatant (s) and pellet (p). The band marked with an asterisk results from proteolysis of β2. MW, molecular weight. (**D**) Coomassie-stained SDS-PAGE of clathrin cage assembly assays using 2.5 μM clathrin and 1.5 μM adaptors (as indicated), overnight at 21°C, centrifuged to separate clathrin cages (p) from supernatants (s). (**E**) Coomassie-stained SDS-PAGE of liposome pulldown assays. Liposomes were sequentially incubated with adaptors and clathrin, then centrifuged to separate unbound material (s) from the liposome pellet (p).

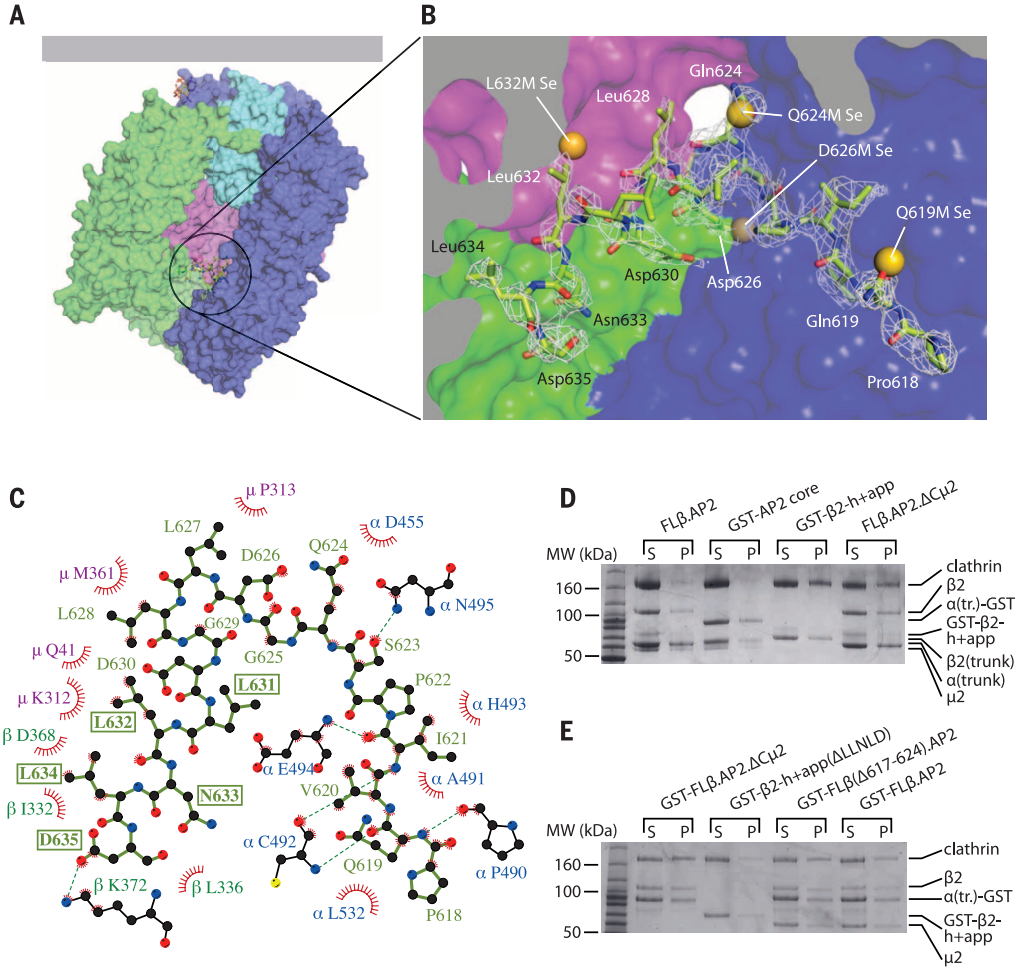


Fig. 2. The AP2 β2 subunit LLNLD clathrin binding motif is buried in the center of the core. Overall (**A**) and closeup (**B**) views of the structure of βhingeHis$_6$.AP2. The residues of the hinge resolved in the structure are shown in green as a stick representation. The AP2 core is depicted in a surface representation, colored as in Fig. 1. The residues of the buried hinge are indicated in (B), with electron density shown as mesh ($2mF_o - DF_c$ map, contoured at 0.34 e Å^{-3}). Q, Gln. Also shown are the positions of the selenium (Se) sites found in the bowl for each of the methionine (M) mutants indicated, showing good agreement with the positions of the corresponding wild-type residues that were mutated. Individual log-likelihood gradient maps are shown in fig. S3. (**C**) Ligplot+ (*25*) diagram showing interactions between buried hinge residues (in pale green) with residues of α (blue), μ2 (magenta), and β2 (dark green). Red fans indicate hydrophobic interactions; dashed green lines indicate hydrogen bonds. The residues of the clathrin-binding motif are boxed. See also fig. S4. A, Ala; C, Cys; E, Glu; G, Gly; H, His; I, Ile; K, Lys; P, Pro; S, Ser; and V, Val. (**D**) Clathrin cage assembly assays. (D) is identical to Fig. 1D (2.5 μM clathrin, 1.5 μM adaptors) with the addition of the FLβ.AP2.ΔCμ2 lane. (**E**) Assays performed as in (D) but at 28°C and with 2 μM clathrin and 4 μM adaptors as shown.

resembles that of the locked conformation of the AP2 core, but additional protein difference electron density was visible in the center of the AP2 core (fig. S2). Crystallographic analysis of AP2s truncated at Leu^{636} and Gln^{619} of β2 suggested that this electron density corresponded to the region of β2 between these points (*11*). A series of mutant AP2s with single methionine substitutions throughout the hinge region was created, the mutants crystallized as selenomethionyl derivatives, and their structures solved (fig. S3). This allowed us to assign unambiguously this density to residues 618 to 634 of β2 (including the clathrin box at residues 631 to 635) and refine the structure (Fig. 2, A and B; fig. S2; and movies S1 and S2). There are two regions of contact: a β sheet interaction between β2 residues 618 to 624 and α trunk residues 490 to 493 and the packing of the clathrin box itself and the short helix immediately preceding it with residues of C-μ2 and the β2 trunk (Fig. 2C and fig. S4). In this position, the LLNLD clathrin box is inaccessible, explaining FLβ.AP2's lack of clathrin binding (Fig. 1), because deletion of only the LLNLD clathrin motif in GST-β2-h+app abolishes clathrin recruitment (fig. S5). The β2 618 to 636 region is well conserved across a wide range of species (fig. S6) and between β2 and β1 (the equivalent subunit of the AP1 adaptor). This suggests that, in AP1, clathrin binding will be similarly regulated by membrane attachment, albeit stimulated mainly by binding to guanosine 5′-triphosphate (GTP)–bound Arf1 (*16*, *17*). Interfering with the interactions that trap the clathrin box in the AP2 core should release the hinge, allowing increased clathrin recruitment. Indeed, deletion of C-μ2 (termed FLβ.AP2.ΔCμ2), disrupting key interactions with β2 625 to 635 (that includes the clathrin motif; fig. S4), had a profound effect, resulting in efficient clathrin binding and cage assembly in solution (Fig. 2D and fig. S7). Deletion of the hinge residues 617 to 624, removing the largely backbone-mediated interaction with 490 to 493 of the α subunit (fig. S4), resulted in a modest but significant increase in AP2-mediated clathrin polymerization in solution at physiological pH [25% ± 3.1% clathrin polymerized (mean ± SEM, three experiments) versus 9.9% ± 3.8%; difference tested by Student's *t* test, $P = 0.037$ (Fig. 2E)].

The structure suggests a mechanism by which clathrin binding is triggered by AP2's membrane recruitment in the cell. Aligning the open and locked conformations on residues 480 to 510 of the α subunit [a translation-libration-screw group used in refinement (*5*) that juxtaposes the buried hinge fragment] revealed that the membrane and cargo-bound open conformation is incompatible with the autoinhibitory sequestration of the hinge (Fig. 3 and figs. S4 and S8): The β2 trunk now blocks the point of entry of the hinge into the bowl, and the relocation of C-μ2 removes one face of the pocket in which the helical β2 hinge segment rests (Fig. 2C and fig. S4). Thus, transition of AP2 from the locked to the open conformation, triggered by association with the plasma membrane, stimulates clathrin binding by releasing the clathrin box–containing β2 hinge from the center of the core (*5*).

To address whether cargo binding is absolutely required to stimulate clathrin recruitment, we prepared synthetic liposomes supplemented either with PtdIns(4,5)P_2 alone or with a mixture of PtdIns(4,5)P_2 and a lipid-linked Yxxϕ motif and mixed these with FLβ.AP2 and clathrin, both at plausible cellular concentrations of 0.4 μM (*18*) (Fig. 4A). As expected, FLβ.AP2 bound more tightly to the cargo-containing liposomes (Fig. 4A) (*5*, *14*). However, the ratio of clathrin to AP2 present in the cargo-containing liposome pellets was significantly greater (26.5% ± 5.3%) than in the PtdIns(4,5)P_2-only liposomes (5.2% ± 1.9%; means ± SEM, four experiments; difference tested by Student's *t* test, $P = 0.0094$). This finding suggests that PtdIns(4,5)P_2- and cargo-bound FLβ.AP2 is able to recruit clathrin more efficiently than FLβ.AP2 bound only via PtdIns(4,5)P_2, consistent with PtdIns(4,5)P_2 driving the conformational change in AP2 that is then stabilized by cargo binding (*5*, *19*).

Last, we sought to determine whether AP2 alone is sufficient to initiate and drive clathrin-coated bud formation on appropriate membranes. When FLβ.AP2-loaded PtdIns(4,5)P_2- and lipid-linked Yxxϕ cargo-supplemented liposomes were incubated with clathrin and the results examined by negative stain electron microscopy (EM) (Fig. 4B), we observed numerous clathrin-coated buds, of ~80-nm diameter. Ultrathin sectioning revealed that the buds encapsulated invaginated membrane or vesicles of 30- to 40-nm diameter, similar to CCVs isolated from brain (Fig. 4, D and E). Fewer buds were found on PtdIns(4,5)P_2 liposomes incubated with FLβ.AP2 and clathrin (Fig. 4, C and F). We were unable to find buds on NiNTA liposomes similarly treated with FLβ.AP2 (Fig. 4, C and F), but some clathrin-coated buds were found on NiNTA liposomes incubated with clathrin and C-μ2–deleted FLβ.AP2 (FLβ.AP2.ΔCμ2), whereas His_{12}-tagged GST-β2-h+app produced ample buds on NiNTA liposomes (Fig. 4, C and F). Thus, once activated by binding to its physiological ligands, AP2 is sufficient to drive clathrin-coated bud formation (at least in vitro); no other clathrin adaptors, including those currently described as driving membrane curvature, are required.

AP2 is the most abundant endocytic clathrin adaptor (*20*) and the first to be recruited to sites of CCP formation (*2*, *8*). AP2 knockdown results in a ~12-fold reduction in CCP formation in HeLaM cells (*21*). Together with our findings that

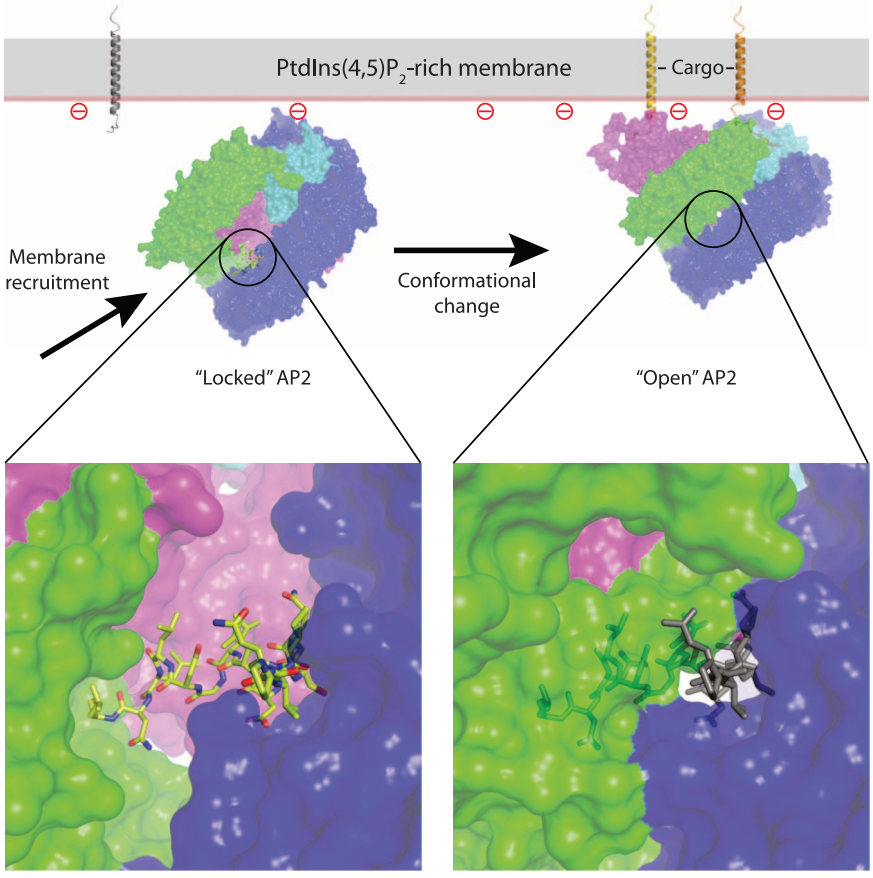


Fig. 3. The open, activated form of AP2 is not compatible with the β2 hinge binding back into the core. Release of the clathrin-binding motif stimulated by conformational change. (**Top**) Locked AP2 core, in solution or transiently bound to the plasma membrane via PtdIns(4,5)P_2 (left), and open AP2 stably attached to the membrane via multiple PtdIns(4,5)P_2s and cargo. (**Bottom**) Views of the hinge binding site in each conformational state; in the open state (right), the hinge residues from the locked state βhingeHis$_6$.AP2 structure are superposed onto the open structure and shown in gray.

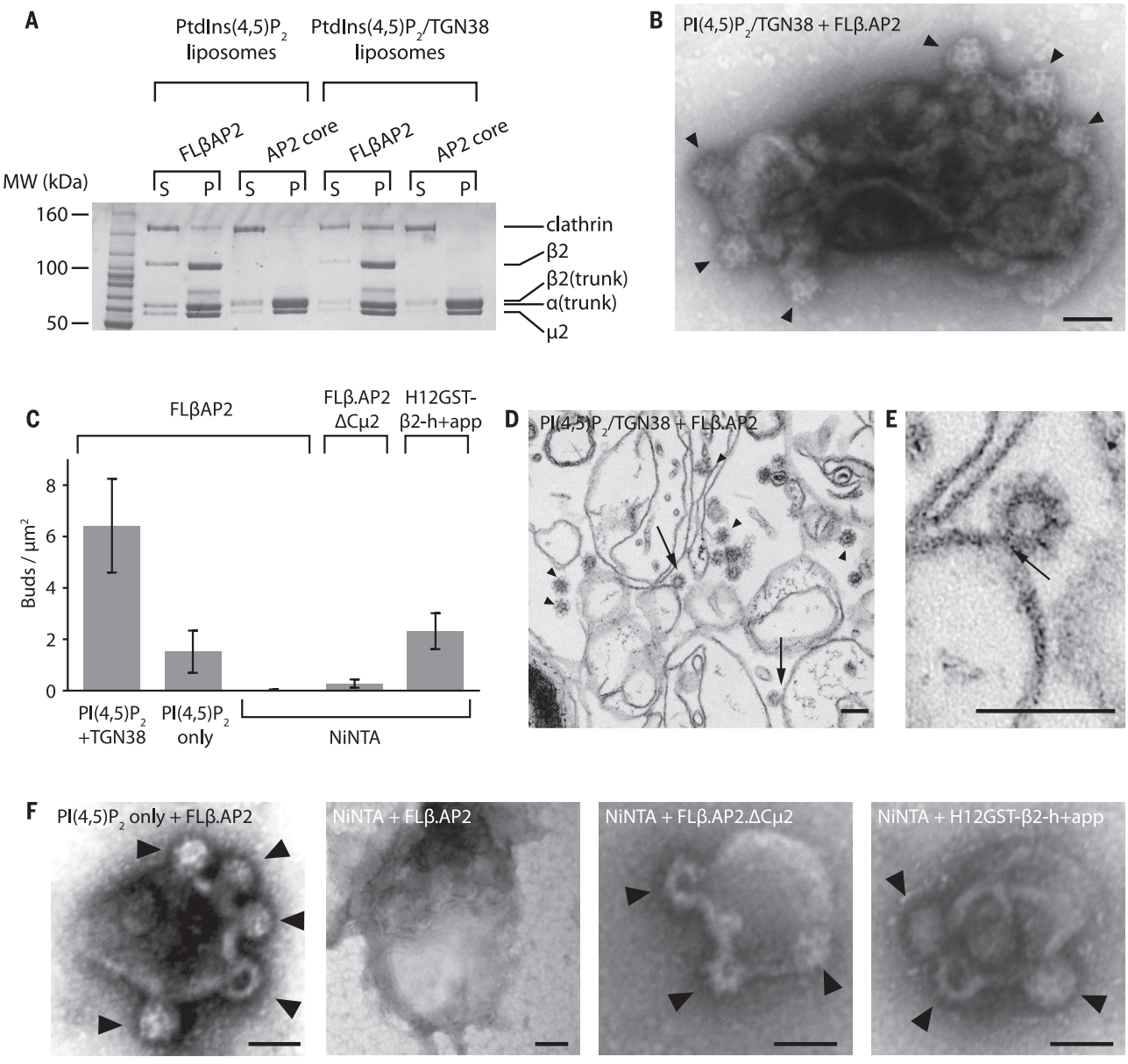


Fig. 4. AP2 and clathrin are sufficient to generate clathrin-coated buds on membranes. (**A**) Clathrin recruitment to liposomes. Synthetic liposomes supplemented with PtdIns(4,5)P_2, or with PtdIns(4,5)P_2 and TGN38 peptide (as indicated), were incubated with adaptor and clathrin as shown (both at 0.4 μM); supernatants (s) and pellets (p) were then separated and analyzed by gel electrophoresis. (**B**) Liposomes supplemented with PtdIns(4,5)P_2 and lipid-linked TGN38 internalization were incubated sequentially with FLβ.AP2 and clathrin and analyzed by negative stain EM, showing clathrin-coated membrane buds (arrowheads). (**C**) Mean number of buds formed per μm^2 of membrane, estimated for various combinations of lipid and adaptor. Note that no buds were found on PtdIns(4,5)P_2 liposomes with or without TGN38 incubated sequentially with the AP2 core and clathrin or with clathrin only (fig. S9). Error bars indicate SEM, three experiments. (**D** and **E**) Liposomes supplemented with PtdIns(4,5)P_2 and lipid-linked TGN38 internalization incubated sequentially with FLβ.AP2 and clathrin and analyzed by ultrathin sectioning. Arrowheads indicate examples of clathrin-coated structures; arrows indicate coated buds where the connection to the liposome is visible. (E) shows an enlarged image of a bud showing the "neck." (**F**) Examples of liposomes supplemented with the lipids indicated [PtdIns(4,5)P_2 or NiNTA-DGS] incubated sequentially with adaptors (as indicated) and clathrin, examined by negative stain EM. Some buds produced by FLβ.AP2 on PtdIns(4,5)P_2-only liposomes seemed less invaginated than those shown here; this can be seen more clearly in ultrathin sections (fig. S10).

PtdIns(4,5)P_2-activated and cargo-stabilized AP2 is sufficient to drive bud formation on liposomes, these data suggest that in vivo the dominant mechanism for endocytic CCP initiation will be the recruitment of AP2 to PtdIns(4,5)P_2-enriched sites in its locked form with its clathrin binding autoinhibited, followed by transition to the open form if sufficient PtdIns(4,5)P_2 is present (*5*, *19*). AP2's conformational change will expel the β2 hinge, allowing clathrin triskelia to bind. The presence of cargo will stabilize AP2's open form and increase its dwell time on the membrane (*5*, *14*, *19*, *22*), thus increasing the chances of it binding clathrin and forming a sufficiently stable nucleating structure. Once a small nucleus of AP2 and clathrin has formed, further AP2, clathrin, and other clathrin adaptors that bind the α appendage can then be recruited in random order to produce a CCP, which can ultimately be severed from the membrane (*3*, *23*, *24*).

REFERENCES AND NOTES

1. P. N. Dannhauser, E. J. Ungewickell, *Nat. Cell Biol.* **14**, 634–639 (2012).
2. E. Cocucci, F. Aguet, S. Boulant, T. Kirchhausen, *Cell* **150**, 495–507 (2012).
3. L. M. Traub, *PLOS Biol.* **9**, e1001037 (2011).
4. B. M. Collins, A. J. McCoy, H. M. Kent, P. R. Evans, D. J. Owen, *Cell* **109**, 523–535 (2002).

5. L. P. Jackson *et al.*, *Cell* **141**, 1220–1229 (2010).
6. L. M. Traub, *Nat. Rev. Mol. Cell Biol.* **10**, 583–596 (2009).
7. E. M. Schmid, H. T. McMahon, *Nature* **448**, 883–888 (2007).
8. M. J. Taylor, D. Perrais, C. J. Merrifield, *PLOS Biol.* **9**, e1000604 (2011).
9. E. ter Haar, S. C. Harrison, T. Kirchhausen, *Proc. Natl. Acad. Sci. U.S.A.* **97**, 1096–1100 (2000).
10. M. A. Edeling *et al.*, *Dev. Cell* **10**, 329–342 (2006).
11. Materials and methods are available as supplementary materials on *Science* Online.
12. S. Zaremba, J. H. Keen, *J. Cell Biol.* **97**, 1339–1347 (1983).
13. R. Lindner, E. Ungewickell, *J. Biol. Chem.* **267**, 16567–16573 (1992).
14. S. Höning *et al.*, *Mol. Cell* **18**, 519–531 (2005).
15. J. Hirst *et al.*, *Mol. Biol. Cell* **24**, 2558–2569 (2013).
16. L. M. Traub, J. A. Ostrom, S. Kornfeld, *J. Cell Biol.* **123**, 561–573 (1993).
17. X. Ren, G. G. Farías, B. J. Canagarajah, J. S. Bonifacino, J. H. Hurley, *Cell* **152**, 755–767 (2013).
18. M. Beck *et al.*, *Mol. Syst. Biol.* **7**, 549 (2011).
19. D. Loerke *et al.*, *PLOS Biol.* **7**, e57 (2009).
20. G. H. Borner *et al.*, *J. Cell Biol.* **197**, 141–160 (2012).
21. A. Motley, N. A. Bright, M. N. Seaman, M. S. Robinson, *J. Cell Biol.* **162**, 909–918 (2003).
22. A. P. Liu, F. Aguet, G. Danuser, S. L. Schmid, *J. Cell Biol.* **191**, 1381–1393 (2010).
23. F. M. Brodsky, *Annu. Rev. Cell Dev. Biol.* **28**, 309–336 (2012).
24. F. Aguet, C. N. Antonescu, M. Mettlen, S. L. Schmid, G. Danuser, *Dev. Cell* **26**, 279–291 (2013).
25. R. A. Laskowski, M. B. Swindells, *J. Chem. Inf. Model.* **51**, 2778–2786 (2011).

ACKNOWLEDGMENTS

We would like to thank the I02, I03, and I04-1 beamline staff at the Diamond Lightsource; A. McCoy and P. Evans for crystallographic advice; C. Oubridge for advice and assistance with SeMet mapping of the hinge residues; N. Bright, C. Savva, and S. Miller for advice and assistance with EM; C. Smith for reagents; and H. Böning and H. Ungewickell for expert technical assistance. D.J.O. and B.T.K. are supported by a Wellcome Trust Principal Research fellowship (090909/Z/09/Z). S.H. is supported by a grant of the German Science Foundation (SFB 635, TP A3). S.C.G. is supported by a Sir Henry Dale fellowship from the Wellcome Trust and the Royal Society (098406/Z/12/Z). CIMR is supported by a Wellcome Trust Strategic Award (079895). Coordinates have been deposited in the Protein Data Bank with PDB ID 4uqi.

SUPPLEMENTARY MATERIALS

www.sciencemag.org/content/345/6195/459/suppl/DC1
Materials and Methods
Figs. S1 to S11
Tables S1 and S2
References (*26*–*38*)
Movies S1 and S2

15 April 2014; accepted 24 June 2014
10.1126/science.1254836

ACTIN CYTOSKELETON

Mechanism of actin filament pointed-end capping by tropomodulin

Jampani Nageswara Rao, Yadaiah Madasu, Roberto Dominguez*

Proteins that cap the ends of the actin filament are essential regulators of cytoskeleton dynamics. Whereas several proteins cap the rapidly growing barbed end, tropomodulin (Tmod) is the only protein known to cap the slowly growing pointed end. The lack of structural information severely limits our understanding of Tmod's capping mechanism. We describe crystal structures of actin complexes with the unstructured amino-terminal and the leucine-rich repeat carboxy-terminal domains of Tmod. The structures and biochemical analysis of structure-inspired mutants showed that one Tmod molecule interacts with three actin subunits at the pointed end, while also contacting two tropomyosin molecules on each side of the filament. We found that Tmod achieves high-affinity binding through several discrete low-affinity interactions, which suggests a mechanism for controlled subunit exchange at the pointed end.

The proteins that cap the ends of the actin filament play important roles in actin-driven processes such as cell migration and organelle trafficking by controlling the addition and dissociation of actin subunits at filament ends. Several proteins cap the barbed end of the filament, including capping protein (CP) and some gelsolin-family members (*1*, *2*). In contrast, tropomodulin (Tmod) is the only protein known to cap the pointed end of tropomyosin (TM)–coated actin filaments (*3*). Four Tmod isoforms work in conjunction with one of several TM isoforms to stabilize actin structures characterized by a uniform distribution of the lengths of actin filaments. These structures include the sarcomere of cardiac and skeletal muscle cells and the spectrin-based membrane skeleton (*3*, *4*).

The mechanism by which Tmod caps the pointed end is poorly understood. Quantification in skeletal muscle and erythrocytes led to the proposal that two Tmod molecules cap the pointed end (*5*, *6*). In vitro, however, one Tmod molecule is sufficient to block pointed-end elongation of TM-coated filaments (*7*), consistent with the distinctive domain architecture of Tmod, which harbors two actin- and two TM-binding sites. Thus, the N-terminal ~160–amino acid region is mostly unstructured in isolation (*8*), but contains three predicted helical segments that bind TM, actin, and TM in that order (*9*, *10*). This region displays TM-dependent capping activity (*9*). Most of the C-terminal region (human Tmod1 residues 161 to 359) consists of a leucine-rich repeat (LRR) domain (*11*). This region displays limited capping activity on its own (*9*). Although Tmod binds with nanomolar affinity to the pointed end (*12*), and even greater affinity in the presence of TM (*7*), it does not form an absolute cap. Instead, Tmod functions as a "leaky" cap, determining the length of the actin filaments while allowing for the controlled addition or dissociation of actin subunits at the pointed end (*13*). In the absence of high-resolution structures of the pointed end, rationalization of the existing data is difficult, and several models exist, featuring either one (*10*, *11*) or two (*5*, *6*) Tmod molecules at the pointed end.

Actin polymerization prevents crystallization of capping complexes. We thus attempted crystallization of the N- and C-terminal actin-binding sites (ABS1 and ABS2) of Tmod in complex with monomeric actin. However, both sites bound with weak affinity to monomeric actin (see below), and polymerization persisted during crystallization. A solution was found by fusing ABS1 and ABS2 C-terminally to gelsolin segment 1 (GS1) via a nine–amino acid flexible linker [crystallization strategies are described in (*14*)]. The Tmod fragments extended beyond the actin-binding sites defined previously (*9*, *15*–*17*), with ABS1 and ABS2 comprising human Tmod1 residues 50 to 101 and 160 to 349, respectively (Fig. 1A). Notably, ABS1 and ABS2 both bound actin:GS1 with 1:1 stoichiometry and with similar affinities [dissociation constant (K_D) = 7.5 and 10.5 μM for ABS1 and ABS2, respectively] when not connected by a linker (Fig. 1, B and C). Similar binding affinities were obtained at two different temperatures, 10°C and 20°C, and with adenosine 5′-triphosphate (ATP)– or adenosine 5′-diphosphate (ADP)–actin (fig. S1).

The complexes of ATP-actin with GS1-ABS1 and GS1-ABS2 crystallized under slightly different conditions, and with different unit cell parameters (*14*) (table S1). The structures were determined to 1.8 and 2.3 Å resolution for ABS1 and ABS2, respectively (Fig. 1, D and E, and fig. S2, A and B). Both structures were well defined in the electron density maps (fig. S2, C and D). The flexible linkers between GS1 and the Tmod fragments, and residues 50 to 57 and 100 to 101 of ABS1 and 160 to 169 of ABS2, were not visualized. These residues likely do not interact with actin, because the C termini of ABS1 and ABS2 projected away from actin, and weak electron density that could not be modeled was also observed projecting away from actin at their N termini. A structure of ABS1 was also obtained with ADP-actin at 2.15 Å resolution and showed a conformation similar to that observed with ATP-actin (*14*). Crystals of ABS2 could not be obtained with ADP-actin.

The Tmod structures differed substantially from previously characterized actin complexes (*18*); whereas most actin-binding proteins bind in the cleft between actin subdomains 1 and 3, ABS1 and ABS2 bound at the pointed end of the actin monomer, and on the side of subdomains

Department of Physiology, Perelman School of Medicine, University of Pennsylvania, Philadelphia, PA 19104, USA.
***Corresponding author: E-mail: droberto@mail.med.upenn.edu**

2 and 1 (Fig. 1, D and E, and movies S1 and S2). An unusual feature of the structures was an interaction with the deoxyribonuclease I (DNase I)–binding loop in actin. As a result, this loop, which is disordered in most actin structures, was ordered in the Tmod complexes, albeit with different conformations in the two structures.

ABS1 extended beyond the α helix suggested previously, with a total of 42 residues (P58 to K99) mediating the interaction (Fig. 1, A and D). ABS1 adopted a rather extended conformation and contacted three out of the four actin subdomains. The α helix was longer than anticipated, comprising residues 64 to 77. This helix played a crucial role in the interaction, by forming a bridge across the nucleotide-binding cleft on top of actin subdomains 4 and 2. As a result, the nucleotide cleft was slightly more closed in this structure than in that of ABS2.

The interactions of ABS2 were also more extensive than anticipated and involved contacts along the entire region Y170 to L344. Residues Y170 to N179 formed a loop that interacted with the DNase I–binding loop in actin. Several additional contacts were mediated by the LRR domain, whose boundaries differed compared to the description of the structure of uncomplexed chicken Tmod1 residues 179 to 344 (*11*). The LRR motif is defined as a β-strand–loop–α-helix module (*19*). The loop of the motif is called the "ascending loop," whereas the loop connecting one motif to the next is called the "descending loop." By this criterion, Tmod contains not five but four-and-a-half LRR motifs (Fig. 1A). The ascending loops typically mediate protein-protein interactions (*19*), and this principle was conserved in Tmod, where the ascending loops interacted on the back side (according to the classical view) of actin subdomains 2 and 1 (Fig. 1 A and E). Most LRR domains have N- and C-terminal caps, which shield the hydrophobic core of the domain from solvent exposure (*19*). In Tmod, these caps consisted of α helices that ran diagonally to the first and last LRR motifs: D182 to N193 and Q321 to N336. The C-terminal cap continued as an uninterrupted α

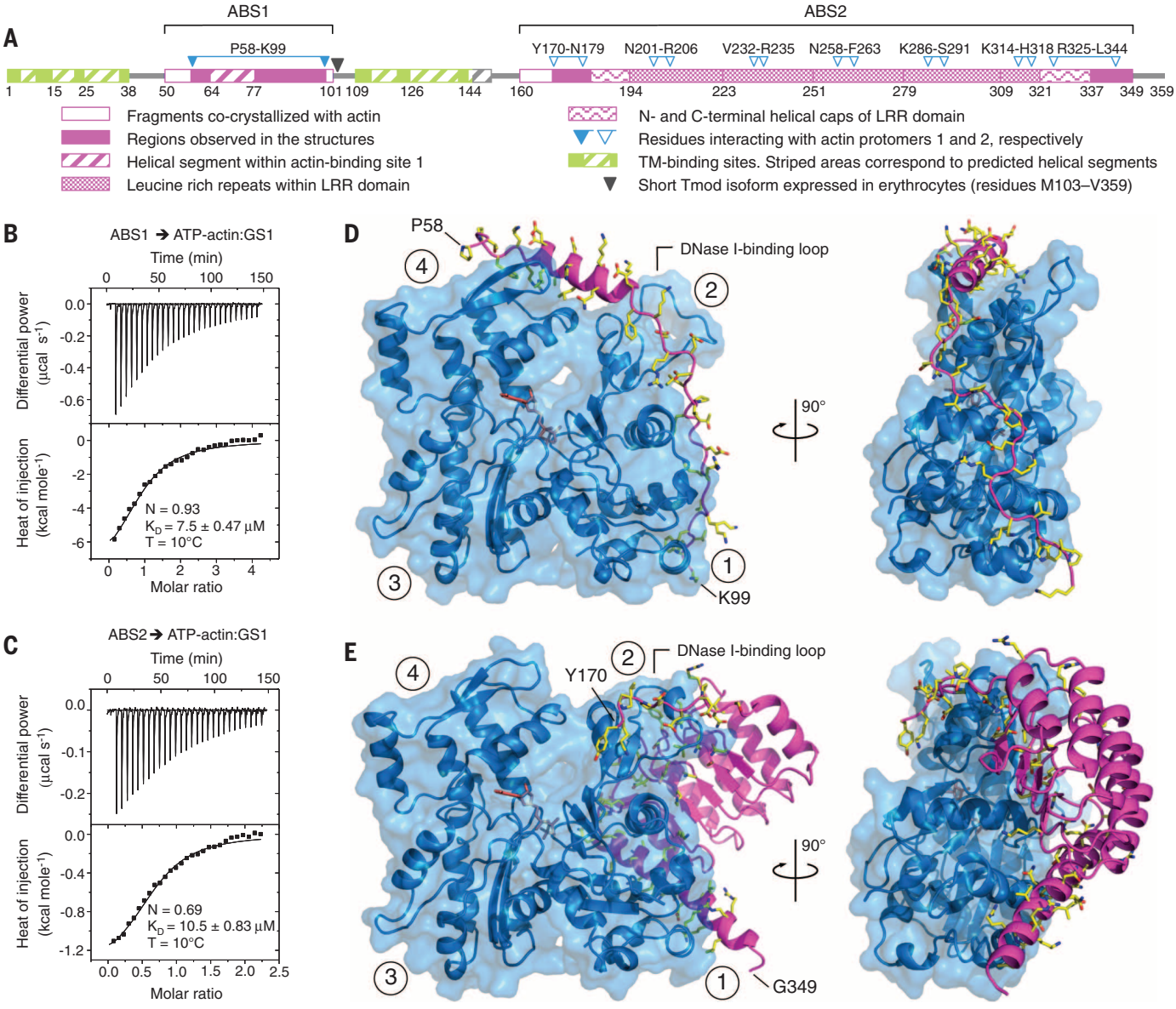


Fig. 1. Structures of Tmod's ABS1 and ABS2 bound to actin. (**A**) Domain diagram of human Tmod1, showing the interactions of ABS1 and ABS2 with actin. (**B** and **C**) Isothermal titration calorimetry (ITC) titrations of ABS1 (400 μM) (B) and ABS2 (632 μM) (C) into 20 and 60 μM ATP-bound actin:GS1. For both titrations, the best fit of the data corresponds to a one-site binding isotherm. The reported errors correspond to the SD of the fits. (**D** and **E**) Two perpendicular views of the structures of ABS1 (D) and ABS2 (E) bound to actin (blue). GS1, fused N-terminally to the two Tmod domains, is omitted from this figure, but shown in fig. S2. The side chains of Tmod residues that fall near actin are shown (colored by atom type: carbon, yellow; oxygen, red; nitrogen, blue). Circled numbers indicate actin subdomains 1 to 4. Note that subdomains 2 and 4 are exposed at the pointed end of the actin filament.

helix that ended with residue T348. This helix interacted along most of its length (R325 to L344) with actin subdomain 1.

The structures of ABS1 and ABS2 were unequivocally overlaid onto the pointed end of the actin filament (*20*), producing a model of the pointed end that was then tested by mutagenesis (*14*). First, the structures showed that Tmod could only bind at the pointed end, because both ABS1 and ABS2 covered surfaces that are buried in the filament. Second, ABS1 and ABS2 must bind to two different protomers at the pointed end, because their binding surfaces partially overlapped (fig. S3A). Third, the binding surfaces of ABS1 and ABS2 also overlapped when they were superimposed onto the second and first protomers of the filament, respectively (fig. S3B). This arrangement also placed the two actin-binding sites asymmetrically on one side of the filament, increasing the distance that must be covered by the intervening sequence (residues 100 to 170) that contains the second TM-binding site. In contrast, no overlap was observed when ABS1 and ABS2 were superimposed onto the first and second protomers of the filament, respectively (Fig. 2A). This arrangement naturally positioned ABS2 at the interface between the first three subunits of the filament, where Tmod residues in contact with actin were highly conserved (fig. S4A). This model, and

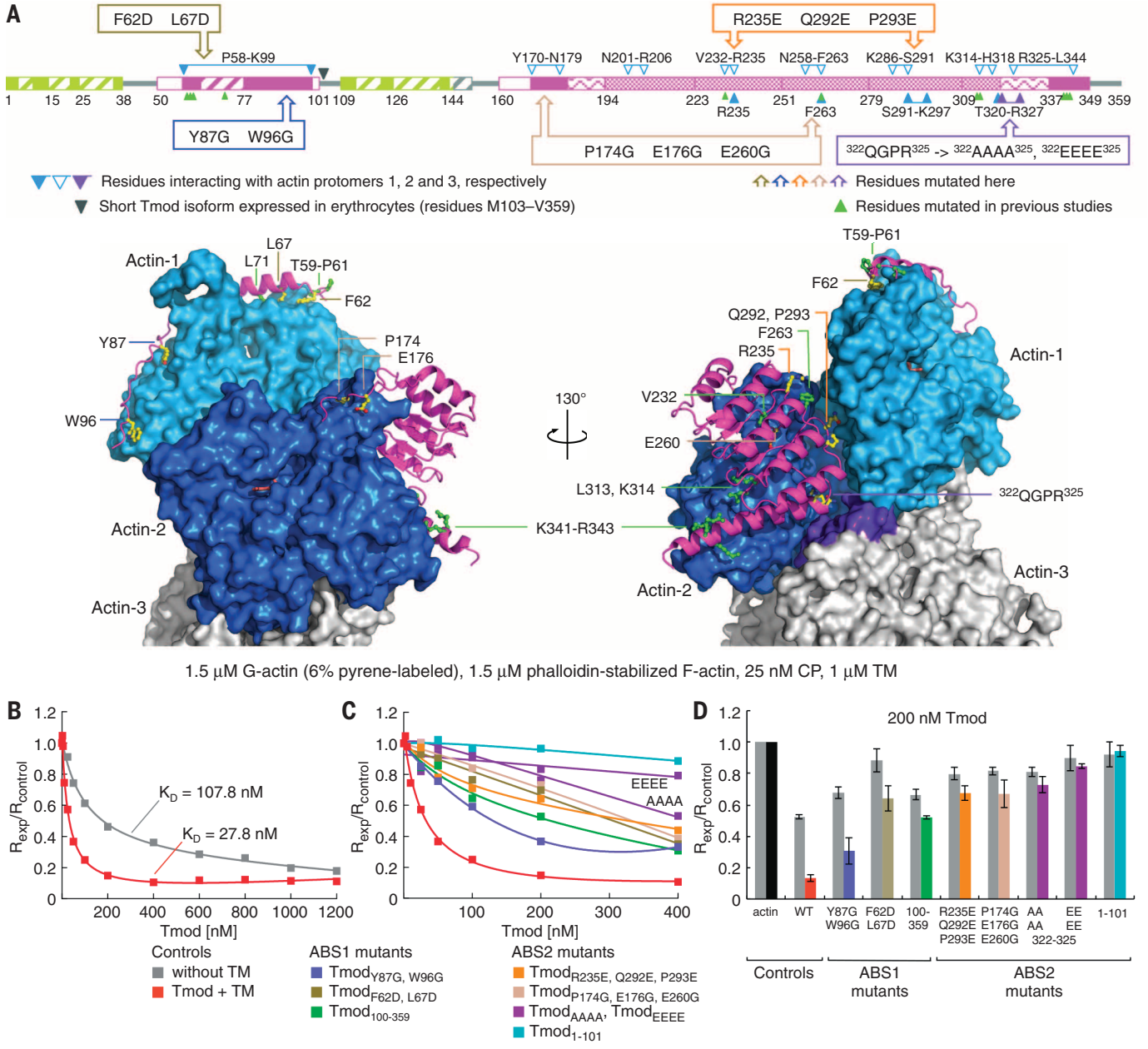


Fig. 2. Testing the interactions of Tmod at the pointed end by mutagenesis. (**A**) Representation of the mutants studied here on a domain diagram of Tmod and on the structures of ABS1 and ABS2 superimposed onto the first two protomers (marine and blue) at the pointed end of the filament model (*20*) (see also movie S3). Residues mutated here are colored by atom type (carbon, yellow; oxygen, red; nitrogen, blue). Also shown are residues mutated in previous studies (green). Note that ABS1 only interacts with the first protomer, whereas ABS2 contacts the first three protomers of the filament. The third protomer is colored gray, except for the area that contacts ABS2, which is colored purple. (**B**) Normalized pointed-end elongation rates of filament seeds as a function of Tmod concentration, with or without TM (conditions given on top). (**C**) Normalized pointed-end elongation rates of filament seeds as a function of mutant Tmod concentration, and in the presence of TM (the individual titrations are shown in fig. S7). Each mutant is represented by a different color (keys are given on the bottom). (**D**) Comparison of the normalized pointed-end elongation rates at 200 nM Tmod with or without (gray bars) TM.

especially the location of the N termini of ABS1 and ABS2, was further consistent with the azimuthal sliding of TM on the surface of the filament (fig. S5), which occurs upon Ca^{2+} binding to troponin and myosin binding to the filament (*21*). The two extreme positions of TM on the filament, blocked and open, are represented by electron microscopy (EM) structures of actin-TM (*22*) and actin-TM-myosin (*23*). The full extent of TM's sliding is estimated to be ~35° (*21*), which greatly restricts the available surface for Tmod binding at the pointed end and strongly supports the model proposed here.

Key interactions of Tmod with the first three protomers of the filament (Fig. 2A and fig. S4) were tested by mutagenesis and pointed end–capping assays. In these assays, the barbed end must be tightly capped, because faster dynamics at this end can mask subunit exchange at the pointed end. Traditionally, gelsolin has been used to cap the barbed end in Tmod studies (*7*, *10*, *12*, *15*–*17*). We found, however, that CP and not gelsolin should be used in these assays (fig. S6, A to D), because monomer sequestration and filament severing by gelsolin interfered with its barbed end capping activity (*14*).

The optimal concentration of TM for our experiments was 1 μM (*14*) (fig. S6, E to H). Thus, the concentration dependence of Tmod capping was determined in the absence or the presence of 1 μM TM (Fig. 2B and fig. S7, A and B). TM enhanced Tmod's capping efficiency about fourfold, resulting in a K_D of 28 nM compared to 108 nM in the absence of TM. These affinity values could be directly compared, because the same stock of filament seeds was used in the experiments. Generally, however, the affinity values depend on the number of pointed ends, which varies from experiment to experiment. Although substantial, a ~4-fold increase in affinity was far below the 1000-fold increase and picomolar affinity reported previously (*7*), which prompted several repetitions of the experiments with identical results. A nanomolar rather than picomolar affinity of Tmod at the pointed end seems more consistent with the observation of pointed-end monomer exchange in sarcomeres (*13*).

We analyzed eight Tmod mutants in elongation assays (Fig. 2, figs. S4 and S7, and movie S3). Erythrocytes express a short Tmod isoform (residues 103 to 359) (*24*), which reinforces an idea suggested by the structures; Tmod is better described as consisting of two TM-actin–binding modules. Thus, we expressed constructs 1 to 101 and 100 to 359 to test the importance of each module. Other mutations were introduced within full-length Tmod and targeted the α helix and tail region of ABS1, and interactions of ABS2 with the first three protomers of the filament. Although TM increased the capping efficiency of the mutants, they all displayed reduced activity compared to wild-type Tmod, supporting the importance of these residues for Tmod-actin interactions (Fig. 2, C and D, and fig. S7, C to J). The most severe capping defects were observed with the deletion or mutations of the C-terminal TM-actin–binding module. Particularly, replacing residues 322 to 325 at the beginning of the C-terminal α helix with AAAA or EEEE had the most pronounced effect, consistent with the key location of this region at the interface between the first three protomers of the filament. Mutations reported to affect actin binding and capping (*9*, *15*–*17*) also tended to localize to the contact surface with subunits of the filament (Fig. 2A, fig. S4, and movie S3).

These results are consistent with a model in which a single Tmod molecule caps actin filaments

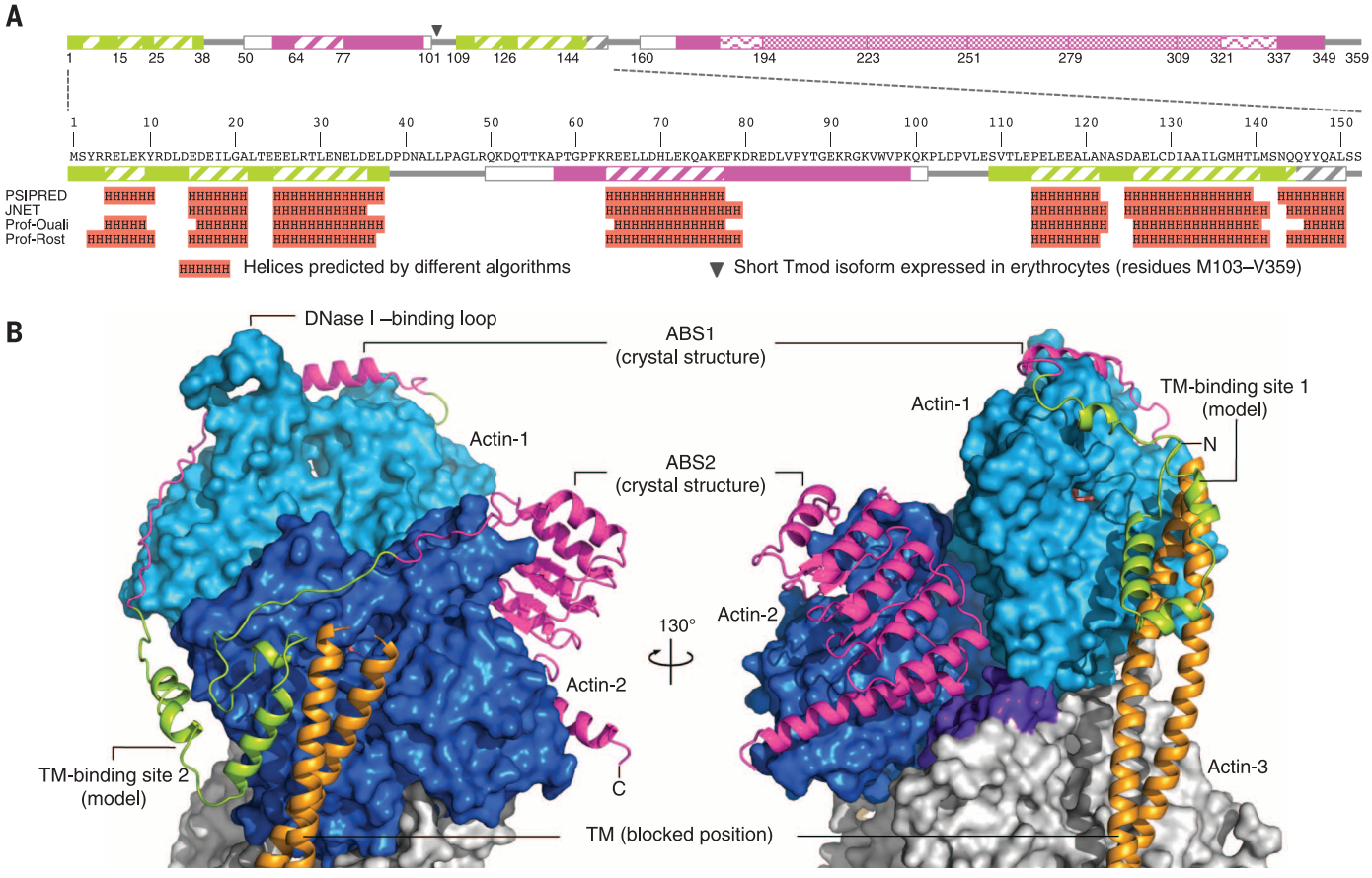


Fig. 3. Model of the pointed end. (**A**) Domain diagram of Tmod (according to Fig. 1A), showing a secondary-structure prediction of the N-terminal region by several algorithms (*14*). The prediction suggests that the two TM-binding sites, which are similar in size, also share a similar fold, consisting of a three-helix bundle. (**B**) Model of the pointed end, with the structures of the complexes of actin with ABS1 and ABS2 (magenta) superimposed onto the first two protomers of the filament (marine and blue). ABS2 also contacts the third protomer (purple-colored area). TM is shown in the stable "blocked" position, which it assumes when bound alone to the filament (*22*). A tentative model of the two TM-binding sites of Tmod (green), based on the results of the secondary-structure prediction and energy minimization (*14*), is shown for reference (see also movie S4).

at the pointed end (Fig. 3 and movie S4). ABS1 interacts only with the first protomer of the filament (interface area: 1549 Å^2) and ABS2 interacts mainly with the second protomer (interface area: 1770 Å^2), although it also contacts protomers 1 and 3 (estimated interface areas: 198 and 125 Å^2, respectively). Secondary-structure prediction using several algorithms further suggests that the two TM-binding sites have a related fold consisting of three helices (*14*). The model of the pointed end proposed here is supported by analysis of several Tmod mutants and by steric constraints imposed by the structure of the filament (*20*) and the blocked (*22*) and open (*23*) positions of TM on the filament.

The structure of the pointed end–binding VCD domain of *Vibrio* VopL was recently determined in complex with an actin trimer (*25*). One of the subunits of the VCD dimer binds in the same location as ABS2, i.e., at the interface between the first three subunits of the filament (fig. S8). VopL is a powerful nucleator, and this activity is strongly enhanced by the presence of actin monomer–binding WH2 domains N-terminal to VCD (*26*, *27*). Similarly, the Tmod-related protein leiomodin is a powerful nucleator (*28*), and this activity is enhanced by the presence of a C-terminal tail that contains a WH2 domain.

Separately, ABS1 and ABS2 interact with monomeric actin with K_Ds of ~10 μM, independent of the nucleotide state on actin, whereas full-length Tmod binds to the pointed end with a K_D of 108 nM, and 28 nM in the presence of TM. Thus, the increased affinity of Tmod at the pointed end results from multiple, relatively weak interactions, involving three actin protomers and two TM molecules on each side of the filament. We suggest that Tmod's interactions at the pointed end are better described in the form of two TM-actin–binding modules. Because of their relative independence and weaker individual affinities, one module can detach from the filament while the other remains bound, which could explain pointed-end subunit exchange in sarcomeres (*13*). Newly incorporated monomers likely consist of ATP-actin, for which the two actin-binding sites of Tmod appear to have an affinity similar to that for ADP-actin, thought to be the predominant species at the pointed end.

REFERENCES AND NOTES

1. J. A. Cooper, D. Sept, *Int. Rev. Cell Mol. Biol.* **267**, 183–206 (2008).
2. S. Nag, M. Larsson, R. C. Robinson, L. D. Burtnick, *Cytoskeleton* **70**, 360–384 (2013).
3. S. Yamashiro, D. S. Gokhin, S. Kimura, R. B. Nowak, V. M. Fowler, *Cytoskeleton* **69**, 337–370 (2012).
4. V. Bennett, A. J. Baines, *Physiol. Rev.* **81**, 1353–1392 (2001).
5. V. M. Fowler, M. A. Sussmann, P. G. Miller, B. E. Flucher, M. P. Daniels, *J. Cell Biol.* **120**, 411–420 (1993).
6. J. D. Moyer *et al.*, *Blood* **116**, 2590–2599 (2010).
7. A. Weber, C. R. Pennise, V. M. Fowler, *J. Biol. Chem.* **274**, 34637–34645 (1999).
8. N. J. Greenfield, A. S. Kostyukova, S. E. Hitchcock-DeGregori, *Biophys. J.* **88**, 372–383 (2005).
9. V. M. Fowler, N. J. Greenfield, J. Moyer, *J. Biol. Chem.* **278**, 40000–40009 (2003).
10. A. S. Kostyukova, A. Choy, B. A. Rapp, *Biochemistry* **45**, 12068–12075 (2006).
11. I. Krieger, A. Kostyukova, A. Yamashita, Y. Nitanai, Y. Maéda, *Biophys. J.* **83**, 2716–2725 (2002).
12. A. Weber, C. R. Pennise, G. G. Babcock, V. M. Fowler, *J. Cell Biol.* **127**, 1627–1635 (1994).
13. R. Littlefield, A. Almenar-Queralt, V. M. Fowler, *Nat. Cell Biol.* **3**, 544–551 (2001).
14. Materials and methods are available as supplementary materials on *Science* Online.
15. A. S. Kostyukova, B. A. Rapp, A. Choy, N. J. Greenfield, S. E. Hitchcock-DeGregori, *Biochemistry* **44**, 4905–4910 (2005).
16. S. Yamashiro, K. D. Speicher, D. W. Speicher, V. M. Fowler, *J. Biol. Chem.* **285**, 33265–33280 (2010).
17. T. Tsukada *et al.*, *J. Biol. Chem.* **286**, 2194–2204 (2011).
18. R. Dominguez, K. C. Holmes, *Annu. Rev. Biophys.* **40**, 169–186 (2011).
19. J. Bella, K. L. Hindle, P. A. McEwan, S. C. Lovell, *Cell. Mol. Life Sci.* **65**, 2307–2333 (2008).
20. T. Fujii, A. H. Iwane, T. Yanagida, K. Namba, *Nature* **467**, 724–728 (2010).
21. P. Vibert, R. Craig, W. Lehman, *J. Mol. Biol.* **266**, 8–14 (1997).
22. X. E. Li *et al.*, *Biophys. J.* **100**, 1005–1013 (2011).
23. E. Behrmann *et al.*, *Cell* **150**, 327–338 (2012).
24. W. Yao, L. A. Sung, *J. Biol. Chem.* **285**, 31408–31417 (2010).
25. J. A. Zahm *et al.*, *Cell* **155**, 423–434 (2013).
26. S. Namgoong *et al.*, *Nat. Struct. Mol. Biol.* **18**, 1060–1067 (2011).
27. B. Yu, H. C. Cheng, C. A. Brautigam, D. R. Tomchick, M. K. Rosen, *Nat. Struct. Mol. Biol.* **18**, 1068–1074 (2011).
28. D. Chereau *et al.*, *Science* **320**, 239–243 (2008).

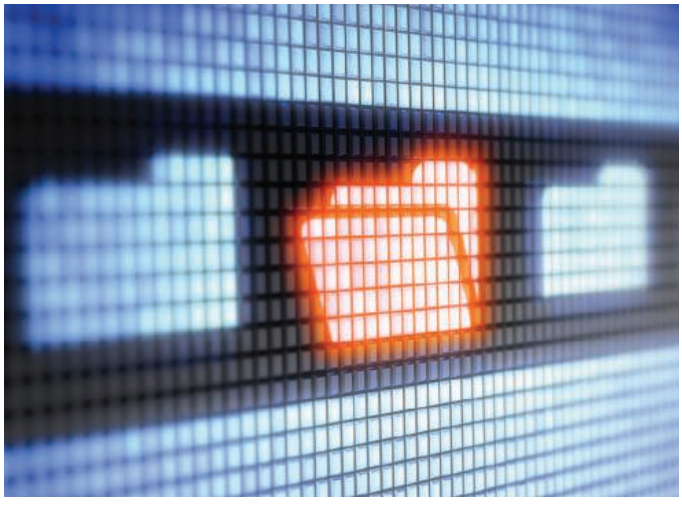
ACKNOWLEDGMENTS

Supported by NIH grant R01 GM073791. X-ray data collection at beamline X6A of the National Synchrotron Light Source was supported by NIH grant GM-0080 and U.S. Department of Energy contract DE-AC02–98CH10886. We thank G. Rebowski for the preparation of actin and TM for this study and W. Lehman and M. Orzechowski for providing the TM models. The structures have been deposited in the Protein Data Bank under codes 4PKG, 4PKH, and 4PKI.

SUPPLEMENTARY MATERIALS

www.sciencemag.org/content/345/6195/463/suppl/DC1
Materials and Methods
Figs. S1 to S8
Movies S1 to S4
Table S1
References (*29*–*55*)

16 May 2014; accepted 24 June 2014
10.1126/science.1256159



The Paperless Lab

Some scientists keep experimental records on sticky notes. Some groups maintain ordering information in the head of a single technician. But for researchers looking for more stable, searchable, and sharable records, digital options such as electronic laboratory notebooks (ELNs) and laboratory information management systems (LIMS) are readily available. Scientists can start with a simple online notebook or choose a complete lab management package to track the entire lifecycle of their projects. By Chris Tachibana

A paper notebook seems like it should last forever. After all, Gutenberg Bibles have survived since the 1400s. Still, paper is not perfect. Consider these true stories: At an Australian university, 30 years of notebooks became a pile of loose pages after the bindings crumbled during relocation. In the United States, a postdoc spent days combing through three-ring binders for experimental details requested by reviewers. In a positive example of going paperless, a Swiss contract manufacturing organization wowed clients with real-time, online chromatography runs of their samples. Electronic laboratory tools have definite advantages, but scientists have been reluctant adopters. The major barriers for going digital are cost, the activation energy required to change work habits, and the daunting number of options.

Where to Start

LIMSwiki is an excellent starting point for laboratory informatics newbies. The online resource is a community service from the Laboratory Informatics Institute, a trade organization founded in 2006 by **LabLynx**, a vendor of browser-based research management software. LabLynx emphasizes transparency, for example in pricing, and LIMSwiki provides prices when possible in its up-to-date vendor descriptions. "We've tried to maintain neutrality throughout," says Shawn Douglas, LIMSwiki curator, "avoiding marketing and self-promotion. The wiki is an evolving tool, and we're always looking for quality contributors."

LIMSwiki provides definitions for terms such as ELN (electronic laboratory notebook, generally used to document experiments) and LIMS (laboratory information management systems, traditionally used for tracking standardized processes such as production). But the distinction between informatics products is blurring, says Markus Dathe, good manufacturing practice and computer system validation coordinator at **Roche**, because "convergence is happening." ELNs, LIMS, and equipment software are expanding functions, interconnecting, and overlapping. Informatics packages increasingly aim to cover the entire lifecycle of an R&D project including reagent inventories, regulatory forms, and work requests in addition to experimental details. Most researchers start small, though, with a homegrown ELN with protocols in text documents and electronic data files.

"Everyone sees the value of ELNs, from scientists to principal investigators to lab managers," says Erik Alsmyr, senior director of software development for the **Accelrys** Notebook (previously Contur's iLabber) for small-to-medium-sized research groups. Alsmyr says most labs start with all-purpose organizing and sharing software such as Evernote or SharePoint, then realize they need more storage capacity or intellectual property (IP) protection. Electronic systems provide 24/7 global access to your records, says Alsmyr, and most commercial ELNs are compliant with regulatory requirements for electronic records, for example Part 11 of the Code of Federal Regulations Title 21, which covers the U.S. Food and Drug Administration, and European Union Annex 11 for the European market.

Researchers are still slow adopters, though, particularly at universities. That's why **LabArchives** offers a free ELN in addition to a subscription-based version with more storage and features. "Our research says that in academia, about 95% of scientists still use a paper notebook," says Earl Beutler, LabArchives' chief executive officer. Beutler, whose entire family are scientists (including a Nobel Prize winner), thinks it's time for labs to go digital. "I've worked around smart, technologically proficient scientists my entire life," he says, "and I'm amazed that their state-of-the-art is still taking a photo of a gel, printing it out, and gluing it into a paper notebook."

Realizing that adhesives disintegrate and notes on laptops don't have the strongest IP protection, universities are buying informatics site licenses that cover entire departments, says Beutler. This removes the cost barrier for scientists and ensures proper archiving of potentially patentable results. LabArchives also targets an audience that doesn't have paper nostalgia: students. "Many of our users are academic researchers who teach, so we created our classroom ELN at their request," says Beutler. "It lets instructors provide background information and give and grade assignments electronically. The largest class it's

PHOTO: PAVEL IGNATOV/SHUTTERSTOCK.COM

Upcoming Features

Metabolomics—September 19 ■ *Genomics—October 3* ■ *Cell Culture—November 21*



In this [nearly sci-fi] vision of the future laboratory, scientists simply do their work while an automated tracking system simultaneously keeps records.

been used in was more than 2,000 students."

Tammy Morrish is an academic researcher who went digital from day one, setting up her laboratory with **Labguru**, a web-based research management system. As a postdoc, Morrish kept a homemade database of project resources but wanted an advanced, sharable system when she started as an assistant professor at the **University of Toledo** Biochemistry and Cancer Biology Department. That's a great time to set up a new system, she says, because you know all the mice, cell lines, and plasmids you have available for projects.

Morrish praises Labguru's customer service and says the system is a huge timesaver. It streamlines ordering by putting product numbers, vendors, and current orders in one place, she says. Labguru holds her laboratory's mouse records with full genotypes, and plasmid information including maps. Morrish says the system is particularly helpful for locating items. "Think how much time we waste looking for things," she says. "Now when I need something, even if other people aren't around to ask, I can type it into the database and find it. Of course," she adds, "people have to put things back where they found them." Her lab has a technician who checks inventories against the database weekly.

At a higher level, the system facilitates group interactions, for example by making data sharing easy. It also teaches best practices. "It helps students learn that with any database," says Morrish, "you have to enter information correctly and consistently or you won't be able to find it."

Going Digital But Maintaining Control

Science-based businesses also appreciate the efficiency of digital research management, but long-term stability is a high priority, too. "The challenge is assuring the accessibility and usability of data 20 years from now," says Dathe. Choosing a major informatics supplier such as IDBS, PerkinElmer, or Accelrys might give some assurance of permanence, but the market is so dynamic that any vendor will likely undergo changes. In the past decades, Thermo Fisher Scientific acquired InnaPhase; PerkinElmer purchased Labtronics, CambridgeSoft and ArtusLabs; Accelrys, which has its own lengthy merger and acquisition history, was recently acquired by the French software company Dassault. Still, after consolidating, companies strive to retain users. "We still carry software developed in the 1990s and we've always shown customers a path forward," says Leif Pedersen, senior vice president at Accelrys.

Nonetheless, industries are not uniformly adopting laboratory informatics. Although agencies such as the Food and Drug Administration encourage electronic documentation, Dathe says, "The pharmaceutical industry is generally conservative, and it's often easier and cheaper to stay with a paper system that is known to be accepted by regulatory agencies."

At **LEO Pharma** in Denmark, head of discovery informatics and data management Ulrik Nicolai de Lichtenberg developed a model for committing to a commercial informatics system. Start with in-depth stakeholder analyses, he says. Define your needs and goals and "how much pain you can put up with," meaning the money, time, and effort available for implementing a new system. Realize that your ELN or LIMS is just a part of an information ecosystem. LEO Pharma chose the Accelrys ELN for its Medicinal Chemistry R&D Department, but the ELN is just one element in a comprehensive infrastructure designed by de Lichtenberg's team. Their system will capture, validate, and permanently store records so they are accessible, searchable, and legally defensible in case of IP disputes. It's a complex project and de Lichtenberg recommends seeking advice from independent consultants who understand the ever-changing informatics market.

Looking to the Cloud And Beyond

Michael Elliott, chief executive officer of **Atrium Research & Consulting**, advised de Lichtenberg and endorses his approach. "Don't get enamored with a demo," he says. "Look under the hood and check out the capabilities of an informatics system." Clients dream of a single system that streamlines process management and securely and permanently stores data while rapidly retrieving needed information. An ideal system would even find "dark data"—previous work that could answer current research questions but is buried in disorganized files. Clients want scalability, a user-friendly interface, and outstanding global support. However, products vary in these capabilities, says Elliott. "Don't choose based on a presentation or brand name. Think carefully about your needs now and in the future."

If expandability and ease of use are priorities, a cloud-based system, for example from Core Informatics, might be the answer. In principle, the cloud can house unlimited amounts of data and has a familiar interface since accessed is through a web browser. Brower-based systems don't require specialized software, so they're easy to upgrade. Informatics vendors are also creating user-friendly modular packages. Similar to choosing mobile phone apps, users select only the components they need.

Also on the horizon is greater mobility and compatibility. Researchers are taking smartphones and tablets into the laboratory so informatics developers are making products compatible with handheld devices. Increasingly, data needs to be compiled across different instruments and informatics platforms, so Pedersen says he is personally pushing for increased standardization to facilitate information sharing. Ever the continued>

PHOTO: BRUCE ROLFF/SHUTTERSTOCK.COM

realist, though, Elliott says progress in standardization is slow because even within a single department, users might employ different terminology and definitions. The force that could drive both standardization of scientific informatics and better data integration, says Elliott, "is the move toward more collaborative work."

To the wish list of informatics improvements, Dathe adds features that give data context: when and where they were collected and for what project. Data should be linked to relevant molecular and clinical information and the entire data-generating process, including the type and status of equipment used. "Without context," says Dathe, "the mountain of data we can collect is meaningless."

Featured Participants

Accelrys
www.accelrys.com

Atrium Research & Consulting
www.atriumresearch.com

LabArchives
www.labarchives.com

Labguru
www.labguru.com

LabKey Software
www.labkey.com

LabLynx
www.lablynx.com

LIMSwiki
www.limswiki.org

LEO Pharma
www.leo-pharma.com

Roche
www.roche.com

University of California, Santa Cruz
www.ucsc.edu

University of Toledo
www.utoledo.edu

Additional Resources

Core Informatics
www.corelims.com

Evernote
www.evernote.com

GitHub
www.github.com

IDBS
www.idbs.com

Jekyll
www.jekyllrb.com

OpenWetWare
www.openwetware.org

PerkinElmer
www.perkinelmer.com

Thermo Fisher Scientific
www.thermofisher.com

Being Open-Minded

Scaling the data mountain is Britt Piehler's job. Piehler is president of **LabKey Software**, which develops tools for data management and integration. The trend toward globalization and multisite collaboration, he says, means project managers must coordinate data collected at far-flung sites under diverse conditions with a variety of instruments. "That's where LabKey comes in," says Piehler. "We build tools for specific tasks, usually data integration for multisite collaborative projects that need to standardize heterogeneous data." An unusual feature of LabKey Software is that its product is open source.

"We grew out of the academic community," says LabKey's Science Outreach Director Elizabeth Nelson, "so we believe it's an advantage for the software platform to be freely available." Open source code allows researchers to tailor their systems, says Piehler, and building and sharing LabKey tools creates a community.

If the code is free, what does LabKey offer? "Customization," says Piehler. LabKey Software experts can create tools that directly address Dathe's call for giving context to data, for example by adding demographic information. And in August 2013, open source and open access came together via LabKey to promote scientific transparency and reproducibility. For a clinical trial of a vasculitis therapy published in the *New England Journal of Medicine,* the LabKey open source platform was used to create a web portal with free public access to participant-level data, stripped of identifying information.

Researchers who are committed to transparency and are also do-it-yourselfers have a choice of open source workflow management tools. Carl Boettiger, an ecology and evolution postdoctoral researcher at the **University of California, Santa Cruz** has traveled the entire DIY lab notebook journey. Boettiger started keeping publicly accessible lab records in the OpenWetWare platform. "It's a bit radical," says Boettiger. "Anyone can go in and edit other peoples' notes, although that rarely happens." After OpenWetWare, Boettiger moved to platforms that give him increasing control over his research records, starting with WordPress, which is usually used for blogging. Boettiger now uses the online software development site GitHub as his notebook and Jekyll website-generating software to publish his notebook online.

A blog-type ELN creates a robust, cached history of your research, says Boettiger. It discourages fraud because any changes leave records. You choose what is public, private, and password protected. And think of the advantages when talking to people at conferences or answering reviewer requests, he says. You can just pull up records on a handheld device to see what you tried and when, and how it worked out.

What's Next

"The trends in laboratory records," says Boettiger, "are toward more open and collaborative, more secure, and more automated." Although Boettiger and Dathe should have different perspectives as an ecology researcher in Santa Cruz and a pharma development and information technology specialist in Basel, respectively, they share a nearly sci-fi vision of the future laboratory. In this vision, scientists simply do their work while an automated tracking system simultaneously keeps records. Barcoding will note reagents, samples, and instruments used, providing context to the data for subsequent analysis. The entire process will be recorded, showing the provenance of every byte and definitively establishing IP claims. "It will give a much more extensive record that can be transparent or shared if you want," says Boettiger. A fully automated system would simplify research by capturing experimental details with no manual data entry. Then, all we'd need is a robot to return reagents to the right shelves.

Chris Tachibana is a science writer based in Seattle, USA, and Copenhagen, Denmark.

DOI: 10.1126/science.opms.p1400087

SOPs and Methods Platforms

The Thermo Scientific Lab Execution System (LES) is an all-inclusive informatics solution that gives scientists complete control over their methods and standard operating procedures (SOPs) without having to purchase, integrate, and validate software from multiple vendors. The system is web-based, built on and fully integrated with the Thermo Scientific enterprise-level lab information management system (LIMS) platform, allowing the LES functionality to be accessed from the LIMS or from any web browser. Combined with the instrument integration capabilities of Thermo Scientific Integration Manager, and the raw data storage and retrieval capabilities of the company's SDMS (Data Manager), the new LES offers customers the most comprehensive paperless lab solution available today. The LES enables lab managers and scientists across all industries to achieve full instrument integration, including managing their own methods and workflow; retrieving and archiving any kind of raw scientific data; and exporting the results across the organization in the format required by the recipient.

Thermo Fisher Scientific
For info: 800-395-5467
www.thermoscientific.com/les

Sample Management Software

Mosaic 6.0 has been developed progressively over the last 12 years in response to the evermore sophisticated requirements in the management of compounds, biologicals, reagents, and standards. Mosaic supports sample supply workflows in all sizes of life science organizations in industry and academia, from multi-continent, enterprise-wide installations, to those in a single lab. The key to this flexibility is the scalable and modular software infrastructure, providing a comprehensive solution to sample management, and satisfying the need to improve throughput while maintaining sample integrity and inventory accuracy. Offering seamless integration with third-party IT infrastructure, Mosaic modules are available for: inventory tracking, ordering, and sample processing, including integration with laboratory automation. Mosaic 6.0 provides new Assay Requesting functionality, enabling sample bank operators to aggregate assay requests, thereby increasing efficiency and reducing waste. Users of Mosaic 6.0 will also benefit from improved interfaces for inventory management that enable convenient inventory search functions.

Titian
For info: 508-366-2234
www.titian.co.uk



Automated Liquid Handler Management

ArtelWare is a software application that is designed for use with the MVS Multichannel Verification System. ArtelWare enables MVS users to track and manage the performance of their automated liquid handlers over time. ArtelWare aggregates the standardized measurements from the MVS for all of a user's liquid handlers, providing detailed, actionable performance information, and a new level of insight for the management of these critical laboratory tools. The Artel MVS and the ArtelWare software deliver valuable benefits to a wide range of research fields. Users can quickly visualize the tip-by-tip status of any device as well as view performance over time, even across multiple labs. Action limits can either be pre-assigned or determined based on the data. ArtelWare also provides the tools to manage and optimize instrument maintenance by viewing historical information on individual device availability and reliability. With ArtelWare, automation customers can reduce time spent on false "hits," increasing overall lab productivity.

Artel
For info: 888-406-3463
www.artel-usa.com

Imaging System Software

The new WITec Suite software, for WITec imaging systems, was developed to acquire and process large data volumes of large-area, high-resolution measurements, and 3-D imaging while providing speed, performance, and usability. Through the software architecture and graphical user interface an integrated and consolidated functionality is available incorporating the various techniques and measurement modes from Raman, to AFM, to SNOM, fluorescence, and luminescence. An intelligent computer resource management provides the capabilities for the generation and visualization of even large data sets. The high-speed data acquisition allows for example the measurement and recording of over 1,300 Raman spectra in only one second. Furthermore data sets including several million image pixels, each containing the information that can be generated, processed, and imaged smoothly. Another focus of WITec Suite is the improved and simplified usability. The software design provides a clear and intuitive menu guidance and an individually adjustable user.

WITec
For info: +49-731-140-700
www.witec.de

Sample Comparison Software

The latest version of GeneMarker Software now includes an integrated replicate comparison tool for use in ecology, agricultural, and clinical research. The replicate comparison tool automatically groups replicate samples within a project and provides immediate flagging to notify researchers of any discordant allele calls. The tool eliminates the time consuming manual review of replicate sample electropherograms. Linked navigation allows the researcher to immediately view the electropherograms of replicates with discordant allele calls for a streamlined workflow. There are several different scenarios where the replicate comparison tool will be useful in the laboratory, including analysis of low template DNA samples. Wildlife genotyping laboratories will benefit from the replicate comparison tool in areas such as evaluating loci for allele drop out; or to confirm putative replicates from DNA samples obtained indirectly from hair traps or dung. Users can export the concordant genotypes in a combined table, or link directly to other embedded GeneMarker software applications.

SoftGenetics
For info: 888-791-1270
www.softgenetics.com

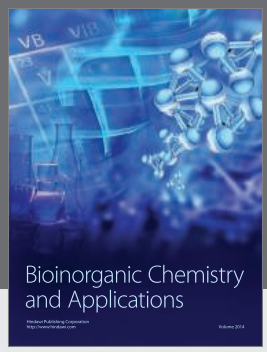
Electronically submit your new product description or product literature information! Go to www.sciencemag.org/products/newproducts.dtl for more information.

Newly offered instrumentation, apparatus, and laboratory materials of interest to researchers in all disciplines in academic, industrial, and governmental organizations are featured in this space. Emphasis is given to purpose, chief characteristics, and availability of products and materials. Endorsement by *Science* or AAAS of any products or materials mentioned is not implied. Additional information may be obtained from the manufacturer or supplier.













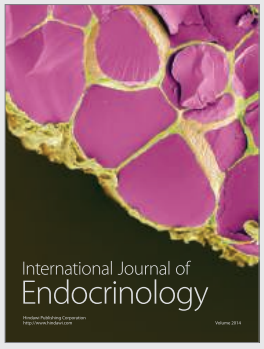


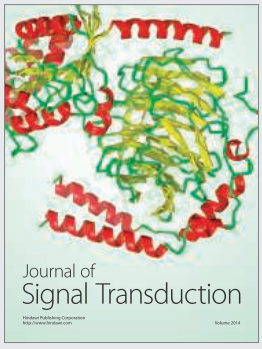


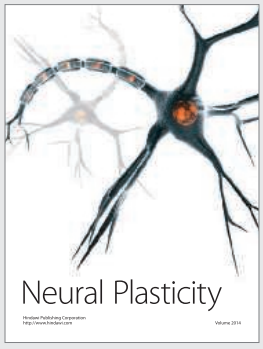


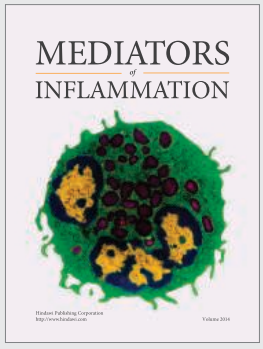
Hindawi

Submit your manuscripts at
http://www.hindawi.com

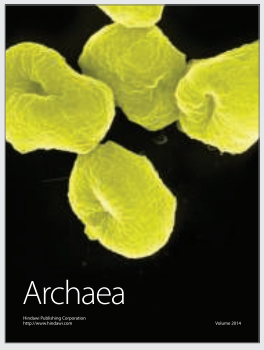


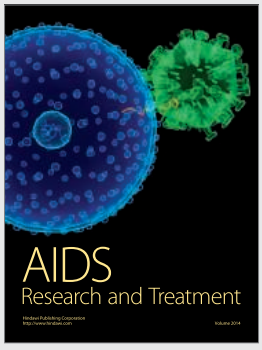


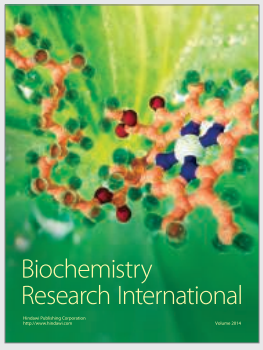


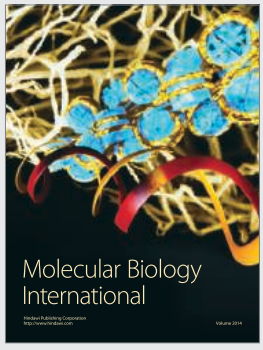


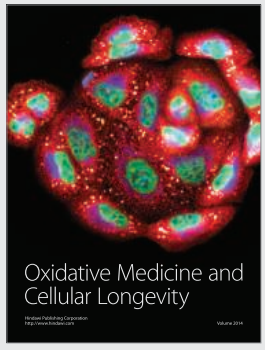




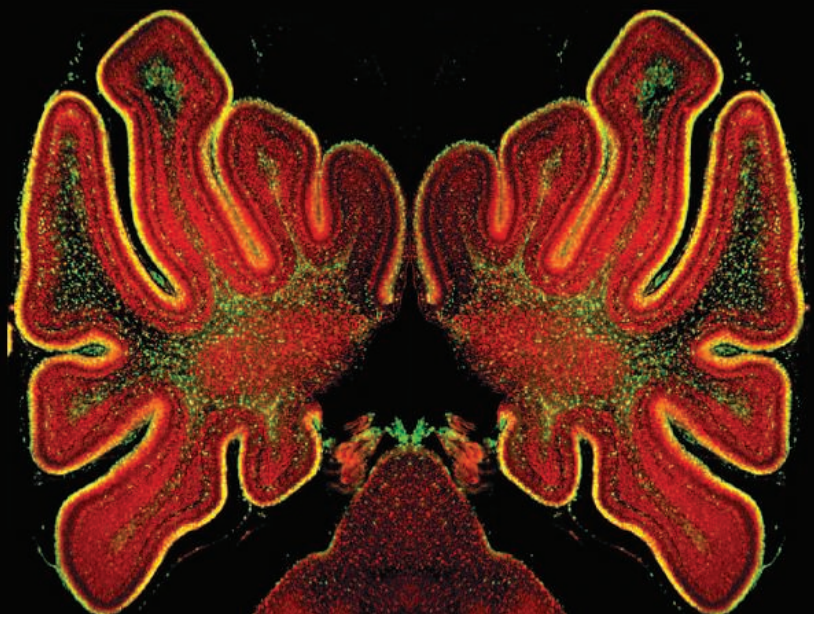








Advances in Neurotechniques: Methods that Reveal the Structure and Function of the Brain



Wednesday, August 13, 2014

12 noon Eastern, 9 a.m. Pacific,
5 p.m. UK, 6 p.m. Central Europe

During this webinar, speakers will:

- Provide an overview of new neuro-techniques
- Shed light on how to use these new technologies to advance research
- Present their research using optogenetics and CLARITY
- Answer your questions live during the webinar!

Register Now!

webinar.sciencemag.org

Elucidating the mind's inner workings is one of the remaining challenges facing scientists today. Since Ramón y Cajal's first illustrations of neuronal structures, neuroscientists have benefited from new ways to visualize the microscopic components within the brain. The development of new, advanced imaging techniques holds the promise for elucidating a better understanding of the how the brain works. Already, cutting-edge tools such as optogenetics and CLARITY offer researchers novel methods for peering into the structure and function of the brain. This webinar will explore the most recent neurotechniques and how these are being used to advance our knowledge of the brain.

Speakers



Karl Deisseroth, M.D., Ph.D.
Stanford University
Stanford, CA



Viviana Gradinaru, Ph.D.
Caltech
Pasadena, CA

Webinar sponsored by

Leica MICROSYSTEMS

Brought to you by the *Science*/AAAS Custom Publishing Office

Science AAAS

@SciMagWebinars

NEW ENGLAND BioLabs® Inc.
enabling technologies in the life sciences

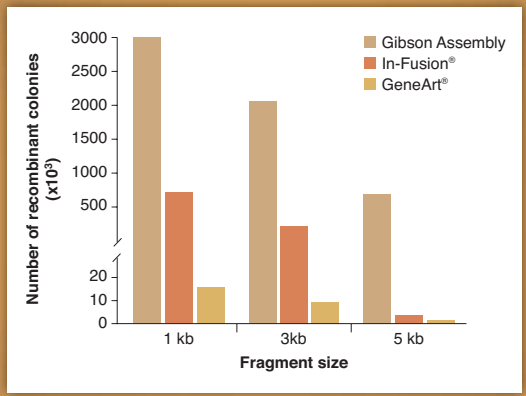
Make ends meet.

Gibson Assembly® Cloning Kit

New England Biolabs has revolutionized your laboratory's standard cloning methodology. The Gibson Assembly Cloning Kit combines the power of the Gibson Assembly Master Mix with NEB 5-alpha Competent *E. coli*, enabling fragment assembly and transformation in just under two hours. Save time, without sacrificing efficiency.

Making ends meet is now quicker and easier than ever before, with the Gibson Assembly Cloning Kit from NEB.

Gibson Assembly Cloning Kit provides robust transformation efficiencies



Assembly reactions containing 25 ng of linear pUC19 vector and 0.04 pmol of each fragment were performed following individual suppliers' recommended protocols and using the competent cells provided with the kit. The total number of recombinant colonies was calculated per 25 ng of linear pUC19 vector added to the assembly reaction.

NEBuilder™ for Gibson Assembly

Visit **NEBGibson.com** to view the latest tutorials and to try our primer design tool.

IN-FUSION® is a registered trademark of Clontech Laboratories, Inc.
GENEART® is a registered trademark of Life Technologies, Inc.
GIBSON ASSEMBLY® is a registered trademark of Synthetic Genomics, Inc.

SGI-DNA

Some components of this product are manufactured by New England Biolabs, Inc. under license from Synthetic Genomics, Inc.

immunogenomics 2014

September 29 - October 1, 2014

HudsonAlpha Biotechnology Campus
Huntsville, Alabama, USA

Join us at the intersection of Immunology and Genomics!

Keynote Speakers

Christophe Benoist, Harvard Medical School
Mary Ellen Conley, University of Tennessee, College of Medicine, Memphis
Mark Davis, Howard Hughes Medical Institute;
Stanford University School of Medicine

Session Chairs

Lou Bridges, University of Alabama at Birmingham, AL, USA • **Jean-Laurent Casanova**, Howard Hughes Medical Institute, Rockefeller • **Alain Fischer**, Imagine Institute, Necker Hospital, Paris, France • **Dan Littman**, New York University, NY, USA • **Sara Marsal**, University of Barcelona, Spain • **Kristen Mueller**, *Science* • **Harlan Robins**, University of Washington/Fred Hutchinson Cancer Research Center

Session Speakers

Scott Boyd, Stanford University School of Medicine, CA • **Zhijian James Chen**, UT Southwestern, TX • **Yanick Crow**, University of Manchester, UK • **Malek Faham**, Sequenta, CA • **Wendy Garrett**, Harvard University School of Public Health, MA • **Peter Gregersen**, Feinstein Institute for Medical Research, NY • **Jian Han**, HudsonAlpha Institute for Biotechnology, AL • **Lionel Ivashkiv**, Hospital for Special Surgery, NY • **Thirumala-Devi Kanneganti**, St. Jude Children's Research Hosp. • **Julian Knight**, Merton College , University of Oxford, UK • **Mike Lenardo**, National Institutes of Health, Washington D.C. • **Xochitl Morgan**, Harvard University School of Public Health, MA • **Barbara Methe**, J. Craig Venter Institute, MD • **Kees Murre**, University of California, San Diego, CA • **Richard M. Myers**, HudsonAlpha Institute for Biotechnology, AL • **Soumya Raychaudhuri**, Broad Institute, MA • **Lars Steinmetz**, European Molecular Biology Laboratory, Germany • **Barbara Stranger**, University of Chicago, IL USA

Platinum Sponsors

BAY CITY CAPITAL

iRepertoire, Inc.

Gold Sponsors

UAB COMPREHENSIVE ARTHRITIS, MUSCULOSKELETAL, AND AUTOIMMUNITY CENTER

Silver Sponsors

GenapSys

illumina

Bronze Sponsors

SEQUENTA

follow @immunogenomics on twitter

Register today at immunogenomics.com

presented by

HUDSONALPHA INSTITUTE FOR BIOTECHNOLOGY

Science AAAS

eppendorf



Impress Yourself

The new Eppendorf Cell Culture Consumables

The all new product line of Eppendorf Cell Culture Consumables will truly delight your cells. Its outstanding design, reliability and purity is based on more than 50 years of experience.
Products created by experts, developed for perfectionists. Impress yourself!

> Unsurpassed quality, clarity, purity and sterility, providing reliable cell culture conditions
> Significantly improved design for more safety and consistency
> Maximum safety and confidence during storage and transportation



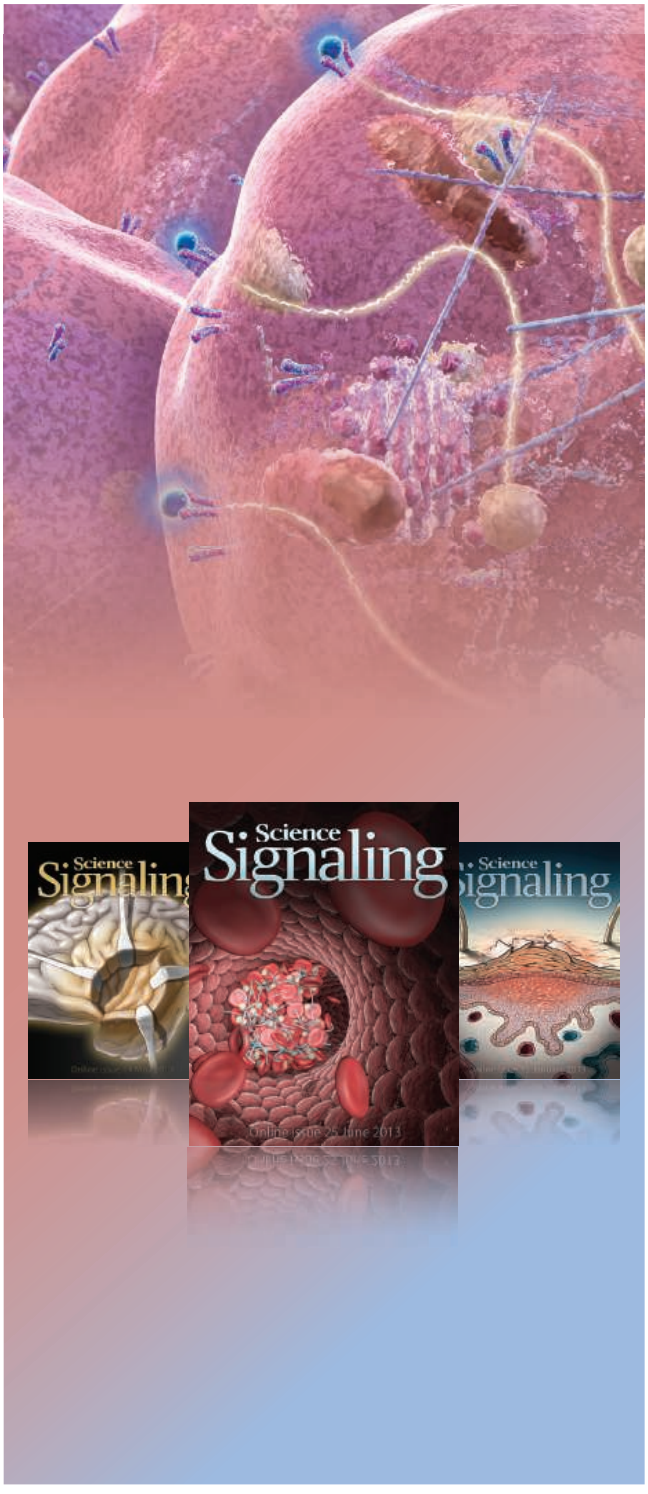
www.eppendorf.com/ccc

Eppendorf® and the Eppendorf logo are registered trademarks of Eppendorf AG, Hamburg, Germany.
All rights reserved, including graphics and images. Copyright © 2014 by Eppendorf AG.

Science Signaling

The Leading Journal for Cell Signaling

Publishing key findings of broad relevance in the multidisciplinary field of cell signaling



Submit your research

ScienceSignaling.org

Recommend to your library

ScienceOnline.org/recommend

Join the ranks of high-profile papers published in *Science Signaling*:

Cancer Biology
Vemurafenib Potently Induces Endoplasmic Reticulum Stress–Mediated Apoptosis in BRAFV600E Melanoma Cells
D. Beck *et al.* (F. Meier), *Sci. Signal.* **6**, ra7 (2013)

Neuroscience
Requirement for Nuclear Calcium Signaling in *Drosophila* Long-Term Memory
J.-M. Weislogel *et al.* (H. Bading), *Sci. Signal.* **6**, ra33 (2013)

Cell and Molecular Biology
A Nontranscriptional Role for HIF-1α as a Direct Inhibitor of DNA Replication
M. E. Hubbi *et al.* (G. L. Semenza), *Sci. Signal.* **6**, ra10 (2013)

Immunology
Monovalent and Multivalent Ligation of the B Cell Receptor Exhibit Differential Dependence upon Syk and Src Family Kinases
S. Mukherjee *et al.* (A. Weiss), *Sci. Signal.* **6**, ra1 (2013)

Computational and Systems Biology
Cross-Species Protein Interactome Mapping Reveals Species-Specific Wiring of Stress Response Pathways
J. Das *et al.* (H. Yu), *Sci. Signal.* **6**, ra38 (2013)

Chief Scientific Editor
Michael B. Yaffe, M.D., Ph.D.
Massachusetts Institute of Technology

Editor
Nancy R. Gough, Ph.D.
AAAS, Washington, DC

Science Signaling
AAAS

sciencesignalingeditors@aaas.org

Bat man wins young scientist prize in Stockholm. Are you next?

Science & SciLifeLab PRIZE FOR YOUNG SCIENTISTS



Photo: Nancy Evelyn - UGA

The 2014 *Science* and SciLifeLab Prize is now open and we are looking for new bright ideas. Are you like Daniel Streicker? Are you a recent PhD graduate eager to win a prize? Daniel is a true "bat man" having spent many hours in dark caves studying bats, to better understand how infectious diseases emerge and establish in new host species. It is for this work that Daniel was published in the journal *Science*, December 6, 2013, as the Grand Prize winner of the 2013 *Science* & SciLifeLab Prize for Young Scientists.

The journal *Science* and SciLifeLab have come together to recognize and celebrate excellence in PhD Research. The *Science* & SciLifeLab Prize has been established to support young scientists at the start of their career.

The four categories for the 2014 prize are: Cell and Developmental Biology; Genomics and Proteomics; Environment; and Translational Medicine. The Grand Prize winner will receive 25,000USD and the other three Category Prize winners will receive 3,000USD each. The Grand Prize winning essay will be published in *Science* and the Category Prize winners will be published in *Science* online.

The deadline for submissions is August 1, 2014.
For further details and to enter, please visit: www.sciencemag.org/scilifelabprize

For over 130 years the journal Science has been the world's leading journal of original scientific research, global news and commentary.

SciLifeLab is a collaboration among four universities in Stockholm and Uppsala, Sweden, and is a national center for molecular biosciences with focus on health and environmental research.

This prize is made possible with the kind support of the Knut and Alice Wallenberg Foundation.

Science AAAS

SciLifeLab

Knut och Alice Wallenbergs Stiftelse

By **Jim Austin**

A scientific partnership

In late June, the *Proceedings of the National Academy of Sciences* (*PNAS*) published an article showing that elite male scientists hire fewer women (as postdocs and graduate students) than other male scientists or elite women do. Almost as striking as the article's main result is the makeup of its authorship team. They are a couple: Jason Sheltzer, a graduate student studying cancer biology at the Massachusetts Institute of Technology (MIT) in Cambridge, and Joan C. Smith, a software engineer in Twitter's Cambridge office. This interview has been edited for brevity and clarity.

Q: Tell us about your backgrounds and how you met.
A: Sheltzer: I majored in molecular biology at Princeton University and then went to grad school in biology at MIT. I'm studying how changes in chromosome number affect cell physiology and cancer progression. Joan and I met on OKCupid. We started chatting about our mutual love of Richard Feynman and hydrogen atoms. We met up at a local cafe and haven't looked back since!
Smith: I have a Bachelor of Science in physics from MIT, and I'm a software engineer at Twitter. From just a few dates, it was obvious that we valued the same things (work, science, feminism), had complementary personality quirks, and got along exceptionally well.



"Elite male faculty in the life sciences hire particularly few women."

Q: How did you start working together?
A: Sheltzer: I was analyzing some microarray data, and I reached the limit of what I knew how to do in terms of data analysis. So I described the scientific question to Joan, and in about 30 minutes, she had set up a Python script to answer it. Collaborating with Joan really expands the range of questions that I'm able to address.

Q: Where did the data for your *PNAS* article come from?
A: Sheltzer: Joan and I started counting the grad students and postdocs from the websites of a few biology labs. We soon found a striking pattern—elite male faculty in the life sciences hire particularly few women—but we also found that it would be difficult to get a large enough sample size to make the results robust and representative of the life sciences as a whole. I had recently sold my car, so we ended up spending the money I had made to hire freelance data scrapers to collect more lab information than we could on our own.

Q: Are there any other important points buried in the article?
A: Sheltzer: It's quite striking how a small number of "elite" labs function as gateways to the professoriate. We found that about 10% of all faculty members are members of the National Academy of Sciences, but about 60% of new faculty members did a postdoc with a member of the National Academy. I think that this says something about the insular nature of academic science. It probably limits the scope of scientific questions that new investigators study. They're mostly coming from established labs working on established topics.

Q: What skills are needed to do data-intensive research?
A: Smith: Since the data is effectively limitless, the primary bounds need to be imposed by your scientific question. Figuring out which pieces of data need to go next to each other in a table is a good chunk of the hard part of data analysis. Beyond that, you have to know at least the basics of programming, and you have to have enough of a background in math that you have the confidence to figure out some new statistical method or tool that you haven't seen before. But in the end, the only things you really need are a computer, Google, time, and the confidence it takes to figure stuff out.

Q: How do you envision the future of your partnership?
A: Sheltzer: Professionally, we're working on a paper together using Joan's data-analysis ability to parse through gene-expression data from more than 20,000 cancer patients. Personally, I'm hoping that we get a cat soon. ■

Jim Austin is the editor of Science *Careers—@SciCareer Editor on Twitter. Do you have an interesting career story? Send it to SciCareerEditor@aaas.org.*

ILLUSTRATOR: ROBERT NEUBECKER

Downloaded from www.sciencemag.org on July 27, 2014

Published by AAAS